FINAL REPORT

ONR CONTRACT NUMBER N00014-92-C-0173

MICHAEL PHILPOTT

IBM ALMADEN RESEARCH CENTER

650 HARRY ROAD

SAN JOSE, CALIFORNIA 95120-6099

JANUARY 10, 2001

TABLE OF CONTENTS

Section 1: Summary of Research

1. Basic Objectives

The primary objective of the proposal was the design and execution of computer experiments designed to provide the first detailed picture of the dynamics of adsorption of ions and small neutrals on metal electrode surfaces as well as any concomitant changes in the electric double layer. Using molecular dynamic (MD) and Monte Carlo (MC) statistical techniques video movies of these simulations became an integral part of the effort, since visual aids sharpen our perceptions and allow us to visualize the dynamics of these processes better than charts and graphs.

After having established the first objective, a detailed analysis was performed of the electric double layers of charged nonmetallic surfaces with a special focus on charged (polar) organic surfaces like those found in polymer coated electrodes (e.g. Nafion), surfactant layers such as: self assembled monolayers, Langmuir-Blodgett films, soap films and lipid bilayers. The simulations include the dynamics of both the aqueous phase and the molecules comprising the organic substrate. Bilayers of lipids are particularly interesting because they serve to model some properties of biological membranes. The archetypes that have been considered are i) a free standing soap film consisting of a bilayer with polar head groups (carboxylic acid, sulphate,...) sandwiching a water film, and ii) a model for a lipid bilayer consisting of an alkanoate or acylsulphate bilayer in tail-to-tail configuration with polar head groups facing outwards in contact with aqueous electrolyte.

2. Environment

Over the past fifty years electrochemists have accumulated a vast amount of knowledge concerning the workings of metal electrode-aqueous electrolyte interfaces. A fairly detailed picture of adsorption on the surface and concurrent structural changes in the inner and outer part of the double layer has evolved. We call this the standard model. In the last decade many new experimental techniques (STM, SERS, SURS, FTIR, SHG, ex situ UHV, SFG, EXAFS, GIXS) together with improvements in time tested techniques like chronocoulometry, differential capacitance, ellipsometry, etc., applied to single crystal electrodes are providing new detailed information on the atomic scale. The richness in the interfacial structure being experimentally observed clearly requiring a much more detailed picture than currently available. The standard model with its flat charged hard wall electrode is under attack!

At the foundation of the standard model are a series of physically appealing but simple calculations that use experimental data in an internally consistent way or fashion simple intuitive models to explain particular experiments. The electrode-electrolyte interface consists of two parts. In the compact part there is a layer of the specifically adsorbed ions and water molecules in actual contact with the smooth (flat) metal. Outside of this layer is the diffuse region where the distribution of ions is believed to fall off to bulk values according to the Gouy-Chapman theory. Attempts to develop a more rigorous theory have focussed on better representation of the metal and, a better formulation of the

statistical theory. Additionally, there have been simulations of the structure of water at solid surfaces. However, all this work has assumed the metal to be at the potential of zero and long range coulomb forces cut off aft 1.0 to 1.5 nm.

What was missing in these simulations was an attempt to rigorously derive the consequences of the standard model and modifications one might conceive of, for example, a more realistic representation of the metal surface which would include the atomic topography. This was the first goal of this proposal.

MD/MC simulations of aqueous electrolytes near metal are made difficult by the existence of long range forces (r^n, n=1,2,3) and images in the periodic boundary and in the metal surface. In principle, the computation effort (time) grows as O (N^2) in charged particle number N.

3. Strategy

To achieve the stated goal the strategy was to develop custom MD or MC simulation codes for dynamics and structure. To avoid the coulomb sum bottleneck describe above our strategy was to implement the fast multipole method. When appropriate IBM's extensive quantum chemistry codes were used to calculate potentials. Additionally, the latest IBM computer hardware was used for computation and visualization.

4. Pertinent Results

The structure of the aqueous part of the double layer was derived with a variety of codes in terms of time dependent water and ion probability distribution functions averaged parallel to the metal surface. Electric fields and potentials were calculated from the microscopic charge density profiles. These calculations provided a consistent microscopic picture of ions and water in a double layer including the species next to the charged surface (inner layer), in the 'diffuse layer' (also called the screening layer) and in the bulk zone. The effect of finite sized ions and water are clearly evident, as is the effect of the electric field on the orientation of surface water molecules.

Independent of the numerical approach that was chosen the water structure near charged metal was shown to be no numerical artifact. In 1M NaCl the double layer is about 1 nm thick (about three layers of water) while in 3M solution the screening layer was found to be narrower than a water molecule. Water layers at the surface significantly affect the distribution of ions near the metal, creating features in the probability distribution that are not describable in the Gouy-Chapman-Stern model.

A more detailed summary was published in Philpott, M. R., Glosli, J. N., "Molecular Dynamics Simulation of Interfacial Electrochemical Processes: Electrical Double Layer Screening" ....American Chemical Society, 13-30 (1997). A copy of this book chapter is included together with copies of all other publications, reports, and abstracts of presentations that were the results of this contract.

Section 2: Publications

1. Philpott, M. R., Glosli, J. N., "Molecular Dynamics Simulation of Adsorption of Ions From Aqueous Media onto Charged Electrodes" J. Chem. Phys., ***96***(9), 6962-6969 (1992).

2. Philpott, M. R., Barnes, L. A., Liu, B., "Adsorption of Sulfate on Metal Electodes" NTIS, ***2***, 1-19 (1993).

3. Philpott, M. R., Glosli, J. N., "Molecular Dynamics Modeling of Electric Double Layers with Spectroscopic Applications" NTIS, ***6***, 1-4 (1993).

4. Philpott, M. R., Glosli, J. N., "Molecular Dynamics Modeling of Electric Double Layer" NTIS, ***4***, 1-16 (1993).

5. Philpott, M. R., Glosli, J. N., "Adsorption of Hydrated Halide Ions on Charged Electrodes. Molecular Dynamics Simulation" NTIS, ***1***, 1-55 (1993).

6. Philpott, M. R., Glosli, J. N., "Molecular Dynamics Computer Simulations of Charged Metal Electrode-Aqueous Electrolyte Interfaces" Theoretical and Computational Approaches to Interface Phenomena, 75-100 (1994).

7. Philpott, M. R., Zhu, S.-B., "Interaction of Water with Metal Surfaces" Journal Chem. Phys., ***100***(9), 6961-6969 (1994).

8. Philpott, M. R., Zhu, S.-B., Glosli, J. N., "Comparison of Water Models in Simple Electric Double Layers" NTIS, ***11***, 1-28 (1994).

9. Philpott, M. R., Zhu, S.-B., Glosli, J. N., "Molecular Dynamics Study of Aqueous Electrolyte Solutions Near a Structured Sphere" NTIS, ***12***, 1-12 (1994).

10. Philpott, M. R., Zhu, S.-B., Glosli, J. N., "Screening of Charged Electrodes in Aqueous Electrolytes" NTIS, ***10***, 1-10 (1994).

11. Philpott, M. R., Glosli, J. N., "Electric Potential Near a Charged Metal Surface in Contact with Aqueous Electrolyte" Journal of Electroanalytical Chemistry, ***409***, 65-72 (1996).

12. Philpott, M. R., Glosli, J. N., "Molecular Dynamics Study of Interfacial Electric Fields" Electrochimica Acta. ***41(14)***, 2145-2158 (1996).

13. Philpott, M. R., Glosli, J. N., In: *Solid-Liquid Electrochemical Interfaces*, Chap. 2, "Molecular Dynamics Simulation of Interfacial Electrochemical Processes: Electric Double Layer Screening," ACS Symp. Ser. ***656***, 13-30 (1997).

Section 3: Presentations

1. Philpott, M. R., Glosli, J. N., " Molecular Dynamics Modeling of Electric Double Layers" June 10, 1992.

2. Philpott, M. R., Glosli, J. N., " Molecular Dynamics Modeling of Electric Double Layers with Spectroscopic Applications" October 28, 1992.

3. Philpott, M. R., Barnes, L. A., "Adsorption of Sulphate on Metal Electrodes" October 18, 1992.

4. Philpott, M. R., Glosli, J. N., "Fast Multipole Method in Simulations of Electric Double Layers" June 6, 1992.

5. Philpott, M. R., Glosli, J. N., " Molecular Dynamics Simulation of Adsorption of Ions from Aqueous Media onto Charged Electrodes" November 5, 1991.

6. Philpott, M. R., Glosli, J. N., "Adsorption of Hydrated Halide Ions on Charged Electrodes. Molecular Dynamics Simulation" June 22, 1992.

7. Philpott, M. R., Glosli, J. N., "Molecular Dynamics Modeling of Electric Double Layers" October 21, 1992.

8. Philpott, M. R., Barnes, L. A., Liu, B., "Adsorption of Sulphate on Metal Electrodes" June 10, 1992.

9. Philpott, M. R., Glosli, J. N., "Fast Multipole Method in Simulations of Aqueous Systems" October 19, 1992.

10. Philpott, M. R., Glosli, J. N., "Molecular Dynamics Modeling of Electronic Double Layers" April 8, 1993.

11. Philpott, M. R., Glosli, J. N., Zhu, S.-B., "Molecular Dynamics Study of Interfacial Electric Fields" May 20, 1994.

12. Philpott, M. R., "Virbrational Spectroscopy of Molecules on Surfaces. Theory and Experiment" December 28, 1994.

13. Philpott, M. R., Zhu, S.-B., "Molecular Dynamics Modeling of Electric Double Layer Near Flat and Spherical Surfaces as Well as Metallic Tips" May 28, 1994.

14. Philpott, M. R., Glosli, J. N., Zhu, S.-B., "Molecular Dynamics Modeling of Electric Double Layers Near Flat, Spherical and 'Tiped' Surfaces" May 28, 1994.

15. Philpott, M. R., Glosli, J. N., "Molecular Dynamics Computer Simulations of Charged Metal Electrode-Aqueous Electrolyte Interfaces" January 7, 1994.

16. Philpott, M. R., Glosli, J. N., "Electric Potential Near a Charged Metal Surface in Contact with Aqueous Electrolyte" October 20, 1995.

17. Philpott, M. R., Glosli, J. N., "Molecular Dynamics Study of Interfacial Electric Fields" October 20, 1995.

18. Philpott, M. R., Glosli, J. N., "Molecular Dynamics Simulation of the Adsorption of Benzene on Charged Metal Electrodes in the Presence of Aqueous Electrolyte" May 8, 1995.

19. Philpott, M. R., Glosli, J. N., "Molecular Dynamics Simulation of Ions, Neutrals and Water in Electric Double Layers Between Charged Metal Electrodes" March 17, 1995.

20. Philpott, M. R., Glosli, J. N., "Molecular Dynamics Simulation of Ions, Neutrals and Water in Electric Double Layers Between Charged Metal Electrodes" March 17, 1995.

21. Philpott, M. R., Glosli, J. N., "Molecular Dynamics Simulations of the Electrode-Aqueous Electrolyte Interface" March 17, 1995.

22. Philpott, M. R., Glosli, J. N., "Molecular Dynamics Simulation of Interfacial Electrochemical Processes: Electric Double Layer Screening" May 7, 1996.

23. Philpott, M. R., Glosli, J. N., Roberts, J., "Molecular Dynamics Simulation of Adsorption, Deposition and Dissolution at Aqueous Electrochemical Interfaces" July 3, 1996.

Molecular dynamics simulation of adsorption of ions from aqueous media onto charged electrodes

James N. Glosli and Michael R. Philpott
IBM Research Division, Almaden Research Center, San Jose, California 95120-6099

(Received 11 November 1991; accepted 30 January 1992)

Molecular dynamics simulation of 216 water molecules (ST2 model) between charged flat electrodes 2.362 nm apart showed layering with a few molecules at each surface that broke H bonds with the bulk and oriented their charges towards the electrode. Compared to uncharged electrodes, the atomic and molecular distributions were unsymmetric. When a lithium and an iodide ion were substituted at random for two water molecules, the iodide ion contact adsorbed on the anode with no water molecules between it and the electrode. The iodide ion appeared weakly solvated on the solution side to water molecules that preferred to engage in hydrogen bonding with the network of the bulk solvent. In contrast, the lithium ion adsorbed without losing its primary solvation shell of six water molecules and was never observed further than two water molecules removed from the electrode. Its average position corresponded to an ion supported on a tripod of three waters. The average solvation number was not changed upon adsorption in this configuration. These qualitative observations and some quantitative results afford striking confirmation on the one hand and new insight on the other of some aspects of the standard model of the adsorption of ions on electrode surfaces. Time durations for simulations were generally between 200 and 800 ps with a basic integration time step of 2 fs.

I. INTRODUCTION

In this paper, we explore aspects of the adsorption of ions from aqueous solution using molecular dynamics simulation of a relatively simple model. Adsorption is one of the fundamental processes controlling the structure and dynamics of electrochemical double layers. The goal is insight and understanding concerning the local environment around the adsorbate. The total number of molecules was chosen small in order to explore time scales up to a nanosecond in duration and to check the dynamical stability of the adsorbed ions. This turned out to be important because the simulations showed that ions with strongly bound water undergo motion akin to slow "bumping" against a charged surface. Some important interactions are treated approximately, but by focusing where possible on comparisons, it is believed that these approximations do not effect qualitative behavior. For example, long-range Coulomb interactions are cut off at 0.82 nm. This is perhaps the most serious deficiency, but its consequences are global and not expected to alter our conclusions concerning local water structure around the ions.

There is vast literature describing electrochemical double layers and the adsorption of ions from aqueous electrolyte solution onto charged electrodes. On the basis of clever experimentation and deductive reasoning using simple models, electrochemists have evolved a detailed "standard model" of the disposition of ions, water, and organics adsorbed on the electrode in the range of potentials where the electric double layer is thermodynamically stable.[1-5] Early experiments relied on precision measurements of electric current. In the mid-1940s, Grahame[1] used a dropping mercury electrode to avoid surface contamination and in classic experiments measured the capacitance of the double layer as a function of potential and electrolyte composition. This was the beginning of the modern era of electrochemistry and the origin of the standard model of the interface.

Consider a solvated ion approaching the surface by a diffusion process biased by an attractive electrostatic potential. Before the ion can make contact, some of the weakly bound water molecules between the electrode and the ion are displaced. The thermodynamic equilibrium involves a balance of opposing interactions. The most important are electrostatic interaction between ion and electrode, enthalpies of hydration of ion and surface atoms, and entropy of displaced water molecules. Generally speaking, large ions (iodide and cesium) contact adsorb, whereas small ions (fluoride and lithium) do not. Experimental verification of contact adsorption has been demonstrated by a variety of techniques including: differential capacitance,[3] radio tracer,[6] Fourier transform infrared (FTIR),[7] and surface exafs.[8,9] The molecular dynamics simulation described below is the first to show clearly that contact adsorption occurs for the large radius ion and not for solvated small radius ions.

According to the standard model, the electric double layer consists of two parts—a compact part adjacent to the electrode and a diffuse part stretching from the compact layer into the bulk electrolyte. The thickness of the diffuse layer is very dependent on ionic strength. For 0.1 M solutions it is about 2 nm in extent. The delimiter between the two zones, the outer Helmholtz plane (OHP), is defined as the plane of closest approach of the nuclei of fully solvated ions that do not contact adsorb. For metal electrodes, the compact part is thought to consist of two water layers mixed with contact adsorbed ions and visiting counterions. Interpretation of experimental capacitance measurements suggests that the compact layer can be subdivided further into inner and outer

 0021-9606/92/096962-08$06.00

rts. The dividing plane, called the inner Helmholtz plane HP), cuts through the centers of contact adsorbed ion. So r choice of the LiI system has the advantage that contact sorbed iodide defines the IHP on one electrode and adrbed hydrated lithium ion defines the OHP on the second ectrode.

Ions have been classified according to their adsorbing ility by Anson.[10] Inside the compact layer the specifically lsorbed ions accumulate on the electrode driven there by e Gibbs free energy of adsorption. They can change the gn of the charge felt by ions in the diffuse layer. Put another ay, negative ions such as iodide adsorb strongly on negatily charged metal electrodes, requiring the diffuse layer to reen a larger effective charge. Likewise, adsorption of ans on positively charged metal electrodes can lead to an verall negative charge to be screened by the diffuse layer. he thermodynamics of contact adsorption has been well udied within the framework of the standard model. Useful bles of Gibbs free energies are given in a number of texts see, e.g., Bockris and Reddy).[11] The main point for this iscussion is that for large radius ions, the water–electrode nd ion–electrode interactions are roughly constant and oposing. The determining effect is the variation in ion–water nteraction. Large radius ions with deeply buried charge end to adsorb strongly.

The second part of the electric double layer, called the liffuse part, consists of fully hydrated ions moving under the nfluence of thermal forces in the combined electric fields of he metal electrons and the adsorbed ions. The diffuse layer, lescribed by Gouy–Chapman theory,[3–5] screens the charge on the electrode. Direct measurement of the diffuse layer listribution has been described recently using x-ray fluorescence from zinc ions.[12] The calculations described here say nothing about the diffuse layer. To calculate the diffuse layer a much larger simulation cell is needed together with the ability to simulate for nanoseconds.

The molecular dynamics simulations reported in this paper complement some of the previous work relevant to electrochemical double layers. Rigorous statistical mechanical models using correlation functions to describe ion distributions and including structure on the metal side were developed by Henderson, Schmickler, and co-workers.[13,14] *Ab initio* calculations of the electronic structure of adsorbates on small metal clusters provided information about adsorption site bonding and geometry.[15–17] There have been a number of molecular dynamics and Monte Carlo studies of water near surfaces. The closest was a simulation for 19 ps of eight LiI and 200 water molecules between uncharged plates.[18] This was insufficient to study ionic adsorption of hydrated species. In recent work, Heinzelman,[19] Spohr,[20] and Berkowitz[21] considered adsorption of water on model platinum electrodes in the absence of charge on the electrodes. The platinum–water potential included orientational factors. Water between charged surfaces has been considered by Hauptman *et al.*,[22,23] Marchesi,[24] and by Kjellander and Marcelja[25] for water between mica and lecithin layers. Ions were not included in these studies. Recently several papers have addressed the problem of dielectric saturation in bulk and thin films of water[26,27] for a range of field strengths encompassing the value used here.

In the work described here, we start from a relatively well-understood system initially explored by Lee, McCammon, and Rossky.[28] The calculations reported below first consider water in the field between charged plates and then the effect of this field on a system obtained by substituting LiI for two water molecules.

II. BASIC MODEL

Many models of the water molecule have been proposed for use in computer simulations of bulk water and aqueous electrolytes. At present, the popular models are designated—ST2,[29,30] TIP4P,[31] and SPCE.[32] In the calculations reported here, we have elected to use ST2 not because it more faithfully reproduces bulk water properties, but because the extensive molecular dynamics calculations by Heinzinger and Spohr[19,20] have yielded a complete set of parameters for alkali metal ions and halide ions solvated by ST2 water.

A. Interaction energy

In the ST2 model, the Coulomb interaction between water molecules is represented as sum of $1/r$ interactions between atomic point charges softened for small molecular separation by a switching function S.[29] Without the switching function, the network of H bonds is too rigid. The short-range part of the intermolecular interaction was modeled by a Lennard-Jones potential between the atoms. All molecule–molecule interactions (both $1/r$ and Lennard-Jones potentials) were cut off in a smooth fashion at molecular separation $R = 0.82$ nm by a truncation function T. Both surfaces were treated as flat featureless plates with a uniform electric charge density of $+\sigma$ and $-\sigma$ on the $-z_0$ and $+z_0$ plates, respectively ($z_0 = 1.181$ nm). This gave rise to a uniform electric field $E = 4\pi K\sigma$ in the z direction, where K the electrostatic coupling constant had the value 138.936 kJ nm/(mol e^2) in the units used in this calculation. Non-Coulombic interactions between the walls at $z = \pm z_0$ and all the ions and water molecules were represented by the 9-3 potential (henceforth called the wall potential) introduced by Lee *et al.*[28] There was one 9-3 potential for each surface. This wall interaction is the same for all ions and molecules. In this aspect, our model of the electrode–electrolyte interface is simpler than the standard model. The complete interaction energy U is

$$U = \sum_{\substack{\alpha\in A_i \\ \beta\in A_j \\ i<j}} \left\{ \frac{Kq_\alpha q_\beta}{r_{\alpha\beta}} S(R_{ij}, R_L^{ij}, R_U^{ij}) + 4\epsilon_{\alpha\beta}\left[\left(\frac{\sigma_{\alpha\beta}}{r_{\alpha\beta}}\right)^{12} - \left(\frac{\sigma_{\alpha\beta}}{r_{\alpha\beta}}\right)^{6}\right]\right\} T(R_{ij})$$

$$+ \sum_\alpha \left\{ -q_\alpha E z_\alpha + \left[\frac{A_\alpha}{(z_\alpha + z_0)^9} - \frac{B_\alpha}{(z_\alpha + z_0)^3}\right] + \left[\frac{A_\alpha}{(z_\alpha - z_0)^9} - \frac{B_\alpha}{(z_\alpha - z_0)^3}\right]\right\}, \quad (1)$$

III. WATER BETWEEN FLAT CHARGED ELECTRODES

A. Uncharged electrodes

This case was studied by Lee, McCammon, and Rossky.[28] Their geometry was adopted in this paper and provided a useful existing frame of reference against which to compare results. We have repeated all their published calculations using the same parameter set and get essential agreement.

The simulation of pure ST2 water was performed in two parts. First, the system was simulated for 250 ps at a constant temperature of 2.411 kJ/mol with configurations stored every 0.5 ps. The average of the total energy was calculated for the last 200 ps and was equal to $E_{\text{total}} = -35.23 \pm 0.1$ kJ/mol. Next, an initial configuration for a constant energy run was generated by taking the last configuration of the constant temperature run and scaling its velocities such that the total energy would equal the average energy of the constant temperature simulation (-35.23 kJ/mol). This configuration was evolved for 200 ps at constant energy and samples were collected every 0.1 ps. The average temperature was found to equal 2.40 ± 0.03 kJ/mol (289 K). The consistency between the constant temperature and energy runs suggests that both runs have sampled a representative part of the equilibrium ensemble.

For a bin size of 0.0236 nm (1/100 of the gap between the electrodes), the oxygen and hydrogen z-dependent number densities are shown in Fig. 1. They resemble those of Lee *et al.*[28] quite closely. Superimposed is the 9-3 wall potential with scale given on the right-hand side. Some points of interest are that the broad first O atom peak falls in the range of the weakly attractive well of the wall potential, the "foot" of the H density extending 0.1 nm (OH bond length) past the point where the wall potential first becomes repulsive because the latter acts only on the O atom and not on the H atoms. The peak in H density near the surface occurs at smaller $|z|$ than in the O density profile, consistent with an ice-like structure in which one OH bond points toward the surface.

B. Charged electrodes

In this section, we discuss the results of a simulation for water between oppositely charged plates. The plate at $z = -z_0$ carried the positive charge. The uniform electric field was equivalent to a surface charge density of $0.11e/\text{nm}^2$ or about 2×10^7 V/cm. This is at the upper end of field gradients believed to occur in electric double layers. The simulation was done at a constant energy of $E_{\text{total}} = -35.23$ kJ/mol for 200 ps. The average of the temperature was calculated over the last 150 ps of this run and had the value 2.49 ± 0.02 kJ/mol (300 K).

Figure 2 shows the density profiles for H and O atoms in the direction z perpendicular to the electrodes. The first feature of note is the pronounced asymmetry induced in all the densities. There are sharper peaks near the positive electrode ($z<0$). The sharper peak is interpreted as better wetting in the field which orients and packs more water molecules near the surface. This occurs where the electrostatic force is comparable to the Lennard-Jones interaction. At larger $|z|$, where the r^{-9} repulsion dominates, the electrostatic interaction has no effect on the distribution of molecules. The O density profile is not bodily shifted relative to the zero field case, but the first peak shifts and sharpens in a move to a

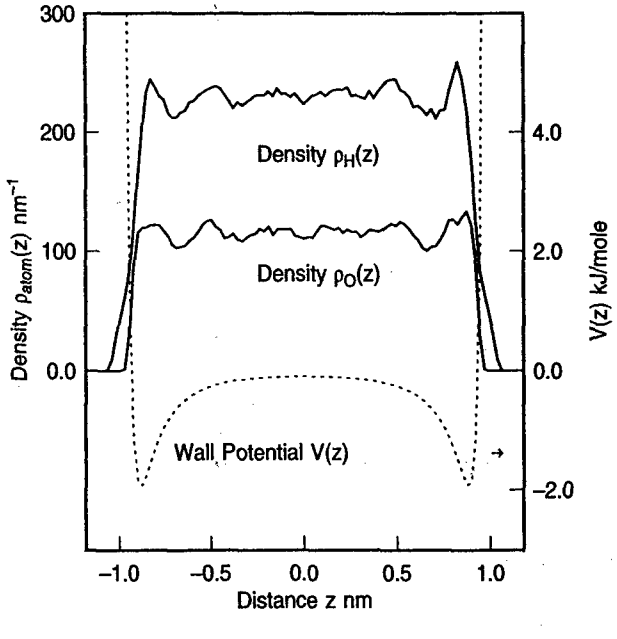

FIG. 1. Some properties of the water ST2 model in zero electric field. Number density profiles for hydrogen H and oxygen O as a function of position between the electrodes. Broken line shows the weakly attractive wall potential.

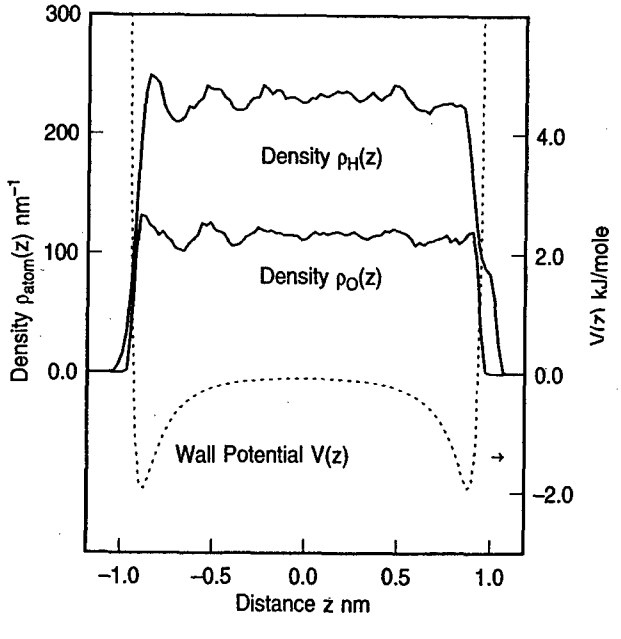

FIG. 2. Some properties of the water ST2 model in a strong electric field (2×10^7 V/cm). Number density profiles for hydrogen H and oxygen O as a function of position between the electrodes.

more negative z value. The same is true for H except that H density has a new feature, a pronounced shoulder at $z = 1.0$ nm not present in the corresponding zero field density.

Figure 3 shows the change in H density when the field is turned on. Also plotted, for reference purposes, is the H density with field on. The shoulder on the right-hand side of the H density can be identified to molecules oriented with the positive charge towards the negative electrode to increase their electrostatic interaction. It coincides with $z = 1.0$ nm positive lobe of the difference density $\Delta\rho_{\mathrm{H}}(z)$. These molecules will be partially decoupled from the bulk as a result. The number of molecules contributing to this feature is small and was estimated to be one. This number was determined by subtracting from the "field-on" density, the "field-off" density to give the $\Delta\rho_{\mathrm{H}}(z)$ shown in Fig. 3. In the case of H, the integral of the difference $\Delta\rho_{\mathrm{H}}(z)$ over a small range of z near the negative electrode was found to be slightly greater than two. Essentially, the same number was obtained when this procedure was repeated for the point charge PC in the vicinity of the positive electrode. On the average, one molecule at each surface is reoriented as a result of turning on the field.

Figure 4 shows the charge density $\Delta\rho_q(z)$ for the entire ensemble averaged in the xy direction and plotted as a function of z. For reference, the density of the H atoms is also shown. The charge density for field on and field off are shown. Note that in the case of field off, the distribution has been shifted down to avoid congestion. For field on, the large negative exaltation at $z = -1.0$ nm and large positive exaltation at $z \doteq 1.0$ nm are due to water molecules orienting their charge to reduce electrostatic interactions. In zero field, the exaltations are much weaker and positive, indicating some H atoms are pointing toward the surface. This

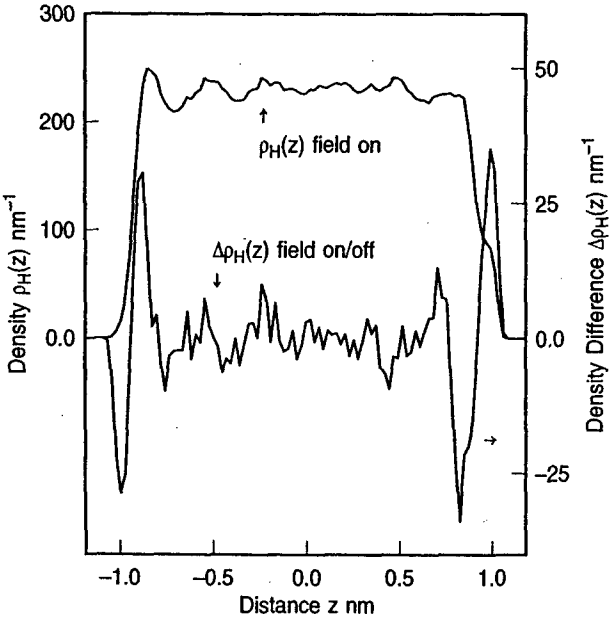

FIG. 3. Some properties of the water ST2 model in a strong electric field. The change in H atom distribution for electric field on and off.

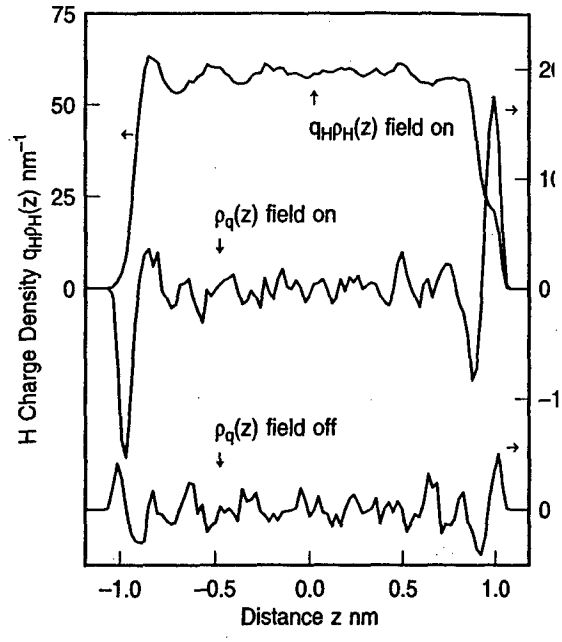

FIG. 4. Some properties of the water ST2 model in a strong el Charge density profiles for field on and field off. The H atom der is shown for reference.

means that for the ST2 model, the waters can optim getics of H bonding interactions by adopting an or with some H atoms pointing toward the weakly a surface.

IV. SOLVATED IONS BETWEEN FLAT CHARGE ELECTRODES

In this section, we describe adsorption of lith iodide ions on charged electrodes ($\sigma = 0.1$ $E = 2\times10^7$ V/cm) These ions represent extreme adsorption. Experimentally, iodide is believed to co sorb, whereas lithium ions being strongly hydrate not lose any waters from the first coordination sh initial configuration consisted of the molecules and i $6\times6\times6$ cubic lattice with parameter 0.31 nm, witl sites selected at random. After performing a const perature equilibration run, long simulations up tc were performed at constant energy $E_{\mathrm{total}} = -$ kJ/mol to gather statistics. An average temper 2.40 ± 0.01 kJ/mol ($T = 289$ K) was found. Figure the distribution of the two ions and water across between the two electrodes. To facilitate interpret the density curves, the plot is annotated with a nu circles with diameters equal to the Lennard-Jones σ eters of the ions and water. Also, for the same reas wall potential is superimposed on the same plot. As ed, the two ions are adsorbed on electrodes with the sign in charge. However, it is clear that the way in wl ions are adsorbed is different. Lithium is hydrated a not approach the electrode much closer than the dia a water molecule. Iodide in contrast makes physical with the electrode; there are no water molecules be

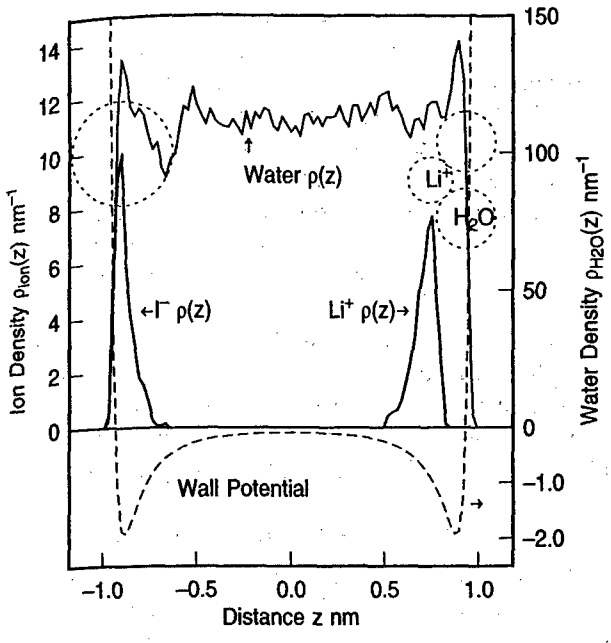

FIG. 5. Distribution of Li^+, I^-, and 214 water molecules in a strong electric field (2×10^7 V/cm) across the gap between the charged plates. The wall potential is shown for reference. Circles are Lennard-Jones radii for the ions and water.

and the electrode. In several simulations, the electric field was reversed after 200 ps or more, forcing the ions to migrate across the simulation cell to the opposite electrode. Forcing the ions to transport across the film must induce considerable mixing. Density profiles calculated after flipping the field were essentially mirror images of the earlier ones. This supported our assumption that equilibrium was established in about 100 ps and that it was adequate to start accumulate statistics after an equilibration period of this magnitude.

A. Position of the iodide ion

In Fig. 5, the iodide distribution is localized against the wall (bin size is 0.0236 nm and the wall potential is the same for all molecules). The peak is at $z = -0.90$ nm, the closest approach is $z \leqslant -0.97$ nm, and the farthest distance is $z \simeq -0.83$ nm. On the average, the iodide ion center is midway between the minimum and the repulsive region [defined by $V(z) \geqslant 0$] of the wall potential. The range of z displacements of the iodide ion center is approximately 0.25 nm for the simulation shown in Fig. 5. Even during a fluctuation which places the iodide at its greatest distance from the electrode, there is no room for a water molecule to press between the wall and ion. It remains in contact with the wall and is to be regarded as contact adsorbed. This is the first example of a molecular dynamic simulation of the electrochemical contact adsorption phenomenon.

Now consider the pair correlation function for water around the iodide ion. Since the ion is adsorbed, the environment on the surface side of the ion can be very different from the environment on the side away from the surface. With this in mind, the pair correlation was evaluated by counting only water molecules that were within a cone with a half-angle of 60° whose axis was parallel to the z axis and vertex which was coincident with the ion. There are two such cones. One that opened into the surface and the other which opened away from the surface, which we call the surface and bulk cones, respectively. To make the normalization explicit, $g(r)$ is defined as

$$g_{H_2O} = \frac{1}{\pi r^2 \rho_0} \frac{d}{dr} \langle n(r) \rangle, \tag{4}$$

where $n(r)$ is the number of water molecules within both the cone and a distance r from the ion and $\rho_0 = 33$ particles/nm^3 is the mean density of water in the central region between the plates. In Fig. 6, we show the I/water pair correlation function averaged over the bulk cone. The pair correlation function averaged over the surface cone was negligible, signifying the absence of solvent molecules between the ion and the wall at all times. This is completely consistent with the density distribution of Fig. 5.

B. Position of lithium ion

The lithium ion z distribution is shown on the right-hand side ($z > 0$) in Fig. 5. Figure 7 shows the pair correlation function for water around the Li ion. There are separate functions for both bulk and surface cones. The latter measures water between the ion and the wall. Unlike the case for iodide displayed in Fig. 6, there is a measurable pair correlation function for waters between the wall and ion. In fact, the first peak corresponding to the primary solvation shell is at

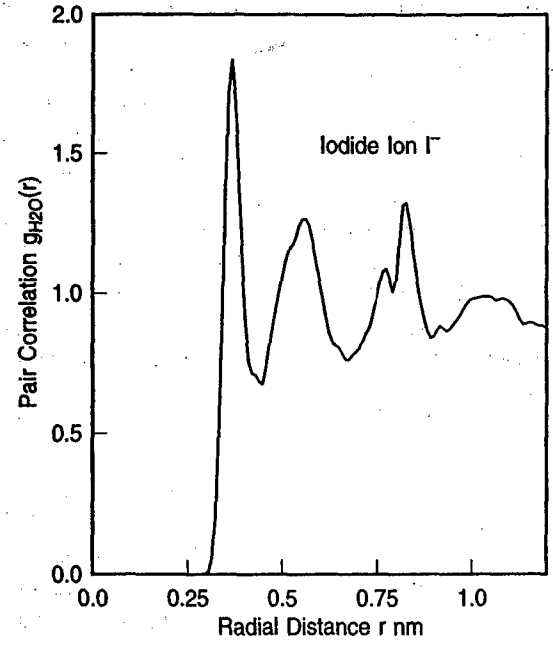

FIG. 6. The pair correlation function for water distributed around the adsorbed I ion. Only the distribution within the bulk cone (half-angle of 60°) is shown. There are no water molecules between the iodide and electrode in the surface cone.

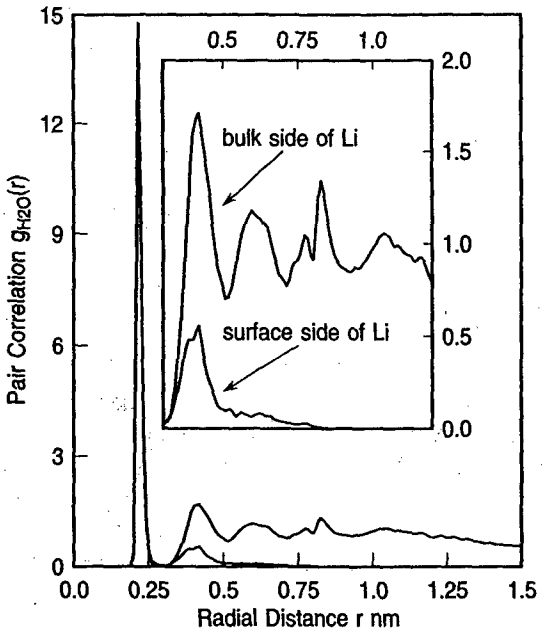

FIG. 7. The pair correlation function for water around an adsorbed Li ion. The inset shows distributions inside cones (half-angle of 60°) oriented towards bulk and surface.

the same radial position. The inset in Fig. 7 is the secondary and further region at greater resolution. The secondary solvation shell is broad, indicating the very considerable mixing with the bulk. Integration out to the primary shell radius confirmed the presence of six strongly coordinated water molecules.

The hydrated lithium ion can be visualized as a large object consisting of a central ion surrounded by six water molecules in the shape of a bipyramidal octagon. This object can adsorb to the surface with one, two, or three vertices (spherical waters in this model) down. Iodide by contrast behaves as if it is spherical. As the simulation proceeds, this large "rough" object bumps and rolls over the charged electrode as it is subject to fluctuations in the hydrogen bonded solvent surrounding it. This picture allows us to interpret features of the lithium distribution of Fig. 5 not found for iodide. The distribution is: (i) peaked further from the wall; (ii) broader (larger full width at half-maximum); and (iii) never approaches within ~0.1 nm of the hard repulsive region at $z = 0.934$ nm.

The Li ion distribution is confined between $z = 0.425$ and 0.827 nm. The main peak for Li^+ occurs at $z = 0.76$ nm. Compare these hypothetical distances calculated assuming the ion and water are hard spheres. A lithium separated from the hard wall by one water molecule $[|z| = |0.934 - 0.5(\sigma_{Li} + \sigma_O)|]$ is located at $z = 0.66$ nm, and at $z = 0.61$ nm when the water center occurs at the wall potential minimum.

The peak position $z = 0.76$ nm is compatible with the hydrated Li ion having three of its attached waters simultaneously in contact with the wall. For this orientation, the position of the Li nucleus (hard sphere model) would be at $z = 0.73$ nm with the waters centered at the minimum i wall potential ($V = V_{min}$ at $z = 0.884$ nm) and at $z =$ nm when the water centers are positioned at the hard (at $z = 0.934$ nm). The position of closest approach of t ion in the distribution in Fig. 5 is $z = 0.827$ nm. The considerable splay of the solvating waters from their n nal octahedral positions around the ion. Examinatic three-dimensional computer graphics images showed the lithium never contact adsorbed even though the s tion shell was distorted.

At positions farthest from the electrode, the lithiu was well separated, with the centers of water in its pri solvation shell outside the attractive minimum of the potential. However, there is not room for two water cules as can be easily visualized by looking at Fig. 5.

C. Water and the charge density distributions

Figure 8 shows total charge density derived from rate densities for the two ions, H and PC atoms, refer against the water density distribution (water and oxyg essentially the same). The total charge density looks qu tively very similar to the case of water without ions sho Fig. 4.

The water density peaks show sharp structure cl both walls where the electric field and the local ion strongly orient the solvent molecules. There is also a ' in the water distribution at a position corresponding radius of the iodide. This corresponds to exclusion solvent by the ion. The area involved corresponds to a imately three water molecules. The volume displaced

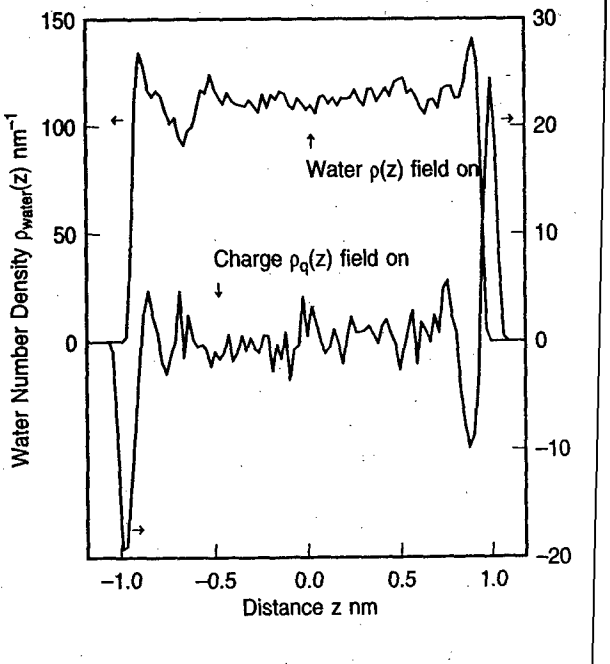

FIG. 8. The charge density profile across the ion–water mixture i electric field (2×10^7 V/cm). For reference, the water distributi shown. Apart from small shifts in peak positions, the shape of t density resembles that shown in Fig. 4 for water.

dide's Lennard-Jones radius is equivalent to approximately 2.7 water molecules. Clearly the weaker solvation of iodide together with its volume is responsible for the apparent hole.

V. SUMMARY AND COMMENT ON APPLICATIONS TO ELECTROCHEMISTRY

This paper has demonstrated the value of molecular dynamics calculations applied to models of electrified interfaces. The model used here, though very simple, appears capable of simulating aspects of a broad range of phenomena known to occur at electrodes. Additionally, microscopic insight has been provided in the form of pictures of how ions and water orient in the presence of an electric field at a surface. The bumping of fully solvated ions against the surface and the concommitant distortion of the hydration sphere as the ion approaches closer than the diameter of a water molecule, discussed briefly above, has implications for electron transfer reactions such as those that occur in the desolvation of metal ions and deposition of metal. In fields much larger than the ones used in the present study, small ions such as lithium contact adsorb. In passing, we also note that it is possible to study ion transport across small films using this model. In a number of simulations, we reversed the field and followed the migration of the ions across the water film as they switched sides. In this case, the water molecules reoriented within a few picoseconds, well before the ions started to leave the electrode. Transit times of tens of picoseconds were observed with the weakly solvated iodide traveling faster in accord with the known ionic conductivities at infinite dilution in bulk water.

ACKNOWLEDGMENTS

This research was supported in part by the Office of Naval Research. R. Rafey is thanked for assistance with visualization graphics. M.R.P. thanks J.C.C. for nine months of unfathomable patience.

[1] D. C. Grahame, Chem. Rev. **41**, 441 (1947).
[2] J. O. Brockris, M. A. Devanathan, and K. Müller, Proc. R. Soc. London, Ser. A **274**, 55 (1963).
[3] J. O. Brockris and A. Gonzalez-Martin, *Spectroscopic and Diffraction Techniques* (Kluwer, Dordrecht, 1990), pp. 1–54.
[4] J. R. MacDonald, J. Electroanal. Chem. **223**, 1 (1987).
[5] R. Parsons, Chem. Rev. **90**, 813 (1990).
[6] P. Zelenay, L. M. Rice-Jackson, and A. Wieckowski, J. Electroanal. Chem. **283**, 389 (1990).
[7] K. Kunimatsu, W. G. Golden, H. Seki, and M. R. Philpott, Langmuir **1**, 245 (1985).
[8] L. Blum, H. Abruna, J. White, J. G. Gordon, G. Borges, M. G. Samant, and O. R. Melroy, J. Chem. Phys. **85**, 6732 (1986).
[9] O. R. Melroy, M. G. Samant, G. L. Borges, J. G. Gordon, L. Blum, J. H. White, M. J. Albarelli, M. McMillan, and H. D. Abruna, Langmuir **4**, 728 (1988).
[10] F. Anson, Acc. Chem. Res. **8**, 400 (1975).
[11] J. O. Bockris and A. K. Reddy, *Modern Electrochemistry* (Plenum, New York, 1973).
[12] M. J. Bedzyk, G. M. Bommarito, M. Caffrey, and T. L. Penner, Science **248**, 55 (1990).
[13] W. Schmickler and D. Henderson, Prog. Surf. Sci. **22**, 323 (1986).
[14] D. Henderson, *Trends in Interfacial Electrochemistry* (Reidel, Dordrecht, 1986), p. 183.
[15] P. S. Bagus, C. J. Nelin, W. Mueller, M. R. Philpott, and H. Seki, Phys. Rev. Lett. **58**, 559 (1987).
[16] P. S. Bagus, C. J. Nelin, K. Herman, and M. R. Philpott, Phys. Rev. Rapid Commun. **36**, 8169 (1987).
[17] P. S. Bagus, G. Pacchioni, and M. R. Philpott, J. Chem. Phys. **90**, 4287 (1989).
[18] E. Spohr and K. Heinzinger, J. Chem. Phys. **84**, 2304 (1986).
[19] K. Heinzelman, *Computer Modelling of Fluids Polymers and Solids, NATO ASI Series C* (Kluwer, Dordrecht, 1990), pp. 357–404.
[20] E. Spohr and K. Heinzinger, Ber. Bunsenges. Phys. Chem. **92**, 1358 (1988).
[21] K. Raghavan, K. Foster, K. Motakabbir, and M. Berkowitz, J. Chem. Phys. **94**, 2110 (1991).
[22] J. Hauptman, J. W. Halley, and Y. J. Rhee, J. Chem. Phys. **91**, 467 (1989).
[23] Y. J. Rhee, J. W. Halley, J. Hauptman, and A. Rhaman, Phys. Rev. B **40**, 36 (1989).
[24] M. Marchesi, Chem. Phys. Lett. **97**, 224 (1983).
[25] R. Kjellander and S. Marcelja, Chem. Scr. **25**, 73 (1985).
[26] H. E. Alper and R. M. Levy, J. Phys. Chem. **94**, 8401 (1990).
[27] M. Watanabe, A. M. Brodsky, and W. P. Reinhardt, J. Phys. Chem. **95**, 4593 (1991).
[28] C. Y. Lee, J. A. McCammon, and P. J. Rossky, J. Chem. Phys. **80**, 4448 (1984).
[29] F. H. Stillinger and A. Rahman, J. Chem. Phys. **60**, 1545 (1974).
[30] O. Steinhauser, Mol. Phys. **45**, 335 (1982).
[31] W. L. Jorgensen, J. Chandrasekhar, J. D. Madura, R. W. Impey, and M. L. Klein, J. Chem. Phys. **79**, 926 (1985).
[32] H. J. Berendsen, J. R. Grigera, and T. P. Straatsma, J. Phys. Chem. **91**, 6269 (1987).
[33] W. G. Hoover, Rev. Phys. Chem. **34**, 103 (1983).
[34] D. J. Evans and G. P. Morris, Comput. Phys. Rep. **1**, 297 (1984).
[35] M. P. Allen and D. J. Tildesley, *Computer Simulation of Liquids* (Oxford University, Oxford, 1987), pp. 88–90.

ADSORPTION OF SULFATE ON METAL ELECTRODES

IBM RESEARCH DIV.
SAN JOSE, CA

14 APR 1993

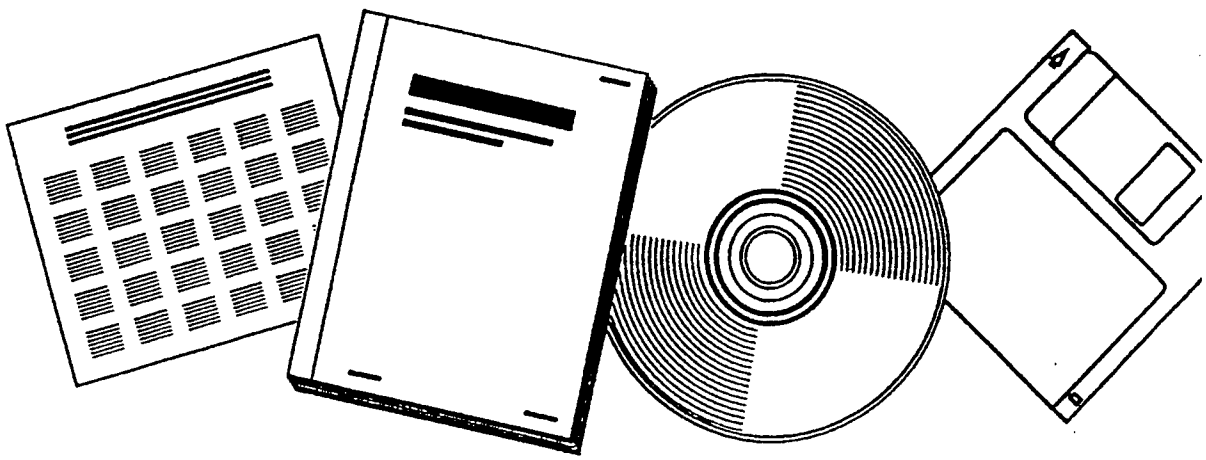

U.S. DEPARTMENT OF COMMERCE
National Technical Information Service

OFFICE OF NAVAL RESEARCH

Grant No. _____

R&T Code N00014-92-C-0173

Technical Report #02

ADSORPTION OF SULFATE ON METAL ELECTRODES

by

Leslie A. Barnes
Michael R. Philpott
Bowen Liu

Prepared for publication

in the

Electrochemical Society Proceedings '93

IBM Research Division, Almaden Research Center,
650 Harry Road, San Jose, CA 95120-6099

1993

Adsorption of Sulfate on Metal Electrodes

Leslie A. Barnes *, Michael R. Philpott and Bowen Liu
IBM Research Division, Almaden Research Center
650 Harry Road, San Jose, California 95120-6099

Abstract

The adsorption of sulfate (SO_4^{2-}) and bisulfate (HSO_4^-) on copper has been studied using *ab initio* calculations at the SCF level of theory, to aid in the interpretation of *in situ* experimental data from the electrochemical interface, in particular optical and surface X-ray measurements. The calculations are designed to give qualitative insight rather than quantitative accuracy. Optimized structures and harmonic frequencies and intensities are computed for isolated sulfate and bisulfate, and qualitative agreement with experimental data is demonstrated. The effect of a uniform electric field on sulfate is also studied. The structures of $Cu^0SO_4^{2-}$ and $Cu^0HSO_4^-$ are optimized. The bonding is dominantly ionic, with consequential small orientational dependence of the adsorbed ligand. We also compute structures for the larger $Cu_4^0SO_4^{2-}$ cluster. The sulfate ion is found to favour a "3-down" adsorption geometry with sulfate oxygens occupying on-top sites over the previously postulated "1-down" structure invoked to explain the early surface exafs experiments.

1 Introduction

Understanding the adsorption of sulfate on surfaces is a challenging scientific problem that is also of significant technological interest in connection with battery chemistry, dissolution of metals in acids, electroplating and polishing, and the incipience of oxide films. Recent optical and surface X-ray measurements of metal electrodes in contact with aqueous sulfate media have been explained with hypothetical models, with sulfate (SO_4^{2-}) and it's hydrolysis product bisulfate (HSO_4^-) in specific orientations adsorbed on the metal surface [1]–[6]. Figure 1 shows some of these models.

The high symmetry (T_d) and many vibrational modes of sulfate that are exclusively IR or Raman allowed make it a potentially useful probe of forces influencing orientation and of the local field within the electrochemical double layer. Bisulfate, with lower symmetry, has more vibrational frequencies which may be IR or Raman allowed, some of which overlap with sulfate modes. This complicates interpretation

*Mailing Address: Mail Stop RTC-230-3, NASA Ames Research Center, Moffett Field, California 94035-1000

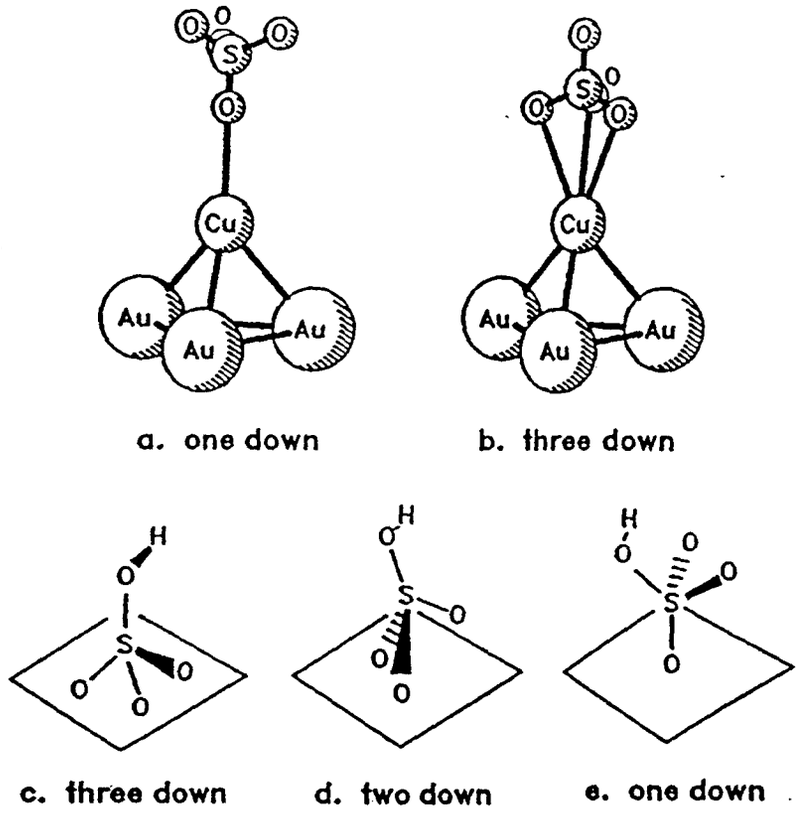

Figure 1: Proposed Sexafs model of sulfate on upd Cu monolayer on Au(111) surface along with some optical models for bisulfate.

of the experimental data, where both sulfate and bisulfate may be present. From a computational viewpoint, the larger size of sulfate and bisulfate make the calculation and interpretation of structures and spectra more difficult than for smaller ligands such as carbon monoxide or cyanide [7]. Nevertheless, because of the existence of several proposed structures on Cu surfaces [5, 6] and the variety of other data bearing on adsorption site geometry and structure [8]–[11], it is clear that model *ab initio* quantum chemical calculations could play a crucial role in elucidating geometry, structure and bonding at the adsorption site.

The goal of the present work is to use a series of simple models to explore the interaction of sulfate and bisulfate with metal surfaces and aid in the interpretation of *in situ* experiments. Previous calculations have studied Cu clusters with small ligands like O, CO, and CN^- [12]–[14]. On silver clusters the ligands F^-, Cl^-, Br^-, I^-, azide N_3^-, and thiocyanate SCN^- have been studied [15]–[18]. The polyatomic and potentially polydentate ligands SO_4^{2-} and HSO_4^- are more demanding of computational resources due to the larger number of atoms and electrons and the variety

performed [10]. Other structure determinations have used STM [30] and AFM [31] to obtain geometric information about the effect of sulfate on metal adatom sites on gold surfaces.

Optical spectroscopy has provided important information about adsorption of bisulfate and sulfate on metals and also how vibrational frequencies change on adsorption and with changes in electrode potential. In particular *in situ* surface FTIR spectroscopy [1]–[4], [32], has shown how sulfate, bisulfate and water adsorb on polycrystalline and single crystal surfaces and single crystals with submonolayer of under potentially deposited metals. Finally, we point out that other optical spectroscopies such as second harmonic generation and sum frequency generation [33] have provided some information concerning the interaction of adsorbed sulfate on metal electrodes over a wide range of potentials [34, 35].

3 Methods

For isolated SO_4^{2-} and HSO_4^- we carry out *ab initio* all-electron SCF calculations using analytical derivative methods to determine optimal geometries, harmonic frequencies, and both IR and Raman intensities. The SCF method is expected to give bond stretches which may be 10–20% too high compared to experiment. However, the results should be qualitatively correct. For SO_4^{2-}, we have also carried out geometry optimizations and frequency calculations in the presence of an applied electric field. These were carried out under the constraint that the S position was fixed. We have also computed IR intensities for SO_4^{2-} in the presence of an applied field, but not Raman intensities. For the single copper atom and copper cluster calculations with sulfate or bisulfate, we carry out *ab initio* all-electron SCF calculations using analytical derivative methods to determine optimal geometries, with the constraint of C_{3v} symmetry for $Cu^0SO_4^{2-}$ and C_s symmetry for $Cu^0HSO_4^-$. The $Cu_4^0SO_4^{2-}$ calculations were constrained so that the Cu_4 geometry was fixed at that of bulk Cu metal on the (111) surface [36] and the $Cu_4^0SO_4^{2-}$ cluster had C_{3v} symmetry.

The sulfur basis is derived from the (12*s* 7*p*) primitive Gaussian set of Dunning and Hay [37], contracted to [6*s* 4*p*] and supplemented with two *d* functions with exponent 0.9 and 0.3. The oxygen basis is the (9*s* 5*p*) primitive Gaussian basis set of Huzinaga [38], contracted to [4*s* 2*p*] according to Dunning [39]. This is supplemented with a diffuse *p* function with exponent 0.059 [37] and a *d* function with exponent 0.72 [40]. The basis for hydrogen is the (4*s*) primitive Gaussian set of Huzinaga, contracted to [2*s*] according to Dunning and Hay, and supplemented with a single *p* function with exponent 1.0. For Cu we use the (14*s* 9*p* 5*d*) primitive Gaussian basis set of Wachters [41], contracted to [8*s* 4*p* 3*d*] using his contraction scheme 2. Two diffuse *p* functions, as recommended by Wachters, and the diffuse *d* function of Hay [42] are added, yielding a final basis set of the form (14*s* 11*p* 6*d*)/[8*s* 6*p* 4*d*]. This basis should be adequate to describe the dominantly electrostatic interaction between the Cu 4*s* electron and SO_4^{2-} or HSO_4^- units.

of potential binding modes. We first examine the isolated sulfate and bisulfate ions, and then look at the effect of a strong electric field on sulfate. We then model the binding to the surface first with a single Cu atom, and then progress to larger clusters with four metal atoms, looking at geometries and relative binding energies, using all electron *ab initio* SCF Hartree-Fock calculations and analytical derivative methods. A more complete description of additional calculations for sulfate and bisulfate including adsorption on ten atom Cu clusters will be reported elsewhere [19].

This paper is organized in the following way. In § 2 we provide a survey of the experimental data. In § 3 we discuss the theoretical methods used, and in § 4 we present our results and discussion, first presenting results for SO_4^{2-} and HSO_4^-, then $Cu^0SO_4^{2-}$, $Cu^0HSO_4^-$ and $Cu_4^0SO_4^{2-}$.

2 Survey of Experimental Data

In this section we briefly describe some of the more important experimental work that this paper impacts. There are three main areas: adsorption, structure, and optical spectroscopy.

In aqueous solution sulfate belongs to the class of anion known to undergo specific adsorption [20, 21] in the range of electrode potential corresponding to a thermodynamically stable electrochemical double layer. In this process more weakly bound water molecules between the electrode and the ion are displaced and the ion makes physical contact with the surface atoms of the metal. This is the origin of the term "contact adsorption". Early discussions of this phenomena also considered whether a chemical bond was formed, but conventional wisdom now describes the adsorption as primarily physisorption. In practice contact adsorption results from a balance of opposing free energy interactions of the following type: electrostatics, enthalpies of hydration of ion and surface atoms, and entropy of displaced water molecules. Generally speaking, large ions (eg. I^-, Cs^+) contact adsorb whereas small ions (eg. F^-, Ca^+) do not. The contact adsorption series for noble and coinage metal electrodes immersed in aqueous electrolyte is $BF_4^- < PF_6^- < ClO_4^- < F^- < HSO_4^- < SO_4^{2-} < Cl^- < SCN^- < Br^- < I^-$ [21, 22]. Verification of contact adsorption for sulfate and bisulfate on metals has been demonstrated by a variety of classical electrochemical techniques including cyclic voltammetry [23]–[25], differential capacitance [26], and radio tracer analysis [27]–[29].

Structure determinations by surface X-ray scattering have proved very important because actual geometric information has been derived. For example Blum *et al.* [5, 6] proposed the first structure for sulfate adsorption. These results are particularly important because it was proposed that sulfate may occupy an on-top site with the Cu-O-S bond parallel to the normal of the (111) surface plane. Complimentary X-ray studies have been reported for various Au surfaces [8, 9]. Similar on-top site geometries have been proposed for adsorption on Cu(100), obtained by emersing the electrode from acidic sulfate solution prior to tranfer into UHV where LEED was

S–O1	2.80

S–O1	2.70
S–O2	3.06
S–O3	2.72
∠O3–S–O3	113.3°

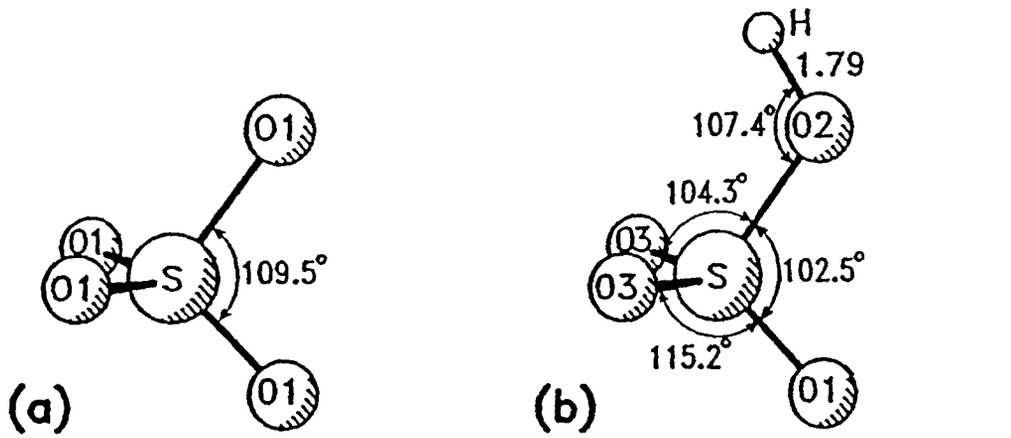

Figure 2: Isolated SO_4^{2-} and HSO_4^- structures. Bond lengths are in a.u. and angles are in degrees (1 a.u. = 0.529177 Å).

The programs CADPAC [43] and the Cambridge Direct SCF [44] are used, implemented on an IBM 3090/300J and RISC SYSTEM/6000 computers at the IBM Almaden Research Center. CADPAC was modified to compute frequencies and intensities in the presence of an applied electric field according to the methods of Duran *et al.* [45].

4 Results and Discussion

4.1 Isolated SO_4^{2-} and HSO_4^- ions

To illustrate the qualitative accuracy of the calculations, we consider here the structure and vibrational frequencies of isolated SO_4^{2-} and HSO_4^-. We emphasize, however, that our results are for "gas-phase" species — so the comparison with experiment will only be qualitative. Nevertheless, the results are useful.

The structure of isolated SO_4^{2-} and HSO_4^- are illustrated in Figure 2. Isolated SO_4^{2-} has tetrahedral symmetry (T_d point group), whereas HSO_4^- has a single plane of symmetry (C_s point group). The computed bond distance for SO_4^{2-} of 2.80 a.u. is in good agreement with the experimental value of 2.82 a.u., which is the value in the Na_2SO_4 crystal and also is the average value in the K_2SO_4 crystal [36]. The computed

Table 1: Summary of the SO_4^{2-} harmonic frequencies and intensities

Mode	Freq. cm^{-1}	IR int. km/mol	Raman int. $Å^4$/amu	Expt. Freq.[a] cm^{-1}
$\nu_2(e)$	471	0	2.3	451
$\nu_4(t_2)$	666	50	2.4	618
$\nu_1(a_1)$	1035	0	24.6	981
$\nu_3(t_2)$	1174	605	8.2	1104

[a] Aqueous Na_2SO_4 [49]

structure of HSO_4^- is also in general agreement with data from crystal structures of $KHSO_4$ [46] and NH_4HSO_4 [47]. For example, in $KHSO_4$ the S–O3 distance is around 2.72 a.u., whereas the S–O1 distance is longer at around 2.77 a.u., due to hydrogen bonding with other HSO_4^- units in the crystal. The S–O2 distance is around 2.96 a.u. in the crystal, shorter than the theoretical result, again an effect due to hydrogen bonding in the crystal. The O–H distance is only 1.37 a.u. in $KHSO_4$ and NH_4HSO_4, compared with the 1.79 a.u. value found here. This difference is larger than could reasonably be expected. However, as discussed by Nelmes [47], the "expected" O–H bond distance in other hydrogen bonded systems is in the range 1.8–1.9 a.u. For example, the O–H distance in H_2SO_4 [2, 48] is 1.83 a.u. Therefore the theoretical value seems very reasonable. Regarding the angles, there is again qualitative agreement, except for the ∠S–O–H which is not unexpected based on the bond distance differences. For example, in $KHSO_4$, the ∠O3–S–O2 is around 105°, compared with 104° theoretically, and the ∠O3–S–O1 is 111° compared with 115° theoretically. There is some difficulty making direct comparisons, due to hydrogen bonding and other "crystal" effects — however, the theoretical results are qualitatively correct. Thus, for HSO_4^-, the lengthening of the S–OH bond distance and the shortening of the other S–O distances compared with the S–O distance in SO_4^{2-} is seen in both the experimental and theoretical results, and the changes in the bond angles are also in the same general direction.

The computed frequencies and intensities for SO_4^{2-} are given in Table 1 and are in good agreement with the aqueous Na_2SO_4 results, although the symmetric stretch is too high, as expected at the SCF level of theory. In general, frequencies which are too high also correlate with bond distances which are too short at the SCF level of theory — however, external media effects in the solution or crystal environment make specific comparison between the frequencies and bond lengths difficult. In fact the agreement between the computed and experimental frequencies is somewhat fortuitous — the aqueous results will undoubtedly be affected by factors such as hydrogen bonding [49], whereas the effect of electron correlation has not been

Table 2: Comparison of computed HSO_4^- frequencies and intensities with experiment

	Freq. cm^{-1}	IR int. km/mol	Raman int. $Å^4$/amu	Expt. Freq.[a] cm^{-1}
a″	130	93	2.3	145
a′	441	4	1.5	447
a″	476	11	1.1	418[b]
a′	616	52	2.8	576
a″	641	71	2.8	589
a′	642	27	3.8	610
a′	861	330	9.5	883
a′	1157	123	18.4	1022
a′	1258	132	3.0	1044
a″	1351	521	4.7	1194
a′	1409	467	4.0	—[c]
a′	4176	73	61.2	3510

[a] Frequencies from Raman spectrum of NH_4HSO_4 crystal (See reference [49] and references therein)

[b] There is another a″ mode reported at 407 cm^{-1}

[c] Frequencies in the range 1360–1390cm^{-1} have been reported from IR spectra of molten $KHSO_4$ (See reference [49] and references therein)

accounted for in the calculations. However, the qualitative agreement is good, the pattern of vibrational levels being well reproduced. For the intensities there are no absolute measurements. However, it is known that ν_3 is the most intense IR band for SO_4^{2-}, and that ν_1 is the most intense Raman band, which is clearly demonstrated in the theoretical results.

The computed harmonic frequencies and intensities of HSO_4^- are given in Table 2. We denote them according to their symmetry label in the C_s point group. We also present experimental frequencies for HSO_4^- in the NH_4HSO_4 crystal, taken from the work of Dawson *et al.* [49]. We see overall qualitative agreement between the theoretical and experimental frequencies, with the S–O stretches being somewhat too high as found for SO_4^{2-}, except for the S–OH stretch which is too low, possibly correlating with the error found for the S–OH bond distance, which was too long. Quantitative agreement should not be expected due to both limitations in the theory and other effects such as additional hydrogen bonding in the solid, which is expected to lower the experimental O–H stretching frequency. As far as the intensities are concerned, the computed results seem to be in fair agreement with the experimentally observed values in that the most intense Raman band experimentally is the 1022–1044 cm^{-1} band and this corresponds to the 1157 cm^{-1} band in the theoretical calculations.

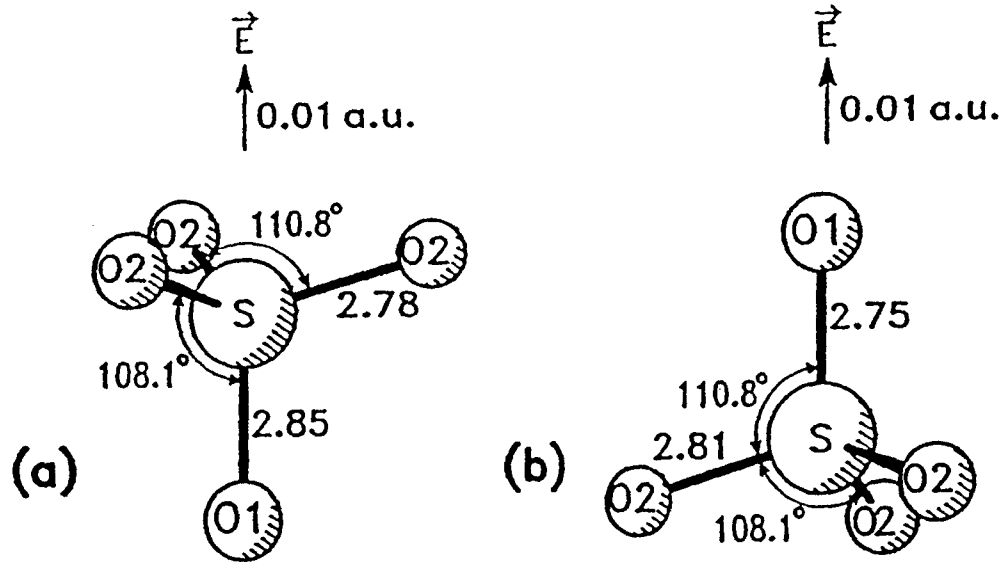

Figure 3: SO_4^{2-} structure in the presence of an electric field along a C_3 axis. Bond lengths are in a.u. and angles are in degrees (for the electric field, 1 a.u. = 5.14221x10^9 V/cm).

Furthermore the order and relative intensity of the four bands at 642, 862, 1157, and 1258 cm^{-1} are not expected to change because all these modes have the same symmetry. Overall, the theoretical methods used here give useful qualitative, though not quantitative, results.

4.2 SO_4^{2-} in the presence of an electric field

In this section we consider the effect of an applied electric field on the structure, frequencies and IR intensities of SO_4^{2-}. This analysis is useful as a simple model of electric field effects at an electrode surface, and also in the analysis of binding in the copper plus sulfate clusters. The magnitude of the field was fixed at 0.01 a.u. (5x10^7 V/cm), corresponding to the strong electric field expected in the electrochemical double layer [13, 50].

The effect of the applied field on the structure of SO_4^{2-} is illustrated in Figure 3. The field is applied along a C_3 axis, with a positive and negative sign, and the SO_4^{2-} unit has C_{3v} symmetry in both cases, with different bond distances and angles. Considering first Figure 3(a), we see that the S–O1 bond has lengthened significantly from the isolated ion value of 2.80 a.u., whereas the S–O2 bond has shortened. However, the shortening effect is smaller since the S–O2 bond lies at a greater angle to the applied field. The bond angles show effects consistent with the distances. The O1–S–O2 angle has *decreased* from the isolated ion value of 109.5°, whereas the O2–S–O2 angle has *increased*. Thinking of the S position as fixed, we see that all the O atoms have

Table 3: Summary of the SO_4^{2-} frequencies (cm^{-1}) and IR intensities (km/mol) with an electric field along S–O1 (C_{3v} symmetry)

	−0.01[a] a.u.		+0.01[b] a.u.	
	ν	IR int.	ν	IR int.
$\nu_2(e)$	471	0.1	471	0.1
$\nu_4(e)$	666	54.2	665	44.6
$\nu_4(a_1)$	664	37.8	667	58.8
$\nu_1(a_1)$	1015	138.2	1028	20.3
$\nu_3(e)$	1210	583.0	1136	626.3
$\nu_3(a_1)$	1113	517.3	1248	547.5

[a] The orientation of the field corresponds to Figure 3(a)
[b] The orientation of the field corresponds to Figure 3(b)

moved in the direction opposite to the applied field, as may be expected due to their negative charge. Reversing the direction of the applied field (Figure 3(b)) has the expected effect — the O atoms all move in the opposite direction, so that the bond distances and angles change in the opposite sense but by about the same magnitude as for the first field direction.

The computed harmonic frequencies and IR intensities for SO_4^{2-} in the presence of an applied electric field are given in Table 3, which are to be compared with the isolated ion results of Table 1. The frequencies in Table 3 are identified by the original labels ($\nu_1 - \nu_4$) used in Table 1, as the assignment is quite clear even though the symmetry is lower. We see that the t_2 modes of the T_d point group have split into a_1 and e modes for the C_{3v} point group in the presence of the applied field. Also, ν_2 and ν_4 are barely affected by the applied field, presumably because these modes involve motions which are predominantly perpendicular to the applied field. Because of their low IR and Raman intensity, these modes are difficult to detect experimentally.

Of more interest are ν_1 and ν_3, as these are intense in the Raman and IR regions, respectively (see Table 1). Although we have not computed Raman intensities in the presence of an applied field, it is likely that ν_1 will still be the most intense Raman band in this case also. From Table 3, for the -0.01 a.u. field, we see that the lengthening of the S–O1 bond (Figure 3(a)) results in a reduction of the $\nu_1(a_1)$ mode by about 20 cm^{-1} and the $\nu_3(a_1)$ mode by about 60 cm^{-1}, a large effect. In addition, ν_1 has gained some IR intensity, possibly due to interaction with the intense $\nu_3(a_1)$ mode. The $\nu_3(e)$ mode has increased in frequency by about 35 cm^{-1}, reflecting the shorter S–O2 bond distance. We note that ν_1 involves both S–O1 and S–O2 stretches, so that in the presence of the applied field there is a balance between effects which increase ν_1 (shortening the three S–O2 distances) and decrease ν_1 (lengthening the

S–O1 distance).

From the +0.01 a.u. results of Table 3, we see that reversing the direction of the applied field has a similar effect on the frequencies as for the bond distances. The $\nu_1(a_1)$ mode is again reduced in frequency, although the effect is smaller than for the –0.01 a.u. field. This shows, however, that an intuitive guess based on the bond distances is not entirely appropriate for predicting the frequency shifts — in this case, the additional $\nu_3(a_1)$ mode has an effect on the $\nu_1(a_1)$ mode, in one case moving down in frequency and the other case moving up. It is probable that this shift in $\nu_3(a_1)$ has a subtle but important effect on $\nu_1(a_1)$ for the –0.01 a.u. field case, increasing the IR intensity and reducing the frequency. Further evidence for this may be seen from the IR intensity of $\nu_1(a_1)$ in the +0.01 a.u. field case — the increase is much smaller than for the –0.01 a.u. case, because $\nu_3(a_1)$ has moved up in frequency rather than down. The $\nu_3(e)$ modes are shifted down in frequency for the +0.01 a.u. field case, as expected.

If we were to consider the metal surface to be perpendicular to the applied field direction, then we must keep in mind the fact that the e modes will not be observable on a surface. This is because the IR intensity arises from a dipole moment derivative which is parallel to the "surface", which will be cancelled by image charge effects (ie. the surface selection rule). Therefore it is the a_1 modes which are the most important, as these involve dipole moment derivatives which are perpendicular to the "surface". These simple model calculations indicate that the orientation of the SO_4^{2-} molecule on the surface may be determined by the frequency shift of the intense $\nu_3(a_1)$ mode.

4.3 $Cu^0SO_4^{2-}$ results

In this section we consider two $Cu^0SO_4^{2-}$ structures, illustrated in Figure 4, denoting them as "1-down" and "3-down", respectively. There are other structures which may be important — for example, there is a "1.5 down" structure with a Cu–O1–S angle of 122°. This lies around 2 kcal/mol below the 1-down structure. In the current work we consider only the C_{3v} structures, postponing discussion of alternative structures to future work [19]

The interaction of SO_4^{2-} with the Cu atom is mainly electrostatic, dominated by charge-induced dipole interactions. Remembering that SO_4^{2-} has no permanent dipole moment, this means that the binding energy of SO_4^{2-} to a single Cu atom is not especially sensitive to the orientation of the SO_4^{2-} unit. The 4s electron on Cu polarizes away from the SO_4^{2-} unit, forming an sp hybrid orbital in order to both reduce the repulsion and create an attractive electrostatic interaction by forming a positive region of charge on the SO_4^{2-} side of the atom — an induced dipole. The interaction is strong — the binding energy of the structure illustrated in Figure 4(a) is around 37 kcal/mol. For comparison, at an equivalent level of theory the binding energy of Cu^0H_2O is less than 1 kcal/mol (a Van der Waals complex), whereas the binding energy of Cu^+H_2O is strong at around 32 kcal/mol.

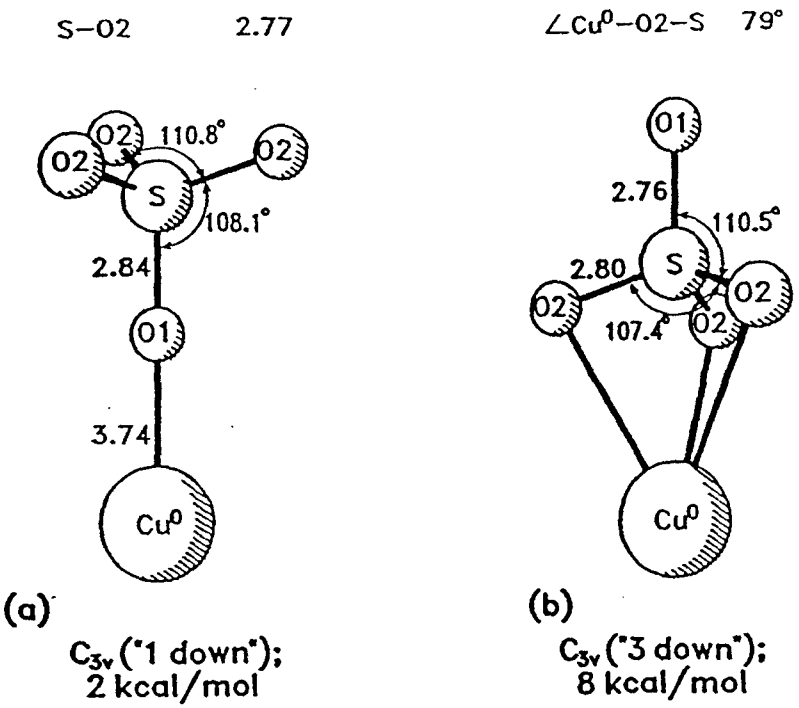

Figure 4: Summary of $Cu^0SO_4^{2-}$ structures in C_{3v} symmetry. Bond lengths are in a.u. and angles are in degrees.

The two structures are separated energetically by 6 kcal/mol. The Cu–O bond distances in each case are very different. The Cu–O1 distance of the 1-down structure is reasonable — for example, the early surface exafs experiments [5] found a value of 3.9 a.u. The Cu–O2 distance of 4.83 a.u. for the 3-down structure is much greater — in this case the limiting factor is the inability of the SO_4^{2-} unit to distort sufficiently to allow a stronger interaction between the O2 atoms and the Cu, combined with the repulsion between the formally positively charged S and the positive charge due to the induced dipole on the Cu atom. The fact that there are three O2 atoms involved in the interaction offsets these factors to some extent.

It is of interest to compare the bond lengths and angles of the SO_4^{2-} unit in $Cu^0SO_4^{2-}$ (Figure 4) with those of SO_4^{2-} in the presence of an applied field (Figure 3). For the 3-down structure, we note that the S–O2 distance is the same as in free SO_4^{2-}, in contrast to Figure 3(b), where it is slightly longer. However, the O2–S–O2 angle is smaller for the 3-down structure than in Figure 3(b). These differences are due to the more localized nature of the electrostatic interaction between Cu and SO_4^{2-} compared with the uniform electric field of Figure 3. Overall, however, there is a remarkable similarity between the SO_4^{2-} unit in the 1-down structure and the applied field structure of Figure 3(a), and the SO_4^{2-} unit in the 3-down structure and the applied field structure of Figure 3(b). This is due to the dominantly electrostatic nature of the interaction of SO_4^{2-} with Cu — the Cu atom with an induced dipole is quite similar to an applied electric field, as far as the SO_4^{2-} unit is concerned. In

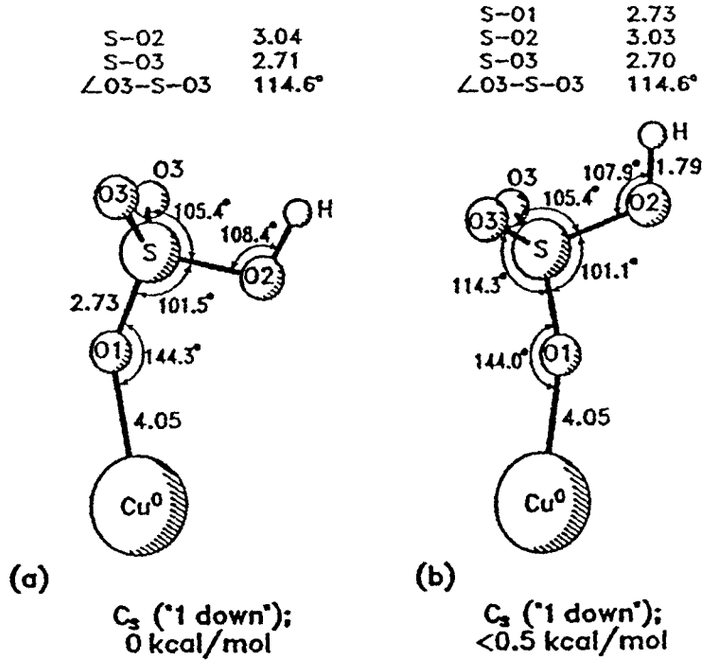

Figure 5: Summary of $Cu^0HSO_4^-$ structures in C_s symmetry. Bond lengths are in a.u. and angles are in degrees.

future work [19] we will consider whether this also applies to the frequency shifts for the SO_4^{2-} unit in $Cu^0SO_4^{2-}$. At the present time we simply state that they are expected to be qualitatively similar to those found for SO_4^{2-} in the presence of an applied field.

4.4 $Cu^0HSO_4^-$ structure

We now consider two $Cu^0HSO_4^-$ structures, illustrated in Figure 5. As for $Cu^0SO_4^{2-}$, there are other possible structures. However, these are the lowest energy structures which we have found.

There are two important differences between SO_4^{2-} and HSO_4^-, both due to the presence of the H in HSO_4^-. The first is the reduced charge of HSO_4^-, which results in a smaller charge-induced dipole interaction in $Cu^0HSO_4^-$. This is illustrated by the reduced binding energy of $Cu^0HSO_4^-$, only around 14 kcal/mol, less than half that of $Cu^0SO_4^{2-}$. The second difference is the presence of a permanent dipole moment in HSO_4^-. Considering Figure 2(b), the permanent dipole is oriented in the S–O2–H plane, approximately perpendicular to the O3–S–O3 plane, passing through the S with the positive end at the OH end of the molecule. There will be an effect which tends to orient the dipole to maximize the dipole-induced dipole interaction. However, this is a secondary effect compared with the charge-induced dipole interaction. This is illustrated by the two structures shown here — the orientation of the dipole is

different in each case, yet the structures have very similar energies.

The Cu–O1 bond distance is longer in $Cu^0HSO_4^-$ than $Cu^0SO_4^{2-}$, reflecting the lower binding energy of $Cu^0HSO_4^-$. Comparing the HSO_4^- structure in $Cu^0HSO_4^-$ with the isolated HSO_4^- structure of Figure 2(b), we see similar effects to the SO_4^{2-} structural changes in $Cu^0SO_4^{2-}$, but again these are not as large since the interaction is weaker. In addition, the symmetry is lower. The S–O1 bond distance is greater in $Cu^0HSO_4^-$ compared with HSO_4^-, and the S–O2 and S–O3 distances are shorter. The angles also change in a way consistent with that found for SO_4^{2-} in $Cu^0SO_4^{2-}$ — the negatively charged oxygens move toward the positive side of the Cu, whereas the positively charged H moves away. This decreases the O1–S–O2 angle, for example, and increases the S–O2–H angle.

There are several other possible structures for $Cu^0HSO_4^-$ when compared to $Cu^0SO_4^{2-}$, mainly because of the lower symmetry of HSO_4^- compared to SO_4^{2-}. However, the most important difference between $Cu^0SO_4^{2-}$ and $Cu^0HSO_4^-$, that is the weaker binding leading to smaller geometric distortions of HSO_4^- in $Cu^0HSO_4^-$, will also apply in these other cases. This also means that, if HSO_4^- and SO_4^{2-} adsorb on a Cu surface with a similar orientation, the frequency shifts for HSO_4^- may be expected to be smaller than for SO_4^{2-}. However, since the frequency shifts are very dependent on the orientation, this cannot be taken as a general rule.

4.5 $Cu_4^0SO_4^{2-}$ structures

In this section we present results for two structures of $Cu_4^0SO_4^{2-}$, illustrated in Figure 6. These are chosen to illustrate important limitations in the single copper atom model, but also to illustrate the utility of that model in the qualitative understanding of the interaction of SO_4^{2-} and a copper surface.

One valid question is why consider the single copper atom calculations at all, given that we are also presenting the Cu_4 results. There are several reasons — firstly, it is computationally feasible to compute harmonic frequencies and IR intensities for $Cu^0SO_4^{2-}$ and related systems. Although we have not presented these results here, this will appear in future work [19]. Secondly, the $Cu^0SO_4^{2-}$ results give good insight into the nature of the Cu–SO_4^{2-} interaction, without the additional complications of cluster artifacts which may appear (see below). Finally, the single copper calculations serve as a starting point from which to plan the more computationally intensive Cu_4 calculations.

The four atom copper cluster used here illustrates the additional binding possibilities of SO_4^{2-} on the Cu(111) surface — the 3-down and 1-down models now contain interactions with *three* copper atoms. Before discussing $Cu_4^0SO_4^{2-}$, however, we must note some additional limitations of the cluster model.

For the Cu_4 and the $Cu_4^0SO_4^{2-}$ clusters, we have currently used a closed-shell singlet coupling of the Cu 4*s* electrons. There are other possible couplings — in particular, several triplet states, which we will be studying in future work. Whether

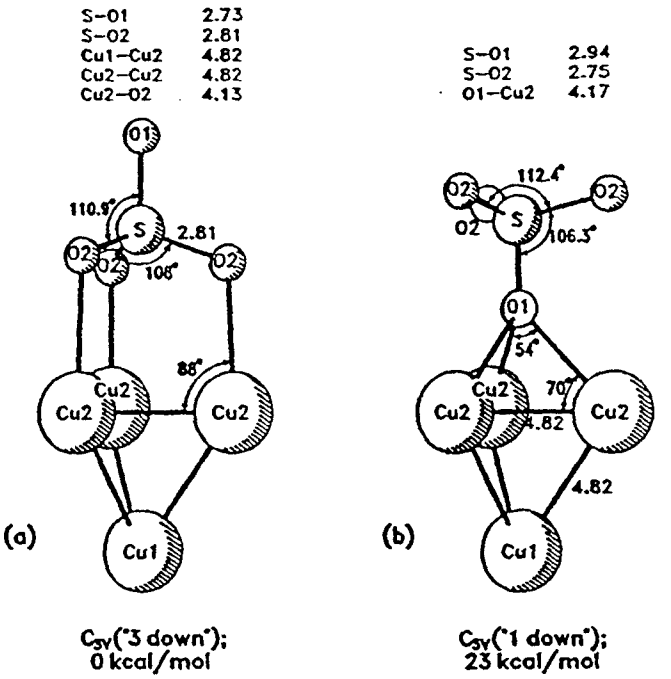

Figure 6: Summary of $Cu_4^0SO_4^{2-}$ structures showing ontop and three fold hollow sites. Bond lengths are in a.u. and angles are in degrees.

a singlet or triplet coupling of the electrons is chosen, there are problems which arise from using the cluster model. Cu_4 is in reality a small molecule with a valence shell of 4*s*-like electrons, rather than an accurate model of a metal surface. The occupation of the valence shell leads to an asymmetric charge distribution in C_{3v} symmetry, so that Cu1 in Figure 6 carries a net negative charge and the three Cu2 atoms carry an equal net positive charge, for the closed-shell singlet coupled case. This gives the cluster an overall dipole moment which in this orientation favours the binding of a negative ion such as SO_4^{2-}, and so absolute binding energies are not well defined. However, relative binding energies should still be qualitatively useful.

The two structures of Figure 6 illustrate the importance of multidentate bonding for SO_4^{2-} on copper. The 3-down structure is much more stable than the 1-down structure over the 3-fold hollow site. The binding energy of SO_4^{2-} to Cu_4 (closed shell singlet coupled) for the 3-down structure is 54 kcal/mol, compared with 31 kcal/mol for the 1-down structure. The binding energy for the 3-down structure is also much higher than that of SO_4^{2-} bound to Cu (37 kcal/mol, § 4.3). Some part of the increased binding energy for the Cu_4 cluster in the 3-down orientation is due to the permanent dipole moment of the Cu_4 cluster. However, the large difference of 23 kcal/mol between the 3-down and 1-down cases for $Cu_4^0SO_4^{2-}$ indicates that the 3-down structure may be favoured on Cu(111). Interestingly, the Cu–O distances are very similar for both cases, just over 4.1 a.u. However, the interaction of three negatively charged O atoms in the 3-down case obviously leads to a much stronger interaction than the

1-down case. The Cu–O bond length of 4.1 a.u. is reasonable when compared with the surface exafs value of 3.9 a.u. discussed previously. However, we do not expect quantitative agreement.

It is useful to compare the structures of the SO_4^{2-} units in Figure 6 with the earlier Figures 3 and 4. The SO_4^{2-} unit for the 3-down structure of Figure 6(a) is quite similar to that of Figure 3(b), indicating again a dominantly electrostatic interaction. Compared to the $Cu^0SO_4^{2-}$ result (Figure 4(b)), the angles of the SO_4^{2-} unit in the $Cu_4^0SO_4^{2-}$ 3-down structure indicate less distortion, due to the oxygens being in a more favourable position in the $Cu_4^0SO_4^{2-}$ structure. The 1-down $Cu_4^0SO_4^{2-}$ structure, although much higher in energy, is still interesting. We see again qualitative similarities to the earlier results of Figures 3(b) and 4(b). However, the distortions of the angles and the S–O1 bond distance are much greater in the 1-down $Cu_4^0SO_4^{2-}$structure. Although the interaction is probably still dominantly electrostatic for the 1-down structure, the very long S–O1 bond distance may be indicative of the formation of a weak chemical bond between the Cu_4 cluster and the SO_4^{2-} unit. Comparing the bond lengths and angles of the $Cu_4^0SO_4^{2-}$ 1-down structure with those of HSO_4^- (Figure 2(b)), we see qualitative similarities. Althought the distortions are not as large in $Cu_4^0SO_4^{2-}$ as in HSO_4^- it is clear that the 1-down structure is some way along to a chemically bonded species, in contrast to the 3-down structure, which is electrostatically bound.

Regarding frequency shifts for SO_4^{2-} in $Cu_4^0SO_4^{2-}$, we simply note from the geometric distortions of the SO_4^{2-} units that they are expected to be qualitatively similar to those found for SO_4^{2-} in the presence of an applied field, and the 1-down shifts may be larger than the 3-down shifts.

5 Conclusions

A series of model calculations have been presented which aim at helping to interpret the results of *in situ* experimental data on the adsorption of SO_4^{2-} and HSO_4^- on metal surfaces. The current calculations are aimed at adsorption on copper, but the qualitative nature of the results means that the conclusions may generalize to other metals. The geometry optimization, harmonic frequency and intensity calculations for isolated SO_4^{2-} and HSO_4^- indicate useful qualitative accuracy. The application of a strong uniform electric field to SO_4^{2-} gave insight into the response of SO_4^{2-} to the local field in the electrochemical double layer, and also gave insight into the nature of the bonding of SO_4^{2-} to Cu and Cu_4. The frequency shifts computed for SO_4^{2-} in the presence of the applied field could be straightforwardly interpreted in terms of the geometrical distortions caused by the field. However, the calculations show that there are some subtle effects for the frequency shifts due to the interaction of modes of the same symmetry which are not obvious from intuitive arguments based on the geometrical distortions. In addition, the calculations show that the frequency shift of the most intense a_1 mode may serve to indicate the adsorption geometry of SO_4^{2-} on

Cu(111), assuming C_{3v} symmetry.

The interaction between Cu^0 and SO_4^{2-} or HSO_4^- is dominantly ionic, a charge-induced dipole interaction, so there is not a large energetic difference between the different structures. The binding energy of SO_4^{2-} to Cu or Cu_4 is quite high, whereas the binding energy HSO_4^- to Cu is lower due to the reduced charge of HSO_4^-, giving a reduced charge-induced dipole interaction. The similarity of the structure of the SO_4^{2-} unit in the presence of an applied field with that in $Cu^0SO_4^{2-}$ serves to illustrate the ionic nature of the bonding. The lower binding energy of HSO_4^- compared with SO_4^{2-} means, that for an equivalent adsorption orientation, the frequency shifts observed for HSO_4^- may be less than for SO_4^{2-}. However, since the frequency shifts are very dependent on adsorption geometry, this statement cannot be taken as general.

The $Cu_4^0SO_4^{2-}$ calculations illustrate that, even accounting for artifacts due to the cluster model, the 3-down multidentate structure of $Cu_4^0SO_4^{2-}$ is energetically much more favourable than the 1-down hollow site adsorption for Cu(111). This is mainly due to the very favourable position of the oxygen atoms over the Cu atoms on Cu(111). The comparison of the SO_4^{2-} structure in $Cu_4^0SO_4^{2-}$ with the earlier structures indicates that the qualitative nature of the frequency shifts for SO_4^{2-} may be deduced from the geometric distortions of the SO_4^{2-} units. Finally, the structure of the SO_4^{2-} unit in the 1-down $Cu_4^0SO_4^{2-}$ cluster indicates the possible formation of a weak chemical bond when compared to the 3-down $Cu_4^0SO_4^{2-}$ structure, which is electrostatically bound.

Continuing and future work includes the consideration of more structures for $Cu^0SO_4^{2-}$ and $Cu^0HSO_4^-$, the computation of harmonic frequencies and IR intensities for these species, the optimization of additional structures for the larger $Cu_4^0SO_4^{2-}$ structures and the consideration of even larger clusters such as $Cu_{10}^0SO_4^{2-}$. When combined with the current results, these should give more insight into the interaction of SO_4^{2-} and HSO_4^- with metals and metal surfaces.

6 Acknowledgements

This work has been supported in part by the Office of Naval Research. L. A. B. would like to thank J. E. Rice and P. S. Bagus for helpful discussions.

References

[1] K. Kunimatsu, M. G. Samant, H. Seki, and M. R. Philpott, J. Electroanal. Chem. 243, 203 (1988).

[2] K. Kunimatsu, M. G. Samant, and H. Seki, J. Electroanal. Chem. 258, 163 (1989).

[3] M. G. Samant, K. Kunimatsu, H. Seki, and M. R. Philpott, J. Electroanal. Chem. 280, 391 (1990).

[4] P. W. Faguy, N. Markovic, R. R. Adzic, C. A. Fierro, and E. B. Yeager, J. Electroanal. Chem. 289, 245 (1990).

[5] L. Blum, H. D. Abruna, J. White, J. G. Gordon II, G. L. Borges, M. G. Samant, and O. R. Melroy, J. Chem. Phys. 85, 6732 (1986).

[6] O. R. Melroy, M. Samant, G. L. Borges, J. G. Gordon II, L. Blum, J. H. White, M. J. Albarelli, M. McMillan, and H. D. Abruna, Langmuir 4, 728 (1988).

[7] M. R. Philpott, R. Corn, W. G. Golden, K. Kunimatsu, and H. Seki, Raman and Infrared Spectroscopy of Molecules Adsorbed on Metal Electrodes, in *Dynamics on Surfaces*, edited by B. Pullman, J. Jortner, A. Nitzan, and B. Gerber, pp. 401–412, D. Reidel, Holland, 1984, Proceedings of the 11th Jerusalem Symposium on Quantum Chemistry and Biology, April 30-May 3, 1984.

[8] A. Tadjeddine, D. Guay, M. Ladouceur, and G. Tourillon, Phys. Rev. Lett. 66, 2235 (1991).

[9] G. Tourillon, D. Guay, and A. Tadjeddine, J. Electroanal. Chem. 289, 263 (1990).

[10] C. B. Ehlers and J. L. Stickney, Surf. Sci. 239, 85 (1990).

[11] D. M. Kolb, Ber. Bunsenges Phys. Chem. 92, 1175 (1988).

[12] P. S. Bagus and F. Illas, Phys. Rev. C 47, 10852 (1990).

[13] P. S. Bagus, C. J. Nelin, W. Müeller, M. R. Philpott, and H. Seki, Phys. Rev. Lett. 58, 559 (1987).

[14] C. J. Nelin, P. S. Bagus, and M. R. Philpott, J. Chem. Phys. 87, 2170 (1987).

[15] P. S. Bagus, G. Pacchioni, and M. R. Philpott, J. Chem. Phys. 90, 4287 (1988).

[16] G. Pacchioni, P. S. Bagus, and M. R. Philpott, Z. Phys. **D12**, 543 (1989).

[17] M. Samant, R. Viswanathan, H. Seki, P. S. Bagus, C. J. Nelin, and M. R. Philpott, J. Chem. Phys. 89, 583 (1988).

[18] M. Samant, K. Kunimatsu, R. Viswanathan, H. Seki, G. Pacchioni, P. S. Bagus, and M. R. Philpott, Langmuir 7, 1261 (1991).

[19] L. A. Barnes, B. Liu, and M. R. Philpott, Model Studies of the Adsorption of Sulfate and Bisulfate on Copper, to be published (1992).

[20] F. Anson, Accounts Chem. Res. **8**, 400 (1975).

[21] J. O. Bockris and A. K. N. Reddy, *Modern Electrochemistry*, Plenum Press, New York, 1973.

[22] G. Valette, J. Electroanal. Chem. **122**, 285 (1981).

[23] R. I. Tucceri and D. Posadas, J. Electroanal. Chem. **191**, 387 (1985).

[24] W. Stoeckel and R. Schumacher, Ber. Bunsenges Phys. Chem. **91**, 345 (1987).

[25] S. Strbac and R. R. Adzic, J. Electroanal. Chem. **249**, 291 (1988).

[26] J. Clavilier, A. Hamelin, and G. Valette, C. R. Acad. Sci. Paris **C265**, 221 (1967).

[27] P. Zelenay, L. M. Rice-Jackson, and A. Wieckowski, J. Electroanal. Chem. **283**, 389 (1990).

[28] P. Zelenay, L. M. Rice-Jackson, J. Gawlowski, and A. Wieckowski, Surf. Sci. **256**, 253 (1991).

[29] P. Zelenay and A. Wieckowski, J. Electrochem. Soc. **139**, 2552 (1992).

[30] O. M. Magnussen, J. Hotlos, R. J. Nichols, D. M. Kolb, and R. J. Behm, Phys. Rev. Lett. **64**, 2929 (1990).

[31] S. Manne, P. K. Hansma, J. Massie, V. B. Elings, and A. A. Gewirth, Science **251**, 183 (1991).

[32] D. B. Parry, M. G. Samant, H. Seki, M. R. Philpott, and K. Ashley, In Situ FTIR Study of Bisulfate and Sulfate Adsorption on Gold Electrodes, with and without Under Potential Deposition of Copper, submitted for publication, Langmuir, (1992).

[33] Y. R. Shen, *Principles of Nonlinear Optics*, Wiley, New York, 1984.

[34] D. J. Campbell and R. M. Corn, J. Phys. Chem. **91**, 345 (1987).

[35] J. M. Robinson and G. L. Richmond, Electrochim. Acta **34**, 1639 (1989).

[36] R. W. G. Wyckoff, *Crystal Structures*, volume 3, Wiley Interscience, New York, second edition, 1965.

[37] T. H. Dunning, Jr. and P. J. Hay, Gaussian Basis Sets for Molecular Calculations, in *Modern Theoretical Chemistry*, edited by H. F. Schaefer, III, volume 3, chapter 1, pp. 1–27, Plenum Press, 1977.

[38] S. Huzinaga, J. Chem. Phys. **42**, 1293 (1965).

[39] T. H. Dunning, Jr., J. Chem. Phys. **53**, 2823 (1970).

[40] R. Ahlrichs and P. R. Taylor, J. Chim. Phys. **78**, 316 (1981).

[41] A. J. H. Wachters, J. Chem. Phys. **52**, 1033 (1970).

[42] P. J. Hay, J. Chem. Phys. **66**, 4377 (1977).

[43] R. D. Amos and J. E. Rice, 'CADPAC: The Cambridge Analytic Derivatives Package', issue 4.0, Cambridge, 1987.

[44] C. W. Murray and R. D. Amos, 'The Cambridge Direct SCF Program', Cambridge, 1989.

[45] M. Duran, J. L. André, A. Lledós, and J. Bertrán, J. Chem. Phys. **90**, 328 (1989).

[46] F. A. Cotton, B. A. Frenz, and D. L. Hunter, Acta. Cryst. **B31**, 302 (1975).

[47] R. J. Nelmes, Acta. Cryst. **B27**, 272 (1971).

[48] Handbook of Chemistry, The Chemical Society of Japan, 11-651 (1984).

[49] B. S. Dawson, D. E. Irish, and G. E. Toogood, J. Phys. Chem. **90**, 334 (1986).

[50] P. S. Bagus, C. J. Nelin, K. Herman, and M. R. Philpott, Phys. Rev. Rap. Commun. **36**, 8169 (1987).

MOLECULAR DYNAMICS MODELING OF ELECTRIC DOUBLE LAYERS WITH SPECTROSCOPIC APPLICATIONS

IBM ALMADEN RESEARCH CENTER
SAN JOSE, CA

14 APR 1993

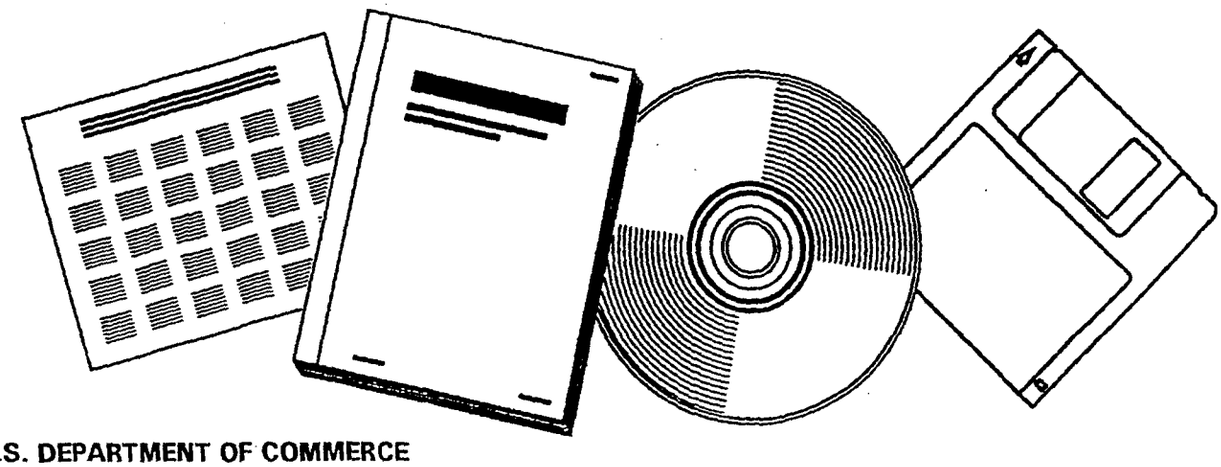

U.S. DEPARTMENT OF COMMERCE
National Technical Information Service

OFFICE OF NAVAL RESEARCH

Grant No. _____

R&T Code N00014-92-C-0173

Technical Report #06

MOLECULAR DYNAMICS MODELING OF ELECTRIC DOUBLE LAYERS WITH SPECTROSCOPIC APPLICATIONS

by

Michael R. Philpott
J. N. Glosli

Prepared for publication

in the

Electrochemical Society Symposium, Hawaii

IBM Research Division, Almaden Research Center,
650 Harry Road, San Jose, CA 95120-6099

1993

Molecular Dynamics Modeling of Electric Double Layers with Spectroscopic Applications

M. R. Philpott and J. N. Glosli†

IBM Research Division, Almaden Research Center
650 Harry Road, San Jose CA 95120-6099
†Lawrence Livermore National Laboratory
University of California, Livermore CA 94550

Molecular dynamics is used to model the structure and dynamics of electric double layers at a charged metal surface and to ask questions of spectroscopic interest. In particular: What is the molecular basis for changing the position of the outer Helmholtz plane (OHP) thereby tuning the electric field across the inner layer? Another topic is the microscopic basis of modulation spectroscopies like SNIFTIRS Our MD simulations of an immersed electrode show features corresponding to: compact layer, diffuse layer, highly oriented water layer next to the metal when the electrode is charged and ions are present, penetration of nominally diffuse layer species into inner layer, ion pair formation between contact adsorbed ion and diffuse layer ion when the electrode is uncharged, poorly oriented surface water when the electrode is uncharged. All these properties arise from the model with the restriction that charge on the metal and aqueous phase sums to zero, ie., $q_M + q_{ions} = 0$.

Molecular Dynamics Modeling of Electric Double Layers with Spectroscopic Applications

Michael R. Philpott and James N. Glosli†
IBM Research Division, Almaden Research Center
650 Harry Road, San Jose, CA 95120-6099
†Lawrence Livermore National Laboratory,
University of California, Livermore, CA 94550

Introduction and Model

We use molecular dynamics (MD) to model the structure and dynamics of electric double layers at a charged metal surface and to ask questions of spectroscopic interest. In particular: What is the molecular basis for changing the position of the outer Helmholtz plane (OHP) thereby tuning the electric field [1, 2] across the inner layer? Another topic is the microscopic basis of modulation spectroscopies like SNIFTIRS [3]. Our MD simulations of an immersed electrode show features corresponding to: compact layer, diffuse layer, highly oriented water layer next to the metal when the electrode is charged and ions are present, penetration of nominally diffuse layer species into inner layer, ion pair formation between contact adsorbed ion and diffuse layer ion when the electrode is uncharged, poorly oriented surface water when the electrode is uncharged. All these properties arise from the model with the restriction that charge on the metal and aqueous phase sums to zero, ie., $q_M + q_{ions} = 0$.

Interaction with the metal was represented by a 9-3 potental for Pauli repulsion and attractive dispersive interactions, and an image potential for interaction with the conduction electrons. On the side opposite the metal the electrolyte was constrained by the 9-3 potential of a 'dielectric-like' bounding surface. This boundary limited the extent of the fluid phase, and kept the calculations tractable. System composition was $mM^{+} + nX^{-} + (N\text{-}m\text{-}n)H_2O$

where N is the number of water molecules in the absence of ions, and (m,n)=(0,0),(1, 0),(0, 1),(1, 1),(2, 1),... . Heinzinger parameters [4] for st2 water model and alkali halides MX were used. Electrostatic fields were calculated exactly (no cut offs) by the fast multipole method.

Double Layer on Charged Electrode

We display a sample result here (see Figure 1) for a system composed of one Li^+, two I^- and 155 waters in a cubic simulation cell with edge length 1.862 nm and periodically replicated in the (x,y) plane. The metal surface at z = 0.932 nm has $q_M = +|c|$ (anodic). Figure 1 shows the density profiles averaged over the xy plane as a function of z for all components of the system. The iodide distribution is sharply peaked near 0.7 nm just inside the repulsive portion (dash line) of the 9-3 potential. The iodide distribution is compact and the Li^+ distribution is diffuse. At negative z the Li density has the gradual fall off expected for an electrostatically bound species. The main component of the Li density ends at 0.05 nm which we interpret as the position of the OHP, being approximately two water diameters from the repulsive wall at z = 0.682 nm. In the region between 0.05 and 0.3 nm the cation has finite probability of penetrating the inner layer. This process is not part of usual Stern-Gouy-Chapman theory. The structure near the metal surface in the densities for water, H, and PC (point charge of the st2 model) arises from an oriented layer of water with a PC pointing at the metal. This an important result of our model with implications for modulation spectroscopy.

Application to Surface Spectroscopy

The idea of altering the position of the outer plane to change the field across the inner layer has been proposed many times [1, 2]. This effect can be modeled with the primative system used here. Based on the total charge distribution given in Figure 1 we see that the iodide and oriented surface waters determine the charge

density near the metal. Note the positive charge peak at 0.65 nm. It and weaker positive peaks near 0.4 and 0.2 nm make it difficult for positive ions to approach the interface even though the latter carries net negative charge because of two adsorbed anions. Two opposing effects operate as cation size is increased, and their balance determines the field effect. First the OHP will move to more negative z due to larger radius and electrostatic repulsion from the positive charge peaks. Second at larger radii the cation hydration shell is softer making it easier for the ion to penetrate the inner layer. In Figure 1 the tail between 0.0 and 0.3 nm indicates how difficult this is for Li ion with its strongly bound solvation shell. More calculations exploring this effect are in progress and will be presented at the meeting.

Conclusion and Acknowledgement

Molecular dynamics calculations show that a simple model based on sound chemical ideas reproduces phenomena familiar from experiments on the electrochemical interface. Important new insights arise concerning the time averaged electric fields across the inner layer which in turn deepen our understanding of spectroscopic probes.

This work was supported in part by the Office of Naval Research.

References

1 A. Bewick, private communication, 1987. Tetralkyl ammonium cations used to alter OHP position

2 K. Ashley, M. G. Samant, H. Seki, and M. R. Philpott, J. Electroanal. Chem. **270**, 349-364 (1989).

3 S. Pons, T. Davidson, and A. Bewick, J. Electroanal. Chem. 160, 63 (1984).

4 K. Heinzinger, *Computer Modelling of Fluids Polymers and Solids*, (Kluwer,Dordrecht, 1990), pp. 357-404.

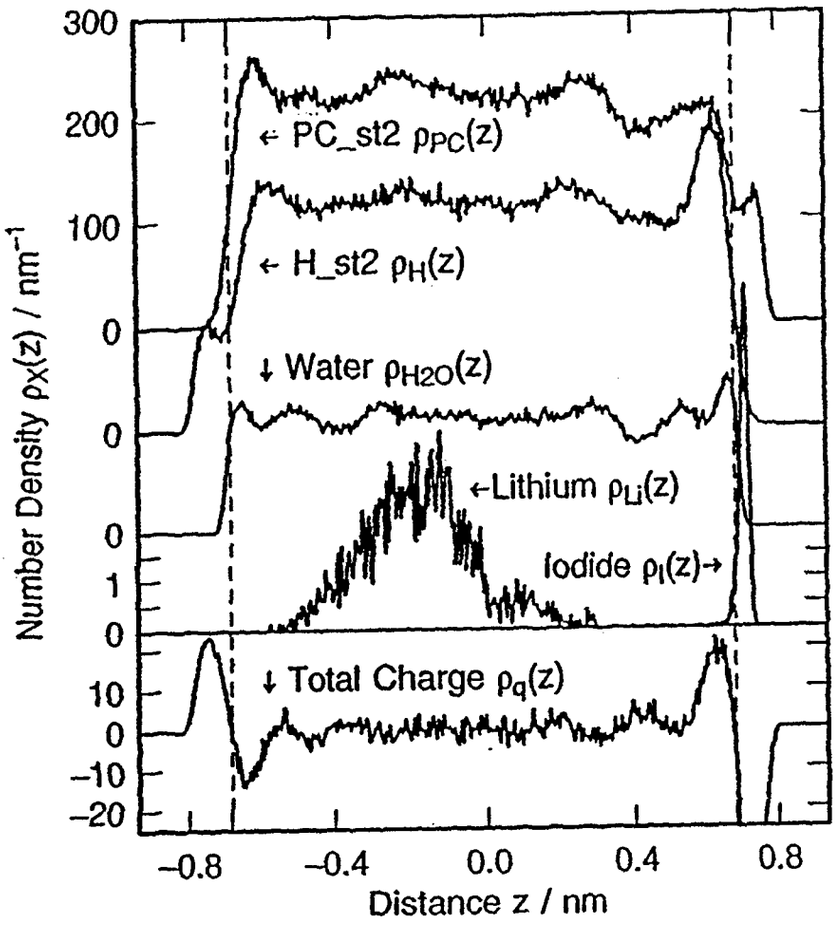

Figure 1. Density profiles for two I^-, one Li^+ and 155 st2 water molecules next to immersed electrode. Anodically charged electrode $q_M = +|e|$. Iodide distribution is compact and Li^+ diffuse. Metal on rhs, dielectric constraining boundary on lhs. Distance across the cell 1.892 nm. Repulsive portion of wall, dashed line, at $|z| = 0.682$ nm. Temperature 290K.

MOLECULAR DYNAMICS MODELING OF ELECTRIC DOUBLE LAYER

IBM ALMADEN RESEARCH CENTER
SAN JOSE, CA

14 APR 1993

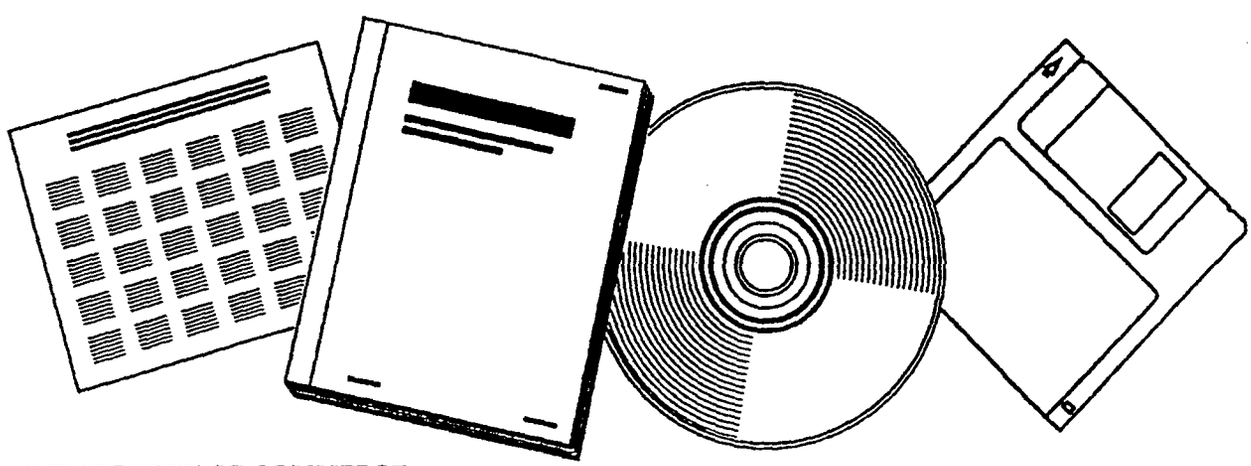

U.S. DEPARTMENT OF COMMERCE
National Technical Information Service

OFFICE OF NAVAL RESEARCH

Grant No. _____

R&T Code N00014-92-C-0173

Technical Report #04

MOLECULAR DYNAMICS MODELING OF ELECTRIC DOUBLE LAYER

by

James N. Glosli
Michael R. Philpott

Prepared for publication

in the

Electrochemical Society Symposium Proceedings

IBM Research Division, Almaden Research Center,
650 Harry Road, San Jose, CA 95120-6099

1993

MOLECULAR DYNAMICS MODELING OF ELECTRIC DOUBLE LAYERS

James N. Glosli and Michael R. Philpott
IBM Research Division, Almaden Research Center
650 Harry Road, San Jose, CA 95120-6099

Constant temperature molecular dynamics calculations of a simple model of a charged metal electrode immersed in electrolyte show the following features known to exist experimentally : incipience of a compact layer, formation of a diffuse layer, presence of highly oriented water layer next to the metal, penetration of nominally diffuse layer species into inner Helmholtz region, ion pair formation between contact adsorbed ion and diffuse layer ion. All these effects emerge from calculations with the same basic model when either the electrolyte composition or the electrode charge are changed. The systems studied had the general composition nI^-+mLi^++(158 - n - m)H_2O where (n,m) = (0,0), (1, 0), (0, 1), (1, 1), and (2, 1). The simulation cell had one metal electrode and one constraining dielectric surface. The surface charge on the metal was q_M=0,±e the latter corresponding to electric fields of about $\pm 5\times 10^7$ V/cm. Net charge in aqueous phase fixed at $q_{Aq}=-q_M$ The st2 water model and parameters for lithium iodide were used in the calculations. The temperature was 290K. The fast multipole method for long range coulomb interactions was used to calculate all electrical forces. This is the first application of molecular dynamics combined with the fast multipole method to study properties of electric double layers at a metal surface.

INTRODUCTION

This paper describes exploratory molecular dynamics simulations of electric double layers composed of water and monovalent ions adjacent to a metal surface modeled by a Lennard-Jones 9-3 potential and an image potential. The goal of this work was not to describe a particular electrochemical system in great detail, rather it was to determine whether a broad range of double layer phenomena (1, 2) were accessible to simulation using simple models based on the parameters that described bulk properties. For this reason we did not seek to model any particular metal surface, but rather chose only to imbue our model with minimum characteristics of a metal. In choosing ions we selected for known extremes of behaviour. Lithium ion was chosen because it is strongly hydrated and does not normally contact adsorb (same as physisorb) on noble metal electrodes (1). Consequently lithium ion is expected to be confined to the diffuse part of any electric double layer that forms. Iodide was chosen because it does contact adsorb and could participate in any compact layer that formed next to the electrode. These attributes of the st2 model Li and I ions were demonstrated by Glosli and Philpott (3, 4) for charged dielectric electrodes. In calculations with ions adjacent to metals electrostatic interactions can

be large and long ranged due to the large dipole constituted by the ion and its image. Consequently when large scale interfacial structures organize in ionic systems it is imperative that the 'electrostatics' be calculated efficiently and with sufficient accuracy. For this reason we use the fast multipole method (fmm) of Greengard and Rokhlin (5), described briefly in a companion paper (6), to calculate the electrostatic interactions thereby avoiding the use of cut-offs, reaction fields and the like.

What is remarkable about the results of the calculations reported here is that systems with a few independent ions display the richness of features found experimentally. Beyond the scope of this present report is an in depth study of concentration effects. We describe only some preliminary work on effects accompanying an increase in electrolyte concentration. This section is concluded with a brief summary of previous studies in this area. There have been simulations of films of pure water between uncharged dielectric walls (3, 7-9), and charged dielectric walls (3, 4, 10, 11). Some of this work is noteworthy because of a predicted phase transition (10, 11). There have been numerous reports for uncharged metal walls (12-16), (17-20), including one for jellium (18) and several for corrugated platinum surfaces (15-17, 19, 20) predicting water at on top sites oxygen down on Pt(111) and Pt(100). There have also been some for electrolyte solutions between uncharged and charged dielectric walls (3, 4, 21, 22) emphasizing spatial distributions and hydration shell structure. There have been studies for electrolytes between uncharged metal walls (15, 23, 24). The work of Rose and Benjamin (24) is particularly interesting because umbrella sampling was used to calculate the free energy of adsorption. Finally we mention the studies of water between charged metal walls (25), and electrolytes between charged metal walls (25). In a lot but not all of this work the long range coulomb interactions were treated in an approximate way. The exceptions relied on the Ewald method or some modification. However the question of full image inclusion and the shape of the containing boundary has to be resolved even in some of these studies. Spherical boundaries are not appropriate for systems with a slab geometry. For the slab one has to perform the conditionally convergent Coulomb sums in a manifestly plane wise fashion (26). This is a old problem that has occurred in other areas of physics in connection with long range electromagnetic fields inside samples of arbitrary shape. It will not be discussed further here.

THE MODEL

The immersed electrode was modelled as follows. Integral charge in the aqueous phase q_{Aq}, was exactly balanced by charge on the metal q_M. This is an essential constraint of our immersed electrode model. The advantage of the model is we have less than half the number of water molecules needed to simulate a system with two metal electrodes. The metal was represented by two linearly superimposed potentials. Pauli repulsion and dispersive attractive interactions were represented by a 9-3 potential, and the interaction with the conduction electrons by an image potential. In the calculations described here the image plane and origin plane of the 9-3 potential were coincident. This was tantamount to choosing the image plane and the nuclear plane of the metal surface to be coincident. This was acceptable in our scheme because the Lennard-Jones core parameters σ are all large and the 'thickness' of the repulsive wall is also large (ca. 0.247 nm). On the other side of the simulation cell the electrolyte solution was constrained by the 9-3 potential of the second bounding surface (1.862 nm from the image plane of the metal). We refer to the second surface as a dielectric surface, it's main role was to limit the extent of the fluid phase and thereby make the calculations tractable. The simulation cell

was a cube with edge 1.862nm. It was periodically replicated in the xy directions parallel to the electrode surface plane. In summary of what's right with the model can be listed briefly. Long range coulomb interactions were included in essentially an exact way since all images generated by the metal surface were counted. The average 'mean field' molecular polarizabilities that get bulk properties right were included in the parameters defining the water model. Important effects omitted in this treatment: metal surface topology especially different sites, molecular polarizabilities, and molecular distortions.

In all the calculations reported here we use the parameters of the Stillinger (27, 28) st2 water model and the interaction parameters with Li and I ions developed by Heinzinger and coworkers (29). The st2 water molecule model consists of a central oxygen atom (O_st2 or O for short) surrounded by two hydrogen atoms (H_st2 or H for short) and two massless point charges (PC_st2 or PC for short) in a rigid tetrahedral arrangement (bond angle = $\cos^{-1}(1/\sqrt{3})$). The O-H and O-PC bond lengths were 0.10 nm and 0.08 nm respectively. The only Lennard-Jones 'atom' in st2 model is the oxygen atom. The hydrogen H_st2 and point charges PC_st2 interact with their surroundings (i.e. other atoms and surfaces) only via Coulomb interactions. Their charges are q_H=0.23570|e| and q_{PC}=-q_H. The O atom has zero charge. The Li and and I ions were treated as non-polarizable Lennard-Jones atoms with point mass and charge. The atom-atom interaction parameters are taken from Heinzinger's review (29). The (ε,σ) pairs are (0.3164, 0.3100), (0.1490, 0.2370) and (0.4080, 0.5400) for O_st2, Li ion and I ion respectively. The units are ε in kJ/mole and σ in nm . The usual combining rules were enforced for unlike species, namely: $\varepsilon_{AB} = (\varepsilon_{AA}\varepsilon_{BB})^{1/2}$ and $\sigma_{AB} = \frac{1}{2}(\sigma_{AA} + \sigma_{BB})$. The switching function interval ends R_L^{IJ} and R_U^{IJ} all vanish except for st2/st2 pairs, where $R_L^{ST2,ST2}$=0.20160 nm and $R_U^{ST2,ST2}$=0.31287 nm.

The atom-surface interaction parameters were those used by Lee at al (7), A=17.447x10^{-6} kJ(nm)^6/mole and B=76.144x10^{-3} kJ(nm)^3/mole for O, I ion and Li ion. The A and B parameters for H_st2 and PC_st2 were set to zero. The potential corresponding to these parameters describe a graphite-like surface. The Coulomb interaction between molecules was represented as sum of $1/r$ interactions between atomic point charges. These interactions were softened for small molecular separation in the established manner (7) by a switching function S . As already mentioned the short range part of the intermolecular interaction was modeled by Lennard-Jones potential between the atoms of each molecule. All molecule-molecule Lennard-Jones type interactions were cut-off in a smooth fashion at a molecular separation $R = 0.68$ nm by a truncation function T . The atoms of each molecule also interacted with the surfaces at $z = \pm z_o$ where z_o = 0.931 nm. Both surfaces were treated as flat featureless plates with a uniform electric charge density of σ on the metal plate at $+z_o$. This gave rise to a uniform electric field, $E = 4\pi K\sigma$, in the z-direction where

K the electrostatic coupling constant had the value 138.936 kJ.nm/(mole.e^2) in the units used in this calculation. Recall total charge on the electrode was q_M/e =0, ±1. The complete interaction energy U is,

$$U = \sum_{\substack{\beta\in A_j \\ i<j}} \left(\left\{ \frac{Kq_\alpha q_\beta}{r_{\alpha\beta}} \left[S(R_{ij}, R_L^{ij}, R_U^{ij}) - 1 \right] + 4\varepsilon_{\alpha\beta} \left[\left(\frac{\sigma_{\alpha\beta}}{r_{\alpha\beta}} \right)^{12} - \left(\frac{\sigma_{\alpha\beta}}{r_{\alpha\beta}} \right)^{6} \right] \right\} T(R_{ij}) + \frac{Kq_\alpha q_\beta}{r_{\alpha\beta}} \right) \qquad [1]$$

$$+ \sum_\alpha \left\{ -q_\alpha E z_\alpha + \left(\frac{A_\alpha}{(z_\alpha + z_o)^9} - \frac{B_\alpha}{(z_\alpha + z_o)^3} \right) + \left(\frac{A_\alpha}{(z_\alpha - z_o)^9} - \frac{B_\alpha}{(z_\alpha - z_o)^3} \right) \right\}$$

where i and j were molecular indices, and, α and β were atomic indices. The symbol A_i represented the set of all atoms of molecular i . The symbol R_{ij} was the distance between the center of mass of molecules i and j. The symbol $r_{\alpha\beta}$ was the distance between atoms α and β. For small R we followed the practice of modifying the the coulomb energy between st2 molecules and ions by the switching function $S(R, R_L, R_U)$ given by,

$$S(R, R_L, R_U) = \begin{cases} 0 & R < R_L \\ \dfrac{(R - R_L)^2 (3R_U - 2R - R_L)}{(R_U - R_L)^3} & R_L < R < R_U \\ 1 & R_U < R \end{cases} \qquad [2]$$

The values of R_L and R_U were dependent on the types of the molecular species that were interacting.

As mentioned above the tails of the Lennard-Jones pair interactions were cut off by the truncation function T. The form of T was given by,

$$T(R) = \begin{cases} 1 & R < R_L^T \\ \left(1 - \left(\dfrac{R - R_L^T}{R_U^T - R_L^T} \right)^m \right)^n & R_L^T < R < R_U^T \\ 0 & R_U^T < R \end{cases} \qquad [3]$$

The same truncation function has been applied to all non Coulombic molecular interactions, with R_L^T=0.63 nm and R_U^T=0.68 nm. The integers m and n controlled the smoothness of the truncation function at R_L^T and R_U^T respectively. In this calculation $n = m = 2$ which insured that energy was smooth up to first spatial derivatives.

Bond lengths and angles were explicitly constrained by a quaternion formulation of the rigid body equations of motion (30). The equations of motion were expressed as a set of first order differential equations and a fourth order multi-step numerical scheme with a 2 fs time step was used in the integration. At each time step a small scaling correction was made to the quaternions and velocities to correct for global drift. Also the global center of mass velocities in the x and y directions was set to zero at each time step by shifting the molecular translational velocities.

ELECTRODES IMMERSED IN ELECTROLYTE

This section describes briefly our studies of the immersed electrode using the model described in the last section. In the absence of ions 158 water molecules corresponded to about 4.5 layers of water. The layer was not complete in the sense that in the Lee model (7) the 216 water molecules organized roughly into six layers. Most of the simulations were run for 100 ps to anneal the film and then for a further 900 ps to gather configurations used in the construction of the density profiles shown in the figures. The density plots in Figures 1 and 2 used configurations stored every 1.0 ps. The density plots in Figures 3 to 6 used configurations stored every 0.5 ps.

158 st2 Waters. Immersed Metal Electrode

Uncharged Electrode. Figure 1 displays water component (molecule center of mass H_2O, proton H_st2, and point charge PC_st2) density profiles $\rho(z)$ for 158 st2 water molecules averaged in the xy plane with a bin size of 0.005 nm. The simulation time was 0.9 ns with configurations stored every 1 ps. There are four clearly visible peaks in H_st2, PC_st2 and H_2O, with some 'pile up' at the walls. Compared to the previous calculations of Glosli and Philpott (3, 4) the presence of the metal's image plane has almost no effect on the densities. The charge density shows weak positive deviations from zero at the boundaries due to the longer length of the O-H bond (0.1 nm) compared to the O-PC bond (0.08 nm). Qualitatively this appears little different from the two dielectric surface (3) result.

Anodically Charged Electrode. The results for field on resemble those published earlier for 216 st2 water molecules (3) in a weaker field of 2×10^7 V/cm (equivalent to 0.11 e/(nm)^2). In the current simulation the field is about three times stronger and the film effectively 0.3 nm thinner. Figure 2 shows the density profiles for a field that repelled protons away from the metal. Notice that there is an overall loss in structure in the water density, which appeared distinctly flatter than the corresponding profile in zero field (compare Figure 1). There was a distinct peak at the dielectric surface for H_st2 atoms that caused the left hand peak in the charge density. There was about 1.7e of charge in this peak and about -0.5e units in the adjacent negative going peak due to PC_atoms in the the first layer of water at the dielectric electrode. This negative charge comes from the main peak in the PC_density profile at -0.65 nm. At the metal electrode the oscillation in the charge density was less pronounced but qualitatively the same. The minimum at 0.75 nm was due to the distinct shoulder in the PC atom density and the peak at 0.6 nm was due to main peak in the H atom density at about 0.6 nm (see Figure 2).

In agreement with the earlier study, we see in the charge density a region that over compensated the charge next to the surface followed immediately by a layer of charge of opposite sign that in turn partially compensated the first. These layers were closer together than the diameter of a water molecule and were due to closer packing of water molecules at the surface. This packing was the result of partial breaking of H-bonds by the applied electric field and 9-3 surface field.

I^- and 157 Waters. Compact Layer on an Anodically Charged Metal

Iodide represents one extreme case of adsorption. Experimentally iodide is known to contact adsorb, in contrast to hydrated lithium ion which does not. The simulation cell contained one iodide ion and 157 st2 water molecules. In this simulation the field across the system was an attractive field for anions equivalent to that generated by -1 unit of electronic charge smeared uniformly over the z=+0.931 nm plane. Figure 3 shows density profiles for all the components of the system as a function of distance across the gap. The bin size used in accumulating the densities was approximately 0.005 nm.

The high field behaviour of one iodide ion in 157 waters was found to be similar to that found previously for iodide in LiI and 214 waters between charged dielectric electrodes (3, 4). Basically the iodide distribution here consisted of one sharp peak indicating that the ion spends almost all its time at the repulsive wall boundary of the metal, and this high field behaved like a strong contact adsorber. The narrowness of the distribution indicated that only short time excursions were made away from the surface. Figure 3 shows it to be rarely removed more than 0.1 nm from contact. The anion density profile was sharply peaked at z = 0.700 nm very close to the beginning of the repulsive wall at 0.684 nm. The point of closest approach was about 0.74 nm, and that farthest retreat was about 0.65 nm. In the charge density profile the iodide contributed a sharp negative peak on top of a rather broad negative density region centered around 0.72 nm due to the PC atoms of the first layer of water. We discuss this water layer next.

There was significant structure in water, H and PC densities near the metal boundary. The water density displayed four pronounced maxima and one minimum (see Figure 3): narrow peak at -0.67 nm due to water pile up at the dielectric boundary, a broad peak at 0.28 nm followed by an equally broad minimum at 0.43 nm likely due to water exclusion from the vicinity of iodide due to it's size, a peak at 0.56 nm due to 'non oriented surface water' and a sharp peak at 0.66 nm due to highly oriented surface water with one PC atom pointed directly at the metal.

This last feature must along with the sharp iodide peak be considered a key feature of the inner region of the double layer. The strongly oriented layer of surface water one molecule thick occurred when the applied field and anion and image field reinforced. The two peaks at z = 0.74 and 0.63 nm (δz = 0.11 nm) in the PC density arose from the negative charge on the same molecule, one pointing directly at the metal and the other away at the tetrahedral angle. The surface peak in the H density at 0.62 nm was approximately twice the area (over background) but at same position, clearly indicating that it belonged to the same highly oriented surface layer.

The PC density as mentioned already had two components near the surface. The peak at 0.74 nm contributed approximately -1.5|e| to the total negative charge (about -2.5|e|) in the large negative peak in the total charge density at 0.70 nm. Between -0.6 nm and 0.4 nm the H and PC densities are computed to be almost identical, so that this region was always neutral. Comparing the charge densities of pure water and this system we see that the presence of the ion and it's image created extensive polarization of the water. The metal boundary showed strong polar regions with alternating sign extending to out z = 0.2 nm as a result of water structure resulting from shielding of the fields of the charged electrode, adsorbed iodide ion, and the first layer of oriented water.

Li^+ and 157 waters. Diffuse Layer on a Cathodically Charged Metal

Figure 4 shows density profiles of the single lithium ion (normalized to unity), 157 waters, H and PC components, and the charge density across the system with a bin size of 0.005 nm. The density plots in this Figure used configurations from 100 ps to 1000 ps, stored every 0.5 ps.

In this simulation the field was reversed, the charge on the metal being -1.0lel, so that the positive ion was attracted to the metal on the right side of the figure. First thing to notice is the over all similarity to Figure 3 in the water, H and PC profiles except that the profiles for H and PC are reversed in the case of Li compared to I due to change in field direction. This means that there was a highly oriented layer of surface water with protons H pointing directly at the metal. This reversal was of course quite consistent given the reversal in the field and the fact that the direction of ion field and that of it's image were also reversed. The peak heights were larger in the present case for three reasons. First the protons H_st2 could get closer to the image plane than in the case of PC_st2 because O_H bond was longer. Second the field of the Li ion and its image was spread over a larger area of the electrode because it is located further from the electrode. Third the Li ions primary hydration shell penetrates to the wall and contributes localized water to the distributions.

The density profile for Li defines a bimodal diffuse region between -5.5 and 5.5 nm with a minimum at 0.15 nm. Throughout this region the total charge was mostly zero. The distance of closest approach to the hard wall of the metal was approximately 0.13 nm or the radius of a water molecule. At this extremum the primary hydration shell of the lithium ion has to be mixed in with the highly oriented layer of water at the surface. The positive ion felt the influence of its image and was 'splayed' against the hard wall thereby affording a further reduction in the distance of approach to less than $0.5(\sigma_{Li}+\sigma_O)$. Glosli and Philpott (3, 4) have discussed the adsorption of hydrated ions and their possible distances of approach. At the minimum of the bimodal Li ion distribution the distance from the hard wall was approximately 0.54 nm, which should be compared with 0.60 nm the distance corresponding to separation from the wall by two water molecules. The interpretation of the Li distribution now seems clear. The peak between -0.55 and 0.15 nm is most likely a diffuse layer component with distance of closest approach being the outer Helmholtz plane, whilst the somewhat weaker diffuse-like component closer to the metal represents the smaller statistical probability of penetrating past the outer plane into the inner layer. This latter process depends strongly on the exact nature of the forces acting at the surface (crystal plane sites, size of the ion, etc.) and in some experimental systems and might well be absent altogether. What is important here is the idea that nominally diffuse layer ions can penetrate the outer plane and comingle with inner layer species. As mentioned already the ability of an ion to do this will depend critically on double layer structure and topography of the electrode surface.

Li^+, I^- and 156 Waters. Weakly Oriented Water at the PZC

In this simulation the applied field was zero so there was no charge on the metal electrode. In some ways this case mimics the potential of zero charge (pzc). The main electrostatic fields are now amongst the charges making up the ions and water and their images in the metal surface at z = 0.931 nm. Figure 5 displays the density profiles for water, protons H_st2, point charges PC_st2, each ions and the total charge density as a function of position across the film.

Some of the features were similar to those discussed already. Emphasize here is on major points of difference. The surface electric fields due to ions and their images were weaker since there was no net applied field and the image fields of the ions tend to cancel on the average. We note first of all that all the water related densities were flatter across the whole film, the H and PC surface peaks appear only as shoulders, just as in the case already examined of water in zero field. This means that first layer of water was not well oriented as in the previous two examples. This is of course consistent with the experimental finding that at the pzc water is less well bound. Consistent with this conclusion was the observation that the charge density was positive at the extreme edge of the film. This is consistent with the known result for water without ions (3) and the charge profile displayed in Figure 1.

Note that the iodide density has a tail not present in any of the simulations with non-zero fields, that overlaps the tail of the Li ion distribution. This was a new feature that signals the possible formation of temporary ion pairs in the double layer. In this case the contact adsorbed ion attracted compensating ion of opposite sign from out of the diffuse layer. In the present case the separation between iodide peak and nearest Li peak was approximately 0.55 nm. This would seem to rule out an ion pair configured with nuclei along the surface normal with interposed water molecule from the primary solvation shell of the cation. This configuration would require a separation of 0.7 nm for all centers to be colinear.

That this interaction could locally alter the diffuse layer can be seen by comparing the diffuse regions of Li ion in Figure 4 with that shown in Figure 5. The idea of altering the position of the outer plane to change the field across the inner layer has been proposed many times. We cite only one example from our own experimental work (31). References to the work of Bewick can be found there. Clearly this phenomenon could be studied further even with the primitive model used here.

The minimum in the bimodal Li ion distribution was at approximately -0.1 nm. At this position the Li ion was separated from the hard wall by 0.784 nm, much more than two water molecules. At the pzc the Li ion was not bound by a charge originating on the metal. It was bound by the field of the contact adsorbed species and its image. Since this was a dipole field the attraction between the iodide and lithium ions was weak. The Li ion in the density between -0.55 and -0.10 nm may be metastable and may well displace to larger separations if the water film were thicker.

Li^+, two I^- and 155 waters. Diffuse and Compact Layers

In this simulation there was a field of approximately $5x10^7$ V/cm attracting negative ions to the metal. Figure 6 displays the density profiles for all components of the system and the charge density. The simulation time was 1000 ps with the first 100 ps discarded for equilibration, configurations were stored every 0.5 ps.

Note that both iodide ions were adsorbed in a sharply peaked distribution that resembled the single adsorbed iodide distribution in Figure 3 than the iodide distribution with the tail seen in Figure 5 of the last section. The single Li ion occupies a (possibly weakly bimodal) diffuse-like distribution between -0.6 nm and 0.3 nm. At large negative z this distribution has a gradually fall off that would be expected for an electrostatically bound species. In contrast the tail of Li ion in Figure 4 drops quickly suggesting it was modified by the presence of the confining dielectric wall. On the positive side the main component of the distribution ends at 0.05 nm. This latter position was 0.63 nm from the hard wall, and was roughly at the same place for the outer plane of Figure 4. The region between 0.05 and 0.3 nm defines, as in Figure 4, the region of greatly reduced probability of penetrating into inner layer and contacting the adsorbed iodide ions.

It was noticeable that the water structure near the metal surface was less well defined than for either a single iodide or a single lithium ion. The reason for this was another new effect, water displacement from the interface as large ions contact adsorb. There was less water to orient next to the metal, and the density profiles mirror this fact.

CONCLUSIONS

In the introduction the question was could the behaviour of molecules and ions near a metal surface be qualitatively modeled with bulk parameters. Broadly speaking the answer appears to be yes. This means that the range of phenomena predicted is consistent with experimental observation. It does not mean that in any specific case we can model detailed behaviour. We have shown how a simple model suffices to reproduce many phenomena familiar from experiments on electric double layers at the electrolyte-metal interface. A key tool was the use of the fast multipole method to accurately and efficiently calculate coulomb interactions so that long range electric fields were computed correctly. This is very important for polar systems. The phenomena described included: contact adsorption of large ions on metals driven by image interactions, diffuse layers of strongly hydrated species, an oriented boundary layer of water next to the electrode when it is charged, relatively poorly oriented water next to uncharged electrode, and a zone of overlap between ions of opposite sign again when the electrode is not charged.

Finally we point out that these calculations suggest that modelling the electrochemical interface can be readily extended to such diverse systems as: nanosized structures, microelectrodes, and polymer coated electrodes. A more detailed analysis of phenomena such as these will be presented elsewhere.

ACKNOWLEDGEMENTS

This research was supported in part by the Office of Naval Research.

REFERENCES

(1) J. O. Bockris and A. K. Reddy, *Modern Electrochemistry, Vol.2* (Plenum Press, New York, 1973).

(2) J. O. Bockris and A. Gonzalez-Martin, *Spectroscopic and Diffraction Techniques in Interfacial Electrochemistry, NATO ASI Series C* (Kluwer,Dordrecht,Holland, 1990), pp. 1-54.

(3) J. N. Glosli and M. R. Philpott, J. Chem. Phys. **96**, 6962-6969 (1992).

(4) J. N. Glosli and M. R. Philpott, J. Chem. Phys. **in press**, (1993).

(5) L. Greengard and V. Rokhlin, J. Comp. Phys. **73**, 325-348 (1987).

(6) J. N. Glosli and M. R. Philpott, ECS Symposium Fall 1992 Proceedings, **Toronto**, (1993).

(7) C. Y. Lee, J. A. McCammon, and P. J. Rossky, J. Chem. Phys. **80**, 4448-4455 (1984).

(8) J. P. Valleau and A. A. Gardner, J. Chem. Phys. **86**, 4162-4170 (1987).

(9) Y. J. Rhee, J. W. Halley, J. Hautman, and A. Rahman, Phys. Rev. B **40**, 36-42 (1989).

(10) A. M. Brodsky, M. Watanabe, and W. P. Reinhardt, Electrochimica Acta **36**, 1695-1697 (1991).

(11) M. Watanabe, A. M. Brodsky, and W. P. Reinhardt, J. Phys. Chem. **95**, 4593 (1991).

(12) N. Parsonage and D. Nicholson, J. Chem. Soc. Faraday Trans. 2, **82**, 1521 (1986). pages 1521-1535

(13) N. Parsonage and D. Nicholson, J. Chem. Soc. Faraday Trans. 2, **83**, 663 - 673 (1987). pages 663 - 673

(14) A. A. Gardner and J. P. Valleau, J. Chem. Phys. **86**, 4171-4176 (1987).

(15) E. Spohr and K. Heinzinger, Electrochimica Acta **33**, 1211-1222 (1988).

(16) E. Spohr and K. Heinzinger, Ber. Bunsenges. Phys. Chem. **92**, 1358-1363 (1988).

(17) K. Heinzinger and E. Spohr, Electrochimica Acta **34**, 1849-1856 (1989).

(18) J. Hautman, J. W. Halley, and Y. Rhee, J. Chem. Phys. **91**, 467-472 (1989).

(19) K. Foster, K. Raghavan, and M. Berkowitz, Chem. Phys. Lett. **162**, 32-388 (1989).

(20) K. Raghavan, K. Foster, K. Motakabbir, and M. Berkowitz, J. Chem. Phys. **94**, 2110-2117 (1991).

(21) R. Kjellander and S. Marcelja, Chemica Scripta **25**, 73-80 (1985).

(22) E. Spohr and K. Heinzinger, J. Chem. Phys. **84**, 2304-2309 (1986).

(23) J. Seitz-Beywl, M. Poxleitner, and K. Heinzinger, Z. Naturforsch. **46A**, 876 (1991).

(24) D. A. Rose and I. Benjamin, J. Chem. Phys. **95**, 6856-6865 (1991).

(25) K. Heinzinger, Pure Appl. Chem. **63**, 1733-1742 (1991).

(26) G. E. Schacher and F. W. de Wette, Phys. Rev. **136A**, 78-91 (1965).

(27) F. H. Stillinger and A. Rahman, J. Chem. Phys. **60**, 1545 (1974).

(28) O. Steinhauser, Mol. Phys. **45**, 335-348 (1982).

(29) K. Heinzinger, *Computer Modelling of Fluids Polymers and Solids,* (Kluwer,Dordrecht, 1990), pp. 357-404.

(30) M. P. Allen and D. J. Tildesley, *Computer Simulation of Liquids* (Oxford University Press, Oxford, 1989), pp. 88-90.

(31) K. Ashley, M. G. Samant, H. Seki, and M. R. Philpott, J. Electroanal. Chem. **270**, 349-364 (1989).

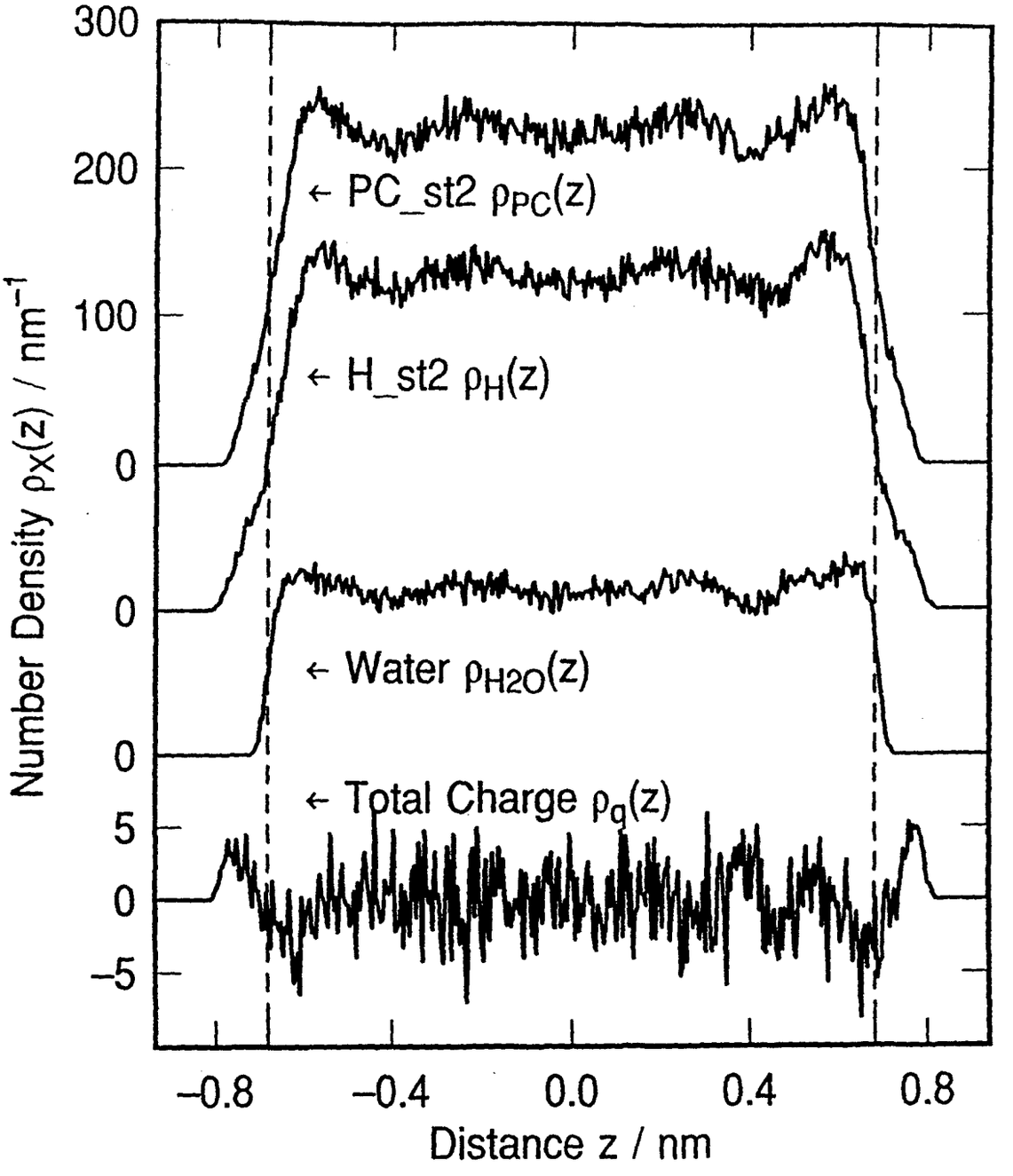

Figure 1. Water in zero field. Density profiles for 158 st2 water molecules adjacent to uncharged metal electrode on right side. Left side confining boundary is a dielectric surface with no image field. Gap between surfaces is $\Delta z = 1.862$ nm.

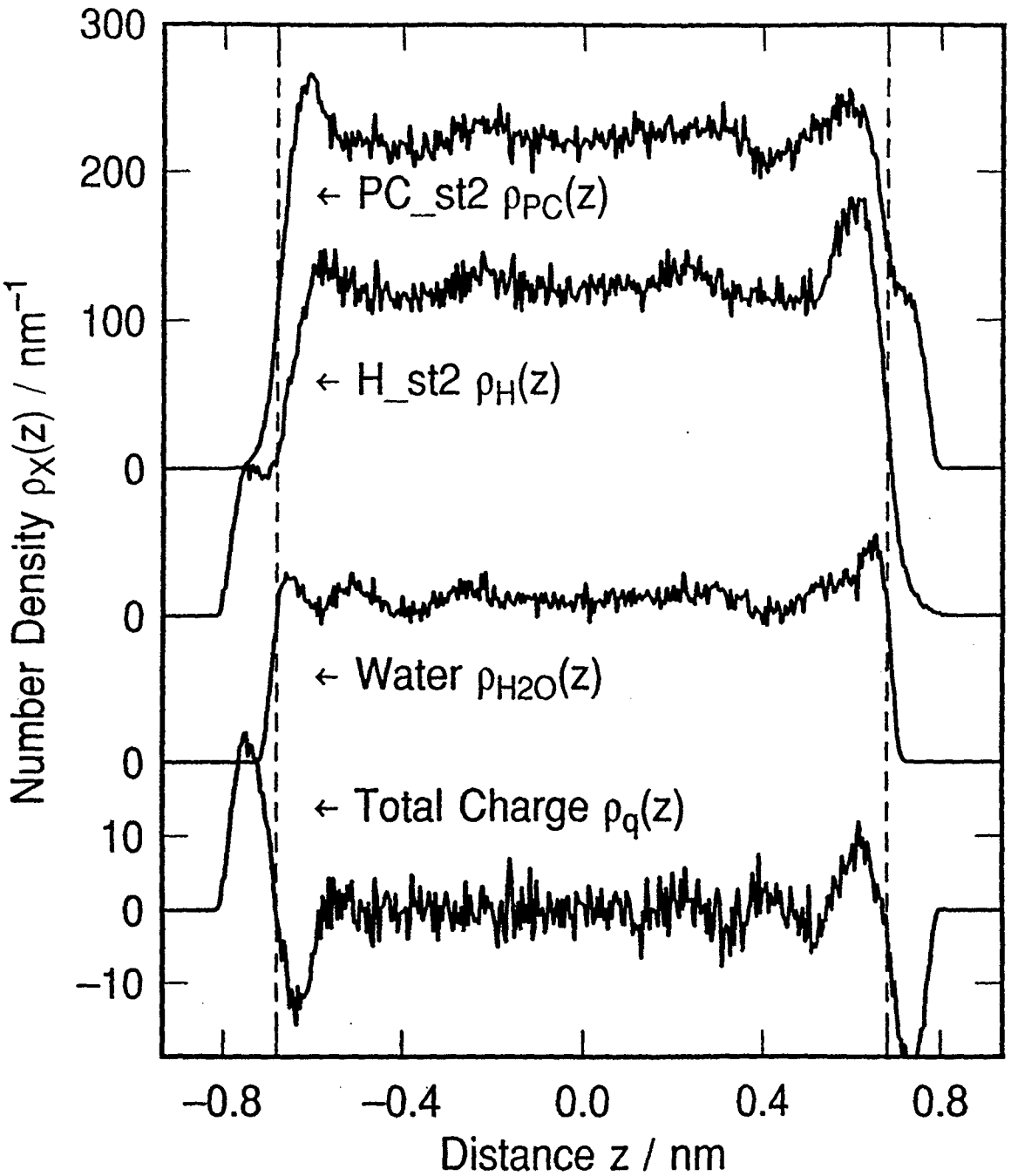

Figure 2. Water in field of 5×10^7 V/cm. Density profiles for 158 st2 water molecules adjacent to charged metal electrode on right side. Right confining boundary is a dielectric surface with no image field. Gap between surfaces is $\Delta z = 1.862$ nm.

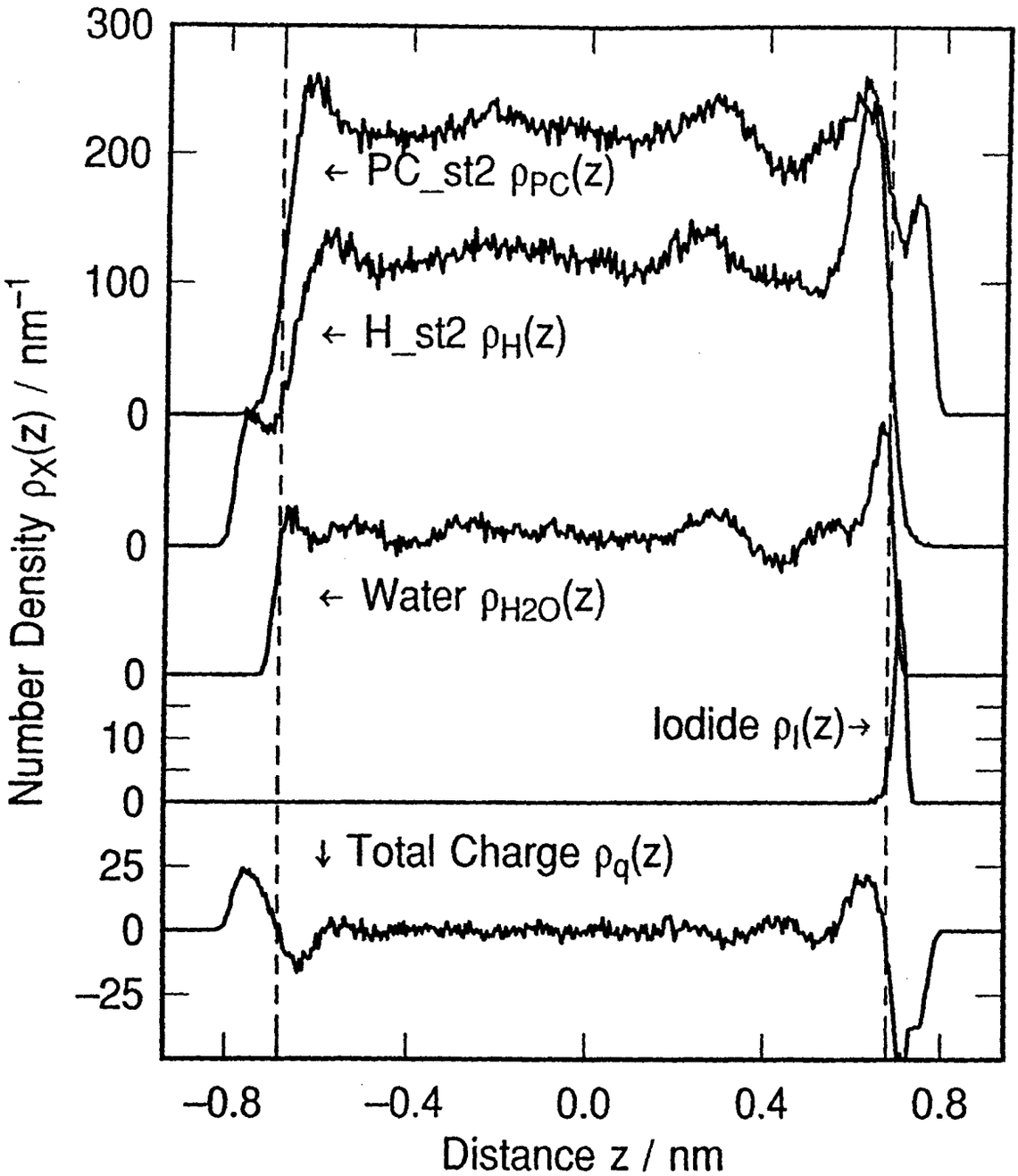

Figure 3. Density profiles for one iodide ion I^- and 157 st2 water molecules between a charged metal electrode and the dielectric boundary. The metal has anodic bias equivalent to a field of 5×10^7V/cm. Image plane at z = 0.931 nm . Repulsive portion of the wall potentials begin at |z| = 0.682 nm.

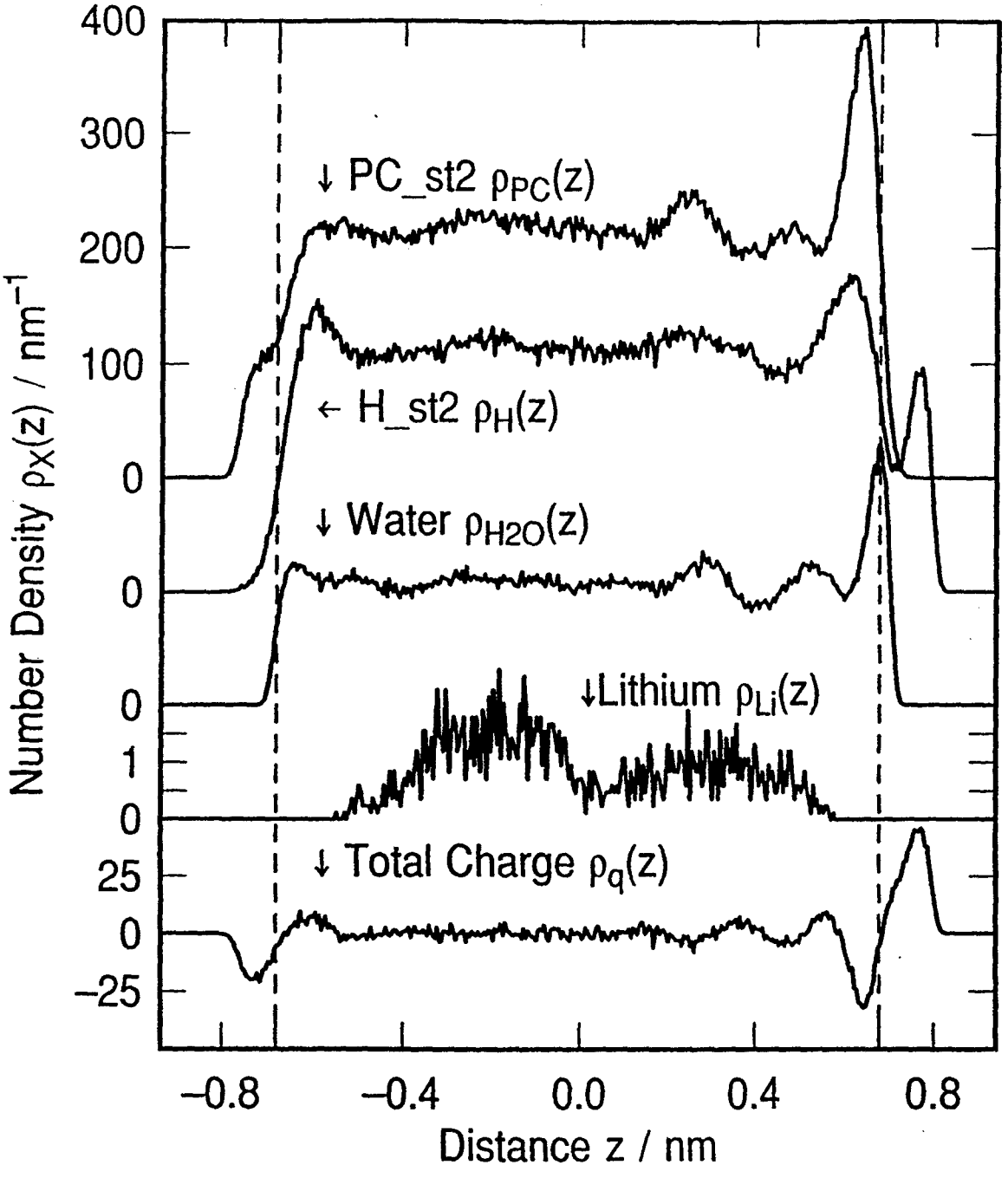

Figure 4. Density profiles for one Li^+ ion and 157 st2 waters near an immersed electrode with cathodic bias. Metal electrode on right hand side, dielectric on the left. Image plane at z = 0.931 nm and repulsive wall at |z|=0.682 nm.

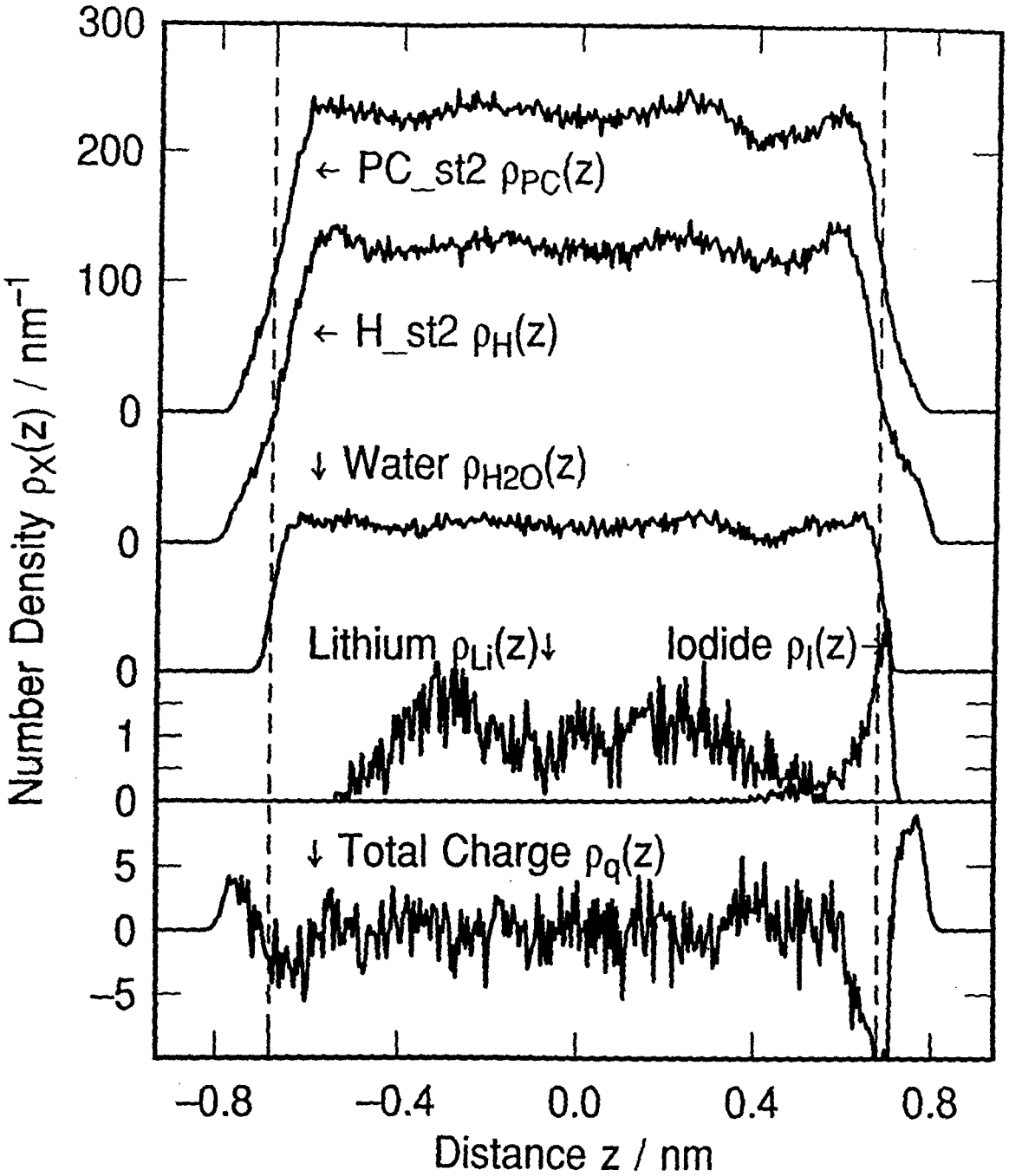

Figure 5. Density profiles for one Li^+ ion, one I^- ion and 156 st2 waters near an uncharged immersed electrode. Metal electrode on right hand side, dielectric on the left. Image plane at z = 0.931 nm and repulsive walls at |z|=0.682 nm.

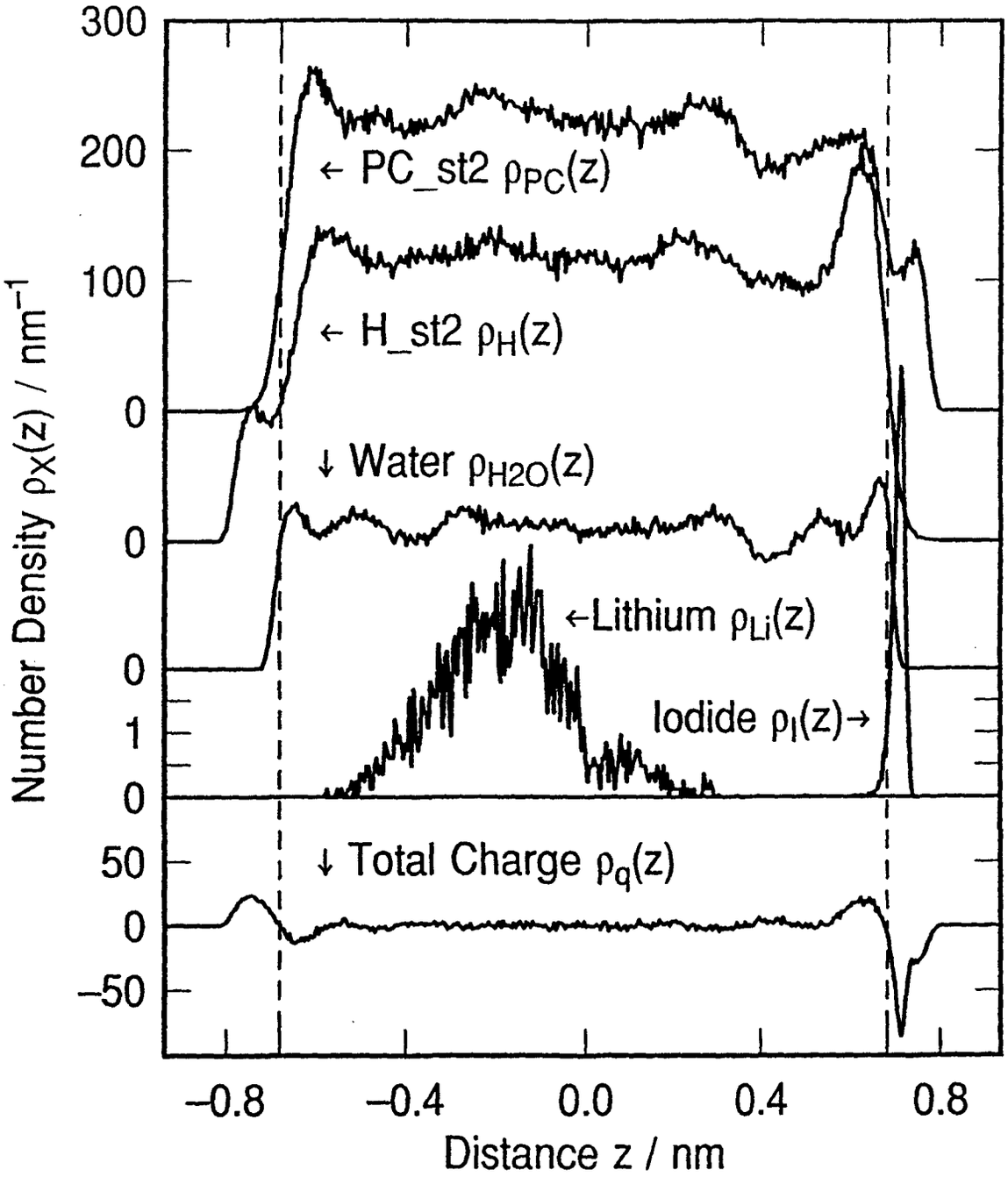

Figure 6. Density profiles for two I^-, one Li^+ and 155 st2 water molecules next to immersed electrode. Anodic bias corresponding to static electric field of 5×10^7 V/cm.

ADSORPTION OF HYDRATED HALIDE IONS ON CHARGED ELECTRODES. MOLECULAR DYNAMICS SIMULATION.

James N. Glosli
and
Michael R. Philpott

IBM Research Division
Almaden Research Center
650 Harry Road
San Jose, CA 95120-6099

ABSTRACT

Constant temperature molecular dynamics has been used to simulate the adsorption of hydrated halide ions $X^- = F^-$, Cl^-, Br^- and I^-, and lithium ion Li^+ on a flat uniformly charged surfaces. The simulations were done with either 214 water molecules and two ions (Li^+ and X^-) in a box 2.362 nm deep or with 430 water molecules and the two ions in a box 4.320 nm deep. The boxes were periodically replicated in the xy directions. The magnitude of the surface charge on the box ends was ± 0.11 c/(nm)^2, corresponding to an electric field of 2×10^7 V/cm. The lateral dimensions of the simulation cell were 1.862 nm × 1.862 nm (x × y) in each case. All of the water molecules and ions interacted with the end walls via a weak 9 - 3 potential. The ST2 water model and parameters optimized for alkali halides interacting with the model ST2 water molecule were used in the calculations. Common practices of truncating the interactions at a finite distance (0.82 nm) and switching off Coulomb interactions at small distances were followed. The temperature was set at T = 2.411 kJ/mole (290 K).

Some of the properties calculated were: distribution density profiles for ions and water across the gap important for comparisons with Gouy-Chapman theory, adsorbed ion - water pair correlation functions, the number of water molecules in the first and second hydration shells of the ions as a function of time. The time spent by a water molecule in the hydration shell was calculated to be approximately ten times longer for lithium than any other ion. The correlation between distance from the electrode and hydration number was studied and generally found to be pronounced for the larger anions. Comparison of the dynamics of the common ion Li^+ for different anions revealed the subtle influence of a transcell interaction in the 2.362 nm thick film.

In the given field the smallest ions Li^+ and F^- remained fully solvated at all times. Chloride behaved quite differently. Part of the time this ion was far enough away from the electrode to be fully hydrated and part of the time it was in physical contact (ie., physisorbed) on the

coordinates of ions, time dependence of ion hydration numbers, time averaged distribution of ions and water across the electrolyte film, and the ion-water pair correlation functions. The first property showed that the transition to contract adsorption first occurs for Cl^- in the given electric field. The second showed how solvation shells were affected as the adsorbed ions jittered back and forth under opposing influences of thermal forces and the combined attraction of the electric and wall forces.

All the frequently used water models (ST2, TIPS and SPCE) (7-9), have parameters optimized to bulk properties. Consequently none may be adequate to describe quantitatively a water molecule outside a mean field approximation to it's bulk environment. Our strategy to side step this difficulty is to perform calculations on a series of related ions in the expectation that by considering a series with the same charge and a graduated property like radius, the water-ion-wall interactions will span the experimental range of phenomena observed as ions approach a charged surface. The presence of the Li^+ counter ion in all the calculations provides a useful sanity check against pathological conditions that might arise due to the assumptions like finite cut-off of long range interactions. With the exception of Xe-Pt(111) system (10) there are no well proven or tested molecule- or ion-surface potentials. Consequently we are currently unable to connect directly with either ex situ measurements e.g., I^- on Pt(111) or Cl^- on Ag(100) performed by transferring emersed electrodes into UHV (11) or in situ surface crystallographic measurements like Sexafs and Xanes of under potentially deposited (upd) metals (12, 13).

In one respect the model used here was simpler than the set of assumptions constituting the standard model (2) of ionic adsorption on metal electrodes. In our model all species were attracted to the electrodes by the same 'wall' potential. This potential and the static electric field were not subject to the 0.82 nm cut-off applied to all the intermolecular interactions.

I.INTRODUCTION

In a previous paper (1), constant energy molecular dynamics simulations of the adsorption lithium and iodide ions from aqueous solution onto charged surfaces were described. This paper continues this study with an investigation of the halide series (fluoride, chloride, bromide, and iodide) characterized by increasing ionic radius and decreasing hydration enthalpies, adsorbed on an idealized flat charged surface situated at the ends of a box replicated periodically in the lateral (xy) directions.

Capacitance, chronocoulombic, spectroscopic and ellipsometric measurements of ions adsorbed at electrochmeical interfaces have long been interpreted using a standardized model (2-4). It has been shown that the larger ions adsorb with at least partial loss of the inner solvation shell. For metal electrodes this process is called contact adsorption, and on some noble metals a series has been determined in which higher members displace lower ones from the surface (2, 5). A fuller discussion was given in the first paper (1). It is a goal of this paper to understand more about the transition from adsorbed but fully solvated ion to adsorbed ion in physical contact with the surface when there is a static electric field attracting the ion to the surface. We tacitly assume this local property of the ions is not greatly affected by gross misshandling of the long range electrostatic fields of the interface through the application of the cut-off. The field chosen is at the upper end of fields in thermodynamically stable double layers. In weaker fields the average position of the ion was closer to film center (6). We show how essential features of the contacting process can be modeled with a system consisting of two ions and 214 water molecules sandwiched between charged nonmetallic plates 2.362 nm apart. More elaborate calculations with 430 waters, two ions and plates 4.320 nm apart were performed to check for transcell interactions between adsorbed ions. Such interactions were indeed found. The study revealed new features about the way the adsorption process proceeds. Properties calculated and reported here include: time dependence of the z

electrode with no water molecules interposed between it and the electrode. Bromide favoured contact adsorption over full hydration most of the time. Iodide was observed to be contact adsorbed almost all of the time. These simulations provide new insights on the behavior of strongly hydrated ions at surfaces and how the transition from non-contact to 'contact' adsorption occurs.

The ST2 parameters describing lithium and to a lesser extent fluoride are suspect because in the case of lithium ion the hydration enthalpy calculated is too large compared to experiment (14-16). It is possible that the adsorption of the smallest ions Li^+ and F^- as fully hydrated species in the $2x10^7$ V/cm field could be artifacts due to the exaggerated hydration enthalpy. However this argument does not affect our general conclusions if only because the applied static field used is at the upper end of fields encountered in electrochemical double layers and if more realistic model parameters had weaker hydration interactions there would still be fields where the small ions would adsorb fully hydrated. In weaker fields than the one used in this paper the ions relax towards film center (6). We will discuss the effect this could have on the interpretation of the calculations more fully in a later section.

Another point of concern is the electrical discharge of contact adsorbed ions. In the older papers and text books (2, 17) halide adsorption is treated as a physisorption phenomenon. However there is exceptionaly good experimental evidence that argues strongly that this is far too simplistic a picture. After contact adsorption a large polarizable ions like iodide on metals Au and Pt can 'discharge' and become chemisorbed (11, 18-21). Discharge of ions and the formation of chemisorbed species is outside the scope of the classical molecular dynamics scheme used here. tains its full charge.

We close this section with a brief review of recent MD calculations in the general area of solid - aqueous interfaces. In a very early study, the Mainz group (22, 23), followed the evolution of eight LiI and 200 water molecules between Lennard - Jones walls for 10 and 20 ps. They were only able to calculate short time correlation functions and not the adsorption process which required a longer simulation than they were able to do at the time. Rose and Benjamin (24) have described MD simulations of a single Na^+ and a single Cl^- ion in a slab of 512 waters (flexible SPC model (25),) between two Pt(100) surfaces. The geometry and potentials were those devised

by Heinzinger and coworkers (26, 27). For Pt(100) the first monolayer of water was strongly bound. A result of significance was the calculation of the Helmholtz free energy of adsorption in zero electric field. The anion was more strongly bound than the cation. More recently Seitz-Beywl et al (28) have studied hydration of Li^+ and I^- separately in three layers of water at the Pt surface. They used the flexible water model of Bopp et al (29), in a simulation lasting 7.5 ps. The work reported here is complementary to that cited and described above.

There is also continuing interest in thin films of water and electrolytes in connection with a possible phase transition (30, 31), vibrational relaxation dynamics, hydrogen bond formation dynamics (32, 33), and the interaction of water with metals treated as jellium half spaces (34).

This paper is arranged as follows. Section II describes the models used for ions and water and details of computation. Sections III through VII describe the results for the halide ions, and the last section summarizes the main results and conclusions for this series of simulations.

II. THE MODEL

In the calculations described here we use the water model originally devised by Stillinger (7, 35), and commonly referred to as the ST2 model. Although this model required more computer time because it contains four charged and one uncharged point particles, this draw back is more than compensated by the extensive set of Lennard-Jones parameters for use with all the alkali metal cations and halide anions. These parameters were developed in a series of molecular dynamics calculations by Heinzinger and Spohr (26, 27).

Interaction Energy

The Coulomb interaction between molecules was represented as sum of $1/r$ interactions between atomic point charges. These interactions were soften for small molecular separation by a switching function $S(R)$. This switching function was introduced by Stillinger (7), and was clearly documented by Steinhauser (35). The short range part of the intermolecular interaction was modeled by Lennard-Jones potential between the atoms of each molecule. All molecule-molecule interactions (both $1/r$ and Lennard-Jones potentials) were cut-off in a smooth fashion at molecular separation $R = 0.82$ nm by a truncation function $T(R)$. The atoms of each molecule also interacted with surfaces at $z = \pm z_o$. Both surfaces were treated as flat featureless plates with a uniform electric charge density of $+\sigma$ and $-\sigma$ on the $-z_o$ and $+z_o$ plates respectively. This gave rise to a uniform electric field, $E = 4\pi K\sigma$ in the positive z-direction where the electrostatic coupling constant K had the value 138.936 KJ•nm/(mole• e^2) in the units used in this calculation. Non Coulombic interactions between the walls and all the atoms were represented by the 9-3 potential (wall potential) introduced by Lee et al (36). The complete interaction energy U is,

$$U = \sum_{\substack{\alpha \in A_i \\ \beta \in A_j \\ i<j}} \left\{ \frac{K q_\alpha q_\beta}{r_{\alpha\beta}} S(R_{ij}, R_L^{ij}, R_U^{ij}) + 4\varepsilon_{\alpha\beta} \left[\left(\frac{\sigma_{\alpha\beta}}{r_{\alpha\beta}} \right)^{12} - \left(\frac{\sigma_{\alpha\beta}}{r_{\alpha\beta}} \right)^{6} \right] \right\} T(R_{ij}) \tag{1}$$

$$+ \sum_{\alpha} \left\{ - q_\alpha E z_\alpha + \left(\frac{A_\alpha}{(z_\alpha + z_o)^9} - \frac{B_\alpha}{(z_\alpha + z_o)^3} \right) + \left(\frac{A_\alpha}{(z_\alpha - z_o)^9} - \frac{B_\alpha}{(z_\alpha - z_o)^3} \right) \right\}$$

where i and j were molecular indices, and, α and β were atomic indices. Here A_i was the set of all atoms of molecule i , R_{ij} was the distance between the center of mass of molecules i and j, and The symbol $r_{\alpha\beta}$ was the distance between atoms α and β. For small R the Coulomb energy was modified by the switching function $S(R, R_L, R_U)$ given by,

$$S(R, R_L, R_U) = \begin{cases} 0 & R < R_L \\ \dfrac{(R - R_L)^2 (3R_U - 2R - R_L)}{(R_U - R_L)^3} & R_L < R < R_U \\ 1 & R_U < R \end{cases} \tag{2}$$

The values of R_L and R_U were dependent on the types of the molecular species that were interacting.

As mentioned above the tails of Coulomb and Lennard-Jones pair interactions were cut off by the truncation function $T(R)$. The form of $T(R)$ was given by,

$$T(R) = \begin{cases} 1 & R < R_L^T \\ \left(1 - \left(\dfrac{R - R_L^T}{R_U^T - R_L^T} \right)^m \right)^n & R_L^T < R < R_U^T \\ 0 & R_U^T < R \end{cases} \qquad (3)$$

The same truncation function was applied to all molecular interactions, with $R_L^T = 0.779$ nm and $R_U^T = 0.820$ nm. The integers m and n controlled the smoothness of the truncation function at R_L^T and R_U^T respectively. In these calculations $n = m = 2$ which insured that the energy had smooth first spatial derivatives.

Equations of motion

All molecules, in this study, were considered as a rigid collection of point atoms. That is all bond lengths and angles within a molecule were fixed. To evolve a collection of these molecules a quaternion formulation of the rigid body equations of motion was used (37). The center of mass position ($\mathbf{R}_i$) and velocity ($\mathbf{V}_i$) was used to describe the translational degrees of freedoms of molecule i. The orientational motion of the molecule was described by the quaternion $\mathbf{q}_i = (q_i^0, q_i^1, q_i^2, q_i^3)$ and the rotational velocity ($\boldsymbol{\omega}_i^b$), as measured in the body frame of the molecule. The one exception to this was for monatomic molecules, in which case the orientational degrees of freedom were not needed.

The discussion of the equations of motion begin by considering the potential energy U. From equation 1, it can be seen that the potential energy can be treated as a scalar function of the variables ($\mathbf{R}_1,..., \mathbf{R}_N; \mathbf{r}_1,..., \mathbf{r}_n$), where N is the number of molecules and n is the number of atoms in the entire system.

$$U = U(\mathbf{R}_1,..., \mathbf{R}_N; \mathbf{r}_1,..., \mathbf{r}_n) \qquad (4)$$

Of course not all these variables are independent. However for the purposes of the following two definitions they are treated as independent variables.

$$\mathbf{f}_\alpha \equiv \nabla_{\mathbf{r}_\alpha} U, \qquad \mathbf{F}_i \equiv \nabla_{\mathbf{R}_i} U. \tag{5}$$

The total force $\mathbf{F}_i^T$ and torque τ_i, can be expressed in terms of $\mathbf{f}_\alpha$ and $\mathbf{F}_i$ as

$$\mathbf{F}_i^T = \mathbf{F}_i + \sum_{\alpha \in A_i} \mathbf{f}_\alpha \qquad \tau_i = \sum_{\alpha \in A_i} (\mathbf{r}_\alpha - \mathbf{R}_i) \times \mathbf{f}_\alpha, \tag{6}$$

The translational motion of the molecule is described by the first order ordinary differential equation,

$$\frac{d\mathbf{R}_i}{dt} = \mathbf{V}_i \qquad M_i \frac{d\mathbf{V}_i}{dt} = \mathbf{F}_i^T. \tag{7}$$

For the rotational motion it is convenient to work in the body axis of the molecule, where the moment of inertia $\hat{I}_i$ is diagonal and time independent. It is useful to define the operator $\hat{Q}_i$

$$\hat{Q}_i = \begin{bmatrix} -q_i^1 & -q_i^2 & -q_i^3 \\ q_i^0 & -q_i^3 & q_i^2 \\ q_i^3 & q_i^0 & -q_i^1 \\ -q_i^2 & q_i^1 & q_i^0 \end{bmatrix} \tag{8}$$

and the body frame rotational force

$$\mathbf{F}_i^R = \tau_i^b - \omega_i^b \times (\hat{I}_i^b \omega_i^b). \tag{9}$$

Using these quantities above, the following first order ordinary differential equations can be written to describe the rotational motion

$$\frac{d\mathbf{q}_i}{dt} = \hat{Q}_i \omega_i^b \qquad \hat{I}_i^b \frac{d\omega_i^b}{dt} = \mathbf{F}_i^R. \tag{10}$$

This set of equations conserve the total energy for time independent potentials (U) . A constant temperature ensemble may be simulated by introducing a velocity dependent term in the acceleration terms to constrain the total kinetic energy. The constant temperature equations of motion are written as,

$$\frac{d\mathbf{R}_i}{dt} = \mathbf{V}_i, \qquad M_i \frac{d\mathbf{V}_i}{dt} = \mathbf{F}_i^T - \gamma \mathbf{V}_i$$

$$\frac{d\mathbf{q}_i}{dt} = \hat{Q}_i \omega_i^b, \qquad (\hat{I}_i)^b \frac{d\omega_i^b}{dt} = \mathbf{F}_i^R - \gamma \omega_i^b. \tag{11}$$

$$\gamma = \left(\sum_i \mathbf{V}_i \mathbf{F}_i^T + \omega_i^b \mathbf{F}_i^b\right)/(2K)$$

This choice of γ ensures that the total kinetic energy of the systems is constant.

Model for water molecules and ions.

In the ST2 model the water molecule consisted of a central oxygen atom (O_ST2) surrounded by two hydrogen atoms (H_ST2) and two massless point charges (PC_ST2) in a rigid tetrahedral arrangement (bond angle = $\cos^{-1}(1/\sqrt{3})$). The O_ST2/H_ST2 and O_ST2/PC_ST2 bond lengths were 0.10 nm and 0.08 nm respectively. The oxygen atom was the only Lennard-Jones 'atom' in ST2 water. The hydrogen and point charges interacted with their surroundings (i.e. atoms and surfaces) by Coulomb interactions only. The ions were treated as non polarizable Lennard-Jones 'atom' with point mass and charge.

Interaction Parameters.

The atom-atom and atom-surface interaction parameters are given in Table I. These parameters are taken from work of Heinzinger and Spohr (26, 27). The combining

rules for unlike species were: $\varepsilon_{AB} = (\varepsilon_{AA}\varepsilon_{BB})^{1/2}$, $\sigma_{AB} = \frac{1}{2}(\sigma_{AA} + \sigma_{BB})$. The switching function interval ends R_L^{ij} and R_U^{ij} all vanish except for ST2/ST2 pairs, where $R_L^{ST2,ST2} = 0.20160$ nm and $R_U^{ST2,ST2} = 0.31287$ nm.

Simulation details

The systems considered had either 216 or 432 molecules and ions. In the main set of simulations a system of 214 water ST2 molecules, one Li ion and one halide ion were studied. For all systems the molecules were confined to a rectangular simulation box with dimensions 1.862 nm × 1.862 nm ×2.362 nm (x × y × z) and periodic boundary conditions in the x and y directions. In the calculations with 432 molecules the simulation box had the same x and y dimensions and was 4.230 nm thick in the z direction. Initially the molecules were randomly disposed on a cubic lattice with lattice parameter 0.31 nm. The equations of motion were integrated by a fourth order multi-step numerical scheme with a 2 fs time step. With this scheme the time step to time step rms fluctuation of quaternions length and energy/temperature was about 0.0002% and 0.0009%/0.002% respectively. Though small, these changes could lead to global drift, so at each time step a small scaling correction was made to the quaternions and velocities. Also the global center of mass velocities in the x and y directions was set to zero at each time step by shifting the molecular translational velocities

All calculations were performed on an IBM RS/6000 model 540 operating at 16 Mflop. For the simulations involving 432 molecules and ions a 100 ps simulation with 2 fs time step took approximately 25 hours.

Ion-water pair correlation functions.

The ion - water pair correlation functions for all the ions were calculated in the manner described in the first paper (1). Figure 1 shows the result for all the ions studied in this paper, the distribution including only water molecules in a cone with

half angle 60° pointing into the bulk with axis parallel to the z axis. For chloride, bromide, and iodide the second peak appeared identical. The third peak in the figure contained a narrow minimum at 0.8 nm. This is indicated by the arrows in Figure 1. This feature was due to the seam in the water distribution due to the truncation of all interactions between 0.779 and 0.820 nm (see Eqn.3).

Cross correlation values.

The correlation between two variable v and w was tested by evaluating the cross correlation factor β,

$$\beta = \frac{< vw > - < v > < w >}{\sqrt{(< vv > - < v >^2)(< ww > - < w >^2)}} \tag{12}$$

where $< \phi >$ denote the average of ϕ . If v and w are completely uncorrelated, β vanishes and if v and w are highly correlated, the magnitude of β will be close to one. The cross correlation factor was used to explore the correlation between the ion's position and hydration number

Residence and Exchange Times

It was of interest to consider the mean residence time of a water molecule in a ion's hydration shell. The hydrations shell's inner and outer radii r_i and r_o respectively are determined by the minimums of the ion-water pair correlations function. A water molecule is consider to have entered the hydration shell when the water-ion separation r satisfies the relationship, $r_i(1+\delta) < r < r_o(1-\delta)$ for the first time. The parameter δ is a small number that filters out water molecules that only make very short time excursions into the shell. For this calculation δ is chosen to be 0.1 . A water molecule is then consider to have left the hydration shell when $r < r_i(1-\delta)$ or $r_o(1+\delta) < r$ In this case δ filter out events where a water molecule makes a short time excursion out of the shell. We consider the residence of this water molecule about

the ion to be the time between these two events. Then mean residence time T_R is approximated by averaging this time over all water molecules than both enter and leave the hydration shell during the simulation.

A related measure of the rate of change of the hydration shell, is the mean time of change of the hydration shell. This is simply the average time between events where the set of water molecules that constitute the hydration shell changes. In this paper a hydration shell is consider to have changed if it membership differs from the original for more than 1ps A stable hydration shell is considered to be created when its membership remains unchanged for more that 1ps. The mean time to change :.fT sub C is defined as the time to change of a stable hydration shell averaged over all stable shells created in the simulation.

III.RESULTS FOF LiF

Figure 2 shows the time evolution of the z coordinate (see left side vertical scale) of the lithium ion and fluoride ion for a time period lasting 1000 ps, in a cell also containing 214 water molecules. The broken lines at $|z| = 0.934$ nm at top and bottom of the figure indicate where the hard wall part of the surface potential begins i.e., where $V(z) = 0$. The configurations used in constructing this figure were 1 ps apart. In the starting configuration both ions were located near the cathode corresponding to time t and position z given by $(t, z) = (0, -0.5)$. In Figure 2 this corresponds to a point near the bottom left edge. Under the influence of the electric field the fluoride ion migrated the greatest distance, traversing most of the water layer to reach the anode corresponding to the broken line at $z = 0.934$ nm at the top of the figure. It took approximately 100 ps for the fluoride ion to traverse the film. It is not unreasonable to assume that during this time the solvent underwent considerable mixing, and that sufficient time lapsed sufficient time for the whole system to settle into the part of phase space describing equilibrium of the ions and associated waters. Notice that in the applied field the path of the z coordinate of the fluoride ion for the first 100 ps was not a monotonically increasing function of time. The initial movement was best described as a steady drift with superimposed high frequency jitter most likely due to interactions of the ion's primary solvent shell with surrounding solvent. This type of motion has been frequently seen in our studies of hydrated ions, and may well be typical of ions pushing through a H-bonded network. For times greater than 100 ps the time dependence of the z coordinate of both ions looks qualitatively the same. The range of positions for the ion was about 0.4 nm, not much more than the diameter of a water molecule ($\sigma = 0.31$ nm). The time averaged position of the fluoride ion was -0.668 nm, about one water diameter from the hard wall region ($|z| = 0.934$ nm).

Also shown in Figure 2 as a function of time for each ion are the numbers of water molecules in the first and second solvation shells. The data was sampled every 5 ps not every 1 ps as for the z coordinates. The radii of the solvation shells were chosen to be at the minima in the calculated ion-water pair correlation functions. For lithium these were at r = 0.2785 nm (first shell) and r = 0.500 nm (second shell). For fluoride these were at r = 0.3405 nm (first shell) and r = 0.5527 nm (second shell).

It can be seen that for lithium the first shell contained six waters with very infrequent excursions to five and seven. There was one event that lasted more than five picoseconds (see bottom right in Figure 2). The time averaged first hydration shell number was n = 6.01 . This is consistent with the calculation of Szasz et al (38), who reported the same value for bulk electrolyte, and the neutron scattering experiments of Newsome et al (39), and Hewish et al (40). The mean time to change T_c of the first solvation shell was between about 25 ps and 35 ps. This was in the range of all the other calculated values for the lithium ion with different anions. Table II summarizes the hydration water residence times for all the ions. In the case of lithium the residence time was about 100 ps for the first shell. This was about an order of magnitude larger than for the second shell, and approximately consistent with the mean time between changes (25 x 6 vs. 106 ps). These numbers are consistent with those reported for ions in a bulk environment in the interesting paper of Impey et al (15). Roughly the residence times on Li^+ ions in different LiX solutions were the same, with the larger values associated with greater statistical uncertainty. It was also three times greater than residence time for water in the first shell of fluoride ion. For the first shell there did not appear to be much correlation between position and hydration number for the first shell. The calculated correlation coefficient was 0.1. In the second shell the hydration number fluctuated between seven and sixteen, with a calculated average value of 11.4, displayed a strong correlation with distance from the electrode. The correlation coefficient of 0.5 supported the visual impression. The

mean time to change of the second shell was a not much larger than the sample interval and so not reliable, except to say that it was of the order of 1 ps. The picture that emerged was that the lithium ion and it's first shell be considered as a rather stiff or even as a rigid object, surrounded by a compliant second shell.

For fluoride the first shell contained seven waters with frequent excursions to six and seven, and a few to five. The average first shell hydration number was 6.8. The mean time between changes of the first shell was 3 ps. This was an order of magnitude smaller than for lithium. The residence time (see Table II) for hydration water was about 25 ps, in the 216 molecule system, and a little longer (33 ps) in the larger system. The differences are not large enough to be considered significant. There was no apparent correlation between first shell hydration number and position, and this was reflected in the calculated correlation of 0.18. In the second shell the hydration number fluctuated between ten and twenty two, with an average value of 15.4. There was a correlation with distance from the electrode about the same as in the second shell of lithium. The correlation coefficient was 0.57.

Figure 3 shows the density profiles for lithium and fluoride ions (normalized to unity) and water (normalized to 214) across the gap. Only configurations with time greater than 100 ps were used in accumulating this density profile. The figure also shows schematically a cartoon of the relative positions of the ions and water molecules in the first hydration shell closest to the surface. Clearly in the density 'peak' position both ions are hydrated. Not surprisingly the cation has a peak closer to the electrode since it is the ion with the smaller radius. The lithium peak position was at -0.709 nm and the fluoride was at 0.661 nm. The average positions were -0.668 nm (Li^+) and 0.628 nm (F^-). The difference 0.05 nm should be compared to the difference in Lennard-Jones radii which is 0.08 nm. The range of positions of both ions is very similar, a little less than 0.5 nm in each case. The hydrated ions have the density profile of a particle trapped in a well undergoing Brownian motion. For convenience

the main features of the densities for ions and water are collected into Tables III and IV.

The water density profile has interesting features. The larger peak at -0.803 nm was due to water in the first layer of the sample. When structure in the water distribution is compared with the ions it is clear that the larger size of the anion is responsible for the shallow minimum located near 0.66 nm. This conclusion was further substantiated by the increase in size of this feature with size of the anion. This will be seen clearly in later figures of density profiles. Calculations of the density profiles for water center of mass and the hydrogen atoms were also performed. The most interesting feature of these calculations was a small but distinct peak in the hydrogen distribution near the cathode at -0.992 nm. This was due to protons oriented towards the electrode.

Figure 4 shows density profiles calculated with the wider box (4.230 nm) containing twice as many molecules and ions. The hard wall was located at $z = \pm 1.868$ nm. Notice that the density profiles are narrower (smaller full width at half maximum). The reason for this was traced to smaller fluctuations in the positions of the ions because of weaker transcell interactions. The plots of z vs. t (time) did not show the same range of movement seen in Figure 2. Also the ions were more strongly adsorbed as judged by their peak positions, which were each closer to their respective electrodes. The peak positions relative to the hard wall are listed in Table III. For fluoride the distance from peak to hard wall was 0.13nm compared to 0.27 nm for the thinner film with 216 molecules and ions. The cartoon for the fluoride ion shows in to be closer to the electrode in Figure 4 compared to Figure 3. There was also a small shift to the electrode for the cation, but it was smaller due to stronger binding of the waters of hydration. With a cut off radius of 0.82 nm the ions did not couple directly by Coulomb interactions. There was no overlap of the range of the interactions that would be possible at times in the 2.362 nm thick sample.

There is some concern that the transcell ion attraction in the thin films may be an artifact due to the truncation of the Coulomb potentials of the sort recently described by Bader and Chandler. (41). Bader and Chandler identified an artificial, truncation induced attraction between ion of like charge, however argue that for ions of unlike charge such artifacts should be reduced. This and the fact that the transcell attraction is decreasing with film thickness argue that we are not seeing such truncation induce effects.

Figure 4 also showed that the water at the interface was quieter, as measured by the peaks and troughs in the water density profile. Major feature positions are recorded in Table IV. Note first that the density in the middle of the films was about the same. The peaks corresponding to surface water were higher at both surfaces relative to bulk for the 432 molecule system compared to the 216 system. Corroborating this notion was the deeper water exclusion trough near the fluoride ion, implying a higher degree of time averaged organization around the anion.

V. RESULTS FOR LiCl

Figure 5 shows the time evolution of the z coordinate for the lithium ion and chloride ion in a 216 molecule and ion simulation. Shown also is the time dependence of the number of water molecules in the first and second solvation shells for chloride. Lithium is not shown because it was essentially identical to the result already plotted in Figure 2. The starting configuration was the same as previously described for LiF. Note first that the time dependence of the lithium ion was qualitatively the same as in the LiF simulation and is not discussed further here. The time dependence of the z coordinate for chloride was different to fluoride. During the first 100 ps of the LiCl simulation hydrated Cl^- moved faster under the influence of the electric field and arrived at the anode sooner than fluoride did under similar conditions. This observation is significant since it is in qualitative agreement with experimentally measured transport numbers in dilute solutions (42-44). This difference was due to the larger effective radius of hydrated fluoride which binds its solvation shells more tightly than the chloride ion. In passing we note that the chloride ion z coordinate also showed jitter similar to that already described for fluoride in Figure 2.

For times greater than 100 ps the time dependence of the z coordinate of chloride looks qualitatively different from the strongly hydrated ions fluoride and lithium. First note that the chloride nucleus occasionally touches and penetrates the hard wall, which in zero electric field occurs at $|z| = 0.934$ nm. This means that chloride spends some time contact adsorbed, in contrast to fluoride which never made direct physical contact with the electrode.

Inside the box in Figure 5 the data for the first and second solvation shells of chloride was sampled every 5 ps not every 1 ps as for the z coordinates. The radii of the solvation shells were chosen to be at the minima in the calculated chloride ion-water pair correlation functions. For chloride these were at $r = 0.3758$ nm (first shell) and $r = 0.6558$ nm (second shell).

For chloride the first shell fluctuated mostly in the range five to seven with excursions to three and occasionally as high as ten (not shown in the time spanned in figure 5). The average hydration numbers for the first and second hydration shells averaged over 900 ps were 6.1 and 20.8 respectively. The first number is consistent with the pioneering studies of Dietz et al (45), who calculated 6.5 $\pm$0.5 for the chloride ion in bulk electrolyte. There was an apparent correlation between first shell hydration number and position when the ion was close to the electrode. The calculated correlation was 0.51. For times greater than 100 ps the second shell hydration number fluctuated between twelve and thirty seven. The averaged hydration number was 20.8 for the second shell. Again there was apparent correlation with distance from the electrode and the calculated correlation was 0.81, higher than for the shells of smaller ions. The residence time for water on chloride was about 15 ps for the large system and a little smaller for the small system (see Table II). It was not dependent on shell indicating that the shells are mixing in comparable fashion consistent with water being weakly bound. This was the common description for all except the two smallest ions.

Figure 6 shows the z dependent density profiles for lithium and chloride ions (normalized to unity) and water (normalized to 214) across the film. Only configurations with times greater than 100 ps were used in accumulating these density profiles. The total simulation time was actually 1100 ps more than shown in the figure, so that for chloride statistics were collected for a total duration of 1000 ps. The main peak (average) of lithium ion occurred at -0.732 nm (-0.679 nm) with closest approach at -0.827 nm and furthest position at z = -0.283 nm. Values are tabulated in Table III. The lithium distribution resembles that for LiF quite closely.

For chloride the main peak (average) was at 0.709 nm (0.747 nm), closest at 0.968 nm and farthest point at z = 0.449 nm. The range of displacements of the chloride ion was about 0.5 nm. This was greater than shown in Figure 4 which only showed the first nanosecond, a large excursion away from the electrode occurred between 1000

ps and 1100 ps. Clearly the statistics were not sufficient to give a smooth distribution, and it is possible that the density is bimodal for a gap of 2.362 nm. If the density profile is bimodal then a calculation of the potential of mean force (46) will show two minima. This latter conclusion was also suggested by the rapidity of the transition from contact to non-contact adsorbed configuration (see Figure 4). It was considered not worthwhile to pursue this aspect further with the model used in this paper. The figure also shows schematically a cartoon of the relative positions of the ions and water molecules in the first hydration shell closest to the surface. Only when the chloride ion is furthest from the electrode at z = 0.5 nm, is it possible for the ion to be surrounded by a complete first solvation shell. The position of closest approach is slightly greater than 0.934 nm because the attractive electric field acts to pull the ion into the repulsive region. Also shown in Figure 6 is the water density distribution. Chloride being a larger anion than fluoride gives rise to a deeper minimum located near 0.66 nm the position of the main peak (at z = 0.71 nm) in the ion density. Other features in common with the fluoride simulations were the sharpness of the surface water peaks (at |z| = 0.898 nm) and a separate peak in the calculated proton distribution at z = -0.992 nm near the anode (not shown in Figure 6).

Figure 7 displays the density profile results for the thicker 4.230 nm film. Note the dramatic change in distributions for both ions. Each was found to be sharper and occupying a narrower range of Δz. The full widths at half maximum were comparable to those found for all the other thicker systems. The cartoon of hydration around the chloride ligand in Figure 7 showed that the anion was more strongly adsorbed than in the 2.3 nm film. The half widths and position shifts are consistent with the view that transcell coupling mediated by water polarization is responsible for the much broader distributions seen in the 2.36 nm films. The chloride distribution remained wider than any other ion in similar cells, suggestive of the behavior seen in the thinner film. Chloride behaved intermediate between adsorbed as a hydrated ion and adsorbed

in contact. The water exclusion zone near $z = 1.6$ nm resembled that seen already for the fluoride ion in Figure 4. All the water density profiles were remarkably similar, a fact reflected in part by the similarity in the values in Table IV.

VI.RESULTS FOR LiBr

Figure 8 displays the time dependence of the z coordinate of the lithium ion and a bromide ion during a simulation lasting 1000 ps. Unlike all the simulations presented so far this one started with an equilibrated system in which the ions were adsorbed on the electrodes. It was found that starting with the cubic lattice lead to the formation of an ion pair. The procedure used for bromide was to start with the 6 × 6 × 6 cubic array as before but in an electric field ten times stronger. The simulation was run in high field for 10 or 20 ps until both ions were in contact with the oppositely charged wall. In fields of 1.5×10^8 V/cm and greater even the cation was contact adsorbed. With the ions separated the field was then reset at $2x10^7$ V/cm. Dashed horizontal lines define the hard wall region of the wall potential starting at |z| = 0.934 nm. This is effectively the boundary surface of the electrode. Note that the bromide ion frequently touched the boundary, and so in this model is a moderate contact adsorber, more strongly bound than chloride in Figure 4, but not as strongly bound as iodide (vide ultra).

The time dependence of the z coordinate of the lithium ion was a little different to that found for LiCl and LiBr. The range of displacements is clearly smaller, which results in the distribution being narrower. We return to this subject later.

Shown in Figure 8 as a function of time for each ion are the numbers of water molecules in the first and second solvation shells of the bromide ion. The data was sampled every 5 ps not every 1 ps as for the z coordinates. The radii of the solvation shells were chosen to be at the minima in the calculated ion-water pair correlation functions. For bromide these were at r = 0.4024 nm (first shell) and r = 0.6588 nm (second shell), same as for chloride.

For bromide the contents of the first shell fluctuated between five and six waters with infrequent excursions to four and occasional jumps to values as high as nine. The

average value was 5.6 for the first shell. The higher values were only weakly correlated with positions further from the electrode. The correlation coefficient for the first shell was calculated to be 0.37. In the second shell the hydration number fluctuated between ten and twenty six. The hydration average value was 16.8 and the correlation coefficient was 0.86, implying a strong correlation with distance from the electrode. Table II shows the residence times follow the pattern established for chloride.

Figure 9 shows the distribution of Li^+, Br^-, and 214 water molecules in a strong electric field ($2x10^7$ V/cm) across the gap between the charged plates. The wall potential is shown for reference. Circles have the Lennard-Jones radii for the ions and water. The configurations were collected in the time interval 100 ps < time < 1000 ps. The range of bromide positions was: farthest z = 0.661 nm, closest z = 0.968 nm, and peak (average) position at approximately 0.874 nm (-0.861 nm). At the closest approach the negative ion lay inside the repulsive regime of the wall potential. In this simulation the anion engages in moderate contact adsorption, stronger than chloride but not as strong as in the case of iodide. Note the again the presence of the shallow minimum in the water distribution near the average position of the anion. This minimum is slightly more pronounced than in the case of chloride. It is due to exclusion of water molecules from the interface by the larger volume of the ion.

The results of simulations with a twelve (4.230 nm) water layer system are shown in Figure 10. The trend to contact adsorption with larger ionic size was continued. Again there was a narrow lithium distribution characteristic of the thicker film. What was of interest in comparing the density profiles in Figures 9 and 10, was their similarity. In all the other LiX systems the 2.36 and 4.23 nm films show how the transcell interaction drops in going to the thicker cell.

The transcell interactions between Li^+ and Br^- appeared weaker in thin cell compared say to LiF and LiCl. As with LiI, to be discussed in the next section, it appeared that as contact adsorption increased then the more the anion decoupled from the bulk

water and the smaller the perturbation on the cation due to movement of the anion perpendicular to the surface. As seen from the Figure 10 and the positions tabulated in Table III the lithium cation peak at z = -1.692 nm had moved a little closer to the hard wall, and the density profile was somewhat sharper. Indeed the lithium position was close to that for a lithium ion without an anion but trapped against the cathode by the static field used in all these simulations (6).

VII. RESULTS FOR LiI

The case of lithium iodide solutions at constant energy were described in the first (1) paper. New results are presented here for simulations done at constant temperature. Iodide represents the extreme case of contact adsorption. Experimentally iodide is known to contact adsorb on metals at potentials corresponding to thermodynamically stable electric double layers. in contrast to lithium ions which do not. Time dependence of the z coordinate of the lithium ion and a iodide ion during a simulation lasting 400 ps is shown in Figure 11. The sampling interval in these calculations was 0.5 ps, smaller than in all the previous calculations described so far which were all at 1.0 ps. The starting configuration was one previously obtained in the earlier study (1). As before the dashed horizontal lines define the repulsive region of the wall potential starting at $|z| = 0.934$ nm. This is effectively the boundary surface of the electrode. Note that the iodide ion spends almost all its time at the boundary, and in this model is classified as a strong contact adsorber. It makes only short time excursions away from the surface, and is rarely found more than 0.1 nm removed from contact.

Also shown in Figure 11 as a function of time for the iodide ion are the numbers of water molecules in the first and second solvation shells. The data was sampled every 2.5 ps not every 5 ps as for the hydration number plots in the figures for LiF, LiCl, and LiBr. The radii of the solvation shells taken from the calculated ion-water pair correlation functions were at $r = 0.4289$ nm (first shell) and $r = 0.6765$ nm (second shell).

For iodide the first shell fluctuated between two and eight, with four, five and six being the most frequent occupation number. The average value was 5.4 for the first shell with a correlation of 0.29 (weak, corresponding to no apparent correlation visible in Figure 11) between first shell hydration number and position. Because the ion was so strongly adsorbed the correlation was small. In the second shell the hydration

number fluctuated between eleven and twenty five. The average value was 16.8. A weak correlation with distance from the electrode was apparent, the calculated correlation was 0.63.

As shown in Figure 12 the essential features of the iodide distribution emerge even after a simulation running for 400 ps. The distribution of the Li^+ ion and the 214 water molecules looks very similar to LiF and LiCl solutions. In this simulation the anion exhibits strong contact adsorption. The anion density profile was sharply peaked (average) at z = 0.921 nm (0.886 nm) very close to the hard wall. The point of closest approach was 0.992 nm, and that farthest from the electrode was at 0.685 nm. The water distribution in Figure 9 has more noise than the one shown in Figure 6 for LiCl solution because of poorer statistics resulting from a simulation time of 400 ps duration. In spite of this the shallow minimum in the water distribution due to the ion displacing water was clearly visible near 0.70 nm. Table IV gives the salient features of all the water distributions.

In Figure 13 the results of the thick film density profile are displayed. As before the system was allowed to equilibrate for 100 ps before averaging over configurations collected during the next 900 ps. The iodide density distribution was the sharpest, of all the halide profiles for all the systems studied here. The peak value of nearly 14 nm^{-1} in the thick film compared to 11 nm^{-1} in the six layer film. A comparison of water density profiles showed them all to be very similar, with all the distribution differences occurring near the walls. The differences that did exist seemed to be related to the degree and strength of hydration of the adsorbed ions. Consistent with weaker coupling across this thicker film, the water distribution near the cathode where the Li^+ was adsorbed were superimposable for different anions in systems with 432 molecules and ions.

VIII. RESULTS FOR WEAKER FIELDS

This section resumes the discussion of the quality of water and ion parameters for surface studies begun in the introduction.

It has been pointed out (8) that small ion parameters over estimate the of hydration by as much as 25%. Consequently in the field we are using $2x10^7$ V/cm in our simulations, the ability of small ions like fluoride F^- and lithium Li^+ to adsorb with intact primary solvation shell is exaggerated compared to the larger ions. The magnitude of this field is at the upper end for stable electrochemical double layers so it is of interest to know what happens in weaker fields.

However it is an experimental fact that small ions like Li^+ and fluoride F^- do not chemisorb on to metals in the double region of electrode potentials, and this phenomenon is attributed to their strongly held primary solvation shells. There are even anions (PF_6^-, BF_6^- and ClO_4^-) that adsorb more weakly than fluoride (5), in that they distrurb the interface even less (lower capacitance). Consequently although the ST2 parameters for Li^+ do not qualitatively model the adsorption process at the value of the static field used here, the series of Heinzinger's anion parameters does model adsoption changes along the series. We do not expect this modelling to be quantitative, for example by predicting the value of the threshold field above which the lithium ion to be contact adsorbed.

To explore the static field dependence we calculated the density profile for a single Li^+ ion with 215 water molecules and a single I^- ion in 215 ST2 waters, for different values of the applied field. All other conditions in these simulations were the same as before.

For fields about seven times higher (ca.$1.5x10^8$V/cm), like the ones used in the calculations of Brodsky and Reinhardt (30, 31), the lithium ion was contact adsorbed and it was observed that all the waters of the film oriented with dipoles ||z. The

behaviour in the regime of weaker fields is more relevant to the present study. As the field was weakened the density profile of Li^+ ion shifted towards the middle of the water film. In zero field the density profile $\rho_{ion}(z)$ was a broad bell-like distribution with the tails reaching out to about $|z| = 0.5$nm. This result is consistent with that reported by Wilson et al (47) for a single sodium ion in a 2.0 nm thick film of water with two liquid - vapour boundaries, and can be interpreted as the ions migrating to maximize their polarization energy in the solvent. Relaxation times were found to be longer than 1 ns, because of the large configuration space explored. Consequently it was not possible to get good statistics by accumulating configurations with brute force dynamics. This problem could be better tackled using umbrella sampling (24) or some scheme to simplify the long time dynamics like those used to studied polypeptides (48).

In the case of iodide the peak in the density profile $\rho_{ion}(z)$ for a given field always occurred at a point closer to the charged wall than was the case for lithium ion. This is consistent with the previous calculations for I^- ion, and suggests that the establishment of the solvent structure around this large anion occurs gradually as the field is weakened and the ion pulls pulls back from the wall.

What can be concluded from these results? First because of differences in ionic radii the smaller ions will be more strongly hydrated than larger ions. As the strength of the field is increased ions with more strongly bound solvation shells will tend to spend more time contact adsorbed. Conversely, in the absence of a strong universally binding interaction such as an image interaction, the adsorbed ions will shift away from the electrode as the field is weakened. An exception will occur for large hydrophobic ions which might remain adsorbed in a configuration that maximized solvent entropy (it is well established that large neutral organics eg., benzene, are adsorbed most strongly at the potential of zero charge) (49).

IX. SUMMARY

The simulations described here have revealed some of the static and dynamical complexities of the adsorption of hydrated ions onto charged surfaces. The main features were as follows. i) The small ions Li^+ and F^- did not make contact with electrode in fields of $2x10^7$V/cm because of their strongly bound first solvation shells. There was a balance between electric and Lennard-Jones attraction and thermal fluctuations. In the thin film polarization coupling mediated by water molecules increased the size of the fluctuations experienced by the ions. ii) In the model used here chloride was the first ion to exhibit contact adsorption. In the 2 nm film it appeared to have a bimodal distribution. iii) The presence of adsorbed ions implies the presence of localized water held in place by the field of the ion and it's associated hydrogen bond network. The presence of large interfacial ions also means there is a depletion zone where fewer waters are located. iv) The time dependence of the first shell hydration numbers for lithium and fluoride corroborate the picture. The residence time of a water molecule on lithium ion was a factor of four longer compared to fluoride. The first solvation shell of chloride and the bigger ions were found to be all very dynamic with residence times around 10 ps according to the model used here. Exchange of water between the first shell and the bulk was less than about 1ps.

Finally we point out that their are significant physical effects not modeled in the present study. In particular rigid non polarizable models exhibit dielectric saturation. To more accurately account for relaxation around small ion core one clearly needs to enhance the models in significant ways outside the scope of the present study. In the extremely high fields near small ion cores water molecules will distort electronically and geometrically. To account for these effects commonly adopted enhancements include replacement of the repulsive r^{-12} core potentials with softer ones fashioned after exp(-ar), or better still a sum of exponentials obtained from a quantum chemistry

calculation, polarizable ions and neutral water molecules, and flexible water molecules. Work on incorporating these effects in useable models is in progress in our laboratory.

ACKNOWLEDGEMENT

This research was supported in part by the Office of Naval Research. R.Rafey is thanked for assistance with visualization graphics.

References

(1) J. N. Glosli and M. R. Philpott, J. Chem. Phys. **96**, 6962-6969 (1992).

(2) J. O. Bockris and A. K. Reddy, *Modern Electrochemistry, Vol.2* (Plenum Press, New York, 1973).

(3) R. Parsons, Chem. Rev. **90**, 813-826 (1990).

(4) C. Gutierrez and C. Melendres, *Spectroscopic and Diffraction Techniques in Interfacial Electrochemistry, NATO ASI Series C* (Kluwer,Dordrecht,Holland, 1990).

(5) G. Valette, J. Electroanal. Chem. **122**, 285 - 297 (1981).

(6) J. N. Glosli and M. R. Philpott, unpublished calculations (1992).

(7) F. H. Stillinger and A. Rahman, J. Chem. Phys. **60**, 1545 (1974).

(8) W. L. Jorgensen, J. Chandrasekhar, J. D. Madura, R. W. Impey, and M. L. Klein, J. Chem. Phys. **79**, 926-935 (1983).

(9) H. J. Berendsen, J. R. Grigera, and T. P. Straatsma, J. Phys. Chem. **6269**, 6267 (1987).

(10) J. A. Barker, C. T. Rettner, and D. S. Bethune, Chem. Phys. Lett. **188**, 471 - 476 (1992).

(11) J. L. Stickney, S. D. Rosasco, G. N. Salaita, and A. T. Hubbard, Langmuir. **1**, 66 - 71 (1985).

(12) M. F. Toney, J. G. Gordon, and O. R. Melroy, SPIE Proceedings **1550**, xxx - xxx (1991).

(13) T. Tadjeddine, D. Guay, M. Ladouceur, and G. Tourillon, Phys. Rev. Lett. **66**, 2235 - 2238 (1991).

(14) M. Mezei and D. L. Beveridge, J. Chem. Phys. **74**, 6902 - 6910 (1981).

(15) R. W. Impey, P. A. Madden, and I. R. McDonald, J. Phys. Chem. **87**, 5071 - 5083 (1983).

(16) J. Chandrasekhar, D. C. Spellmeyer, and W. L. Jorgensen, J. Amer. Chem. Soc. **106**, 903-910 (1983).

(17) J. O. Brockris, M. A. Devanathan, and K. Müller, Proc. Roy. Soc.(London) **A274**, 55-79 (1963.).

(18) R. F. Lane and A. T. Hubbard, J. Phys. Chem. **79**, 808 - 815 (1975).

(19) A. T. Hubbard, Chem. Rev. **88**, 633 - 656 (1988).

(20) M. R. Deakin and O. Melroy, J. Electroanal. Chem. 239, 321 - 331 (1988).

(21) M. R. Deakin and O. Melroy, J. Electroanal. Chem. 243, 343 - 351 (1988).

(22) G. I. Szasz, K. Heinzinger, and W. O. Riede, Z. Naturforsch. 36a, 1067 - 1075 (1981).

(23) E. Spohr and K. Heinzinger, J. Chem. Phys. 84, 2304-2309 (1986).

(24) D. A. Rose and I. Benjamin, J. Chem. Phys. 95, 6856-6865 (1991).

(25) H. J. Berendsen, J. P. Postsma, W. F. van Gunsteren, and J. Hermans, *Intermolecular Forces* (Reidel, Dordrecht, Holland, 1981), p. 331.

(26) E. Spohr and K. Heinzinger, Ber. Bunsenges. Phys. Chem. 92, 1358-1363 (1988).

(27) K. Heinzinger, *Computer Modelling of Fluids Polymers and Solids,* (Kluwer,Dordrecht, 1990), pp. 357-404.

(28) J. Seitz-Beywl, M. Poxleitner, and K. Heinzinger, Z. Naturforsch. 46A, 876 (1991).

(29) P. Bopp, G. Jansco, and K. Heinzinger, Chem. Phys. Letters 98, 129-133 (1983).

(30) M. Watanabe, A. M. Brodsky, and W. P. Reinhardt, J. Phys. Chem. 95, 4593 (1991).

(31) A. M. Brodsky, M. Watanabe, and W. P. Reinhardt, Electrochimica Acta 36, 1695-1697 (1991).

(32) S. Zhu and G. W. Robinson, J. Chem. Phys 94, 1403-1410 (1991).

(33) S. Zhu, T. G. Fillingim, and G. W. Robinson, J. Phys. Chem. 95, 1002-1006 (1991).

(34) J. Hautman, J. W. Halley, and Y. Rhee, J. Chem. Phys. 91, 467-472 (1989).

(35) O. Steinhauser, Mol. Phys. 45, 335-348 (1982).

(36) C. Y. Lee, J. A. McCammon, and P. J. Rossky, J. Chem. Phys. 80, 4448-4455 (1984).

(37) M. P. Allen and D. J. Tildesley, *Computer Simulation of Liquids* (Oxford University Press, Oxford, 1989), pp. 88-90.

(38) G. I. Szasz, K. Heinzinger, and G. Palinkas, Chem. Phys. Lett. 78, 194 (1981).

(39) J. R. Newsome, J. E. Enderby, and G. W. Neilson, J. Phys. C 13, L923 (1980).

(40) N. A. Hewish, J. E. Enderby, and W. S. Howells, J. Phys. C 16, 1777 (1983).

(41) J. S. Bader and D. Chandler, J. Phys. Chem. 96, 6423 - 6427 (1992).

(42) J. Burgess, *Metal Ions in Solution* (Halsted Press, John Wiley, New York, 1978).

(43) A. L. Horvath, *Handbook of Aqueous Electrolyte Solution* (Halsted Press, John Wiley, New York, 1985), pp. 196, 240.

(44) J. O. Bockris and A. K. Reddy, *Modern Electrochemistry, Vol.1* (Plenum Press, New York, 1973).

(45) W. W.Dietz, W. W.O.Reide, and K. K.Heinzinger, Z. Naturforsh. 37A, 1038 (1982).

(46) G. Ciccoti, M. Ferrario, J. T. Hynes, and R. Kapral, Chem. Phys. 129, 241-251 (1989).

(47) M. A. Wilson, A. Pohorille, and L. R. Prattd, Chem. Phys. 129, 209 - 212 (1989).

(48) G. R. Hu, G. R. Flemming, K. F. Freed, and A. Perico, Chem. Phys. 158, 395 - 408 (1991).

(49) F. Anson, Accts Chem. Res. 8, 400-407 (1975).

Table I The interaction parameters $(q, \varepsilon, \sigma, A, B)$ and mass (m) for all atoms used in the simulations, where $q_o = e$, $\varepsilon_o = 1 KJ/mole$, $\sigma_o = 1 nm$, $A_o = 17.447 \times 10^{-6} KJ \bullet nm^6/mole$, $B_o = 76.144 \times 10^{-3} KJ \bullet nm^3/mole$, and $m_o = 1 AMU$. The ε and σ for unlike atom pairs is formed from the combination rules, $\varepsilon_{AB} = \sqrt{(\varepsilon_{AA}\varepsilon_{BB})}$ and $\sigma_{AB} = (\sigma_{AA} + \sigma_{BB})/2$.

	q/q_o	$\varepsilon/\varepsilon_o$	σ/σ_o	m/m_o	A/A_o	B/B_o
O_ST2	0.0000	0.316	0.310	16.0	1	1
H_ST2	0.2357	0.000	0.000	1.000	0	0
PC_ST2	−0.2357	0.000	0.0	0.0	0	0
Li	1.0000	0.149	0.237	6.9	1	1
F	−1.0000	0.050	0.400	19.0	1	1
Cl	−1.0000	0.168	0.486	35.5	1	1
Br	−1.0000	0.270	0.504	79.9	1	1
I	−1.0000	0.408	0.540	129.9	1	1

Table II. Summary of hydration water residence times with the one sigma errors for LiX (X = F,Cl,Br,I) in water films with 216 molecules (2.362nm) and 432 molecules (4.320nm).

	LiF	LiCl	LiBr	LiI
2.362 nm film with 216 molecules				
Li^+ ion, 1st shell	122±25	168±43	115±43	
Li^+ ion, 2nd shell	12±0.5	12±0.4	12±0.5	
X^- ion, 1st shell	25±1.8	12±0.6	11±0.6	
X^- ion, 2nd shell	13±0.4	13±0.4	12±0.4	
4.320 nm film with 432 molecules				
Li^+ ion, 1st shell	106±14	97±12	87±17	130±22
Li^+ ion, 2nd shell	10±0.3	9±0.3	10±0.3	9±0.3
X^- ion, 1st shell	33±2.7	16±1.2	14±0.8	11±0.6
X^- ion, 2nd shell	15±0.6	16±0.6	16±0.6	15±0.5

Table III. Summary of density profile results of halide ions in two water films. All positions relative to closest wall at |z| = 0.934 (for 2.362nm film) and |z| = 1.868nm (for 4.320nm film).

	Li^+ [a]	F^-	Cl^-	Br^-	I^-
2.362nm film					
$z_{near} - z_h$ [b]	+0.084	-0.084	+0.034	+0.058	+0.058
$z_{pk} - z_h$ [c]	+0.225	-0.273	-0.225	-0.036	-0.013
$z_{far} - z_h$ [d]	+0.580	-0.556	-0.509	-0.320	-0.249
4.320nm film					
$z_{near} - z_h$ [b]	+0.044	-0.007	+0.062	+0.062	+0.062
$z_{pk} - z_h$ [c]	+0.202	-0.176	-0.044	-0.017	-0.017
$z_{far} - z_h$ [d]	+0.414	-0.440	-0.335	-0.308	-0.202

a lithium from LiF simulation

b z_{near}, point of nearest approach to electrode

c z_{pk}, position of peak in the density

d z_{far}, position of farthest point from electrode

Table IV. Summary of water density profile results for LiX (X = F,Cl,Br,I) two water films. All positions measured in nm relative to nearest hard wall at $|z_h| = 0.934nm$ (for 2.362nm film) and $|z_h| = 1.808$ (for 4.320nm film). The number in parentheses is the value in nm^{-1} of the density profile

	LiF	LiCl	LiBr	LiI
2.362nm film				
Peak on anion side	-0.060 (147)	-0.036 (143)	-0.036 (142)	-0.036 (135)
Minimum on anion side	-0.273 (103)	-0.273 (95)	-0.296 (93)	-0.273 (91)
Peak on cation Side	0.036 (133)	0.036 (140)	0.036 (138)	0.036 (138)
4.320nm film				
Peak on anion side	-0.044 (157)	-0.044 (150)	-0.044 (152)	-0.044 (141)
Minimum on anion side	-0.255 (96)	-0.282 (93)	-0.255 (90)	-0.255 (87)
Peak on cation Side	0.044 (146)	0.044 (149)	0.017 (151)	0.017 (147)

FIGURE CAPTIONS

Figure 1. Ion-water pair correlation functions for lithium and the halide ions. The four correlation functions for the lithium ions are superimposed showing their essential equivalence. For chloride, bromide, and iodide the second peak near 0.55 nm are also essentially the same within numerical error. The dip at 0.82 nm indicated by the arrows was due to the truncation function.

Figure 2. Time dependence of the z coordinate of the lithium ion and a fluoride ion during a simulation lasting 1000 ps. At time t = 0 ps both ions start out near the cathode. It takes the anion about 100 ps to migrate across the gap. Note that the electric fields keep the ions separated and restricted to vicinity of their respective electrodes. The ions are not free to diffuse throughout the gap. Dashed horizontal lines define the beginning of the hard wall repulsive region of the potential starting at |z| = 0.934 nm. This is effectively the boundary surface of the electrode.

Figure 3. Distribution of Li^+, F^-, and 214 water molecules in a strong electric field ($\sim 2 \times 10^7$ V/cm) across the gap between the charged plates. Wall potential shown for reference. Circles are Lennard-Jones radii for the ions and water. In this simulation the anion never contact adsorbs. Contrast this with the results of the simulation for LiCl, LiBr, and LiI. Note the shallow minimum in the water distribution near the average position of the anion.

Figure 4. Distribution of Li^+, F^-, and 430 water molecules in a strong electric field ($\sim 2 \times 10^7$ V/cm) across the gap between the charged plates. Wall potential

shown for reference. Circles are Lennard-Jones radii for the ions and water. In this simulation the anion never contact adsorbs. Contrast this with the results of the simulation for LiCl, LiBr, and LiI. Note the shallow minimum in the water distribution near the average position of the anion.

Figure 5. Time dependence of the z coordinate of the lithium ion and a a chloride ion during a simulation lasting 1000 ps. At time t = 0 ps both ions start out near the cathode. It takes the anion less than 100 ps to migrate across the gap. Note that the electric fields keep the ions separated and restricted to vicinity of their respective electrodes. The ions are not free to diffuse throughout the gap. Dashed horizontal lines define the hard wall region of the potential starting at $|z| = 0.934$ nm. This is effectively the boundary surface of the electrode. Unlike fluoride the chloride ion does touch the boundary, and in this model is able to contact adsorb in weak fashion.

Figure 6. Distribution of Li^+, Cl^-, and 214 water molecules in a strong electric field ($\sim 2 \times 10^7$ V/cm) across the gap between the charged plates. Wall potential shown for reference. Circles are Lennard-Jones radii for the ions and water. In this simulation the anion makes weak contact adsorption. Contrast this with the results of the simulation for LiBr and LiI, where the contact adsorption is more frequent and therefore stronger. Note the shallow minimum in the water distribution near the average position of the anion.

Figure 7. Distribution of Li^+, Cl^-, and 430 water molecules in a strong electric field ($\sim 2 \times 10^7$ V/cm) across the gap between the charged plates. Wall potential shown for reference. Circles are Lennard-Jones radii for the ions and water. In this simulation the anion makes weak contact adsorption. Contrast this

with the results of the simulation for LiBr and LiI, where the contact adsorption is more frequent and therefore stronger. Note the shallow minimum in the water distribution near the average position of the anion.

Figure 8. Time dependence of the z coordinate of the lithium ion and a bromide ion during a simulation lasting 1000 ps. Note that the electric fields keep the ions separated and restricted to vicinity of their respective electrodes. The ions are not free to diffuse throughout the gap. Dashed horizontal lines define the repulsive region of the wall potential starting at $|z| = 0.934$ nm. This is effectively the boundary surface of the electrode. Note that the bromide ion frequently touches the boundary, and so in this model is a moderate contact adsorber.

Figure 9. Distribution of Li^+, Br^-, and 214 water molecules in a strong electric field ($\sim 2 \times 10^7$ V/cm) across the gap between the charged plates. Wall potential shown for reference. Circles are Lennard-Jones radii for the ions and water. In this simulation the anion engages in moderate contact adsorption. Contrast this with the results of the simulation for LiF where there is no contact and LiI where the iodide makes strong contact. Note the shallow minimum in the water distribution near the average position of the anion.

Figure 10. Distribution of Li^+, Br^-, and 430 water molecules in a strong electric field ($\sim 2 \times 10^7$ V/cm) across the gap between the charged plates. Wall potential shown for reference. Circles are Lennard-Jones radii for the ions and water. In this simulation the anion engages in moderate contact adsorption. Contrast this with the results of the simulation for LiF where there is no

contact and LiI where the iodide makes strong contact. Note the shallow minimum in the water distribution near the average position of the anion.

Figure 11. Time dependence of the z coordinate of the lithium ion and a iodide ion during a simulation lasting 400 ps. Note that the electric fields keep the ions separated and restricted to vicinity of their respective electrodes. The ions are not free to diffuse throughout the gap. Dashed horizontal lines define the hard wall region of the potential starting at $|z| = 0.934$ nm. This is effectively the boundary surface of the electrode. Note that the iodide ion spends almost all its time at the boundary, and in this model is classified as a strong contact adsorber. It makes only short time excursions away from the surface.

Figure 12. Distribution of Li^+, I^-, and 214 water molecules in a strong electric field ($\sim 2 \times 10^7$ V/cm) across the gap between the charged plates. Wall potential shown for reference. Circles are Lennard-Jones radii for the ions and water. In this simulation the anion exhibits strong contact adsorption. The density profile is sharply peaked very close to the repulsive wall. Contrast this with the results of the simulation for LiF where there is no contact. Note the shallow minimum in the water distribution near the average position of the anion.

Figure 13. Distribution of Li^+, I^-, and 432 water molecules in a strong electric field ($\sim 2 \times 10^7$ V/cm) across the gap between the charged plates. Simulation time 1000ps. Wall potential shown for reference. Circles are Lennard-Jones radii for the ions and water. In this simulation the anion exhibits strong contact adsorption. The density profile is sharply peaked very close to the repulsive

wall. Contrast this with the results of the simulation for LiF where there is no contact. Note the shallow minimum in the water distribution near the average position of the anion.

F1

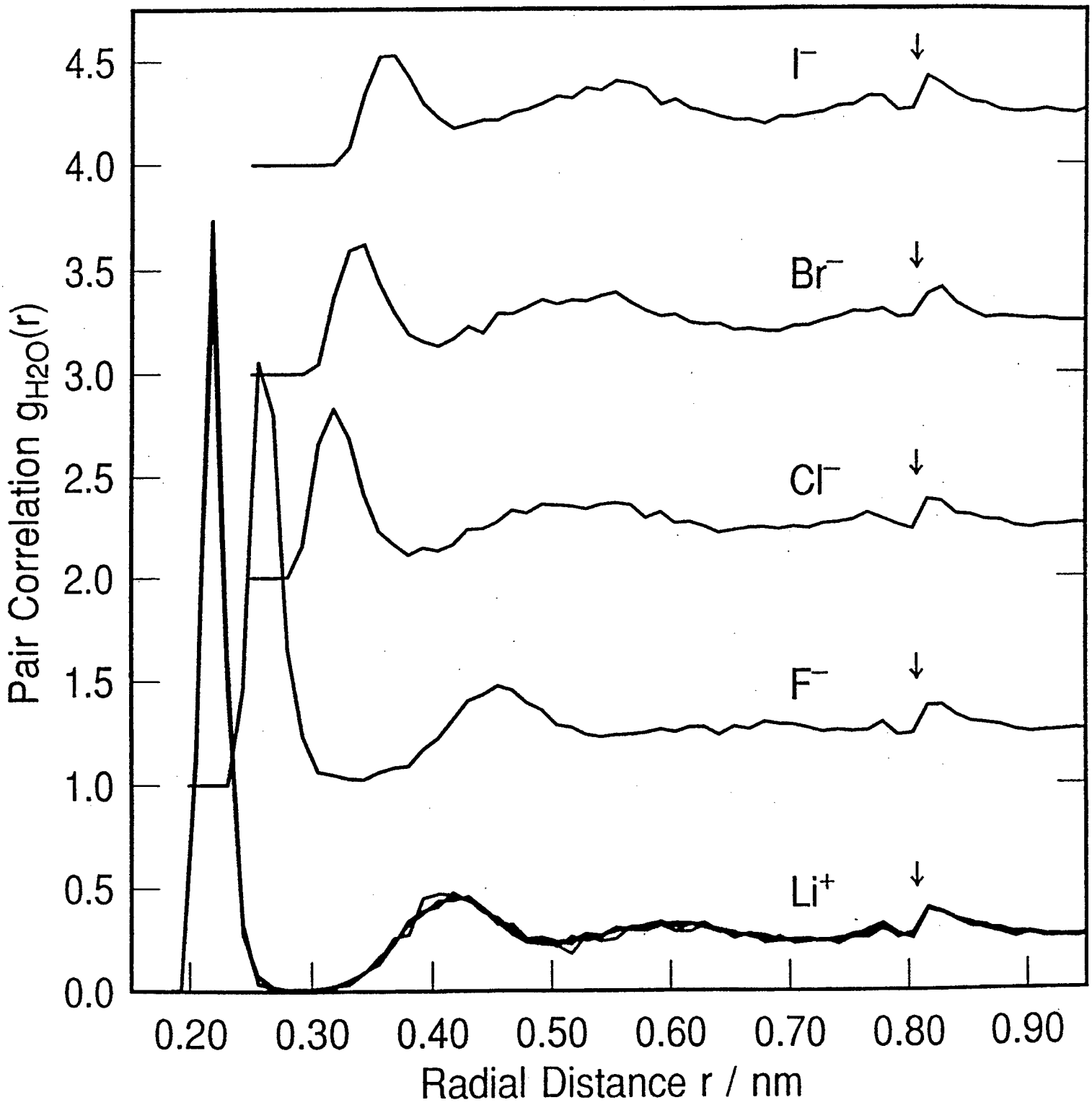
Pair Correlation $g_{H2O}(r)$
4.5
4.0
3.5
3.0
2.5
2.0
1.5
1.0
0.5
0.0
I^-
Br^-
Cl^-
F^-
Li^+
0.20
0.30
0.40
0.50
0.60
0.70
0.80
0.90
Radial Distance r / nm

F2

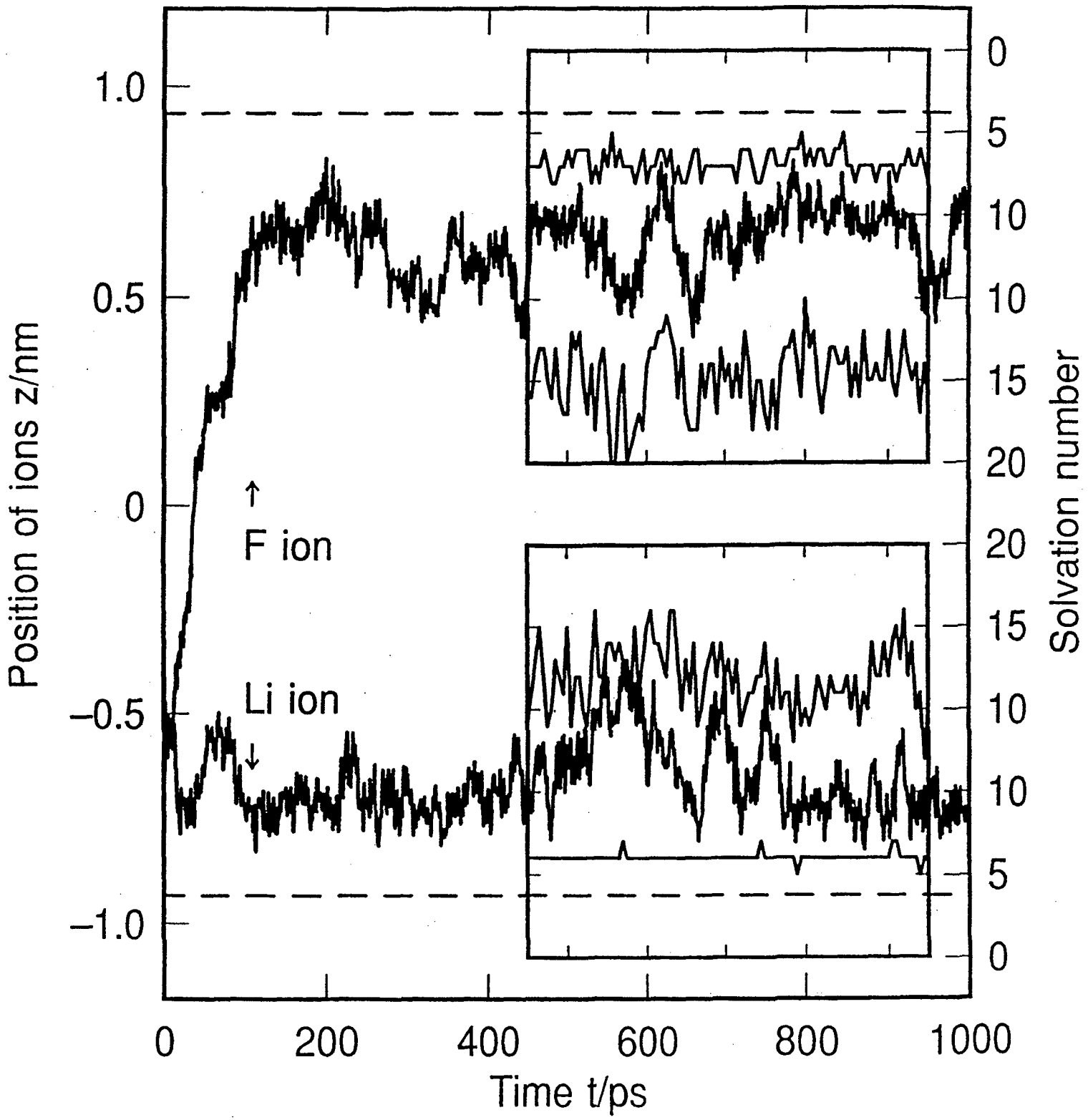
1.0
0.5
0
−0.5
−1.0
Position of ions z/nm
↑
F ion
Li ion
↓
0
5
10
10
15
20
20
15
10
10
5
0
Solvation number
0
200
400
600
800
1000
Time t/ps

F3

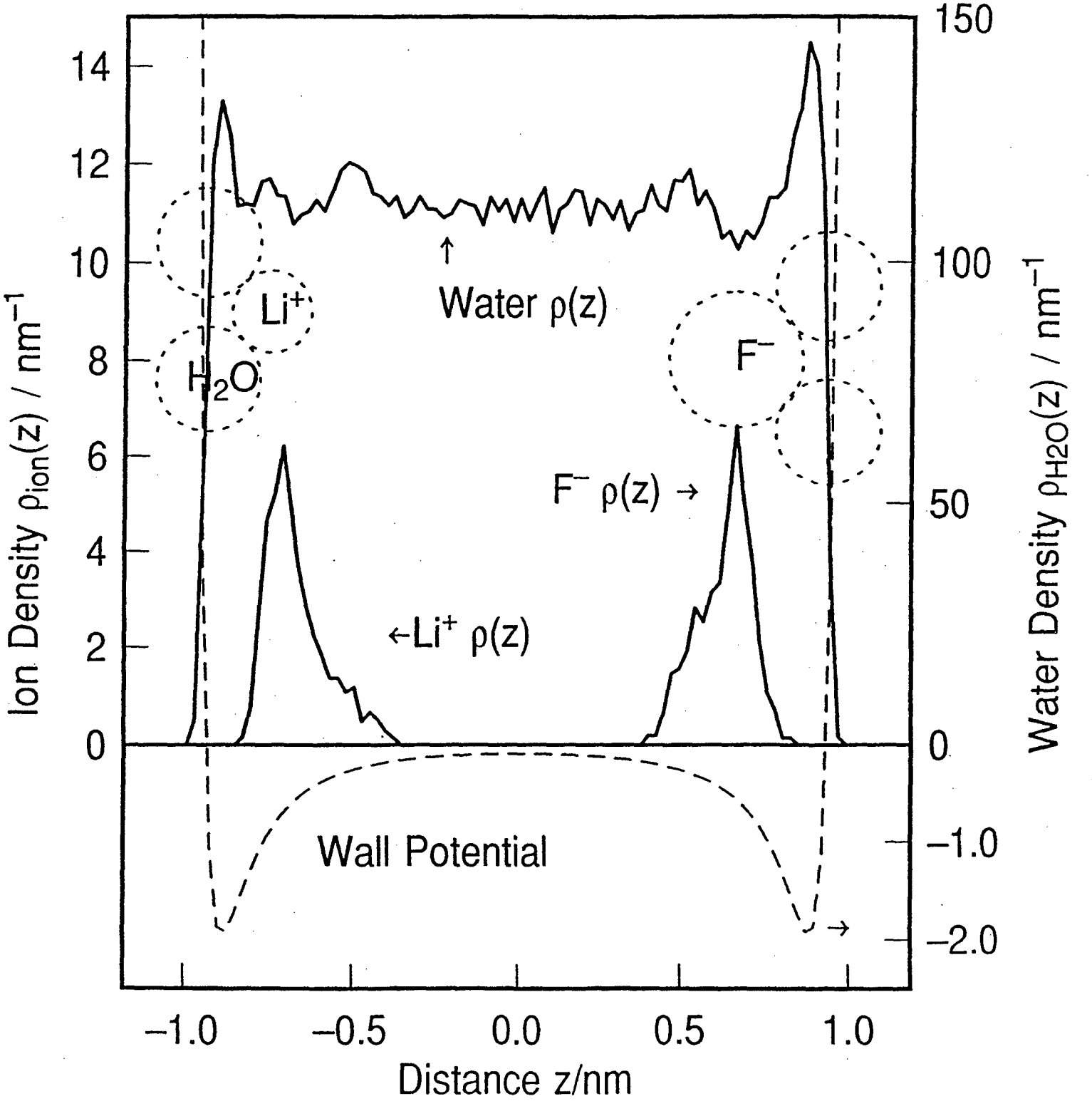
Ion Density $\rho_{ion}(z)$ / nm^{-1}
Water Density $\rho_{H2O}(z)$ / nm^{-1}
Distance z/nm
Water ρ(z)
Li+
H2O
F−
F− ρ(z) →
←Li+ ρ(z)
Wall Potential
14
12
10
8
6
4
2
0
150
100
50
0
−1.0
−2.0
−1.0
−0.5
0.0
0.5
1.0

F4

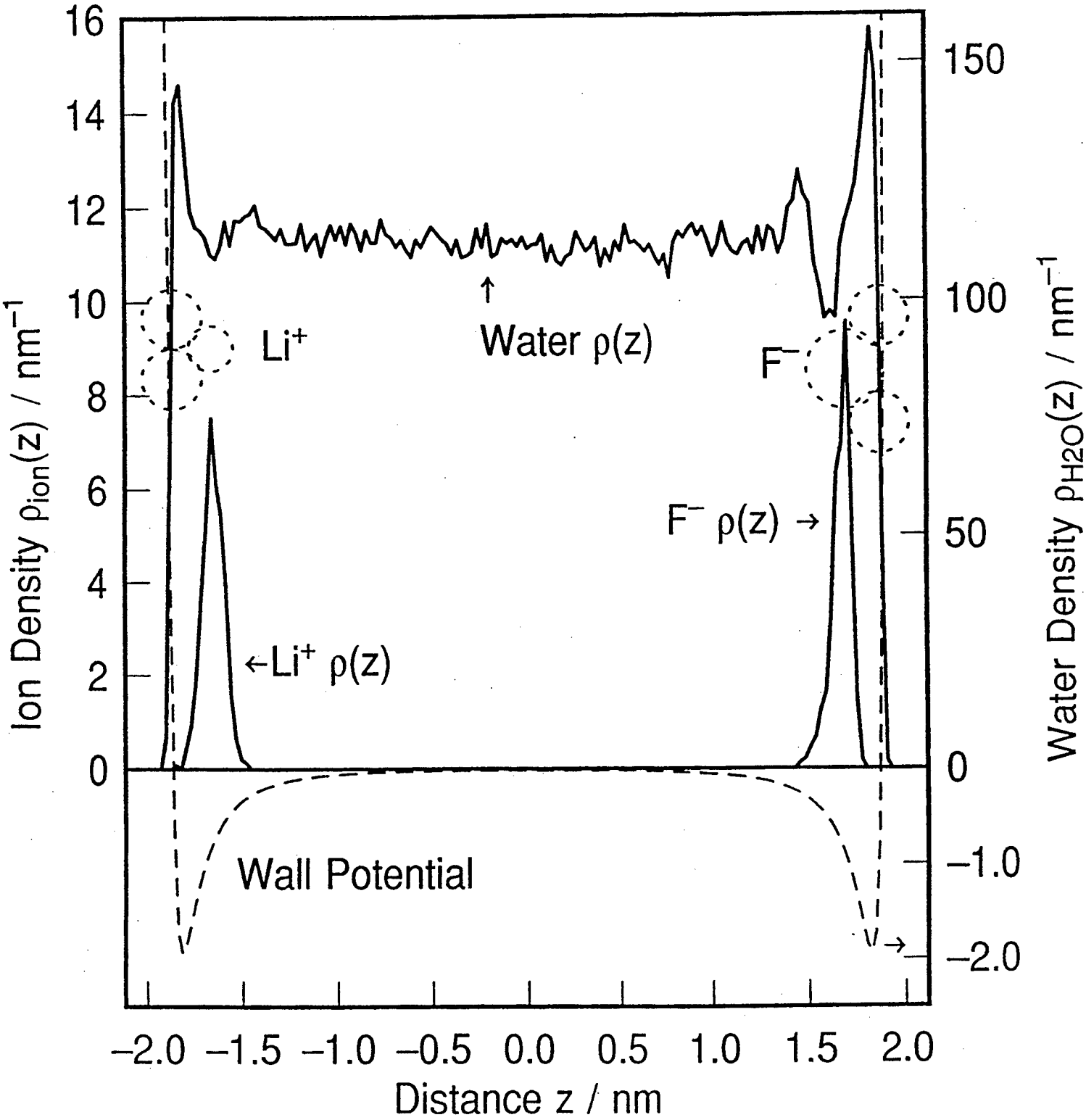
16
14
12
10
8
6
4
2
0
Ion Density $\rho_{ion}(z)$ / nm^{-1}
150
100
50
0
−1.0
−2.0
Water Density $\rho_{H2O}(z)$ / nm^{-1}
Li+
Water ρ(z)
F−
F− ρ(z) →
←Li+ ρ(z)
Wall Potential
−2.0 −1.5 −1.0 −0.5 0.0 0.5 1.0 1.5 2.0
Distance z / nm

F5

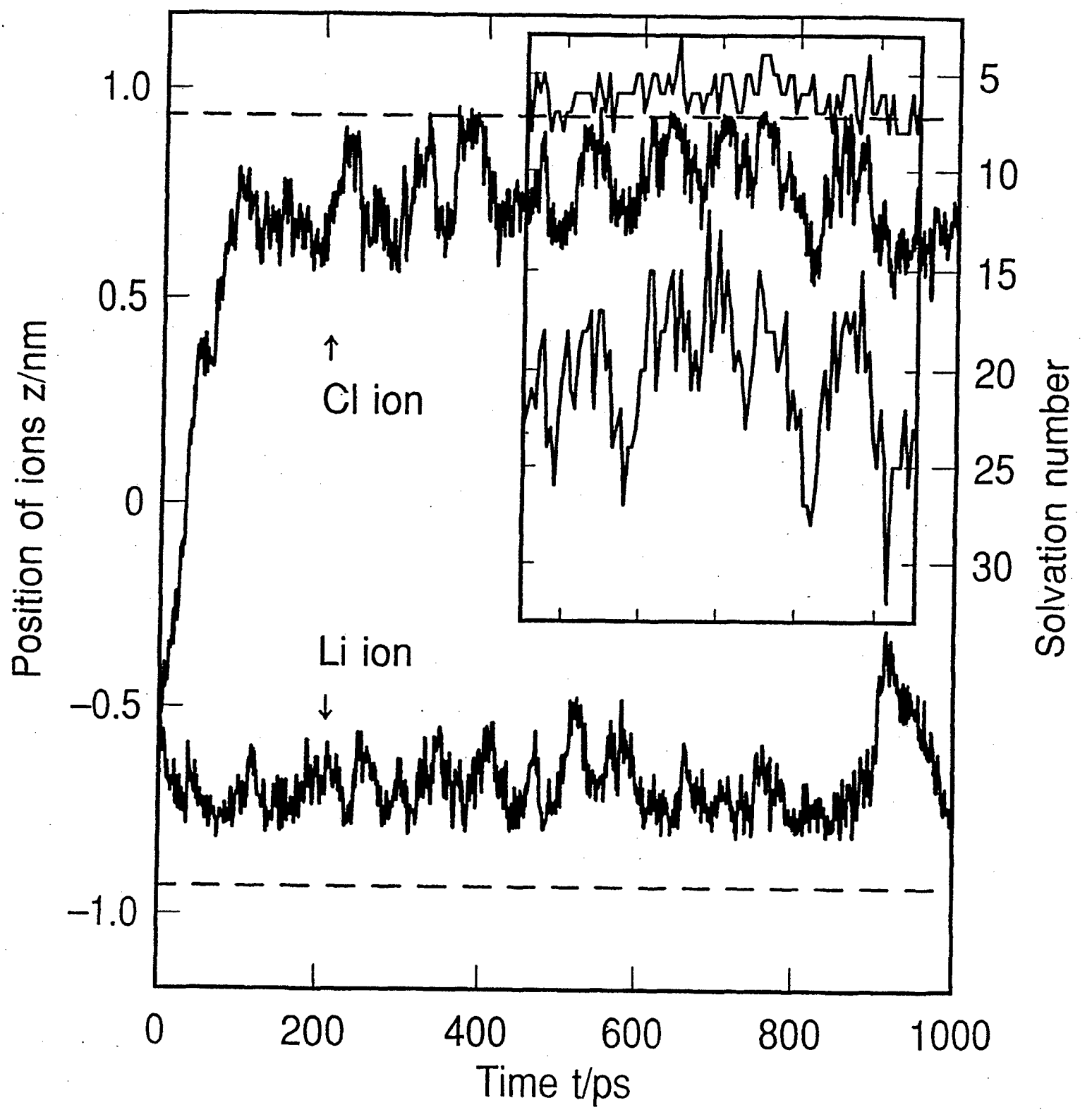
1.0
0.5
0
−0.5
−1.0
Position of ions z/nm
Cl ion
Li ion
5
10
15
20
25
30
Solvation number
0
200
400
600
800
1000
Time t/ps

F6

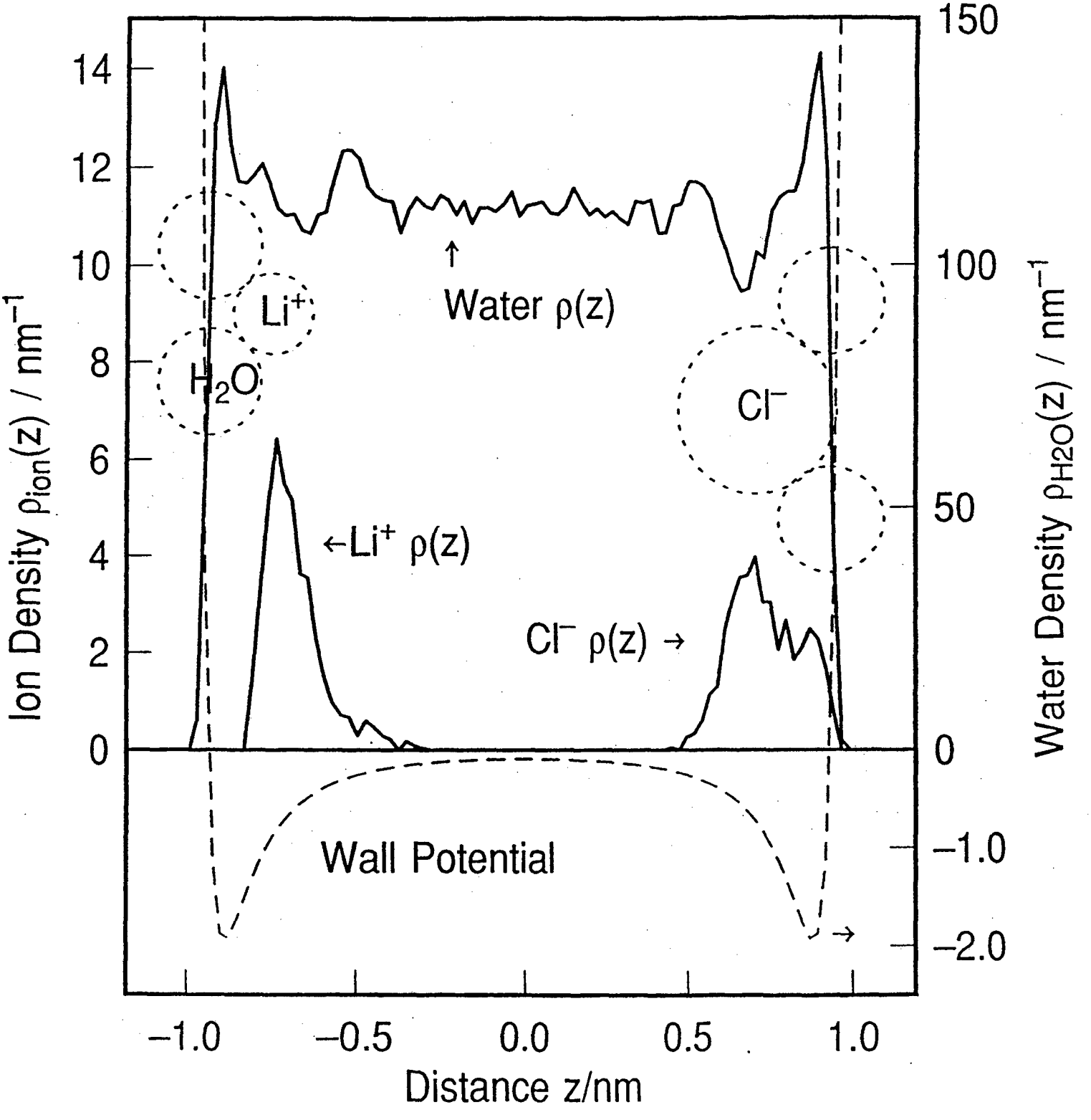
14
12
10
8
6
4
2
0
150
100
50
0
−1.0
−2.0
Ion Density $\rho_{ion}(z)$ / nm^{-1}
Water Density $\rho_{H2O}(z)$ / nm^{-1}
Li$^+$
H_2O
Cl$^-$
Water ρ(z)
←Li$^+$ ρ(z)
Cl$^-$ ρ(z) →
Wall Potential
→
−1.0
−0.5
0.0
0.5
1.0
Distance z/nm

F7

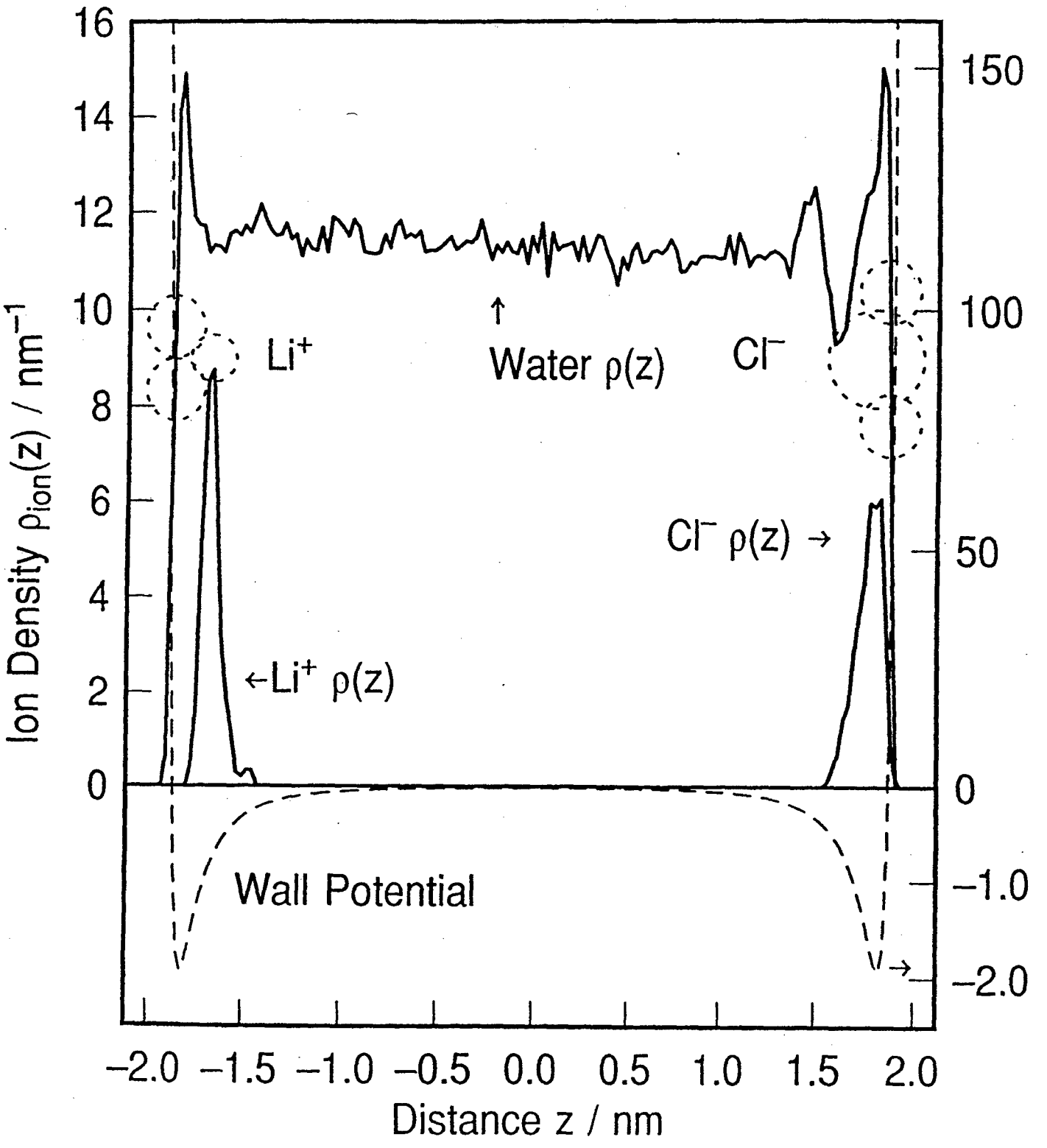
16
14
12
10
8
6
4
2
0
150
100
50
0
−1.0
−2.0
Ion Density $\rho_{ion}(z)$ / nm^{-1}
Water Density $\rho_{H2O}(z)$ / nm^{-1}
Li$^+$
Water $\rho(z)$
Cl$^-$
Cl$^-$ $\rho(z)$ →
←Li$^+$ $\rho(z)$
Wall Potential
→
−2.0 −1.5 −1.0 −0.5 0.0 0.5 1.0 1.5 2.0
Distance z / nm

F8

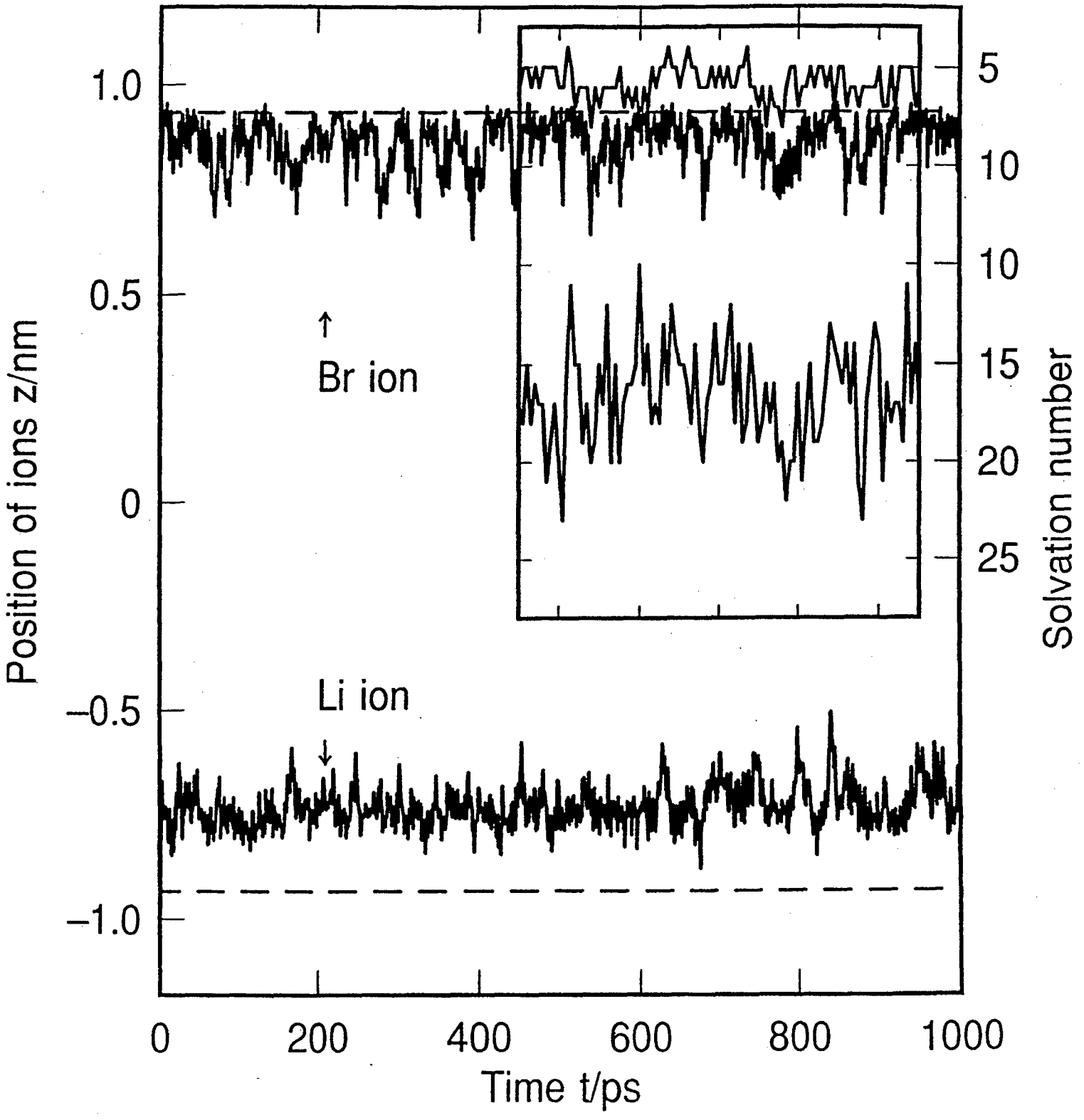
1.0
0.5
0
−0.5
−1.0
Position of ions z/nm
↑
Br ion
Li ion
↓
5
10
10
15
20
25
Solvation number
0
200
400
600
800
1000
Time t/ps

F9

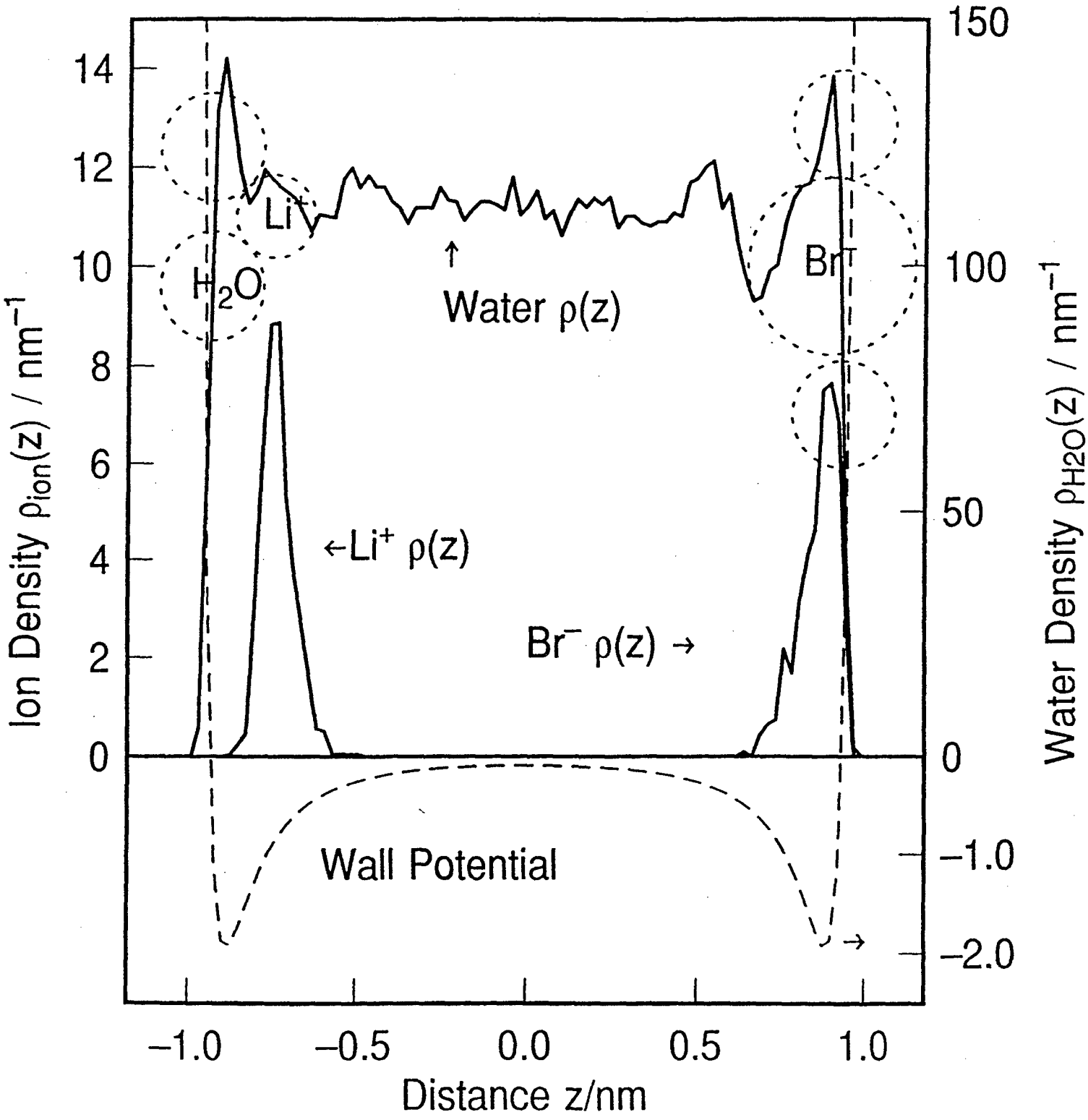
Ion Density $\rho_{ion}(z)$ / nm^{-1}
Water Density $\rho_{H2O}(z)$ / nm^{-1}
Distance z/nm
Li
H_2O
Br
Water ρ(z)
←Li$^+$ ρ(z)
Br$^-$ ρ(z) →
Wall Potential
14
12
10
8
6
4
2
0
150
100
50
0
−1.0
−2.0
−1.0
−0.5
0.0
0.5
1.0

F10

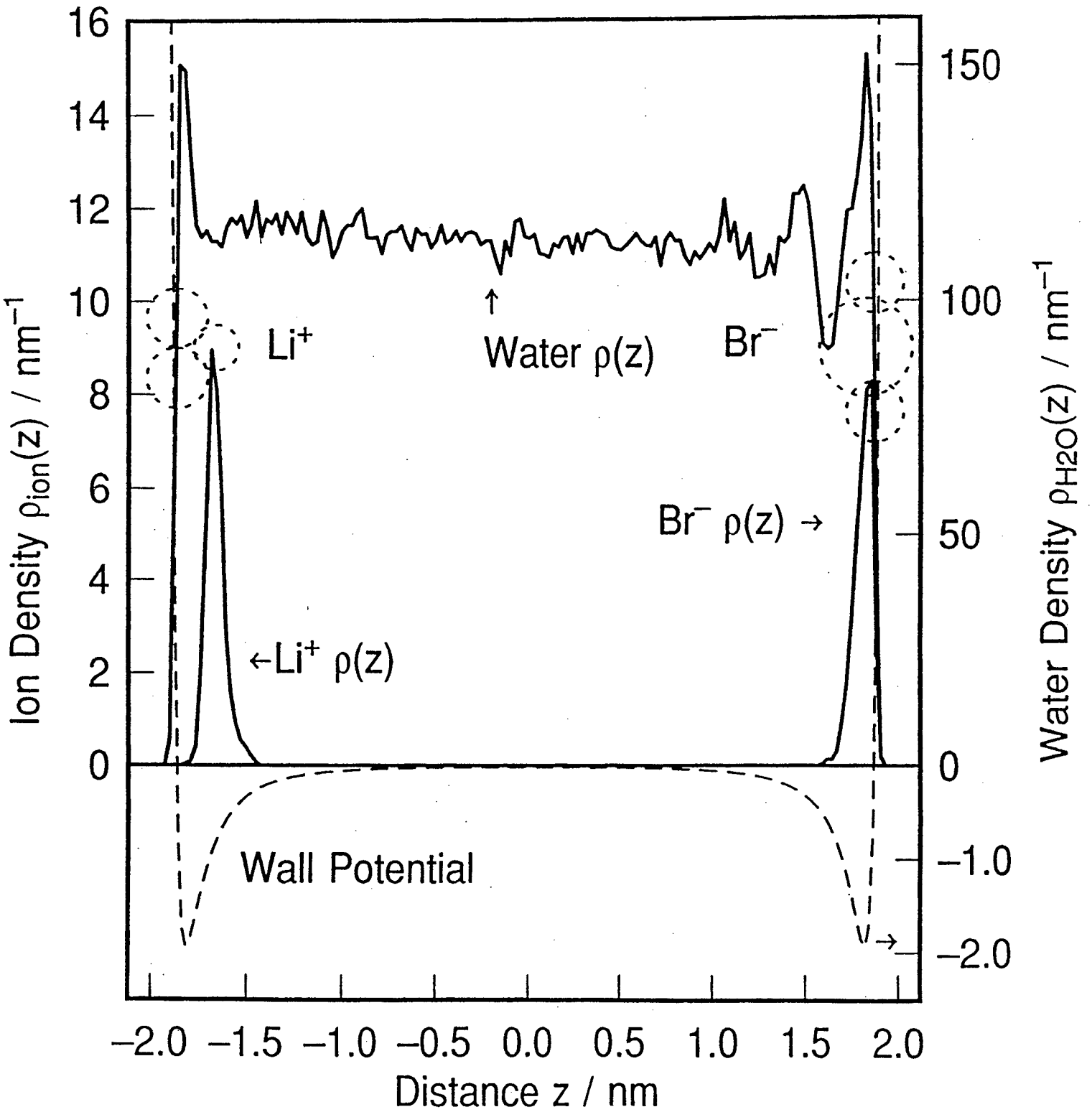
16
14
12
10
8
6
4
2
0
150
100
50
0
−1.0
−2.0
Ion Density $\rho_{ion}(z)$ / nm^{-1}
Water Density $\rho_{H2O}(z)$ / nm^{-1}
Li$^+$
Water ρ(z)
Br$^-$
Br$^-$ ρ(z) →
←Li$^+$ ρ(z)
Wall Potential
→
−2.0 −1.5 −1.0 −0.5 0.0 0.5 1.0 1.5 2.0
Distance z / nm

F11

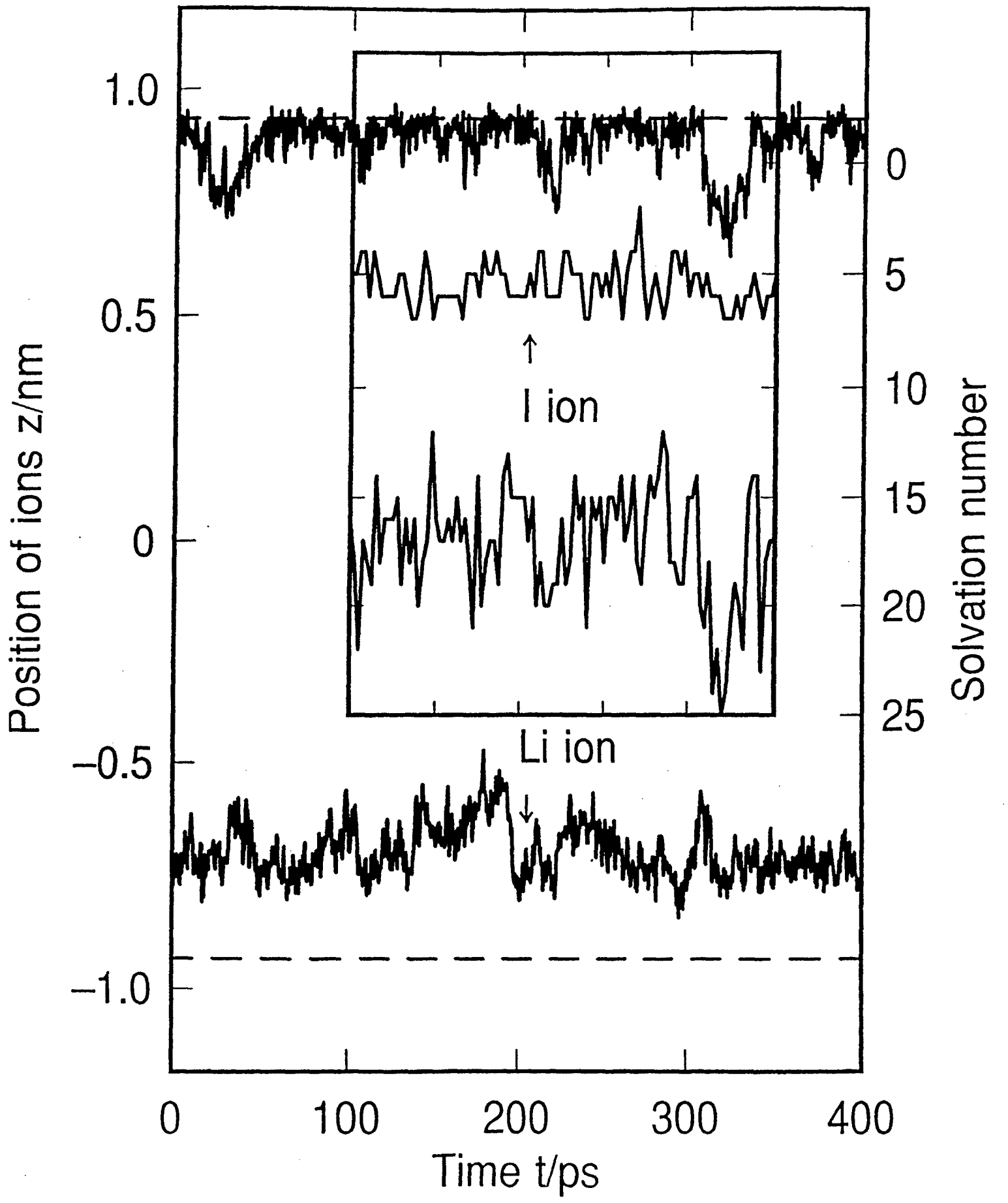
1.0
0.5
0
−0.5
−1.0
Position of ions z/nm
0
5
10
15
20
25
Solvation number
I ion
Li ion
0
100
200
300
400
Time t/ps

H12

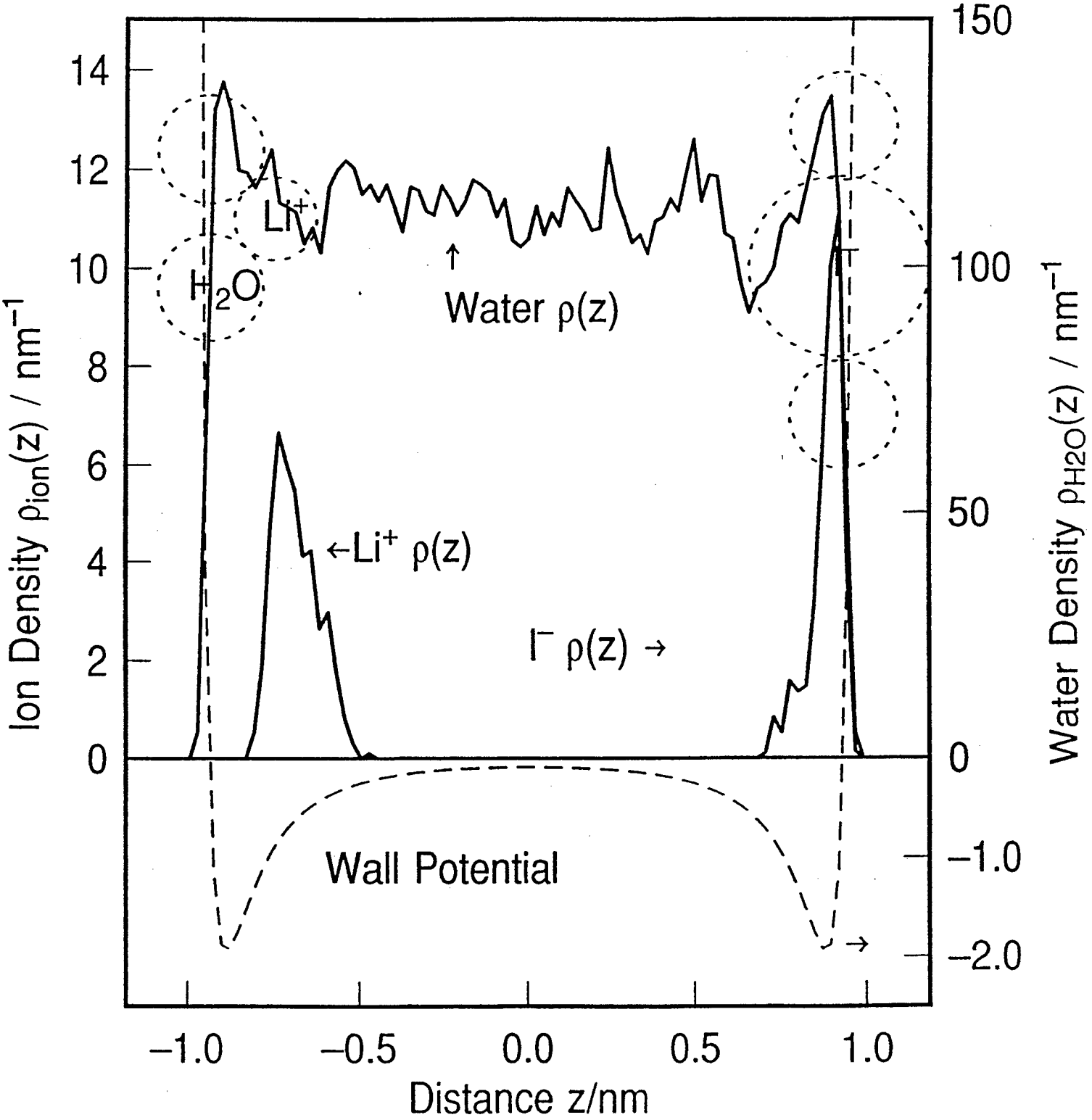
Ion Density $\rho_{ion}(z)$ / nm^{-1}
Water Density $\rho_{H2O}(z)$ / nm^{-1}
Distance z/nm
Li^+
H_2O
Water ρ(z)
←Li^+ ρ(z)
I^- ρ(z) →
Wall Potential
→
14
12
10
8
6
4
2
0
150
100
50
0
−1.0
−2.0
−1.0
−0.5
0.0
0.5
1.0

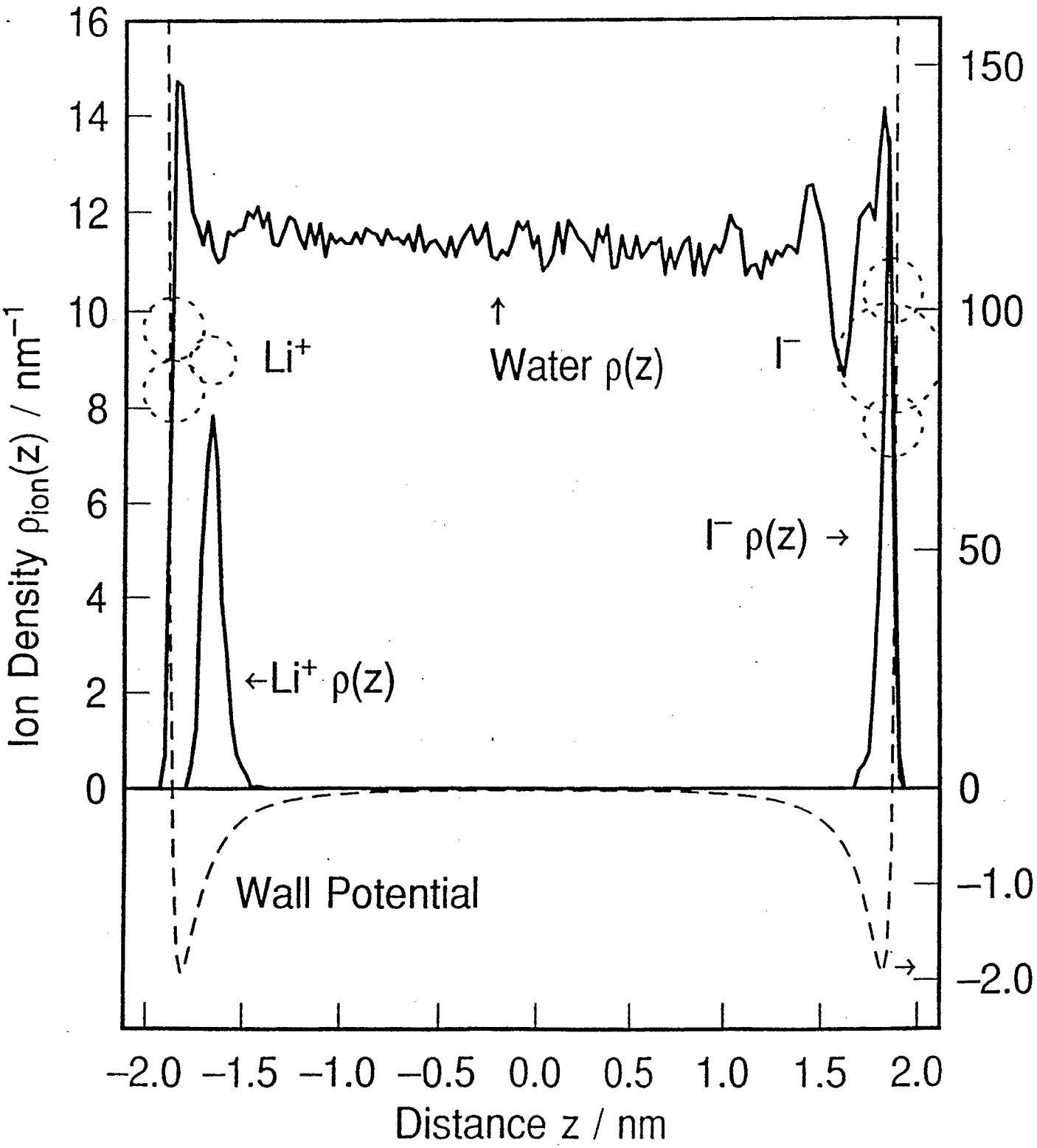
16
14
12
10
8
6
4
2
0
Ion Density $\rho_{ion}(z)$ / nm^{-1}
150
100
50
0
−1.0
−2.0
Li+
Water ρ(z)
I−
I− ρ(z) →
←Li+ ρ(z)
Wall Potential
V →
−2.0 −1.5 −1.0 −0.5 0.0 0.5 1.0 1.5 2.0
Distance z / nm

MOLECULAR DYNAMICS COMPUTER SIMULATIONS OF CHARGED METAL ELECTRODE-AQUEOUS ELECTROLYTE INTERFACES

Michael R. Philpott and James N. Glosli†

IBM Almaden Research Center
650 Harry Road, San Jose CA 95120-6099
†Lawrence Livermore National Laboratory
Livermore CA 94550

INTRODUCTION

When two different substances are joined material flows across the interface (sometimes almost imperceptibly) until the chemical potentials of the component species are equalized. When the sustances are solid or liquid and some of the chemical species are charged then the interface developes a net electrical polarization due to the formation of an electric double layer. The existence of electric double layers was first recognized by von Helmholtz [1] who studied them in the last century. In many chemical and biological systems the electric double layer exerts a profound effect on function. For example in aqueous electrolyte solution the electric field of a charged object (electrode surface or an ion) is completely shielded by the movement of ions of opposite sign toward the surface until charge balance is achieved. The distribution of ions around charged objects is described simply by the classical theories of Gouy[2-4] and Chapman[5] for flat surfaces and by the theory of Debye and Hückel[6] for spherical ions.

The main goal of this program of study is to give a molecular basis for understanding the structure and dynamics of electric double layers at charged metal-aqueous electrolyte interface. The aim is to unify current separate descriptions of surface adsorption and solution behavior, and ultimately to include a detailed treatment of the surface crystalography and electronic properties of the metal. A key element in this effort is the correct treatment of electrostatic interactions among ions, polar neutrals and their images in the metal. In our work this is achieved with the use of the fast multipole method of Greengard and Rokhlin[7-10]. The fast multipole method was specifically designed for efficient computation of long range coulomb interactions. In our simulations we have used it to in the calculation of all electrical forces, including direct space and image interactions.

Theoretical and Computational Approaches to Interface Phenomena
Edited by H.L. Sellers and J.T. Golab, Plenum Press, New York, 1994

Because we calculate the electrostatic interactions accurately, without the use of finite cut-offs, this work also has important implications concerning the way in which ions and water distributions in biological[11] and clay suspensions[12] systems should be calculated.

Four previous publications summarize the work completed prior to that described in this report[13-16]. Through systematic computer simulations we have shown that a relatively simple model suffices to describe the adsorption of halide anions and alkali metal cations on neutral and charged metal surfaces. These calculations show qualitatively many of the features known to occur experimentally at electrochemical interfaces in the thermodynamically stable region of the electric double layer. Most notable are the existence of: highly oriented water layer next to the charged metal, contact adsorption layer of the larger ions, and a diffuse region of strongly hydrated ions. The contact adsorbed ions comprise the compact layer in electrochemical interfaces. In our model, contact adsorbed ions are physisorbed because there is no provision to describe covalent bonds. Typical electric fields found in our calculations correspond to $5x10^9$ V/m, and these arise from image charge densities on the electrode of about $0.1e/nm^2$. One by product of our simulations is to point up some of the limitations in current electrochemical concepts. Consider for example the outer Helmholtz plane which defines the position of closest approach of hydrated ions to the elctrode surface. This plane is shown in numerous textbook and review article illustrations[17, 18]. Our simulations show that the plane really corresponds to a narrow zone where ions of the diffuse layer ions penetrate with increasing difficulty the closer they are to the electrode surface. In this zone some mixing with contact adsorbed species can occur which is not possible in the old picture.

In the last fifteen years there have been many simulations of water and electrolyte solutions near surfaces. Some of these studies have contributed greatly to our understanding of electrochemical interfaces. For completeness some of this work is summarized here. Films of pure water between uncharged dielectric walls[13, 19-21], and charged dielectric walls[13, 14, 22, 23]. Some of this work is noteworthy because of a predicted phase transition[22, 23]. There have been numerous calculations reported for uncharged metal[24-27] walls[28-32], including one for jellium[30] and several for corrugated platinum surfaces[27-29, 31, 32] predicting that water adsorbs weakly at top sites with oxygen down on Pt(111) and Pt(100). There have also been some calculations for electrolyte solutions between uncharged and charged dielectric walls[13, 14, 33, 34] emphasizing spatial distributions and hydration shell structure. There have been studies for electrolytes between uncharged metal walls[27, 35, 36]. The work of Rose and Benjamin[36] is particularly interesting because umbrella sampling was used to calculate the free energy of adsorption. Finally we mention the studies of water between charged metal walls[37], and electrolytes between charged metal walls[37]. In much but not all of the work just summarized, the long range coulomb interactions were treated in an approximate way. The commonest approximation was to cut off all interactions beyond a certain radius like 0.10 nm. Some workers used the Ewald method or a planar modification of the method to compute the sum of long range fields correctly. Curiously many of the other summation methods, like the planewise method of de Wette [38] seem not to have been used at all. The reason why it is important to calculate the long range fields accurately is to capture the macroscopic part. The dipole component of the field is conditionally convergent and the sum must be performed in a manner consistent with the physical boundaries. This is a rather old problem which has a partial mapping onto the problem of calculating the macroscopic electromagnetic field inside a sample of arbitrary shape. Space and time (!) prevent us from pursuing this connection here.

CAPILLARY THERMODYNAMICS

Our present understanding of electric double layers and their importance in surface electrochemistry has its origin in the dropping mercury electrode experiments of Grahame[39, 40]. The basic experiment consists of measuring the radius of a sessile mercury drop as a function of electrode potential and electrolyte composition. One can then use the electrocapillary equations of Lippmann[41] to relate radius of the drop to the interfacial surface tension and so in turn to the charge on the electrode. Thermodynamic arguments are then used deduce the surface excess concentration of adsorbed cations, anions and neutral organics on the electrode surface[17, 18, 39, 40, 42, 43].

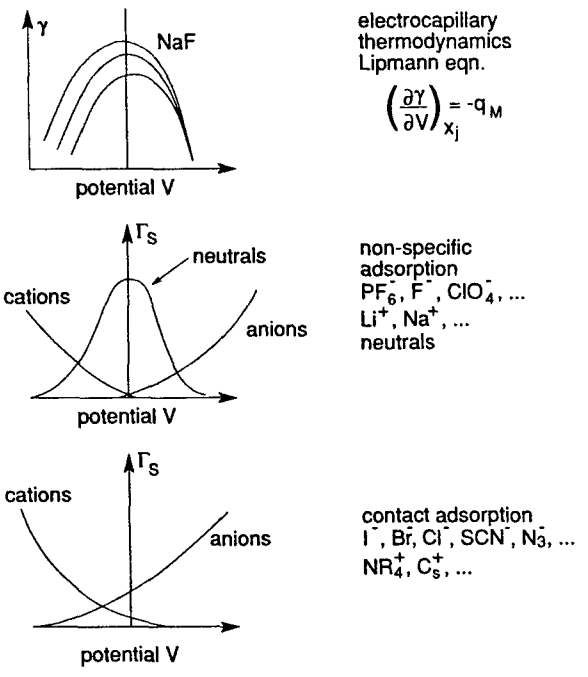

Figure 1. Schematic diagram depicting thermodynamics of adsorption: (a) plot of surface tension γ vs electrode potential V for different electrolyte compositions, (b) surface concentration Γ_S vs potential V for neutrals and strongly hydrated ions, (c) Γ_S vs potential V for contact adsorbing ions.

Figure 1 summarizes the important aspects of thermodynamic studies. For example at the top of Figure 1 the surface tension γ is depicted versus electrode potential for aqueous NaF at different concentrations. The Lippmann equation

$$\left(\frac{\partial \gamma}{\partial V}\right)_{TPN_j} = -q_M \qquad [1]$$

can be used to determine the charge on the mercury drop directly, and in turn the differential capacitance can be calculated. Contact adsorbed ions give a large contribution to the capacitance compared to ions in the diffuse layer, and this has be used to separate their

contributions in mixed solutions. The middle Figure 1 shows highly schematic curves for the adsorption of neutral organics and strongly hydrated ions on noble metals. The organics adsorb most strongly when the charge on the electrode is small because the water layer nearest the metal is then least strongly bound and more easily displaced by the organic adsorbate. The final part Figure 1c shows the adsorption isotherms for larger ions, in particular it depicts behaviour like that observed for iodide and the pseudohalides CN^- and thiocyanate SCN^-. For more discussion see the review paper by Anson[44]. For solid electrodes less direct methods are used to obtain the relevant data for a thermodynamic analysis. If the differential capacitance[45, 46]

$$C(V) = \left(\frac{\partial q_M}{\partial V} \right)_{TPN_j} \qquad [2]$$

can be measured in a way that inner layer and diffuse layer contributions can be separated then a variety of integration techniques can be used to determine the charge on the electrode. From these quantities the other important thermodynamic variables such as the surface concentrations Γ_S (depicted schematically in middle and bottom of Figure 1) can be obtained using the thermodynamic analysis starting from Eqn (1).

THE TRADITIONAL MODEL

On the basis of experimental methods like differential capacitance, chronocoulombmetry, ellipsometry, and UV-visible spectroscopy, wielded with consummate skill a detailed picture of the electric double layer adjacent to metal surfaces has been devised[18, 47]. We will refer to this picture as the 'traditional model'. The main features of this model are shown schematically in Figure 2 for that part of the double layer close to the electrode surface. Drawings similar to this one can be found in many textbooks and review articles on interfacial electrochemistry[48-50]. The metal is flat and carries charge (negative shown), the aqueous subphase is divided into two parts, called diffuse and compact regions. Additionally next to the charged surface there is a highly oriented layer of water shown in Figure 2 with protons oriented towards the surface. The anion is shown adsorbed in contact (physisorbed) and the strongly hydrated cations are shown no closer than two water molecules. The inner Helmholtz plane (IHP) is defined as the plane through the nuclei of the contact adsorbed anions and a similar plane through cations at their distance of closest approach is called the outer Helmholtz plane (OHP). Beyond the OHP the distribution of ions is assumed to be described by the Gouy-Chapman theory, which in it's simplest form assumes the ions are charged point-like objects and the solvent is a dielectric continuum with appropriate bulk properties. Close to the electrode the 'traditional model' calculates system properties based on static distributions or uses lattice statistics. The diffuse region in this picture[18] starts two solvent molecules from a flat electrode surface and stretches out several nanometers into the bulk electrolyte. The electrostatics and ionic distributions in this diffuse part were first described by the Gouy-Chapman theory[2-5] which predates even the Debye-Hückel[6] model of ionic atmospheres in bulk electrolytes. The ions in the diffuse layer screen the net charge of metal and any ions occupying in the compact part of the double layer. Traditionally the structure of the compact region is thought of as being rather static and resembling a parallel plate capacitor with a gap of atomic separations (0.1 - 0.2 nm). The flat surface model dates from times before the ability to make useable single crystal electrode surfaces, the advent of synchrotron sources and facilities to do surface X-ray analysis. Even so quite a consid-

erable effort has been directed toward developing better model of the metal side. In this regard the work of Halley et al[51-53] and Schmickler[54] is particularly significant. These groups have developed theories based on jellium electrode models of the charged metal surface that attempts to capture important physics causing features in measured capacitance vs. potential curves. Focussing more on the electrolyte subphase Henderson and coworkers[55] have developed a correlation function approach and an analysis that shows that in their very reasonable model there is no sharp division between the diffuse and inner Helmholtz planes. This is in contrast to the ideas conveyed by the pictures found in many textbooks and Figure 2.

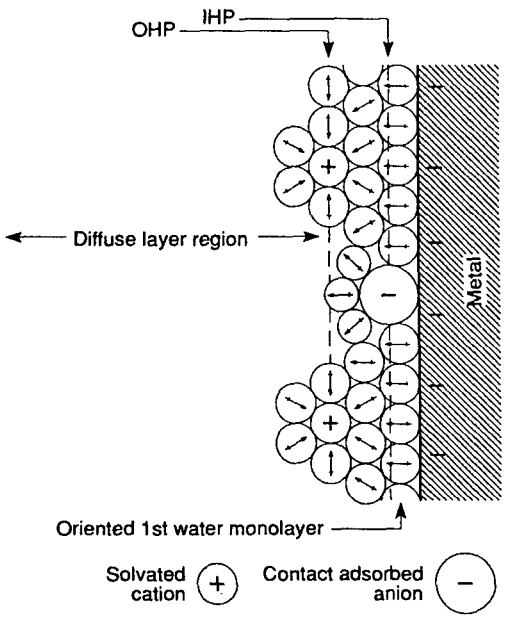

Figure 2. Schematic diagram depicting the 'traditional model' of the electric double layer found in many review articles and introductory texts on electrochemistry.

It must be pointed out that many of molecular dynamics studies performed to date have not recognized the importance of solving the electrostatics problem accurately. Intense long range fields exist at the interface because of the large dipole normal to the surface formed by the ions and their electrical images are all in phase. This problem spills over into other areas where electrostatics is important, for example most studies of water around biological objects are wrong in the way in which the dielectric polarization of water is calculated because long range correlations are lost when interactions are cut off at a finite distance. Workers in this field often resort to using distance dependent dielectric functions to shield ionized groups attached to the object's surface.

The experimental picture of electrochemical surfaces is currently undergoing rapid change due to numerous advanced in situ and ex situ UHV surface science probes of the electrochemical interface. The new synchrotron based X-ray surface crystal structure probes like grazing incidence X-ray scattering (GIXS), X-ray standing wave (XSW), surface extended X-ray absorption fine structure (SEXAFS) techniques have allowed surface geometries to be measured for the first time[56-59]. Recent studies by Hubbard and

coworkers[46] reveal changes in charge state of the ion as the surface concentration is increased, changes that have analogies in UHV surface science studies of the metalization of semiconductors These studies show contact adsorption to be a complex process that can evolve into chemisorption at high coverages even if the initial step is physisorption. Local probes like scanning tunneling microscopy (STM) and atomic force microscopy (AFM) give images with local atomic scale features. The next few years will likely see major revisions in our experimental understanding of the less dynamic part of the electrochemical double layers.

MODEL FOR THE IMMERSED ELECTRODE

Consider a system consisting of two electrodes immersed in aqueous electrolyte solution as shown schematically in Figure 3. Reading from left to right there are three regions: the anode on the left, the bulk region at the center, and the cathode region on the right. If the electrodes are uncharged then in all three regions the electrolyte phase would be electrically neutral. Now when the externally applied (battery) potential is altered so that the electrodes become charged (the case shown schematically in Figure 3) the electrolyte responses by screening the electric field and the three regions acquire different net charge. One with excess anions (left) screens the positive charge on the left electrode, a bulk region in which the electric field is zero, and one with an excess of cations (right). When the charge on each electrode is included with the adjacent 'zone' of electrolyte the net charge in each region is zero.

These simple considerations suggest we can try to model an immersed electrode with it's adjacent screening region and do not have to model the whole cell as was done in two previous publications[13, 14]. This approach is useful because it reduces the number of water molecules in the calculation, however it imposes a constraint in the form of charge neutrality and requires us to choose a 'good' boundary to separate the bulk region and immersed region. We can test the boundary by scaling the size of the system to capture some bulk-like behavior. Scaling by a factor of ten suggests that four layers of water is a minimum sized system.

Our immersed electrode model therefore consists of a layer of electrolyte between two walls. The wall on the left carries no charge it is simply a restraining wall and ideally should allow a continuous transition to the bulk electrolyte region. The complete system of electroltye and electrode (always chosen to be on the right hand side in our calculations) is neutral, unless we deliberately choose to stress the system with an uncompensated charge on the right hand metal electrode. In practice we have performed both types of calculation for reasons described in more detail later. Later we will show an important result that water behaves in an uncompensated field as if the excess ionic charge were higher.

Since there is integer charge in the aqueous phase q_{Aq}, and the image charge on the metal q_{im} satisfies the equation $q_{im} + q_{aq} = 0$. In our calculations we also consider cases (to be discussed at length later) where there is additional charge q_{uc} on the electrode with the restriction that $q_T = q_{im} + q_{uc} = ne$ where $n = 0, \pm 1, \pm 2, \ldots$.

In Figure 3 if one thinks of the vertical dash line as symbolizing the restraining wall then in reality the vertical line will be very close to the corresponding electrode for a macroscopic sized cell. Integral electrode charge is an essential constraint in this immersed electrode model. We stress again that the main advantage of the model is that

only about half the number of water molecules are needed to simulate a system with two metal electrodes. For the restraining barrier we choose a 9-3 potential. The origin for this restraining potential is at 1.862 nm from the image plane of the metal. We refer to this restraining potential surface as the dielectric surface, and as already mentioned it's only function is to limit the extent of the fluid phase and thereby make the calculations more tractable. In all the calculations reported here the simulation cell was a cube with edge 1.862nm. The cube was periodically replicated in the xy directions parallel to the electrode surface plane. Again we mention that we have performed some scaled up calculations on cells with larger edge length by up to a factor 2 and found very similar features to those described for the smaller cells.

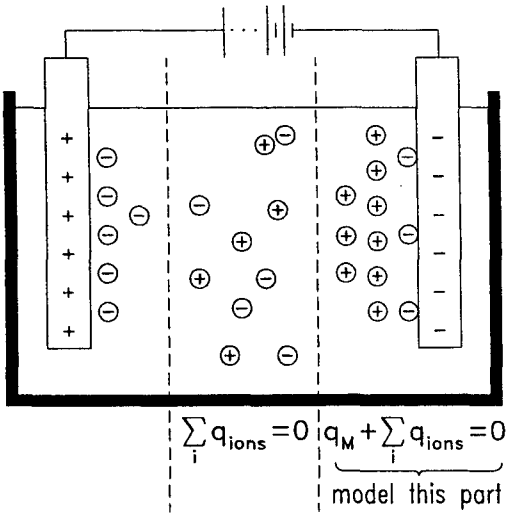

Figure 3. Immersed Electrode Model. Schematic diagram of the electrochemical cell showing the immersed electrode configuration on the right side. Vertical broken lines symbolize the transition region from diffuse layer to bulk electrolyte where the solution is electrically neutral.

MODEL FOR WATER, IONS AND THE METAL SURFACE

In all the calculations reported here we have used the parameters of the Stillinger[60, 61] ST2 water model and the extensive interaction parameter set for alkali metal ions and halide ions developed by Heinzinger and coworkers[62]. Figure 4 shows a schematic of the ST2 water model, a simple ion and the smoothly truncated Lennard-Jones potential. The ST2 water molecule model consists of a central oxygen atom (O_ST2 or O for short) surrounded by two hydrogen atoms (H_ST2 or H for short) and two massless point charges (PC_ST2 or PC for short) in a rigid tetrahedral arrangement (bond angle = $\cos^{-1}(1/\sqrt{3})$). The O-H and O-PC bond lengths were 0.10 nm and 0.08 nm respectively. This small difference in bond lengths means that the water_ST2 model and its electrostatic image (i.e., $q \rightarrow -q$) behave similarly. The only Lennard-Jones 'atom' in ST2 model is the oxygen atom. The hydrogen H and point charges PC interact with their surroundings (i.e., other atoms and surfaces) by Coulomb interactions only. Their charges are q_H= 0.23570|e| and q_{PC}= $-q_H$. The O atom carries no charge. The alkali metal ion and halide ion were treated as non-polarizable Lennard-Jones atoms with central point mass and

charge. Figure 4 shows an ion schematically next to the water model. The atom-atom interaction parameters are taken from Heinzinger's review[28, 62].

Next we describe the interaction between water and ions and the metal and restraining wall. The metal was represented by two linearly superimposed potentials. Pauli repulsion and dispersive attractive interactions were modelled by a 9-3 potential, and the interaction of charges with the conduction electrons by a classical image potential. In the calculations described here the image plane and origin plane of the 9-3 potential were coincident. This was tantamount to choosing the image plane and the nuclear plane of the metal surface to be coincident. This was acceptable in our scheme because the Lennard-Jones core parameters σ are all large and the 'thickness' of the repulsive wall is also large (ca. 0.247 nm).

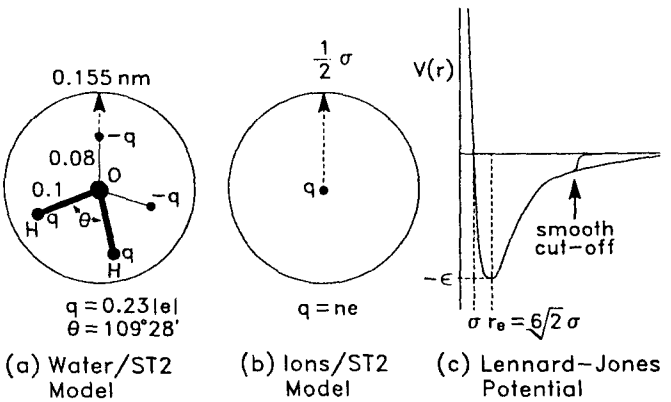

Figure 4. The Ion and Water Models. Schematic diagram summarizing the key features of the model for ST2 water and the ions. Water and ions are treated as non polarizable Lennard-Jones atoms with embedded charges. Shown on the left is a schematic drawing of the Lennard-Jones potential with smooth cut-off.

CALCULATION OF THE ELECTROSTATIC INTERACTIONS

Electrostatic sums are conditionally convergent and great care must be exercised in using cut-offs and different boundary conditions. The Coulomb field computation grows as N^2 (N number of charged particles) unless special measures are adopted. We use the fast multipole method (fmm) devised by Greengard and Roklin[7], in which the cpu time grows as N. The cross over point in efficiency for direct sum versus fmm can be as small as N = 1000 (about 250 ST2 water molecules). The original papers of Greengard should be consulted for details of this clever algorithm. Some discussion of the use of fmm in electrochemical simulations has been given by Glosli and Philpott[15].

TOTAL POTENTIAL ENERGY OF THE SYSTEM

The Coulomb interaction between molecules was represented as sum of $1/r$ interactions between atomic point charges. For the ST2 water model these interactions result in H-bonds that are too strong when the PC and H atoms are close. These interactions were softened for small molecular separation in the way described by Stillinger[60] and Lee et

al[19] by introducing a switching function S that modifies specified atomic coulomb interactions at small separations. The short range part of the intermolecular interaction was modeled by Lennard-Jones potential between atom pairs on each molecule. All molecule-molecule Lennard-Jones type interactions were cut-off in a smooth fashion at a molecular separation $R = 0.68$ nm by a truncation function T. The atoms of each molecule also interacted with the surfaces at $z = \pm z_o$ where z_o = 0.931 nm. Both surfaces were treated as flat featureless plates with a uniform electric charge density of σ on the metal plate at $+ z_o$ if there is an uncompensated charge on the metal, otherwise $\sigma = 0$ This gave rise to a uniform electric field, $E = 4\pi K\sigma$, in the z-direction where K the electrostatic coupling constant had the value 138.936 kJ.nm/(mole.e^2) in the units of this paper. The complete interaction energy U was given by the following formula

$$U = \sum_{\substack{\beta\in A_j \\ i<j}} \left(\left\{ \frac{Kq_\alpha q_\beta}{r_{\alpha\beta}} \left[S(R_{ij}, R_L^{ij}, R_U^{ij}) - 1 \right] + 4\varepsilon_{\alpha\beta} \left[\left(\frac{\sigma_{\alpha\beta}}{r_{\alpha\beta}} \right)^{12} - \left(\frac{\sigma_{\alpha\beta}}{r_{\alpha\beta}} \right)^{6} \right] \right\} T(R_{ij}) + \frac{Kq_\alpha q_\beta}{r_{\alpha\beta}} \right) \qquad [3]$$

$$+ \sum_\alpha \left\{ - q_\alpha E z_\alpha + \left(\frac{A_\alpha}{(z_\alpha + z_o)^9} - \frac{B_\alpha}{(z_\alpha + z_o)^3} \right) + \left(\frac{A_\alpha}{(z_\alpha - z_o)^9} - \frac{B_\alpha}{(z_\alpha - z_o)^3} \right) \right\}$$

where i and j were molecular indices, and α and β were atomic indices. The symbol A_i represented the set of all atoms of molecular i . The symbol R_{ij} was the distance between the center of mass of molecules i and j. The symbol $r_{\alpha\beta}$ was the distance between atoms α and β. For small R we followed the practice of modifying the the coulomb energy between ST2 molecules and ions by the switching function $S(R, R_L, R_U)$ given by,

$$S(R, R_L, R_U) = \begin{cases} 0 & R < R_L \\ \dfrac{(R - R_L)^2 (3R_U - 2R - R_L)}{(R_U - R_L)^3} & R_L < R < R_U \\ 1 & R_U < R \end{cases} \qquad [4]$$

The values of R_L and R_U were dependent on the types of the molecular species that were interacting. As mentioned above the tails of the Lennard-Jones pair interactions were cut off by the truncation function T. The form of T was given by,

$$T(R) = \begin{cases} 1 & R < R_L^T \\ \left(1 - \left(\dfrac{R - R_L^T}{R_U^T - R_L^T} \right)^m \right)^n & R_L^T < R < R_U^T \\ 0 & R_U^T < R \end{cases} \qquad [5]$$

The same truncation function has been applied to all non Coulombic molecular interactions, with R_L^T=0.63 nm and R_U^T=0.68 nm. The integers m and n controlled the smoothness of the truncation function at R_L^T and R_U^T respectively. In this calculation $n = m = 2$ which insured that energy has continous first spatial derivatives.

All the atom-atom and atom-surface interaction parameters are given in Table I. For example we see that the (ε,σ) pairs are (0.3164, 0.3100), (0.1490, 0.2370) and (0.4080, 0.5400) for O_ST2, Li ion and I ion respectively. The units of the well depth ε are kJ/mole and the van der Waals σ is in nm . The usual combining rules were enforced for unlike species, namely: $\varepsilon_{AB} = (\varepsilon_{AA}\varepsilon_{BB})^{1/2}$ and $\sigma_{AB} = \frac{1}{2}(\sigma_{AA} + \sigma_{BB})$. The st2 model switching

function (see later) interval ends R_L^{IJ} and R_U^{IJ} both vanish except for st2/st2 water pairs, where $R_L^{ST2,ST2}$=0.20160 nm and $R_U^{ST2,ST2}$=0.31287 nm.

The atom-surface parameters describing interaction with nonconduction electrons were chosen to be the same as those used by Lee at al[19], A=17.447x10^{-6} kJ(nm)^6/mole and B=76.144x10^{-3} kJ(nm)^3/mole for O, I ion and Li ion. The A and B parameters for H_st2 and PC_st2 were set to zero. The potential corresponding to these parameters describe a graphite-like surface. Real metals would have much larger ε ours were deliberately chosen to be small so as to permit coulombic interactions to dominate the physics.

Table I. The interaction parameters (q, ε, σ, A, B) and mass (m) for all atoms used in the simulations, where $q_o = e$, $\varepsilon_o = 1KJ/mole$, $\sigma_o = 1nm$, $A_o = 17.447 \times 10^{-6} KJ \cdot nm^6/mole$, $B_o = 76.144 \times 10^{-3} KJ \cdot nm^3/mole$, and $m_o = 1AMU$. The ε and σ for unlike atom pairs are formed using the combination rules $\varepsilon_{AB} = \sqrt{(\varepsilon_{AA}\varepsilon_{BB})}$ and $\sigma_{AB} = (\sigma_{AA} + \sigma_{BB})/2$.

	q/q_o	$\varepsilon/\varepsilon_o$	σ/σ_o	m/m_o	A/A_o	B/B_o
O_ST2	0.0000	0.316	0.310	16.0	1	1
H_ST2	0.2357	0.000	0.000	1.000	0	0
PC_ST2	− 0.2357	0.000	0.0	0.0	0	0
Li	1.0000	0.149	0.237	6.9	1	1
F	− 1.0000	0.050	0.400	19.0	1	1
Cl	− 1.0000	0.168	0.486	35.5	1	1
Br	− 1.0000	0.270	0.504	79.9	1	1
I	− 1.0000	0.408	0.540	129.9	1	1

In the equations of motion bond lengths and angles were explicitly constrained by a quaternion formulation of the rigid body equations of motion[63]. The equations of motion were expressed as a set of first order differential equations and a fourth order multi-step numerical scheme with a 2 fs time step was used in the integration. At each time step a small scaling correction was made to the quaternions and velocities to correct for global drift. Also the global center of mass velocities in the x and y directions was set to zero at each time step by shifting the molecular translational velocities.

In the analysis of configurations the first 100 ps were used to equilibrate the system and subsequent configurations were used in compute properties like density profiles. There were exceptions where it was evident that the system had not equilibrated. In practice it was found this occurred frequently in three ion systems, as in the case of a cation in the presence of two coadsorbed iodide ions. All the simulations were run to 1000 ps or longer, so that generally 900 or more configurations one ps apart were used to calculate averages. Typical density plots were derived from bining configurations stored every ps and with bin widths of 0.005 nm or larger.

EQUATIONS OF MOTION

All molecules, in this study, were assumed to be a rigid collection of point atoms, so that all bond lengths and bond angles within a molecule were fixed. To evolve a collection of these molecules a quaternion formulation of the rigid body equations of motion was used[63-65] The center of mass position ($\mathbf{R}_i$) and velocity ($\mathbf{V}_i$) was used to describe the translational degrees of freedoms of molecule *i*. The orientational motion of the molecule was described by the quaternion $\mathbf{q}_i = (q_i^0, q_i^1, q_i^2, q_i^3)$ and the rotational velocity (ω_i^p), as measured in the body frame of the molecule. The one exception to this was for monatomic molecules, in which case the orientational degrees of freedom were not needed.

The discussion of the equations of motion begin by considering the potential energy U. From Eqn 3, it can be seen that the potential energy can be treated as a scalar function of the variables ($\mathbf{R}_1,..., \mathbf{R}_N; \mathbf{r}_1,..., \mathbf{r}_n$), where N is the number of molecules and n is the number of atoms in the entire system.

$$U = U(\mathbf{R}_1,..., \mathbf{R}_N; \mathbf{r}_1,..., \mathbf{r}_n) \qquad [6]$$

Of course not all these variables are independent. However for the purposes of the following two definitions they are treated as independent variables.

$$\mathbf{f}_\alpha \equiv -\nabla_{\mathbf{r}_\alpha} U, \qquad \mathbf{F}_i \equiv -\nabla_{\mathbf{R}_i} U. \qquad [7]$$

The total force $\mathbf{F}_i^T$ and torque τ_i, can be expressed in terms of $\mathbf{f}_\alpha$ and $\mathbf{F}_i$ as

$$\mathbf{F}_i^T = \mathbf{F}_i + \sum_{\alpha \in A_i} \mathbf{f}_\alpha \qquad \tau_i = \sum_{\alpha \in A_i} (\mathbf{r}_\alpha - \mathbf{R}_i) \times \mathbf{f}_\alpha, \qquad [8]$$

The translational motion of the molecule is described by the first order ordinary differential equation,

$$\frac{d\mathbf{R}_i}{dt} = \mathbf{V}_i \qquad M_i \frac{d\mathbf{V}_i}{dt} = \mathbf{F}_i^T. \qquad [9]$$

For the rotational motion it is convenient to work in the body axis of the molecule, where the moment of inertia $\hat{I}_i$ is diagonal and time independent. It is useful to define the operator $\hat{Q}_i$

$$\hat{Q}_i = \begin{bmatrix} -q_i^1 & -q_i^2 & -q_i^3 \\ q_i^0 & -q_i^3 & q_i^2 \\ q_i^3 & q_i^0 & -q_i^1 \\ -q_i^2 & q_i^1 & q_i^0 \end{bmatrix} \qquad [10]$$

and the body frame rotational force

$$\mathbf{F}_i^R = \tau_i^b - \omega_i^b \times (\hat{I}_i^b \omega_i^b). \qquad [11]$$

Using these quantities above, the following first order ordinary differential equations can be written to describe the rotational motion

$$\frac{d\mathbf{q}_i}{dt} = \hat{Q}_i \omega_i^b \qquad \hat{I}_i^b \frac{d\omega_i^b}{dt} = \mathbf{F}_i^R. \qquad [12]$$

This set of equations conserve the total energy for time independent potentials (U) . A constant temperature ensemble may be simulated by introducing a velocity dependent term in the acceleration terms to constrain the total kinetic energy. The constant temperature equations of motion are written as

$$\begin{aligned} \frac{d\mathbf{R}_i}{dt} &= \mathbf{V}_i, & M_i \frac{d\mathbf{V}_i}{dt} &= \mathbf{F}_i^T - \gamma \mathbf{V}_i \\ \frac{d\mathbf{q}_i}{dt} &= \hat{Q}_i \omega_i^b, & (\hat{I}_i)^b \frac{d\omega_i^b}{dt} &= \mathbf{F}_i^R - \gamma \omega_i^b, \end{aligned} \qquad [13]$$

$$\gamma = (\sum_i \mathbf{V}_i \mathbf{F}_i^T + \omega_i^b \mathbf{F}_i^b)/(2K)$$

This choice of γ ensures that the total kinetic energy of the systems is constant.

INTRODUCTION TO THE RESULTS

The purpose of this section is to briefly introduce and explain some of the terms and concepts used in the description and discussion of the results. We define inner layer, inner surface field and the external or as we will also refer to it the 'uncompensated' field.

In our calculations the inner layer is defined to be all ions and molecules in contact with the electrode. Recall that the surface is represented by a 9-3 potential that acts on the center of the molecules and ions. This means that in our model the inner most layer, i.e., the first layer, has a simpler structure because steric effects due to dimension perpendicular to the surface are suppressed. In a more realistic model Pauli repulsion would ensure that the center of water was closer to the surface that the center of an iodide ion. One consequence of our model is that some hydrophobic effects at the surface are accentuated, and some steric effects based on volume are decreased in importance.

In equilibrium states the charge on the flat electrode is just the net image charge, which is equal in magnitude but opposite in sign to the sum of the charges on the ions. In this case there is no field in the bulk because the fields from the ions and their images cancel. When the charge on the electrode is only the image charge, then the potential drop occurs

between the metal surface and the ions. There is essentially no electric field beyond the ions. We call the field generated by the ions and their images the inner surface field. Since the water molecules have large permanent dipole moments those molecules between the ions and the metal will try to align with the field.

It is useful from the theoretical point of view to stress the system by placing extra uncompensated charge on the electrode. In this case there is a field across the sample, just as occurs when we have water without ions between charged plates. We refer to this field as the external, applied or uncompensated electric field. In general then we can think of the total charge on the electrode as the sum of the image charge and the extra uncompensated charge. In passing we emphasize again that in electrochemical systems it is not possible to have uncompensated charge (i.e., unshielded) on an electrode immersed in electrolyte. However, it is possible in principle to place uncompensated charge on an emersed electrode, so that there are physically realizable states resembling those of the immersed model with uncompensated charge. However the uncompensated charge densities reachable in practice are about 100 times smaller than the ones used in this paper. In our calculations with uncompensated charge we have deliberately chosen charge densities equal in magnitude to the image charge density in order to better understand the effect of the surface field on the inner layer of water.

Finally we state again that the inner surface field is localized close to the metal, in contrast to the field of uncompensated charge which extends across the entire sample. At the surface the total surface field consists of the inner field and any applied field due to uncompensated charge.

POSITIVELY CHARGED METAL IN WATER WITHOUT IONS

Water is the common primary chemical species in all the calculations described in this paper and it is important to know its behaviour in electric fields without the additional structure changing effects of ions. In this simulation 158 ST2 model water molecules were confined between the metal surface at $z_0 = 0.931$ nm and the 'dielectric' wall at $z = -z_0$. Gap between surfaces is $\Delta z = 1.862$ nm = L the edge length of the simulation cell. The water film thickness corresponds to about 4.5 layers of water. For comparison we note that in the calculations of Lee, McCammon and Rossky[19] there were 216 water ST2 molecules equivalent to about six layers. The image plane of the metal was at z = 0.931 nm the right hand surface. Left confining boundary is a dielectric surface (with dielectric constant ε=1) with no image field. The repulsive part of the 9-3 potentials on both sides of the box began at |z|=0.682 nm.

There are no ions in this sample. The electric field across the system comes from (uncompensated) positive charge density of $q_T = q_{uc} = +1$ on plate with area L^2, or equiv-

alently an charge density of 0.29e/(nm)^2. The electric field in vacuum due to this charge is about 5.2 GV/m . Density profiles in the z direction were obtained by averaging 900 configurations over the xy plane. These profiles are shown in Figure 5. The total surface field is just the applied field. Since the field attracts negative charge to the metal the water orients with point charges PC_ST2 directed towards the metal. In comparing Figure 5 profiles with similar ones obtained by reversing the direction of the external field (not shown here) we note there is slightly more structure in the negative field than in zero field (not shown here) or the positive field (Figure 5). The structure is most prominent on the metal side because the O-H bond is longer than PC-O bond and so the proton-proton image interaction being larger pulls the water molecule closer to the metal.

In the PC_ST2 density profile in Figure 5 a distinct shoulder occurs at about 0.7 nm clearly inside the repulsive region of the 9-3 potential. This is permitted because the wall potential acts the center of the water molecule not the component atoms. That the system is strongly polarized as shown by the z component of the dipole density $\rho_p(z)$., and the microscopic charge density $\rho_q(z)$. There is a very pronounced oscillation at the surface in both profiles. Given the existence of oscillations in $\rho_{wat}(z)$ these are not unexpected. What is not clear is whether they result from the superposition of two wall effects. This has been checked with larger N simulations where they occur to the same degree implying the oscillation is intrinsic to one surface. The microscopic charge density has a small value in the interior region of the film and a large oscillation centered at approximately 0.7 nm. The dipole polarization shows large negative deviations at both surfaces, and a uniform positive value across the interior. The behaviour of the dipole and charge densities is that consistent with a high dielectric response material.

All the simple rigid water models display dielectric saturation at high fields because reorientation is the possible relaxation process, and when the molecules are all highly oriented the dielectric is saturated. In the fields in the calculations used by Brodsky et al[22, 23] water was highly oriented and close to saturation, since their system like the one studied here polarizes by molecular reorientation. We have also repeated our calculations in fields up to 1.5 times stronger and find that the interior polarization increases linearly, implying that dielectric saturation has not occurred. However the response of molecules near the surface is different and the dipolar density did not increase linearly with the external field. This is consistent with the presence of more highly oriented and more densely packed water molecules next to the surfaces.

The question of dielectric response of thin films and near surfaces in larger systems is of great interest. If we assume linear response of the electric polarization to an external field then the dielectric constant is given by

$$\frac{\varepsilon_0}{\bar{\varepsilon}} = 1 - \frac{1}{2zq_T}\int_{-z}^{z} \bar{P}_z(z')\,dz' \qquad [14]$$

In the integrand $\overline{P}_z$ is the dipole density parallel to the surface normal (z) averaged over the xy plane. The electrode charge is q_T, and the integration limit is bounded $z < L/2$. The central portion of the dipole density is linear in the applied field, and appears to provide a convenient 'quick' and unambiguous way to calculate the dielectric 'constant' $\bar{\varepsilon}_{zz}$. However in practise this is not easily realized because to check convergence one must evaluate the integral for very large system to avoid interference from the walls.

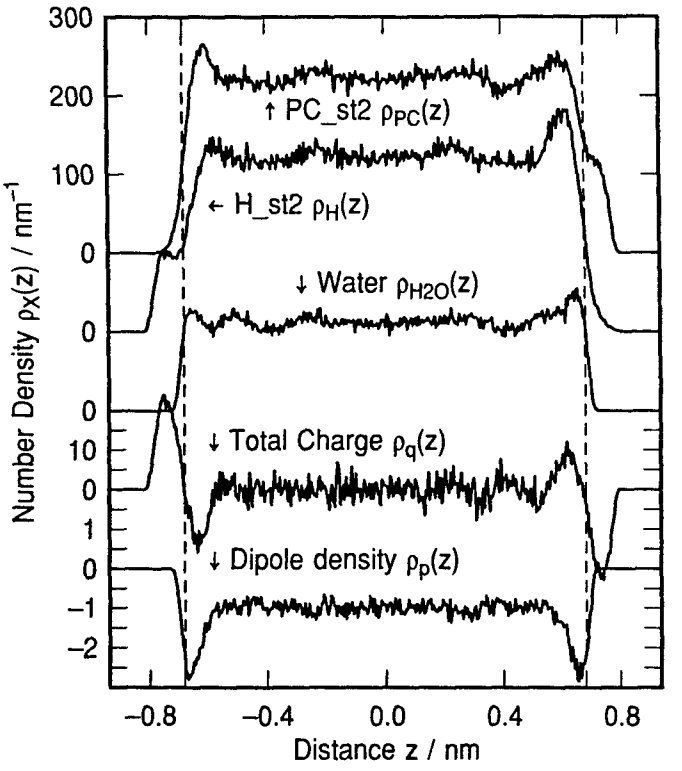

Figure 5. Water without any ions between charged plates with $q_T = q_{uc} = +1$. Component density profile plots for 158 ST2 water molecules adjacent to charged metal electrode on right side. The total electric charge density on the electrode is one positive electron on the simulation plate of area L^2, where L = 1.862 nm. 0.29 e/(nm)^2 The vacuum electric field is approximately 5 GV/m.

FLUORIDE SOLUTIONS. STRONG ELECTRIC FIELD EFFECTS

In this section we discuss several simulations performed with one and two fluorides in the cell (effective ionic concentrations of 0.35 M and 0.70 M respectively) containing 157 and 156 water molecules respectively. We will show that at the higher concentration there is

more dense oriented layer of surface water and that the inner surface electric field drives the effect.

Figure 6 shows some representative results for one fluoride ion in the form of density profiles for the fluoride ion and the atomic components of water. In this calculation $q_T = q_{im} = +1$ and $q_{uc} = 0$. The surface field arises from the negatively charged fluoride ion

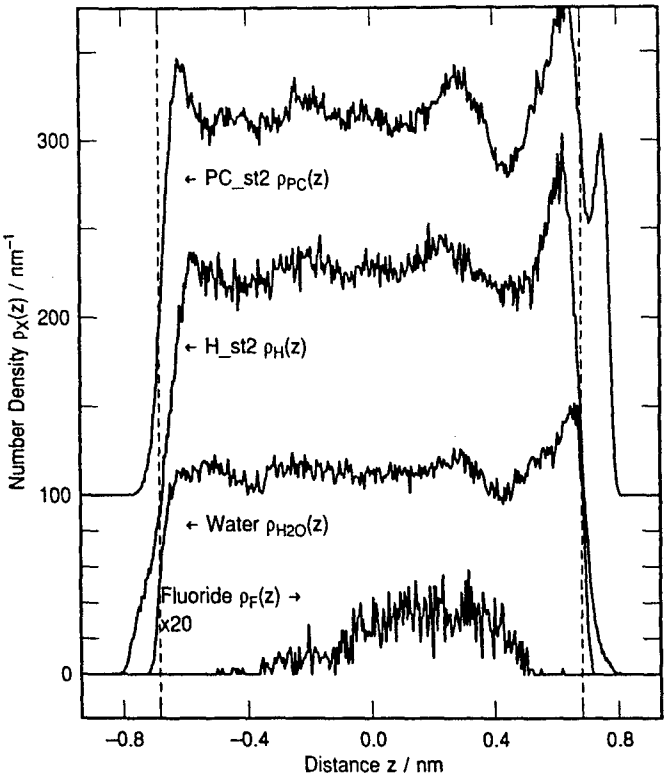

Figure 6. Adsorption of fluoride anions. Density profiles for one fluoride F⁻ and 157 ST2 water molecules between a metal electrode and the dielectric boundary. Charge on the metal $q_T = q_{im} = +1$. Image plane at z = 0.931 nm . Repulsive portion of the wall potentials begin at |z| = 0.682 nm. Note oriented water layer forming near the metal (rhs) with point charge (PC top curve) pointing at metal.

and its image. Because the ion is distributed uniformly in the xy plane the surface electric field is similar to that inside a capacitor (with a 1.4 nm gap). Features in the water density profiles near the metal surface resemble those already seen for water without ions in Figure 5.

Features on the left at the dielectric boundary do not compare well, in fact they resemble water in zero field (not shown here). These results show that in the single ion case there is no field at the dielectric and a high field at the metal surface. This indicates that the inner field felt by surface waters is similar to the externally applied field in the absence of ions. Closer comparison shows that at the metal side the water peaks are uniformly stronger. In particular the PC_ST2 density profile shows a distinct peak near 0.75 nm, to be compared with the shoulder at 0.7 nm in Figure 5. The extra height and structure may be due to water in the solvation sheath of the fluoride ion at its position of closest approach. Recall that the fluoride ion is strongly hydrated and shows no propensity to contact adsorb. Fluoride remains hydrated even at the point of closest approach (ca. 0.55 nm) to the metal. However at this distance the solvation shell is splayed against the electrode. The distribution is broad (-0.4 nm to 0.5 nm, peak near 0.2 nm) covering almost all accessible configuration space consistent with the ion being strongly hydrated and a permanent resident of the diffuse layer. Note also that the fluoride distribution is diffuse across the entire water film, and there being no hint of a sharp plane or barrier (equivalent to an outer Helmholtz plane OHP in the traditional model) across which the ion is prevented from passing. In these simulations the fluoride behaves more like a strongly hydrated ion in the Grahame model of the electric double layer. Figure 7 shows density profiles for the case of two fluoride ions in the simulation cell with 156 water molecules. The total microscopic charge density is also shown. Charge on the metal $q_T = q_{im} = +2$. The density profile for two fluorides resembles that of a single fluoride except it is shifted further from the metal (range is from -0.5 to 0.5 nm with the peak near 0.0 nm). The electric field due to metal charge and ions is zero near the dielectric boundary as seen by comparing water component profiles with previous two figures. The inner surface field has a much higher value as judged by sharper more intense peaks near the metal surface. The sharp water peak near 0.65 nm has twice the interior density value. Some of this water has one PC pointing at the electrode. Also note that the fluoride density profile is shifted away from the metal surface, consistent with the notion that the compacted layer of surface water hinders the approach of strongly hydrated ions. This effect is consistent with the concept of the OHP being approximately two water molecules distant from the electrode. The position of the first H_ST2 peak, and the near surface oscillation in microscopic charge confirm the overall picture as described.

Next we show the importance of the long range interfacial dipole field by repeating the calculation for one fluoride shown in Figure 6 with an uncompensated field equivalent to a charge of one positive electron on the plate area L^2. The charge on the metal is given by $q_T = q_{im} + q_{uc} = +2$, with $q_{im} = q_{uc} = +1$. Figure 8 shows the density profiles for one

fluoride F^- and 157 ST2 water molecules between a charged metal electrode and a dielectric boundary. Note the similarities in the density profiles for water and its components in the range z > 0 nm in Figures 7 and 8. In this region the density profile almost

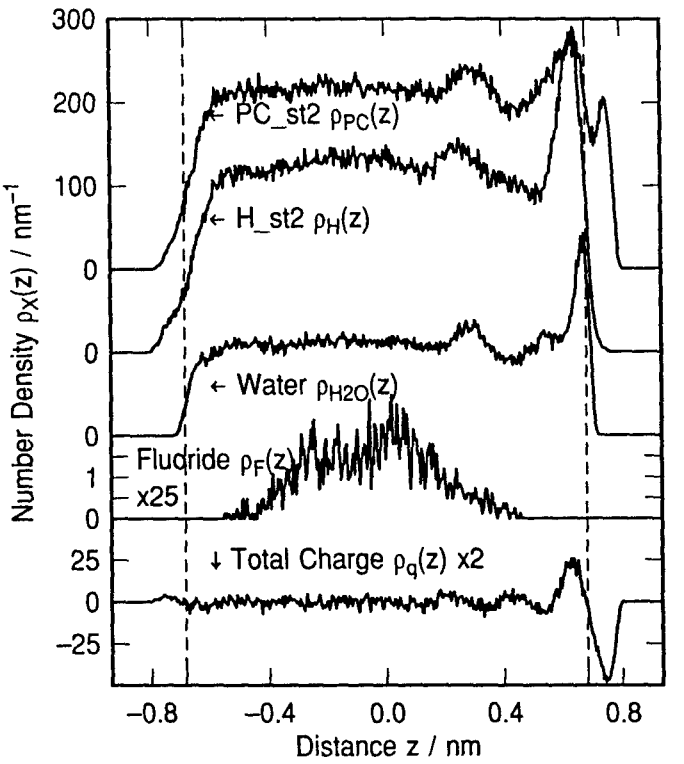

Figure 7. Adsorption of anions continued. Density profiles for two fluoride F^- and 156 ST2 water molecules between a metal electrode and the dielectric boundary. Charge on the metal $q_T = q_{im} = +2$. Image plane at z = 0.931 nm. Repulsive portion of the wall potentials begin at |z| = 0.682 nm. Note the high density oriented water peak near 0.65 nm and the shift in the fluoride distribution away from the metal compared to Figure 6.

superimpose. Since we have shown that the water profiles are sensitive to the electric field it suggests that the inner fields are almost the same in the two cases. Furthermore these calculations show that it is the field in the inner layer and not steric effects due to ions that drives the structural changes.

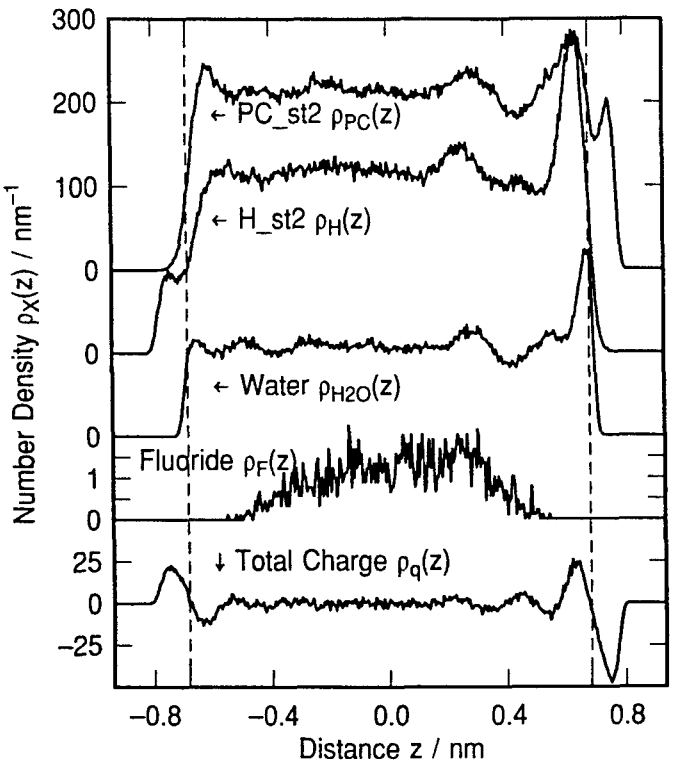

Figure 8. Adsorption of anions continued. Surface electric field effects. The charge on the metal is given by $q_T = q_{im} + q_{uc} = +2$, with $q_{im} = q_{uc} = +1$. Density profiles for one fluoride F^- and 157 ST2 water molecules between a charged metal electrode and a dielectric boundary. Note similarity of water and component density profiles in Figure 7 for z > 0 nm. Image plane at z = 0.931 nm. Repulsive portion of the wall potentials begin at |z| = 0.682 nm.

ELECTRIC FIELD EFFECTS. CASE STUDY OF SODIUM FLUORIDE

In this section we consider the effect of interchanging anions and cations with similar strengths of hydration. We have chosen NaF solutions to explore this case, and have chosen to work also with an uncompensated field ($q_{uc} = \pm 1$) to mimic higher effective concentrations than actually used in the calculation.

Figure 9 shows the density profiles for a simulation with one fluoride F^-, two sodium ions Na^+ and 155 ST2 water molecules between a charged metal electrode and a dielectric boundary. The charge on the metal was $q_T = q_{im} + q_{uc} = -2$, with $q_{im} = q_{uc} = -1$. Note that even though the field has opposite sign there is a superficial similarity of water density profile with those shown in Figure 7 and 8.

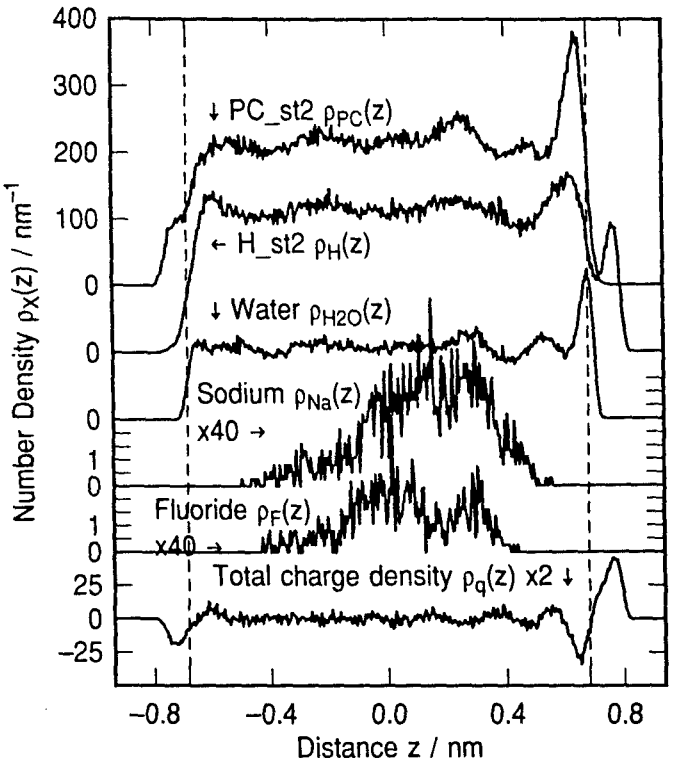

Figure 9. Approximate equivalence interchanged anions and cations, part 1. The charge on the metal was $q_T = q_{im} + q_{uc} = -2$, with $q_{im} = q_{uc} = -1$. Note similarity of water and component density profiles in Figure 7. Density profiles for one fluoride F^-, two sodium ions Na^+ and 155 ST2 water molecules between a charged metal electrode and a dielectric boundary. Image plane at z = 0.931 nm . Repulsive portion of the wall potentials begin at |z| = 0.682 nm.

Figure 10 displays the profiles for two fluoride F^-, one sodium ions Na^+ and 155 ST2 water molecules The charge on the metal was now positive $q_T = q_{im} + q_{uc} = 2$, with $q_{im} = q_{uc} = +1$. Note similarity of water and component density profiles in Figure 7. Note also that the density profiles for Na and F in Figures 9 and 10 when interchanged are almost the same. These calculation extend to mixed electrolytes the conclusion reached in the last section that the water structure in the inner layer is the result of surface electric fields.

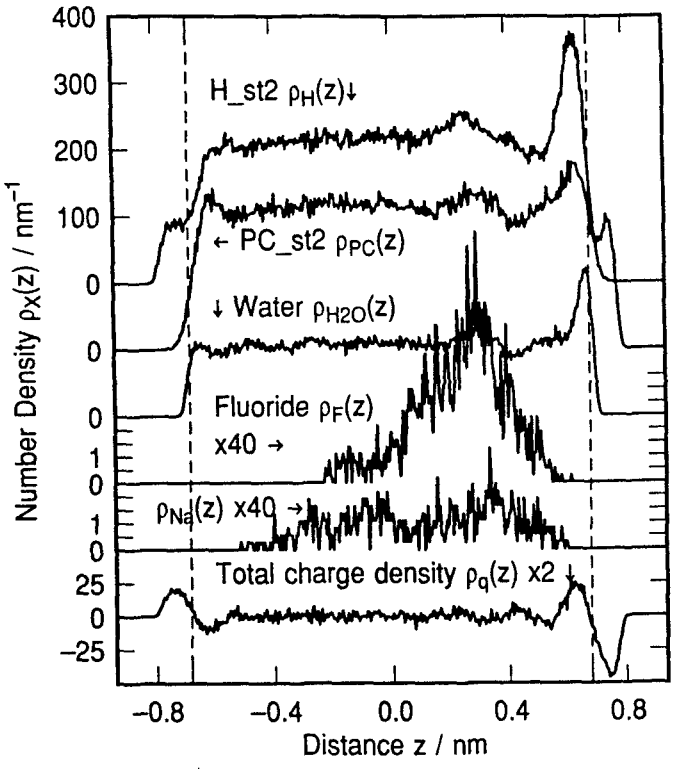

Figure 10. Approximate equivalence interchanged anions and cations, part 2. Note similarity of water and component density profiles in Figure 7. The charge on the metal was positive $q_T = q_{im} + q_{uc} = 2$, with $q_{im} = q_{uc} = +1$. Density profiles for two fluoride F^-, one sodium ions Na^+ and 155 ST2 water molecules between a charged metal electrode and a dielectric boundary. Image plane at z = 0.931 nm . Repulsive portion of the wall potentials begin at |z| = 0.682 nm.

SMALL CATION COADSORBED WITH IODIDE IONS

In this set of simulations we explore another important aspect of adsorption on metal electrodes, namely the ability of strong contact adsorbers like iodide ions I^- to adsorb on positively charged electrodes in sufficient excess to change the sign of the charge at the interface as observed by an ion in the diffuse layer. In this case cations are attracted out of the diffuse layer region to compensate the excess negative ion charge at the interface. The lithium ion was chosen as cation. We have performed these calculations without and with uncompensated charge.

In the first case the charge on the metal was $q_T = q_{im} = +1$, and in the second case $q_T = q_{im} + q_{uc} = 2$. Figure 11 displays the density profiles for all components of the system and the microscopic charge density. The simulation time was 1000 ps with the first 100 ps discarded for equilibration, and then configurations were stored every 1.0 ps.

Note that both iodide ions adsorbed in one sharply peaked distribution mostly inside the onset of the repulsive wall region, but with a small tail out to smaller z positions. The iodide distribution in zero field is characteristically different from the case when an attractive field exists there being a longer tail into the electrolyte indicating a more weakly bound state. The single Li ion occupies a (possibly weakly bimodal) diffuse-like distribution between -0.6 nm and 0.6 nm. The water profiles hint that the inner surface electric field across the first water layer is weak because the iodide charge is so close to the metal, i.e., the waters are outside the main part of the capacitor is this model. Additionally the large size of the iodides tends to exclude some water from the surface.

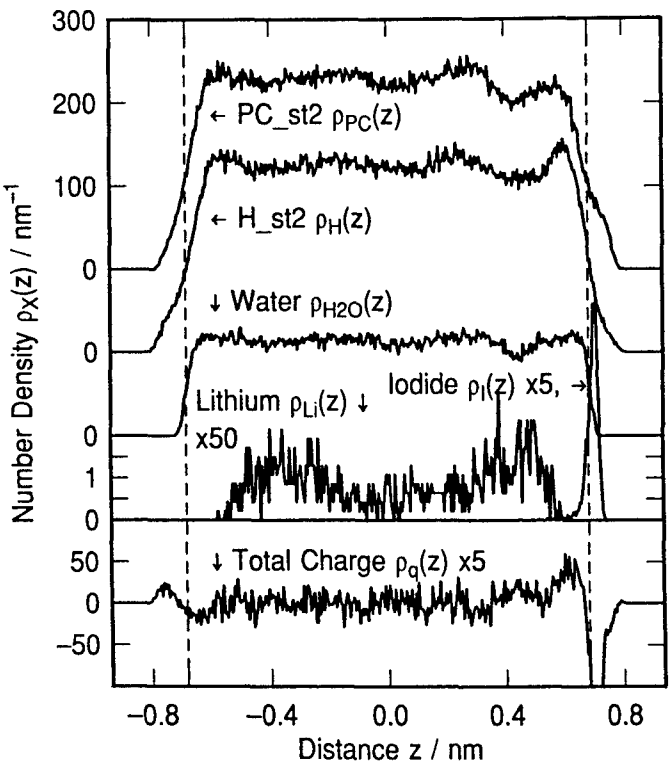

Figure 11. Coadsorption of ions. The charge on the metal was $q_T = q_{im} = +1$. Interface becomes effectively negatively charged after the adsorption of two iodide ions, thereby attracting the positive Li ion. Density profiles for two I^-, one lithium cation Li^+ and 155 ST2 water molecules using the immersed electrode model.

In the second case the charge on the metal was $q_T = q_{im} + q_{uc} = +2$ due to the presence of the extra charge $q_{uc} = +1$. The net charge on the electrode repells the lithium ion. Figure 12 displays the density profiles for all components of the system and the charge density. The simulation time was 1000 ps with the first 100 ps discarded for equilibration, configurations were stored every 0.5 ps. Note that both iodide ions were adsorbed in a sharply

peaked distribution that resembles the single adsorbed iodide distribution calculated by Glosli and Philpott[16]. The single Li ion occupies diffuse-like distribution between -0.6 nm and 0.3 nm and peaks around -0.1 nm. The region between 0.0 and 0.3 nm defines a region of reduced probability of penetrating into inner layer and contacting either the wall or the adsorbed iodide ions.

It is noticeable that the water structure near the metal surface though less well defined than in the case of adsorbed fluoride (see Figures 7, 8 or 10) shows more structure than in Figure 11. Overall the structure resembles water in the field of a positively charged electrode as shown in Figure 5. Some artifacts are expected due to some surface PC reaching the high field region between the iodide layer and the metal.

A final word of caution. The statistics for lithium ions in the simulations described in this section are not as good as in previous calculations. The presence of two iodides on the surface creates a rough surface and the calculations should be run several nanoseconds to permit the positive ion to explore all configuration space.

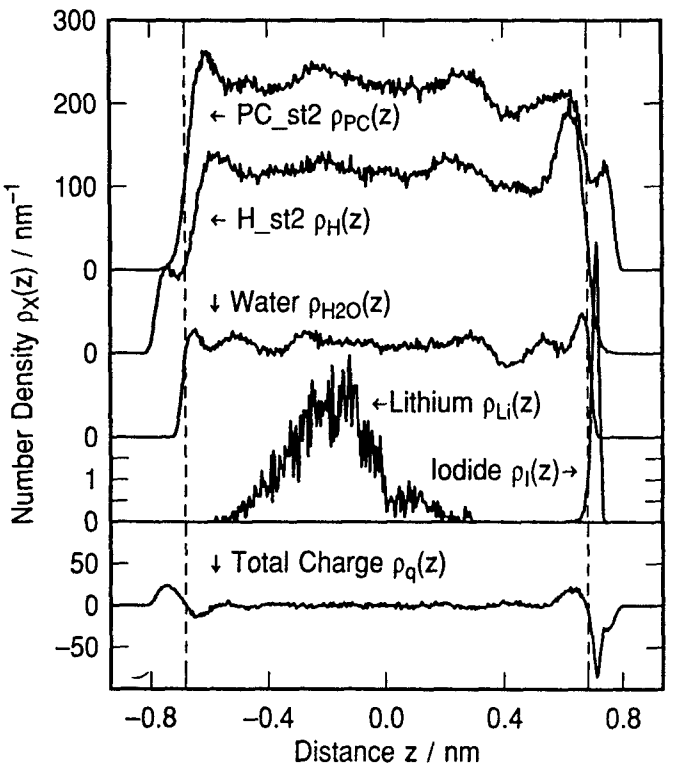

Figure 12. Coadsorption of ions continued. Density profiles for two I^-, one Li^+ and 155 ST2 water molecules next to immersed electrode. The charge on the metal was $q_T = q_{im} + q_{uc} = +2$.

CONCLUSIONS

In this paper we have shown how a simple model suffices to mimic many phenomena familiar from experiments on electric double layers at the electrolyte-metal interface. There was emphasis on electrostatic interactions and understanding the role played by the inner surface field in driving structural changes in the surface water layer. This is expected to be important for all polar systems. A key element of the calculations was the use of the fast multipole method to accurately and efficiently calculate coulomb interactions so that macroscopic electric fields were computed correctly. Among the phenomena studied were: an oriented boundary layer of water at the electrode when it is charged, penetration of nominally diffuse layer species like hydrated fluoride into the inner layer, and attraction of cations to a positively charged electrode induced by contact adsorption of large ions like iodide.

Finally we point out that the techniques described in this report with minor modifications can be extended to more complex systems, for example: microelectrodes, polymer coated electrodes, biological membranes, globular protein surfaces, and clay surfaces.

ACKNOWLEDGEMENTS

This research was supported in part by the Office of Naval Research.

REFERENCES

1 H. L. von Helmholtz, Ann. Physik **89**, 211 (1853).
2 G. Gouy, Ann. chim. phys. **8**, 291 (1906).
3 G. Gouy, J. Physique **9**, 457 (1910).
4 G. Gouy, Ann. phys. **7**, 129 (1917).
5 D. L. Chapman, Phil. Mag. **25**, 508 (1913).
6 P. Debye and E. Hückel, Physik. Z. **24**, 185 (1923).
7 L. Greengard and V. Rokhlin, J. Comp. Phys. **73**, 325-348 (1987).
8 L. F. Greengard, *The Rapid Evaluation of Potential Fields in Particle Systems*. (The MIT Press, Cambridge, Massachusetts, 1987).
9 J. Carrier, L. Greengard, and V. Rokhlin, Siam J. Sci. Stat. Comput. **9**, 669 (1988).
10 L. Greengard and V. Rokhlin, Chemica Scripta **29A**, 139-144 (1989).
11 R. B. Gennis, *Biomembranes. Molecular Structure and Function.* (Springer-Verlag, New York, 1989), pp. 235-269.
12 H. van Olphen, *Clay Colloid Chemistry* (Kreiger, Malabar Florida, 1991).
13 J. N. Glosli and M. R. Philpott, J. Chem. Phys. **96**, 6962-6969 (1992).
14 J. N. Glosli and M. R. Philpott, J. Chem. Phys. **98**, 9995-10008 (1993).
15 J. N. Glosli and M. R. Philpott, Electrochem. Soc. Symposium Proc. **93-5**, 80-90 (1993).
16 J. N. Glosli and M. R. Philpott, Electrochem. Soc. Symposium Proc. **93-5**, 90-103 (1993).

17 J. O. Bockris and A. K. Reddy, *Modern Electrochemistry, Vol.1* (Plenum Press, New York, 1973).

18 J. O. Bockris and A. K. Reddy, *Modern Electrochemistry, Vol.2* (Plenum Press, New York, 1973).

19 C. Y. Lee, J. A. McCammon, and P. J. Rossky, J. Chem. Phys. **80**, 4448-4455 (1984).

20 J. P. Valleau and A. A. Gardner, J. Chem. Phys. **86**, 4162-4170 (1987).

21 Y. J. Rhee, J. W. Halley, J. Hautman, and A. Rahman, Phys. Rev. B **40**, 36-42 (1989).

22 A. M. Brodsky, M. Watanabe, and W. P. Reinhardt, Electrochimica Acta **36**, 1695-1697 (1991).

23 M. Watanabe, A. M. Brodsky, and W. P. Reinhardt, J. Phys. Chem. **95**, 4593 (1991).

24 N. Parsonage and D. Nicholson, J. Chem. Soc. Faraday Trans. 2 **82**, 1521-1535 (1986).

25 N. Parsonage and D. Nicholson, J. Chem. Soc. Faraday Trans. 2 **83**, 663 - 673 (1987).

26 A. A. Gardner and J. P. Valleau, J. Chem. Phys. **86**, 4171-4176 (1987).

27 E. Spohr and K. Heinzinger, Electrochimica Acta **33**, 1211-1222 (1988).

28 E. Spohr and K. Heinzinger, Ber. Bunsenges. Phys. Chem. **92**, 1358-1363 (1988).

29 K. Heinzinger and E. Spohr, Electrochimica Acta **34**, 1849-1856 (1989).

30 J. Hautman, J. W. Halley, and Y. Rhee, J. Chem. Phys. **91**, 467-472 (1989).

31 K. Foster, K. Raghavan, and M. Berkowitz, Chem. Phys. Lett. **162**, 32-388 (1989).

32 K. Raghavan, K. Foster, K. Motakabbir, and M. Berkowitz, J. Chem. Phys. **94**, 2110-2117 (1991).

33 R. Kjellander and S. Marcelja, Chemica Scripta **25**, 73-80 (1985).

34 E. Spohr and K. Heinzinger, J. Chem. Phys. **84**, 2304-2309 (1986).

35 J. Seitz-Beywl, M. Poxleitner, and K. Heinzinger, Z. Naturforsch. **46A**, 876 (1991).

36 D. A. Rose and I. Benjamin, J. Chem. Phys. **95**, 6856-6865 (1991).

37 K. Heinzinger, Pure Appl. Chem. **63**, 1733-1742 (1991).

38 G. E. Schacher and F. W. de Wette, Phys. Rev. **136A**, 78-91 (1965).

39 D. C. Grahame., Chem. Rev. **41**, 441 (1947).

40 D. C. Grahame., J. Amer. Chem. Soc. **79**, 2093 (1957).

41 G. Lippmann, Ann. Chim. Phys. (Paris) **5**, 494 (1875).

42 H. D. Hurawitz, J. Electroanal. Chem. **10**, 35 (1965).

43 E. Dutkiewicz and R. Parsons, J. Electroanal. Chem. **11**, 100 (1966).

44 F. C. Anson, Accts Chem. Res. **8**, 400-407 (1975).

45 R. Parsons, Chem. Rev. **90**, 813-826 (1990).

46 A. T. Hubbard, Chem. Rev. **88**, 633 - 656 (1988).

47 J. O. Bockris and A. Gonzalez-Martin, *Spectroscopic and Diffraction Techniques in Interfacial Electrochemistry, NATO ASI Series C* (Kluwer,Dordrecht,Holland, 1990), pp. 1-54.

48 J. W. Albery, *Electrode Kinetics* (Clarendon Press, Oxford, 1975).

49 L. Antropov, *Theoretical Electrochemistry* (Mir Publishers, Moscow, 1972).

50 J. O. Bockris and S. U. Khan, *Quantum Electrochemistry* (Plenum Press, New York, 1979).

51 J. W. Halley, B. Johnson, D. Price, and M. Schwalm, Phys. Rev. B **31 B**, 7695-7709 (1985).

52 J. W. Halley, Supperlattices and Microstructures **2**, 165-172 (1986).

53 J. W. Halley and D. Price, Phys. Rev. B **35 B**, 9095-9102 (1987).

54 W. Schmickler and D. Henderson, Prog. Surf. Sci. **22**, 323 (1986).

55 D. Henderson, *Trends in Interfacial Electrochemistry* (Reidel, Dordrecht, Holland, 1986), p. 183.

56 O. R. Melroy, M. G. Samant, G. L. Borges, J. G. Gordon, L. Blum, J. H. White, M. J. Albarelli, M. McMillan, and H. D. Abruna, Langmuir **4**, 728 (1988).

57 M. F. Toney, J. G. Gordon, and O. R. Melroy, SPIE Proceedings **1550**, 140 (1991).

58 M. F. Toney, J. N. Howard, J. Richer, G. L. Borges, J. G. Gordon, O. R. Melroy, D. G. Wiesler, D. Yee, and L. B. Sorensen, Nature (1994).

59 T. Tadjeddine, D. Guay, M. Ladouceur, and G. Tourillon, Phys. Rev. Lett. **66**, 2235 - 2238 (1991).

60 F. H. Stillinger and A. Rahman, J. Chem. Phys. **60**, 1545 (1974).

61 O. Steinhauser, Mol. Phys. **45**, 335-348 (1982).

62 K. Heinzinger, *Computer Modelling of Fluids Polymers and Solids,* (Kluwer,Dordrecht, 1990), pp. 357-404.

63 M. P. Allen and D. J. Tildesley, *Computer Simulation of Liquids* (Oxford University Press, Oxford, 1989), pp. 88-90.

64 D. J. Evans, Mol. Phys. **34**, 317-325 (1977).

65 D. J. Evans and S. Murad, Mol. Phys. **34**, 327-331 (1977).

Interaction of water with metal surfaces

Sheng-Bai Zhu and Michael R. Philpott
IBM Research Division, Almaden Research Center, San Jose, California 95120-6099

(Received 29 November 1993; accepted 20 January 1994)

A new class of potential suitable for modeling the adsorption of water on different metal sites is described. The new potentials are simple in form and convenient for use in computer simulations. In their real space form they comprise three parts: A pairwise sum of spatially anisotropic 12-6 potentials, a pairwise sum of isotropic short range potentials, and an image potential. Two modifications of the potential are developed. In the first, the anisotropic potential acts only on the oxygen atom and not on the protons. In the second, the potential acts on all the atoms of the water molecule. In practical calculations it is convenient to transform the potential to a reciprocal space form in the manner described by Steele [Surf. Sci. **36**, 317 (1973)]. Adsorption of water at top, bridge, and hollow sites on (100), (110), and (111) surfaces of Pt, Ni, Cu, and Al were studied using two fitting parameters and the results compared with previous theoretical calculations.

I. INTRODUCTION

Understanding the properties and dynamic behavior of water in the vicinity of metallic surfaces is of fundamental importance in electrochemistry, catalysis, and the study of corrosion. A variety of experimental techniques exist capable of providing data about surface adsorbed water, e.g., those described in the review of Thiel and Madey,[1] surface infrared spectroscopy by O'Grady[2] and Melendres,[3] and the x-ray technique described by Toney and co-workers.[4] Computer simulations play an important role by providing detailed microscopic insight about the water multilayers, which is currently unavailable from laboratory experiments. A matter of primary importance for performing a computer simulation is, of course, the knowledge of the relevant interactions. Our purpose in this paper is to describe a new simple potential function useful for molecular dynamics simulations of metal–aqueous interfaces. The weight of experimental and theoretical evidence to be surveyed briefly later, supports the adsorption of water with oxygen atom down on the top site of a metal surface. In contrast a pairwise sum of 12-6 Lennard-Jones (LJ) potentials predicts the binding energy order for adsorption as hollow>bridge>top sites. It is also clear that the electronic properties of the metal play a critical role in the interaction with water which is weakly chemisorbed rather than physisorbed, and that the chemisorption bond directs adsorption to the top site. The key idea in our development is the introduction of a simple angular dependence into the traditional 12-6 Lennard-Jones potential to mimic the directionality of the chemisorptive bond.

In the earliest studies the water-surface potential was assumed to have two components, image terms to describe the polarization interaction of molecular charge with the conduction electrons and 12-6 Lennard-Jones terms to account for Pauli repulsion and the dispersion attraction interaction with all electrons in the core and conduction band. We will refer to this latter part as the core term. Earlier efforts[5–8] described the interaction of a molecule and the conduction electrons of a metal often by truncating the image potential to the leading term. In practical computations, the core potential part often appears in its integrated form which, within the first-order approximation, is a 10-4 or 9-3 potential. These models, though reasonable at first sight, fail to predict orientational properties of water molecules chemisorbed on the surface of a transition metal. Existing experimental data[1] for the work function change suggest that the water dipoles tend to orient perpendicular to the surface rather than parallel to it. In the case of low index faces where the metal atoms are explicitly taken into account, the above-mentioned water-wall potential leads to a conclusion that the preferred adsorption is on the hollow sites of the surface.[5] This contradicts the weight of evidence that an adsorption on top of the metal atom is the preferred site, as indicated by both the experimental observations[9] and the quantum mechanical calculations.[10–14] It is therefore a challenge to find a water–metal surface potential function that is simple in form and still describes the observed preferences.

Extended Hückel molecular orbital calculations of a water molecule on top of a cluster of five platinum atoms[10] were used by Spohr and Heinzinger[15] and Spohr[16] to fit the water-surface potential to a set of exponential functions. Berkowitz and co-workers[17,18] have prescribed potential functions for water–Pt(100) and water–Pt(111) interfaces based on the Heinzinger–Spohr form, but incorporating the lattice symmetry and corrugation explicitly. These potentials usefully describe the chemisorption bonding, but not the image contribution or its contribution to long range interfacial electric fields. In a quite separate approach Siepmann and Sprik[19] have modified the bond-angle-dependent potentials developed for covalent solids[20] by the use of overlapping Gaussian charge distributions centered at the metal atoms, as a compromise between the image charge formalism and a microscopic description of the electronic structure. These more complicated potential models are in qualitative agreement with more elaborate *ab initio* calculations and existing experimental data.

Finally, we make a comment about Xe on Pt, another weak chemisorption system. Recently, Barker and Rettner[21] have used a large body of energy and angle resolved gas-surface scattering data to derive a benchmark potential for the Xe–Pt(111) system. For water–metal systems there is currently no single molecule-surface scattering data and a

 0021-9606/94/100(9)/6961/8/$6.00

much less sophisticated approach to deriving a potential is desirable.

II. POTENTIAL ENERGY FUNCTION

The physisorption of molecules on insulators has been usefully modeled in many cases using a pairwise sum of atom–atom Lennard-Jones 12-6 potentials and r^{-1} Coulomb potentials. The extension of this model to a metal would describe the molecule-core electron interaction with a Lennard-Jones (LJ) potential and the molecule-conduction electron interaction with an image potential. In practice the Lennard-Jones potential also includes Pauli repulsion and attractive dispersion interactions for all the electrons making up the metal. This does not work for water, or for that matter the adsorption of Xe atoms on Pt.[21] Many-body effects other than those giving the asymptotic image interaction are expected to be important for the adsorption on metals. It is not correct to treat a metal surface as a simple assembly of uncorrelated atoms; nonadditive interactions should be incorporated. However, to obtain a concise potential in a form which is convenient for adjusting parameters and useful in computer simulations, it would be very helpful if one could treat the many-body contribution in an approximate but effective manner. In this section, we show that this possibility indeed exists. Introducing angular dependence into the traditional LJ potential can make the top site most favored for a water molecule in an oxygen down geometry.

The two potentials described below are labeled A1 and A2, the latter being the all atom model. In both there is a LJ potential modified by incorporation of angular dependence. Instead of spherical symmetry, the repulsive and attractive parts have the symmetry of an ellipsoid of revolution. Several interactions contribute to angular dependent terms: First is the chemisorptive bond interaction involving mixing of orbitals from the metal and oxygen, another comes from the interaction between the permanent dipole moment of the adsorbed molecule and the induced moment of the solid atom.[22] Repulsions due to overlap of electron clouds at short separations are also considered in this modification. In addition, extra terms proportional to r^{-n} are introduced to mimic short-range bonding that pulls the oxygen atom closer to the top atom. These angular dependent, short-range interactions allow better modeling of the adsorption of water on metal surfaces. In simulations where metal atom dynamics and surface reconstruction are not considered, it is useful to explicitly incorporate surface lattice translational symmetry using the method first proposed by Hove and Krumhansl[23] and subsequently universally adopted.[24,25]

In both models, the potential for one molecule interacting with the metal is written

$$V_{\text{w-met}}=V_{\text{w-cond}}+V_{\text{w-core}}, \tag{1}$$

where the first term represents the water molecule-conduction electron potential and the second term the molecule-core electron contribution. As usual, we approximate the first term by a classical image potential. The image charge q_{image} of a classical point charge q is located at the symmetrical position below the image plane and has the magnitude[26]

$$q_{\text{image}}=\frac{1-\epsilon_r}{1+\epsilon_r}\ q. \tag{2}$$

The "correct" choice of the image plane position has been the subject of much debate. It is not deeper into the metal than the first nuclear plane for low index faces. This is the position we will assume. For a grounded ideal metal, the relative permittivity ϵ_r is infinite, and $q_{\text{image}}=-q$. For a molecule modeled by point sites, each point charge interacts with all the image charges by means of a Coulomb potential

$$V_{\text{w-cond}}=\sum_{l,k}\frac{q_l q_k}{2r_{lk}}, \tag{3}$$

where the index l stands for the real charge and k for the image charge with r_{lk} being their distance apart. Since the polarization response of the surface changes with the addition of new molecules, Eq. (3) describes a nonadditive surface polarization.

The second term in Eq. (1) contains the anisotropic short-range potential and the short-range r^{-n} potential (n integer) and so requires much more detailed description.

$$V_{\text{w-core}}=V_{\text{w-an}}+V_{\text{w-isr}}, \tag{4}$$

where $V_{\text{w-isr}}$ is the isotropic short-range part and $V_{\text{w-an}}$ contains the anisotropic part. The anisotropic contribution comes from many-body effects including the polarization of core electrons of the metal atoms. Next we construct both these parts separately using pairwise sums and then use translational periodicity to reduce them to usable forms. Henceforth we drop explicit reference to water (label w).

To begin, consider a perfect crystal surface in which the basic vectors of the lattice are $\mathbf{a}_1$ and $\mathbf{a}_2$. Next consider a point particle p at $\mathbf{r}_p=(\boldsymbol{\rho}_p,z_p)$ where z_p is the perpendicular distance above the surface and $\boldsymbol{\rho}_p$ is the projection of $\mathbf{r}_p$ onto the surface plane. The label p stands for O or either of two H atoms. For convenience we choose the x axis to be parallel to $\mathbf{a}_1$ and take origin to be at the inversion center of the first lattice plane. Let the atoms j of the surface plane be located at

$$\mathbf{l}_j=n_{1j}\mathbf{a}_1+n_{2j}\mathbf{a}_2 \tag{5}$$

then the distance between atom j and the particle p is written

$$r_{pj}=\sqrt{\rho_{pj}^2+z_{pj}^2}, \tag{6}$$

where $\rho_{pj}^2=x_{pj}^2+y_{pj}^2$, and x_{pj},y_{pj},z_{pj} are the components of the vector

$$\mathbf{r}_{pj}=\mathbf{r}_p-\mathbf{l}_j. \tag{7}$$

In this frame the anisotropic part of the potential has the form

$$V_{\text{an}}(p;\mathbf{r}_p)=4\epsilon_{ps}\sum_j\left[\left(\frac{\sigma_{ps}^2}{(\alpha\rho_{pj})^2+z_{pj}^2}\right)^6-\left(\frac{\sigma_{ps}^2}{(\rho_j/\alpha)^2+z_{pj}^2}\right)^3\right] \tag{8}$$

which, in essence, is a generalization of the well-known 12-6 Lennard-Jones interaction. Here α is a scaling parameter that

cts differently on the repulsive and attractive parts and gives ıe potential its anisotropy between directions in the xy lane and the z axis. In our calculations α was set equal to .8, since much smaller values would not be consistent with veakly chemisorbed molecules. The summation in Eq. (8) is aken over all atoms j of the surface.

The short-range isotropic contribution can, in general, be lescribed as

$$V_{\rm isr}(n,p;\mathbf{r}_p)=-4\epsilon_{ps}\sum_j \frac{C_n(p)\sigma_{ps}^n}{r_{pj}^n}, \tag{9}$$

where C_n is a fitting parameter with n being an integer. The scale factors σ_{ps} and ϵ_{ps} are separated for mathematical convenience.

Now that we have described the form of the water–core interactions for the two models we can write down the complete potentials for the two cases. In the first model (A1) we have

$$V_{\rm A1}=V_{\rm w\text{-}cond}+V_{\rm an}(\mathrm{O};\mathbf{r}_{\rm O})+V_{\rm isr}(8,\mathrm{O};\mathbf{r}_{\rm O}) -\sum_{\rm H} V_{\rm isr}(6,\mathrm{H},\mathbf{r}_{\rm H}). \tag{10}$$

In the second model (A2) we have

$$V_{\rm A2}=V_{\rm w\text{-}cond}+V_{\rm an}(\mathrm{O};\mathbf{r}_{\rm O})+V_{\rm isr}(10,\mathrm{O};\mathbf{r}_{\rm O}) +\sum_{\rm H}[V_{\rm an}(\mathrm{H};\mathbf{r}_{\rm H})+V_{\rm isr}(10,\mathrm{H};\mathbf{r}_{\rm H})]. \tag{11}$$

Note that in the second model A2, both the oxygen and hydrogen atoms in water interact with the metal atoms through the anisotropic Lennard-Jones potential, and the short-range interaction now has an inverse tenth power dependence. This latter change is needed to describe the atomic polarization under strong electric field near the metal surface. The physical origin of such electrostatic field is the deformation of the electron cloud within a metal.[27–29] We shall show that model A2 improves the binding energy, the equilibrium distance, and the adsorption via hydrogen atoms over model A1 but at the cost of more complexity.

Following the derivation of Steele,[24,25] the lattice sum in Eq. (8) is transformed to reciprocal space

$$V_{\rm an}(p;\mathbf{r}_p)=\frac{8\pi\epsilon_{ps}\sigma_{ps}^2}{A_{\rm cell}}\left\{\frac{\sigma_{ps}^{10}}{10\alpha^2 z^{10}}-\frac{\alpha^2\sigma_{ps}^4}{4z^4} +\sum_{g_j} G(g_j;\mathbf{g}_j\cdot\boldsymbol{\rho})\left[\frac{\sigma_{ps}^{10}}{60\alpha^7}\left(\frac{g_j}{2z}\right)^5 K_5(g_j z/\alpha) -\alpha^4\sigma_{ps}^4\left(\frac{g_j}{2z}\right)^2 K_2(\alpha g_j z)\right]\right\}. \tag{12}$$

In the above equation, the label p is omitted on the right-hand side from $\boldsymbol{\rho}$ and z, $A_{\rm cell}$ is the surface area of a unit lattice cell, $K_m(\xi)$ stands for mth order modified Bessel function of the second kind, and $G(g_j;\mathbf{g}_j\cdot\boldsymbol{\rho})$ includes contributions from all the trigonometric factors $\cos(\mathbf{g}_j\cdot\boldsymbol{\rho})$ with the restriction that the magnitude of $\mathbf{g}_j$ is a constant, equal to g_j.

Analogously the short-range component $V_{\rm isr}$ can be written

$$V_{\rm isr}(n,p;\mathbf{r}_p)=-\frac{8\pi\epsilon_{ps}\sigma_{ps}^2 C_n(P)}{A_{\rm cell}}\left[\frac{1}{n-2}\left(\frac{\sigma_{ps}}{z}\right)^{n-2} +\sum_{g_j} G(g_j;\mathbf{g}_j\cdot\boldsymbol{\rho})\frac{2\sigma_{ps}^{n-2}}{(n/2-1)!} \times\left(\frac{g_j}{2z}\right)^{n/2-1} K_{n/2-1}(g_j z)\right] \tag{13}$$

in terms of the same set of geometric factors G. Note that the G factors depend on the symmetry of the lattice plane and are different for (111), (100), and (110) planes.

We conclude with explicit lists of the geometric factors for each of the three main low index planes starting with the square lattice. For the (100) plane where $|\mathbf{a}_1|=|\mathbf{a}_2|=a/\sqrt{2}$ and $A_{\rm cell}=a^2/2$, the lengths of the two-dimensional $\mathbf{g}_j$ vectors in the reciprocal lattice space are given by

$$g_j=\frac{2\pi}{a}(g_{j1}^2+g_{j2}^2)^{1/2}, \tag{14}$$

where a is the lattice constant, g_{j1} and g_{j2} are integers, which satisfy g_j=constant. Accordingly, we write the dot product of $\mathbf{g}_j$ and $\boldsymbol{\rho}$ as

$$\mathbf{g}_j\cdot\boldsymbol{\rho}=\frac{2\pi}{a}(g_{j1}x+g_{j2}y). \tag{15}$$

Straightforward manipulation of Eqs. (14) and (15) leads to the following explicit expressions for the first five leading terms of the corrugation factors G:

$$G(g_1;\mathbf{g}_1\cdot\boldsymbol{\rho})=\cos\beta_x x+\cos\beta_y y,$$

$$G(g_2;\mathbf{g}_2\cdot\boldsymbol{\rho})=2\cos\beta_x x\cos\beta_y y,$$

$$G(g_3;\mathbf{g}_3\cdot\boldsymbol{\rho})=\cos 2\beta_x x+\cos 2\beta_y y,$$

$$G(g_4;\mathbf{g}_4\cdot\boldsymbol{\rho})=2(\cos 2\beta_x x\cos\beta_y y+\cos\beta_x x\cos 2\beta_y y),$$

and

$$G(g_5;\mathbf{g}_5\cdot\boldsymbol{\rho})=2\cos 4\beta_x x\cos 4\beta_y y,$$

corresponding to $g_1=\beta_x$, $g_2=\sqrt{2}\beta_x$, $g_3=2\beta_x$, $g_4=\sqrt{5}\beta_x$, and $g_5=2g_2$. In the above equations, $\beta_x=\beta_y=2\sqrt{2}\pi/a$.

The situation for (110) surface is similar, except for $|\mathbf{a}_1|=|\mathbf{a}_2|/\sqrt{2}=a/\sqrt{2}$. Accordingly, Eq. (14) is replaced by

$$g_j=\frac{2\pi}{a}(2g_{j1}^2+g_{j2}^2)^{1/2} \tag{16}$$

which leads to

$$\mathbf{g}_j\cdot\boldsymbol{\rho}=\frac{2\pi}{a}(\sqrt{2}g_{j1}x+g_{j2}y).$$

Since the Fourier series converges relatively slowly at small z for this surface, we keep the first ten terms, corresponding to $g_1=2\pi/a$, $g_2=\sqrt{2}g_1$, $g_3=\sqrt{3}g_1$, $g_4=2g_1$, $g_5=\sqrt{6}g_1$,

$g_6=2g_2$, $g_7=3g_1$, $g_8=\sqrt{11}g_1$, $g_9=2g_3$, and $g_{10}=4g_1$. These corrugation components have the form of

$$G(g_1;\mathbf{g}_1\cdot\boldsymbol{\rho})=\cos\beta_y y,$$

$$G(g_2;\mathbf{g}_2\cdot\boldsymbol{\rho})=\cos\beta_x x,$$

$$G(g_3;\mathbf{g}_3\cdot\boldsymbol{\rho})=2\cos\beta_x x\cos\beta_y y,$$

$$G(g_4;\mathbf{g}_4\cdot\boldsymbol{\rho})=\cos 2\beta_y y,$$

$$G(g_5;\mathbf{g}_5\cdot\boldsymbol{\rho})=2\cos\beta_x x\cos 2\beta_y y,$$

$$G(g_6;\mathbf{g}_6\cdot\boldsymbol{\rho})=\cos 2\beta_x x,$$

$$G(g_7;\mathbf{g}_7\cdot\boldsymbol{\rho})=\cos 3\beta_y y+2\cos 2\beta_x x\cos\beta_y y,$$

$$G(g_8;\mathbf{g}_8\cdot\boldsymbol{\rho})=2\cos\beta_x x\cos 3\beta_y y,$$

$$G(g_9;\mathbf{g}_9\cdot\boldsymbol{\rho})=2\cos 2\beta_x x\cos 2\beta_y y,$$

and

$$G(g_{10};\mathbf{g}_{10}\cdot\boldsymbol{\rho})=\cos 4\beta_y y$$

with $\beta_x=g_2$ and $\beta_y=g_1$.

In the case of (111) plane, $|\mathbf{a}_1|=|\mathbf{a}_2|=a/\sqrt{2}$ and $A_{\text{cell}}=\sqrt{3}a^2/2$. The magnitude of $\mathbf{g}_j$ is evaluated by

$$g_j=\frac{4\pi}{\sqrt{3}}\ (g_{j1}^2+g_{j2}^2-g_{j1}g_{j2})^{1/2}, \tag{17}$$

which gives $g_1=2\beta_y$, $g_2=\sqrt{3}g_1$, $g_3=2g_1$, $g_4=\sqrt{7}g_1$, $g_5=3g_1\cdots$ with $\beta_x=2\sqrt{2}\pi/a$ and $\beta_y=2\beta_x/\sqrt{3}$. For such configuration, the dot product

$$\mathbf{g}_j\cdot\boldsymbol{\rho}=\frac{2\pi}{a}\ [(2g_{j1}-g_{j2})x/\sqrt{3}+g_{j2}y], \tag{18}$$

yielding the first five terms in the Fourier series:

$$G(g_1;\mathbf{g}_1\cdot\boldsymbol{\rho})=\cos 2\beta_y y+2\cos\beta_x x\cos\beta_y y,$$

$$G(g_2;\mathbf{g}_2\cdot\boldsymbol{\rho})=\cos 2\beta_x x+2\cos\beta_x x\cos 3\beta_y y,$$

$$G(g_3;\mathbf{g}_3\cdot\boldsymbol{\rho})=\cos 4\beta_y y+2\cos 2\beta_x x\cos 2\beta_y y,$$

$$G(g_4;\mathbf{g}_4\cdot\boldsymbol{\rho})=2(\cos 3\beta_x x\cos\beta_y y+\cos 2\beta_x x\cos 4\beta_y y+\cos\beta_x x\cos 5\beta_y y),$$

$$G(g_5;\mathbf{g}_5\cdot\boldsymbol{\rho})=\cos 6\beta_y y+2\cos 3\beta_x x\cos 3\beta_y y.$$

In most cases, only the first few expansion terms are necessary to achieve sufficient accuracy. However, for some extreme conditions, there may be a need to keep more terms.

TABLE I. Potential parameters (Ref. 33) and lattice constants (Ref. 30) for various metals.

Metals	ϵ (kJ/mol)	σ (nm)	a (nm)
Al	37.84	0.262	0.405
Cu	39.49	0.234	0.362
Ni	50.14	0.228	0.352
Pt	65.77	0.254	0.392

TABLE II. Potential parameters. $\alpha=0.8$, $\sigma_w=0.316$ nm, $\sigma_O=0.286$ nm, $\sigma_H=0.256$ nm, $\epsilon_w=0.650$ kJ/mol, $\epsilon_O=0.229$ kJ/mol, $\epsilon_H=0.0845$ kJ/mol.

Metals	C_{10} (O)	C_{10} (H)	C_8 (O)	C_6 (H)
Al	1.60	0	2.32	1.3
Ni	1.25	0.8	1.85	1.1
Pt	1.28	1.2	1.43	0.75

III. RESULTS AND DISCUSSION

In this section we describe calculations with the two forms of the potential for different low index planes of some fcc metals. In all the calculations, we set $\alpha=0.8$, which reduces the effective radius for the repulsion and increases the radius for the attraction through inverse dependence in the second term of Eq. (8), when the projection vector $\boldsymbol{\rho}_{pj}$ is not null. The simple point charge model SPC/E is used to represent the water molecule. Its geometry, partial charges, and Lennard-Jones parameters are used for model A1. For model A2, the Lennard-Jones parameters were replaced by taking the oxygen as a neon atom with $\sigma_O=0.286$ nm, $\epsilon_O=0.229$ kJ/mol,[30] and hydrogen as a helium, with $\sigma_H=0.256$ nm, and $\epsilon_H=0.0845$ kJ/mol.[31]

The Lennard-Jones parameters for the metals were taken from the literature. Table I lists the potential parameters evaluated from a variety of crystalline state physical properties at a wide range of temperatures[32,33] and the lattice constants[30] for a selected set of metals. To get the coupling parameters (so-called mixed Lennard-Jones parameters) needed for the two forms of potential described in the last section we used the parameters just described and the well-known Kong's combining rules.[34] This limits the number of the fitting parameters to the two C's in Eqs. (9)–(11), except in the case of Al where there was only one parameter. In passing we comment that since the Lennard-Jones radii and energies used in A2 do not depend on the particular model readjustment of parameters for other water models that have different geometry and point charges is straightforward.

Reported in Table II are the coefficients for the angular independent, short-range interactions in V_{isr} of Eqs. (9)–(11) obtained by a fit to the *ab initio* binding energies of water on Ni(111),[14] Pt(100),[10] and Al(100).[11] For the case of aluminum, we simplified the calculation further by setting $C_{10}(\text{H})=0$. In this study, we define the atop site as the posi

TABLE III. Adsorption energies of water on nickel surfaces (in units of kJ/mol). A: *A* top; B: bridge site; H: hollow site; A1, A2: present work; YW: Ref. 14; SS: Ref. 19; same for Tables IV–VI.

	A1	A2	YW	SS
(100) A	−45.07	−44.69	...	−49.0
(100) B	−28.53	−28.12	...	...
(100) H	−21.43	−22.89	...	...
(110) A	−46.59	−44.58	...	−55.9
(110) B	−29.30	−26.95	...	...
(110) H	−13.00	−18.17	...	...
(111) A	−44.54	−44.86	−44.35	−43.5
(111) B	−30.07	−29.34	−29.71	−28.3
(111) H	−28.50	−26.65	−28.65	−27.4

TABLE IV. Adsorption energeis of water on aluminum surfaces (in units of kJ/mol). MH: Ref. 11.

	A1	A2	MH
(100) A	−51.19	−52.33	−51.14
(100) B	−23.72	−22.13	−24.12
(100) H	−15.16	−16.83	−14.47
(110) A	−53.06	−52.53	···
(110) B	−24.91	−21.57	···
(110) H	−7.64	−13.08	···
(111) A	−50.14	−52.18	···
(111) B	−25.19	−23.00	···
(111) H	−23.14	−21.45	···

tion right above a metal atom, the bridge site as the position above the middle point of the $\mathbf{a}_1$ vector, and the hollow site is the one with a second layer metal atom underneath. There is a complication that we did not consider in our calculations. According to the calculations of Yang and Whitten[14] for Ni, the adsorption energy for the hollow site with no second layer metal atom underneath is 9.59 kJ/mol larger than the one with the atom. We considered this effect to be beyond the scope of the present model and so we took an average value of the two, −28.65 kJ/mol, as the criterion for comparison. It should also be mentioned that all the quantum-mechanical calculation results are based on small clusters, and may depart from the surface results significantly.

Although the fitting procedure is for specific low index faces, the parameters determined are equally applicable to other types of crystallographic structure as well as to discrete atomic layers. This can clearly be seen from Tables III–V where comparisons with results from other potential functions and/or molecular orbital calculations are given. Keep in mind that two assumptions are implicit in the above statement: pairwise additivity approximation for non-Coulombic interactions and the validity of the combining rule. Also note that the adsorption energies were calculated for a molecular orientation with the oxygen atom closest to the surface ("oxygen atom down") and with the vector bisecting the H–O–H bond angle perpendicular to the interface, and the line connecting the two hydrogen atoms parallel to the x axis (parallel to $\mathbf{a}_1$). These calculated results are consistent with experimental measurements,[9,35–38] although quantitative determination of the adsorption energy of water on metal surface is difficult and the data are not currently available.

According to our calculations, the equilibrium distances between the oxygen atom of the water molecule and the Ni(111) surface at atop, bridge, and hollow sites are, respectively, 0.25, 0.26, 0.27 nm for model A1 and 0.22, 0.24, 0.24 nm for model A2, compared with 0.206, 0.209, 0.210 nm of Yang and Whitten.[14] Both our models predict an equilibrium distance that is too large compared to the *ab initio* calculations. Model A2 is marginally "better" than A1 in yielding the bond distances that are smaller and closer to the cluster calculation. Experience with the Xe–Pt potential offers useful insight here. Barker and Rettner[21] pointed out that quantum chemistry cluster calculations which attempt to approximate the r^{-n} attractive dispersion interactions by exponentials will tend to give equilibrium bond distances that are too short.

According to the calculation of Yang and Whitten,[14] the adsorption energy of water on Ni(111) surface is shifted upward by 5.02 kJ/mol when the molecule on the atop site rotates about the C_{2v} axis by 90° so the H–H line becomes parallel to the y axis. In our model, the energy difference turns out to be much smaller since the distances from the hydrogen nuclei to the nearest Ni atom remain the same after the rotation. It seems that the energy shift observed by Yang and Whitten arises from some binding contributions absent in the present model.

It is informative to examine the energy variation with respect to ϕ which is defined as the angle between the molecular dipole moment vector and the z axis normal to the surface. In particular, rotating the water molecule on the Ni(111) surface (keeping z_O fixed at the equilibrium distance) by ϕ=49.75° in the xz plane increases the binding energy to 164 kJ/mol for model A1 and to −2.94 kJ/mol for model A2 at atop site, to 135 and −21.5 kJ/mol at the bridge site, and to 70.1 and −17.4 kJ/mol at the hollow site. On the other hand, the value calculated by Yang and Whitten[14] for the atop site at ϕ=52.25° is 25.10 kJ/mol. There is a 5° difference in the H–O–H bond angle of the SPC/E model compared to the geometry of water in the *ab initio* cluster. However we have chosen ϕ such that one of our O–H bonds makes the same angle relative to the z axis as in the Yang–Whitten calculation. Clearly A1 overestimates the rotational barrier while A2 underestimates the rotational barrier.

By allowing the molecular dipole to change its direction along the yz plane, using ψ to measure the angle between the dipole vector and the surface normal, we are able to study

TABLE V. Adsorption energies of water on platinum surfaces (in units of kJ/mol). SH: Ref. 16; RFMB: Ref. 18; HB: Ref.10; FRB: Ref. 17.

	A1	A2	SS	SH	RFMB	HB	FRB
(100) A	−48.35	−48.58	−43.3	−35.7	···	−48.25	−39.5
(100) B	−34.42	−28.26	−22.2	−16.3	···	···	−22.0
(100) H	−27.80	−22.32	−20.7	−12.1	···	−27.94	−8.2
(110) A	−48.24	−48.00	···	···	···	···	···
(110) B	−33.82	−27.27	···	···	···	···	···
(110) H	−19.61	−17.38	···	···	···	···	···
(111) A	−48.71	−49.19	···	···	−40.7	···	···
(111) B	−36.23	−29.29	···	···	−26.1	···	···
(111) H	−34.54	−27.36	···	···	−23.9	···	···

TABLE VI. Adsorption energies of water on copper surfaces (in units of kJ/mol). RLL: Ref. 12.

	A1	A2	RLL
(100) A	−38.57	−37.87	−36.66
(100) B	−24.01	−24.08	···
(100) H	−17.71	−19.60	···
(110) A	−40.41	−37.33	···
(110) B	−24.57	−23.17	···
(110) H	−10.69	−15.69	···
(111) A	−38.08	−38.38	···
(111) B	−25.47	−24.97	···
(111) B	−23.91	−23.49	···

dependence of the binding energy upon molecular tilt. Successively tilting the water molecule in increments of 10° from the surface normal (ψ=0) changes the binding energy at the top site to −43.65 (ψ=10°), −40.86 (ψ=20°), −35.86 (ψ=30°), −28.09 (ψ=40°), −16.55 (ψ=50°), 0.32 (ψ=60°) kJ/mol for model A1 and to −44.89, −44.96, −45.06, −45.10, −44.95, −44.32 kJ/mol for model A2. By comparison, the corresponding values of Yang and Whitten were: −47.28, −48.12, −48.12, −45.19, −41.00, −35.98 kJ/mol. The energies computed from A1 show a monotonic increase, the quantum calculation result displays a minimum around ψ=20°–30°. For model A2, the energy minimum is around ψ=30°–40°. These discrepancies should not affect the computer simulation results significantly since they only affect the water in contact with the surface and decrease rapidly with increasing distance z.

The Lennard-Jones parameters obtained from thermodynamic data suggest that Cu, Ag, Au, and Ni form a single class, and Pt yet another with stronger binding. Using the fitting coefficients of Ni, we are able to predict the energies for adsorption on copper surfaces. The results are given in Table VI, and show that the predicted binding energy of water molecule right above a metal atom of Cu(100), −38.57 kJ/mol at 0.25 nm for model A1 and −37.87 kJ/mol at 0.22 nm for model A2, is in accord with the *ab initio* results of Ribarsky and co-workers,[12] namely −36.66 kJ/mol at 0.220 nm.

All the potential surfaces depicted in Tables III–VI indicate a preference for water to adopt orientations in which water dipole moment points away from the interface and the oxygen sits down on the surface with the on top site being the site with greatest binding energy. If more experimental data were available the potentials described here could be further refined.

Using the parameters reported in Tables I and II, we plot the potential energy curves calculated from the analytical formulas derived in Sec. II for one oriented water molecule adsorbed at different sites on low index faces of platinum. The results are shown by the curves in Figs. 1–3. For comparison, we also plot the potential energies (data points) obtained from the direct summation of pairwise interaction. Both sets of calculations explicitly included the top two layers of metal surface atoms and approximated the remainder of the crystal by means of the 9-3 potential that comes from treating the remaining half-space in the continuum limit. As

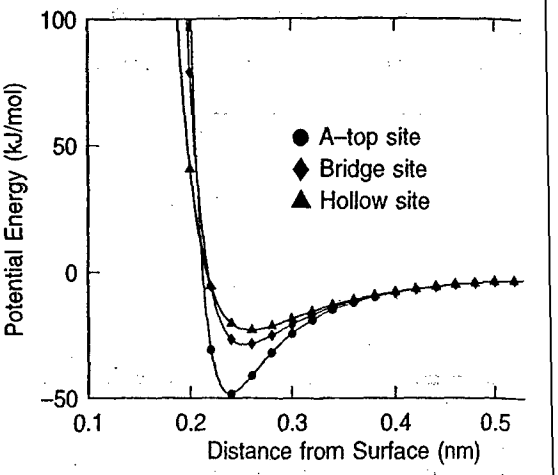

FIG. 1. Water–Pt(100) potential (model A2) as a function of oxygen atom from surface plane. The molecule lies in y=con with dipole moment vector parallel to surface normal and ox down. Symbols: direct sums of pairwise energy. Curves: Fourie pansion.

can be seen there, the agreement between these tw computations is excellent. The largest deviations, ha ible in the plots, occur when the particle-wall distanc short. Since the use of the transformed form of the energy is computationally much more economica summation of pairwise interaction is not necessary puter simulations unless inclusion of the thermal m the metal atoms is desired. In Figs. 1–3, about 75 adsorption energy on the atop site comes from the int with the nearest metal atom. For the bridge site, on t hand, the contribution from the two nearest neigl about 65%. By comparing the potentials at distance than 0.35 nm in Figs. 1–3 we see that the corrugatio tial decays very rapidly with distance z from the m

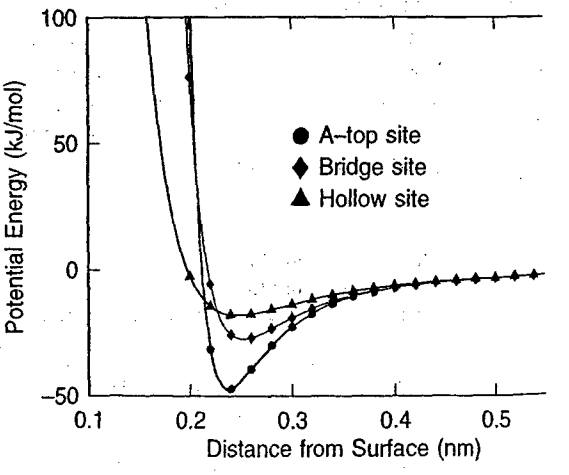

FIG. 2. Water–Pt(110) potential (model A2) as a function of di oxygen atom from surface plane. The molecule lies in y=const with dipole moment vector parallel to surface normal and oxy down. Symbols: direct sums of pair-wise energy. Curves: Four expansion.

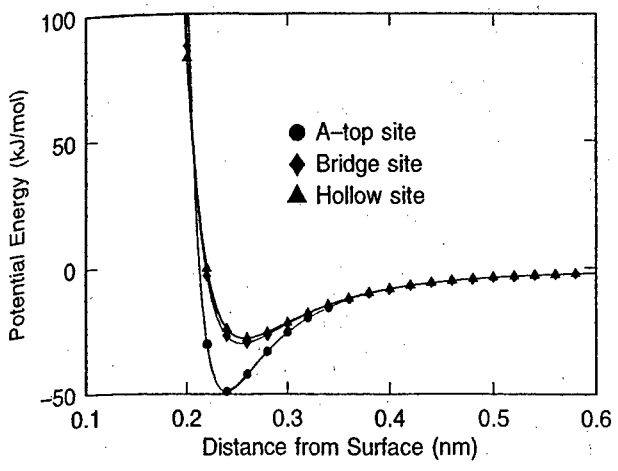

FIG. 3. Water–Pt(111) potential (model A2) as a function of distance of oxygen atom from surface plane. The molecule lies in y=constant plane with dipole moment vector parallel to surface normal and oxygen atom down. Symbols: direct sums of pair-wise energy. Curves: Fourier series expansion.

face. However if the first layer of water is strongly bound in an ordered array then indirect effects of corrugation will be felt further out.

When angle dependence of the potential is turned off [α=1 and $C_n(p)$=0], the top site becomes the site of weakest binding. This is shown for the Pt(111) surface and model A2 in Fig. 4. Figure 4 shows how anisotropy is important in lowering energy of the top site and in decreasing the metal–oxygen bond distance. As mentioned above, introduction of the angular dependent, short-range interactions to represent chemical bonding is essential for mimicing water adsorption on metallic surfaces. The Lennard-Jones potential function does not produce the correct preferential adsorption site. By adding the angular dependent, short-range interactions, the potential well for atop site deepens and shifts towards small z, while for the bridge and hollow sites the influence is just opposite. This reverses the preference order for adsorption energies. The contribution from image interactions is also shown in Fig. 4.

In Fig. 5 we plot the total energy of H_2O–Pt(100) system versus the O-surface separation. The molecular orientation is such that one O–H bond vector is perpendicular to the horizontal surface plane with one hydrogen pointing directly at the surface. The other O–H bond lies in the xz plane pointing away from the surface at an oblique angle. This mimics the situation where chemisorption is through the hydrogen atom. For such a configuration, we obtain the binding energies of −27.03 kJ/mol at 0.33 nm for the atop site, −16.87 kJ/mol at 0.35 nm for the bridge site, and −14.43 kJ/mol at 0.352 nm for the hollow site (model A2). The corresponding values from the molecular orbital calculation of Holloway and Bennemann[10] are −24.18 kJ/mol at 0.265 nm for the first position and −5.94 kJ/mol at 0.268 nm for the third position. Model A1 does not predict any significant adsorption via hydrogen atom. Note that the shift in minima for oxygen versus hydrogen down is approximately 0.1 nm. This is the shift observed by Toney *et al.*[4] in the experiments with bulk water next to a silver surface when the electric field is reversed. This is an added reason for adopting potentials with the form described here.

Compared with other analytical potential functions, the present one is physically more meaningful. It contains a small enough number of fitting parameters to not overly prejudice the physics. In addition, the functional form is universal for studying water adsorption on various metal surfaces and can be directly used for systems in which the metal atoms are explicitly taken into account. As new experimental or theoretical data on the adsorption energy, etc., becomes

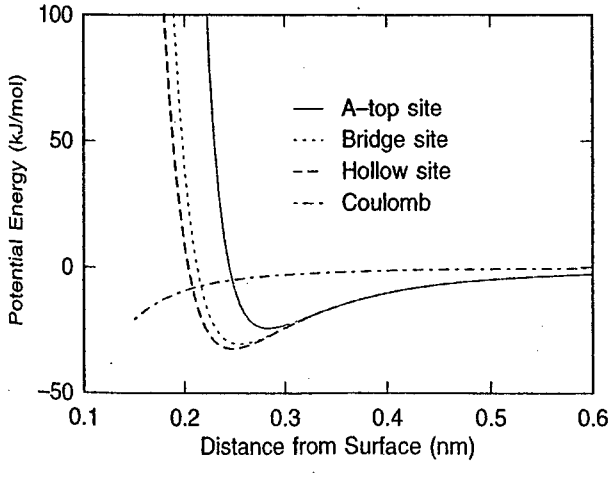

FIG. 4. Water–Pt(111) potential without anisotropic and short-range isotropic terms. The potential is a sum of the conventional 12-6 Lennard-Jones interaction and the Coulomb interaction between real and image charges. The Coulombic image potential is also plotted separately to show its weak z dependence. The molecule lies in y=constant plane with dipole moment vector parallel to surface normal and oxygen atom down.

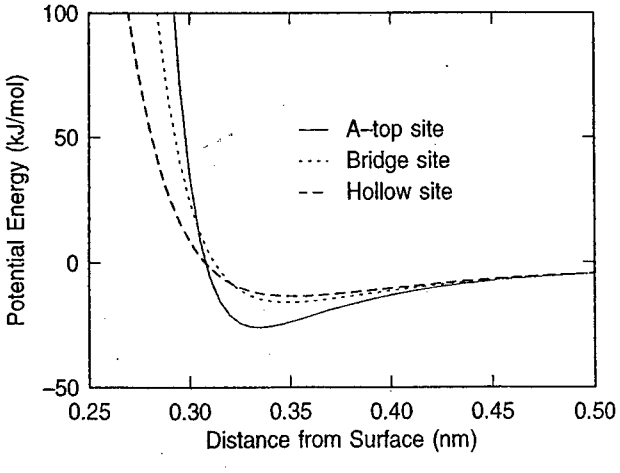

FIG. 5. Water–Pt(100) potential (model A2) with H atom down. The potential is plotted as a function of distance of oxygen atom from the surface plane. The molecule lies in y=constant plane with one O–H bond perpendicular to the surface. Note shift in minima by approximately 0.1 nm and reduced binding energies compared to the oxygen atom down orientation shown in Fig. 1.

available, it will be very easy to modify the potential function and refine the parameters. One possible channel of improvement of the present model is to add nonadditive interactions such as electric polarizations or other many-body interactions explicitly. Work on modifying the potentials to include electric polarization is in progress.

ACKNOWLEDGMENTS

This work was supported in part by the Office of Naval Research. The authors are grateful to Dr. John A. Barker for helpful discussions.

[1] P. A. Thiel and T. E. Madey, Surf. Sci. Rep. **7**, 211 (1987).
[2] A. E. Russell, A. S. Lin, and W. E. O'Grady, J. Chem. Soc. Faraday Trans. **89**, 195 (1993).
[3] C. A. Melendres, B. Beden, G. Bowmaker, C. Liu, and V. A. Maroni, Langmuir **9**, 1980 (1993).
[4] M. F. Toney, J. N. Howard, J. Richer, G. L. Borges, J. G. Gordon, O. R. Melroy, D. G. Weisler, D. Yee, and L. B. Sorensen, Nature (in press).
[5] E. Spohr and K. Heinzinger, Chem. Phys. Lett. **123**, 218 (1986).
[6] N. G. Parsonage and D. Nicholson, J. Chem. Soc. Faraday Trans. 2 **82**, 1521 (1986).
[7] N. G. Parsonage and D. Nicholson, J. Chem. Soc. Faraday Trans. 2 **83**, 663 (1987).
[8] A. A. Gardner and J. P. Valleau, J. Chem. Phys. **86**, 4171 (1987).
[9] G. B. Fisher and J. L. Gland, Surf. Sci. **94**, 446 (1980).
[10] S. Holloway and K. H. Bennemann, Surf. Sci. **101**, 327 (1980).
[11] J. E. Müller and J. Harris, Phys. Rev. Lett. **53**, 2493 (1984).
[12] M. W. Ribarsky, W. D. Luedtke, and U. Landman, Phys. Rev. B **32**, 1430 (1985).
[13] C. W. Bauschlicher, Jr., J. Chem. Phys. **83**, 3129 (1985).
[14] H. Yang and J. L. Whitten, Surf. Sci. **223**, 131 (1989).
[15] E. Spohr and K. Heinzinger, Ber. Bunsenges. Phys. Chem (1988).
[16] E. Spohr, J. Phys. Chem. **93**, 6171 (1989).
[17] K. Forster, K. Raghavan, and M. Berkowitz, Chem. Phys. L (1989).
[18] K. Raghvan, K. Foster, K. Motakabbir, and M. Berkowitz, J. C **94**, 2110 (1991).
[19] J. I. Siepmann and M. Sprik, Surf. Sci. Lett. **279**, L185 (199
[20] F. H. Stillinger and T. A. Weber, Phys. Rev. B **31**, 5262 (198
[21] J. A. Barker and C. T. Rettner, J. Chem. Phys. **97**, 5844 (199
[22] N. N. Avgul and A. V. Kiselev, in *Chemistry and Physics* (Dekker, New York, 1970), Vol. 6.
[23] J. Hove and J. A. Krumhansl, Phys. Rev. **92**, 569 (1953).
[24] W. A. Steele, Surf. Sci. **36**, 317 (1973).
[25] W. A. Steele, *The Interaction of Gases with Solid Surfaces* Oxford, 1974).
[26] J. D. Jackson, *Classical Electrodynamics* (Wiley, New York, 1
[27] B. Mrowka and A. Recknagel, Phys. Z. **38**, 758 (1937).
[28] J. C. P. Mignolet, Discuss. Faraday Soc. **8**, 105 (1950).
[29] J. H. Kaspersma, Ph.D. thesis, Catholic University of Nijmeg lands, 1972.
[30] *American Institute of Physics Handbook*, 3rd ed. (McGraw Company: New York, 1982).
[31] J. O. Hirschfelder, C. F. Curtiss, and R. B. Bird, *Molecular The and Liquids* (Wiley, New York, 1954).
[32] T. Halicioğlu and G. M. Pound, Phys. Status Solidi A **30**, 61
[33] C. Kittel, *Introduction to Solid State Physics*, 6th ed. (Wiley, 1986).
[34] C. L. Kong, J. Chem. Phys. **59**, 2464 (1973).
[35] H. Ibach and S. Lehwald, Surf. Sci. **91**, 187 (1980).
[36] T. E. Madey and F. P. Nezter, Surf. Sci. **117**, 549 (1982).
[37] F. P. Nezter and T. E. Madey, Surf. Sci. **127**, L102 (1983).
[38] R. H. Stulen and P. A. Thiel, Surf. Sci. **157**, 99 (1985).

Intermolecular energy-band dispersion in oriented thin films of bis(1,2,5-thiadiazolo)-*p*-quinobis(1,3-dithiole) by angle-resolved photoemission

Shinji Hasegawa, Takehiko Mori, Kenichi Imaeda, Shoji Tanaka, Yoshiro Yamashita, and Hiroo Inokuchi
Institute for Molecular Science, Myodaiji, Okazaki 444, Japan

Hitoshi Fujimoto
Department of Environmental Science, The Graduate School of Science and Technology, Kumamoto University, Kumamoto 860, Japan

Kazuhiko Seki
Department of Chemistry, Faculty of Science, Nagoya University, Nagoya 464-01, Japan

Nobuo Ueno
Department of Materials Science, Faculty of Engineering, Chiba University, Inage-ku Chiba 263, Japan

(Received 27 July 1993; accepted 20 January 1994)

Angle-resolved ultraviolet photoemission spectra using synchrotron radiation were measured for oriented thin films of bis(1,2,5-thiadiazolo)-*p*-quinobis(1,3-dithiole) (BTQBT) on graphite. From the photon energy dependence of normal emission spectra, the energy-band dispersion of π-bands were observed for the highest (HOMO) and next highest (NHOMO) bands. This is the first observation of intermolecular dispersion in a single-component organic molecular crystal. The results demonstrate that the BTQBT molecules have a strong intermolecular interaction, which can be derived from the introduction of a covalent interaction between sulfur atoms in addition to the usual intermolecular interaction by van der Waals forces.

INTRODUCTION

The energy-band dispersion relation, $E=E(k)$, is a fundamental basis for understanding the basic properties of solids, such as electrical conductivity and optical properties. Angle-resolved ultraviolet photoemission spectroscopy (ARUPS) using synchrotron radiation is a powerful technique for directly measuring the valence band dispersion. The technique is well established for inorganic solids, and the band structures of various metals and semiconductors have been extensively studied.[1,2]

For typical organic solids, the energy-band dispersion has been difficult to observe, since (i) the band width is small (at most 0.1 eV) due to weak intermolecular van der Waals interaction,[3] and (ii) it is difficult to prepare well-oriented samples required for the ARUPS measurement. A few experiments have, however, been reported during the past ten years.[4–9] Seki *et al.*[4,5] and Ueno *et al.*[6] first reported the observation of intramolecular energy-band dispersion of σ-bands for oriented thin films of hexatriacontane $CH_3(CH_2)_{34}CH_3$ and cadmium arachidate $[CH_3(CH_2)_{18}COO]_2Cd$. Later, Fujimoto *et al.*[7] observed the dispersion over the whole Brillouin zone for hexatriacontane, and Ueno *et al.*[8] obtained the complete energy-band dispersion for pentatriacontan-18-one $CH_3(CH_2)_{16}CO(CH_2)_{16}CH_3$. Since the intramolecular (interatomic) interaction due to covalent chemical bonds is stronger than the intermolecular one, these compounds exhibit a sufficiently large band width ($\approx$5 eV) to be observed experimentally. Recently, Schmeisser *et al.*[9] observed the intermolecular energy-band dispersion of π-bands for oriented thin films of dicyanoquinonediimine (DCNQI)-metal complex, which were prepared using an ingenious method by Wachtel *et al.*[10] Due to the strong charge transfer interaction between adjacent molecules and metal ions, the band width of the complex is sufficiently large ($\approx$0.5 eV) to be observed.

Bis(1,2,5-thiadiazolo)-*p*-quinobis(1,3-dithiole) (BTQBT) (Fig. 1) is a novel single-component organic semiconductor. In contrast to multicomponent systems such as complexes which have charge transfer interactions, single-component semiconductors were designed to have a strong intermolecular interaction by introducing a covalent interaction of chalcogen atoms in addition to the usual intermolecular interaction by van der Waals forces.[11] For example, tertathiafulvalene (TTF) derivatives containing long alkyl chains[12] or telluro substituents[13] show low resistivities of 10^4–10^5 Ω cm at room temperature. BTQBT consists of electron-withdrawing 1,2,5-thiadiazole rings fused to a strongly electron-donating 2,2′-*p*-quinobis(1,3-dithiole). As shown in Fig. 1, the BTQBT molecules in a single crystal form a two-dimensional network by the short $S\cdots S$ contact of 3.26 Å which is much shorter than the sum of their van der Waals radii 3.70 Å, and the network sheets are stacked with a small spacing of 3.45 Å to form molecular columns.[14] The short contacts between sulfur atoms are expected to lead to a strong intermolecular interaction in the solid state. The resistivity of a single crystal grown by sublimation is low (2.7×10^5 Ω cm) along the column axis.[15] The crystal also shows a Hall effect which is rarely observed in organic semiconductors.[15] However, the band structure derived from

 0021-9606/94/100(9)/6969/5/$6.00

Comparison of Water Models in Simple Electric Double Layers

Sheng-Bai Zhu and Michael R. Philpott
IBM Research Division
Almaden Research Center
650 Harry Road
San Jose, CA 95120-6099

James N. Glosli
Lawrence Livermore National Laboratory
Livermore, CA 94550

August 9, 1994

Abstract

The three bulk water models (SPCE, TIP4P and ST2) are compared in molecular dynamics simulations of electric double layers consisting of a monovalent ion (Na^+ or Cl^-), water as solvent, and a flat metal electrode. The goal is to identify features of the double layer that are sensitive to the model and those that are not. The simulations are done with zero external field and one non-zero applied field. All electrostatic image interactions due to the ion and the point charges constituting the water molecules are included in the calculation. All the models give rise to several well defined solvent density oscillations at the metal surface and the first peak in particular can be strongly accentuated by an external electric field. The Na^+ ion occupies a diffuse zone in which its first solvation shell remains intact even when drawn to the electrode by an external field. One striking difference occurs for the ST2 water compared to the other models. In a cathodic external field the Na^+ ion does not concentrate near the electrode. There are

also quantitative differences in the electric potential profiles. Effects of replacing Na^+ with Cl^- are also studied. It was observed that there was less structure in the water density profiles with solvated anions. The Cl^- ion occupies a diffuse zone that extends to the surface where it makes occasional contact and its solvation shell greatly distorted. In an external field the chloride ion forms a compact layer at the metal with no diffuse component to its distribution. Significant differences in using different water models are observed and are interpreted on the basis of the relative strength of the solvation and the stiffness of the liquid.

1 Introduction

In this paper we use constant (N,V,T) molecular dynamics computer simulations to study the sensitivity [1, 2] of the main properties of electric double layers to the model used. The same model for the metal electrode is used throughout. The ion parameters were those optimized for the bulk solutions. We will show that all the models have major solvent structural features in common, with the simple point charge (SPCE) model and the transferable intermolecular potential (TIP4P) model being similar in many respects. The importance of this work is in identifying model independent features likely to exist in real systems and differences associated with particular models. All electrostatic interactions between ions and water and the electrostatic images of ions and water in the model are included in the calculation.

Electric double layers are formed when aqueous ionic solutions contact charged plates. The ions migrate toward the charged surface until the field of the surface charge is completely shielded outside a narrow zone (less than a few nanometers thick at 0.1 M salt concentration) next to the metal. The region where zero average field begins marks the edge of the bulk electrolyte. In the bulk region the electrolyte solution is neutral, the average electric field is zero, and the water molecules are not preferentially oriented. According to the traditional electrochemical textbook model [3, 4, 5], the electric double layer consists of a diffuse part of mobile ions and water stretching into the bulk electrolyte and a compact part comprising the charged metal surface region and contact adsorbed species. In the diffuse layer, fully hydrated ions move under the combined influence of thermal forces from neighboring species and interactions with metal plates as well as external fields. Distri-

butions in the diffuse layer are described by the Gouy-Chapman theory [6, 7] which takes no account of the detailed nature of the ions other than the magnitudes of their charges and treats the solvent as a continuous fluid with given dielectric constant. In the compact layer, if one exists for the system under study, ions physisorb without electronic discharge or chemisorb and form a bond with some degree of covalent character [4]. In this part of the electric double layer, the properties have been described by the Stern [8], Frumkin [9], Grahame [10], or Bockris, Devanathan, and Muller [11] models. In particular the Bockris, Devanathan, and Muller model [11] assumed the compact region consisted of two layers of solvent containing contact adsorbed ions. An obvious disadvantage of the traditional model is the absence of predictions concerning water (the majority species!) perturbations due to visiting counter ions, the loss of some or all of the solvation sheath of contacting ions, and the formation of chemical bonds between ions, water and the surface.

During the last fifty years the traditional model evolved through the analysis of numerous experiments designed to measure surface coverages as a function of electrolyte composition and externally applied potential. Recent UHV experiments [4] have revealed that some of the traditional views regarding contact adsorption must be reassessed, for example, iodide ions discharge on Pt(111) surfaces at high coverage. Problems concerning change in electronic structure with coverage are beyond the scope of the present paper. However classical molecular dynamics computer simulations can add detailed insights at the atomic scale, including information about the temporal and structural aspects of molecular organization in the electric double layer. In these systems water molecules are perturbed by ions, external fields, and the atoms making up the solid surface. There is a growing literature describing computer simulations of water in perturbed systems. Subjects of recent studies are: aqueous electrolyte solutions, pure water near charged or uncharged surfaces, and water-ion complexes in the vicinity of charged or uncharged surfaces. A recent review of water in perturbed states has been published by Zhu and coworkers [12].

All the computer simulations of double layer problems so far published have used water models developed for the bulk state. Most of these models are within the framework of pairwise additive potentials which treat the polarization effect in an average way through effective charges. An important question naturally arises: whether the mean field approximation is still a valid

description, or to what extent it is a reasonable description, for studying perturbed water where the molecular environment is spatially inhomogeneous. There is, unfortunately, no straightforward answer for this question since microscopic information of double layers has not been available from current experiments and the existing water models can only reproduce at most a few experimental data. They may be appropriate in some aspects but inappropriate in others. The lack of a criterion for the 'truth' causes difficulty in directly testing the reliability of a water model for solving electric double layer problems. In this paper, we simply compare molecular dynamics simulation results of three most commonly employed water models, namely SPCE [13], TIP4P [14], and ST2 [15], in otherwise identical conditions. These models respectively represent a three-site, four-site, and five-site version of rigid and non-polarizable water molecules. Particular attention will be paid on differences and similarities of the simulation results. If the results are qualitatively different, at least one of these models is inappropriate in describing the properties studied. On the other hand, similarities in results indicate these models are almost equivalent in these aspects. It, of course, does not necessarily mean that these properties really correspond to real physical features of electrolytes near charged solid surfaces.

2 Model

In each simulation the cell contained a single ion, either Na^+ as the cation or Cl^- as the anion (0.35 M concentration), and a total of 157 water molecules, sandwiched between two walls one representing the metal electrode and the other the neutral restraining wall. The cells are replicated to infinite parallel to the xy plane of the metal. We call this the immersed electrode model [16]. In this model, a full treatment of all electrostatic interactions is performed. This means interactions between the ion, all the water molecules, and all the electrostatic images of the ion and all the water molecules (due to the presence of a single metal surface). In the absence of an external field the net charge on the metal electrode is the image charge of the ion in the aqueous subphase, which has a fluctuating position and is opposite in sign to that of the ion. The total charge on the metal in the case of Na^+ was $q_T = q_{im} = -e$, where e denotes the electron charge. A very high surface electric field exists across the metal-solution interface, which drops rapidly to zero as the

dielectric boundary is approached. The water molecules were represented by one of the three models mentioned above, and the ion parameters were chosen to be consistent with the water model. All these water models have been used extensively to study liquid water and electrolyte solutions and all have reasonable success in explaining selected bulk phase properties. To stress the system and mimic the effect of even higher salt concentration on the water layers near the electrode we also performed calculations with an external electric field applied in a direction that reinforced the existing field due to the ion and its electrostatic image. The total charge on the metal in the case of Na^+ was $q_T = q_{im} + q_{ext} = -2e$ with the uniformly distributed component $q_{ext} = -e$. Although systems under external electric field do not exist at equilibrium in nature, we consider this a useful ploy to examine how system responds initially to a change in field, and as shown by Philpott and Glosli [16], how even higher same ion concentrations alter the water structure next to the electrode.

Several approximations are implicit in the present study. Through the use of bulk water models, a basic assumption involved in the non-polarizable water models is that the molecular environment is spatially isotropic so that the polarization effects may be treated in an average way by introducing effective point charges. This assumption will break down when 'perturbations' from neighboring solutes, external fields, interfaces etc., deviate greatly from the mean field of the bulk phase. It seems reasonable to think this will occur when the molecule is in the first layer next to the electrode. Also omitted here are the geometric distortions of the molecular framework which may be significant in the presence of intense fields [17, 18, 19, 20, 21] such as the cases occur around polyvalent ions. We can only minimize this effect here by restricting the systems studied to monovalent ions. The rigid geometry and the absence of polarizability mean that the dipole moment is fixed at a mean value appropriate for the bulk phase. In turn this means that dielectric saturation could occur in smaller electric fields than observed experimentally, and will be manifest by completely oriented water molecules. For each system, the ion-water interactions were optimized on the basis of bulk phase. It is therefore to be expected that the results obtained from different model calculations may be differentiated when interfacial phenomena are investigated. Our general goal is to examine the consistency of these models in describing the properties of electric double layers.

The water-ion mixture is confined between flat featureless plates 1.862

nm apart. The left hand plate (see Fig. 1) at z = -0.931 nm is a dielectric, it interacts with all molecules and ions by the 9-3 potential of Lee, McCammon, and Rossky [22]. This potential represents the interaction of water and ions with the core electrons of the wall. The explicit form of the water-wall and ion-wall 9-3 potentials for a solid with density ρ is [23]:

$$u_{9-3} = 2\pi\rho\epsilon_w\sigma_w^3\left[\frac{2}{45}\left(\frac{\sigma_w}{z-z_w}\right)^9 - \left(\frac{\sigma_w}{z-z_w}\right)^3\right], \tag{1}$$

where ϵ_w and σ_w are the Lennard-Jones energy and radius for the wall potential. The coordinate z, measured perpendicular to the interface, is the distance of the mass center of ion or the distance of the oxygen atom of the water molecule. This choice of wall potential neglects the interaction of the hydrogen atoms with the wall. The right hand plate at z = 0.931 nm represents a metal surface. In addition to the same 9-3 potential for core interactions, the interaction of charges on ions or on the charge sites inside each water molecules with conduction electrons is modeled by an electrostatic image potential. For all these systems, the image plane is chosen to be coincident with the origin plane of the 9-3 potential, which passes through the nuclei of the metal atoms on the first layer at z = 0.931 nm.

A number of schemes have been developed in past years to treat long range electrostatic fields. In this work, we employ the fast multipole method (FMM) proposed by Greengard and Rokhlin [24, 25, 26, 27], which is computationally more economical than the Ewald summation [28, 29, 30] and, compared with other methods, is easy to use in combination with complex boundary conditions [31, 32]. Additionally it is well suited to vector and parallel machines, and the error in computation is controlled by changing the number of terms retained in the multipole expansions. The first application of FMM to electrochemical problems were the molecular dynamics calculations of dielectric constant of bulk SPCE water by Glosli and Philpott [32].

Table 1 lists the potential parameters employed for the systems studied in this paper, together with the relevant references. Here ϵ_O and σ_O represent the Lennard-Jones energy and radius of water-water interaction, ϵ_{OI} and σ_{OI} label the same quantities for the ion-water interaction. For systems in an external electric field, the additional electric field strength in vacuum was 5.22×10^7 V/cm, equivalent to a surface charge density of 0.288 e/nm^2.

Although, on average, the electrostatic image of the ion has the same surface charge density, its influence on the solution depends on the behavior of the ion and, therefore, is not exactly identical with the external field.

Constant (N, V, T) molecular dynamics calculations were performed on each system, for simulation times of one nanosecond in all cases except the system Na^+ in ST2 water where the calculation was run for 2 ns. This provided a cross-check to against artifacts from poor statistics. A time step of 2 fs is used for integrating the equations of motion. For each simulation, the first 100 ps was used to equilibrate the system at a temperature of 294K, and the remainder is to accumulate data. The sample box is a cube with the edge length of 1.862 nm and was periodically replicated along the x and y directions parallel to the electrode surface.

3 Results and Discussion

In this section the results of the simulations are presented in terms of probability distributions for the chemical components (water, H atoms and ions) averaged over the x and y directions. After averaging the distributions, which we will also refer to loosely as density profiles, show only a dependence on z, the coordinate perpendicular to the surface. They usefully characterize the main structural features of the electric double layers. In addition, we have calculated the total microscopic charge and the z component of the dipole moment of water (vector component parallel to the surface normal). For convenience we first discuss systems containing Na^+ and Cl^- separately and later focus on points of difference. Some large differences are to be expected because asymmetry in the water models and the reversal in the interfacial field for cations compared with anions.

3.1 Systems Containing Na^+ Ions

Figures 1 to 3 display the basic results. The solid curves correspond to no external field, a physically acceptable state. The combination of broken and solid lines indicate the main change occurring when a field is turned on. This external static electric field is always in the direction to pull the ion to the metal surface, so that the total surface field could be as high as 10 GV/m. As has been shown elsewhere [16], the field at the metal surface

(only) is equivalent to having an extra ion in the system. For additional emphasis in all the figures presented in this paper, the label 'e' signifies how the distributions change in the presence of the external field. Broken vertical lines at $|z| = 0.682$ nm, indicate the location of the 'effective' walls which are defined as the planes parallel to the solid surfaces where the 9-3 wall potential crosses zero. In each figure, the metal electrode is on the right side with the image plane on the extreme edge of the figure ($z = 0.931$ nm), and the uncharged restraining (dielectric) wall is on the left at z = -0.931 nm.

We discuss the main features first starting with the majority species water. In surveying the results plotted in Figures 1 to 3 we conclude that the water and proton distributions calculated for all three models are in basic qualitative agreement. In zero external field, the water distributions are slightly asymmetric with respect to the central plane ($z = 0$). This difference is due to the charge-image charge interaction, and arises from the intrinsically different nature of the solution-surface interactions occurring at the metal surface compared to the dielectric surface. The effect on the density profiles is weak for neutral water and strong for the H atoms.

All three water density profiles exhibit broad maxima at -0.5, -0.2 (indistinct), 0.3 and 0.6 nm. These peaks, due to layering at the surfaces are more distinct on the metal side ($z > 0$). In all three figures there is a small sharp peak on the edge of the profile near 0.7 nm. It is most visible in Figures 2 and 3 for TIP4P and ST2 models. When the field is turned on it becomes the sharpest feature in the water profile. This peak is due to a few water molecules with mass centers localized near 0.68 nm at the edge of the repulsion zone. We address the question of how the orientation of these water molecules differs from the majority of waters near the surface after describing the proton (H atom) distributions.

As with water center of mass, the H atom distributions are very similar for all three models. There is asymmetry with respect to $z = 0$. This is especially true on the metal side because our model allows H atoms to get closer to the image plane. The main peaks are at 0.2 (broad), 0.55 (broad) and 0.76 nm (sharp). The proton peak at ca. 0.76 nm is particularly distinct because these protons are attracted by a strong image electrostatic field and since they do not feel the 9-3 wall potential directly, they can penetrate the exclusion zone for the oxygen and ions created by the repulsive 9-potential. The peak at 0.76 nm is clearly associated with water molecules of mass center near 0.68 nm. When the field is turned on, the electric field near the metal surface

is almost doubled and so more protons are attracted to the metal and the 0.76 nm peak doubles in height. The height of the first peak in the hydrogen number density ρ_H is about 90% of that in the oxygen number density ρ_O and their peak-to-peak separation is about 0.08 nm. In addition, the ratio of the number of hydrogen atoms in the first layer (defined as the portion between the first peak near the metal surface and the corresponding liquid-solid interface) to the number of oxygen atoms in the first layer (similarly defined) is about 0.6. These values suggest there is a large probability to have one proton pointing at the metal rather than having the dipole aligned perpendicular to the surface (the ultimate high field configuration).

It is natural to ask if the packing of water molecules next to the metal is increased. In the absence of strong surface electric fields, the interfacial water molecules tend to be oriented with some of their hydrogen atoms pointing away from the liquid phase, and some involved in H-bonding to a second layer [22]. The orientational ordering and packing of the water molecules near the metal surface is disrupted by the high surface electric field between the ions and their images, with the result that some hydrogen bonds break allowing more water molecules to pack closer. The increased local density of water is the expected packing phenomenon in the interfacial region, resulting from the hydrogen bond breaking. Also some solvent structure breaking will occur because of disruption due to the proximity of the cation.

Next we discuss the z component of dipole density profile. The three models show similar behavior near the metal with and without an applied external field. For all the models there is a prominent peak at 0.68 nm from oriented water at the surface. As expected the peak has a tail towards the bulk side signifying a decrease in orientation as the distance from the surface increases. In the interior of the film the dipole density drops to a low value signifying shielding of the charge of ions and their images. In the applied field the dipole profile is peaked at both surfaces (edge effect) and for $|z| < 0.6$ nm is approximately uniformly polarized. This latter behavior is as expected for a dielectric exhibiting orientational polarization. In zero field the peak at 0.68 nm arises because of orientational saturation at the position where the electric field due to the ions is greatest. There is also a weak broad maximum between 0.2 and 0.4 nm due to ion induced orientation of the water molecule. The model ST2 shows a distinctive difference near the second boundary z = -0.931 nm. There is practically no dipole oscillation at -0.68 nm. Models SPCE and TIP4P have a small but significant variation in dipole density

between -0.7 and -0.6 nm compared to ST2. As a result for the different models, the electric potential will vary in significantly different ways in the range $-0.931 < z < -0.4$ nm.

We have also calculated the total charge density across the system. Though we do not show it in the figures we describe it briefly. Most noticeable are oscillations presumed due to water packing variations. For the Na^+-water systems without external electric field, the two planar models, SPCE and TIP4P, produce almost identical total charge density ρ_q. In both models ρ_q display a prominent peak near the electrode, followed with a deep minimum. Some small difference in ρ_q may come from the shift of the negative charge in TIP4P. The main structure in the charge density ρ_q near the wall comes from oriented and localized water molecules. There is a peak (at 0.76 nm) in ρ_q contributed from the hydrogens, coincidence with the first peak in ρ_H at approximately 0.76 nm. Since the density profiles for the hydrogen atoms and water molecules are relatively insensitive to the water model, the difference in the peak amplitude of ρ_q must be mainly a consequence of the different charge value carried by the hydrogens. Indeed, the partial charge carried by the hydrogen nuclei in ST2 is almost one half of those in SPCE and TIP4P, and the peak in ρ_q is reduced by about the same ratio. Another effect that perturbs the charge density profile is the molecular geometry. For the ST2 molecule, the negative charges are moved along the tetrahedral directions by 0.08 nm. This causes a shallower minimum near the metal wall, shifted towards the center of the film. Such contributions also affect ρ_q near the dielectric wall. However, the minima in systems Na^+/ST2 and Na^+/ST2/e (field on) differ with the other four to an even larger extent partly because of the contribution made by the sodium cation.

The largest differences among these systems are the ion density profiles, which play an important role in determining the electric field and potential across the system. In the absence of the applied field, the ions are completely hydrated all of the time and range across the greater part of the film. The sodium ion in ST2 water is localized from $\sim$ -0.3 to 0.3 nm. It shows some propensity to contact the metal surface in the SPCE or TIP4P water molecule systems.

However, the situation becomes qualitatively different in an external field. Although some small shift towards the metal surface is observed for SPCE, the cationic density profiles calculated for systems Na^+/SPCE and Na^+/TIP4P are almost superimposable. In the systems SPCE and TIP4P

there is a reasonable probability for Na^+ to make solvent-bridged contact to the metal surface, a central feature of the Grahame model [10] of the electric double layer. For TIP4P solvent, the probability is slightly reduced. However, for ST2 water there is a greatly reduced probability for the primary solvent shell contacting the electrode. The density profile of the sodium ion looks flat, contrasting the changes observed in the other systems where the surface electric field draws the ion towards the metal. There is some small probability that the cation weakly adsorbs on the dielectric surface, along with its primary solvation sheath (splayed). No contact adsorption is observed on the metal surface.

The entirely different behavior for ions observed in the planar solvents SPCE and TIP4P compared to the three dimensional ST2 solvent molecule is very important since it influences the conclusion about the nature of the adsorbed ions. In order to avoid possible artifacts introduced from poor statistics and/or equilibrium, we doubled the simulation time for the system Na^+/ST2 from 1 ns to 2 ns and observed no significant changes. This confirms that the simulation results should be qualitatively reliable and previously described effect real for this model.

3.2 Systems Containing Cl^- Ions

In figures 4 to 6 the probability profiles for the three water systems and chloride are shown. In the absence of an external field we observe no qualitative differences among the three models. A contributing factor is the larger radius of the chloride ion and weaker primary hydration.

The main peaks of ρ_{H_2O} are broad and are located at -0.6, 0.3 and 0.6 nm. There is a hint of a broad peak between -0.2 and -0.3 nm in ST2 water. Along the series SPCE, TIP4P to ST2 a small peak grows in near 0.65 nm on top of the broader peak at 0.60 nm. In the presence of the applied field, the left shoulders of ρ_{H2O} are raised in the same order. This structure resembles the one seen in the cation systems in shape and position. Careful inspection shows that for anions this weak peak is always at smaller z. The shift is due to the reversal in the orientation of water in the surface electric field generated by the anions.

In the external field, the 0.65 nm peak grows in sharply, becoming the sharpest feature in the water profile. However the peak is not as sharp or intense as in the case of sodium ions discussed in the last section. The reason

is because the chloride ion contact adsorbs in the applied field there is a drop in the electric field on the left side of the ions so that the field experienced by the water molecules in the first layer is weaker by approximately a factor two (this is in contrast to the sodium ion case where the field due to the ions decays slowly over the diffuse region).

In zero field, the H atom profiles are similar. The main peaks occur at -0.6 (edge), 0.3, and 0.6 nm (main peak). The ST2 model has an additional broad maximum near -0.2 nm. The main peak at 0.6 nm also grows by approximately a factor two (compared to ρ_{H_2O}). In the applied field both protons are repelled and their is no evidence that the distributions split as in the case with cation fields. A new feature in the H distributions in the external field is the appearance of a small distinct peak at -0.75 nm. In the applied field the water molecules orient across the film so that protons poke outward at the dielectric boundary.

Unlike the situation for the Na^+-water systems, the density profiles of ion for the Cl^--water systems shown in Figs. 4-6 are all quite broad and diffuse and show little variation with model. The difference between the adsorption behavior of anion and cation becomes larger in the external electric field because all the chlorides localize on the electrode. In zero field, the Cl^- density profiles are all diffuse with a small but finite chance for contact adsorption. When the anodic external electric field is applied, all the anions strongly contact adsorbed on the metal surface. In the SPCE or TIP4P environment, the anion is very seldom found far from the electrode, though there is a small statistical probability that the anion will desorb temporarily in the case of TIP4P. When the adsorbed chloride peak heights are compared, it is seen that chloride density profile ρ_{Cl} in ST2 (see Figure 6) has the highest amplitude and narrowest full width at half maximum, implying most localization in this case.

The dipole density for water, ρ_D, shown in Figures 4-6 indicate that the orientational ordering of the water molecules from the three models do not deviate from each other significantly except at the dielectric surface. As discussed earlier in the case of the sodium ion, the ST2 dipole profile is much flatter coming off the dielectric wall. The similarity in the rest of the zero field profile stems from similarities in the chloride ion distributions. When the external field is applied, the dipole distribution functions are similar to the situation in pure water because in each model the ion is localized (contact adsorbed) entirely on the metal. The peaks near $|z| = 0.65$ nm are from 'end

effect' due to the walls and on the metal side they are also caused by intense surface field contributed from the chloride ion.

3.3 Further Discussions

It is well known [36] that the adsorption behavior is, to a large extent, controlled by the competition among the ion-water, ion-surface, water-water, and water-surface interactions. Referring to Table I where the potential parameters used in the simulations are given, we find that the differences in ϵ_{OI} and σ_{OI} between systems Na^+/SPCE and Na^+/ST2 are much smaller than those between systems Na^+/SPCE and Na^+/TIP4P. Therefore, the differences in behavior of Na^+ ions seen in ρ_{Na} cannot be due to the spherically symmetric Lennard-Jones potential. It must therefore be a consequence of some angular-dependent interactions. At small distances the Coulomb interaction between ion and water depends strongly on the model employed because of their different geometries and charge distributions, and consequently different higher multipole moments.

For a better understanding of the electrical properties, we plot the electrical potential profiles across the electrolyte in Fig. 7, setting the average of the potential on the dielectric plate to be zero, as a reference point. The electrical potential profiles are calculated from the charge distribution along the z direction. These curves show that the electrical potential in the central part ($|z| \leq\sim 0.6$ nm) of the Na^+/ST2 and Cl^-/ST2 films without external field are nearly zero, while for systems Na^+/SPCE, Na^+/TIP4P, Cl^-/SPCE, and Cl^-/TIP4P, the potential drops by almost -0.6 V. In this sense, the central parts of systems Na^+/ST2 and Cl^-/ST2 display approximately bulk behavior. There is no such region in the SPCE and TIP4P solutions. A simple interpretation of the phenomenon is based on the well-known fact that the bulk ST2 water is more structured than SPCE and TIP4P. Therefore, the former persists under the perturbation, while the latter two are more fragile.

In accord with the polarization and net charge distributions described earlier, the electric potentials for systems Na^+/SPCE and Na^+/TIP4P in zero field have two minima around $|z| \approx 0.6$ - 0.65 nm. In the presence of the applied field, the minima around the metal surface are about 600 mV deep, while for system Na^+/ST2, it is much shallower. This explains the broad unstructured diffuse region occupied by the cation and its hydration shell in

system Na^+/ST2/e described above.

In all the cases studied, the hydration shell of Na^+ was complete. We have calculated pair correlation functions for the ions and water molecules. It is interesting to note that the first peak of Na^+-TIP4P pair correlation function is located near 0.25 nm, much larger than the mixed Lennard-Jones radius of 0.19 nm (see Table I). This would imply that the solvation structure of Na^+-TIP4P is relatively weak. In contrast, the first peak of the Na^+-ST2 radial distribution function is located at $\sim$ 0.24 nm, much shorter than the mixed $\sigma_{OI} = 0.273$ nm, indicating a strong attractive electrostatic interaction on average. The hydration numbers for systems Na^+/ST2 in zero and non-zero external field are almost 20% higher than those of the other four systems.

In contrast to the cation solutions, the hydration number for Cl^- decreases in the order of SPCE, TIP4P, and ST2. The propensity of Cl^- to adsorb on the surface increases in the same order, as expected. Because of the anionic adsorption, there is a significant reduction in the hydration number when the external electric field is turned on. Since the interaction of Cl^- with the ST2 molecule is weaker than the interactions with the other types of solvent molecules, there is a greater loss in the first hydration shell for ST2 ($\sim$ 32%) than for SPCE ($\sim$ 26%) and TIP4P ($\sim$ 24%).

According to the calculation of bulk solution by Heinzinger [35], the ST2 water molecules in the first hydration shell of Na^+ ion are oriented with strong preference to form a tetrahedral structure. For planar water molecules such as SPCE and TIP4P, the hydrated ion has the largest probability to be located in the same plane of the water molecule. As pointed out by Heinzinger [35], the preferential orientation of water molecules in the first hydration shell of an ion belongs to one of the rare cases where the simulation results depend sensitively on the model employed. All these results consistently show that the potential models with stronger angular dependence like ST2 form stiffer hydration shells compared to less structured liquids such as SPCE and TIP4P. Our simulation results also show that the hydration structure of cations in ST2 solution does not vary with the external field, whereas in SPCE and TIP4P solutions there were some changes albeit small ones. The discussion thus far suggests that the cation-water interaction, especially in the case of ST2 solution, is very strong compared to the interactions with the metal wall. Therefore, the movement of the hydrated cation is accompanied with the surrounding water molecules. On average, more water molecules in the ST2 medium than in the SPCE or TIP4P media move with the cation.

The interaction between Na^+ ion and ST2 water is stronger than in the case of SPCE or TIP4P water and the ST2 liquid is more strongly hydrogen-bonded. As a consequence, there is a greater tendency for Na^+ to be hydrated in the ST2 environment than adsorb to the electrode.

4 Conclusions

Molecular dynamics simulations were performed on two different ions in three different water models, with zero applied field and with an external applied field. All electrostatic interactions between ions, water molecules, and their electrostatic images in the metal have been accurately computed with the FMM. Our goal was, through detailed comparison of the computed results, to gain some insight concerning the relative usefulness of these models at aqueous interfaces. These models have been initially developed in the bulk phase and later have been widely applied to studying water in perturbed states. The application to surface problems may invalidate some implicit approximations involved in their original derivations (in particular, the use of fixed charges). For the most part it was found that the density profiles of the water properties are relatively insensitive to the models, though there were some discrepancies that were discussed in the last section. Since the charges are buried inside Lennard-Jones spheres their influence on the dynamics is muted. This is not so in the case of electrical properties. Even cursory examination of Figures 1 to 6 shows that the dipole density profiles vary much more from model to model than do the water and hydrogen density profiles. This is due, in part, to the different molecular geometry and charge distribution in these models, and in part to energetic competition among various interactions.

Some common features in the water structure were observed for the three models. In particular, the water structure near the metal surface was sensitive to the magnitude and direction of the surface field. In the absence of an external field the surface electric field arises primarily from the density profile of the ion. If the ion is not contact adsorbed then the surface water molecules see a large field that disrupts H-bonds and orients water dipoles with the field. Contact adsorbed ions are less effective because their high field region lies closer to the surface and contains few molecules. The variation in water density peaks with external field verifies this conclusion.

In the absence of the electric field, the ionic solute, whether positively or negatively charged, distributes diffusely. Greater variation is found for the hydrogen density profiles, suggesting the occurrence of molecular reorientation under the influence of the electric field of the ions. Applying the external field further increases the molecular alignment. Because of the strong Coulomb interaction between the charges and their images, the interfacial water molecules are bound to the metal surface, giving rise to a higher density layer. This was also seen in earlier simulations of similar systems [16, 37, 38, 39, 40, 41].

An interesting conclusion of the present work is the qualitatively different adsorption behavior of the sodium ion in different media. In ST2 solution the cation is strongly hydrated and does not adsorb as testified by the density profile. In contrast, in the SPCE and TIP4P environments, it shows a strong propensity to be adsorbed via the first hydration shell. The adsorption behavior of the anion is strongest for ST2 and weakest for the other two. This variation is related to the hydration structure which reflects the energetic competition between water-ion and water-water interactions. This raises an important question whether a model based on effective potentials in the bulk state is a reasonable approximation in studying the electric double layer problems? Some properties are insensitive to the model and can be well described by simple models, but others are not. Of course, studying two ions does not provide enough information to decide. What is need are calculations for a series of related cations and anions. Such calculations have been performed for alkali metal and halide ions in ST2 water [42] where we have learned that many known electrochemical trends can be modeled. However what we learn from this work is that details in these trends are going to be very model sensitive until new models are developed for water and ions that address the peculiar aspects of interfaces. In particular we need a model that incorporates electric polarizability and attributes that mimic weak chemisorption [43].

References

[1] S.-B. Zhu and C. F. Wong, J. Chem. Phys. 98, 8892 (1993).

[2] S.-B. Zhu and C. F. Wong, J. Chem. Phys. 98, 9047 (1993).

[3] J. O'M. Bockris and S. U. Khan, *"Quantum Electrochemistry"* (Plenum Press: New York, 1979).

[4] A. T. Hubbard, Chem. Rev. 88, 633 (1988).

[5] R. Parsons, Chem. Rev. 90, 813 (1990).

[6] G. Gouy, J. Phys. 9, 457 (1910).

[7] D. L. Chapman, Philos. Mag. 25, 508 (1913).

[8] O. Stern, Z. Electrchem. 30, 508 (1924).

[9] A. N. Frumkin, Trans. Faraday Soc. 36, 117 (1940).

[10] D. C. Grahame, Chem. Rev. 41, 441 (1947).

[11] J. O'M Bockris, M. A. V. Devanathan and K. Mueller, Proc. Roy. Soc. (London) A274, 55 (1963).

[12] S.-B. Zhu, S. Singh, and G. W. Robinson, Adv. Chem. Phys. 85(3), 627 (1994).

[13] H. J. C. Berendsen, J. R. Grigera, and T. P. Straatsma, J. Phys. Chem. 91, 6269 (1987).

[14] H. J. Jorgensen, J. Chandrasekhar, J. D. Madura, R. W. Impey, and M. L. Klein, J. Chem. Phys. 79, 926 (1983).

[15] F. H. Stillinger and A. Rahman, J. Chem. Phys. 60, 1545 (1974).

[16] M. R. Philpott and J. N. Glosli, in *"Theoretical and Computational Approaches to Interface Phenomena"*, Eds. H. Sellers and J.T. Golab (Plenum Press: New York, 1994).

[17] P. Bopp, Pure & Appl. Chem. 59, 1071 (1987).

[18] S.-B. Zhu and G. W. Robinson, Z. Naturforsch. 46a, 221 (1990).

[19] S.-B. Zhu and G. W. Robinson, J. Chem. Phys. 94, 1403 (1991).

[20] S.-B. Zhu, J.-B. Zhu, and G. W. Robinson, Phys. Rev. A44, 2602 (1991).

[21] S.-B. Zhu and G. W. Robinson, J. Chem. Phys. 97, 4336 (1992).

[22] C. Y. Lee, J. A. McCammon, and P. J. Rossky, J. Chem. Phys. 80, 4448 (1984).

[23] W. A. Steele, Surf. Sci. 36, 317 (1973).

[24] L. F. Greengard, *"The Rapid Evaluation of Potential Fields"* (MIT Press: Cambridge, MA, 1987).

[25] L. Greengard and V. Rokhlin, J. Comp. Phys. 73, 325 (1987).

[26] J. Carrier, L. Greengard, and V. Rokhlin, Siam J. Sci. Stat. Comput. 9, 669 (1988).

[27] L. Greengard and V. Rokhlin, Chemica Scripta A29, 139 (1989).

[28] P. P. Ewald, Ann. Physik 54, 519 (1917).

[29] P. P. Ewald, Ann. Physik 54, 557 (1917).

[30] M. Born and K. Huang, *"Dynamical Theory of Crystal Lattices"* (The Clarendon Press: Oxford, England, 1954).

[31] J. N. Glosli, Unpublished results.

[32] J. N. Glosli and M. R. Philpott, Proceedings of the Symposium on *"Microscopic Models of Electrolyte Interfaces"*, Vol. 93-5, 80 (The Electrochemical Society, Inc.: Pennington, 1993).

[33] J. Caldwell, L. X. Dang, and P. A. Kollman, J. Am. Chem. Soc. 112, 9144 (1990).

[34] J. Chandrasekhar, D. C. Spellmeyer, and W. L. Jorgensen, J. Am. Chem. Soc. 106, 903 (1984).

[35] K. Heinzinger, Physica, B131, 196 (1985).

[36] J. O'M. Bockris and A. K. N. Reddy, *"Modern Electrochemistry"* Vol. 2 (Plenum Press: New York, 1973).

[37] J. N. Glosli and M. R. Philpott, J. Chem. Phys. 96, 6962 (1992).

[38] J. N. Glosli and M. R. Philpott, Proceedings of the Symposium on *"Microscopic Models of Electrolyte Interfaces"*, Vol. 93-5, 90 (The Electrochemical Society, Inc.: Pennington, 1993).

[39] J. N. Glosli and M. R. Philpott, J. Chem. Phys. 96, 6962 (1993).

[40] D. A. Rose and I. Benjamin, J. Chem. Phys. 95, 6856 (1991).

[41] T. Matsui and W. L. Jorgensen, J. Am. Chem. Soc. 114, 3220 (1992).

[42] M. R. Philpott and J. N. Glosli, unpublished calculations

[43] S.-B. Zhu and M. R. Philpott, J. Chem. Phys. 100, 6961 (1994) Interaction of Water with Metal Surfaces, submitted December 93.

Table 1 Potential Parameters

Water	Ion	ϵ_O (kJ/mol)	σ_O (nm)	ϵ_{OI} (kJ/mol)	σ_{OI}	Ref.
SPCE	Na^+	0.650	0.316	0.544	0.216	[33]
SPCE	Cl^-	0.650	0.316	0.418	0.432	[33]
TIP4P	Na^+	0.649	0.315	6.724	0.190	[34]
TIP4P	Cl^-	0.649	0.315	0.493	0.442	[34]
ST2	Na^+	0.317	0.310	0.358	0.273	[35]
ST2	Cl^-	0.317	0.310	0.168	0.486	[35]

Figure Captions

Fig. 1 Density profiles of water molecules, their hydrogen atoms, the ion, and the orientational polarization of the water molecules for System Na^+-SPCE. The label e indicates the results obtained in the presence of the applied field.

Fig. 2 Density profiles of water molecules, their hydrogen atoms, the ion, and the orientational polarization of the water molecules for System Na^+-TIP4P. The label e indicates the results obtained in the presence of the applied field.

Fig. 3 Density profiles of water molecules, their hydrogen atoms, the ion, and the orientational polarization of the water molecules for System Na^+-ST2. The label e indicates the results obtained in the presence of the applied field.

Fig. 4 Density profiles of water molecules, their hydrogen atoms, the ion, and the orientational polarization of the water molecules for System Cl^--SPCE. The label e indicates the results obtained in the presence of the applied field.

Fig. 5 Density profiles of water molecules, their hydrogen atoms, the ion, and the orientational polarization of the water molecules for System Cl^--TIP4P. The label e indicates the results obtained in the presence of the applied field.

Fig. 6 Density profiles of water molecules, their hydrogen atoms, the ion, and the orientational polarization of the water molecules for System Cl^--ST2. The label e indicates the results obtained in the presence of the applied field.

Fig. 7 Electric potential profiles calculated from the charge distributions. The curves for systems Na^+/SPCE and Na^+/SPCE/e are very similar to the curves for systems Na^+/TIP4P and Na^+/TIP4P/e and so are not shown in this figure. The electric potential profiles for systems containing Cl^- ion has a similar behavior.

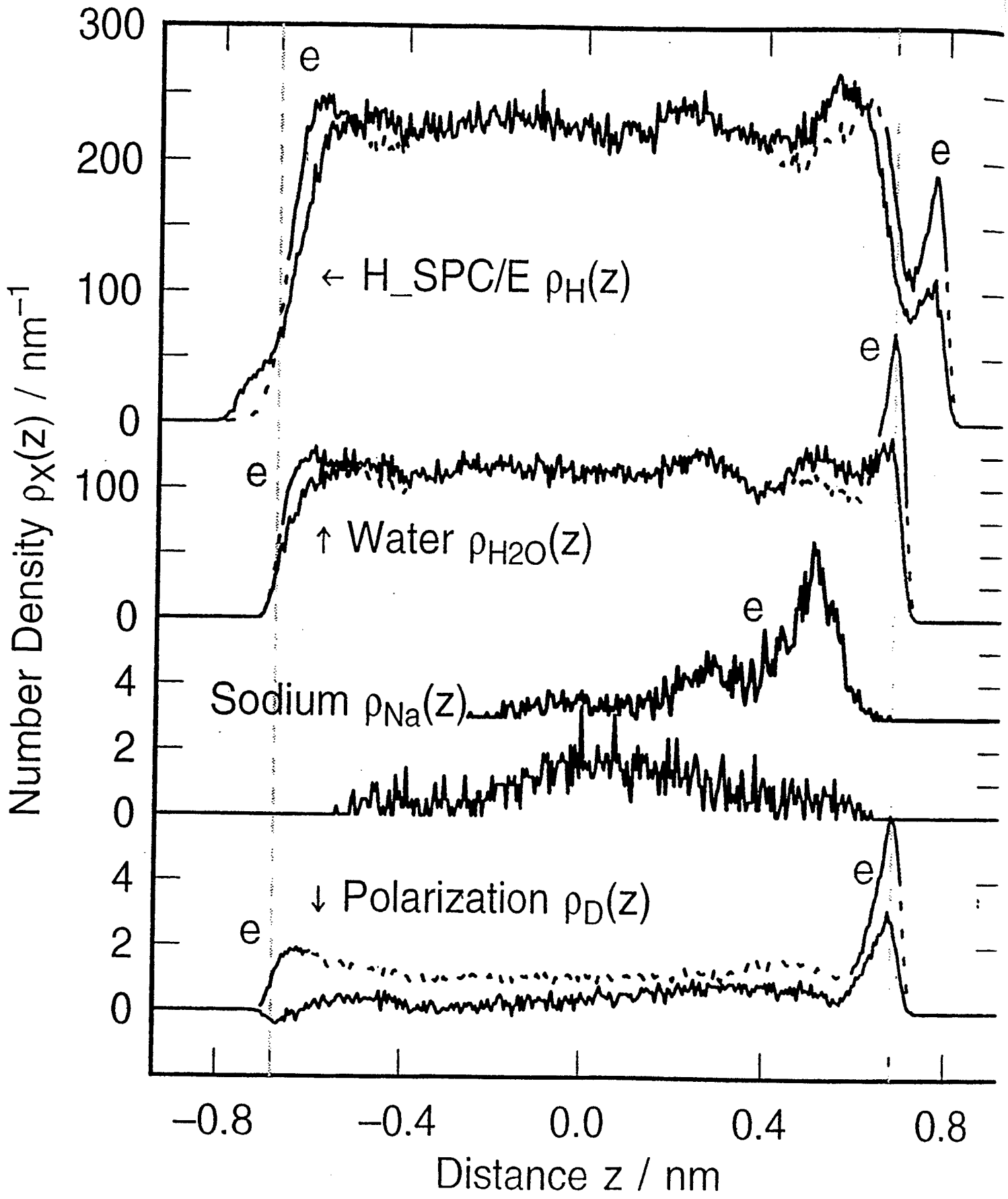
300
200
100
0
100
0
4
2
0
4
2
0
e
e
e
e
e
e
← H_SPC/E $\rho_H(z)$
↑ Water $\rho_{H2O}(z)$
Sodium $\rho_{Na}(z)$
↓ Polarization $\rho_D(z)$
Number Density $\rho_X(z)$ / nm^{-1}
−0.8
−0.4
0.0
0.4
0.8
Distance z / nm

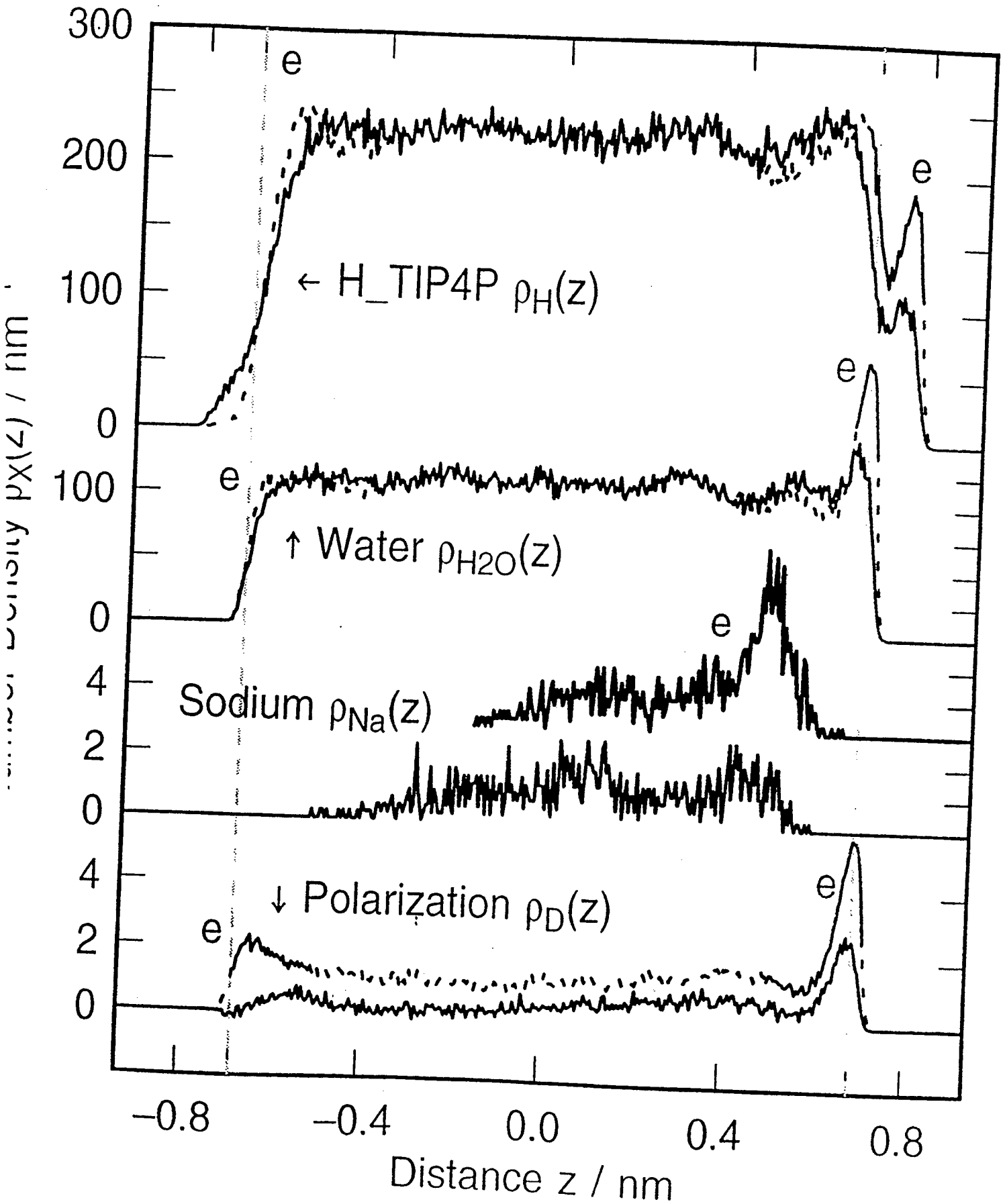
300
200
100
0
100
0
4
2
0
4
2
0
e
e
e
e
e
e
e
← H_TIP4P $\rho_H(z)$
↑ Water $\rho_{H2O}(z)$
Sodium $\rho_{Na}(z)$
↓ Polarization $\rho_D(z)$
−0.8
−0.4
0.0
0.4
0.8
Distance z / nm

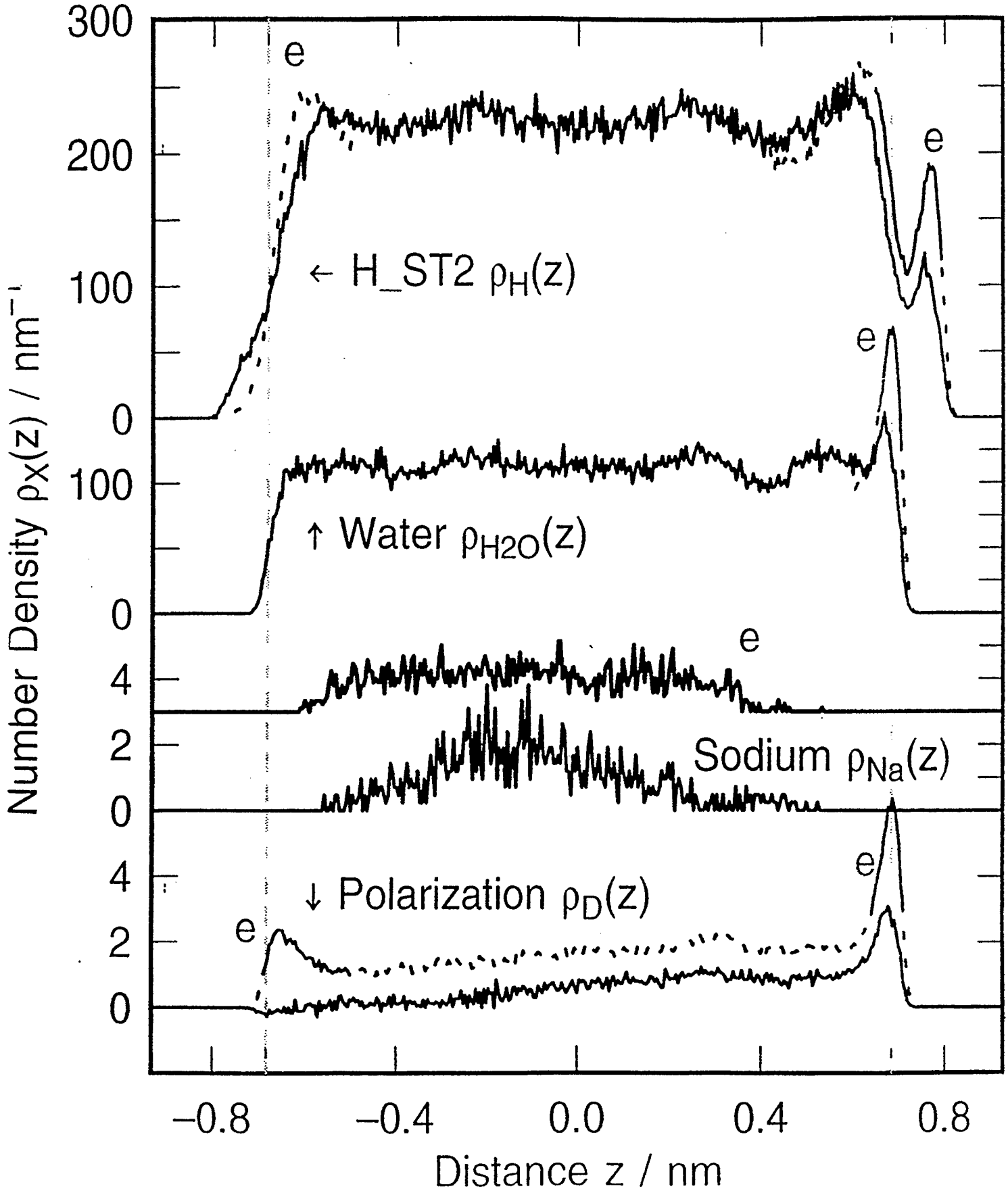
300
200
100
0
100
0
4
2
0
4
2
0
e
e
e
e
e
e
← H_ST2 ρH(z)
↑ Water ρH2O(z)
Sodium ρNa(z)
↓ Polarization ρD(z)
Number Density ρX(z) / nm⁻¹
−0.8
−0.4
0.0
0.4
0.8
Distance z / nm

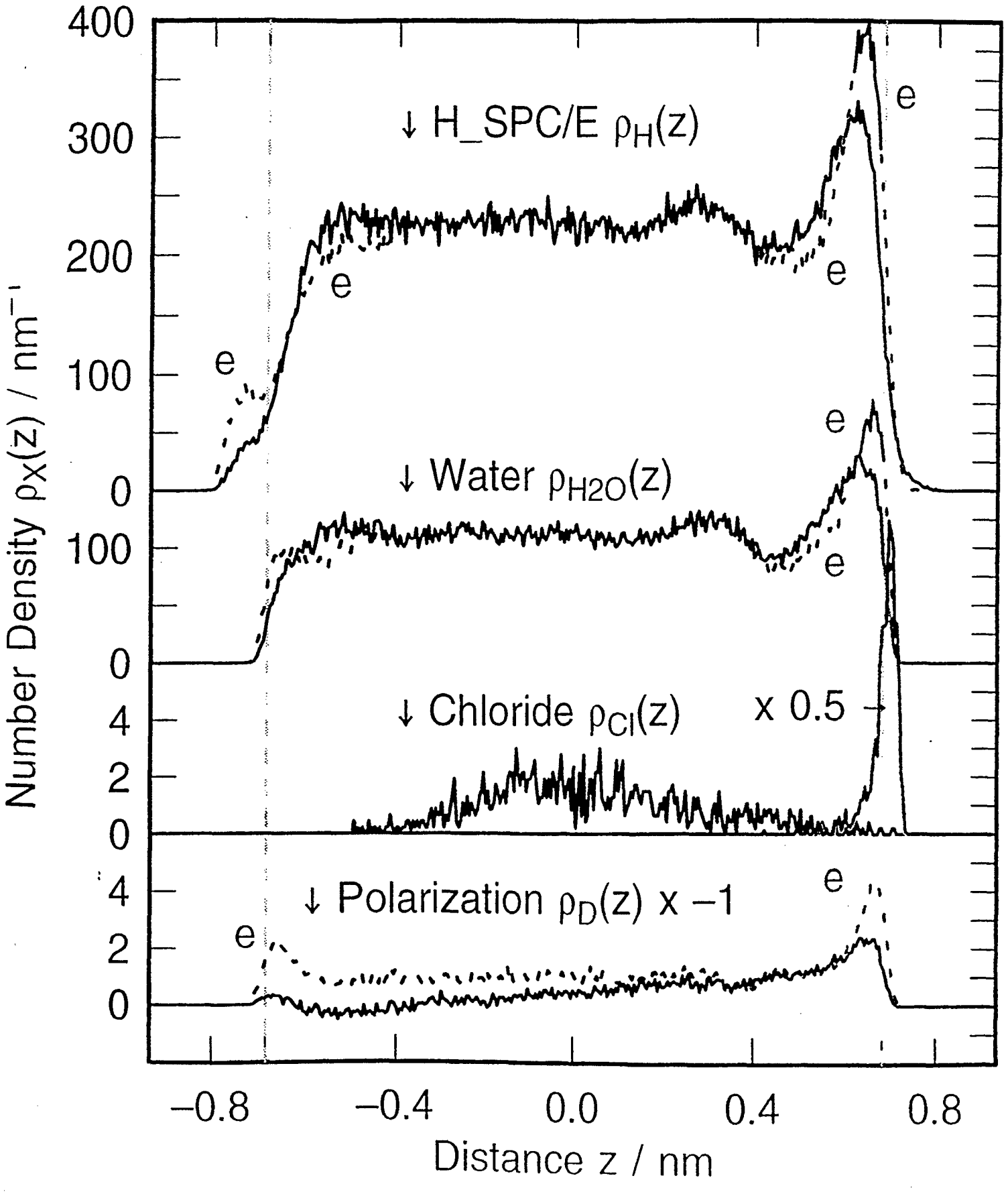
400
300
200
100
0
100
0
4
2
0
4
2
0
↓ H_SPC/E $\rho_H(z)$
↓ Water $\rho_{H2O}(z)$
↓ Chloride $\rho_{Cl}(z)$
x 0.5
↓ Polarization $\rho_D(z)$ x −1
e
Number Density $\rho_X(z)$ / nm^{-1}
−0.8
−0.4
0.0
0.4
0.8
Distance z / nm

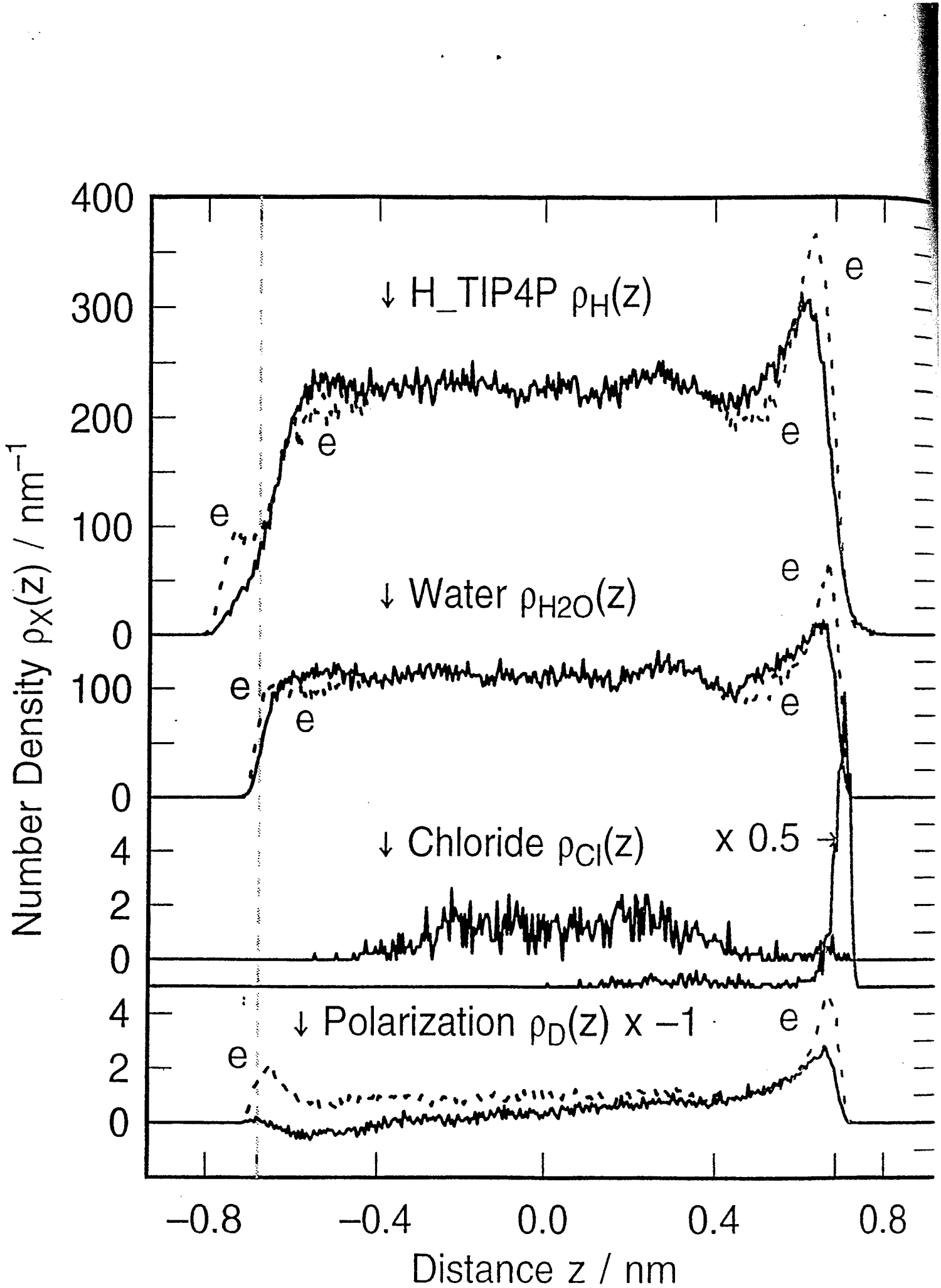
400
300
200
100
0
100
0
4
2
0
4
2
0
↓ H_TIP4P $\rho_H(z)$
↓ Water $\rho_{H2O}(z)$
↓ Chloride $\rho_{Cl}(z)$
x 0.5
↓ Polarization $\rho_D(z)$ x −1
e
Number Density $\rho_X(z)$ / nm^{-1}
−0.8
−0.4
0.0
0.4
0.8
Distance z / nm

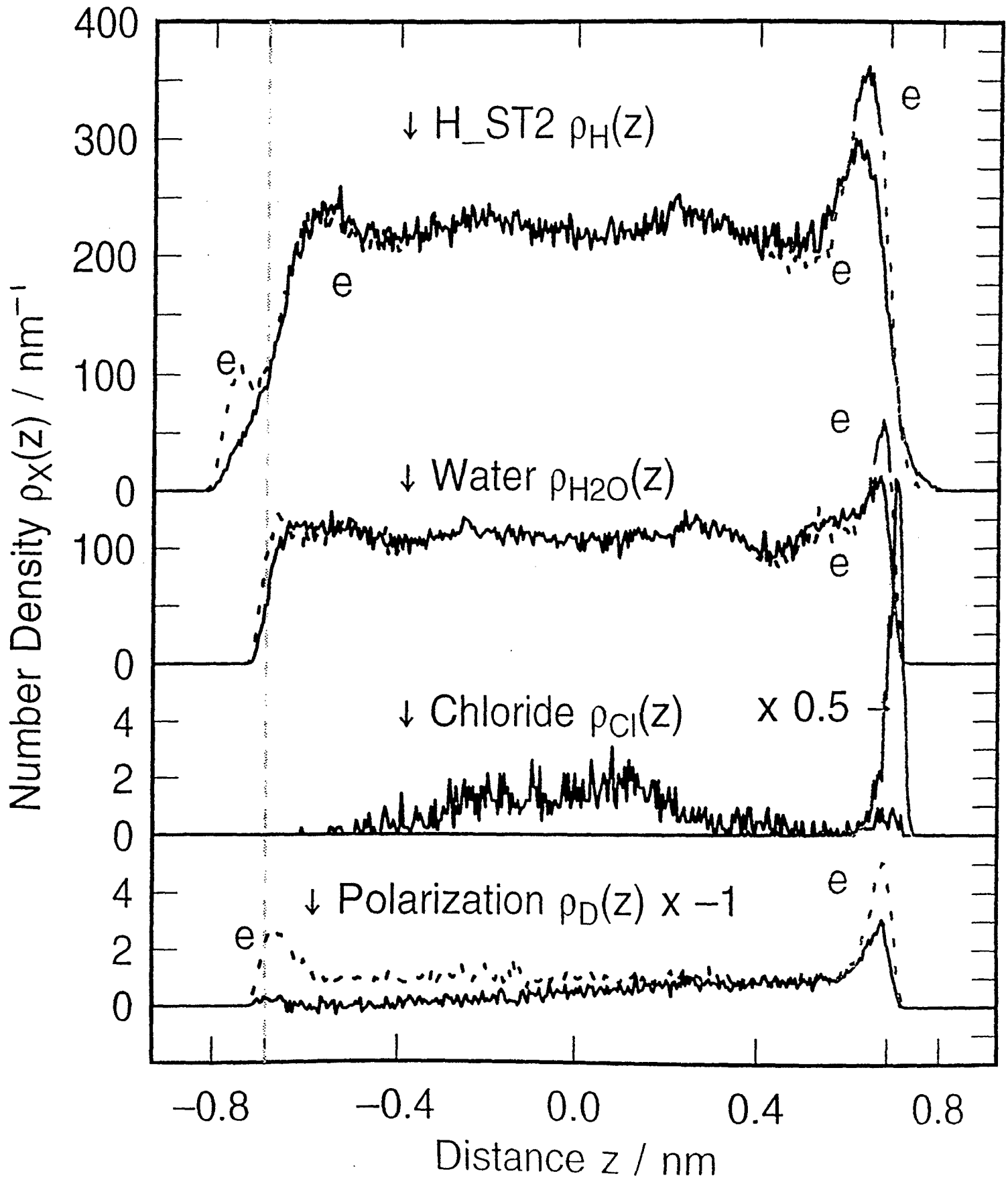
400
300
200
100
0
100
0
4
2
0
4
2
0
↓ H_ST2 $\rho_H(z)$
↓ Water $\rho_{H2O}(z)$
↓ Chloride $\rho_{Cl}(z)$
x 0.5
↓ Polarization $\rho_D(z)$ x −1
e
Number Density $\rho_X(z)$ / nm^{-1}
−0.8
−0.4
0.0
0.4
0.8
Distance z / nm

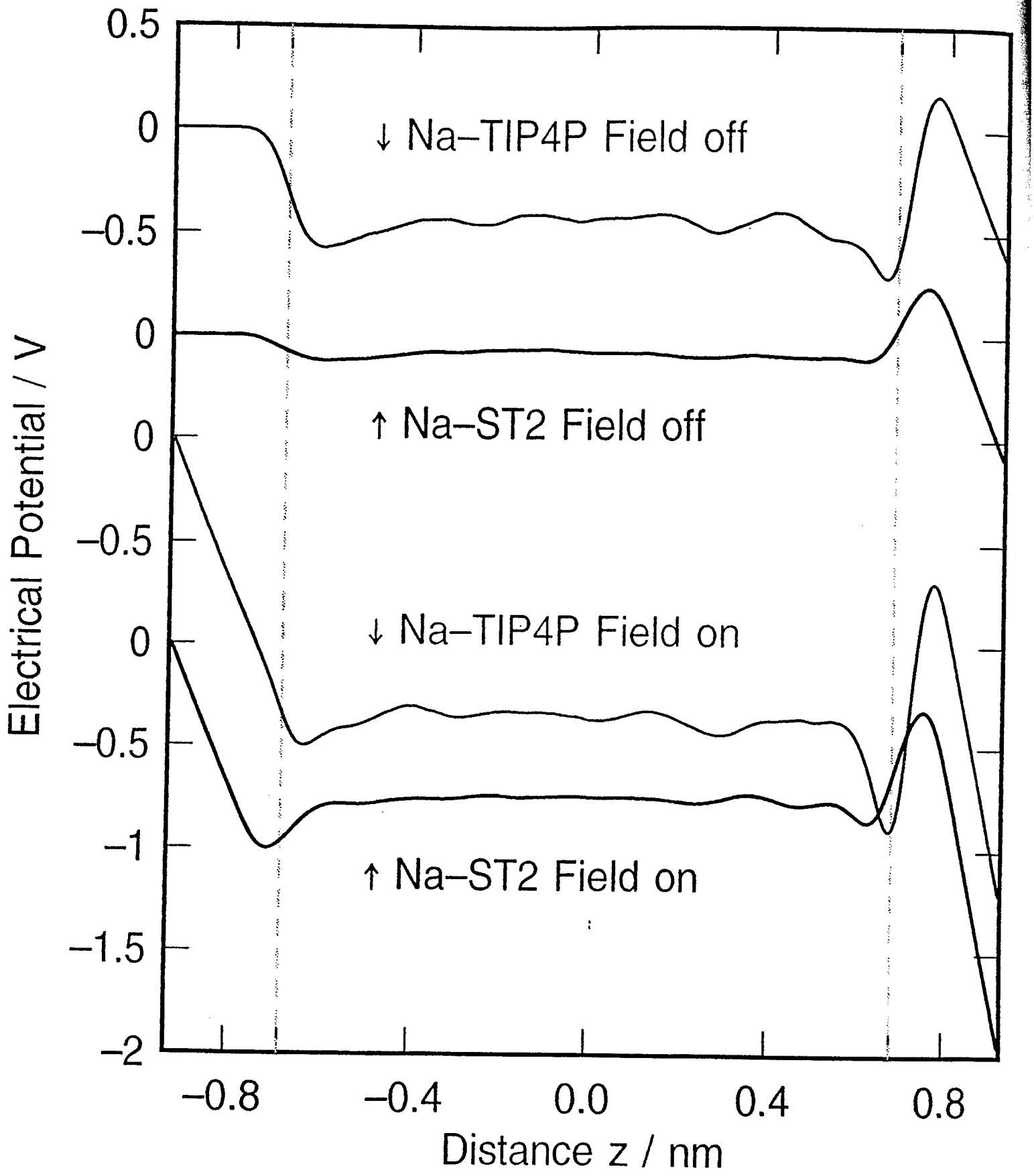
0.5
0
−0.5
0
0
−0.5
0
−0.5
−1
−1.5
−2
↓ Na–TIP4P Field off
↑ Na–ST2 Field off
↓ Na–TIP4P Field on
↑ Na–ST2 Field on
Electrical Potential / V
−0.8
−0.4
0.0
0.4
0.8
Distance z / nm

Molecular Dynamics Study of Aqueous Electrolyte Solutions near a Structured Sphere

Sheng-Bai Zhu and Michael R. Philpott
IBM Research Division
Almaden Research Center
650 Harry Road
San Jose, CA 95120-6099

James N. Glosli
Lawrence Livermore National Laboratory
Livermore, CA 94550

August 22, 1994

Abstract

Molecular dynamics studies of water and ions around a charged small compact globular object are described. The hypothetical molecular ion C_{60}^{--} is used as the globular model. It is found that the cesium cation is in physical contact on the spherical surface much of the time with an incomplete hydration shell. The chloride ion spends part of the time in a solvent-separated adsorption configuration and part of the time in the diffuse region. No adsorption of the sodium ion onto the spherical surface is observed.

1 Introduction

This communication describes the first molecular dynamics study of water and ions around a charged small compact globular object about 1 nm in

diameter and includes accurate and efficient treatment of all electrostatic interactions. The goal of this work is to gain some basic understanding of the organization of water and ions in electric double layers around 'spherical' objects since this is relevant, albeit on a somewhat larger scale, to the microscopic environment around small colloid particles, compact proteins and polyelectrolytes. In previous studies the Poisson-Boltzmann equation for large spherical ions has been studied analytically by calculating the singlet and pair correlation function using the Ornstein-Zernike equation, as for example in the work of Henderson and coworkers [1, 2, 3, 4]. In the present article, we choose C_{60} molecule as the prototype 'structured sphere' because it possesses a computationally manageable size and has a characterized set of interaction parameters based on a considerable number of molecular dynamics simulations [5, 6, 7, 8, 9]. This paper is not meant to be a study of actual C_{60} ions in solution.

So far, computer simulations of electrochemical double layers have been mainly performed for aqueous electrolyte solutions near flat structureless surfaces [10, 11, 12, 13, 14, 15] and flat atomically structured surfaces [16, 17, 18, 19]. From a computational point of view, flat surfaces can be thought to be spheres with infinitely large radius so that one anticipates some common features between the two types of systems. In particular the first peak in the radial distribution function of a large sphere goes over into the density probability function in the coordinate z measured along the surface normal. Likewise a contact ion pair goes over into contact adsorption (also called specific adsorption) on the flat electrode surface, though in the case of metals the electrostatic image interactions differ. Because of the surface curvature changes, one also anticipates some features that differ in each case.

2 Molecular Dynamics Method

Constant (N, V, T) molecular dynamics simulations are carried out for two dilute aqueous solutions. The first is composed of 502 ST2 water molecules [20], four sodium cations, two chloride anions, and one C_{60} molecule on which each C atom carries the charge $-e/30$ so that the total on the molecular ion is $-2e$. The second is composed of 506 ST2 water molecules, two cesium cations, and one C_{60}^{--} molecular ion. For both the cases, the simulation cell has the dimensions of $2.5054 \times 2.5054 \times 2.5054$ nm^3, and periodic boundary

conditions in three orthogonal directions are used. Each simulation lasts 1 ns, with the first 200 ps being used to equilibrate the system. Detailed description of the simulation method was given in previous papers [11, 12, 13, 14, 15].

Before proceeding, we remind the reader that C_{60} or buckminsterfullerene [21] is a soccer ball-like molecule with 60 carbon atoms sitting on the vertices of a truncated icosahedron. Each carbon atom interacts with the atoms comprising the solution components through Lennard-Jones potentials and a Coulomb potential. The ion-ion, ion-carbon, and water-carbon interactions are similarly modeled. The Lennard-Jones parameters of the carbon atom are taken from Steele's work on graphite [22]. The ion-water interactions are modeled by the 12-6 Lennard-Jones function between the ion and the oxygen atom of the water and the Coulomb potentials among charged sites. The Lennard-Jones parameters of the ions are taken from Heinzinger's results [23].

3 Adsorption and Hydration

The adsorption of the ions onto the structured sphere is partially described by the radial distribution functions (RDFs), g_{H_2OC60}, g_{NaC60}, g_{ClC60}, and g_{CsC60}. If there is adsorption onto specific sites like the hollow site of a six membered ring then simple radial distributions based on the assumed spherical symmetry will not be adequate. However they clearly represent a good starting point for initial discussions. As shown in Fig. 1, there is a distinct first hydration shell surrounding the structured sphere with its highest local density $\sim$ 0.65 nm away from the center of mass of C_{60} and the minimum around 0.74 nm which gives a coordination number of $\sim$ 38 for the system containing sodium and chloride ions and $\sim$ 39 for the system containing cesium ions. The two RDFs for water are remarkably similar especially when we realize that, as will be discussed later, the RDF for Cs^+ ion shows one ion to be contact adsorbed.

The ion-C_{60} radial distribution functions indicate that the Cs^+ ion makes a contact pair whereas, in contrast, the smaller ions Na^+ and Cl^- do not and appear in diffuse regions only. We discuss the cesium cation RDF first. In Figure 1 the bottom curve shows that the RDF for Cs^+ consists of a sharp peak at approximately 0.7 nm followed by a broad diffuse region devoid of

structure. The Cs^+ peak is consistent with a contact adsorbed ion because its position relative to the first water peak is equal to half the difference in the Lennard-Jones radii for water oxygen ($\sigma = 0.310$ nm) and cesium ($\sigma = 0.392$ nm). This strong adsorption tendency is not unexpected because there is a Coulombic attraction between the Cs^+ cation and C_{60}^{---} anion and the large size of the cation means a weaker hydration energy and unfavorable mixing entropy [24].

The RDF for chloride ion-C_{60} is broad and diffuse with the hint of a wide maximum near 0.85 nm and a weak minimum at approximately 1.05 nm. The distance of closest approach is approximately 0.65 nm, indicating that the anion occasionally touches the surface of C_{60} but does not form a stable contact pair. The broad peak in g_{ClC60} lying between the first and second peaks in the water-C_{60} RDF, g_{H_2OC60}, could be explained by some small tendency to take part in solvent-separated adsorption on the sphere. The solvent-induced interaction is attractive for the two like ions [25]. If we assume the chloride ions, whose distance from the center of mass of C_{60} is less than 1.05 nm where a weak minimum in g_{ClC60} is found, as solvent-separated adsorbing species, then the probability for such configurations would be about 26%.

The radial distribution function for the sodium cation-C_{60} in Figure 1 shows no probability for an approach closer than approximately 0.75 nm. At this point the C_{60} anion and Na^+ cation are separated by one water molecule. At the position of the first weak maximum in g_{NaC60} at approximately 0.9 nm the separation is equivalent to two water molecules. We conclude therefore that although the Coulomb interaction between the sodium ion and the C_{60} ion is attractive, the probability for observing a solvent-separated adsorption of the cation onto the anion is very small, since the cation is fully hydrated and the sodium-water interaction is very strong. By comparing the adsorption behavior of Na^+ with that of Cl^-, it is clear that the size of the ion plays a critical role in the adsorption process. Theories and many experimental results have shown that larger ionic size corresponds to a more negative entropy change and a less negative enthalpy change when the ion is transfered from nonpolar solvent to the aqueous environment [26]. In other words, large ions behave hydrophobically [27] and have a stronger tendency to be excluded from the solution.

Figure 2 describes the hydration structure of the ions through the ion-O and ion-H radial distribution functions. The central pair of plots for Na-H and Na-O in Figure 2, shows the sodium ion to be most strongly hydrated

with distinct first and second shells. The hydration structures of the sodium cation and the chloride anion are not significantly perturbed by the C_{60} molecular ion and are very similar to the ions in the bulk NaCl solution [28]. On the other hand, the hydration shell of the cesium ion is not always complete and the average hydration number reduces from 8.3 in the absence of the C_{60} [28] to 7.5 in the presence of the C_{60}. The values for the first peaks of g_{CsO} and g_{CsH}, 3.4 and 2.2, in Figure 2 are much smaller than their values in the bulk solutions, that is, 4.7 and $\sim$ 5 [28]. This significant decrease of the peak values for the Cs-O and Cs-H radial distribution functions is a consequence of the contact adsorption of the cation onto the C_{60} ion as discussed above in connection with the RDFs plotted in Figure 1.

In Figure 2 the first peak of g_{ClH} is shifted by ~ 0.1 nm, about the O-H bond length, compared with g_{ClO}. This suggests that the water molecules nearest to the anion have a preferred orientation with one O-H bond pointing directly towards the anion. For the sodium cation, the first peak of g_{NaH} is about 0.06 nm farther than the first peak of g_{NaO}. This shift corresponds to the configuration where one lone pair of the ST2 water points directly at the cation.

These conclusions concerning the orientation of water molecules in the hydration shells of the ions are confirmed by the curves in Figure 3. Here we plot the average orientations of the water molecules as functions of the distance between the oxygen atom of the water and the given ion. To measure the molecular orientation, we introduce the variable θ, which is the angle between the water dipole and the ion-O connecting line. If one O-H bond vector of the water molecule lies exactly on the line connecting the oxygen atom to the ion ($\theta = 125.25°$) or if one lone pair vector points directly towards the ion ($\theta = 54.75°$), then the average $< \cos\theta >$ would be ± 0.58. As indicated by the first two curves (from the top) in Figure 3, the water molecules surrounding C_{60} tend to be oriented with their dipoles pointing towards the center of the negatively charged sphere. Within the first hydration shell for Na^+ and Cl^-, the average $< \cos\theta >$ remains approximately constant, ~ 0.65 for sodium cation and ~ -0.6 for the chloride anion. For purposes of comparison, we note that in a bulk solution simulation without the C_{60} molecular-ion, Heinzinger and Vogel [28] found that the mean values of $\cos\theta$ are 0.69 for Na^+ and -0.65 for Cl^-. These values are slightly larger than the values obtained in this work. The orientational ordering of the water molecules surrounding the cesium ion is severely disturbed by the oppositely

charged C_{60} molecular ion. If the C_{60} ion were absent, these dipoles would have their orientations similar to those of the water molecules around the Na^+ cation (the third curve in Fig.3).

4 Conclusions

The first layer of water is oriented with its dipole pointing towards the center of the 'spherical' doubly charged C_{60} anion. The cesium cation is in physical contact on the spherical surface about 10% of the time. The smaller ions occupy extensive diffuse layers around the C_{60} molecular ion. No adsorption of the sodium ion onto the spherical surface is observed. Its distance of closest approach is one water molecule, with a separation of two or more water molecules more likely. The chloride ion appears to spend part of the time in a solvent-separated adsorption configuration and part of the time in the diffusion region. The hydration structures of the sodium cation and the chloride anion are not significantly perturbed by the presence of the C_{60} molecule. The hydration shell of the cesium ion is incomplete and the orientations of the water molecules around Cs^+ are severely disturbed by the surface of C_{60}.

5 Acknowledgments

This research was supported in part by the Office of Naval Research. We thank Donald Bethune for the coordinates of C_{60}.

References

[1] D. Henderson, F. F. Abraham, and J. A. Barker, Mol. Phys. 31 (1976) 1291.

[2] D. Henderson and M. Plischke, Proc. Roy. Soc. A 410 (1987) 409.

[3] D. Henderson and M. Plischke, J. Phys. Chem. 92 (1988) 7177.

[4] M. Lozada-Cassou and D. Henderson, J. Chem. Phys. 83 (1985) 361.

[5] Guo, Y.; Karasawa, N.; Goddard, W. A. III Nature 1991, 351, 464.

[6] Cheng, A.; Klein, M. L. J. Phys. Chem. 1991, 95, 6750.

[7] Sprik, M.; Cheng, A.; Klein, M. L. J. Phys. Chem. 1992, 96, 2027.

[8] Cheng, A.; Klein, M. L. Phys. Rev. 1992, B 45, 1889.

[9] Sprik, M.; Cheng, A.; Klein, M. L. Phys. Rev. Lett. 1992, 69, 1660.

[10] T. Matsui and W. L. Jorgensen, J. Am. Chem. Soc. 114 (1992) 3220.

[11] J. N. Glosli and M. R. Philpott, J. Chem. Phys. 96, 6962 (1992).

[12] J. N. Glosli and M. R. Philpott, Proceedings of the Symposium on *"Microscopic Models of Electrolyte Interfaces"*, Vol. 93-5, 90 (The Electrochemical Society, Inc.: Pennington, 1993).

[13] J. N. Glosli and M. R. Philpott, J. Chem. Phys. 96, 6962 (1993).

[14] S.-B. Zhu, M. R. Philpott, and J. N. Glosli, submitted to J. Chem. Phys.

[15] S.-B. Zhu, M. R. Philpott, and J. N. Glosli, in preparation.

[16] E. Spohr and K. Heinzinger, J. Chem. Phys. 84 (1986) 2304.

[17] Spohr, E,: Heinzinger, K. Electrochim Acta 1988, 33, 1211.

[18] Rose, D. A.; Benjamin, I. J. Chem. Phys. 1991, 95, 6856.

[19] Heinzinger, K.; Seitz-Beywl, J.; Poxleitner, M. Proceedings of the Symposium on *"Microscopic Models of Electrolyte Interfaces"*, Vol. 93-5, 63 (The Electrochemical Society, Inc.: Pennington, 1993).

[20] F. H. Stillinger and A. Rahman, J. Chem. Phys. 60 (1974) 1545.

[21] Kroto, H. W.; Heath, J. R.; O'Brien, S. C.; Curl, R. F.; Smalley, R. E. Nature, 1985, 318, 162.

[22] W. A. Steele, *"The Interaction of Gases with Solid Surfaces"* (Pergamon: New York, 1974).

[23] K. Heinzinger, Physica 131B (1985) 196.

[24] S.-B. Zhu, unpublished results.

[25] S.-B. Zhu and G. W. Robinson, J. Chem. Phys. 97 (1992) 4336.

[26] "The Chemical Physics of Solvation"; Ed. by R. R. Dogonadze, E. Kálmán, A. A. Kornyshev, and J. Ulstrup; Elsevier; Amsterdam, 1985.

[27] B. G. Cox, G. R. Hedwig, A. J. Parker, and D. W. Watts, Aust. J. Chem. 27 (1974) 477.

[28] K. Heinzinger and P. C. Vogel, Z. Naturforsch, 31A (1976) 463.

Figure Captions

Fig. 1 Radial distribution functions for water-C60 pair in the NaCl solution, water-C60 pair in the Cs solution, sodium-C60 pair, chloride-C60 pair, and cesium-C60 pair (from top to bottom).

Fig. 2 Hydration structure of the ions. The dotted curves are for ion-O radial distribution functions and the solid curves are for ion-H radial distribution functions.

Fig. 3 Average $\cos\theta$ as a function of the distance between an ion and the oxygen atom. Curves from top to bottom represent the molecular orientations around C60 in the NaCl solution, around C60 in the Cs solution, Na^+, Cl^-, and Cs^+.

F1

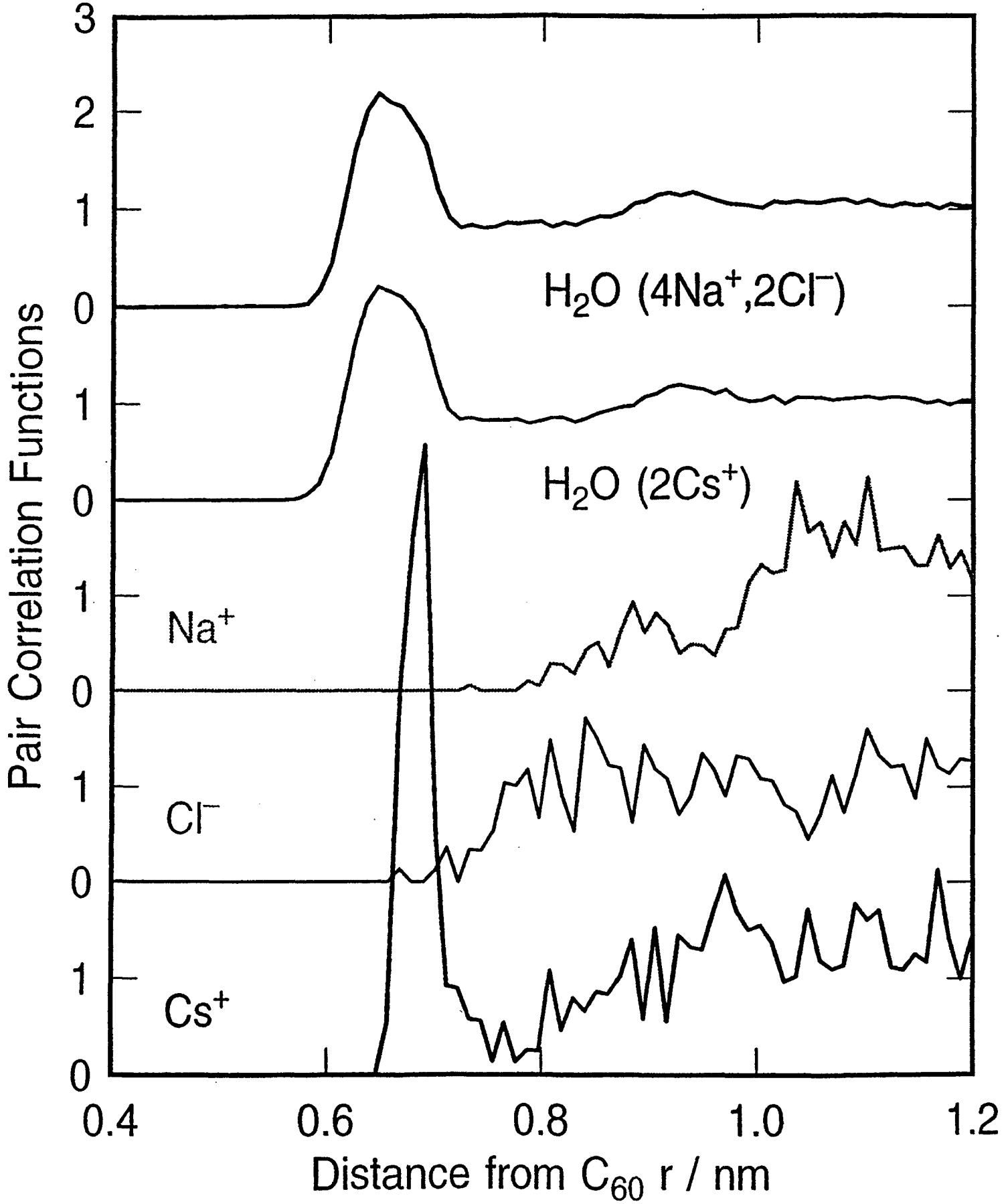
Pair Correlation Functions
3
2
1
0
1
0
1
0
1
0
H_2O ($4Na^+$,$2Cl^-$)
H_2O ($2Cs^+$)
Na^+
Cl^-
Cs^+
0.4
0.6
0.8
1.0
1.2
Distance from C_{60} r / nm

F2

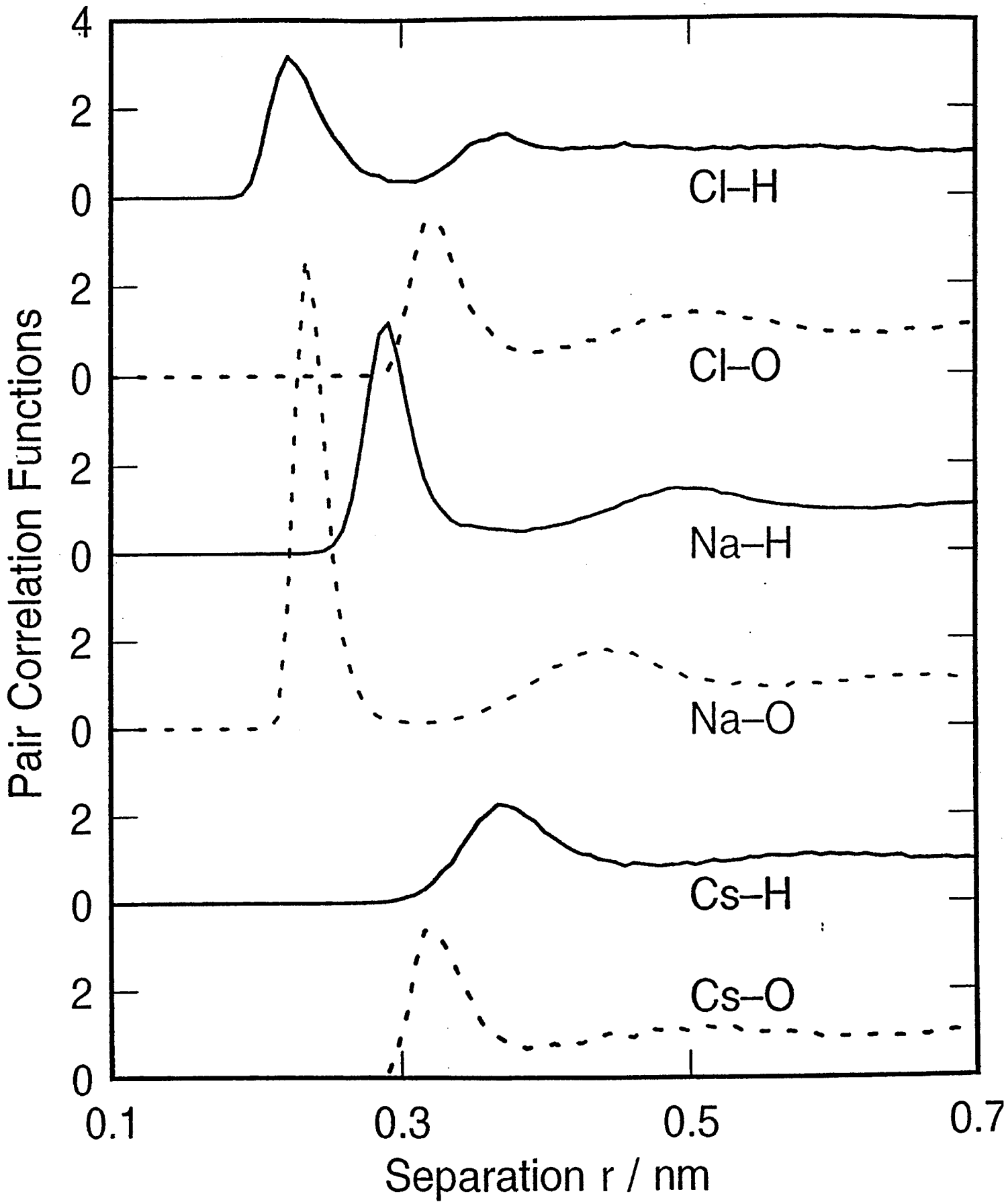
Pair Correlation Functions
4
2
0
2
0
2
0
2
0
2
0
Cl–H
Cl–O
Na–H
Na–O
Cs–H
Cs–O
0.1
0.3
0.5
0.7
Separation r / nm

F3

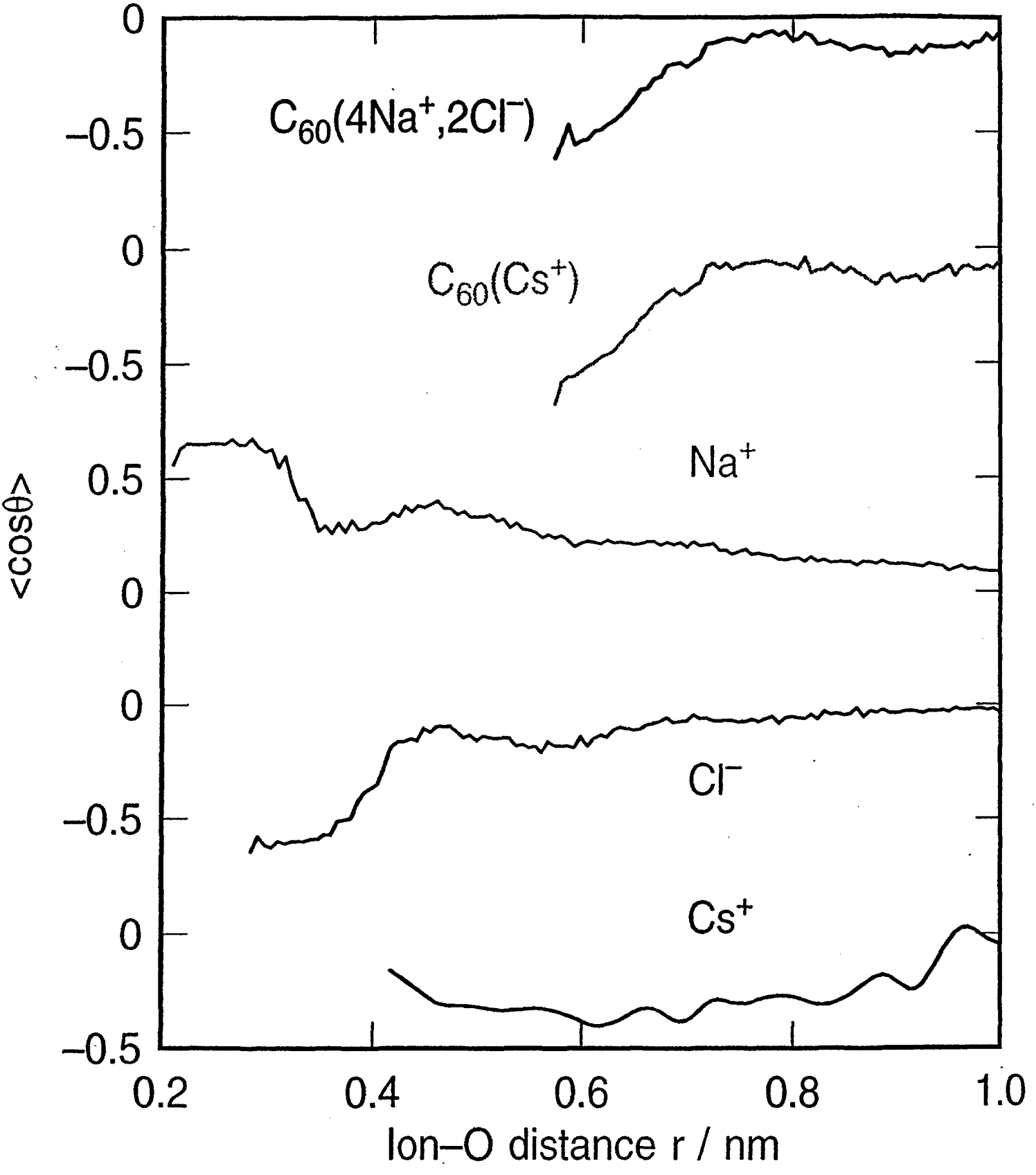
0
−0.5
0
−0.5
0.5
0
0
−0.5
0
−0.5
C60(4Na+,2Cl−)
C60(Cs+)
Na+
Cl−
Cs+
<cosθ>
0.2
0.4
0.6
0.8
1.0
Ion–O distance r / nm

SCREENING OF CHARGED ELECTRODES IN AQUEOUS ELECTROLYTES

Michael R. Philpott
IBM Research Division, Almaden Research Center,
650 Harry Road, San Jose, CA 95120-6099
and
James N. Glosli
Lawrence Livermore National Laboratory,
University of California, Livermore, CA 94550

Abstract

Molecular dynamics simulations are used to demonstrate for the first time that systems about 4 nm thick containing 1200 to 1600 water molecules and NaCl at 1M to 3M concentrations exhibit the main components of electric double layers at charged metal surfaces. In particular for the system chosen there are regions clearly identifiable as a bulk electrolyte zone, a diffuse layer that screens the charge on the electrode and a layer of oriented water localized next to the electrode. The width of the diffuse layer increases with decrease in salt concentration from 0.2 nm at 3 M to 0.5 nm at 1 M. All the calculations are based on the simple point charge model (SPCE) water model and the immersed electrode approximation.

INTRODUCTION

Electric double layers are some of the basic organizations adopted in electrochemical and biological systems to shield fields arising from layers and arrays of charge in contiguous structures. It is therefore quite important to understand their properties using simple models without introducing further approximations. In this letter we describe the first molecular dynamics simulation of a complete electric double layer and detail it's structure from the charged surface of the metal electrode all the way to the bulk electrolyte zone, in terms of water and ion time independent probability distribution functions averaged parallel to the metal surface. These calculations provide a consistent microscopic picture of ions and water throughout a double layer including the species next to the charged surface, in the 'diffuse layer' and in the bulk zone. The effect of finite size of ions and water are clearly evident, as is the effect of the large electric field on the orientation of surface water molecules.

In the calculations reported here the simulation cell has edge length 3.724 nm, with a flat metal plate at z = 1.862 nm and a flat restraining wall at z = -1.862 nm. The cell contains between 1400 to 1600 water molecules and the NaCl concentration is 1M, 2M or 3M. The electric charge density on the flat metal plate is either -9 or -18 Cm^{-2}.

The calculations show that a diffuse layer is formed between the metal and the region of the cell that acts like a bulk electrolyte zone. The ions in the diffuse layer shield the metal charge so that there is no field in the bulk electrolyte zone which is locally approximately neutral. In all previous papers in which molecular dynamics or Monte Carlo simulations of the adsorption of ions on electrodes were considered, there was no demonstration of the simultaneous existence of a diffuse layer and a bulk region. In other words the simulations were not on a scale to permit adsorption in the presence of an established double layer. We believe this is a prerequisite for all calculations to correctly describe the local and global properties of the electric double layer. In all the calculations reported here we use the SPCE water model [1] (three charged (q_H = 0.4238e) mass points, bond angle 109.5°, OH bond length 0.1 nm, inside a Lennard-Jones sphere with radius σ = 0.317 nm and well depth ε= 0.650 kJ/mole) and associated parameters for NaCl[2].

In an attempt to reduce the amount of computer time we use the immersed electrode model[3-5] for a film of electrolyte on a charged metal surface. This approach is useful because it reduces the number of water molecules in the calculation, and because there is only one metal surface (always shown on the rhs in the figures) there are no multiple images in the calculation of electric fields and potentials. In the immersed electrode model the charge on the metal is defined by and completely screened by the
excess charge in the aqueous subphase. It therefore mimics what happens in larger systems. In all previous simulations the number of ions was too small for there to be an identifiable bulk region [3-7]. This turns out not to be the case in the present set of calculations.

The metal was modelled by two linearly superimposed potentials. Pauli repulsion and dispersive attractive interactions were modelled by a 9-3 potential, of the type used by Lee et al[8]. The atom-surface interaction parameters describing interaction with nonconduction electrons were

chosen to be the same as those used by Lee at al[8]. The interactions between ions and water and the conduction electrons was modelled by their respective image potentials.

In the calculations described here the image plane and origin plane of the 9-3 potential were coincident. This was tantamount to choosing the image plane and the nuclear plane of the metal surface to be coincident. This was acceptable in our scheme because the Lennard-Jones core parameters σ are all large and the 'thickness' of the repulsive wall is also large (ca. 0.247 nm). The calculation of the image fields was done very accurately using a code based on the fast multipole method (fmm) and using the physically correct boundary conditions for a system with one metal surface. Neither the direct long range coulomb interaction nor the image interaction were cut off at a finite distances. The fast multipole method developed by Greengard and Rokhlin [9-12] is of order N in the number of charged particles in the system. It is the only viable method for large simulations like the one described here.

Finally some comments on screening of charged surfaces. At high salt concentrations the region with excess ionic charge is microscopically small. A rough estimate of the thickness of the zone in which screening occurs, valid for dilute solutions (< 0.1 M), is given by $d = \kappa^{-1}$ the inverse of the Debye-Hückel screening constant[13]

$$d = \sqrt{\left(\frac{\epsilon kT}{8\pi e^2 n_b \nu^2} \right)} \qquad [1]$$

Here ϵ is the macroscopic dielectric constant of the solvent (approximately 80 for water), ν the valence of the ion (always magnitude one in this paper), and n_b is the bulk concentration of the ions. Typical values of d are: 9.6 nm for 0.001 M, 3.1 nm for 0.01 M, 0.96 nm for 0.1 M, 0.31 nm for 1.0 M, and 0.18 nm for 3 M NaCl solutions. Obviously in high salt concentrations the screening should be more efficient and the screening length smaller, but since the numbers are smaller than the diameter of a water molecule it is not clear if they have any real meaning out of the plane. At high concentrations there are in fact a myriad of difficulties with simple Gouy-Chapman theory[14-16] and many modifications to the theory have been proposed[13]. There are three main problems: first the dielectric constant of water, second the finite size of ions and solvent which represent the lower length scale, and third correlated motion amongst ions and water. For example there is no reason to believe that the appropriate value of ϵ, the dielectric constant of water, is 80 near a surface or in a high electric field where dielectric saturation can occur. This subject has been discussed many times in the electrochemical literature[17]. Therefore we can only take the theoretical values of screening lengths for concentrated solutions as an rough measure of double layer thickness, and should be especially cautious when d is smaller than the size of an ion or solvent molecule.

SCREENING IN SPCE NaCl ELECTROLYTE

This section describes the interaction of hydrated Na^+ cations and Cl^- anions in solvent composed of SPCE water molecules with a charged metal surface. Each simulation was run for one nanosecond or longer, and the instantaneous spatial positions of all the atoms recorded every picosecond. The first 100 ps were discarded as anneal time. Then density probability functions $\rho(z)$ were constructed by averaging over the remaining time and over the x and y coordinates parallel to the metal surface to give functions of z the coordinate in the direction perpendicular to the surface. Figure 1, in particular shows the density profile results for Na^+ cations, Cl^- anions and SPCE water molecules in a 3M salt solution at a temperature of 50° C. Calculations with temperatures as high as 100° C where originally selected to improve the statistics. Temperature dependence of the probability distributions in the range 30 to 100° C is weak. In the 50° C simulation there were 94 Na ions, 86 Cl ions and 1416 water molecules. The charge on the electrode, equal to the image charge, is -(94 - 86)e or -8e, equivalent to a surface charge density of -17.77 Cm^{-2}.

The excess sodium ions, attracted to the electrode by the image charge, screen the electrode charge. The screening charge is concentrated in the peak at 1.45 nm in the sodium density on the right hand side of the simulation box near the point where the 9-3 wall potential passes through zero (z_w = 1.615 nm). The image plane of the metal is located at the extreme the right hand vertical edge of the Figure 1 at z = 1.862 nm. Simple Gouy-Chapman theory would predict an increase in charge to a finite value at the metal surface. There is no peak in simple theory because ions are point-like objects and the solvent is a continuum with a fixed dielectric constant. The peak in the cation distribution at z = 1.45 nm is a consequence of a finite ion radius and the hydration of the ions. The solvent layer at the electrode also effects the position and shape of the cation distribution near the metal. Note that for $|z| < 1.0$ nm the cation distribution is approximately flat at 30 ions nm^{-1}. There is also a small peak on the left hand side at ca. z = -1.4 nm, that is not associated with screening but is instead due to layering of the water molecules at the flat restraining wall. This wall potential goes through zero at z = -1.615 nm. Note that the chloride ion distribution does not show a peak in the same region as the cation peak because negative ions are repulsed by the negatively charged metal electrode.

The chloride probability distribution has no major structural features, certainly no peak like the screening peak at z = 1.45 nm in the Na^+ distribution. Starting from the metal on the right side of Figure 1, the chloride ion distribution rises to a rough plateau that stretches from z = 1.00 nm to z = -1.00 nm. The chloride and sodium ion probabilities are sufficiently similar across the plateau region for us to propose that this has the properties of a bulk zone. This suggestion is supported by the observation of approximate local charge neutrality (ion densities are the same), and very nearly equal integrated densities shown in Figure 2 for each of the concentrations at which the calculations were performed. The integrated density plots all monotonically increase with z from left to right. The initial slopes for z < -1.0 nm are less because of the rise in ion densities from zero at z = -1.615 nm to 'bulk' values for z > -1.0 nm. The solid line is the integrated density for the Na^+ ion and the dash line is for the Cl^- ions. Since the integrated

densities are very similar this means that the electric field is locally very small or zero in the bulk zone defined by $|z| < 1.0$ nm.

Whereas on the basis of one simulation we cannot interpret any of the minor features in the ion profiles, comparison of the three sets in Figure 2 shows the persistence of smaller features near 1.2 nm and 1.4 nm for both ions. We will discuss these features below.

The water density profile shown in Figure 1 displays well pronounced oscillations on both sides of the simulation cell due to the presence of the walls at $|z| = 1.862$ nm. Recall that the 9 - 3 wall potential is the same on both sides. The metal side (right) is distinguished by the existence of the image plane. On the metal side at $z = 1.615$ nm the water density peak is the strongest feature in the system due to localized water next to the metal. The surface electric field reaches its highest value in this region and water is localized as a result of its interaction with the surface field. In this simulation the waters in the first layer are oriented by this strong field and some H bonds to the bulk region are broken. This electric field effect is distinct from localization of water on Pt(100) and Pt(111) surfaces in the simulations of Heinzinger and Spohr[18], and Berkowitz[19, 20]. In these later works the localization is at top sites of the Pt surface due to directed features in the weak chemisorptive potential.

In Figure 2 we show the results of calculations that show the dependence of the ion densities on salt concentration and electrode charge. The 30° C temperature for the 2M and 1M plots was chosen because there did not appear to be a significant improvement in statistics in the earlier 50° C 3M calculation. Each calculation took approximately 3 months on a work station 80 to 90% dedicated to these calculations so it was not possible to run all the calculations at the same temperature. In these plots the Cl density has been smoothed to distinguish it from the Na ion density. Top panel displays the 3M result of Figure 1 in which there were 94 Na ions, 86 Cl ions and 1416 water molecules at 100°C, and the image charge on the electrode is -(94 - 86)e = -8e. The temperature is 50°C. Note the similarity in ion densities between -1.0 and 1.0 nm in all three examples. The middle panel displays the 2M result in which there were 62 Na ions, 58 Cl ions and 1516 water molecules, and the image charge on the electrode is -4e. The temperature is 30°C. The bottom panel displays the 1M result in which there were 32 Na ions, 28 Cl ions and 1576 water molecules, and the image charge on the electrode is again -4e. The temperature is 30° C.

In each panel the cation and anion concentrations are approximately the same for $|z| < 1.0$ nm. This identifies the region of the system with bulk electrolyte properties. Also for each system we show the integrated ion density vs distance z. The integrals are taken from $z = -1.862$ nm to $z = 1.862$ nm., Solid line for the cation and dash line for the anion. Detailed examination shows that in each case for $|z| < 1.0$ nm the integrals are almost indistinguishable. This indicates that the electric field due to the ions is almost zero across the film as expected for a bulk electrolyte.

In each case studied the width of the electric double layer region is small but finite. As an estimate of diffuse layer width we measure from the position of the hard wall ($z = 1.615$ nm) to the point where the difference in integrated ion densities is 0.35 of the difference at the metal (either 8 for 3M or 4 for 1M or 2M). We can compare this with the Debye-Hückel screening

length since this is a e^{-1} measure of diffuse layer thickness in the linearized form of the Gouy-Chapman theory (numbers in parentheses). For the three solutions the measures are: for 3M it is 0.2 nm (0.18 nm), for 2M it is 0.4 nm (0.24 nm), for 1M it is 0.5 nm (0.31 nm). The numbers in parentheses are the Debye shielding lengths calculated using Eqn(1). The estimates based on the ion probability distributions must be regarded as very rough because of the manner they were done. They may change when the simulations are run longer, and are very sensitive to structure in the water layers near the metal. In reality there must be effects due to the finite size of water molecules and ions, and effects due to saturation of molecular polarizability in high electric fields. However there is general agreement in trend and magnitude. This agreement would be lost if the dielectric constant for water were taken to be $\varepsilon = 6$, a value more appropriate for a zone in which the dielectric properties of water are at saturation values[17].

Returning to the topic of fine structure in the ion density profiles we note that on the metal side all the chloride distributions have two weak features at ca. 1.2 and 1.4 nm. Both features appear to be associated with peaks in the cation distribution and may therefore be due to contact pairs or solvent separated pairs. It should be cautioned that the SPCE model for water was not designed with high salt concentrations in mind, so the ion pairs may be more a feature of the model and not nature! This in turn implies that correlation between ions at high salt concentrations effects the distribution near the charged surface. It is interesting to note that there is no apparent association of similarly positioned ion peaks at the restraining wall on the left hand side of Figure 2.

Layering in the water distribution effects the ion distributions. Figure 1 shows a general result confirmed by more extensive simulations, namely ions avoid regions of high water density. On the metal side at right this is at $z = 1.615$ nm where the wall potential is zero, and at $z = 1.25$ nm where there is a secondary water peak. Note that the highly localized water layer next to the electrode creates a large exclusion region for ions of both signs compared to the restraining wall on the left hand side of the cell.

SUMMARY

This letter described the calculation of the structure of an electric double layer in a system large enough to show a bulk-like electrolyte region that occupied a significant portion of the whole simulation cell. Estimates of the width of the diffuse layer were consistently larger than the corresponding Debye-Hückel screening lengths.

The cations and anions density profiles screening the electrode was structured. In the case of cations there was a peak near 1.4 nm. For anions there was a shoulder at the same position. There no sign of similar structure near the restraining wall. Influence of solvent on both distributions near the metal interface was also noted. This simulation places no restrictions on either ion-ion or water-ion correlations, unlike the simple Gouy-Chapman theory where there is no correlation.

The water distribution showed a plane of localized water at the point where the 9 - 3 wall potential passed through zero. This localization involves preferential orientation of the water, and some evidence of up to three layers of water is evident.

ACKNOWLEDGEMENTS

J.D.Gordon and O.Melroy are thanked for critical comments. This research was supported in part by the Office of Naval Research.

REFERENCES

1 H. J. Berendsen, J. R. Grigera, and T. P. Straatsma, J. Phys. Chem. **6269**, 6267 (1987).

2 R. W. Impey, P. A. Madden, and I. R. McDonald, J. Phys. Chem. **87**, 5071 - 5083 (1983).

3 J. N. Glosli and M. R. Philpott, Proceedings of the Symposium on Microscopic Models of Electrode-Electrolyte Interfaces **93-5**, 80-90 (1993).

4 J. N. Glosli and M. R. Philpott, Proceedings of the Symposium on Microscopic Models of Electrode-Electrolyte Interfaces **93-5**, 90-103 (1993).

5 M. R. Philpott and J. N. Glosli, Theoretical and Computational Approaches to Interface Phenomena. (1994).

6 J. N. Glosli and M. R. Philpott, J. Chem. Phys. **96**, 6962-6969 (1992).

7 J. N. Glosli and M. R. Philpott, J. Chem. Phys. **98**, 9995-10008 (1993).

8 C. Y. Lee, J. A. McCammon, and P. J. Rossky, J. Chem. Phys. **80**, 4448-4455 (1984).

9 L. F. Greengard, *The Rapid Evaluation of Potential Fields in Particle Systems*. (The MIT Press, Cambridge, Massachusetts, 1987).

10 L. Greengard and V. Rokhlin, J. Comp. Phys. **73**, 325-348 (1987).

11 J. Carrier, L. Greengard, and V. Rokhlin, Siam J. Sci. Stat. Comput. **9**, 669-686 (1988).

12 L. Greengard and V. Rokhlin, Chemica Scripta **29A**, 139-144 (1989).

13 J. Goodisman, *Electrochemistry: Theoretical Foundations* (Wiley-Interscience, New York, 1987).

14 G. Gouy, Ann. phys. **7**, 129 (1917).

15 D. L. Chapman, Phil. Mag. **25**, 475 (1913).

16 J. O. Bockris and A. K. Reddy, *Modern Electrochemistry, Vol.1* (Plenum Press, New York, 1973).

17 B. E. Conway, J. O. Bockris, and I. A. Ammar, Trans. Faraday Soc. **47**, 756 - 766 (1951).

18 K. Heinzinger, Computer Modelling of Fluids Polymers and Solids, NATO ASI Series C **293**, 357-404 (1990).

19 M. R. Reddy and M. Berkowitz, Chem. Phys. Letters **155**, 173-176 (1989).

20 K. Raghavan, K. Foster, K. Motakabbir, and M. Berkowitz, J. Chem. Phys. **94**, 2110-2117 (1991).

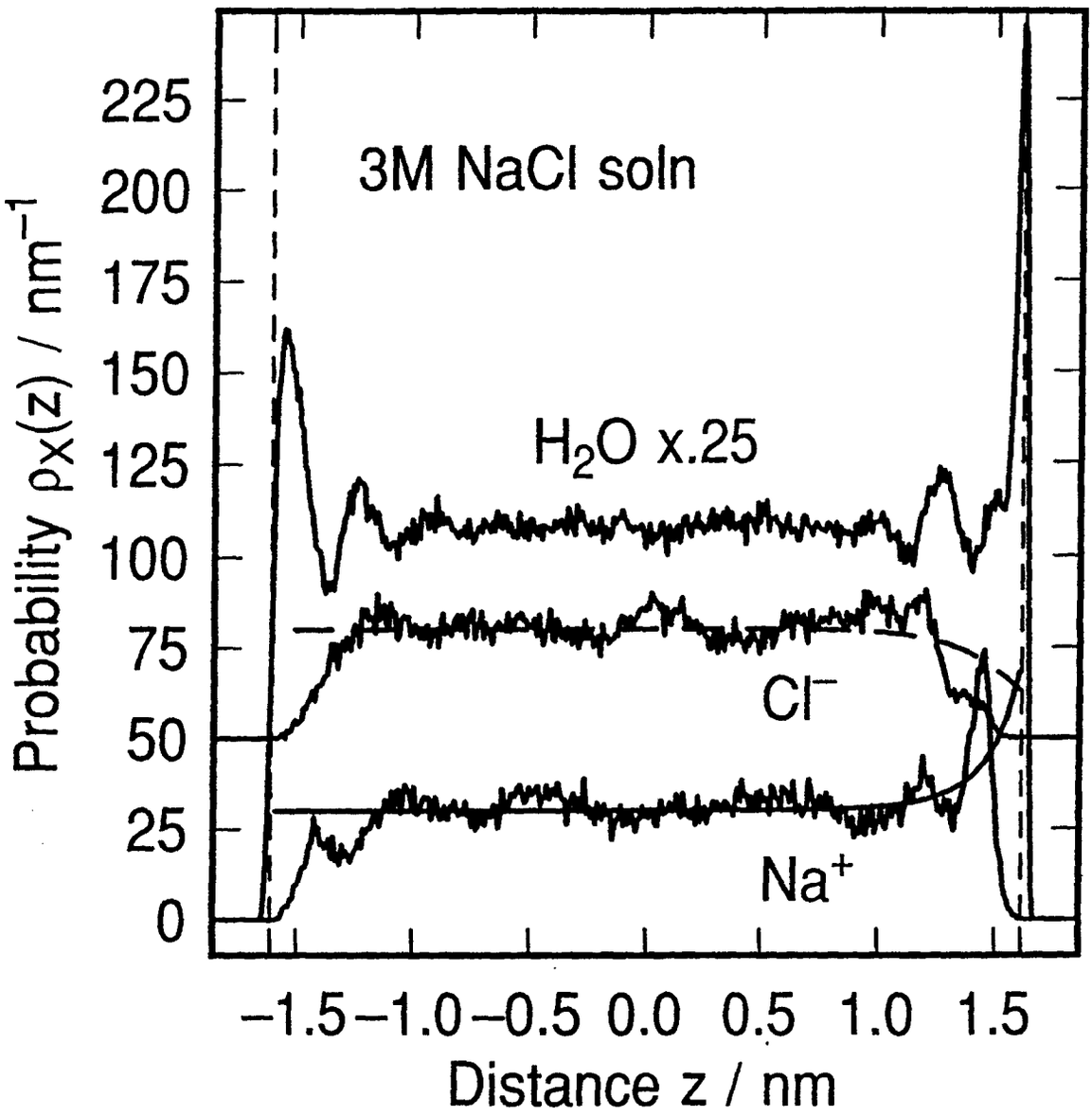

Figure 1. Ion and water probability density distributions for 3M salt solution at 50°C, charge on the electrode q_M = -8e. Composition of the simulation cell: 94 Na^+ ions, 86 Cl^- ions, and 1463 water molecules. Metal electrode on right hand side at z = 1.862nm (position of image plane), restraining wall origin on the left at z = -1.862 nm, positions where the wall potentials on both sides of the simulation cell go through zero at |z|= 1.615 nm are shown by vertical broken lines. Water density shows highly localized surface layer of water near z = 1.62 nm. The cation distribution shows a sharp peak near z = 1.45 nm corresponding to the excess positive ions that screen the negatively charged electrode. The Gouy-Chapman distribution for cations and anions is shown superimposed on the chloride (broken line) and sodium (solid line) ion distribution.

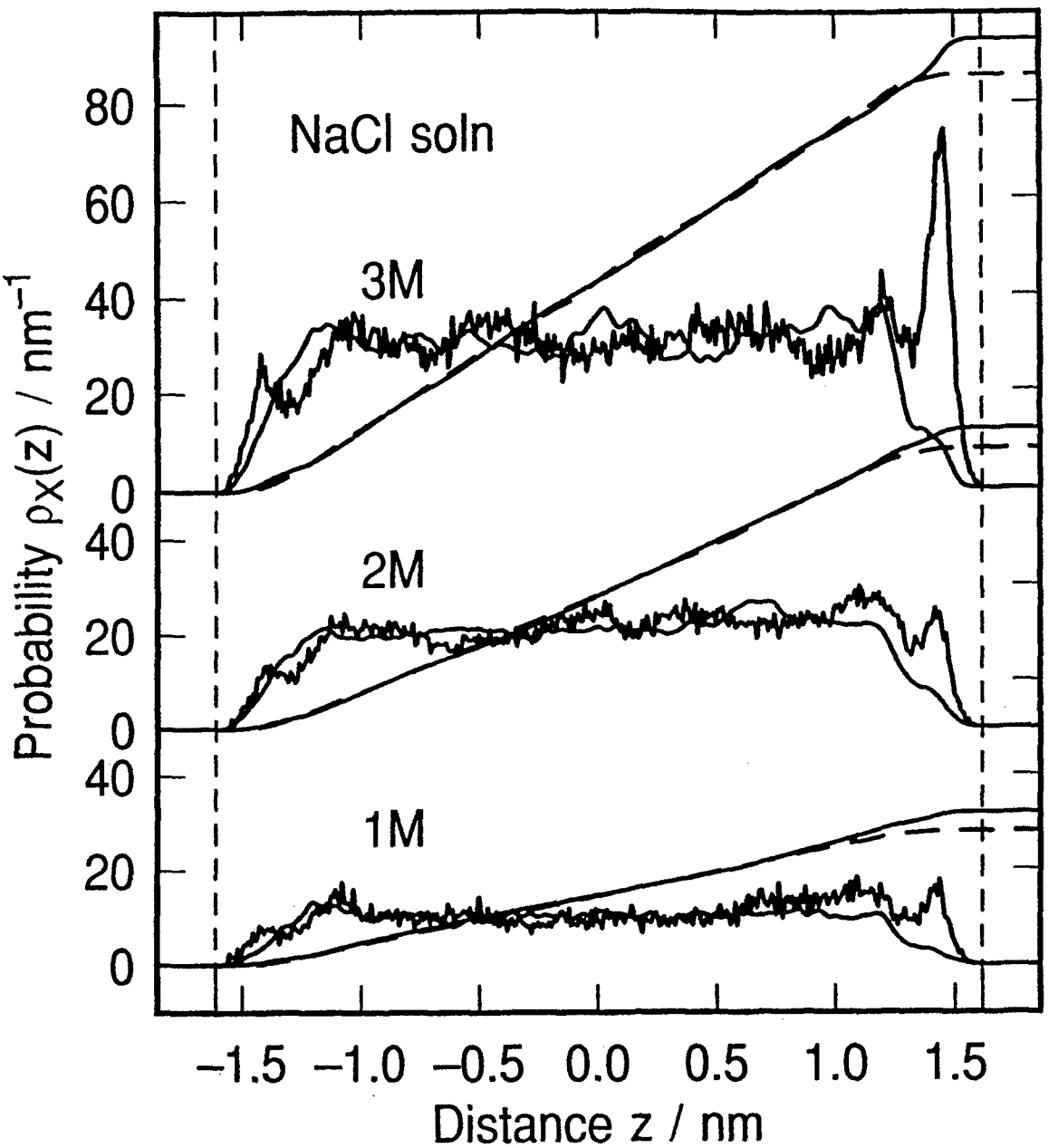

Figure 2. The sodium and chloride ion probability distributions in 3M (50°C, electrode charge -8e), 2M (30°C, electrode charge -4e), and 1M (30°C, electrode charge -4e) aqueous sodium chloride solution. Smoothed curves are for chloride, and the unsmoothed curves are for sodium cations. Metal electrode on right hand side at z = 1.862nm (position of image plane), restraining wall origin on the left at z = -1.862 nm, wall potentials on both sides of the simulation cell go through zero at |z|= 1.615 nm (shown by vertical broken lines). The integral of each ion distribution is plotted , solid line for cation dashed line for the anion. The two integrals diverge near the metal wall, where the excess cations are concentrated and shield the electrode charge. The depletion of the anion distribution has structure that is induced by layering in the water profile. Note that all the distributions show a distance dependence that deviates from the behavior expected qualitatively from the simple Gouy-Chapman theory.

ELSEVIER

Journal of Electroanalytical Chemistry 409 (1996) 65–72

JOURNAL OF ELECTROANALYTICAL CHEMISTRY

Electric potential near a charged metal surface in contact with aqueous electrolyte [1]

Michael R. Philpott [a], James N. Glosli [b]

[a] IBM Almaden Research Center, 650 Harry Road, San Jose, CA 95120-6099, USA
[b] Lawrence Livermore National Laboratory, University of California, Livermore, CA 94550, USA

Received 22 September 1995; in revised form 11 December 1995

Abstract

The time independent electric potential due to water and a lithium ion near a charged metal surface is calculated by space and ensemble averaging of trajectories generated by a molecular dynamics simulation. Since the cation does not contact adsorb, variations in the electric potential near the metal surface are due to water oriented in the electric field of the charged surface. The potential is decomposed into separate contributions from monopoles (from the ions), and dipoles, quadrupoles and octopoles (from the water molecules). At distances greater than about 0.5 nm from the electrode (two to three water molecules) the potential is 'flat' with the quadrupole contributing most due to a near cancellation of the ion and water dipole components. Approaching the surface, weak features are encountered due to water packing and then a big oscillation due to water oriented in a layer next to the electrode. None of these effects are described in theories that approximate water as a continuum fluid.

Keywords: Electric potential; Aqueous electrolyte; Molecular dynamics simulation

1. Introduction

In this paper we describe the calculation of the electric potential across an electrified interface using a molecular dynamics simulation performed at constant N, V, T. The simulation cell consists of one lithium ion and 157 water molecules. Lithium was chosen because it does not lose solvation and contact adsorb on the surface in the range of charge densities used (-0.288 e nm^{-2}) in the calculation. This makes the interpretation of structure near the electrode simpler. We resolve the potential into explicit contributions from the ions and the multipole moments of the water molecules. The variation in the potentials with distance from the electrode shows structure which is related to the distribution of the ion and the distribution and orientation of the water molecules. The features in the electric potential due to water are new and not found in theories that treat the solvent as a dielectric continuum. The explicit calculation of quadrupole and octopole potentials provides insight not available from theories that model the solvent as a point dipole in a sphere.

Fig. 1 (upper part) shows schematically the electric potential of the system when water is assumed to be a simple dielectric continuum. The lower part of Fig. 1 is a cartoon that provides, on the molecular scale, a picture of the double layer near a flat charged metal surface when there are no contact adsorbing ions. Similar pictures can be found in many textbooks and review articles. The water next to the electrode is shown as an oriented monolayer. If this first layer of water is not displaced by the cation at its distance of closest approach then the hydrated cation is two water molecules away from the surface. This is a characteristic feature of the model of Bockris and coworkers [1–3]. In Grahame's model [4] the ion's primary solvation shell can contact the electrode. The plane of closest approach of the positive ion is the outer Helmholtz plane (OHP). The diffuse region in this traditional picture starts two solvent molecules from a flat electrode surface and stretches out many nanometers into the bulk electrolyte. The Gouy and Chapman model [2] provided the first quantitative description of the diffuse layer.

This paper consists of three sections. Section 2 contains a brief description of model and methods. Two complementary methods were used to calculate the electric potential. In Section 3, we first briefly describe the distribution profiles for ions and water molecules obtained from the

[1] This paper is based on a presentation given during the Snowdonia Conference on Electrified Interfaces, Harlech, Wales, UK, 17–21 July 1995.

PII S0022-0728(96)04510-X

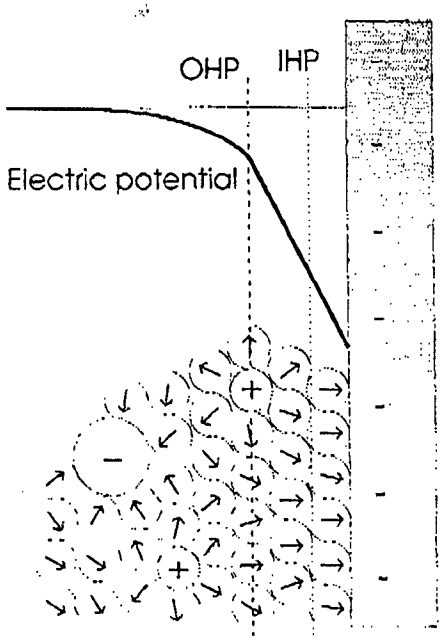

Fig. 1. Schematic diagram of the charged metal electrode|aqueous electrolyte interface. The metal is shown as a flat negatively charged surface and there is a fully hydrated cation at the OHP two water molecules distant. The top part shows a schematic of the electric potential assuming the ions are point charges in a dielectric continuum restricted to the solution side of the OHP.

molecular dynamics simulation, and then the results of the electric potential calculations. These include the results of decomposing the potential into multipole components and a summary of the effect of varying the width of the spatial box used in making the space averages. It is shown how the water quadrupole and octopole multipole structure in the potential is washed out when the box dimension parameter approximates the size of a water molecule.

2. Model and methods

2.1. The screened electrode

Since the electrolyte solution is a conductor, all charged surfaces immersed in the electrolyte are screened by displacement of ions towards the surface in such a way as to shield the bulk solution from the field of the surface charge. The simplest treatment of this phenomena is the Gouy–Chapman theory [2] which treats ions as point charges and all the solvent molecules as if they comprised a dielectric fluid. According to this theory the concentration of monovalent ions has fallen to e^{-1} of its 'surface' value at a distance d from the electrode given by

$$d = \sqrt{\left(\frac{DkT}{8\pi e^2 n_b}\right)} \qquad (1)$$

in unrationalized form.

The inverse d^{-1} is the Debye–Hückel screening constant. Here D is the macroscopic dielectric constant of the solvent, and n_b is the concentration of the ions in the bulk. Typical values of d are: 3.1 nm for 0.01 M, and 0.96 nm for 0.1 M. The derivation of this formula does not hold for high salt concentrations, though it can provide some guidance. For example, at 0.3 M we have $d = 0.55$ nm which is only about twice the size of a water molecule or ion. We conclude that most of the surface charge screening takes place close to the electrode and that a simulation cell with size $L = 1.862$ nm should be just large enough to capture most of the physics.

2.2. Immersed electrode model

The model consists of a layer of electrolyte between two walls. The gap between the walls is the simulation cell edge length $L = 1.862$ nm. The cell contains 157 model ST2 water molecules and one lithium ion. The cell is periodically replicated in the two dimensions xy parallel to the metal surface, but not perpendicular to the surface. The wall on the left ($z = -L/2$) carries no charge, it is a simple restraining wall to hold the electrolyte in place. The wall on the right ($z = L/2$) is the metal with the plane $z = L/2$ the electrostatic image plane. The charge on the metal equals the image charge of the lithium ion. The total charge of the system is zero because the water molecules are individually neutral and the ion and its electrostatic image are opposite in charge. The essential feature of the immersed electrode model is that the charge in solution exactly equals the charge on the metal, and the charge on the metal is the net electrostatic image charge (all the water molecules have electrostatic images but their net charge is zero).

2.3. Model for water and ions

In all the calculations reported here we use the parameters of the Stillinger [5,6] ST2 water model and the interaction parameters for alkali metal ions and water developed by Heinzinger [7]. The ST2 water molecule model consists of a central oxygen atom (O_ST2 or O for short) surrounded by two hydrogen atoms (H_ST2 or H for short) and two massless point charges (PC_ST2 or PC for short) in a rigid tetrahedral arrangement. The O–H and O–PC bond lengths were 0.10 nm and 0.08 nm respectively. This small difference in bond lengths means that the water_ST2 model and its electrostatic image behave similarly. The only Lennard–Jones 'atom' in the ST2 model is the oxygen atom. The hydrogen H_ST2 and point charges PC_ST2 interact with their surroundings (i.e. other atoms and surfaces) only via Coulomb interactions. Their charges are $q_H = 0.23570\,|e|$ and $q_{PC} = -q_H$. The O atom has zero charge. The lithium ion was treated as a non-polarizable Lennard–Jones atom with point mass and charge. For example, the (ε, σ) pairs are (0.3164, 0.3100) and (0.1490, 0.2370) for O_ST2 and Li ion respectively. The

units are ε in kJ mol^{-1} and σ in nm. The Lorentz–Berthelot combining rules were enforced for unlike species, namely: $\varepsilon_{AB} = (\varepsilon_{AA}\varepsilon_{BB})^{1/2}$ and $\sigma_{AB} = 1/2(\sigma_{AA} + \sigma_{BB})$. The Stillinger switching function was used to modify the coulomb interactions between water molecules at close range. All molecule–molecule Lennard–Jones-type interactions were cut-off in a smooth fashion at a molecular separation $R = 0.68$ nm.

2.4. Interaction between water and ions and the walls

The metal was represented by two linearly superimposed potentials. Pauli repulsion and dispersive attractive interactions were represented by a $9-3$ potential, and the interaction with the conduction electrons by an electrostatic image potential. In the calculations described here the image plane and origin plane of the $9-3$ potential were chosen coincident. This was tantamount to choosing the image plane and the nuclear plane of the metal surface to be same plane. This is acceptable in our scheme because the Lennard–Jones core parameters σ are all large and the 'thickness' of the repulsive wall is also large (ca. 0.247 nm). The atom-surface interaction parameters describing interaction with nonconduction electrons were chosen to be the same as those used by Lee at al. [8]. The well depth is approximately equal to thermal energy 'kT' or about 2.4 kJ mol^{-1}.

2.5. Electrostatics

During the molecular dynamics simulations the fast multipole method developed by Greengard and co-workers [9–12] was used to evaluate all long range sums of electrostatic interactions without truncation. The charge on the electrode is the image charge $-|e|$. At any instant during the molecular dynamics run, this charge is not uniformly distributed across the electrode but localized on the surface in such a way as to produce the same electric field and potential as the electrostatic image of the lithium ion and all the water molecules. The field acting on the lithium ion comes from all the water molecules in the cell, all water and ions in the xy periodical replicant cells, and all of the electrostatic images of the contents of all cells in the image plane of the metal. We emphasize again that in this calculation, as in all the others described in this paper, no electrostatic interaction is truncated.

There are two useful ways to calculate the average time independent electric potentials from stored molecular dynamics trajectories. The reason for doing this is to make comparisons with averaged potentials calculated by other theories, e.g. Gouy–Chapman. The first method (the atom approach) uses the charge or partial charge on each atom and the three space coordinates of each atom recorded at regular time separations (usually 1 ps) as input into the generation of a charged source distribution. The source term for Maxwell's equations is the charge density function in vacuum. Without any local spatial averaging this point of view is similar to that followed by Wilson et al. [13,14]. The second way (the molecule method) views the dynamical system as a collection of molecules with internal electrical structure. These are inherently more complex objects than atoms. To specify the electrical properties we need the space coordinates, orientations and electrostatic multipole moments of each ion and molecule in the system. The approach we follow was described by Russakoff [15]. This derivation of a set of macroscopic Maxwell equations from the equations of charged particles in vacuum is summarized in a number of standard texts [16]. We note that though the dynamics are uniquely defined by the models we use, the time independent average fields and potentials that are calculated are not unique because we can broaden the point charge distributions inside the ions and molecules in a spherically symmetric way, and so long as the broadened distributions stay well inside the Lennard–Jones spheres (so that distributions on different molecules do not overlap) then the dynamics are unchanged. This means we can smooth some of the averages within limits set by the geometry of the models and the energetics of collisions. This point has already been pointed out by Wilson et al. [13,17] in their interesting discussion of the properties of the vacuum|water surface.

The atom method uses the distribution of point charges in vacuum. Consider the set of point charges without regard for whether they originate from neutral water molecules or charged ions. In this case the source term for Maxwell fields in vacuum is the microscopic charge density

$$\rho_l(\mathbf{r}, t) = \rho_{\text{metal}}(\mathbf{r}, t) + \rho_{\text{atoms}}(r, t) \tag{2}$$

where

$$\rho_{\text{metals}}(\mathbf{r}, t) = \rho_{\text{metal}}(x, y, t)\,\delta(z - 1/2L) \tag{3}$$

and

$$\rho_{\text{atoms}}(\mathbf{r}, t) = \sum_{j=1}^{N_{\text{atoms}}} q_j \delta\left[\mathbf{r} - \mathbf{r}_j(t)\right] \tag{4}$$

Here N_{atoms} is the number of atoms in the simulation cell and $\mathbf{r}_j$ is the position of the jth atom. The surface charge density on the metal $\rho_{\text{metal}}(x, y, t)$ is time dependent because it depends on the position of the atomic charges. All the charge in the system is described by ρ_l. We can subject this charge density to local space averaging using a test function. Let $f(\mathbf{r})$ be a real positive function localized around $\mathbf{r} = 0$. We define the local spatial average of $F(\mathbf{r}, t)$ by

$$\langle F(\mathbf{r}, t)\rangle = \int d\mathbf{r}' f(\mathbf{r}')\, F(\mathbf{r} - \mathbf{r}', t) \tag{5}$$

The time average can be replaced by an average over configurations at different times

$$\bar{F}(\mathbf{r}) = \lim_{t\to\infty} \frac{1}{t}\int_0^t dt' \langle F(\mathbf{r}, t')\rangle \approx \frac{1}{N_{\text{configs}}} \sum_{i=1}^{N_{\text{configs}}} \langle F(\mathbf{r}, t_i)\rangle \tag{6}$$

The system has translational invariance in the xy plane; therefore $\bar{F}(\mathbf{r})$ is only a function of z. Consequently we consider only test functions $f(z)$ like the localized one-dimensional Gaussian function

$$f(z) = (\pi g^2)^{-1/2} \exp\left[-(z/g)^2\right] \tag{7}$$

We will subsequently refer to g as the Gaussian width or 'bin' width. The metal surface charge density $\rho_{\text{metal}}(x, y, t)$ is replaced by the averaged image charge density which is a constant. The metal image charge is denoted by $\bar{\rho}_{\text{metal}}$. After the configurational averages are performed we get the z-dependent charge density

$$\bar{\rho}_I(z) = \bar{\rho}_{\text{metal}}\delta(z - 1/2L) + \bar{\rho}_{\text{atoms}}(z) \tag{8}$$

where after substituting explicitly for the test function we get

$$\bar{\rho}_{\text{atoms}}(z) = \frac{1}{N_{\text{configs}}} \sum_{i=1}^{N_{\text{configs}}} \sum_{j=1}^{N_{\text{atoms}}} q_j f\left[z - z_j(t_i)\right] \tag{9}$$

The electric field and potential are given by integrating the vacuum Maxwell's equation over the remaining space variable z

$$\bar{E}_{I,z}(z) = \frac{1}{\varepsilon_0}\int_{-\infty}^{z} dz' \bar{\rho}_I(z'),$$

$$\bar{\Phi}_I(z) = -\frac{1}{\varepsilon_0}\int_{-\infty}^{z} dz' \bar{E}_{I,z}(z') \tag{10}$$

The second approach treats the system as a collection of molecules (labels n, positions $\mathbf{r}_n$) composed of atoms (label b, position $\mathbf{r}_{nb}$, charge q_{nb}). The charge density of the system is still the same as $\rho_I(\mathbf{r}, t)$ but with the atoms collected into molecular groups. For the molecule method we write the charge density as follows:

$$\rho_{II}(\mathbf{r}, t) = \rho_{\text{metal}}(x, y, t)\delta(z - 1/2L) + \rho_{\text{mol}}(\mathbf{r}, t) \tag{11}$$

where ρ_{metal} is the same charge density on the metal surface as in the atomic method, and the charge density from the molecules is

$$\rho_{\text{mol}}(\mathbf{r}, t) = \sum_{n=1}^{N_{\text{mol}}} \rho_n(\mathbf{r}, t)$$

$$= \sum_{n=1}^{N_{\text{mol}}} \sum_{b=1}^{N_{nb}} q_{nb}\delta\left[\mathbf{r} - \mathbf{r}_n(t) - \mathbf{r}_{nb}(t)\right] \tag{12}$$

Here N_{mol} is the total number of molecules in the system. The number of atoms in the nth molecule is N_{nb}, and $\mathbf{r}_{nb}$ is the position of the charge q_{nb} measured from the center $\mathbf{r}_n$ of the nth molecule. Note that $\mathbf{r}_n$ and $\mathbf{r}_{nb}$ are time dependent.

Next we perform explicit local spatial averaging with a test function and take the ensemble average. These steps are formally the same as described for the atom method. Then for each molecule (label n) we take the average with respect to the test function $f(z)$, and make a Taylor expansion of atomic coordinates $\mathbf{r}_{nb}$ relative to the molecular centers $\mathbf{r}_m$. This yields the following expression for the averaged charge density by the molecule method:

$$\bar{\rho}_{\text{mol}} = \bar{\rho}(z) - \frac{d}{dz}\bar{P}_z(z) + \frac{d^2}{dz^2}\bar{Q}_{zz}(z) - \frac{d^3}{dz^3}\bar{O}_{zzz}(z) + \ldots \tag{13}$$

where

$$\bar{\rho}(z) = \frac{1}{N_{\text{configs}}} \sum_{i=1}^{N_{\text{configs}}} \sum_{m=1}^{N_{\text{mol}}} f\left[z - z_m(t_i)\right] \sum_{b=1}^{N_{nb}} q_{mb} \tag{14}$$

$$\bar{P}_z(z) = \frac{1}{N_{\text{configs}}} \sum_{i=1}^{N_{\text{configs}}} \sum_{m=1}^{N_{\text{mol}}} f\left[z - z_m(t_i)\right] \sum_{b=1}^{N_{nb}} q_{mb} z_{mb}(t_i) \tag{15}$$

$$\bar{Q}_{zz}(z) = \frac{1}{N_{\text{configs}}} \sum_{i=1}^{N_{\text{configs}}} 1/2 \sum_{m=1}^{N_{\text{mol}}} f\left[z - z_m(t_i)\right] \times \sum_{b=1}^{N_{nb}} q_{mb} z_{mb}(t_i) z_{mb}(t_i) \tag{16}$$

$$\bar{Q}_{zzz}(z) = \frac{1}{N_{\text{configs}}} \sum_{i=1}^{N_{\text{configs}}} \frac{1}{6} \sum_{m=1}^{N_{\text{mol}}} f\left[z - z_m(t_i)\right] \times \sum_{b=1}^{N_{nb}} q_{mb} z_{mb}(t_i) z_{mb}(t_i) z_{mb}(t_i) \tag{17}$$

Here the charge density in the second method has been resolved into contributions from monopoles (ions only in this paper), dipoles, quadrupoles, octopoles, and higher order terms (all from the solvent in this paper).

3. Single metal ion

In this section we first describe briefly the probability density distribution calculated from molecular dynamics trajectories. Then we discuss the contributions that the electrostatic multipoles make to the total electric potential. Finally we discuss the sensitivity of the potential and its components to the width of the test function used in the calculation.

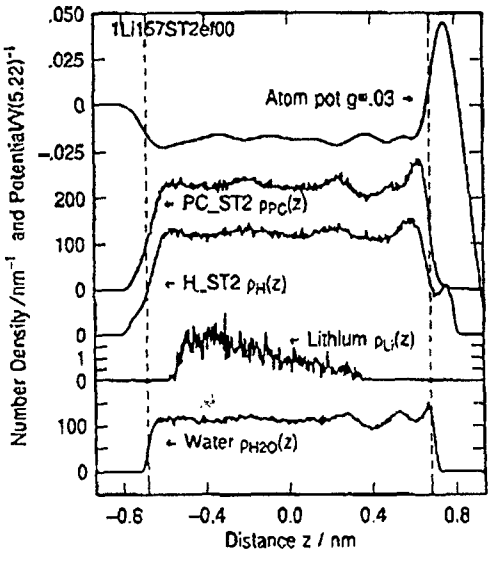

Fig. 2. Electric potential and density profiles for lithium cation Li^+ and 157 STst2 waters near an immersed electrode. Metal electrode on the right hand side, dielectric on the left. Image plane at $z = 0.931$ nm and wall potentials go through zero at $|z| = 0.68$ nm.

The simulation was run for 2000 ps, the first 100 ps of which were used to equilibrate the system. Fig. 2 shows the probability density profiles for the atoms, ions and water averaged over the xy plane. Also shown at the top in Fig. 2 is the electrical potential calculated by the atom method using a Gaussian test function with a width of $g = 0.03$ nm. It is shown with the probability distributions to highlight features due to water as the majority species. Note that in Fig. 2 the scale for water and its components differs from the lithium ion by a factor of 50.

In Fig. 2 the Li^+ ion mass center maps out a diffuse-like region between -0.6 and 0.4 nm. The small ionic radius of Li^+ ensures that its primary solvation shell is tightly bound, making it the core of a much larger composite object. Only in a particularly high surface electric field can this object dissociate and permit the Li^+ cation to contact adsorb on the electrode. The apparent asymmetry of the distribution may be due to the limited width of the cell and consequently no significance is attached to its shape other than it is diffuse in nature. The ion can be pulled closer to the metal by applying an external uncompensated electric field. Uncompensated field cannot be screened completely by ions present in the solution. This is a convenient way to check the sensitivity of an ion to adsorption in higher fields, without having to resort to a separate lengthy computer simulation. When the surface field was roughly equal to that produced by doubling the negative charge on the metal, the lithium ion did not contact adsorb [18,19], whereas all the larger cations (Na^+, K^+, Rb^+, and Cs^+) did contact adsorb.

To check for large effects owing to correlated motion between two Li^+ ions in the same simulation cell we performed the calculations for several hundred picoseconds with a system about four times larger (two lithium ions and 598 water molecules). The water density profiles when appropriately scaled appeared almost exactly the same, and the lithium probability $\rho(z)$ profile was again spread across the cell and formed a diffuse zone with a moderate bias toward the metal. This latter result provides some reassurance that small simulations can give useful information about water structure within two or three layers from the surface.

Near the metal, the ion center did not pass $z = 0.4$ nm. This meant it was never closer than 0.3 nm to the point where the wall potential passed through zero (vertical dashed line at 0.6 nm in Fig. 2). At this point of closest approach there is still room for one water molecule between the ion and the metal. In Grahame's picture of aqueous electric double layers [3,4] water in the primary solvation shell of small ions can touch the electrode surface. In contrast, in the model proposed by Bockris [1,3] the solvated ion does not displace water in the first layer next to the charged metal, and the ion is always at a distance of about two water molecules from the surface. In the simulations described here the ion behaved like the picture due to Grahame. A more detailed model of adsorption in which the ion interacts with atoms and electrons comprising the surface is beyond the scope of the present work. In passing we mention that metal–water potentials exist for platinum and several other metals. Generally, the effective well depths are large, and to calculate distribution profiles requires either very long simulation times (greater than 10 ns) and or the use of specialized sampling techniques [20].

The water profile shows some new structure not seen in water without ions [19,21]. Most interesting is the peak closest to the metal surface at ca. 0.68 nm due to a few localized water molecules. The orientation of these localized water molecules can be determined from the H_ST2 and PC_ST2 probability distributions. The protons on these molecules give rise to the distinct peak at ca. 0.75 nm in the H_ST2 distribution. In the PC_ST2 distribution there is a peak at ca. 0.625 nm that is enhanced more than the second peak in the H_ST2 profile at ca. 0.6 nm. The first water peak at ca. 0.68 nm lies between the first H and PC peaks measured from the metal surface. The positions and relative intensities of these peaks suggests that some of the localized water molecules have one proton pointing at the electrode. This would permit the system to adopt an ice-like configuration with hydrogen bonding to a second layer of water, similar to that discussed by Lee et al. [8]. We do not preclude other waters with two protons pointing at the surface; these would have a dipole normal to the surface which is favored on the basis of simple electrostatics.

Fig. 3 shows the electric potential (atom × 10) across the cell calculated by the atomic charge method with a test function with Gaussian width $g = 0.03$ nm. Also shown are the components of the electric potential coming from

the ions (monopoles) and the point dipoles of the water molecules. The component potentials were calculated by the molecular method. The components are monopole (mono), dipole, and monopole + dipole combined (m + d × 10). Note that for $|z| < 0.6$ nm the monopole and dipole terms almost cancel.

The monopole contribution (mono in Fig. 3) due to lithium ion alone drops monotonically, as expected, for the potential inside a capacitor where the charge on the left is in a diffuse layer spatially separate from the charge on the right plate (metal) at $z = 0.931$ nm. Adding the dipole completely changes the potential (see m + d × 10 curve). The water molecules very effectively screen the field inside the capacitor, except for the region $z > 0.68$ nm where the water distribution drops rapidly to zero. The peak in m + d near 0.7 nm occurs where they no longer cancel and the monopole charge dominates.

Fig. 4 shows some of the higher order electrostatic components of the electric potential. Quadrupole and octopole potentials are from the water molecules. To allow an easy comparison the monopole + dipole combined (m + d) potential is also plotted. Note that the quadrupole potential is approximately constant across the cell except near the metal where the potential has a sharp peak. The octopole potential is everywhere approximately zero except near the metal surface. Adding the quadrupole term (also from water only) brings the atomic and molecular calculations into some measure of agreement The quadrupole contribution to the potential is a negative constant in the region away from the wall potential. This occurs because its contribution to the charge $\langle \rho_{mol}(\mathbf{r}, t)\rangle$ contains a double derivative in space coordinates. The differences are greatest at the surfaces where the atomic method traces charge density smoothly, whereas the molecular method, based on an expansion about molecular centers, requires many high multipoles to describe the field. The dangers of omitting higher multipoles were clearly pointed out by Wilson et al. [13,17] for water without ions.

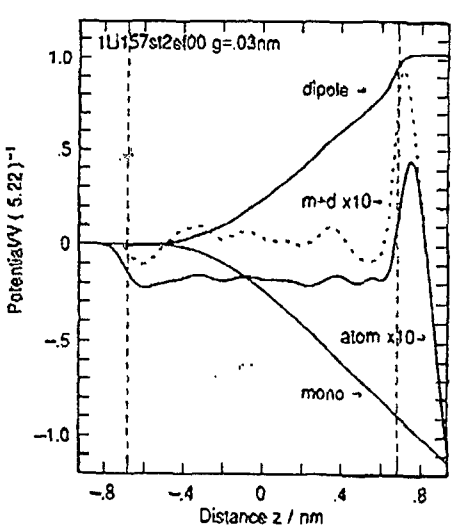

Fig. 3. Electric potential (atom × 10) and components of the potential calculated by the molecular method. The components are monopole (mono), dipole, and monopole + dipole combined (m + d × 10). Note that for $|z| < 0.6$ nm the monopole and dipole terms almost cancel. Simulation cell contains one Li^+ ion and 157 st2 waters with the metal electrode on the right hand side, and dielectric on the left. Image plane at $z = 0.931$ nm and wall potentials go through zero at $|z| = 0.682$ nm.

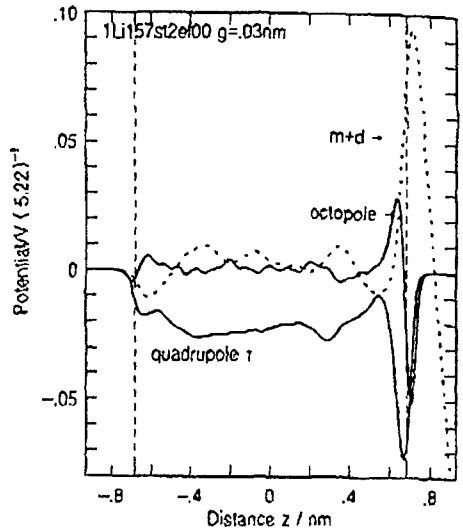

Fig. 4. Higher order electrostatic components of the electric potential. Quadrupole and octopole potentials from the water molecules. For comparison the monopole + dipole combined (m + d) potential is also plotted. Note that the quadrupole potential is approximately constant across the cell except near the metal where the potential has a sharp peak. The octopole potential is everywhere approximately zero except near the metal surface. Simulation cell contains one Li^+ ion and 157 st2 waters with the metal electrode on the right hand side, and dielectric on the left. Image plane at $z = 0.931$ nm and wall potentials go through zero at $|z| = 0.682$ nm.

We close this section with a discussion of changing the length scale over which the test function averaging is performed. The lithium system was chosen because prior work [18,19] and systematic electrochemical experiments [2] have shown that small ions like lithium or fluoride form diffuse screening zones near charged electrodes, and have little tendency to contact adsorb. Fig. 5 shows the relative insensitivity of the monopole and dipole potentials to a change in the Gaussian bin widths for the range $g = 0.03$ to 0.3 nm. The solid curves are for $g = 0.03$ nm and the broken curves for $g = 0.3$ nm. The smearing of monopole (ion) charge for $g = 0.03$ to 0.3 nm did not cause it to overlap the metal so that this component of the electric potential hardly changed. The dipole potential changed most with g, notably for $z > 0.68$ nm since the water density extended all the way to the repulsive region of the wall potential of the metal. Since the monopole and dipole potential almost cancel in the solution phase this makes the m + d potential sensitive to the detailed behavior of the dipole near the surface.

Fig. 6 shows the sensitivity of higher order electrostatic multipole potentials to Gaussian bin widths for the range $g = 0.03$ to 0.3 nm (solid curve for $g = 0.03$ nm, long

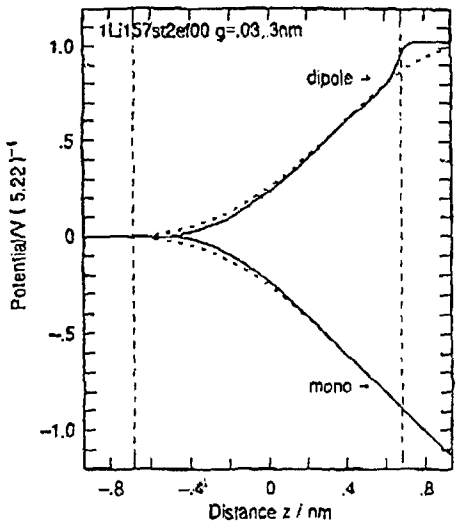

Fig. 5. Insensitivity of low order electrostatic multipole potentials to Gaussian bin widths for the range $g = 0.03$ to 0.3 nm. Monopole and dipole do not change value except the dipole for $z > 0.68$ nm where the water density is very small. Simulation cell contains one Li^+ ion and 157 st2 waters with the metal electrode on right hand side, and dielectric on the left. Image plane at $z = 0.931$ nm and wall potentials go through zero at $|z| = 0.682$ nm.

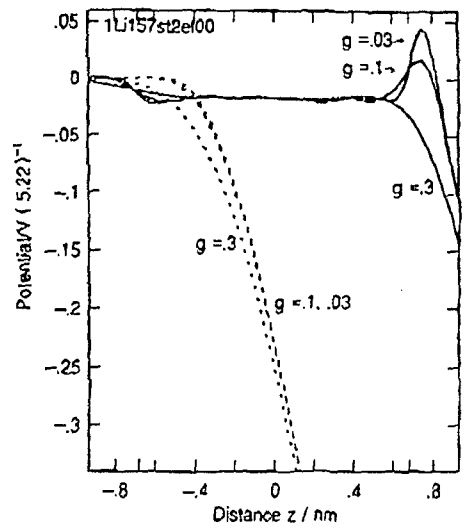

Fig. 7. Sensitivity of the atom method electric potential to Gaussian bin widths for the range $g = 0.03$ to 0.3 nm. The corresponding monopole potentials are plotted for reference. Note that the peak in the potential near 0.8 nm is completely washed out at $g = 0.3$ nm. Simulation cell contains one Li^+ ion and 157 st2 waters with the metal electrode on the right hand side, and dielectric on the left. Image plane at $z = 0.931$ nm and wall potentials go through zero at $|z| = 0.682$ nm.

broken curve for $g = 0.1$ nm, and short broken curve for $g = 0.3$ nm). The surface features of the quadrupole and octopole are washed out by the value $g = 0.3$ nm the size of the water molecule. Note that the quadrupole potential is averaged to a finite value, very roughly constant over the cell. The potential from the octopoles averages to zero over the whole cell for bin widths greater than $g = 0.1$ nm.

The effect of changing the Gaussian width on the total potential is shown in Figs. 7 and 8. In Fig. 7 the sensitivity of the atom potential to the Gaussian bin width is shown (solid curves) for $g = 0.03$ to 0.3 nm. The broken curves show the corresponding monopole potentials. The difference between the two sets of curves is due to the water. Note that the peak in the potential near 0.8 nm is completely washed out at $g = 0.3$ nm. Fig. 8 shows a detail of Fig. 7 in the range of small electric potentials (-0.05 to 0.05). The Gaussian bin widths are the same as before, $g = 0.03$ to 0.3 nm. The corresponding monopole potentials are plotted for reference. Note that the peak in the potential near 0.75 nm is completely washed out by $g = 0.3$ nm.

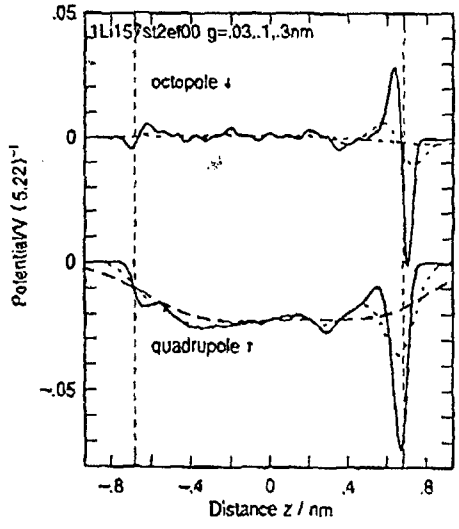

Fig. 6. Sensitivity of higher order electrostatic multipole potentials to Gaussian bin widths for the range $g = 0.03$ to 0.3 nm. Note that the quadrupole loses the surface peak for a width equal to the water molecule dimension 0.3 nm. The octopole potential averages to zero over the whole cell. Simulation cell contains one Li^+ ion and 157 st2 waters with the metal electrode on the right hand side, and dielectric on the left. Image plane at $z = 0.931$ nm and wall potentials go through zero at $|z| = 0.682$ nm.

Figs. 7 and 8 demonstrate that as the size of the bin is increased from $g = 0.03$ nm (0.1 × water molecule dimension) to $g = 1.0$ nm (3 × water molecule dimension) the structure in the electric potential near the surface due to the water profile is lost. The total potential becomes monotonic and resembles the shape of the monopole potential curves calculated using the monopole charge distribution. Since the component of the water dipole perpendicular to the surface is not averaged to zero the atom potential at the surface always remains smaller in magnitude than the monopole potential. We can regard this as an expression of dipole dielectric polarization which remains after Gaussian averaging and reduces the value of the surface potential by roughly an order of magnitude (curves for $g = 0.3$ nm). As expected, the monopole potentials are not as sensitive to the value of the width g as the atomic potentials. This is an interesting qualitative result because it shows the transition from the microscopic scale, where surface water oscillatory structure dominates the potential,

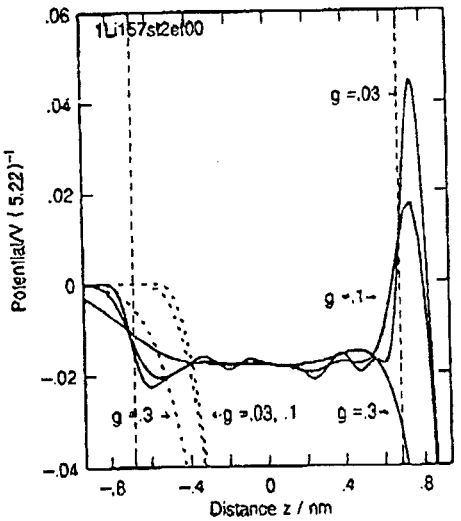

Fig. 8. Detail showing the small potential range (less than 0.05) of the sensitivity of the atom method electric potential to Gaussian bin widths for the range $g = 0.03$ to 0.3 nm. The corresponding monopole potentials are plotted for reference. Note that the peak in the potential near 0.8 nm is completely washed out at $g = 0.3$ nm. Simulation cell contains one Li^+ ion and 157 st2 waters with the metal electrode on the right hand side, and dielectric on the left. Image plane at $z = 0.931$ nm and wall potentials go through zero at $|z| = 0.682$ nm.

to macroscopic scale behavior where water contributes simple scaling of the electric potential.

4. Conclusions

For a system with non-contact adsorbing cations we have used two methods to calculate a time independent electric potential from atom trajectories generated by a constant (N, V, T) molecular dynamics simulation. A key feature of the simulation was the calculation of all long range coulomb interactions including all electric image interactions without truncation. Each method provides some insight into the components of the potential contributed by the ion and the water molecules and the sensitivity of the multipole fields to the scale over which spatial averages were performed. The variation in potential near the metal was due to partially oriented water molecules. The importance of water dipole, quadrupole and octopole potentials was highlighted. Quadrupoles contribute roughly a constant value to the potential in the bulk and oscillatory structure near the surface. A significant contribution from octopoles and higher order multipoles occurred near the surface where the fields are strong and the potential rapidly varying. The insensitivity of monopole and dipole to the spatial bin width was in contrast to the behavior of the quadrupole and octopole.

Acknowledgements

This research was supported in part by the Office of Naval Research. The contributions of JNG were performed under the auspices of US DOE contract W-7405-Eng-48.

References

[1] J.O. Bockris, M.A. Devanathan and K. Müller, Proc. R. Soc. London Ser. A:, 274 (1963) 55.
[2] J.O. Bockris and A.K. Reddy, Modern Electrochemistry, Vol. 2, Plenum, New York, 1973.
[3] E. Gileadi, E. Kirowa-Eisner and J. Penciner, Interfacial Electrochemistry, Addison-Wesley, Reading, MA, 1975.
[4] D.C. Grahame., Chem. Rev., 41 (1947) 441.
[5] F.H. Stillinger and A. Rahman, J. Chem. Phys., 60 (1974) 1545.
[6] O. Steinhauser, Mol. Phys., 45 (1982) 335.
[7] K. Heinzinger, in C.R.A. Catlow, S.C. Parker and M.P. Allen (Eds.), Computer Modeling of Fluids Polymers and Solids, Vol. 293, NATO ASI Series C, Kluwer, Holland, 1990 pp. 357–404.
[8] C.Y. Lee, J.A. McCammon and P.J. Rossky, J. Chem. Phys., 80 (1984) 4448.
[9] L.F. Greengard, The Rapid Evaluation of Potential Fields in Particle Systems, MIT Press, Cambridge, MA, 1987.
[10] L. Greengard and V. Rokhlin, J. Comput. Phys., 73 (1987) 325.
[11] J. Carrier, L. Greengard and V. Rokhlin, Siam J. Sci. Stat. Comput., 9 (1988) 669.
[12] L. Greengard and V. Rokhlin, Chem. Scr. A 29 (1989) 139.
[13] M.A. Wilson, A. Pohorille and L.R. Pratt, J. Chem. Phys., 88 (1988) 3281.
[14] M.A. Wilson, A. Pohorille and L.R. Pratt, Chem. Phys., 129 (1989) 209.
[15] G. Russakoff, Am. J. Phys., 38 (1970) 1188.
[16] J.D. Jackson, Classical Electrodynamics, Wiley, New York, 1975, pp. 54–62.
[17] M.A. Wilson, A. Pohorille and L.R. Pratt, J. Chem. Phys., 90 (1989) 5211.
[18] J.N. Glosli and M.R. Philpott, J. Chem. Phys., 96 (1992) 6962.
[19] J.N. Glosli and M.R. Philpott, J. Chem. Phys., 98 (1993) 9995.
[20] D.A. Rose and I. Benjamin, J. Chem. Phys., 95 (1991) 6856.
[21] M.R. Philpott and J.N. Glosli, in H. Sellers and J.T. Golab (Eds.), Theoretical and Computational Approaches to Interface Phenomena, Plenum, New York, 1994, pp. 75–100.

Pergamon

Electrochimica Acta, Vol. 41, No. 14, pp. 2145–2158, 1996

0013-4686/96 $15.00 + 0.00

PII:S0013-4686(96)00046-1

MOLECULAR DYNAMICS STUDY OF INTERFACIAL ELECTRIC FIELDS

J. N. GLOSLI† and M. R. PHILPOTT‡*

† Lawrence Livermore National Laboratory, University of California, Livermore, CA 94550, USA
‡ IBM Research Division, Almaden Research Center, 650 Harry Road, San Jose, CA 95120-6099, USA

(*Received* 18 *July* 1995)

Abstract—Electric fields and potentials of an equilibrated assembly of ions and water molecules adjacent to a charged metal surface are calculated as a function of perpendicular distance z from the surface from data derived from molecular dynamics trajectories. The spatial distributions of atoms or molecules along direction z are found by ensemble averaging of trajectories followed by averaging with a localized function with a well defined length scale. Two methods were used calculate z dependent charge density distributions. In the first, to be called the atom method, the trajectories of charged atoms are averaged. In the second, called the molecule method, a Taylor expansion of charged atom positions relative to molecular centres is performed and the charge density separated into monopole, dipole, quadrupole, octopole, ... components. These distributions are used to calculate the electric potential and in one example to study the progressive loss of structure due to water as the length parameter is scanned through the dimension of a water molecule. This latter result provides a link between simulations with detailed atomic modelling of intermolecular interactions and electric potentials derived from Gouy–Chapman theory. Illustrative examples are chosen from simulations of aqueous solutions of simple alkali halide electrolytes next to charged and uncharged flat metal surfaces. The smallest system has one ion and 157 water molecules, the largest 60 ions and 1576 water molecules. Copyright © 1996 Elsevier Science Lrd

Key words: molecular dynamics, interfacial electric fields, calculation methods.

1. INTRODUCTION

In this paper we describe the calculation of electrostatic fields arising from ions and polar molecules in equilibrium distributions in front of charged metal electrodes. The focus is on fields within ten water molecule diameters of the electrode–aqueous electrolyte interface. Molecular dynamics simulations are used to calculate the trajectories of ions and polar molecules, which are time and space averaged in a manner to be described to obtain time independent distributions depending only on the coordinate z perpendicular to the surface. These averaged distributions are then used as the source terms in Maxwell's equations to calculate fields and potentials that are in a form that can be compared with potentials derived intuitively from electrochemical knowledge or the results of non-simulation methods like that of Gouy–Chapman–Stern[1–4] theory or Henderson and co-workers more sophisticated correlation function technique[5]. These latter methods solve Poisson's equation with the Boltzmann ansatz and calculate from the charge distribution the electric field and potential across the double layer region. In our work examples are chosen from simulations of aqueous solutions of simple electrolytes next to charged metal surfaces that represent frequently encountered situations in adsorption from electric double layers. All sums of electrostatic interactions are evaluated without spatial cut-offs using the fast multipole method of Greengard and coworkers[6–9].

The cartoon in Fig. 1 depicts the traditional view[10, 11] of the electric double layer in the thermodynamically stable region of electrode potential for a metal with a flat surface. The electric potential due to ions is schematically shown at the top. We will show that near the surface this way of depicting the distance dependence of the potential is wrong

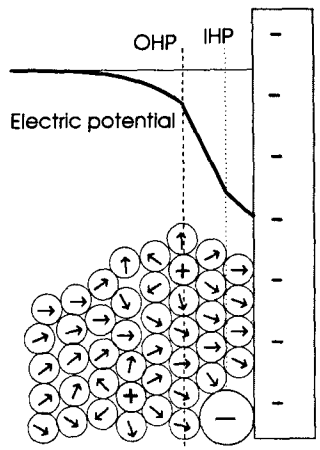

Fig. 1. Schematic diagram of the traditional view of the electric double layer showing a flat negatively charged electrode with contact adsorbed anion and fully hydrated cations at the outer Helmholtz plane (OHP). Electric potential shown schematically at the top.

* Author to whom correspondence should be addressed.

because it neglects the contribution from oriented water molecules. In Fig. 1 the labels IHP and OHP denote the inner and outer Helmholtz planes, respectively. In the cartoon the compact part of the double layer contains an anion in physical contact with a flat surface and a cation two water molecules distant from the electrode as in the model of Bockris, Devanathan and Müller[12]. The diffuse part is symbolized by the labelled arrows which cover the region from the OHP to the bulk electrolyte region.

The calculation of the classical electric field of a set of charges is a well studied problem. Given a set of charges the electric field and potential can be found with arbitrary high accuracy by a number of methods. In molecular dynamics and Monte Carlo simulations Ewald's method has been frequently used. However in systems large number ($N > 200$) of charged or polar species, Ewald methods are slow (time $t \propto N^{1.5}$) compared to the fast multipole method ($t \propto N$) and particle-mesh methods[13] ($t \propto N \log N$). The molecular dynamics simulations described in this paper would not be possible without the use of the fast multipole method to evaluate the long range electrostatic fields. Using the fast multipole method we have performed many simulations on systems containing 600 charged particles and a few simulations on larger systems containing 5000 charged particles and their electrostatic images.

Given that we are able to accurately evaluate long range electrostatic interactions in a molecular dynamics simulation, the next step is the calculation of local electric fields from time averaged charge distributions. This is the main task of the present paper. We concentrate on two methods to calculate time and space averages of charge source functions, and the corresponding electric fields and potentials. The first method, to be called the atom charge method, uses the positions of the atoms and the charge or partial charge of the atoms to calculate a time independent electric charge density. After making averages parallel to the surface this technique yields results equivalent to that described by Wilson, Pohorille and Pratt[14, 15], based on the derivation given in Landau and Lifshitz[16]. The second method (called the molecule method) considers the system in a fundamentally different way. It views the world as a collection of charged or polar molecules. It uses a Taylor series expansion of charged atom coordinates relative to an origin on the molecule to express the electric source in terms of a sequence of electric multipole (monopole, dipole, quadrupole, octopole, . . .) polarization source densities. This method follows the description given in standard texts such as Jackson[17], which is based in part on the lucid description in the paper by Russakoff[18]. By this second method the contribution to the electric field and potential of monopole, dipole, quadrupole, octopole, . . . moments of the molecules can be calculated separately in a systematic way, and could in principle be used to input experimentally measured values of electric multipole moments. Each of the two methods provides its own particular insight in the computation of the fields.

To illustrate the calculation of the fields and potentials we choose examples from on-going work in simulations of aqueous electrochemical interfaces that typify general classes of behaviour. All the systems were composed of water and monovalent ions adjacent to a metal surface. The examples chosen from small scale simulations are: a non-contact adsorbed Li^+ ion, a contact adsorbed I^- ion, a neutral solution of Li^+ and I^- (anion contact adsorbed), a neutral solution of Li^+ and F^- and Li^+ and two iodides $2I^-$ (cation attracted to contact adsorbed anions). As an example of a larger calculation that shows that some of the main features in the small simulations are also found in calculations ten times larger is given at the end of the paper. In this example we discuss a 1 M NaCl salt solution in front of a charged electrode. In this simulation the region of electrolyte that screens the charge on the electrode and the bulk solution are evident.

In our smallest simulations the cell size ($L = 1.862$ nm) is too small for us to be confident that we can do more than describe the average electric field between the metal and the OHP. The decay of the average electric field to zero at the non-metal boundary is the result of charge neutrality in the immersed electrode model. Consequently in the smaller simulations we focus primarily on the interfacial fields within the first three or four water molecules, corresponding to a distance up to about 1 nm from the electrode. In the large simulation with a cell ($L = 3.74$ nm) containing 5000 charges[19], the distribution of ions from the zone where the screening of the charged metal occurs, all the way to the "bulk" electrolyte is observed. In this case we can more confidently interpret the decay of field and potential found in the calculations and identify what corresponds to the diffuse region of the electric double layer. Traditionally the structure of the compact region where ions contact adsorb is thought of as being static and resembling a capacitor of atomic separations. Our model permits the ions to move in and out freely from the diffuse layer and to contact adsorb and desorb. We note that Henderson and co-workers[20] in their work solving the Ornstein-Zernike equation for the electrode–electrolyte interface have shown (as does the work presented here) that there is no sharp division between the diffuse and inner layers, in contrast to the ideas conveyed by the pictures in many textbooks. We summarize the goals of the present work as follows. First, the calculation of averaged electric field and potential for systems of electrochemical interest. Second, to contrast the atom and molecule methods of calculating charge densities and potentials. Third, to qualitatively analyse deviations in the electric potential from the curve for ions in a dielectric fluid in terms of distribution of solvent and ions near the metal surface.

We close this section with a brief mention of important parts of the physics that are still missing. First there is no feature that permits explicit consideration of the metal surface topography and conduction electron densities at the surface. For example, one can go much further and use jellium models or jellium with embedded ions but this is beyond the scope of the current study. Halley and co-workers[21–23] have developed theories based on jellium electrode models of the charged metal

surface and adjacent solution that accounts for aspects of measured capacitance vs potential curves. Cluster calculations have been used to obtain metal–water and metal–ion potentials for use in molecular dynamics simulations that introduce aspects of metal surface corrugation[24–37]. Second there are no effects due to electronic polarizability or geometric distortions of molecules in the high electric fields of the double layer.

2. MODELS AND METHODS

2.1. *The immersed electrode model*

When the electrode potential is altered and charge flows onto the electrode, the composition of the electrolyte next to the electrode adjusts to screen the new charge on the electrode. For dilute solutions (<0.1 M) a rough estimate of the screening layer thickness is $d = \kappa^{-1}$, where κ is the Debye–Huckel screening constant. According to the Gouy–Chapman theory[10] the concentration of monovalent ions has fallen to e^{-1} of its "surface" value at a distance d from the electrode given by

$$d = \sqrt{\left(\frac{\varepsilon kT}{8\pi e^2 n_b}\right)} \qquad (1)$$

Here ε is the macroscopic dielectric constant of the solvent, and n_b is the concentration of the ions in the bulk. Typical values of d are: 3.1 nm for 0.01 M and 0.96 nm for 0.1 M. At higher salt concentrations outside the range of the derivation of this formula we get 0.55 nm for 0.3 M and 0.31 nm for 1 M salt solutions. The formula provides some rough measure perhaps even within a factor 2 (the effective dielectric constant of water near the electrode may be ten times smaller than in the bulk[38]) of the double layer thickness even though the basis of the derivation is not valid. These brief considerations suggest we can use molecular dynamics to simulate an immersed electrode when the salt concentration is about 0.3 M or larger by including the adjacent electrolyte region out to a thickness of about ten water molecules. In this paper we do this first for a small cell about five water molecules thick, expecting only to be able to model the so-called inner part of the double layer where contact adsorption occurs. Later we study a cell about 10 water molecules thick and are able to identify a region in space that has bulk-like properties, lending support to the immersed electrode model as we use it. Our immersed electrode model consists of a layer of electrolyte between two walls. The wall on the left carries no charge; it is simply a restraining wall and ideally would allow a continuous transition to the bulk electrolyte region. The complete system of electrolyte and electrode (always on the right-hand side in all the figures of this paper) is neutral. The approach is useful because it reduces the number of water molecules in the calculation, and because there is only one metal surface, there is only one electrostatic image plane. Finally we point out that in our system the electrical properties of the system are due to three layers: the vacuum half-space occupying: $-\infty < z < -\frac{1}{2}L$; the xy periodically replicated simulation cells: $-\frac{1}{2}L < z < \frac{1}{2}L$; and the metal half-space: $\frac{1}{2}L < z < \infty$. More details and discussion of the immersed electrode model are found elsewhere[39].

2.2. *Models for water and ions*

In the smaller scale simulations reported here we used the parameters of the Stillinger[40, 41] ST2 water model and the interaction parameters with alkali metal ions and halide ions developed by Heinzinger and co-workers[24]. The ST2 water molecule model consists of a central oxygen atom surrounded by two hydrogen atoms and two massless point charges (PC) in a rigid tetrahedral-like arrangement. The charges on the particles are $q_H = 0.23\,570\ |e|$, $q_{PC} = -q_H$ and $q_O = 0$. The alkali metal and halide ions are non-polarizable Lennard–Jones atoms with point mass and charge. The atom–atom interaction parameters are taken from Heinzinger's review[24]. In the larger simulations with a 3.74 nm wide cell containing 1 M NaCl solution the SPCE water model was used primarily because this water model has fewer charges (three compared to four for ST2) and requires less time to compute the electrostatics. The Lennard-Jones potential between the atoms of each molecule was smoothly cut-off at distances of $R = 0.68$ nm.

2.3. *Molecule–wall and ion-wall potentials*

There are two walls. The simplest is the uncharged restraining non-metallic wall on the left-hand side in Figs 2–15. It restrains the fluid by a 9 : 3 potential. The metal wall, on the right-hand side, is represented by two superimposed potentials. The first is a 9 : 3 potential to represent both the Pauli repulsion and dispersive attractive interactions. The second potential is an electrostatic image potential that describes the interaction between a charge in the electrolyte and the conduction electrons of the metal. In the calculations described here the image plane and origin plane of the 9 : 3 potential were coincident. This is equivalent to choosing the image plane and the nuclear plane of the metal surface to be the same. This is acceptable in our scheme because the Lennard-Jones core parameters σ are all large and the "thickness" of the repulsive wall is also large (*ca.* 0.247 nm). The atom–surface interaction parameters describing interaction with non-conduction electrons were chosen to be the same as those of Lee *et al.*[42], $A = 17.447 \times 10^{-6}$ kJ (nm)^6 mol^{-1} and $B = 76.144 \times 10^{-3}$ kJ (nm)^3 mol^{-1} for O, I and Li ions. The A and B parameters for H and PC were set to zero for water molecules. Note that in this model the adsorption well depths of the Lennard-Jones wall potentials is a few kcal mol^{-1}, similar to kT at room temperature, and therefore pretty wimpy.

2.4. *Advantages of the fast multipole method*

Simulations of aqueous electrolyte solutions using molecular dynamics and Monte Carlo methods require the evaluation of the superimposed Coulomb fields of thousands of particles (a 5 nm cube of water contains about 12 500 atoms). In this paper we use the fast multipole method (fmm) of Greengard and Rokhlin[6–9] to evaluate the electric fields acting on

the charged particles during the computer simulation. A number of methods are in use to calculate or approximate long range Coulomb fields. Friedmann and Honig[43] have surveyed some of the empirical dielectric recipes in use in biological simulations. For example recipes like the Hingerty function[44] and other distance dependent dielectric "constants"[45, 46] have been used in simulations of proteins. Direct summation with a cut-off after about 1.00 nm is common in many commercially available codes like Charmm[47] and Amber[45, 48]. There are a number of plane-wise summation methods from crystal physics[49]. For homogeneous systems the reaction field method of Barker[50] is simple and easy to use. This method is not easily applied to liquid–solid interfaces though attempts to extend it have been described[51, 52]. The Ewald method[53–55] has been extensively used when rigour and accuracy are needed. Ewald's summation crudely applied is proportional to N^2 and at best $N^{3/2}$ where N is the number of charges. The fast multipole method (fmm) developed by Greengard and Rokhlin[6–9] is an order N algorithm, and consequently is the only viable method for very large simulations. The fmm technique is attractive because of the ease of implementation of a variety of boundary conditions such as periodic, Dirichlet, Neumann and mixed boundaries and because an adaptive version of the algorithm is available[8] in which regions of low or no charge density are not subdivided when the charge count falls below a specified integer.

3. ELECTROSTATICS OF ELECTROCHEMICAL CELLS

There are many ways that electric fields and potentials can be calculated. For example, at every time step we use the fast multipole method to compute the electric forces acting on every charged particle in the system. We could take the electric field evaluated at a specific particle, say an O atom, at a given instant of time and then either allow the molecule to move and average the field at regular intervals or confine the atom to a spatial well that would then be transported so as to sample all space. This would clearly be useful for interpreting experiments like NMR, but is not in the spirit of Gouy–Chapman theory which attempts to solve the Poisson equation using a Maxwell–Boltzmann ansatz for local charge fluctuations. It is not pursued further here. Instead in this section we describe two methods for getting source distributions to be used to calculate averaged electric fields and potentials for comparison with other theoretical methods which are in the spirit of the Gouy–Chapman approach. The first method assumes that the atoms are fundamental objects and uses the charge or partial charge on each atom and the three space coordinates of each atom recorded at regular time separations (usually 0.5 or 1 ps) as input into the generation of a charged source distribution. We call this the atom approach. The only source term is the charge density function in vacuum. Without any local spatial averaging this point of view is similar to that followed by Wilson, Pohorille and Pratt[14, 15]. The second way, to be called the molecule method, assumes that the system is a collection of molecules that have internal electrical structure. These are inherently more complex objects than atoms. To specify the electrical properties we need space coordinates, orientations and electrostatic multipole moments for each molecule in the system. The approach we follow can be found in the clearly written article by Russakoff[18], or the treatise by de Groot and Suttorp[56]; both sets of authors derive a set of macroscopic equations from Maxwell's equations in vacuum for point charged particles. Their approach is summarized in a number of standard texts[17]. We note that though the dynamics are uniquely defined by the models we use, the time independent average fields and potentials that are calculated are not unique because we can broaden the point charge distributions inside the ions and molecules in a spherically symmetric way and so long as the broaden distributions stay well inside the Lennard-Jones spheres (so that distributions on different molecules do not overlap) the dynamics are unchanged. This means we can smooth some of the averages within limits set by geometry of the models and the energetics of collisions. The point was clearly recognized by Wilson, Pohorille and Pratt[14, 57] in their interesting discussion of the properties of the vacuum–water surface.

The atom method (I) uses the distribution of point charges in vacuum. Consider the set of point charges without regard for whether they originate from neutral water molecules or charged ions. In this case the source term for Maxwell fields in vacuum is the microscopic charge density

$$\rho_I(\mathbf{r}, t) = \rho_{\text{metal}}(\mathbf{r}, t) + \rho_{\text{atoms}}(\mathbf{r}, t). \tag{2}$$

Here

$$\rho_{\text{metal}}(\mathbf{r}, t) = \rho_{\text{metal}}(x, y, t)\delta(z - \tfrac{1}{2}L), \tag{3}$$

and

$$\rho_{\text{atoms}}(\mathbf{r}, t) = \sum_{j=1}^{N_{\text{atoms}}} q_j \delta(\mathbf{r} - \mathbf{r}_j(t)), \tag{4}$$

where N_{atoms} is the number of atoms in the simulation cell and r_j is the position of the j-th atom. The surface charge density on the metal $\rho_{\text{metal}}(x, y, t)$ is time dependent because it depends on the position of the atomic charges. All the charge in the system is described by ρ_I.

We can subject this charge density to local space averaging using a test function. Let $f(\mathbf{r})$ be a real positive function localized around $\mathbf{r} = 0$. We define the local spatial average of $F(\mathbf{r}, t)$ by

$$\langle F(\mathbf{r}, t)\rangle = \int \mathrm{d}\mathbf{r}' f(\mathbf{r}')F(\mathbf{r} - \mathbf{r}', t). \tag{5}$$

The time average

$$\bar{F}(\mathbf{r}) = \lim_{t\to\infty} \frac{1}{t}\int_0^t \langle F(\mathbf{r}, t')\rangle \mathrm{d}t' \tag{6}$$

can be replaced by an average over configurations at different times

$$\bar{F}(\mathbf{r}) = \frac{1}{N_{\text{configs}}} \sum_{i=1}^{N_{\text{configs}}} \langle F(\mathbf{r}, t_i)\rangle. \tag{7}$$

The systems we consider have translational invariance in the xy plane. The function $\bar{F}(\mathbf{r})$ is a function of z only. In light of this we consider only test functions which are functions of z. We use two test functions, a bin-like test function

$$f(\mathbf{r}) = \begin{cases} 1/g, & |z| < \frac{1}{2}g \\ 0, & |z| > \frac{1}{2}g \end{cases} \tag{8}$$

and a localized one-dimensional Gaussian function

$$f(z) = (\pi g^2)^{-1/2} e^{-(z/g)^2}. \tag{9}$$

The metal surface charge density $\rho_{\text{metal}}(x, y, t)$ is replaced by the averaged image charge density which is a constant. The metal image charge is denoted by $\bar{\rho}_{\text{metal}}$. After we have averaged over the many spatial configurations from the molecular dynamics calculation we obtain a z dependent charge density profile given by

$$\bar{\rho}_I(z) = \bar{\rho}_{\text{metal}}\,\delta(z - \tfrac{1}{2}L) + \bar{\rho}_{\text{atoms}}(z) \tag{10}$$

where as in equation (7)

$$\bar{\rho}_{\text{atoms}}(z) = \frac{1}{N_{\text{configs}}} \sum_{i=1}^{N_{\text{configs}}} \langle \rho_{\text{atoms}}(\mathbf{r}, t_i) \rangle. \tag{11}$$

After substituting explicitly for the test function we get

$$\bar{\rho}_{\text{atoms}}(z) = \frac{1}{N_{\text{configs}}} \sum_{i=1}^{N_{\text{configs}}} \sum_{j=1}^{N_{\text{atoms}}} q_j f(z - z_j(t_i)) \tag{12}$$

The electric field is given directly by integrating the vacuum Maxwell's equation. Since we have already averaged over the xy plane the electric field normal to the surface is given by

$$\bar{E}_{I,z}(z) = \frac{1}{\varepsilon_0} \int_{-\infty}^{z} \mathrm{d}z' \bar{\rho}_I(z') \tag{13}$$

The electric potential is given by a second integration

$$\bar{\Phi}_I(z) = -\frac{1}{\varepsilon_0} \int_{-\infty}^{z} \mathrm{d}z' \bar{E}_{I,z}(z') \tag{14}$$

The second approach views the system as a collection of molecules (labels n, positions $\mathbf{r}_n$) composed of atoms (label b, position $\mathbf{r}_{nb}$, charge q_{nb}). The charge density of the system is:

$$\rho_{II}(\mathbf{r}, t) = \rho_{\text{metal}}(x, y, t)\delta(z - \tfrac{1}{2}L) + \rho_{\text{mol}}(\mathbf{r}, t) \tag{15}$$

where ρ_{metal} is the same charge density on the metal surface as in the atomic method, and

$$\rho_{\text{mol}}(\mathbf{r}, t) = \sum_{n=1}^{N_{\text{mol}}} \rho_n(\mathbf{r}, t). \tag{16}$$

Here N_{mol} is the total number of molecules in the system, and

$$\rho_n(\mathbf{r}, t) = \sum_{b=1}^{N_{na}} q_{nb}\,\delta(\mathbf{r} - \mathbf{r}_n - \mathbf{r}_{nb}), \tag{17}$$

is the charge density of the n-th molecule. The number of atoms in the n-th molecule is N_{na}, and $\mathbf{r}_{nb}$ is the position of the charge q_{nb} measured from the centre $\mathbf{r}_n$ of the n-th molecule. Next we perform explicit local spatial averaging with a test function and take the ensemble average. These steps are formally the same as described for the atom method. For each molecule label n we take the average with respect to the test function $f(z)$, then make a Taylor expansion of atomic coordinates $\mathbf{r}_{nb}$ relative to the molecular centres $\mathbf{r}_m$. This yields the following expression for the averaged charge density by the molecule method

$$\bar{\rho}_{\text{mol}}(z) = \bar{\rho}(z) - \frac{\mathrm{d}}{\mathrm{d}z}\bar{P}_z(z) + \frac{\mathrm{d}^2}{\mathrm{d}z^2}\bar{Q}_{zz}(z) - \frac{\mathrm{d}^3}{\mathrm{d}z^3}\bar{O}_{zzz}(z) + \cdots \tag{18}$$

where

$$\bar{\rho}(z) = \frac{1}{N_{\text{configs}}} \sum_{i=1}^{N_{\text{configs}}} \sum_{m=1}^{N_{\text{mol}}} f(z - z_m(t_i)) \sum_{b=1}^{N_{ma}} q_{mb} \tag{19}$$

$$\bar{P}_z(z) = \frac{1}{N_{\text{configs}}} \sum_{i=1}^{N_{\text{configs}}} \sum_{m=1}^{N_{\text{mol}}} f(z - z_m(t_i)) \sum_{b=1}^{N_{ma}} q_{mb} z_{mb}(t_i) \tag{20}$$

$$\bar{Q}_{zz}(z) = \frac{1}{N_{\text{configs}}} \sum_{i=1}^{N_{\text{configs}}} \frac{1}{2} \sum_{m=1}^{N_{\text{mol}}} f(z - z_m(t_i)) \times \sum_{b=1}^{N_{mb}} q_{mb} z_{mb}(t_i) z_{mb}(t_i) \tag{21}$$

$$\bar{O}_{zzz}(z) = \frac{1}{N_{\text{configs}}} \sum_{i=1}^{N_{\text{configs}}} \frac{1}{6} \sum_{m=1}^{N_{\text{mol}}} f(z - z_m(t_i)) \times \sum_{b=1}^{N_{mb}} q_{mb} z_{mb}(t_i) z_{mb}(t_i) \tag{22}$$

Here the charge density in the second method has been resolved into contributions from monopoles (ions only in this paper), dipoles, quadrupoles, octopoles and higher order terms. In principle, experimental moments can be substituted for dipoles, quadrupoles, . . . where these are known.

In the following sections we report simulations designed to typify general electrochemical systems. The distributions displayed in most of the figures were calculated using a one-dimensional binning function with width 0.004 655 nm. In one case to be described in the next section we discuss the effect of changing the size of the region averaged from smaller (0.03 nm) to larger than the dimension of a water molecule.

4. ALKALI METAL ION

This section describes molecular dynamics calculations with one Li^+ cation and 157 ST2 water molecules against a metal surface. The simulation cell is periodically replicated in the xy plane parallel to the metal surface. The simulation was run for 2500 ps, the first 100 ps of which were used to equilibrate the system. The charge on the electrode is the image charge $-|e|$. At any instant this charge is not uniformly distributed across the electrode but localized on the surface in such a way as to produce the same electric field and potential as the electrostatic image of the lithium ion and all the water molecules. The field acting on the lithium ion comes from all the

water molecules in the cell, all water and ions in xy periodically replicated cells, and all of the electrostatic images of the contents of all cells in the image plane of the metal. We emphasize again that in this calculation as in all the others described in this paper no electrostatic interaction is truncated. Figures 2 and 3 show the probability density profiles averaged over the xy direction and electrical potential calculated by the two ways described in Section 3. Note that in Fig. 2 the probability of finding the ion and water have scales differing by fifty. Also plotted in Fig. 2 is the total charge density by the atomic method. The bin size is $L/400 = 0.004\,655$ nm where L is the edge length of the simulation cell.

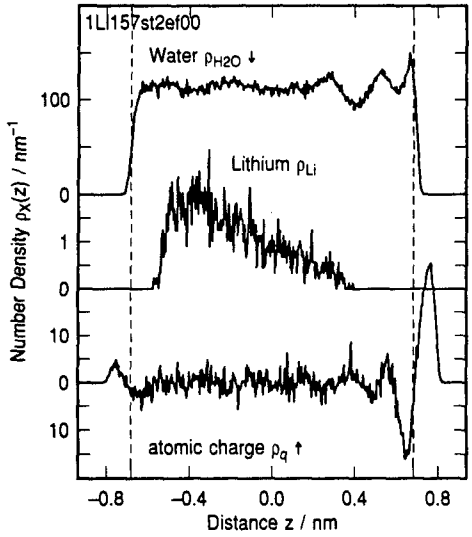

Fig. 2. Density profiles for lithium cation Li^+ ion, 157 ST2 waters and the total atomic charge density ρ near an immersed electrode. Image charge on metal -1 is screened by the Li^+ ion. Metal electrode on right-hand side, restraining wall on the left. Image plane at $z = 0.931$ nm. Wall potentials go through zero at $|z| = 0.682$ nm. Simulation from 100 ps to 2500 ps.

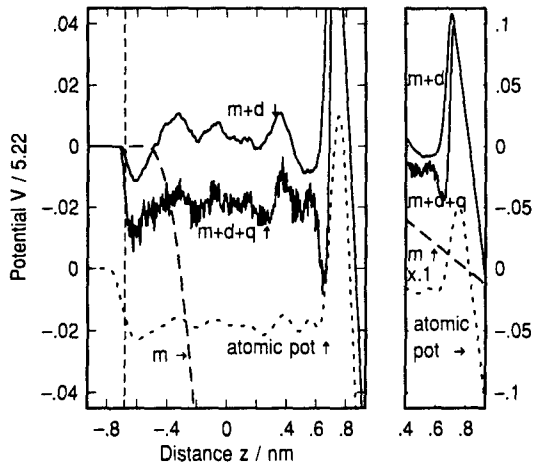

Fig. 3. Potential drop across the system Li^+ ion and 157 ST2 waters in the immersed electrode model. Calculations using atom and molecule methods. Bin size 0.004 655 nm. Molecule method: m monopole only, $m + d$ monopole and dipole, $m + d + q$ monopole, dipole and quadrupole. The right-hand side panel shows the potentials on a larger scale for $z > 0.4$ nm, with the monopole scaled by 0.1. Image charge on metal -1 is screened by the Li^+ ion. Metal electrode on right-hand side, non-metallic restraining wall on the left. Image plane at $z = 0.931$ nm. Wall potentials go through zero at $|z| = 0.682$ nm.

In Fig. 2 we see that the Li^+ ion mass centre mapped out a diffuse-like region between -0.6 and 0.4 nm. The lithium Li^+ ion has the smallest ionic radius of all the monovalent cations. Consequently its hydration shell is very strongly bound making it more difficult for this ion to contact adsorb on the electrode. The asymmetry of the distribution may well be affected by the small width of the cell and consequently no significance is attached to its shape other than it is diffuse in nature. There may possibly be a hydrophobic plating of the ion to the left-hand interface. On the metal side the ion rarely approached closer than 0.3 nm to the repulsive part of the wall potential shown by the dashed line at 0.68 nm in Fig. 2. This is approximately the average of the separate σ parameters for Li^+ and O_ST2 suggesting that the lithium ion remains fully hydrated at the metal surface, and that though surface water restricts the approach of the ion to the metal it does not exclude it. This behaviour of the lithium ion is more like that postulated in Grahame's picture of the double layer[58], than say the Bockris model[12]. To confirm such behaviour would require extending the simulation over many nanoseconds, or performing umbrella sampling[59]. This particular aspect of the problem is not pursued further here.

The water profile shows some new structure not seen in water without ions[39, 60]. Most interesting is the leading peak (closest to the metal surface) at *ca.* 0.68 nm due to a few localized water molecules. The orientation of these localized water molecules can be ascertained from the H_ST2 and PC_ST2 probability distributions (not shown here). The protons on these molecules give rise to the distinct peak at *ca.* 0.75 nm in the H_ST2 distribution. In the PC_ST2 distribution (not shown) there is a peak at *ca.* 0.625 nm that is enhanced more than the second peak in the H_ST2 profile which is at *ca.* 0.6 nm. The first water peak at *ca.* 0.68 nm lies between the first H and PC peaks measured from the metal surface. It appears therefore that some of the localized water molecules have one proton pointing at the electrode.

The atomic charge density profile in Fig. 2 is dominated by neutral water. The large oscillation centred near 0.70 nm is due to partially oriented water. The main positive peak at *ca.* 0.75 nm is due to protons attracted to the metal by their images and the image field of the lithium ion. There are smaller oscillations in the charge profile further from the surface that are more clearly seen if the distribution is smoothed. These tend to follow the oscillations in the water density probability in Fig. 2. The actual lithium charge density is buried under the contribution from the water when the bin size is 0.004 655 nm.

Figure 3 shows the electric potential across the cell calculated by the atomic charge method, and by the molecular method with systematic inclusion of higher electrostatic multipoles. For clarity the dashed vertical line denoting the point $z = 0.628$ nm

where the wall potential goes through zero has been omitted except for the tick mark on the x axis. Since all the curves go off scale near $z = 0.682$ nm all the data for $z > 0.4$ nm have been plotted again on a larger scale and are shown in the right-hand panel. Note too that in this right-hand panel the monopole curve m (broken curve) is scaled by 0.1 to distinguish it from the other curves. The notation in the figures is m = monopole, d = dipole, q = quadrupole. When m and d contributions are combined the curve is labelled $m + d$. When m, d and q contributions are combined the curve is labelled $m + d + q$. Only when three multipoles are included ($m + d + q$ curve) do the potentials calculated by the two methods agree reasonably. Due to the small size of the bin it is necessary to include more higher multipoles before the atom and molecular methods agree quantitatively. The monopole contribution m (dashed line in Fig. 3) due to the lithium ion alone drops monotonically as expected for the potential inside a capacitor where the charge on the left is in a diffuse layer spatially separate from the charge on the right plate (metal) at $z = 0.931$ nm. Adding the dipole completely changes the potential (see $m + d$ curve). The water molecules very effectively screen the field inside the capacitor, except for the region $z > 0.68$ nm where the water distribution drops rapidly to zero. Adding the quadrupole (also from water only) term brings the atomic and molecular calculations into some measure of agreement (note that the atomic and $m + d + q$ potentials are offset by 0.04 in Fig. 3). The quadrupole contribution to the potential is a negative constant in the region away from the wall potential. This occurs because its contribution to the charge $\langle \rho_{\text{mol}}(\mathbf{r}, t) \rangle$ contains a double derivative in space coordinates. The differences are greatest at the surfaces where the atomic method traces charge density smoothly whereas the molecular method, based on an expansion about molecular centres, requires many high multipoles to describe the field.

The variation in potential is rapid near the metal and Fig. 3 shows this variation for the atomic and $m + d + q$ approximation scaled by a factor 0.1. After adjusting for the offset of 0.04 the two curves become identical for $z > 0.8$ nm as expected for a region containing no molecules or ions. Between 0.6 and 0.75 nm the difference between the methods is largest due the difference in source terms. The dangers of omitting higher multipoles was clearly pointed out by Wilson, Pororille and Pratt[14, 57] for water without ions.

Finally we return to the asymmetry in the lithium ion distribution. There are effects due to system size and ion-ion correlation. We have repeated some of the calculations with two lithium ions and 598 water_ST2 molecules for a few hundreds of picoseconds. The water structures appear almost exactly as in the smaller simulations. The lithium probability $\rho(z)$ for the two ion system is spread across most of the cell in a diffuse zone with a moderate bias towards the metal side of the cell. This result is satisfying in that no peculiar or pathological features are revealed implying that the smaller calculations can give useful insight into water structure within about two water layers (*ca.* 0.6 nm from the point where the wall potential becomes repulsive at $z = 0.68$ nm).

We close this section with a discussion of changing the length scale over which the test function averaging is performed. The lithium system is chosen because the ion occupies a diffuse region and does not contact adsorbed on the electrode. The initial smearing of ion charge by the localized Gaussian average does not overlap the metal surface region so that changes near the metal reflect averaging of the local distributions. Figure 4 shows the result of changing the size of the length scale when Gaussian averaging is performed. It shows that as the averaging length scale increases the atom potential loses features at the scale of a water molecule. The parameter g (in nm units) is the width of the function $f_g(z)$ defined in equation (9). There are two families of curves, the broken lines are for the atom (method I) potential with $g = 0.03$, 0.1, 0.3 and 1.0. Though hardly apparant because of the factor $\times$ 20 in ordinate scale, the atom potential with $g = 0.03$ is close in numerical value to the atomic potential shown previously by the dotted curve in Fig. 3. The $g = 1.0$ is extreme because it is close to half the box edge $\frac{1}{2}L = 0.931$ nm. The behaviour of the $g = 1.0$ monopole shows there is some smeared charge beyond the left-hand wall. What Fig. 4 demonstrates is that as the size of the region averaged is increased from $g = 0.03$ nm (0.1 $\times$ water molecule dimension) to $g = 1.0$ nm (3 $\times$ water molecule dimension) the structure in the electric potential near the surface due to the water profile is lost. The total potential becomes monotonic and resembles the family of monopole potential curves calculated using the monopole charge distribution. Since the component of the water dipole perpendicular to the surface is not averaged to zero the atom potential at the surface

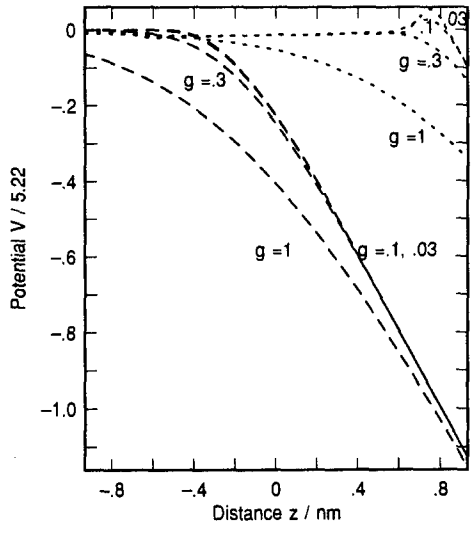

Fig. 4. Potential drop across the system Li^+ ion and 157 ST2 waters in the immersed electrode model. Calculations using atom and molecule methods with Gaussian widths $g = 0.03$, 0.1, 0.3, 1.0 nm. Curves for monopole potentials (broken lines) and the total potential by the atom (dotted lines) method. Oscillations in the atomic potential clearly visible in Fig. 3 for $z > 0.2$ nm are washed out on the scale of a water molecule $g = 0.3$.

remains smaller in magnitude. The macroscopic dielectric polarization remains and reduces the value of the surface potential by roughly an order of magnitude (curves for $g = 0.3$ nm). As expected the monopole potentials are not as sensitive to the value of the width g as the atomic potentials. This is an important qualitative result because it shows the transition from the microscopic scale, where surface water oscillatory structure dominates the potential, to macroscopic scale behaviour where water contributes a simple scaling of the electric potential.

5. IODIDE ION

In this section we describe simulations for one iodide anion I^- and 157 water molecules interacting with a metal surface. In practice it was found not necessary to run the simulation beyond 500 ps because the ion adsorbed on the metal after approximately 10 ps and remained there. However, for consistency with the other simulations reported in this paper the calculation was allowed to run for 1000 ps. As in the case of lithium the first 100 ps were used to allow the system to equilibrate and were excluded from any statistical analyses. When the ions and water are described by the Heinzinger parameter set[24] we have shown in previous publications that: (i) in fields of 1 GV m^{-1} all the halide ions except fluoride contact adsorbed on non-metal (surface with no electrostatic image interactions) electrodes[61] and (ii) similar behaviour occurred for the model of the metal used here when there was an unscreened external field of 1 GV m^{-1} pulling the ion to the surface[62].

Figures 5 and 6 show the probability density distributions and electric potential for the iodide system. Figure 5 shows the iodide ion distribution peaked at *ca.* 0.7 nm closer to the electrode than

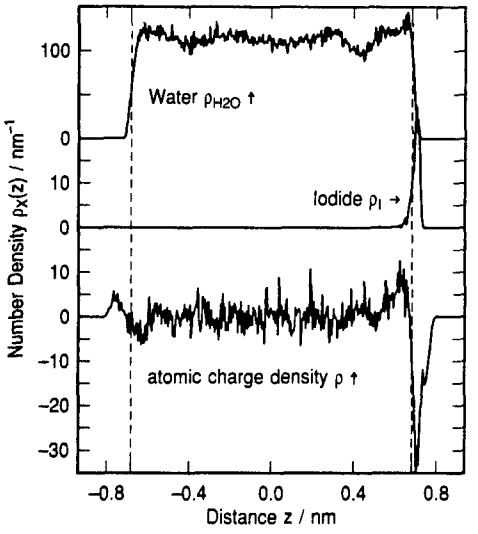

Fig. 5. Density profiles for iodide anion I^- ion, 157 ST2 waters and the total atomic charge density ρ near an immersed electrode. Image charge on metal + 1 is screened by the I^- ion. Metal electrode on right-hand side, restraining wall on the left. Image plane at $z = 0.931$ nm. Wall potentials go through zero at $|z| = 0.682$ nm.

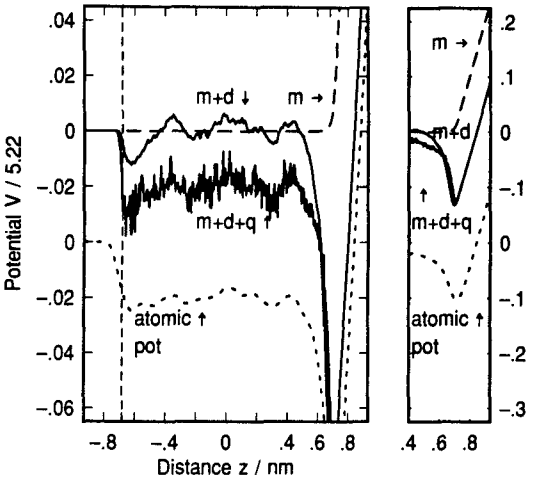

Fig. 6. Potential drop across the system I^- ion and 157 ST2 waters in the immersed electrode model. Calculations using atom and molecule methods. Bin size 0.004 655 nm. Molecule method: m monopole only, $m + d$ monopole and dipole, $m + d + q$ monopole, dipole and quadrupole. Panel on the right-hand side shows the curve for $z > 0.4$ nm on a reduced scale. Image charge on metal + 1 is screened by the I^- ion. Metal electrode on right-hand side, restraining wall on the left. Image plane at $z = 0.931$ nm. Wall potentials go through zero at $|z| = 0.682$ nm.

where the wall potential becomes positive at 0.68 nm. Compared to the previous example (lithium ion, Fig. 2) there is less structure in the water and in the H_ST2 and PC_ST2 component distributions (not shown). In fact apart from a small peak at 0.65 nm the distribution resembles water without ions in zero applied field[39, 62]. The atomic charge distribution displays a medium positive peak at *ca.* 0.65 nm (H_ST2) and two negative peaks at *ca.* 0.7 nm (iodide), and *ca.* 0.75 nm (PC_ST2).

Figure 6 shows the electric potential calculated by the two methods. All components go off scale near $z = 0.682$ nm, and are plotted for $z > 0.4$ nm on a reduced scale ($\times 0.2$ in the right-hand panel). The monopole potential m (broken curve) due to the iodide alone, is zero except close to the wall where the iodide is localized. There it changes swiftly from 0 to a high positive value corresponding to an electric field E_{ion} of approximately -5 GV m^{-1}. The absence of an electric field due to iodide ions means there is little or no reaction from the water molecules and they are less ordered between -0.6 nm and 0.4 nm, and what ordering there is comes from the presence of the surfaces. In Fig. 6 the $m + d$ curve for combined monopole and dipole potentials shows a weaker variation compared to the lithium ion. This means that before $z = 0.4$ nm the charge on the electrode is completely shielded. The curves of the atomic and $m + d + q$ potentials overlap well for $z < 0.4$ nm due primarily to the water quadrupole contribution.

6. NEUTRAL SOLUTIONS: POTENTIAL OF ZERO CHARGE

In this section we compute the properties of a neutral solution of LiI comprised of one Li ion and

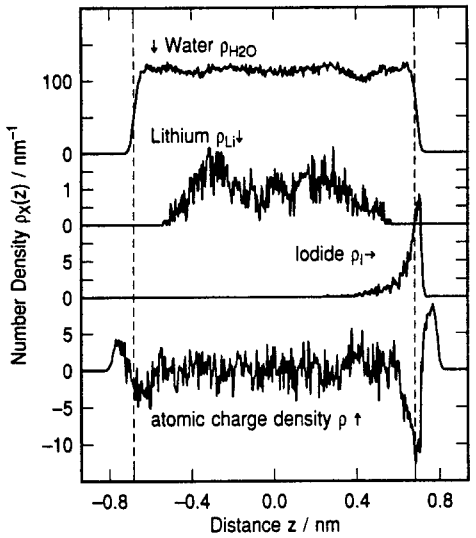

Fig. 7. Density profiles for a neutral solution consisting of one lithium cation Li^+, one iodide anion I^- and 157 ST2 waters and the total atomic charge density near an immersed electrode. Metal electrode on right-hand side, restraining wall on the left. Image plane at $z = 0.931$ nm. Wall potentials go through zero at $|z| = 0.682$ nm.

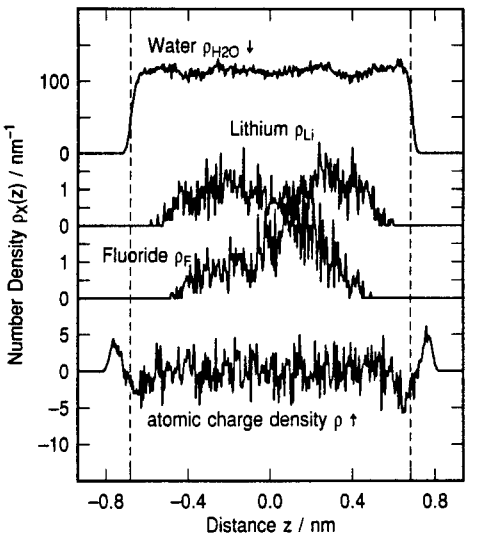

Fig. 9. Density profiles for a neutral solution consisting of one lithium ion Li^+, one fluoride ion F^- and 156 ST2 waters and the total atomic charge density ρ near an immersed electrode. Image charge on metal is zero. Metal electrode on right-hand side, restraining wall on the left. Image plane at $z = 0.931$ nm. Wall potentials go through zero at $|z| = 0.682$ nm.

one I ion and 156 water molecules in the simulation cell, and compare it to the case of LiF with the same number of water molecules. There is no net attractive electric field on either ion because the total electrostatic image charge on the metal is zero. The two systems are quite different because iodide contact adsorbs on the metal and creates a surface localized electric dipole and field. Because the aqueous phase is neutral this simulation models a system at the potential of zero charge. This potential does not have to be zero, it will be very small if the charge distribution in the aqueous subphase is everywhere almost zero. The potential of zero charge is considered the natural reference point from which to measure electrode potentials. The measurement of change of surface tension of liquid metals with electrode potential is the only reliable direct method[63] of determining the *pzc*. The calculation of electric field and potential using the atom charge distribution have been published[64] so in this section we focus on comparing the atom calculations with the molecular method to gain further insight. Figure 7 displays the most important density profiles for the LiI system, and Fig. 8 shows the various components of the electric potential.

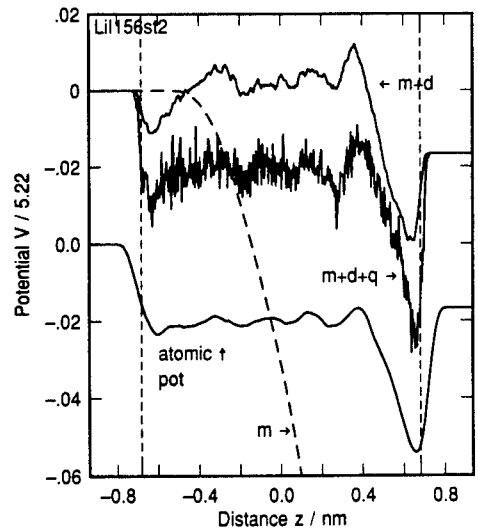

Fig. 8. Electric potential drop across a the neutral solution consisting of one lithium ion Li^+, one iodide ion I^- and 156 ST2 waters next to an immersed electrode. Potential due to atom method shifted by -0.04. Potential from: ions only m, ions and water dipoles $m + d$, ions and water dipole and quadrupole $m + d + q$. Note that the potential $m + d + q$ is almost the same as that calculated from atomic charges. There is no net image charge on the metal. Metal electrode on right-hand side, restraining wall on the left. Image plane at $z = 0.931$ nm. Wall potentials go through zero at $|z| = 0.682$ nm.

In Fig. 8 we note that the monopole potential m drops steeply as it passes through the diffuse layer of lithium ions (much as it did in the case of one lithium ion) because the iodide adsorbed on the metal acts like the second plate in a capacitor. The $m + d$ curve shows that the water dipoles orient in the ion field and shield the ions from each other except close to the metal. As in the previous two examples the water quadrupole shifts the electric potential to lower values by a constant amount. Note that the shift in potential from vacuum to metal, which measures the potential of zero charge, depends on the net dipole moment of the system[65]. The atomic and molecular methods give similar results. Closer results require the inclusion of octopole and higher moments which contribute most near the surface.

We have also performed simulations on LiF under the same conditions that mimic the potential of zero charge. Figure 9 shows the probability distributions.

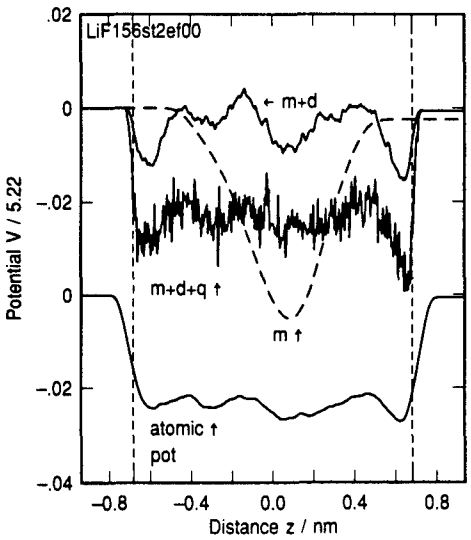

Fig. 10. Electric potential drop across a neutral solution consisting of one lithium ion Li^+, one fluoride ion F^- and 156 ST2 waters next to an immersed electrode. Potential due to atom method is shifted by −0.04. Potential from: ions only m, ions and water dipoles $m + d$, ions and water dipole and quadrupole $m + d + q$. Note that the potential $m + d + q$ is almost the same as that calculated from atomic charges. Metal electrode on right-hand side, restraining wall on the left. Image plane at $z = 0.931$ nm. Wall potential goes through zero at $|z| = 0.682$ nm.

In neutral LiF solution in contrast to LiI solution neither ion adsorbs on the electrode and both are comingled into a diffuse layer that is predominantly neutral across the system. The water distribution looks like water between uncharged plates. Figure 10 displays the electric potentials. As expected the contact potential was calculated as close to zero since the net dipole moment is very small. The monopole potential m shows a minimum related to the apparent bimodal distribution of the lithium ion. The water dipole orients to reduce the local electric field to a small value, with the result that the curve $m + d$ shows weak changes across the film. Adding the quadrupole in $m + d + q$ shifts the whole potential downwards bringing it into close correspondence with the result of the atomic method of calculation. For $z < 0.4$ nm the atomic and $m + d + q$ potentials are similar in shape and value. Higher multipole contributions to the molecular method are needed to bring it into closer correspondence to the atom method near the metal surface.

7. LITHIUM CATION "COADSORBED" WITH IODIDE IONS

In this simulation we explore another important aspect of the adsorption of ions on metal electrodes, namely the ability of strong contact adsorbers like iodide ions I^- to adsorb on positively charged electrodes in sufficient excess to change the sign of the charge at the interface as observed by an ion located in the diffuse layer. In the case under consideration cations will be attracted out of the diffuse layer to compensate the excess negative charge at the interface. The interface can develop a layered structure of alternating charges. First there is positively charged metal, then a narrow layer of contact adsorbed negative ions, and then a layer of compensating cations. In real systems this compensating layer may be part of a diffuse layer or it could be a separate structure. The coadsorption of the cations is required to maintain overall charge neutrality. It is in this sense that we refer to the cations as coadsorbed. Phenomena of this type occur frequently in electrochemistry. In a previous paper we very briefly described results for this system in an external applied field corresponding to uncompensated charge on the immersed electrode. In the present calculation the charge on the electrode due to electrostatic images is $+|e|$. The presence of two adsorbed iodides creates an anisotropic surface electric field and some simulations were run for 3 ns to improve the cation statistics. Even though only small changes in the distribution were observed due to configurations accumulated at later times, we regard the calculated distributions for the cation as being approximate. A preliminary account of the probability distributions of this simulation has been published[39]. This is the first report of the potentials across this cell.

Figure 11 shows the probability density profiles for selected species in solution. There are some similarities in the results for water and the lithium ion for this system and the one discussed in the last section. In particular the water looks quite unstructured compared to hydrated ions, and the Li^+ ion is bimodal. The I^- ion distribution is sharper because the electrode is positively charged.

The initial configuration was a random arrangement of ions and water on a cubic lattice. Both the iodides adsorbed within 50 ps. Note that the iodide distribution is localized at the surface as in the case of one iodide, and the lithium is more diffuse than in the case of a single lithium in the field of its own

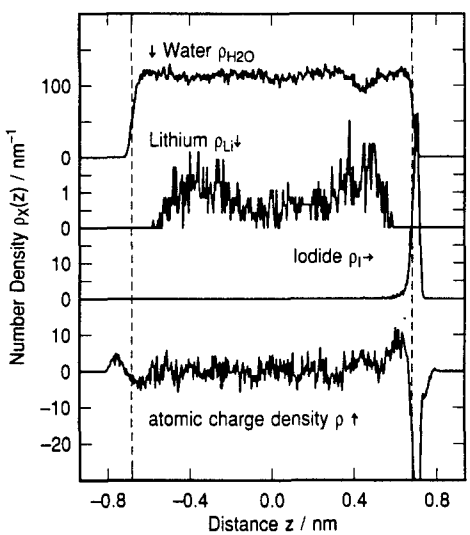

Fig. 11. Density profiles for two iodide ions I^- and one lithium cation Li^+ and 155 ST2 water molecules and total atomic charge density next to an immersed electrode. The net image charge on the metal + 1 is screened by three ions in solution.

electrostatic image charge. Except for slightly accentuated broad structures in the range 0.4 to 0.6 nm, the water distribution resembles the distribution already calculated for zero applied field[62]. In particular we note that there are no new peaks near 0.65 nm indicative of localized surface water. The proton H_ST2 and point charge PC_ST2 components have more structure near the metal than in zero field. This is to be expected since they are charged and the field between them and their images is unscreened. The atomic charge density has a deep minimum at *ca.* 0.7 nm due to iodide and a shoulder at *ca.* 0.75 nm due to the PC_ST2.

Figure 12 shows the electric potential calculated using the two methods. Starting from the left the monopole potential first rises as it passes through the lithium layer, and then drops rapidly as it approaches the sheet of adsorbed iodide, finally it turns upward because the electrode carries a net positive image charge. Apart from the upward turn near the metal this monopole behaviour is qualitatively similar to that depicted for the model in Fig. 1. Our assertion that the traditional models neglect significant contributions from the water can be seen by examination of Fig. 12. There is significant structure in the electric potential calculated by either method induced by orientation and packing distribution of the waters at the surface. The monopole term is completely compensated ($-0.65 < z < 0.4$ nm) by the dipole potential from the water molecules as shown by curve $m + d$ until next to the metal surface where water is more strongly oriented and where the water supply drops rapidly to zero. From 0.4 nm to 0.65 nm the atomic potential closely follows that of one iodide (see Fig. 6). On the right-hand side of Fig. 12 we show the potentials for atomic, monopole m and $m + d + q$ scaled by a factor 0.1.

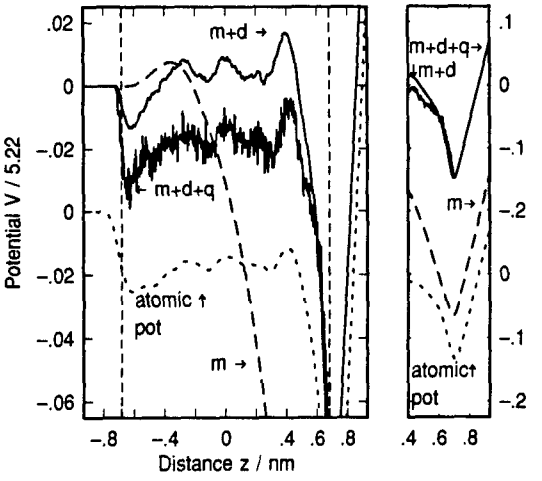

Fig. 12. Electric potential drop across a charged solution consisting of one lithium ion Li^+, two iodide ions I^- and 155 ST2 waters next to an immersed electrode. Potential due to atom method is shifted by −0.04. Potential from: ions only m, ions and water dipoles $m + d$, ions and water dipole and quadrupole $m + d + q$. Note that the potential $m + d + q$ is almost the same as that calculated from atomic charges. Metal electrode on right-hand side, restraining wall on the left. Image plane at $z = 0.931$ nm. Wall potential goes through zero at $|z| = 0.682$ nm. Panel on right shows potentials for $z > 0.4$ nm on a scale 5× larger than the left side.

Scale-up is likely to be an important issue since the size of the system may be too small to allow the diffuse layer lithium ion enough space to distribute without interference from the restraining wall at $z = -0.931$ nm. However, conclusions drawn concerning the behaviour of ions within 1.0 nm of the metal surface will not be very sensitive to the position of the restraining wall. An example of a large system with intact double layer is discussed next.

8. 1 M NaCl SOLUTION

In this final example we describe a simulation with approximately 1600 water molecules and ions in a box with edge length $L = 3.724$ nm. The simulation cell contains 32 Na^+ ions, 28 Cl^- ions and 1576 water molecules. The NaCl concentration is about 1 M. The electrostatic image charge on the electrode surface due to the difference in number of positive over negative ions is $-4\,|e|$ or $0.046\,C\,m^{-2}$. This is essentially the same charge density as in all the earlier smaller simulations with non-zero electrode charge density. Computer time constraints dictated the use of a simple water model. For this reason we chose the SPCE water model (three charged mass points[66]) over the ST2 water model (two charged mass points, two charged zero mass points, one uncharged mass point). The NaCl parameters[67] used are those appropriate for SPCE water. We also experimented with simulations run at elevated temperatures to increase the diffusion rate of the ions in order to get better statistics. In this calculation the temperature was 30°C. The simulation was run for 840 ps with the first 100 ps used to equilibrate the system. On a dedicated IBM RS6000 model 550 work station the calculation takes approximately 10 to 12 weeks.

Figure 13 shows the probability density profiles for the water proton, water mass centre, Na^+ ions and Cl^- ions. The anion distribution (broken line) has been smoothed to permit it to be distinguished from the cation. Also shown rising monotonically from the left are the integrals of the ion densities. The near coincidence of the integrals for $z < 0.7$ nm shows that the electrolyte is approximately charge neutral. For $z > 0.7$ nm the integrated densities systematically diverge as expected for a transition from the locally neutral "bulk" electrolyte into the "diffuse" part of the electric double layer where screening occurs. At $z = 1.0$ nm the divergence in the integrated densities equals the largest previous difference in the two curves, implying that the region $z > 1.0$ nm corresponds to solution shielding the charge on the metal. The Na^+ ion distribution shows well defined structure in the form of a board peak at *ca.* 1.1 nm, and a sharp peak at 1.1 nm. The water and proton distributions appear flat for $|z| < 0.8$ nm. On the metal side the water probability distribution has peaks at 0.9 nm, 1.2 nm and a strong asymmetric peak at 1.6 nm. This latter feature appears to be composite being the superposition of a broad feature at 1.5 nm and a narrow peak at 1.6 nm. The peaks in the proton distribution are at 0.9 nm,

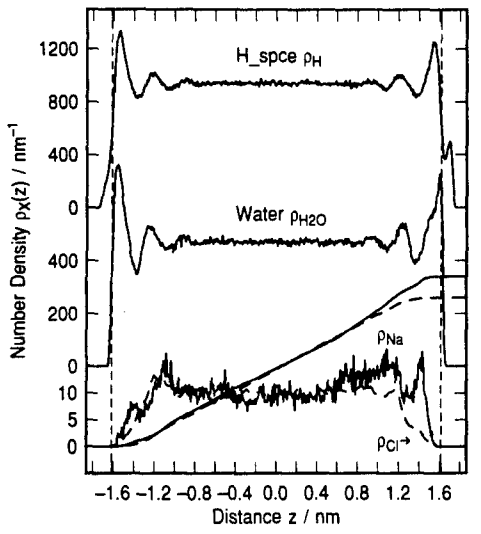

Fig. 13. Screening for 1 M $NaCl_{aq}$ at 30°C. Electrolyte composition: 32 Na^+ ions, 28 Cl^- ions and 1576 SPCE water molecules near an immersed electrode. Image charge on the metal $-4\,|e|$. Metal electrode on right-hand side at $z = 1.862$ nm (position of image plane), restraining wall origin on the left at $z = -1.862$ nm, wall potentials on both sides of the simulation cell go through zero at $|z| = 1.615$ nm. Simulation duration 100 ps to 840 ps.

1.2 nm, 1.55 nm and 1.7 nm. The last peak at *ca.* 1.7 nm comes from protons in water OH bonds pointing at the metal.

Figure 14 shows the atomic charge density for a bin function with width 0.004 655 nm (or $L/800$). We note that the charge density appears flat for $|z| < 0.8$ nm. The contribution from the ionic charge for $z > 0.8$ nm is not evident because the charge on the waters dominates. The electric field was obtained by integration from $-\infty$ to position z. The field is flat with small variations around zero in the region $|z| < 0.8$ nm. Near the metal the electric field undergoes a series of rapid oscillations as it vears upwards. These oscillations are due to the water structure at the interface. The general rise is due to the excess Na^+ charge in the double layer.

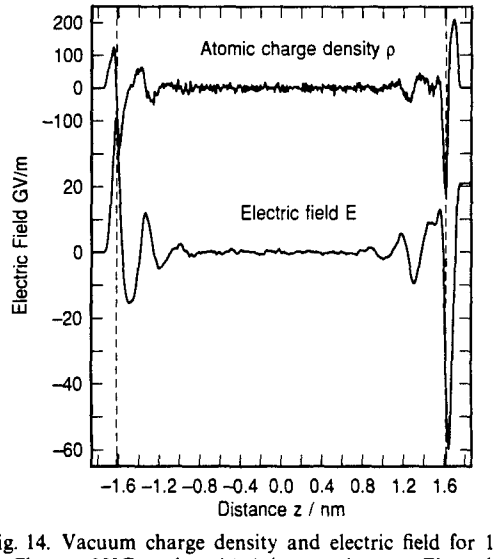

Fig. 14. Vacuum charge density and electric field for 1 M $NaCl_{aq}$ at 30°C and $-4\,|e|$ image charges. Electrolyte composition: 32 Na^+ ions, 28 Cl^- ions and 1576 SPCE water molecules near an immersed electrode. Metal electrode on right-hand side at $z = 1.862$ nm (position of image plane), restraining wall origin on the left at $z = -1.862$ nm, wall potentials on both sides of the simulation cell go through zero at $|z| = 1.615$ nm. Simulation duration 100 ps to 840 ps.

Figure 15 shows the potential calculated using the atom method, and the components of the potential calculated by the molecule method. The contact potential is about -2.0 V, and as in the smaller simulations the potential in the "bulk-like" zone comes from the water quadrupole. The broken curve labelled m is that from the ionic charge. If the system were truly neutral then curve m would be flat and zero all the way to the beginning of the diffuse layer. Clearly the small charge imbalances seen in Fig. 13 do affect the shape of the potential curve and may be an exacting criterion with which to judge these larger simulations. The transition to monotonic decrease starting near $z = 0.7$ nm is another indicator of where the diffuse layer begins in this simulation. Note that $m + d$ shows that the dipole potential completely compensates the monopole. Including the quadrupole to give $m + d + q$ shifts the core region downwards by 3 V and brings the molecular calculation of potential into correspondence with the atom method of calculation. The molecular method has larger extrema near the surface compared to the

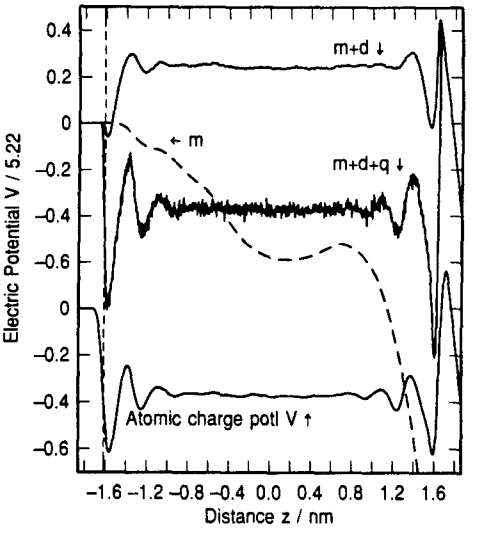

Fig. 15. Electric potential drop across a charged solution consisting of 1 M NaCl solution at 30°C and $-4\,|e|$ image charge on the metal. Potential calculated by the atom method is shifted by -0.8. Molecule method potentials from: ions only m, ions and water dipoles $m + d$, ions and water dipole and quadrupole $m + d + q$. Note that the potential $m + d + q$ is almost the same as that calculated by the atom method. The net image charge on the metal $-4\,|e|$ is screened by a total of sixty ions. Electrolyte composition: 32 Na^+ ions, 28 Cl^- ions and 1576 SPCE water molecules near an immersed electrode. Metal electrode on right-hand side at $z = 1.862$ nm (position of image plane), restraining wall origin on the left at $z = -1.862$ nm, wall potentials on both sides of the simulation cell go through zero at $|z| = 1.615$ nm. Simulation duration 100 ps to 840 ps.

atom method. The reason for this is the very small bin size and the consequential need to include many high order multipoles in the molecule method. However, as required the contact potential is the same in each case. Note also that adding the quadrupole term does not change the contact potential.

In summary this larger simulation has verified that water structure near walls is not an artifact of small size. In 1 M NaCl the double layer is about 1 nm thick and encompasses about three layers of water. These water layers can significantly affect the distribution of ions near the metal creating features in the probability distributions that are not describable in the Gouy–Chapman–Stern model.

9. CONCLUSIONS

In this paper we have shown how the results of molecular dynamics simulations performed at constant N, V, T can be used to calculate the electrostatic field and potential across an electric double layer. Apart from usual molecular dynamics assumptions we used a model for an immersed electrode in which electrode charge was equal to the image charge on the metal. All electrostatics were summed without truncating the long range Coulomb interaction using the fast multipole method. The charge distribution in the system was analysed by two methods. One was based on the charges in atoms in vacuum, the other was based on molecules and required expanding the positions of charge inside a molecule about an origin on each molecule. The later method provided a natural route for decomposing fields into monopole and higher order multipole components. We also showed, by increasing the length scale over which the local average is taken, how microscopic structure due to the water probability distribution is systematically washed away leaving only the macroscopic effect of the water dielectric polarization on the electric surface potential. We also showed using the results of a calculation almost an order of magnitude larger in number of water molecules, that the main features evident in smaller calculations of the probability profiles for water near charged metal surfaces are not greatly affected by scale-up. This implies that small simulations involving a few hundred water molecules provide a useful starting point for studying double layer properties.

In a series of examples starting with single ions in water, and then moving to increasingly more complex cases we explored fields close to the surface and across double layers in some electrochemically interesting examples. The case of lithium was chosen to explore some of the consequences of averaging over length scales from smaller to larger than a water molecule. In the final example of 1 M NaCl we demonstrated the coexistence of bulk and double layer regions in equilibrium in the same simulation. Since the system contained 60 ions there is ample correlation between ions and among ion and water molecules.

Acknowledgements—This research was supported in part by the Office of Naval Research. The contributions of JNG were performed under the auspices of US DOE contract W-7405-Eng-48.

REFERENCES

1. G. Gouy, *J. Physique* **9,** 457 (1910).
2. D. L. Chapman, *Phil. Mag.* **25,** 508 (1913).
3. D. L. Chapman, *Phil. Mag.* **25,** 475 (1913).
4. O. Stern, *Z. Elektrochem.* **30,** 508 (1924).
5. D. Henderson and M. Plischke, *Mol. Phys.* **62,** 801–804 (1987).
6. L. F. Greengard, *The Rapid Evaluation of Potential Fields in Particle Systems.* MIT Press, Cambridge, Massachusetts (1987).
7. L. Greengard and V. Rokhlin, *J. Comp. Phys.* **73,** 325–348 (1987).
8. J. Carrier, L. Greengard and V. Rokhlin, Siam *J. Sci. Stat. Comput.* **9,** 669–686 (1988).
9. L. Greengard and V. Rokhlin, *Chemica Scripta* **29A,** 139–144 (1989).
10. J. O. Bockris and A. K. Reddy, *Modern Electrochemistry, Vol. 2.* Plenum Press, New York (1973).
11. J. O. Bockris and A. Gonzalez-Martin, *Spectroscopic and Diffraction Techniques in Interfacial Electrochemistry*, NATO ASI Series C, Vol. 320, **320,** (1990).
12. J. O. Brockris, M. A. Devanathan and K. Müller, *Proc. Roy. Soc. (London)* **A274,** 55–79 (1963).
13. R. W. Hockney and J. W. Eastwood, *Computer Simulation using Particles.* McGraw-Hill, New York, 1981.
14. M. A. Wilson, A. Pohorille and L. R. Pratt, *J. Chem. Phys.* **88,** 3281–3285 (1988).
15. M. A. Wilson, A. Pohorille and L. R. Pratt, *Chem. Phys.* **129,** 209–212 (1989).
16. L. D. Landau and E. M. Lifschitz, *Electrodynamics of Continuous Media.* Addison-Wesley (1960).
17. J. D. Jackson, *Classical Electrodynamics*, pp. 54–62. Wiley, New York (1975).
18. G. Russakoff, *Amer. J. Phys.* **38,** 1188–1195 (1970).
19. M. R. Philpott and J. N. Glosli, *J. Electrochemical Soc.* **142,** L25–L28 (1995).
20. D. Henderson, *Trends in Interfacial Electrochemistry*, p. 183. Reidel, Dordrecht, Holland (1986).
21. J. W. Halley, B. Johnson, D. Price and M. Schwalm, *Phys. Rev. B* **31B,** 7695–7709 (1985).
22. J. W. Halley and D. Price, *Phys. Rev. B* **35B,** 9095–9102 (1987).
23. D. L. Price and J. W. Halley, *Phys. Rev. B* **38B,** 9357–9367 (1988).
24. K. Heinzinger, in *Computer Modeling of Fluids Polymers and Solids* (Edited by C. R. A. Catlow, S. C. Parker and M. P. Allen). Vol. 293, NATO ASI Series C, pp. 357–404. Kluwer, Holland (1990).
25. G. Nagy and K. Heinzinger, *J. Electroanal. Chem.* **296** (1990).
26. K. Heinzinger, *Pure Appl. Chem.* **63,** 1733–1742 (1991).
27. J. Seitz-Beywl, M. Poxleitner and K. Heinzinger, *Z. Naturforsch.* **46A,** 876–886 (1991).
28. G. Nagy and K. Heinzinger, *J. Electroanal. Chem.* **327** (1992).
29. J. Seitz-Beywl, M. Poxleitner, M. M. Probst and K. Heinzinger, *Int. J. Quantum Chem.* **42,** 1141–1147 (1992).
30. E. Spohr and K. Heinzinger, *Ber. Bunsenges. Phys. Chem.* **92,** 1358–1363 (1988).
31. E. Spohr and K. Heinzinger, *Electrochimica Acta* **33,** 1211–1222 (1988).
32. E. Spohr, *J. phys. Chem.* **93,** 6171–6180 (1989).
33. E. Spohr, *Chem. Phys.* **141,** 87–94 (1990).
34. E. Spohr, *Chem. Phys. Lett.* **207,** 214–219 (1993).
35. M. R. Reddy and M. Berkowitz, *Chem. Phys. Lett.* **155,** 173–176 (1989).

36. K. Raghavan, K. Foster, K. Motakabbir and M. Berkowitz, *J. Chem. Phys.* **94,** 2110–2117 (1991).
37. L. Perera and M. L. Berkowitz, *J. Chem. Phys.* **99,** 4222–4224 and 4236–4237 (1993).
38. B. E. Conway, J. O. Bockris and I. A. Ammar, *Trans. Faraday Soc.* **47,** 756–766 (1951).
39. M. R. Philpott and J. N. Glosli, in *Theoretical and Computational Approaches to Interface Phenomena* (Edited by H. Sellers and J. T. Golab), pp. 75–100. Plenum, New York (1994).
40. F. H. Stillinger and A. Rahman, *J. Chem. Phys.* **60,** 1545 (1974).
41. O. Steinhauser, *Mol. Phys.* **45,** 335–348 (1982).
42. C. Y. Lee, J. A. McCammon and P. J. Rossky, *J. Chem. Phys.* **80,** 4448–4455 (1984).
43. R. A. Friedman and B. Hoenig, *Biopolymers* **32,** 145–159 (1992).
44. B. E. Hingerty, R. H. Richie, T. L. Ferrel and J. E. Turner, *Biopolymers* **24,** 427–439 (1985).
45. P. R. Weiner and P. A. Kollman, *J. Comp. Chem.* **2,** 287–303 (1981).
46. J. A. McCammon, P. G. Wolynes and M. Karplus, *Biopolymers* **18,** 927–942 (1979).
47. B. R. Brooks, R. E. Bruccoleri, B. D. Olafson, D. J. States, S. Swaminathan and M. Karplus, *J. Comp. Chem.* **4,** 187–217 (1983).
48. S. J. Weiner, P. A. Kollman, D. A. Case, U. C. Singh, C. Ghio, G. Alagona, S. Profeta Jr and P. Weiner, *J. Am. chem. Soc.* **106,** 765–784 (1984).
49. G. E. Schacher and F. W. de Wette, *Phys. Rev.* **136A,** 78–91 (1965).
50. J. A. Barker and R. O. Watts, *Mol. Phys.* **26,** 789–792 (1973).
51. N. Parsonage and D. Nicholson, *J. chem. Soc. Faraday Trans. 2,* **82,** 1521–1535 (1986).
52. N. Parsonage and D. Nicholson, *J. chem. Soc. Faraday Trans. 2* **83,** 663–673 (1987).
53. P. P. Ewald, *Ann. Physik* **54,** 519 (1917).
54. P. P. Ewald, *Ann. Physik* **54,** 557 (1917).
55. M. Born and K. Huang, *Dynamic Theory of Crystal Lattices.* Clarendon Press, Oxford (1954).
56. S. R. de Groot and L. G. Suttorp, *Foundations of Electrodynamics.* North-Holland, Amsterdam (1972).
57. M. A. Wilson, A. Pohorille and L. R. Pratt, *J. Chem. Phys.* **90,** 5211–5213 (1989).
58. E. Gileadi, E. Kirowa-Eisner and J. Penciner, *Interfacial Electrochemistry.* Addison-Wesley, Reading, Massachusetts (1975).
59. D. A. Rose and I. Benjamin, *J. Chem. Phys.* **95,** 6856–6865 (1991).
60. J. N. Glosli and M. R. Philpott, *J. Chem. Phys.* **98,** 9995–10008 (1993).
61. J. N. Glosli and M. R. Philpott, *J. Chem. Phys.* **96,** 6962–6969 (1992).
62. J. N. Glosli and M. R. Philpott, in *Microscopic Models of Electrode–Electrolyte Interfaces. Symp. Proc. 93-5* (Edited by J. W. Halley and L. Blum), pp. 90–103. Electrochem. Soc., Pennington, New Jersey (1993).
63. S. D. Argade and E. Gileadi, in *Electroadsorption* (Edited by E. Gileadi), pp. 87–115. Plenum, New York (1967).
64. M. R. Philpott, J. N. Glosli and S. Zhu, *Surface Sci.* **335,** 422 (1995).
65. L. D. Landau and E. M. Lifschitz, *Electrodynamics of Continuous Media,* pp. 99–101. Addition-Wesley (1960).
66. H. J. Berendsen, J. R. Grigera and T. P. Straatsma, *J. phys. Chem.* **91,** 6269–6271 (1987).
67. R. W. Impey, P. A. Madden and I. R. McDonald, *J. phys. Chem.* **87,** 5071–5083 (1983).

Chapter 2

Molecular Dynamics Simulation of Interfacial Electrochemical Processes: Electric Double Layer Screening

Michael R. Philpott[1] and James N. Glosli[2]

[1]IBM Almaden Research Center, 650 Harry Road, San Jose, CA 95120–6099
[2]Lawrence Livermore National Laboratory, University of California, Livermore, CA 94551–9900

The status of computer simulations of electric double layers is briefly summarized and a road map for solving the important problems in the atomic scale simulation of interfacial electrochemical processes is proposed. As examples efforts to simulate screening in electric double layers are described. Molecular dynamics simulations on systems about 4 nm thick, containing up to 1600 water molecules and NaCl at 1M to 3M concentration, displayed the main features of double layers at charged metal surfaces including: bulk electrolyte zone, diffuse ionic layer that screens the charge on the electrode and a layer of oriented water next to the surface.

This paper describes the application of molecular dynamics to chemical processes at the interface between a charged metal electrode and aqueous electrolyte. The long range goal is a scheme for the dynamics of chemical reactions on surfaces important in the electrochemical technology of power sources, electroplating, and corrosion control. The paper begins with a summary of our view of the current state of computer simulation applied to interfacial electrochemistry. The status is accompanied with a commentary on problems. To illustrate progress in the field we describe our simulations of screening of charged electrodes by aqueous electrolytes, including previously unpublished work. Double layers are some of the basic organizations found in electrochemical and biological systems that shield fields of layers and arrays of electric charge in contiguous structures. It is important to understand their properties using models that can be solved without making additional approximations. In this paper the structure of the aqueous part of the double layer is given in terms of time independent water and ion probability distribution functions averaged parallel to the metal surface. Electric fields and potentials are calculated from the microscopic charge density profile. These calculations provide a consistent microscopic picture of ions and water in a double layer including the species next to the charged

surface (inner layer), in the 'diffuse layer' (also called the screening layer) and in the bulk zone. The effect of finite sized ions and water are clearly evident, as is the effect of the electric field on the orientation of surface water molecules.

Status of Molecular Dynamics Simulations

Figure 1 (top) is a sketch of the electric potential using Gouy-Chapman-Stern theory[1] in which the diffuse layer ions are treated as point charges, the water as a a dielectric continuum, and OHP and IHP (outer and inner Helmholtz planes) are introduced to mark the distance of closest approach of strongly hydrated ions and contact adsorbing ions respectively. Figure 1 (bottom) shows a molecular scale cartoon of ions and water near a flat charged metal surface. Ideas embodied by pictures like this together with Gouy-Chapman-Stern theory and the thermodynamic theory of surface excess quantities have been used to analyze and interpret experimental electrochemical data[2-5]. The electric potential shown is not consistent with the cartoon because an oriented layer of water would result in a strong oscillation in the potential. The simulations described here and by others show such oscillations near the electrode. They are not predicted by Gouy-Chapman theory. The advent of risc based work stations allows the testing of atomic scale models with thousands of molecules. Monte-Carlo and molecular dynamics computer simulations of ions and water molecules interacting by simple potentials are routinely performed for a few

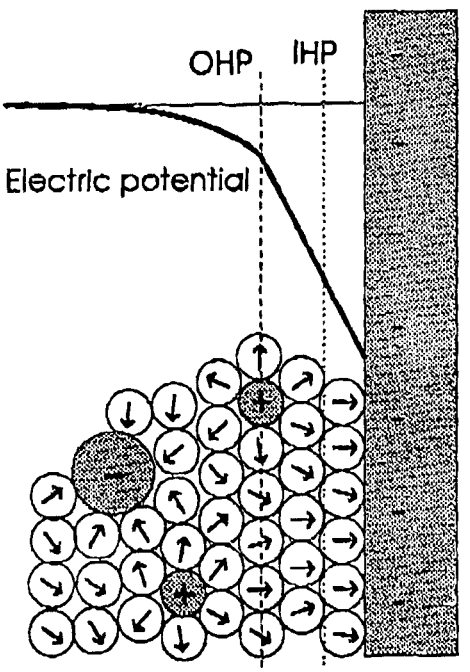

Figure 1. Schematic diagram (top) of electric potential across the double layer based on Gouy-Chapman-Stern model in which the solvent is a continuum dielectric. The cartoon (bottom) depicts a hypothetical arrangement of solvent and ions near a charged surface. Similar pictures are found in electrochemical texts. The labels IHP and OHP mark the inner and outer Helmholtz planes.

thousand water molecules for times up to several nanoseconds. We comment first on electrostatics and potential energy surfaces before other issues.

Electrostatics. In bodies with large but finite numbers of charges, three dimensional sums of electrostatic interactions (eg., ion-ion, dipole-dipole) can be decomposed into separate bulk-like and surface-boundary parts. The latter part is responsible for the phenomenon of conditional convergence when the size of the system is taken to infinity. For electrified interfaces it is essential that the long range part of the electrostatic interaction be computed without truncation in a manner consistent with the boundary conditions. For some geometries (eg., planar) the electric field of surface charge can be calculated by the method of images. There is some evidence from simulations on ions in polar solvents that truncated long range electrostatics result in correlations that cause like charged ions to attract each other. The crystal optics based methods of Ewald and Kornfeld are the simplest for calculating electrostatic fields[6]. The algorithm works for all space group symmetries. At best this method is order $N^{1.5}$ in the number of charges N. There are 2D summation methods that are faster[7, 8]. In our simulations we use the order N fast multipole method (fmm) developed by Greengard and Rokhlin [9-12]. This is a useful method for electrochemical simulations where a variety of boundary conditions (periodic, Dirichlet, Neumann or mixed boundaries) are encountered. It can also be adapted so that regions of low charge density are not subdivided when the charge count falls below a specified integer[11]. It is restricted to cubic simulation cells. The fmm is faster than Ewald for systems exceeding a few hundred charges[13]. Particle-mesh methods have been extensively used for long range r^{-1} potential problems[14]. For most systems P^3M is faster than fmm and can be used with orthorhombic simulation cells[15]. Parallel metal surfaces have an infinite set of multiple electrostatic images that have to be summed in plane-wise fashion[8, 16]. Recently we calculated distributions for ions between parallel metal plates held at a constant potential difference[17, 18]. These distributions defined charge distributions that were used to compute time independent electric fields and potentials across the cell. The effect of additional averaging over space volumes comparable to water molecules was also explored[19, 20]. Though most experiments are done at constant potential, there are very few simulations at constant potential[17, 18].

Molecule-Molecule and Molecule-Metal Potentials. There are continuing improvements in molecule-molecule potentials. High quality efforts are directed at improving the interaction, including electronic polarizability and other tensor properties[21, 22]. There are also potentials that include three body terms explicitly[23]. Possibly the best atom-metal potential is due to Barker[24]. The Barker potential for Xe/Pt(111) is an excellent fit to a large body of experimental data. There have been numerous quantum chemistry studies of ions and water on metal clusters some with applied fields and others on charged clusters to imitate the electrochemical environment (for water references see Zhu[25], for ions on clusters see Pacchioni[26]). So far only a few have been parameterized into forms that can be easily used in an MD code[25, 27-29]. Electric double layers on Ag and Au are thermodynamically stable over wide potential range[30]. It is unfortunate that simulations have focussed almost exclusively on Pt for which there is little experimental

data. The reason is there is an easy to use set of potentials derived from quantum chemistry calculations of small Pt clusters with adsorbed water and ions. In principle cluster calculations performed with Cu, Ag or Au would be more reliable because relativistic orbital contractions and spin orbit effects. are not so important in these sp metals and because the d shell is more tightly bound. Recently several publications have reported cluster calculations for water and ions on Hg[31, 32] including a parameterization to give a pair potential for MD studies.

Dynamics. There are calculations in which the metal is modeled as an Einstein solid with harmonic vibrations[33]. When surface molecules and ions are strongly adsorbed molecular dynamics becomes an inefficient way to study surface processes due to the slow exchange between surface and solution. In this case it is possible to use umbrella sampling to compute distribution profiles[34, 35]. Recently the idea underlying Car-Parrinello was used for macroion dynamics[36, 37] in which the solvent surrounding charged macroions is treated as a continuum in a self consistent scheme for the potential controlling ion dynamics. Dynamical corrections from the solvent can be added. There is a need to develop statistical methods to treat the dynamics of complex objects that evolve on several different time scales.

Interfacial Electron Transfer. There have been several studies of electron transfer reactions[17, 38]and the connection with Marcus's theory[39]. It may be possible to use a Car-Parrinello like scheme on that part of the system directly affecting the electron transfer. There has also been very interesting studies of the ferro-ferri redox couple in solution[40, 41] that address many issues related to electron transfer from an electrode to a hydrated ion. Slow processes can be treated by transition state methods like the ones used in solid state ionic conductivity[42].

Ensembles. One goal of simulations is the calculation of experimental quantities. The most challenging are the Gibbs free energies of adsorption. Currently there is no proven scheme for constant chemical potential simulations of electrolyte adsorption on metals. It seems possible to develop Andersen's method[43] for (N,P,T) ensembles. Another possibility is an analog of the Gibbs ensemble[44] for electrolytes between plates with a bulk sample forming the second phase. In an interesting development the grand canonical Monte Carlo method was used for atomic fluid mixtures in a slit pore[45, 46].

Road Map

The intention is modest though the title of this section sounds pretentious. Given the current state of theory and simulation can we identify a path to useful computation of reactions important to electrochemical technologies? The science problems cover a broad range: deposition and dissolution of metal, formation of oxide layers, electron transfer from electrodes to ions, and charge migration in complex fluid phases. We comment first on the possibility of developing two existing methods, ab initio molecular dynamics and potential energy surface dynamics, to electrochemistry.

Ab Initio Molecular Dynamics. Chemical reactions involve the reorganization of electrons about the nuclei involved in the bond changes. The ab initio molecular dynamics scheme developed by Car and Parrinello[36] permits an accurate de-

scription of both electronic and nuclear rearrangements that occur during a reaction. The penalty for including electronic coordinates explicitly in an electrochemical simulation is the restriction to relatively few water molecules. Liquid water and proton transfer have been studied[47, 48]. The computational problem is immense so that at present the study of hundreds of water molecules takes too long. This number is quite enough for studying H-bonding and dissociation and the dynamics of the hydration of ions but is insufficient to deal with double layer structure or reactions of hydrated ions with charged metals.

Potential Energy Surfaces. For systems where some or all of the dynamics can be described by a potential energy surface (PES) it is possible to avoid solving the electronic Schrodinger equation, and use instead a PES parameterized with experimental data. Several cases already exist. First is the well known S_N2 reaction

$$Cl^- + H_3C-Cl \rightarrow Cl-CH_3 + Cl^-. \qquad [1]$$

The molecular dynamics of this reaction has been studied in water[49]. Another quite different example is the Brenner bond order potential[50] used to describe the dynamics of homolytic bond fission and formation in carbon and hydrogen containing systems[51]. These two examples involve the making or breaking of two electron bonds between low Z atoms. Explicit degrees of freedom for the electrons are avoided though the use of a PES. In gas-surface adsorbate theory considerable progress has been made understanding chemical dissociation reactions and physical sputtering using a combination of LEPS potential for the diatomic on the metal with a many body embedded atom-like potential for the metal[52]. The electrochemical problems are harder. They involve charged metal surfaces, charge transfer in polar environment and dynamics on vastly different time scales.

Road Map. Consider the deposition and dissolution of metal ions on charged surfaces. If systems can be identified where adiabatic potentials describe the nuclear motion then by analogy with the experience gained with the dissociation of diatomics on metal surfaces[52] and with carbon-hydrogen chemistry[53] it should be possible to describe how metal ions adsorb on metals and how metals dissolve. A key step is the calculation of surface charge on the metal and how it fluctuates at adatoms sites. Solvated counter charge amplifies the fluctuations and increases the probability of charge transfer at the site to a degree that metal deposition or dissolution begins[54]. Continuing this avenue it should also be possible to formulate schemes that describe the creation of insoluble metal oxide layers. This would require a model for water decomposition on metals. The central force model which permits water dissociation[55, 56], could be developed for a surface environment. Consider the process where an electron crosses a bridging ligand to an ionic center or organic moiety to a initiate chemical reaction. Some of these reactions could be studied by treating the electron as a quantum particle moving in a potential defined by the classical motion of molecules and ions in the double layer. Solvated electrons in liquids have been studied this way. If the electron cannot be so easily decoupled then a hybrid Car-Parrinello π-orbital scheme might be developed. Finally we comment on ion mobilities in complex fluids in lithium batteries. Progress here may require

ideas borrowed from small polaron motion in solids, using transition state dynamic methods of Bennett[42], or using recent theories of macroion motions[37]. Though we are presently a long way from providing technologically useful information, being able to model aspects of these processes would provide atomic scale insight as to how these technologies work.

Details of the Model

Screening is treated using the immersed electrode model[13, 57, 58]. A layer of electrolyte with an excess of positive ions is confined by a semi-infinite metal on the rhs and a restraining non-metallic wall on the lhs. There is no external electric field. The metal is grounded to zero electric potential. The charge on the electrode equals the image charge of the excess positive ions (-4e or -8e) so that the metal charge is completely screened by the ions in solution. The difference between these and earlier simulations [13, 57-60] is size, here there are enough ions and water to form a bulk electrolyte region where the solution is locally neutral. Because there is only one metal surface (shown on the rhs in all the figures) there are no multiple electrostatic images in the direction perpendicular to the metal[8, 16]. The electric field and potentials are calculated using previously developed methods[19, 20].

This work uses the SPCE water model[61] (three charged mass points, q_H = 0.4238e, bond angle 109.5°, OH bond length 0.1 nm, Lennard-Jones sphere with radius σ = 0.317 nm and well depth ε= 0.650 kJ/mole) and associated parameters for NaCl[62]. The coordinate origin is at the center of the cell, and the axes are perpendicular (z) and parallel (x,y) to the metal surface. The simulation cell has edge length L=3.724 nm, the flat metal plane is at z = 1.862 nm and the flat restraining wall at z = -1.862 nm. The cell contains upto 1600 water molecules and the ion concentrations are approximately 1M, 2M or 3M NaCl. The metal charge density is either -0.046 Cm^{-2} ($-4eL^{-2}$) or -0.092 Cm^{-2} ($-8eL^{-2}$). Contact adsorption of ions is minimized. The cation has a smaller radius than the anion, so its hydration shell is strongly bound making it difficult for it to contact adsorb. The negative metal charge makes it energetically unfavorable for the anions Cl^- to contact adsorb.

Two potentials are used to describe the interaction of water and ions with the metal. A 9-3 potential is used to for the Pauli repulsion and the attractive dispersive interactions between molecules or ions and the metal. The interaction between a charge on an ion or water with the conduction electrons of the metal is modeled with a classical electrostatic image potential. The position of image plane and origin plane (same as the plane through nuclei of the surface) of the 9-3 potential was taken to be coincident. In real materials the image and nuclear planes are not coincident. This is not important in the simulations because the thickness of the repulsive wall is large (ca. 0.247 nm). The 9-3 atom-surface wall parameters describing interaction with nonconduction electrons were chosen to be the same as that used by Lee etal[63], A=17.447x10^{-6} kJ(nm)^6/mole and B=76.144x10^{-3} kJ(nm)^3/mole for the O atom. The A and B parameters for H were set to zero. The potential corresponding to these parameters describe a graphite-like surface. A useful reference point in the wall potential is at z_w=1.615 nm where the 9-3 wall potential changes sign. Each simulation was run for about a nanosecond, and the instantaneous positions of all the

atoms recorded every picosecond. The first 100 ps were discarded as anneal time. The density probability functions $\rho(z)$ were constructed by binning the configurations in bins (width L/800) parallel to the metal surface to give functions of z only.

Screening of Charged Metal Electrodes in SPCE Electrolyte

We begin with remarks on the screening of charged surfaces by aqueous electrolytes. At high salt concentrations the region with excess ionic charge is microscopically small. For dilute solutions (<0.1M) a crude estimate of the screening zone thickness is given by the Debye-Hückel screening length[64]

$$d = \sqrt{\left(\varepsilon kT/(8\pi e^2 n_b \nu^2)\right)} \,. \qquad [2]$$

Here ε is the macroscopic dielectric constant of the solvent (ca. 80 for water), ν the valence of the ion (one in this paper), and n_b is the bulk concentration of the ions. Typical values of d are: 3 nm in 0.01M, 1 nm in 0.1M, 0.3 nm in 1.0M, and 0.2 nm in 3M NaCl solutions. In high salt concentrations the screening should be more efficient and the screening length smaller, but since the length for 1M NaCl is the diameter of a water molecule, and the value for 3M NaCl is even smaller, these values mean nothing without the additional insight provided by MD simulations. At high concentrations there are many problems with simple Gouy-Chapman theory[65-67] and many modifications have been proposed[64]. There are three main problems: the dielectric constant of water in a high surface field, the lower length scale due to the finite molecular size, and correlated motion amongst ions and water. For example there is no reason to believe that the value of ε is 80 near a surface or in a field high enough for dielectric saturation to occur. This aspect has been discussed many times in the electrochemical literature[68]. Though we take the Debye length for concentrated solutions as an rough measure of double layer thickness, we should be very cautious when d approaches the size of a water molecule.

Figure 2 shows the distribution of the ions for three separate calculations with concentrations 1M, 2M and 3M NaCl. The charge on the electrode was -4e for 1M and 2M and -8e for 3M. The temperature was 30°C for 1M and 2M, and 100°C for the 3M NaCl solution. Note that there is no significant contact adsorption. All the peaks in the ion distributions occur away from the position of closest approach z_w=1.612 nm to the metal. This is precisely the situation we contrived for the reasons given before. The ion concentrations are approximately the same for $|z| < 1.0$ nm. This identifies the region of the system with bulk electrolyte properties. For $|z| < 0.5$ nm the two ion profiles are the same within 10 to 20%, for all the simulations. The bulk region is smaller for 1M NaCl because the screening layer is thicker. The integrated ion densities are monotonically increasing curves in Figure 2. They provide a rough measure of overall charge neutrality from the restraining wall to the metal. The vertical arrows indicate roughly where the ion charge densities start to diverge because of screening. Also shown in Figure 2 are the results of a calculation of ion densities using simple Gouy-Chapman theory. For optimal comparison the electrode was assume to start at z=1.612 nm. These superimposed curves show how lack of atomic scale structure limits the application of Gouy-Chapman theory. This is

graphic evidence that there are important details in MD simulations due to hydration, molecular size, and water layering near charged surfaces. In each case the width of the screening layer is too small to justify the description as 'diffuse' (though we will continue to use this term). To estimate the diffuse layer width we measure from the z=1.615 nm (where wall potential changes sign) to the point where the difference in integrated ion densities is e^{-1} of the metal charge (8e for 3M, 4e for 1M and 2M).

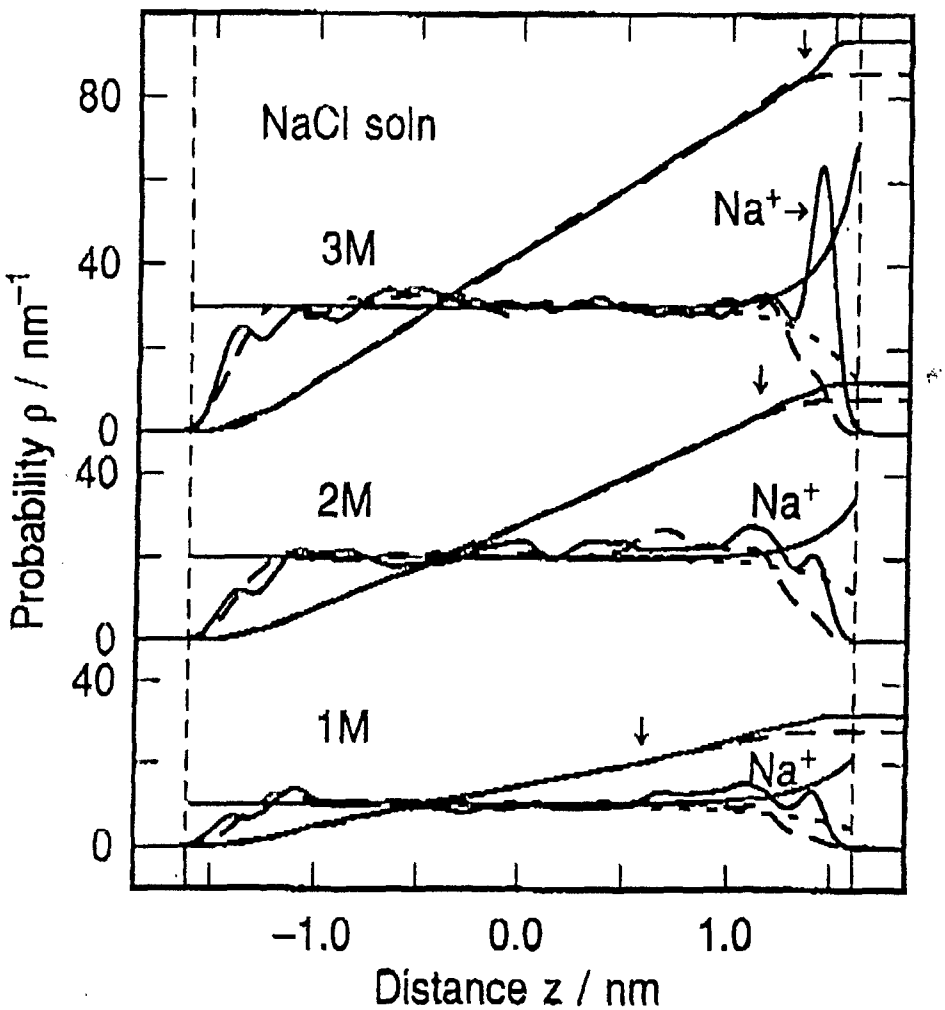

Figure 2. Ion probability distribution profiles for 1M to 3M NaCl solutions. Solid line Na^+ ion, broken line Cl^-. 1M and 2M solution at 30°C and -4e electrode charge, 3M solution at 100°C and -8e electrode charge. Vertical dash lines at |z|=1.615 nm mark where the 9-3 wall potential passes through zero, and beyound which water and ions are repelled. Inclined curves rising monotonically from left to right are the integrals of the corresponding ion distributions. Gouy-Chapman theory ion profiles shown as 'flat' curves for $|z| < 1.615$nm that rise (Na^+) or fall (Cl^-) for $z > 1.0$ nm.

For the solutions we find: 0.5 nm (0.31 nm) for 1M, 0.4 nm (0.24 nm) for 2M, 0.2 nm (0.18 nm) for 3M. The Debye shielding lengths calculated using Eqn(2) are in parentheses. Made with these favorable assumptions the agreement is remarkably close. It would change if we used $\epsilon = 6$, a value more appropriate for a zone in which the dielectric properties of water are at saturation values[68].

Looking at the fine structure in the density profiles we see that on the metal side all the chloride distributions have weak features at ca. 1.2 nm and 1.4 nm. Both appear to be associated with peaks in the cation distribution and may therefore be due to contact pairs or solvent separated pairs. Of course the SPCE model for water was not designed with high salt concentrations in mind, so the ion pairs may be more a feature of the model and not nature. Correlation between ions at high salt concentrations alter the distribution near the charged surface. Note that there is no association of oppositely charged ion peaks at the left wall in Figure 2.

1M NaCl Solution

Figures 3, 4 and 5 show the results of an MD simulation using 1M NaCl solution. The simulation cell contains 32 Na^+ ions, 28 Cl^- ions, and 1576 water molecules at 30°C. The electrostatic charge on the electrode surface due to the difference in number of positive over negative ions is -4|e| or -0.046 Cm^{-2}. The top panel in Figure 3 shows the probability density profiles for the water proton, water mass center, Na^+ ions and Cl^- ions. Both ion distributions have been smoothed to permit clearer identification of variations in density with position. We saw in Figure 2 the near coincidence of the integrals of the ion density for $z < 0.7$ nm which shows that the electrolyte is approximately charge neutral before this point. For $z > 0.7$ nm the integrated densities systematically diverge as expected for a transition from the locally neutral 'bulk' electrolyte into the 'diffuse' part of the electric double layer. The Na^+ ion distribution shows well defined structure in the form of a broad peak at ca. 1.1 nm, and a sharp peak at 1.4 nm. The water and proton distributions appear flat for $|z| < 0.8$ nm. On the metal side the water probability distribution has peaks at 0.9 nm, 1.2 nm, and a strong asymmetric peak at 1.6 nm. This latter feature is a superposition of a broad feature at 1.5 nm and a narrow peak at 1.6 nm. The peaks in the H distribution are at 0.9 nm, 1.2 nm, 1.55 nm, and ca. 1.7 nm. The last peak at 1.7 nm comes from protons in water OH bonds pointing at the metal.

The bottom panel in Figure 3 shows the potential calculated using the atom method, and the components of the potential calculated by the molecule method[19, 20]. The potential at the metal surface is about -2V. The potential in the 'bulk-like' zone comes mainly from the water quadrupole. This is a sensitive feature of the water model. Most water models are parameterized on bulk properties and not sensitive to changes in quadrupole. The electronic polarizability has been included in a average way. Tuning the properties of the water model to correctly account for these subtle effects is an important goal of future research. The monopole curve is from the ionic charge. If the system were truly neutral then the monopole curve would be flat and zero all the way to the beginning of the diffuse layer. The transition to monotonic decrease starting near $z = 0.7$ nm is another indicator of where the diffuse layer begins in this simulation. Note that combined monopole and dipole

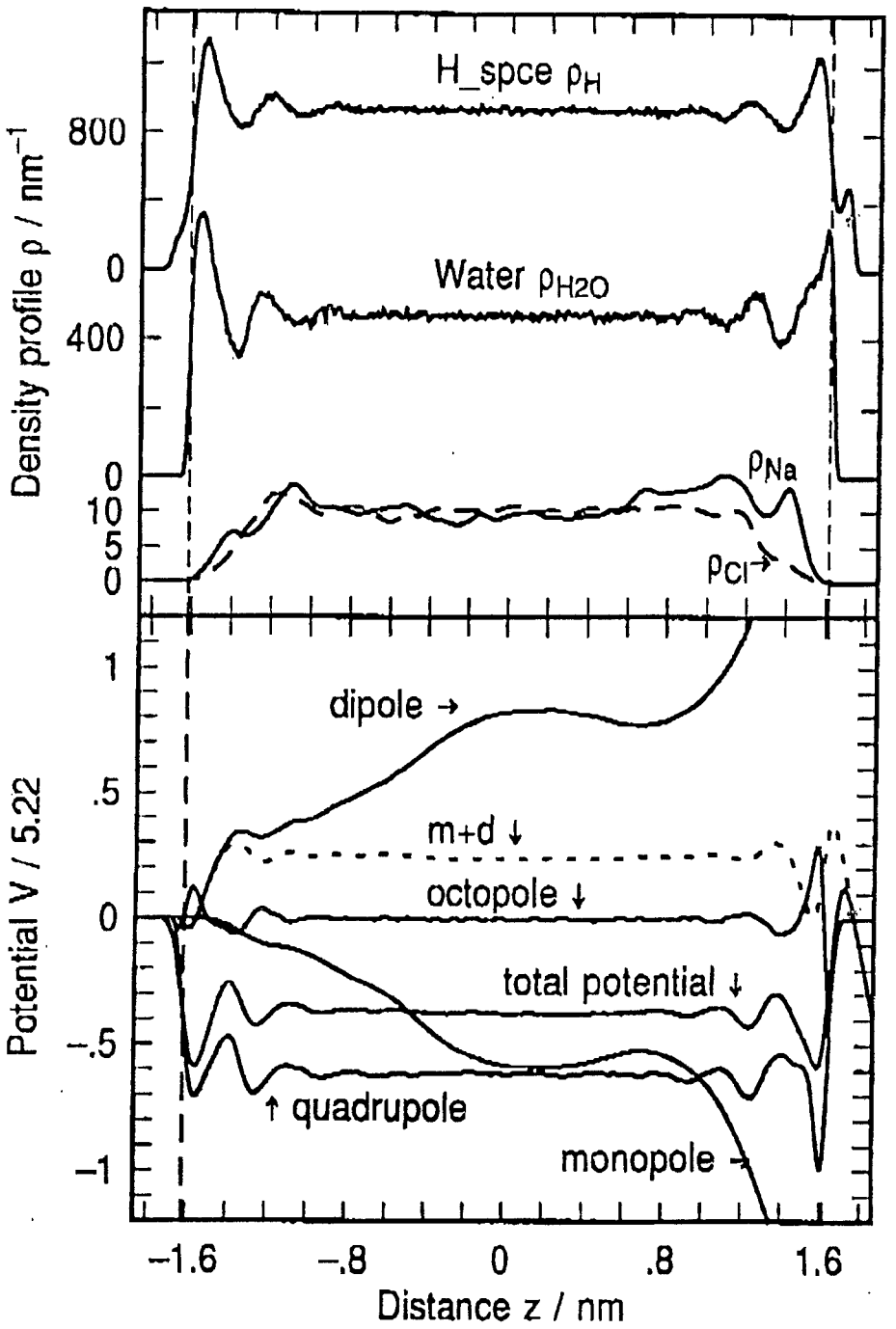

Figure 3. 1M NaCl solution at 30°C and -4e electrode charge. Top. Probability distribution profiles across the cell for H atom, water, and ions N^+ and Cl^-. Bottom. Total electric potential and component (monopole, dipole, combined monopole plus dipole, quadrupole and octopole) electric multipole potentials. The total potential was calculated from the total electric charge distribution. Note that though the monopole and dipole components go off scale their sum is finite and weaker than the quadrupole component of the potential for the SPCE water.

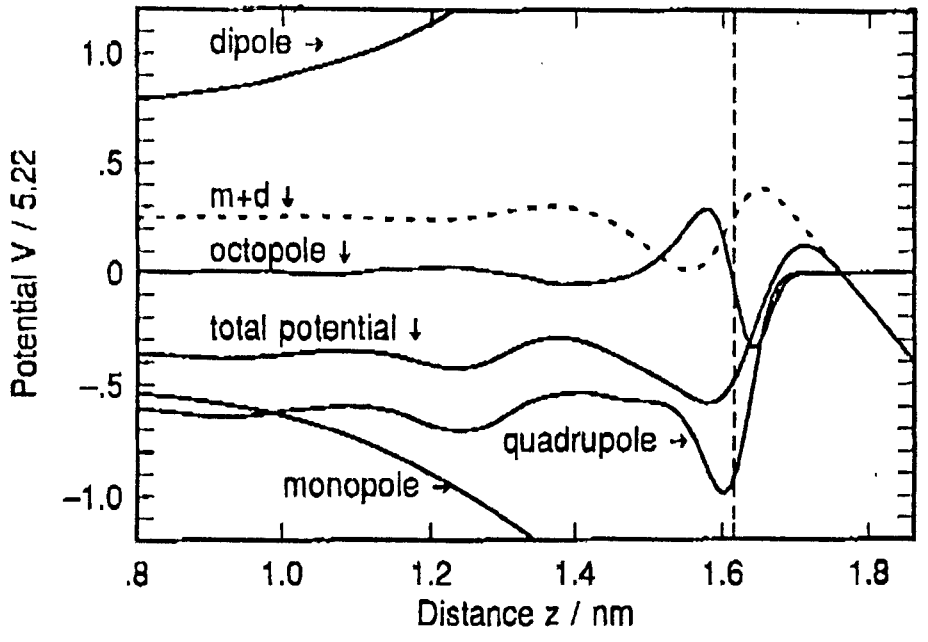

Figure 4. 1M NaCl solution at 30°C and -4e electrode charge. Detail of individual electric multipole component potentials shown in Figure 3 (bottom) for z > 0.8 nm.

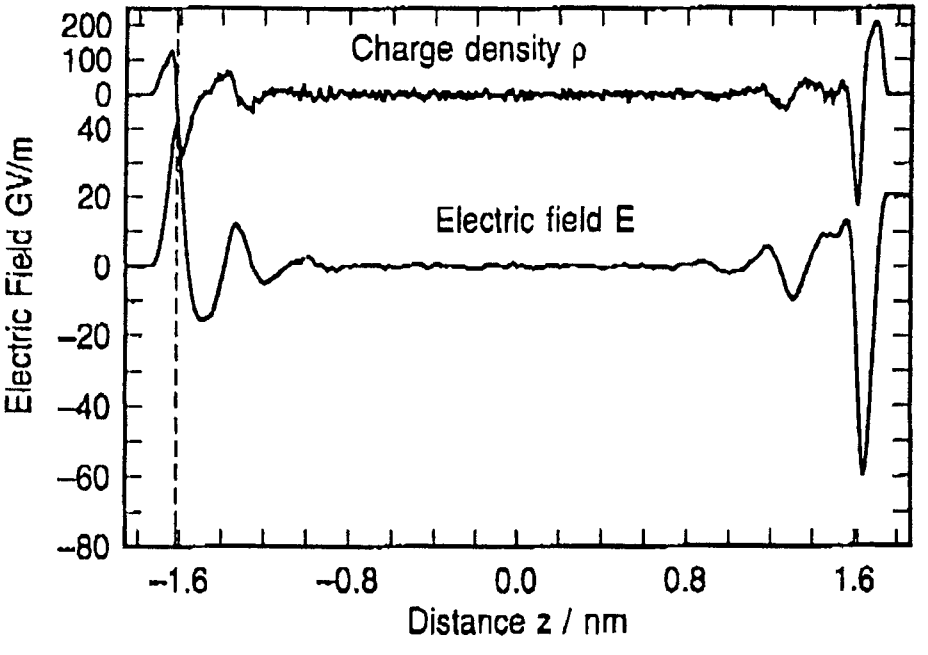

Figure 5. 1M NaCl solution at 30°C and -4e electrode charge. Total microscopic electric charge density and total electric field obtained by integrating the former.

potential curve m+d shows that the dipole potential almost completely compensates the monopole. Adding the quadrupole to m+d shifts the core region downwards by 3V and brings the molecular calculation of potential into fair correspondence with the atom method of calculation. Adding the octopole improves the agreement at the walls. The molecular method has larger extrema near the surface compared to the atom method. The reason for this is the need to include many high order multipoles in the molecule method. However the contact potential is the same in each case since it depends only on m and d[69].

Figure 4 shows a detail of the the potentials shown in Figure 3 (bottom) for the region $z > 0.8$ nm. We note that the monopole and dipole determine the potential at contact. The quadrupole potential is very important in bulk and at the surface. The octopole potential is important near the surface. In the future as water models improve it will be very important to include these terms. Obviously the surface potential relative to bulk solution must include the quadrupole term.. Figure 5 shows the atomic charge density and the electric field along the z axis. Note that the charge density appears flat for $|z| < 0.8$ nm. The contribution from the ionic charge for $z > 0.8$ nm is not evident because the charge on the water molecules dominates. The electric field was obtained by integration of the charge density from $-\infty$ to position z. The field is flat with small variations around zero in the region $|z| < 0.8$ nm. Near the metal the electric field undergoes a series of rapid oscillations due to the water packing structure at the interface. The small overall rise in field from bulk to surface is due to the excess Na^+ charge in the screening layer. The oscillation near $z = -1.615$ nm is due to layering at the restraining wall. This is an unwanted artifact of the immersed electrode model. It does not occur if the water density is decreased to the point that a vapor-liquid interface opens up at the restraining wall. Space prevents discussion of emersed electrodes[70, 71] which have a vapor-liquid interface[72-74] and a liquid-solid interface[75].

2M NaCl Solution

Figure 6 shows the results for a 2M NaCl solution at 30°C. There are 62 Na ions, 58 Cl ions and 1516 water molecules, the image charge on the electrode is -4|e|. The cation and anion concentrations are approximately the same for $|z| < 1.0$ nm. The bulk region appears larger than in 1M NaCl solution consistent with narrower screening zone. There are many similarities between Figures 3 and 6. The detailed proton and water profiles for $z > 1.4$ nm look the same. The bottom panel in Figure 6 shows the total potential calculated using the atom method, and the components of the potential calculated by the molecule method. The contact potential is about -2V, just the same as in the 1M case. The difference between 1M and 2M come mainly from the ion distributions and their direct interaction with the waters. Thus the monopole and dipole potentials are different, but since as already seen for 1M, they cancel each other, the main contribution to the total potential in the bulk region comes from the quadrupole. The water distributions for 1M and 2M are also similar and so are the potentials which come from water. Again if the system were truly neutral the monopole curve would be flat all the way to the edge of the diffuse layer. It is flatter than the 1M case and oscillates about zero before diving down to large

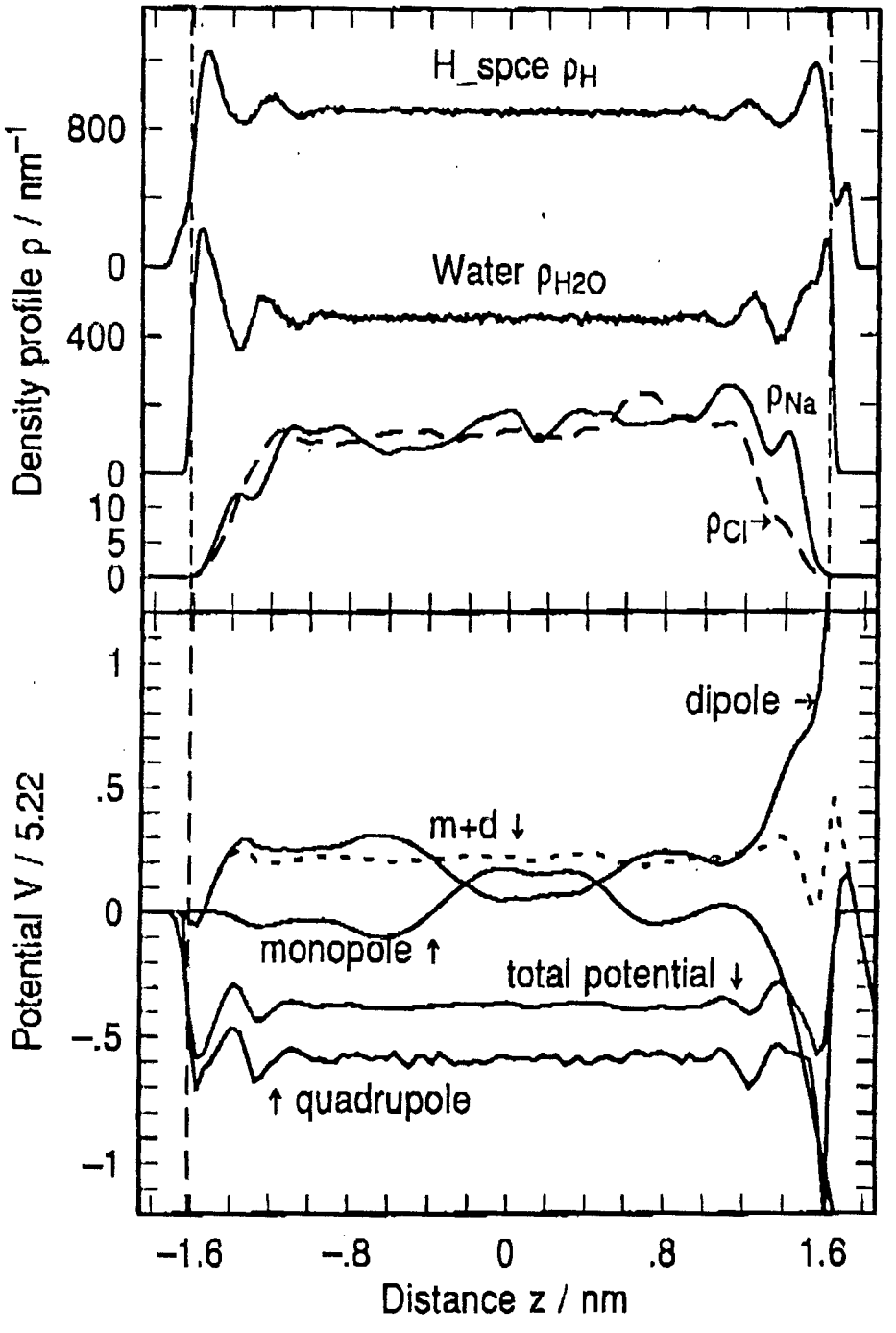

Figure 6. 2M NaCl solution at 30°C and -4e electrode charge. Top, Probability density distribution profiles across the cell for H atom, water, Na^+ and Cl^- ions. Bottom. Total electric potential and component multipole potentials. Total potential calculated by atom method (see text). Note that the combined monopole and dipole components give a flat contribution across most of the cell. Octopole potential not displayed for clarity.

negative values for z > 1.2 nm. A key observation is the dependence of m+d on position. In all the simulations the m+d potentials are similar even though m and d are not. The transition to monotonic decrease starts near z = 1.2 nm is another indicator of where the diffuse layer begins in this simulation. Including the quadrupole shifts the 'core' region down by -3V and brings the molecular calculation of potential into correspondence with the atom potential.

3M NaCl Solution

Figure 7 displays the results for 3M NaCl. There are 94 Na ions, 86 Cl ions and 1463 water molecules at 100°C, and the charge on the electrode is -8|e| or -0.092 Cm^{-2}. Calculations at high temperature were originally selected to improve the statistics. Subsequently the temperature dependence in the range 30 to 100°C was found to be weak. The Na^+ screening charge is concentrated in the peak at 1.45 nm less than one water diameter removed from where the 9-3 wall potential passes through zero (z_w = 1.615 nm). The peak in the cation distribution results from the strong primary hydration shell of the cation. The solvent layer at the electrode also effects the position and shape of the cation distribution near the metal. Note that for |z| < 1.0 nm the cation distribution is approximately flat at 30 ions nm^{-1}. There is also a small peak on the left hand side at ca. z = -1.4 nm, that is not associated with screening but is likely due to layering of the water molecules at the restraining wall. The chloride probability distribution has no major structural features, certainly none like the Na^+ screening peak at z = 1.45 nm. Starting from the metal on the right side of Figure 1, the chloride ion distribution rises to a plateau for |z| < 1.00 nm. The chloride and sodium ion probabilities are sufficiently similar across the plateau region for us to call this the bulk zone. This 3M NaCl simulation has the best statistics, as can be seen by the degree of local charge neutrality (ion densities are the same), and very nearly equal integrated densities shown in Figure 2. The metal charge is twice that of 1M and 2M creating a stronger surface electric field, which results in more oriented waters in the first layer. The height of the proton peaks either side of the main water peak suggest that some H bonds to the bulk region are broken and that OH bonds point directly toward the metal. This electric field effect is distinct from localization of water on Pt(100) and Pt(111) surfaces in the simulations of Heinzinger and Spohr[27], and Berkowitz[28, 29]. In these papers water is localized on top sites of the Pt surface due to directed features in the chemisorptive potential.

The bottom panel of Figure 7 shows the potential calculated using the atom method, and some of the components of the potential calculated by the molecule method. The contact potential is larger due to higher electrode charge. Once again the importance of quadrupole terms is apparant. The m curve due to the ionic charge hovers around zero for z < 1.4 nm. The monopole potential is quite flat outside the screening layer. The transition to monotonic decrease starting near z = 1.4 nm is an indication of where the diffuse layer begins. Again m+d shows that the dipole potential completely compensates the monopole outside the screening zone. Including the quadrupole shifts the core region by -3V and brings the m+d potential into closer correspondence with the total potential calculated by the atom method.

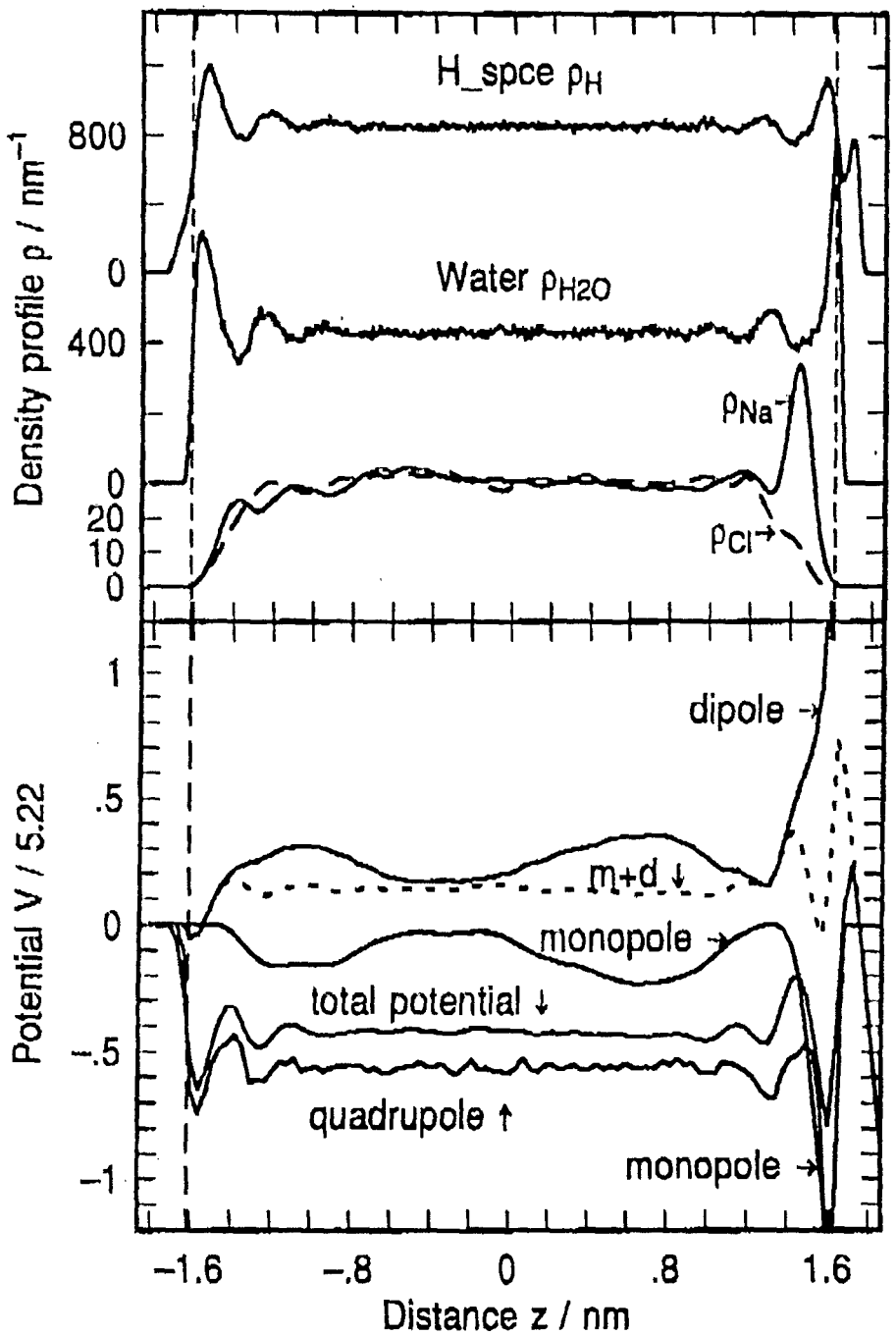

Figure 7. 3M NaCl solution at 30°C and -4e electrode charge. Top. Probability density distribution profiles across the cell for H atoms, water, Na^+ and Cl^- ions. Bottom. Total electric potential and component multipole potentials. Total potential was calculated by atom method (see text). Note that monopole and dipole potentials are flat across most of the cell because the screening zone is narrow for 3M NaCl solution. Octopole potential not displayed for clarity.

Conclusions

In this paper we briefly reviewed the status of MD simulations of electrochemical interfaces and outlined a map of how calculations might further contribute to understanding technology. As an example of current simulation capability we discussed the structure of electric double layers for systems with 1500 water molecules and salt concentrations from 1M to 3M NaCl. Water structure near charged metal walls is not an artifact of small size. In 1M NaCl the double layer is about 1 nm thick (about three layers of water) while in 3M solution the screening layer was narrower than a water molecule. Water layers at the surface significantly affected the distribution of ions near the metal, creating features in the probability distributions that are not describable in the Gouy-Chapman-Stern model.

Acknowledgments. This research was supported in part by the Office of Naval Research. A referee is thanked for helpful comments. The contributions of JNG were performed under the auspices of US DOE contract W-7405-Eng-48.

Literature Cited

1. Gileadi, E., Kirowa-Eisner, E., Penciner, J. *Interfacial Electrochemistry*; Addison-Wesley: Reading, MA, 1975.
2. Grahame., D. C. *Chem. Rev.* **1947**, *41*, 441 - 501.
3. Brockris, J. O., Devanathan, M. A., Müller, K. *Proc. Roy. Soc.(London)* **1963.**, *A274*, 55-79.
4. Dutkiewicz, E., Parsons, R. *J. Electroanal. Chem.* **1966**, *11*, 100-110.
5. Parsons, R. *Chem. Rev.* **1990**, *90*, 813-826.
6. Born, M., Huang, K. *Dynamical Theory of Crystal Lattices*; The Clarendon Press: Oxford, England, 1954.
7. Schacher, G. E., de Wette, F. W. *Phys. Rev.* **1965**, *136A*, 78-91.
8. Rhee, Y. J., Halley, J. W., Hautman, J., Rahman, A. *Phys. Rev. B* **1989**, *40*, 36-42.
9. Greengard, L. F. *The Rapid Evaluation of Potential Fields in Particle Systems*; The MIT Press: Cambridge, MA, 1987.
10. Greengard, L., Rokhlin, V. *J. Comp. Phys.* **1987**, *73*, 325-348.
11. Carrier, J., Greengard, L., Rokhlin, V. *Siam J. Sci. Stat. Comput.* **1988**, *9*, 669-686.
12. Greengard, L., Rokhlin, V. *Chemica Scripta* **1989**, *29A*, 139-144.
13. Glosli, J. N., Philpott, M. R. In *Microscopic Models of Electrode-Electrolyte Interfaces. Symp. Proc. 93-5*; J. W. Halley L. Blum, Ed.; Electrochem. Soc.: Pennington, New Jersey, 1993. 80-90.
14. Hockney, R. W., Eastwood, J. W. *Computer Simulation using Particles*; McGraw-Hill: New York, 1981.
15. Pollock, E. L., Glosli, J. N. *Comput. Phys. Commun.* **1996**, *95*, 93 - 110.
16. Hautman, J., Halley, J. W., Rhee, Y. *J. Chem. Phys.* **1989**, *91*, 467-472.
17. Halley, J. W., Hauptman, J. *Phys. Rev. B* **1988**, *38*, 11704-11710.
18. Philpott, M. R., Glosli, J. N., Roberts, J. *unpublished* **1996.**
19. Glosli, J. N., Philpott, M. R. *Electrochimica Acta* **1996**, *41*, 2145 - 2158.

20. Philpott, M. R., Glosli, J. N. *J. Electroanal. Chem.* **1996**, *409*, 65 - 72.
21. Stone, A. J. *Molec. Phys.* **1985**, *56*, 1065 - 1082.
22. Price, S. L. *Phil. Mag.* **1994**.
23. Dang, L. X., Caldwell, J., Kollman, P. A. *preprint* **1990**.
24. Barker, J. A., Rettner, C. T. *J. Chem. Phys.* **1992**, *97*, 5844 - 5850.
25. Zhu, S., Philpott, M. R. *J. Chem. Phys.* **1994**, *100*, 6961-6968.
26. Pacchioni, G., Bagus, P. S., Nelin, C. J., Philpott, M. R. *Internat. J. Quantum Chem.* **1990**, *38*, 675-689.
27. Heinzinger, K. In *Computer Modeling of Fluids Polymers and Solids*,; C. R. A. Catlow, S. C. Parker, M. P. Allen, Ed.; Kluwer, Holland: 1990; v293, NATO ASI Series C. 357-404.
28. Reddy, M. R., Berkowitz, M. *Chem. Phys. Letters* **1989**, *155*, 173-176.
29. Raghavan, K., Foster, K., Motakabbir, K., Berkowitz, M. *J. Chem. Phys.* **1991**, *94*, 2110-2117.
30. Valette, G. *J. Electroanal. Chem.* **1981**, *122*, 285 - 297.
31. Sellers, H., Sudhakar, P. V. *J. Chem. Phys.* **1992**, *97*, 6644 - 6648.
32. Nazmutdinov, R. R., Probst, M. M., Heinzinger, K. *J. Electroanal. Chem.* **1994**, *369*, 227 - 231.
33. Spohr, E. *Chem. Phys.* **1990**, *141*, 87 - 94.
34. Rose, D. A., Benjamin, I. *J. Chem. Phys.* **1991**, *95*, 6856-6865.
35. Perera, L., Berkowitz, M. L. *J. Phys. Chem.* **1993**, *97*, 13803 - 13806.
36. Car, R., Parrinello, M. *Phys. Rev. Lett.* **1985**, *55*, 2471.
37. Löwen, H., Hansen, J., Madden, P. A. *J. Chem. Phys.* **1993**, *98*, 3275-3289.
38. Straus, J. B., Voth, G. A. *J. Phys. Chem.* **1993**, *97*, 7388-7391.
39. Marcus, R. M. *J. Chem. Phys.* **1965**, *43*, 679.
40. Halley, J. W., Hautman, J. *Ber. Bunsenges. Phys. Chem.* **1987**, *91*, 491-496.
41. Bader, J. S., Chandler, D. *J. Phys. Chem.* **1992**, *96*, 6423 - 6427.
42. Bennett, C. H. In *Algorithms for Chemical Computations*; R. E. Christoffersen, Ed.; ACS Symposium Series 46: Washington DC, 1977. 63-97.
43. Andersen, H. C. *J. Chem. Phys.* **1980**, *72*, 2384-2393.
44. Smit, B. In *Computer Simulation in Chemical Physics*; M. P. Allen D. J. Tildesley, Ed.; Kluwer, Holland: 1993; v397, NATO ASI Series C. 173-209.
45. Nicholson, D., Parsonage, N. G. *Computer Simulation and the Statistical Mechanics of Adsorption*; Academic Press: New York, 1982.
46. Cracknell, R. F., Nicholson, D., Quirke, N. *Mol. Phys.* **1993**, *80*, 885 - 897.
47. Laasonen, K., Sprik, M., Parrinello, M., Car, R. *preprint* **1993**.
48. Tuckermann, M., Laasonen, K., Sprik, M., Parrinello, M. *preprint* **1994**.
49. Bergsma, J. P., Gertner, B. J., Wilson, K. R., Hynes, J. T. *J. Chem. Phys.* **1987**, *86*, 1356-1376.
50. Brenner, D. W. *Phys. Rev. B* **1990**, *42*, 9458-9471.
51. Glosli, J. N., Belak, J., Philpott, M. R. *Electrochem. Soc. Symposium Proc.* **1995**, *95-4*, 25 - 37.
52. DePristo, A. E., Kara, A. *Adv. Chem. Phys.* **1990**, *77*, 163 - 253.
53. Brenner, D. W., Garrison, B. J. *Phys. Rev. B* **1985**, *34*, 1304.
54. Philpott, M. R. *unpublished theory* **1996**.

55. Stillinger, F. H., David, C. W. *J. Chem. Phys.* **1978**, *69*, 1473-1484.
56. Halley, J. W., Rustad, J. R., Rahman, A. *J. Chem. Phys.* **1993**, *98*, 2435-2438.
57. Glosli, J. N., Philpott, M. R. In *Microscopic Models of Electrode-Electrolyte Interfaces. Symp. Proc. 93-5*; J. W. Halley L. Blum, Ed.; Electrochem. Soc.: Pennington, New Jersey, 1993. 90-103.
58. Philpott, M. R., Glosli, J. N. In *Theoretical and Computational Approaches to Interface Phenomena*; H. Sellers J. T. Golab, Ed.; Plenum: New York, 1994. 75 - 100.
59. Glosli, J. N., Philpott, M. R. *J. Chem. Phys.* **1992**, *96*, 6962-6969.
60. Glosli, J. N., Philpott, M. R. *J. Chem. Phys.* **1993**, *98*, 9995-10008.
61. Berendsen, H. J., Grigera, J. R., Straatsma, T. P. *J. Chem. Phys.* **1987**, *90*, 6267.
62. Impey, R. W., Madden, P. A., McDonald, I. R. *J. Phys. Chem.* **1983**, *87*, 5071 - 5083.
63. Lee, C. Y., McCammon, J. A., Rossky, P. J. *J. Chem. Phys.* **1984**, *80*, 4448-4455.
64. Goodisman, J. *Electrochemistry: Theoretical Foundations*; Wiley-Interscience: New York, 1987.
65. Gouy, G. *Ann. phys.* **1917**, *7*, 129.
66. Chapman, D. L. *Phil. Mag.* **1913**, *25*, 475.
67. Bockris, J. O., Reddy, A. K. *Modern Electrochemistry*; Plenum Press: New York, 1973; Vol. 1.
68. Conway, B. E., Bockris, J. O., Ammar, I. A. *Trans. Faraday Soc.* **1951**, *47*, 756 - 766.
69. Landau, L. D., Lifschitz, E. M. *Electrodynamics of Continuous Media*; Addison-Welsey: 1960; 99 - 101.
70. Samec, Z., Johnson, B. W., Doblhofer, K. *Surface Sci.* **1992**, *264*, 440 - 448.
71. Stuve, E. M., Kizhakevariam, N. *Surface Sci.* **1993**, *A 11*, 2217 - 2224.
72. Wilson, M. A., Pohorille, A., Pratt, L. R. *J. Chem. Phys.* **1988**, *88*, 3281 - 3285.
73. Wilson, M. A., Pohorille, A., Pratt, L. R. *Chem. Phys.* **1989**, *129*, 209 - 212.
74. Wilson, M. A., Pohorille, A., Pratt, L. R. *J. Chem. Phys.* **1989**, *90*, 5211 - 5213.
75. Philpott, M. R., Glosli, J. N., Zhu, S. *unpublished* **1996**.

Jun 10, 1992

MOLECULAR DYNAMICS MODELING OF ELECTRIC DOUBLE LAYERS

James N. Glosli
and
Michael R. Philpott

IBM Research Division
Almaden Research Center
650 Harry Road
San Jose, CA 95120-6099

1. Introduction

Adsorption of ions is on of the fundamental processes controlling the structure and dynamics of electric double layers in electrochemical systems. Modern workstations provide a powerful affordable tool to study these systems, through their ability to efficiently solve Newton's equations for thousands of charged particles. In this paper constant temperature molecular dynamics has been used to study water and ions between flat uniformly charged surfaces. The simulations provide new insights on the behaviour of strongly hydrated ions at surfaces and how the transition to 'contact' adsorption occurs.

2. Simulations

Three types of system were examined. First, 214 water molecules and one LiX where X = F, Cl, Br or I, in a cell with dimensions 1.862 nm × 1.862 nm × 2.362nm (x × y × z), where the distance between the plates was 2.362 nm. Second, 215 water molecules and one ion Li^+ or I^- in a cell with the same dimensions. Third, 430 water molecules and one LiX in a cell with the same xy dimensions and z dimension of 4.320 nm. All the water molecules and ions interacted with the walls via the same weak 9 - 3 potential. Although the model used here was simpler than the 'standard model' of the electrochemical interface, it shares many of its essential features. Common practices of truncating all the intermolecular interactions at a finite distance (0.82 nm) and switching off Coulomb interactions at small distances were followed. The surface potential and the static electric field were not subject to truncation. The maximum surface charge was 0.11 e/(nm)^2, corresponding to an electric field of 2×10^7 V/cm. The ST2 water model and parameters optimized for alkali halides interacting with the model ST2 water molecule were used in the calculations. The temperature was set at T = 2.411 kJ/mole (290 K). Time durations for simulations were generally between 200 and 1500 ps, and the basic integration time step was 2 fs. For the simulations described in this paper 100 ps was equivalent to 13 hours of cpu time on an IBM RS/6000 model 540 operating at 16.3Mflop.

3. Results

Properties calculated included time averaged distribution profiles for ions and water in various fields, ion - water pair correlation functions, and residence times for waters on ions. The smallest ion lithium was observed to be fully solvated at all times and in the highest field was separated from the electrode by its primary hydration shell. The Figure shows the density distribution of a Li ion in field. In the Figure the cathode is on the left and the anode right handside. The water number density profile across the normalised to 214 the total number of water molecules in the cell. The broken circles represent in cartoon fashion the cation (and anion). As the field was weaken the ion position further from the surface. Eventually in extended to occupy the center of the film. Small field dynamical behaviour of the lithium with different anion were traced to transcell coupling of the ions. In the 2×10^7 V/cm static field the smallest negative ion fluoride was also found to remain fully solvated and separated from the electrode by its primary solvation shell at all times. This is shown in the Figure. Under the same conditions chloride behaved quite differently, it showed a tendency to make physical contact with the electrode part of the time, with no water molecules interposed between it and the electrode. For chloride adsorption it appeared that simulation times longer than 1 ns were necessary to fully explore configuration space. Bromide behaved more like Iodide favouring contact adsorption over full hydration. Iodide approximates closely the limiting case of contact adsorption. In high field constant energy or constant temperature simulations, the Iodide ion was observed to be contact adsorbed most all of the time. As the field was weakened the Iodide ion, like lithium ion but with differences due to initial stronger 'contact' adsorption, moved out from the positively charged electrode to the core region between the walls.

The time dependent hydration numbers for the first and second solvation shells were calculated and correlations with distance from the electode examined. The first solvation shell of lithium was more stable than fluoride. Water exchanged with the lithium shell about ten times slower than in fluoride. In general the solvation shells of larger ions were very dynamic.

4. Acknowledgement

This research was supported in part by the Office of Naval Research.

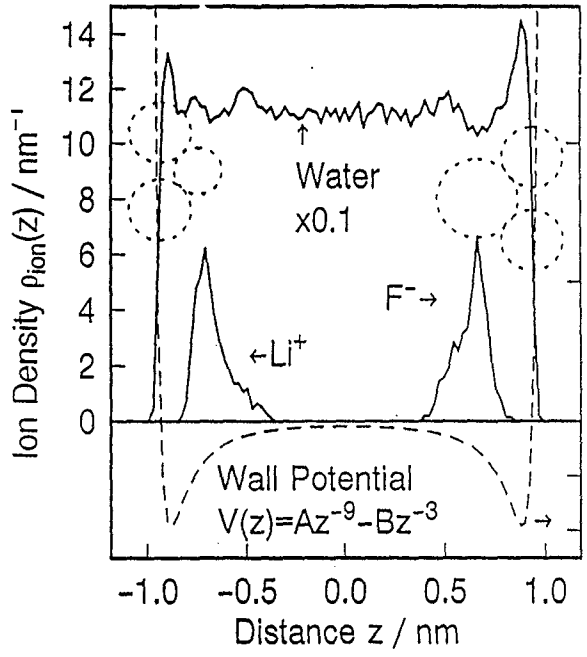

Oct. 28, 1992

Molecular Dynamics Modeling of Electric Double Layers with Spectroscopic Applications

M. R. Philpott and J. N. Glosli†

IBM Research Division, Almaden Research Center
650 Harry Road, San Jose CA 95120-6099
†Lawrence Livermore National Laboratory
University of California, Livermore CA 94550

Molecular dynamics is used to model the structure and dynamics of electric double layers at a charged metal surface and to ask questions of spectroscopic interest. In particular: What is the molecular basis for changing the position of the outer Helmholtz plane (OHP) thereby tuning the electric field across the inner layer? Another topic is the microscopic basis of modulation spectroscopies like SNIFTIRS Our MD simulations of an immersed electrode show features corresponding to: compact layer, diffuse layer, highly oriented water layer next to the metal when the electrode is charged and ions are present, penetration of nominally diffuse layer species into inner layer, ion pair formation between contact adsorbed ion and diffuse layer ion when the electrode is uncharged, poorly oriented surface water when the electrode is uncharged. All these properties arise from the model with the restriction that charge on the metal and aqueous phase sums to zero, ie., $q_M + q_{ions} = 0$.

Molecular Dynamics Modeling of Electric Double Layers with Spectroscopic Applications

Michael R. Philpott and James N. Glosli†
IBM Research Division, Almaden Research Center
650 Harry Road, San Jose, CA 95120-6099
†Lawrence Livermore National Laboratory,
University of California, Livermore, CA 94550

Introduction and Model

We use molecular dynamics (MD) to model the structure and dynamics of electric double layers at a charged metal surface and to ask questions of spectroscopic interest. In particular: What is the molecular basis for changing the position of the outer Helmholtz plane (OHP) thereby tuning the electric field [1, 2] across the inner layer? Another topic is the microscopic basis of modulation spectroscopies like SNIFTIRS [3]. Our MD simulations of an immersed electrode show features corresponding to: compact layer, diffuse layer, highly oriented water layer next to the metal when the electrode is charged and ions are present, penetration of nominally diffuse layer species into inner layer, ion pair formation between contact adsorbed ion and diffuse layer ion when the electrode is uncharged, poorly oriented surface water when the electrode is uncharged. All these properties arise from the model with the restriction that charge on the metal and aqueous phase sums to zero, ie., $q_M + q_{ions} = 0$.

Interaction with the metal was represented by a 9-3 potental for Pauli repulsion and attractive dispersive interactions, and an image potential for interaction with the conduction electrons. On the side opposite the metal the electrolyte was constrained by the 9-3 potential of a 'dielectric-like' bounding surface. This boundary limited the extent of the fluid phase, and kept the calculations tractable. System composition was $mM^+ + nX^- + (N\text{-}m\text{-}n)H_2O$

where N is the number of water molecules in the absence of ions, and (m,n)=(0,0),(1, 0),(0, 1),(1, 1),(2, 1),... . Heinzinger parameters [4] for st2 water model and alkali halides MX were used. Electrostatic fields were calculated exactly (no cut offs) by the fast multipole method.

Double Layer on Charged Electrode

We display a sample result here (see Figure 1) for a system composed of one Li^+, two I^- and 155 waters in a cubic simulation cell with edge length 1.862 nm and periodically replicated in the (x,y) plane. The metal surface at z = 0.932 nm has $q_M = +|e|$ (anodic). Figure 1 shows the density profiles averaged over the xy plane as a function of z for all components of the system. The iodide distribution is sharply peaked near 0.7 nm just inside the repulsive portion (dash line) of the 9-3 potential. The iodide distribution is compact and the Li^+ distribution is diffuse. At negative z the Li density has the gradual fall off expected for an electrostatically bound species. The main component of the Li density ends at 0.05 nm which we interpret as the position of the OHP, being approximately two water diameters from the repulsive wall at z = 0.682 nm. In the region between 0.05 and 0.3 nm the cation has finite probability of penetrating the inner layer. This process is not part of usual Stern-Gouy-Chapman theory. The structure near the metal surface in the densities for water, H, and PC (point charge of the st2 model) arises from an oriented layer of water with a PC pointing at the metal. This an important result of our model with implications for modulation spectroscopy.

Application to Surface Spectroscopy

The idea of altering the position of the outer plane to change the field across the inner layer has been proposed many times [1, 2]. This effect can be modeled with the primative system used here. Based on the total charge distribution given in Figure 1 we see that the iodide and oriented surface waters determine the charge

density near the metal. Note the positive charge peak at 0.65 nm. It and weaker positive peaks near 0.4 and 0.2 nm make it difficult for positive ions to approach the interface even though the latter carries net negative charge because of two adsorbed anions. Two opposing effects operate as cation size is increased, and their balance determines the field effect. First the OHP will move to more negative z due to larger radius and electrostatic repulsion from the positive charge peaks. Second at larger radii the cation hydration shell is softer making it easier for the ion to penetrate the inner layer. In Figure 1 the tail between 0.0 and 0.3 nm indicates how difficult this is for Li ion with its strongly bound solvation shell. More calculations exploring this effect are in progress and will be presented at the meeting.

Conclusion and Acknowledgement

Molecular dynamics calculations show that a simple model based on sound chemical ideas reproduces phenomena familiar from experiments on the electrochemical interface. Important new insights arise concerning the time averaged electric fields across the inner layer which in turn deepen our understanding of spectroscopic probes.

This work was supported in part by the Office of Naval Research.

References

1 A. Bewick, private communication, 1987. Tetralkyl ammonium cations used to alter OHP position

2 K. Ashley, M. G. Samant, H. Seki, and M. R. Philpott, J. Electroanal. Chem. 270, 349-364 (1989).

3 S. Pons, T. Davidson, and A. Bewick, J. Electroanal. Chem. 160, 63 (1984).

4 K. Heinzinger, *Computer Modelling of Fluids Polymers and Solids*, (Kluwer,Dordrecht, 1990), pp. 357-404.

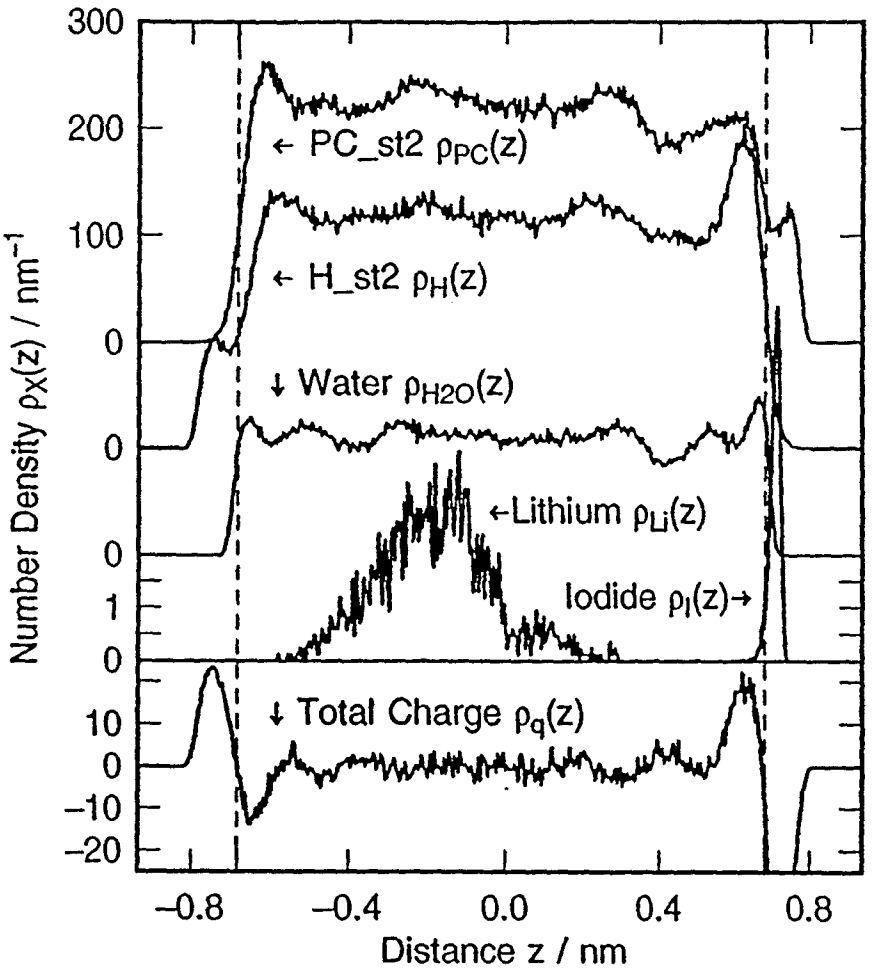

Figure 1. Density profiles for two I^-, one Li^+ and 155 st2 water molecules next to immersed electrode. Anodically charged electrode $q_M = +|e|$. Iodide distribution is compact and Li^+ diffuse. Metal on rhs, dielectric constraining boundary on lhs. Distance across the cell 1.892 nm. Repulsive portion of wall, dashed line, at $|z| = 0.682$ nm. Temperature 290K.

RJ 9066 (80756) October 30, 1992
Chemistry

Oct. 18, 1992

Research Report

ADSORPTION OF SULPHATE ON METAL ELECTRODES

Leslie A. Barnes

NASA Ames Research Center
Mail Stop RTC-210-3
Moffett Field, CA 94035-1000

Michael R. Philpott

IBM Research Division
Almaden Research Center
650 Harry Road
San Jose, California 95120-6099

IBM Research Division

Yorktown Heights, New York • San Jose, California • Zurich, Switzerland

RJ 9066 (80756) October 30, 1992
Chemistry

Adsorption of Sulfate on Metal Electrodes

Leslie A. Barnes *, Michael R. Philpott and Bowen Liu
IBM Research Division, Almaden Research Center
650 Harry Road, San Jose, California 95120-6099

Abstract

The adsorption of sulfate (SO_4^{2-}) and bisulfate (HSO_4^-) on copper has been studied using *ab initio* calculations at the SCF level of theory, to aid in the interpretation of *in situ* experimental data from the electrochemical interface, in particular optical and surface X-ray measurements. The calculations are designed to give qualitative insight rather than quantitative accuracy. Optimized structures and harmonic frequencies and intensities are computed for isolated sulfate and bisulfate, and qualitative agreement with experimental data is demonstrated. The effect of a uniform electric field on sulfate is also studied. The structures of $Cu^0SO_4^{2-}$ and $Cu^0HSO_4^-$ are optimized. The bonding is dominantly ionic, with consequential small orientational dependence of the adsorbed ligand. We also compute structures for the larger $Cu_4^0SO_4^{2-}$ cluster. The sulfate ion is found to favour a "3-down" adsorption geometry with sulfate oxygens occupying on-top sites over the previously postulated "1-down" structure invoked to explain the early surface exafs experiments.

1 Introduction

Understanding the adsorption of sulfate on surfaces is a challenging scientific problem that is also of significant technological interest in connection with battery chemistry, dissolution of metals in acids, electroplating and polishing, and the incipience of oxide films. Recent optical and surface X-ray measurements of metal electrodes in contact with aqueous sulfate media have been explained with hypothetical models, with sulfate (SO_4^{2-}) and it's hydrolysis product bisulfate (HSO_4^-) in specific orientations adsorbed on the metal surface [1]–[6]. Figure 1 shows some of these models.

The high symmetry (T_d) and many vibrational modes of sulfate that are exclusively IR or Raman allowed make it a potentially useful probe of forces influencing orientation and of the local field within the electrochemical double layer. Bisulfate, with lower symmetry, has more vibrational frequencies which may be IR or Raman allowed, some of which overlap with sulfate modes. This complicates interpretation

*Mailing Address: Mail Stop RTC-230-3, NASA Ames Research Center, Moffett Field, California 94035-1000

FAST MULTIPOLE METHOD IN SIMULATIONS OF ELECTRIC DOUBLE LAYERS

James N. Glosli
and
Michael R. Philpott

IBM Research Division
Almaden Research Center
650 Harry Road
San Jose, CA 95120-6099

1. Introduction

Molecular dynamics and Monte Carlo simulations of electrolyte systems require the evaluation of the superimposed Coulomb fields of thousands particles (a mere 5 nm^3 of water contains approximately 4200 atoms). Ewald summation crudely applied is proportional to N^2 and at best $N^{3/2}$ where N is the number of charges. The fast multipole method[1], however, is order N. The method achieves this by using a recursive algorithm based on multipole expansions for the evaluation of the Coulomb fields. The algorithm is able to evaluate these electrostatic potentials (and forces) to an arbitrary small precision in order N steps.

The method has a number of advantages over direct and Ewald sum methods. As already mentioned it is an order N and hence faster for large number of particles (typically N > 1000). As well, within the structure of the algorithm it is easy to impose a variety of boundary conditions on the system. For example in our calculation free, periodic, and metal as well as mixtures of this boundary conditions were all used. The method is also well suited to vector and parallel computation, allowing for the possibility of exploring very large system.

2. Fast Multipole Method

Suppose simulation cell C contains N charged particles. The method divides C (which we will call a level 0 box) into 8 level 1 boxes. Each of these boxes are subdivided into 8 more boxes creating a array of level 2 boxes. This process is repeated until some prescribed level L is reached. The finest level L is chosen to minimize computation and in doing do is proportional to log(N). The boxes formed by the division of a box are called children of the divided box and the divided box is called the parent. The far field due each to box at the finest level is calculated in terms of the multipoles, up to order p. The precision of the method is set by the order p. Next the multipole moments of the parents are created from the children's moments by a linear transformation, starting at the finest level and working upward to level 0.

The strategy now will be to calculate a local expansion for each box that represents the far field potential. Beginning at level zero, the question is asked, which boxes are well separated from the main computational cell? The answer will depend on boundary conditions. For free boundary there is no well separated boxes. For periodic boundary condition it is the array of all images except adjacent images. The local expansion for the level zero box is found by transforming the multipole expansion of each of the well separated boxes. In the case of the free boundary this is trivial since there are no well separated boxes. However in the case of periodic boundary condition there is an infinite number of image boxes, but symmetry enables the local expansion to be calculated easily. The local expansion of a level 1 box can be considered to consist of two parts. One part representing particles included in the local expansion of its' parent and the another part representing all particles in well separated boxes that are not present in the first part. The number of these well separated boxes is finite and bounded. The contribution to the local expansion by particles in the first part is simply found by transforming the origin of the parent's local expansion to the center of the box. The second part is calculated by transforming a finite number of multipole expansions. Once this procedure is applied to all level 1 boxes it is applied recursively to level 2 and so on. Finally a local expansion of all particles in well separated boxes is found for each box at the finest level. What remains to be found is the potential due to particles in adjacent boxes and this is calculated by doing a direct sum over particles in these boxes.

3. Electrochemical Systems

The Figure schematically illustrates electrochemical systems of interest. In the first (a) the simulation cell is replicated throughout 3-D space, to represent an infinite bulk fluid. In cases (b-d) it is replicated laterally in the x-y plane, however the z direction has to be handled differently in each case. In case b the system is a free film or bounded by low dielectric surfaces. In case c the film is bounded by two metals which require the inclusion of images boxes C tilde (generated from C by charge conjugation: $q \rightarrow -q$ and reflection in the xy plane: $z\text{-}z_o \rightarrow z_o\text{-}z$). The bottom right case (d) represents an emersed electrolyte film of finite thickness on a metal electrode. In this case there is only one set of image boxes C tilde.

4. Results

As time permits applications to bulk water and other cases represented in the figure will be presented.

5. Acknowledgement

This research was supported in part by the Office of Naval Research.

6. References

1. L. Greengard and V. Roklin, J. Comput. Physics.73, 325 (1987)

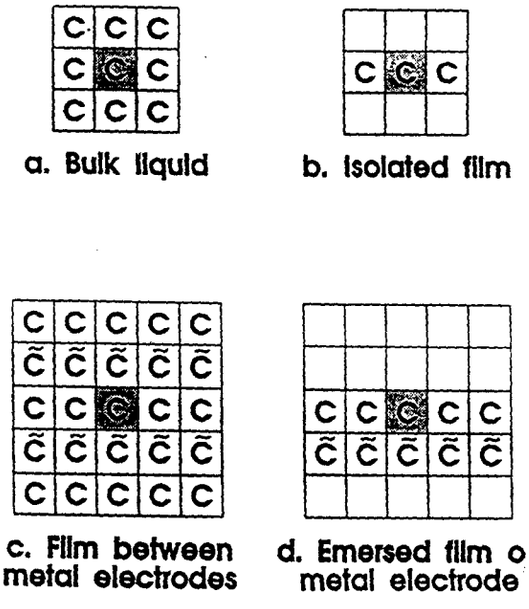

RJ 8491 (76712) November 25, 1991
Chemistry

Research Report

MOLECULAR DYNAMICS SIMULATION OF ADSORPTION OF IONS FROM AQUEOUS MEDIA ONTO CHARGED ELECTRODES

James N. Glosli
Michael R. Philpott

IBM Research Division
Almaden Research Center
650 Harry Road
San Jose, California 95120-6099

Research Division

Yorktown Heights, New York • San Jose, California • Zurich, Switzerland

RJ 8491 (76712) November 25, 1991
Chemistry

MOLECULAR DYNAMICS SIMULATION OF ADSORPTION OF IONS FROM AQUEOUS MEDIA ONTO CHARGED ELECTRODES.

James N. Glosli
Michael R. Philpott

Theory and Computational Physics
IBM Research Division
Almaden Research Center
650 Harry Road
San Jose, CA 95120-6099

ABSTRACT

Molecular dynamics simulation of 216 water molecules (ST2 model) between charged flat electrodes 2.362 nm apart showed layering with a few molecules at each surface that broke H-bonds with the bulk and oriented their charges towards the electrode. Compared to uncharged electrodes the atomic and molecular distributions were unsymmetric. When a lithium and an iodide ion were substituted at random for two water molecules the iodide ion contact adsorbed on the anode with no water molecules between it and the electrode. The iodide ion appeared weakly solvated on the solution side, to water molecules that preferred to engage in hydrogen bonding with the network of the bulk solvent. In contrast the lithium adsorbed without losing its primary solvation shell of six water molecules. The adsorbed cation was never observed two water molecules removed the electrode. The average position corresponded to an ion supported on a tripod of three waters. The solvation number was not changed upon adsorption to this configuration. These qualitative observations and some quantitative results afford striking confirmation on the one hand and new insight on the other of aspects of the standard model of the adsorption of ions on electrode surfaces. Time durations for simulations were generally between 200 and 800 ps, with a basic integration time step of 2 fs.

I. INTRODUCTION

In this paper we explore aspects of the adsorption of ions from aqueous solution using molecular dynamics simulation of a relatively simple model. Adsorption is one of the fundamental processes controlling the structure and dynamics of electrochemical double layers. The goal is insight and understanding concerning the local environment around the adsorbate. The total number of molecules was chosen small in order to explore time scales up to a nanosecond in duration and to check the dynamical stability of the adsorbed ions. This turned out to be important because the simulations showed that ions with strongly bound water undergo motion akin to slow 'bumping' against a charged surface. Some important interactions are treated approximately but by focussing where possible on comparisons it is believed that these approximations do not effect qualitative behavior. For example long range Coulomb interactions are cut off at 0.82 nm. This is perhaps the most serious deficiency, but its consequences are global and not expected to alter our conclusions concerning local water structure around the ions.

There is a vast literature describing electrochemical double layers and the adsorption of ions from aqueous electrolyte solution onto charged electrodes. On the basis of clever experimentation and deductive reasoning using simple models, electrochemists have evolved a detailed 'standard model' of the disposition of ions, water, and organics adsorbed on the electrode in the range of potentials where the electric double layer is thermodynamically stable[1-5] Early experiments relied on precision measurements of electric current. In the mid forties Grahame[1] used a dropping mercury electrode to avoid surface contamination and in classic experiments measured the capacitance of the double layer as a function of potential and electrolyte composition. This was the beginning of the modern era of electrochemistry and the origin the standard model of the interface.

Consider a solvated ion approaching the surface by a diffusion process biased by an attractive electrostatic potential. Before the ion can make contact some of the weakly bound water molecules between the electrode and the ion are displaced. The thermodynamic equilibrium involves a balance of opposing interactions. The most im-

portant are: electrostatic interaction between ion and electrode, enthalpies of hydration of ion and surface atoms, and entropy of displaced water molecules. Generally speaking large ions (iodide, cesium) contact adsorb whereas small ions (fluoride, lithium) do not. Experimental verification of contact adsorption has been demonstrated by a variety of techniques including: differential capacitance[3], radio tracer[6], ftir[7], and surface exafs[8, 9]. The molecular dynamics simulation described below is the first to show clearly that contact adsorption occurs for large radius ion and not for solvated small radius ions.

According to the standard model the electric double layer consists of two parts: a compact part adjacent to the electrode and a diffuse part stretching from the compact layer into the bulk electrolyte. The thickness of the diffuse layer is very dependent on ionic strength, for 0.1M solutions it is about 2 nm in extent. The delimiter between the two zones, the outer Helmholtz plane (OHP), is defined as the plane of closest approach of the nuclei of fully solvated ions that do not contact adsorb. For metal electrodes the compact part is thought to consist of two water layers mixed with contact adsorbed ions, and visiting counter ions. Interpretation of experimental capacitance measurements suggests that the compact layer can be subdivided further into inner and outer parts. The dividing plane, called the inner Helmholtz plane (IHP), cuts through the centers of contact adsorbed ion. So our choice of the LiI system has the advantage that contact adsorbed iodide defines the IHP on one electrode and adsorbed hydrated lithium ion defines the OHP on the second electrode.

Ions have been classified according to their adsorbing ability by Anson[10]. Inside the compact layer the specifically adsorbed ions accumulate on the electrode driven there by the Gibbs free energy of adsorption. They can change the sign of the charge felt by ions in the diffuse layer. Put another, way negative ions like iodide adsorb strongly on negatively charged metal electrodes, requiring the diffuse layer to screen a larger effective charge. Likewise adsorption of anions on positively charged metal electrodes can lead to an overall negative charge to be screened by the diffuse layer. The thermodynamics of contact adsorption has been well studied within the frame work of the standard model. Useful tables of Gibbs free energies are given in a number of texts see for example Bockris and Reddy[11]. The main point for this discussion is that for large radius

ions the water-electrode and ion-electrode interactions are roughly constant and opposing. The determining effect is the variation in ion-water interaction. Large radius ions with deeply buried charge tend to adsorb strongly.

The second part of the electric double layer, called the diffuse part, consists of fully hydrated ions moving under the influence of thermal forces in the combined electric fields of the metal electrons and the adsorbed ions. The diffuse layer, described by Gouy-Chapman theory[3-5], screens the charge on the electrode. Direct measurement of the diffuse layer distribution has been described recently using x-ray fluorescence from zinc ions[12]. The calculations described here tell nothing about the diffuse layer, for this a much larger system is needed together with the ability to simulate for nanoseconds.

The molecular dynamics simulations reported in this paper complement some of the previous work relevant to electrochemical double layers. Rigorous statistical mechanical models using correlation functions to describe ion distributions and including structure on the metal side were developed by Henderson, Schmickler and coworkers[13, 14]. Ab initio calculations of the electronic structure of adsorbates on small metal clusters provided information about adsorption site bonding and geometry[15-17]. There have been a number of molecular dynamics and Monte Carlo studies of water near surfaces. The closest was a simulation for 19 ps of eight LiI and 200 water molecules between uncharged plates[18]. This was insufficient to study ionic adsorption of hydrated species. In recent work Heinzelman[19] Spohr[20] and Berkowitz[21] considered adsorption of water on model platinum electrodes in the absence of charge on the electrodes. The platinum-water potential included orientational factors. Water between charged surfaces has been considered by Hauptman et al[22, 23], Marchesi[24], and by Kjellander and Marcelja[25] for water between mica and lecithin layers. Ions were not included in these studies. Recently several papers have addressed the problem of dielectric saturation in bulk and thin films of water[26, 27] for a range of filed strengths encompassing the value used here.

In the work described here we start from a relatively well understood system first explored by Lee, McCammon and Rossky[28]. The calculation first considers water between

charged plates, and then the effect of the field on a system obtained by substituting LiI for two water molecules.

II. BASIC MODEL

Many models of the water molecule have been proposed for use in computer simulations of bulk water and aqueous electrolytes. At present the popular models are designated: ST2[29, 30], TIP4P[31] and SPCE[32]. In the calculations reported here we have elected to use ST2 not because it more faithfully reproduces bulk water properties but because the extensive molecular dynamics calculations by Heinzinger and Spohr[19, 20] have yielded a complete set of parameters for alkali metal ions and halide ions solvated by ST2 water.

Interaction Energy

The Coulomb interaction between molecules was represented as sum of $1/r$ interactions between atomic point charges. These interaction were soften for small molecular separation by a switching function S. The short range part of the intermolecular interaction was modeled by Lennard-Jones potential between the atoms of each molecule. All molecule-molecule interactions (both $1/r$ and Lennard-Jones potentials) were cut-off in a smooth fashion at molecular separation $R = 0.82$ nm by a truncation function T. The atoms of each molecule also interacted with surfaces at $z = \pm z_o$. Both surfaces were treated as flat featureless plates with a uniform electric charge density of $+\sigma$ and $-\sigma$ on the $-z_o$ and $+z_o$ plates respectively. This gave rise to a uniform electric field, $E = 4\pi K\sigma$, in the z-direction where K the electrostatic coupling constant had the value 138.936 KJ•nm/(mole• e^2) in the units used in this calculation. Non Coulombic interactions between the walls and all the atoms were represented by the 9-3 potential (wall potential) introduced by Lee et al [28]. The complete interaction energy U is,

$$U = \sum_{\substack{\alpha\in A_i \\ \beta\in A_j \\ i<j}} \left\{ \frac{Kq_\alpha q_\beta}{r_{\alpha\beta}} S(R_{ij}, R_L^{ij}, R_U^{ij}) + 4\varepsilon_{\alpha\beta}\left[\left(\frac{\sigma_{\alpha\beta}}{r_{\alpha\beta}}\right)^{12} - \left(\frac{\sigma_{\alpha\beta}}{r_{\alpha\beta}}\right)^{6} \right] \right\} T(R_{ij})$$

$$+ \sum_{\alpha} \left\{ -q_\alpha E z_\alpha + \left(\frac{A_\alpha}{(z_\alpha + z_o)^9} - \frac{B_\alpha}{(z_\alpha + z_o)^3}\right) + \left(\frac{A_\alpha}{(z_\alpha - z_o)^9} - \frac{B_\alpha}{(z_\alpha - z_o)^3}\right) \right\} \qquad (1)$$

where i and j are molecular indices, and, α and β are atomic indices. The symbol A_i represents the set of all atoms of molecular i. The symbol R_{ij} is the distance between the

center of mass of molecules i and j. The symbol $r_{\alpha\beta}$ is the distance between atoms α and β. For small R the Coulomb energy has been modified by the switching function $S(R, R_L, R_U)$ given by,

$$S(R, R_L, R_U) = \begin{cases} 0 & R < R_L \\ \dfrac{(R - R_L)^2(3R_U - 2R - R_L)}{(R_U - R_L)^3} & R_L < R < R_U \\ 1 & R_U < R \end{cases} \qquad (2)$$

The values of R_L and R_U are dependent on the types of the molecular species that are interacting.

As mentioned above the tails of Coulomb and Lennard-Jones pair interactions are cut off by the truncation function T. The form of T is given by,

$$T(R) = \begin{cases} 1 & R < R_L^T \\ \left(1 - \left(\dfrac{R - R_L^T}{R_U^T - R_L^T}\right)^m\right)^n & R_L^T < R < R_U^T \\ 0 & R_U^T < R \end{cases} \qquad (3)$$

The same truncation function has been applied to all molecular interactions, with $R_L^T = 0.779$ nm and $R_U^T = 0.820$ nm. The integers m and n control the smoothness of the truncation function at R_L^T and R_U^T respectively. In this calculation $n = m = 2$ which insured that energy was smooth up to first spatial derivatives.

Model for water and ion molecules.

In the ST2 model the water molecule consists of a central oxygen atom (ST2_O) surrounded by two hydrogen atoms (ST2_H) and two massless point charges (ST2_PC) in a rigid tetrahedral arrangement (bond angle = $\cos^{-1}(1/\sqrt{3})$). The ST2_O/ST2_H and ST2_O/ST2_PC bond lengths are 0.1 nm and 0.08 nm respectively. The only Lennard-Jones 'atom' in ST2 is the oxygen atom. The hydrogen and point charges interact with

their surroundings (i.e. atoms and surfaces) only via the Coulomb interactions. The ions are treated as non polarizable Lennard-Jones 'atom' with point mass and charge.

Interaction Parameters.

The atom-atom and atom-surface interaction parameters are given in Tables I and II. The usual combining rules were enforced for unlike species, namely: $\varepsilon_{AB} = (\varepsilon_{AA}\varepsilon_{BB})^{1/2}$, $\sigma_{AB} = \frac{1}{2}(\sigma_{AA} + \sigma_{BB})$. The switching function interval ends R_L^U and R_U^U all vanish except for ST2/ST2 pairs, where $R_L^{ST2,ST2} = 0.20160$ nm and $R_U^{ST2,ST2} = 0.31287$ nm.

Simulation details

Two separate systems were considered each with 216 molecules. In the first simulation a collection of 216 ST2 water molecules system was studied and in the second a ionic solution of 214 ST2 molecules, one Li ion and one I ion was examined. For both systems the molecules were confined to a rectangular simulation box with dimensions 1.862 nm × 1.862 nm ×2.362 nm (x × y × z) and periodic boundary conditions in the x and y directions. Initially the molecules were randomly disposed on a cubic lattice with lattice parameter 0.31 nm. The systems were consider in both a constant energy and constant temperature ensemble. To constrain the temperature a least constraint method[33, 34] was used. Bond lengths and angles were explicitly constrained by a quaternion formulation of the rigid body equations of motion[35]. The equations of motion were expressed as a set of first order differential equations and a fourth order multi-step numerical scheme with a 2 fs time step was used to integrate them. With this scheme the time step to time step rms fluctuation of quaternions length and energy/temperature was about 0.0002% and 0.0009%/0.002% respectively. Though small these changes could lead to global drift, so at each time step a small scaling correction was made to the quaternions and velocities. Also the global center of mass velocities in the x and y directions was set to zero at each time step by shifting the molecular translational velocities

All simulations were done using an IBM RS/6000 model 540. A 100 ps simulation required 25 hours of cpu time using the water ST2 model. In test runs the water SPCE

model ran 2.4 times faster because there were fewer pairwise Coulomb interactions to sum.

III. WATER BETWEEN FLAT CHARGED ELECTRODES

Uncharged electrodes.

This case was studied by Lee, McCammon and Rossky[28]. Their geometry was adopted in this paper and provided a useful existing frame of reference against which to compare results. We have repeated all their published calculations using the same parameter set and get essential agreement.

The simulation of pure ST2 water was performed in two parts. First, the system was simulated for 250 ps at a constant temperature of 2.411 kJ/mol, with configurations stored every 0.5 ps. The average of the total energy was calculated for the last 200 ps and was equal to $E_{total} = -35.23 \pm 0.1$ kJ/mol. Next an initial configuration for a constant energy run was generated by taking the last configuration of the constant temperature run and scaling it's velocities such that the total energy would equal the average energy of the constant temperature simulation (-35.23 kJ/mole). This configuration was evolved for 200 ps at constant energy and samples were collected every 0.1 ps. The average temperature of was found to equal 2.40±0.03 kJ/mol (289K). The consistency between the constant temperature and energy runs suggest that both runs have sampled a representative part of the equilibrium ensemble.

For a bin size of 0.0236 nm ($2z_o/100$ of the gap between the electrodes) the oxygen and hydrogen z-dependent number densities are shown in Figure 1. They resemble those of Lee et al [28] quite closely. Superimposed is the 9-3 wall potential with scale given on the right hand side. Some points of interest. The broad first O atom peak falls in the range of the weakly attractive well of the wall potential, The 'foot' of the H density extending 0.1 nm (OH bond length) past the point where the wall potential first becomes repulsive because the later acts only on the O atom and not the H atoms. Peak in H density near the surface occurs at smaller |z| than in O density profile, consistent with an ice-like structure in which one OH bond points toward the surface.

Charged Electrodes.

In this section we discuss the results of a simulation for water between oppositely charged plates. The plate at $z = -z_o$ carried the positive charge. The uniform electric

field was equivalent to a surface charge density of $0.11e/nm^{-2}$ or about $2x10^{7}V/cm$. This is at the upper end of field gradients believed to occur in electric double layers. The simulation was done at a constant energy of E_{total}= -35.23 kJ/mol for 200ps. The average of the temperature was calculated over the last 150 ps of this run and had the value 2.49±0.02 kJ/mol (300K).

Figure 2 shows the density profiles for H and O atoms. in the normal direction z The first feature of note is the pronounced asymmetry induced in all the densities. There are sharper peaks near the positive electrode ($z<0$). The sharper peak is interpreted as better wetting in the field which orientates and packs more water molecules near the surface. This occurs where the electrostatic force is comparable to the Lennard-Jones interaction. At larger |z| where the r^{-9} repulsion dominates the electrostatic interaction has no effect on the distribution of molecules. The O density profile is not bodily shifted relative to the zero field case, but the first peak shifts and sharpens in a move to more negative z value. The same is true for H except that H density has a new feature, a pronounced shoulder at z= 1.0 nm, not present in the corresponding zero field density.

Figure 3 shows the change in H density when the field is turned on. Also plotted, for reference purposes, is the H density with field on. The shoulder on right hand side of the H density can be identified to molecules oriented with the positive charge towards the negative electrode to increase their electrostatic interaction. It coincides with z= 1.0 nm positive lobe of the difference density $\Delta\rho_{H}(z)$. These molecules will be partially decoupled from the bulk as a result. The number of molecules contributing to this feature is small and was estimated to be one. This number was determined by subtracting from the 'field on' density the 'field off' density to give the $\Delta\rho_{H}(z)$ shown in Figure 3. In the case of H the integral of the difference $\Delta\rho_{H}(z)$ over a small range of z near the negative electrode was found to be slightly greater than two. Essentially the same number was obtained when this procedure was repeated for the point charge PC in the vicinity of the positive electrode. On the average one molecule at each surface is reoriented as a result of turning on the field.

Figure 4 shows the charge density $\Delta\rho_{q}(z)$ for the entire ensemble averaged in the xy direction, and plotted as a function of z. For reference the density of the H atoms is also

shown. The charge density for field on and field off are shown. Note that in the case of field off the distribution has been shifted down to avoid congestion. For field on, the large negative exaltation at z=-1.0 nm and large positive exaltation at z=1.0 nm are due to water molecules orienting their charge to reduce electrostatic interactions. In zero field the exaltations are much weaker and positive, indicating some H atoms are pointing toward the surface. This means that for the ST2 model the waters can optimize energetics of H bonding interactions by adopting an orientation with some H atoms pointing toward the weakly attractive surface.

IV. SOLVATED IONS BETWEEN FLAT CHARGED ELECTRODES.

In this section we describe adsorption of lithium and iodide ions on charged electrodes ($\sigma = 0.11e/\text{nm}^2, E = 2 \times 10^7$ V/cm) These ions represent extreme cases for adsorption. Experimentally iodide is believed to contact adsorb, whereas lithium ions being strongly hydrated should not lose any waters from the first coordination shell. After performing a constant temperature equilibration run, long simulations up to 800 ps were performed at constant energy $E_{total} = -40.700$ kJ/mol, to gather statistics. An average temperature of 2.40 ± 0.01 kJ/mol(T = 289K) was found. Figure 5 shows the distribution of the two ions and water across the gap between the two electrodes. To facilitate interpretation of the density curves the plot is annotated with a number of circles with diameters equal to the Lennard-Jones σ parameters of the ions and water. As well, for the same reasons, the wall potential is superimposed on the same plot. As expected the two ions are adsorbed on electrodes with the opposite sign in charge. However it is clear that the way in which the ions adsorbed is different. Lithium is hydrated and does not approach the electrode much closer than the diameter of a water molecule. Iodide in contrast makes physical contact with the electrode, there are no water molecules between it and the electrode.

Position of iodide ion.

In Figure 5 the iodide distribution is localized against the wall. Recall that the bin size is 0.0236 nm). Recall that the wall potential is the same for all molecules. The peak is at z = 0.90 nm , closest approach is $z \leq 0.97$ nm, and farthest distance $z \simeq 0.83$ nm. On the average the iodide ion center is mid way between the minimum and the $V(z) \geq 0$ repulsive region of the wall potential. The range of z displacements of the iodide ion center is approximately 0.25 nm for the simulation shown in Figure 5. Even during a fluctuation which places the iodide at its greatest distance from the electrode there is no room for a water molecule to press between the wall and ion. It remains in contact with the wall, and is to be regarded as contact adsorbed. This is the first example a molecular dynamic simulation of the electrochemical contact adsorption phenomenon.

Now consider the pair correlation function for water around the iodide ion. Since the ion is adsorbed the environment on the surface side of the ion can be very different from the environment on the side away from the surface. With this in mind, the pair correlation was evaluated by counting only water molecules that were within a cone with half angle of 60° whose axis was parallel to the z axis and vertex which was coincident with the ion. There are two such cones. One that opened into the surface and the other which opened away from the surface, which we call the surface and bulk cones respectively. To make the normalization explicit g(r) is defined as;

$$g_{H_2O} = \frac{1}{\pi \times r^2 \rho_o} \frac{d}{dr} < n(r) > \qquad (4)$$

where n(r) is the number of water molecules within both the cone and a distance r from the ion and $\rho_o = 33/nm^3$ is the mean density of water in the central region between the plates. In Figure 6 we show the I/water pair correlation function averaged over the bulk cone. The pair correlation function averaged over the surface cone was negligible, signifying the absence of solvent molecules between the ion and the wall at all times. This is completely consistent with the density distribution of Figure 5.

Position of lithium ion.

The lithium ion z-distribution is shown right side ($z > 0$) in Figure 5. Figure 7 shows the pair correlation function for water around the Li ion. There are separate functions for both bulk and surface cones. The latter measures water between the ion and the wall. Unlike the case for iodide displayed in Figure 6, there is a measurable pair correlation function for waters between the wall and ion. Infact the first peak corresponding to the primary solvation shell is at the same radial position. Inset in Figure 7 is the secondary and further regions at greater resolution. The secondary solvation shell is broad indicating the very considerable mixing with the bulk. Integration out to the primary shell radius confirmed the presence of six strongly coordinated water molecules.

The hydrated lithium ion can be visualized as a large object consisting of a central ion surrounded by six water molecules in the shape of a bipyramidal octagon. This object can adsorb to the surface with one, two or three vertices (spherical waters in this model)

down. Iodide by contrast behaves as if is spherical. As the simulation proceeds this large 'rough' object bumps and rolls over the charged electrode as it is subject to fluctuations in the hydrogen bonded solvent surrounding it. This picture allows us to interpret features of the lithium distribution of Figure 5 not found for iodide. The distribution is: i) peaked further from the wall, ii) broader (larger full width at half maximum), and iii) never approaches within ~0.1 nm of the hard repulsive region at z=0.934 nm..

The Li ion distribution is confined between z=0.425 nm and z=0.827 nm The main peak for Li^+ occurs at z=0.76 nm. Compare this hypothetical distances calculated assuming the ion and water are hard spheres. A lithium separated from the hard wall by one water molecule ($|z| = |0.934 - 0.5(\sigma_{Li} + \sigma_O)|$), is located at z=0.66 nm, and at z=0.61 nm when the water center occurs at the wall potential minimum.

The peak position z=0.76 nm is compatible with the hydrated Li ion having three of its attached waters simultaneously in contact with the wall. For this orientation the position of the Li nucleus (hard sphere model) would be at z=0.73 nm with the waters centered at the minimum in the wall potential ($V = V_{min}$ at z=0.884 nm) and at z=0.78 nm when the water centers are positioned at the hard wall (at z=0.934 nm). The position of closest approach of the Li ion in the distribution in Figure 5 is z=0.827 nm. There is considerable splay of the solvating waters from their nomimal octahedral positions around the ion. Careful examination of three dimensional computer graphics images showed that the lithium never contact adsorbed even though the solvation shell was distorted.

At positions farthest from the electrode the lithium ion was well separated, with the centers of water in its primary solvation shell outside the attractive minimum of the wall potential. However there is not room for two water molecules as can be easily visualized by looking at Figure 5

Water and the charge density distributions.

Figure 8 shows total charge density derived from separate densities for the two ions, H and PC 'atoms', referenced against the water density distribution (water and oxygen are

essentially the same). The total charge density looks qualitatively very similar to the case of water without ions shown in Figure 4.

The water density peaks show sharp structure close to the both walls were the electric field and the local ion fields strongly orient the solvent molecules. There is also a 'hole' in the water distribution at a position corresponding to the radius of the iodide. This corresponds to exclusion of solvent by the ion. The area involved corresponds to approximately 3 water molecules. The volume displaced by iodide's Lennard-Jones radius is equivalent to approximately 2.7 water molecules. Clearly the weaker solvation of iodide together with its volume is responsible for the apparant hole.

V. SUMMARY AND COMMENT ON APPLICATIONS TO ELECTROCHEMISTRY.

This paper has demonstrated the value of molecular dynamics calculations applied to models of electrified interfaces. The model used here though very simple appears capable of simulating aspects of a broad range of phenomena known to occur at electrodes. Additionally microscopic insight has been provided in the form of pictures of how ions and water orient in the presence of an electric field at a surface. The bumping of fully solvated ions against the surface and the concomittant distortion of the hydration sphere as the ion approaches closer than the diameter of a water molecule, discussed briefly above, has implications for electron transfer reactions such as occur in the desolvation of metal ions and deposition of metal. In fields much larger than the ones used in the present study small ions like lithium contact adsorb. In passing we also note it is possible to study ion transport across small films using this model. In a number of simulations we reversed the field and followed the migration of the ions across the water film as they switched sides. In this case the water molecules reoriented within a few ps, well before the ions started to leave the electrode. Transit times of tens of picoseconds were observed, with the weakly solvated iodide travelling faster in accord with the known ionic conductivities at infinite dilution in bulk water.

ACKNOWLEDGEMENT

This research was supported in part by the Office of Naval Research. R.Rafey is thanked for assistance with visualization graphics. MRP thanks JCC for nine months of unfathomable patience.

References

[1] D. C. Grahame., Chem.Rev. **41**, 441 (1947).

[2] J. O. Brockris, M. A. Devanathan, and K. Müller, Proc.Roy.Soc.(London) **A274**, 55 (1963.).

[3] J. O. Brockris and A. Gonzalez-Martin, *Spectroscopic and Diffraction Techniques in* (Kluwer,Dordrecht,Holland, 1990), pp. 1-54.

[4] J. R. MacDonald, J.Electroanal.Chem. **223**, 1 (1987).

[5] R. Parsons, Chem.Rev. **90**, 813-826 (1990).

[6] P. Zelenay, L. M. Rice-Jackson, and A. Wieckowski, J.Electroanal.Chem. **283**, 389-401 (1990).

[7] K. Kunimatsu, W. G. Golden, H. Seki, and M. R. Philpott, Langmuir **1**, 245-250 (1985).

[8] L. Blum, H. Abruna, J. White, J. G. Gordon, G. Borges, M. G. Samant, and O. R. Melroy, J.Chem. Phys. **85**, 6732 (1986).

[9] O. R. Melroy, M. G. Samant, G. L. Borges, J. G. Gordon, L. Blum, J. H. White, M. J. Albarelli, M. McMillan, and H. D. Abruna, Langmuir **4**, 728 (1988).

[10] F. Anson, Accts Chem. Res. **8**, 400-407 (1975).

[11] J. O. Bockris and A. K. Reddy, *Modern Electrochemistry* (Plenum Press, New York, 1973).

[12] M. J. Bedzyk, G. M. Bommarito, M. Caffrey, and T. L. Penner, Science **248**, 55 (1990).

[13] W. Schmickler and D. Henderson, Prog.Surf.Sci. **22**, 323 (1986).

[14] D. Henderson, *Trends in Interfacial Electrochemistry* (Reidel, Dordrecht, Holland, 1986), p. 183.

[15] P. S. Bagus, C. J. Nelin, W. Mueller, M. R. Philpott, and H. Seki, Phys.Rev.Lett. **58**, 559-562 (1987).

[16] P. S. Bagus, C. J. Nelin, K. Herman, and M. R. Philpott, Phys.Rev.Rapid Comm. **36:**, 8169-8172 (1987).

[17] P. S. Bagus, G. Pacchioni, and M. R. Philpott, J.Chem.Phys. **90**, (1989).

[18] E. Spohr and K. Heinzinger, J.Chem.Phys. **84**, 2304-2309 (1986).

[19] K. Heinzelman, *Computer Modelling of Fluids Polymers and Solids, NATO ASI Series C* (Kluwer,Dordrecht, 1990), pp. 357-404.

[20] E. Spohr and K. Heinzinger, Ber. Bunsenges. Phys. Chem. **92**, 1358 (1988).

[21] K. Raghavan, K. Foster, K. Motakabbir, and M. Berkowitz, J.Chem.Phys. **94**, 2110 (1991).

[22] J. Hauptman, J. W. Halley, and Y. J. Rhee, J.Chem.Phys. **91**, 467-472 (1989).

[23]Y. J. Rhee, J. W. Halley, J. Hauptman, and A. Rhaman, Phys.Rev.B **40**, 36-42 (1989).

[24]M. Marchesi, Chem.Phys.Lett. **97**, 224-230 (1983).

[25]R. Kjellander and S. Marcelja, Chem.Scripta **25**, 73-80 (1985).

[26]H. E. Alper and R. M. Levy, J.Phys.Chem. **94**, 8401-8403 (1990).

[27]M. Watanabe, A. M. Brodsky, and W. P. Reinhardt, J.Phys.Chem. **95**, 4593-4596 (1991).

[28]C. Y. Lee, J. A. McCammon, and P. J. Rossky, J.Chem.Phys. **80**, 4448-4455 (1984).

[29]F. H. Stillinger and A. Rahman, J.Chem.Phys. **60**, 1545 (1974).

[30]O. Steinhauser, Mol.Phys. **45**, 335-348 (1982).

[31]W. L. Jorgensen, J. Chandrasekhar, J. D. Madura, R. W. Impey, and M. L. Klein, J.Chem.Phys. **79**, 926-935 (1985).

[32]H. J. Berendsen, J. R. Grigera, and T. P. Straatsma, J.Phys.Chem. **6269**, (1987).

[33]W. G. Hoover, A.Rev.Phys.Chem. **34**, 103-127 (1983).

[34]D. J. Evans and G. P. Morris, Comput.Phys.Rep. **1**, 297-344 (1984).

[35]M. P. Allen and D. J. Tildesley, *Computer Simulation of Liquids* (Oxford University Press, Oxford, 1987), pp. 88-90.

TABLES

	$q(e)$	$A(\frac{KJ \bullet nm^6}{mole})$	$B(\frac{KJ \bullet nm^3}{mole})$	mass (AMU)
ST2_O	0.0	17.447×10^{-6}	76.144×10^{-3}	16
ST2_H	0.23570	0.0	0.0	1.0
ST2_PC	− 0.23570	0.0	0.0	0.0
Li	1.0	17.447×10^{-6}	76.144×10^{-3}	6.939
I	− 1.0	17.447×10^{-6}	76.144×10^{-3}	129.9

Table I Charge, A, B, and mass for all atom types.

(ε, σ) $(KJ/mole,nm)$	ST2_O	Li	I
ST2_O	(0.3164,0.3100)	(0.2240,0.2770)	(0.2280,0.4410)
Li	(0.2400,0.2770)	(0.1490,0.2370)	(0.2466,0.3885)
I	(0.2280,0.4410)	(0.2446,0.3885)	(0.4080,0.5400)

Table II The Lennard-Jones' ε and σ for all atoms pairs with nonzero ε.

FIGURE CAPTIONS

Figure 1. Some properties of the water ST2 model in zero electric field. Number density profiles for hydrogen H and oxygen O as a function of position between the electrodes. Broken line shows the weakly attractive wall potential.

Figure 2. Some properties of the water ST2 model in a strong electric field &tilte.$2x10^7$ V/cm. Number density profiles for hydrogen H and oxygen O as a function of position between the electrodes.

Figure 3. Some properties of the water ST2 model in a strong electric field. Change in H atom distribution for electric field on and off.

Figure 4. Some properties of the water ST2 model in a strong electric field. Charge density profiles for field on and field off. The H atom density profile is shown for reference.

Figure 5. Distribution of Li^+, I^-, and 214 water molecules in a strong electric field (&tilte.$2x10^7$ V/cm) across the gap between the charged plates. Wall potential shown for reference. Circles are Lennard-Jones radii for the ions and water.

Figure 6. Pair correlation function for water distributed around adsorbed I ion. Only the distribution within the bulk cone (half angle of 60°) is shown. There are no water molecules between the iodide and electrode in the surface cone.

Figure 7. Pair correlation function for water around an adsorbed Li ion. Inset shows distributions inside cones (half angle of 60°) oriented towards bulk and surface

Figure 8. Charge density profile across the ion-water mixture in a strong electric field &tilte.$2x10^7$ V/cm. For reference the water distribution is also shown. Apart

from small shifts in peak positions the shape of the charge density resembles that shown Figure 4 for water.

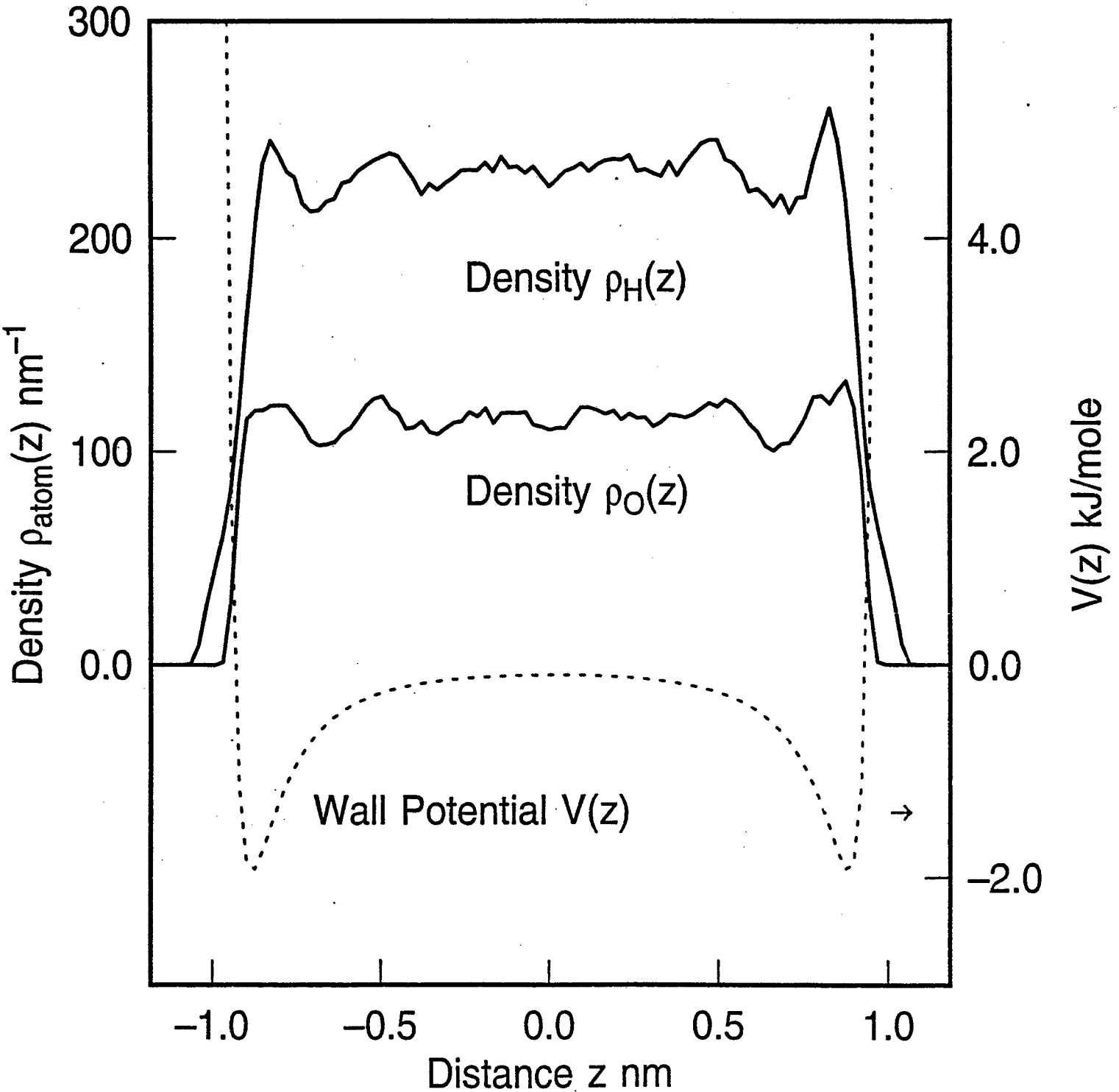
300
200
100
0.0
Density $\rho_{atom}(z)$ nm^{-1}
Density $\rho_H(z)$
Density $\rho_O(z)$
Wall Potential V(z)
4.0
2.0
0.0
−2.0
V(z) kJ/mole
−1.0
−0.5
0.0
0.5
1.0
Distance z nm

Figure 1

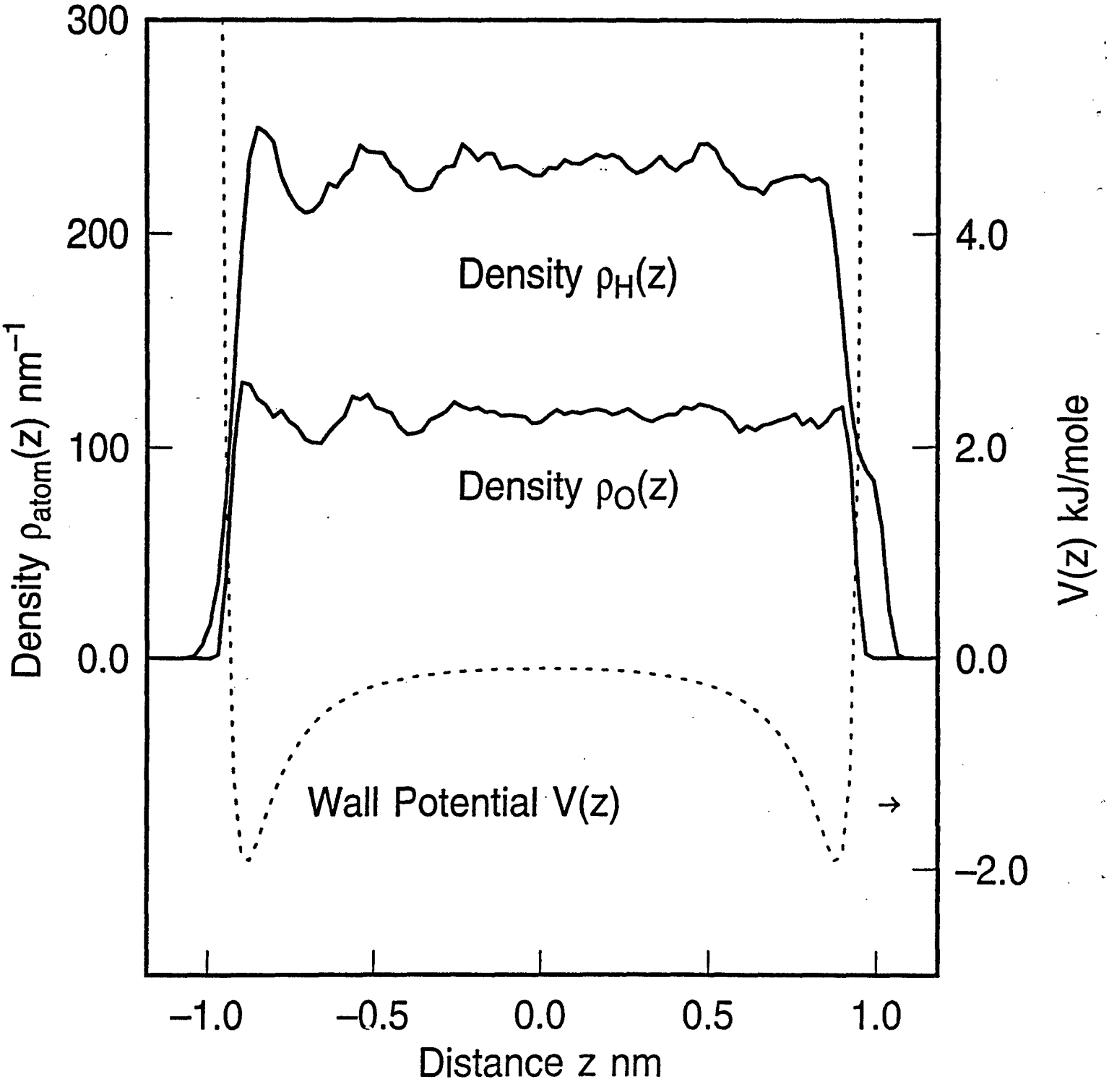
300
200
100
0.0
Density $\rho_{atom}(z)$ nm^{-1}
Density $\rho_H(z)$
Density $\rho_O(z)$
Wall Potential V(z)
4.0
2.0
0.0
−2.0
V(z) kJ/mole
−1.0
−0.5
0.0
0.5
1.0
Distance z nm

Figure 2

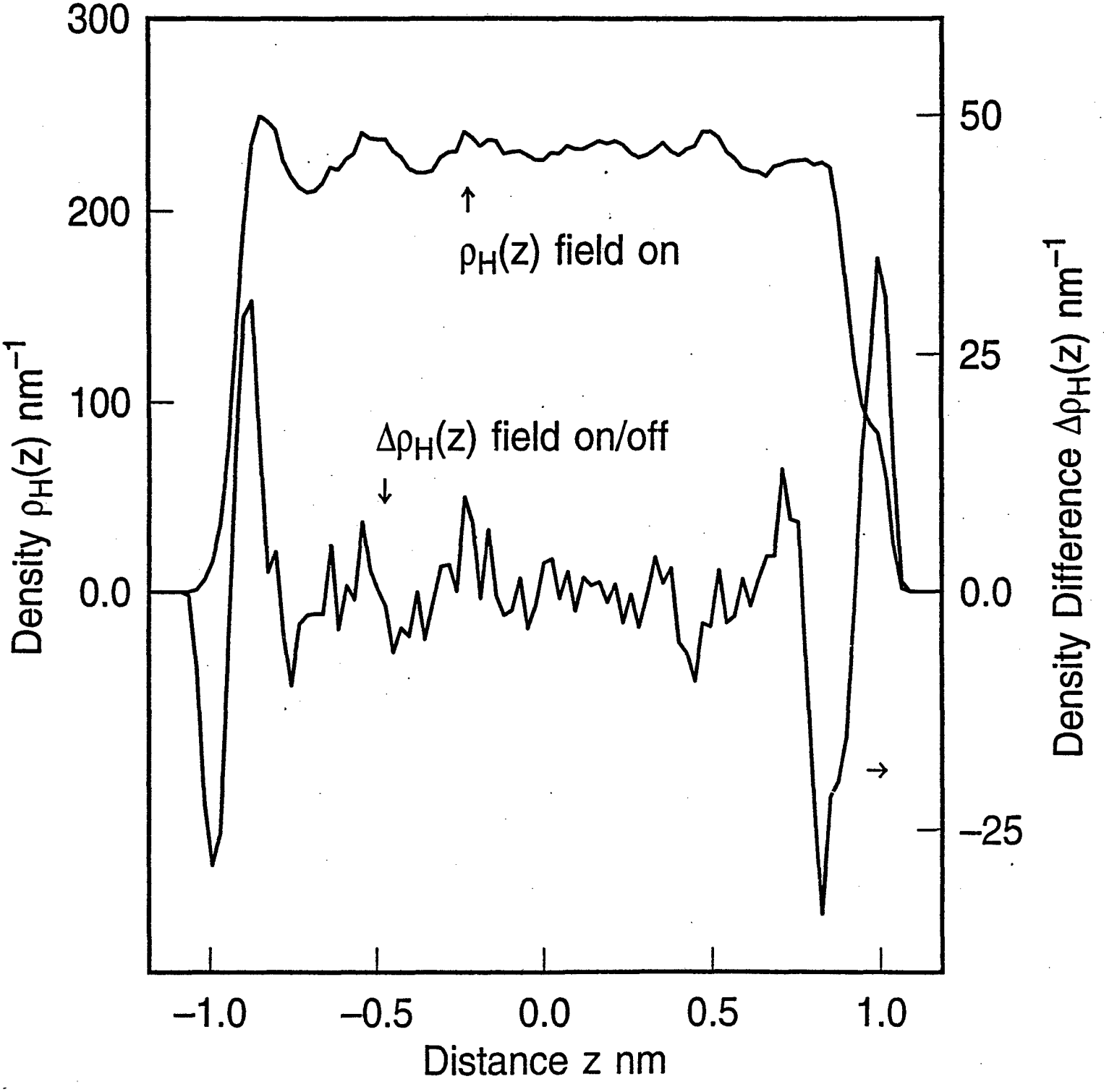
300
200
100
0.0
50
25
0.0
−25
ρ_H(z) field on
$\Delta\rho_H$(z) field on/off
Density ρ_H(z) nm^{-1}
Density Difference $\Delta\rho_H$(z) nm^{-1}
−1.0
−0.5
0.0
0.5
1.0
Distance z nm

Figure 3

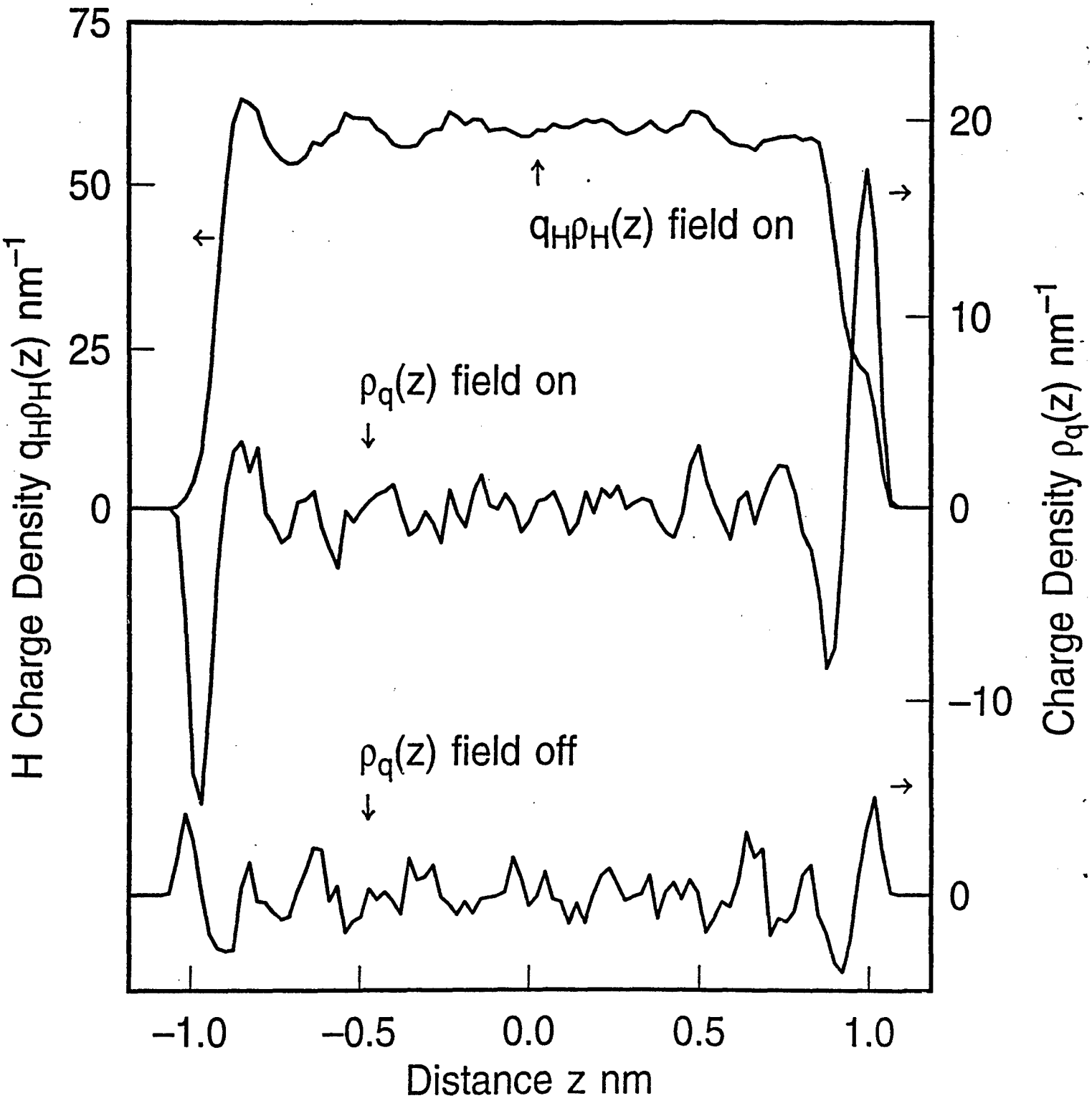
75
50
25
0
20
10
0
−10
0
−1.0
−0.5
0.0
0.5
1.0
Distance z nm
H Charge Density $q_H\rho_H(z)$ nm^{-1}
Charge Density $\rho_q(z)$ nm^{-1}
$q_H\rho_H(z)$ field on
$\rho_q(z)$ field on
$\rho_q(z)$ field off

Figure 4

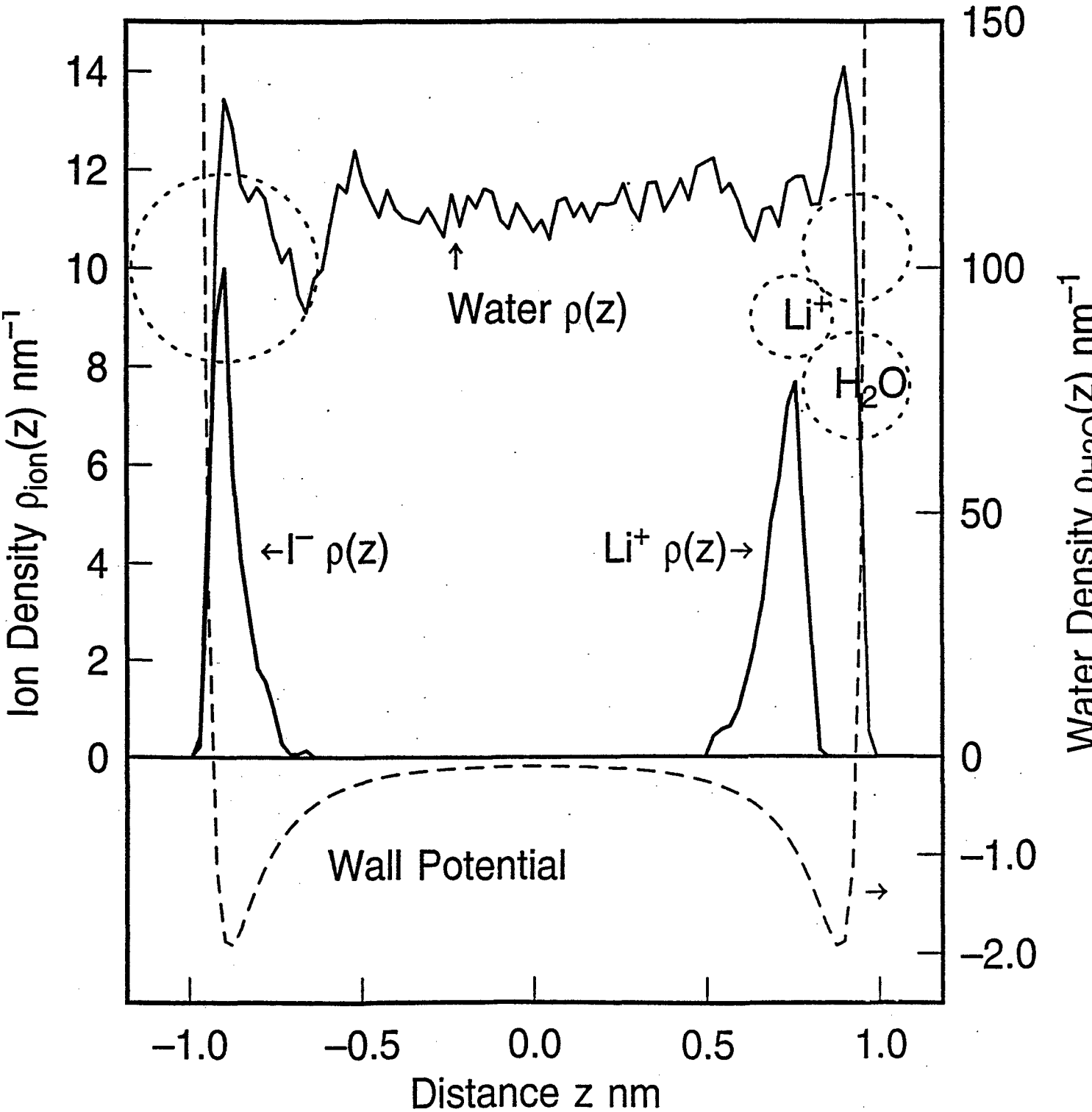
Ion Density $\rho_{ion}(z)$ nm^{-1}
Water Density $\rho_{H2O}(z)$ nm^{-1}
Distance z nm
Water ρ(z)
Li+
H2O
←I− ρ(z)
Li+ ρ(z)→
Wall Potential
14
12
10
8
6
4
2
0
150
100
50
0
−1.0
−2.0
−1.0
−0.5
0.0
0.5
1.0

Figure 5

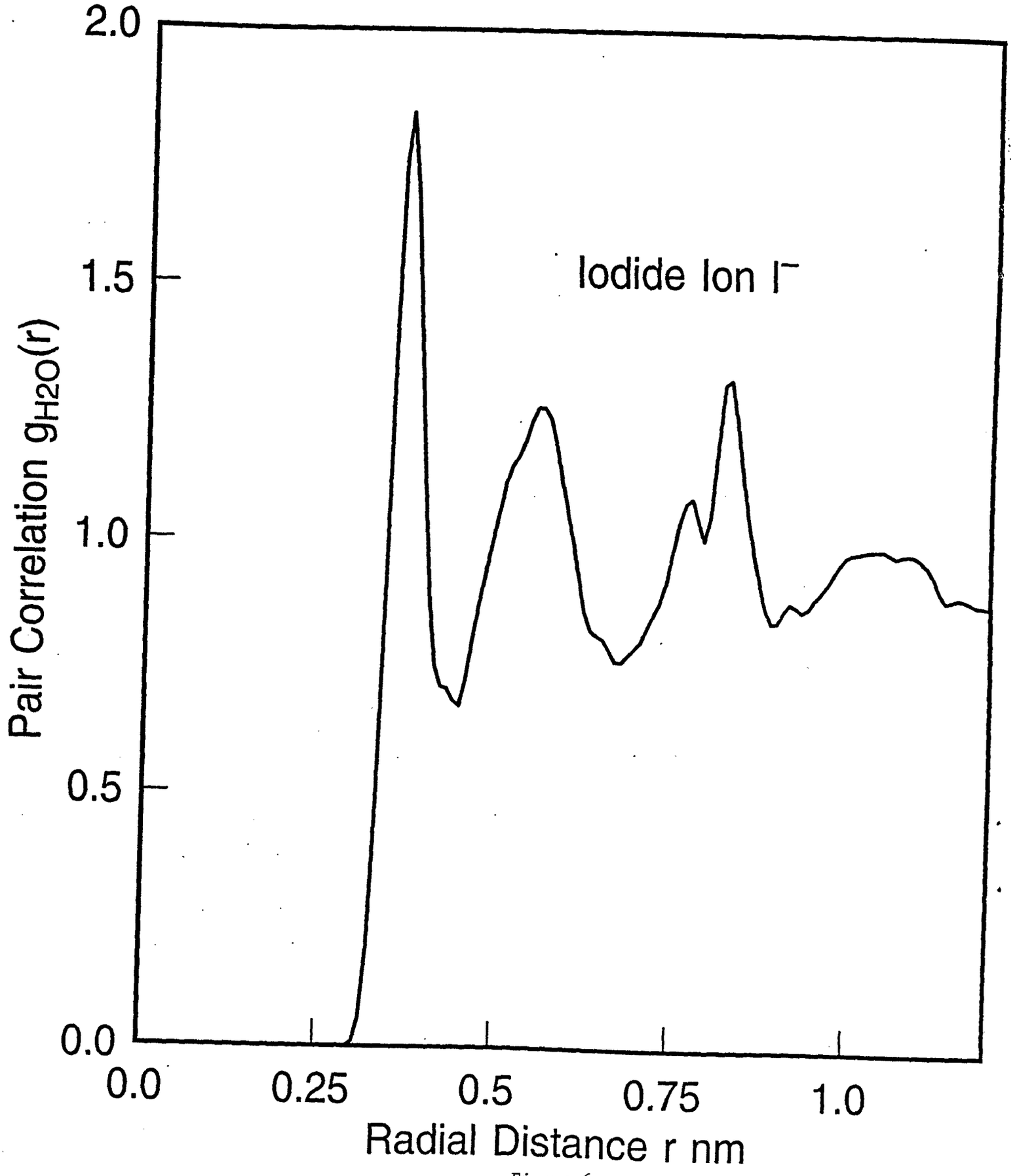
2.0
1.5
1.0
0.5
0.0
Iodide Ion I⁻
Pair Correlation $g_{H2O}(r)$
0.0
0.25
0.5
0.75
1.0
Radial Distance r nm

Figure 6

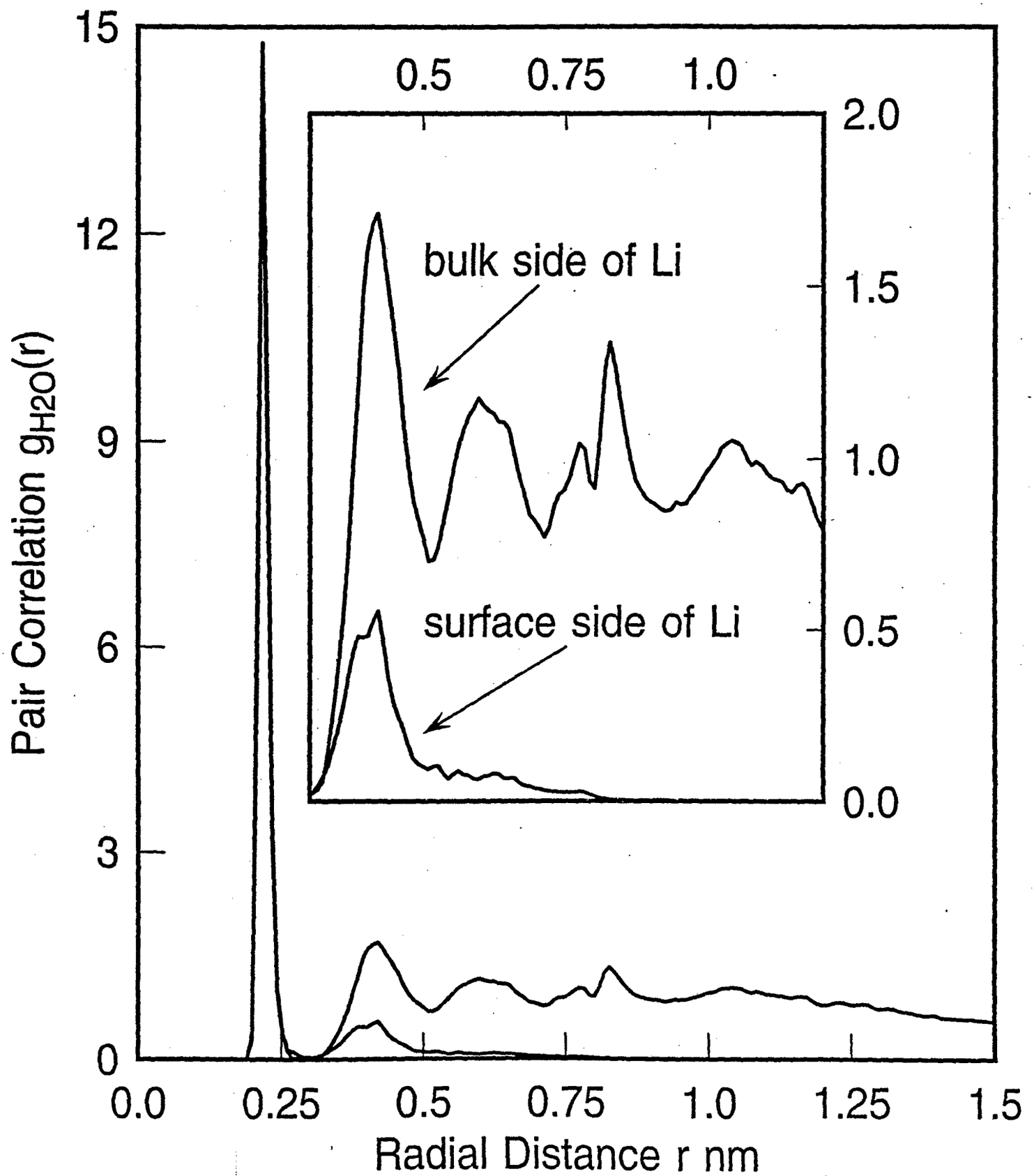
15
12
9
6
3
0
0.0
0.25
0.5
0.75
1.0
1.25
1.5
Radial Distance r nm
Pair Correlation $g_{H2O}(r)$
0.5
0.75
1.0
2.0
1.5
1.0
0.5
0.0
bulk side of Li
surface side of Li

Figure 7

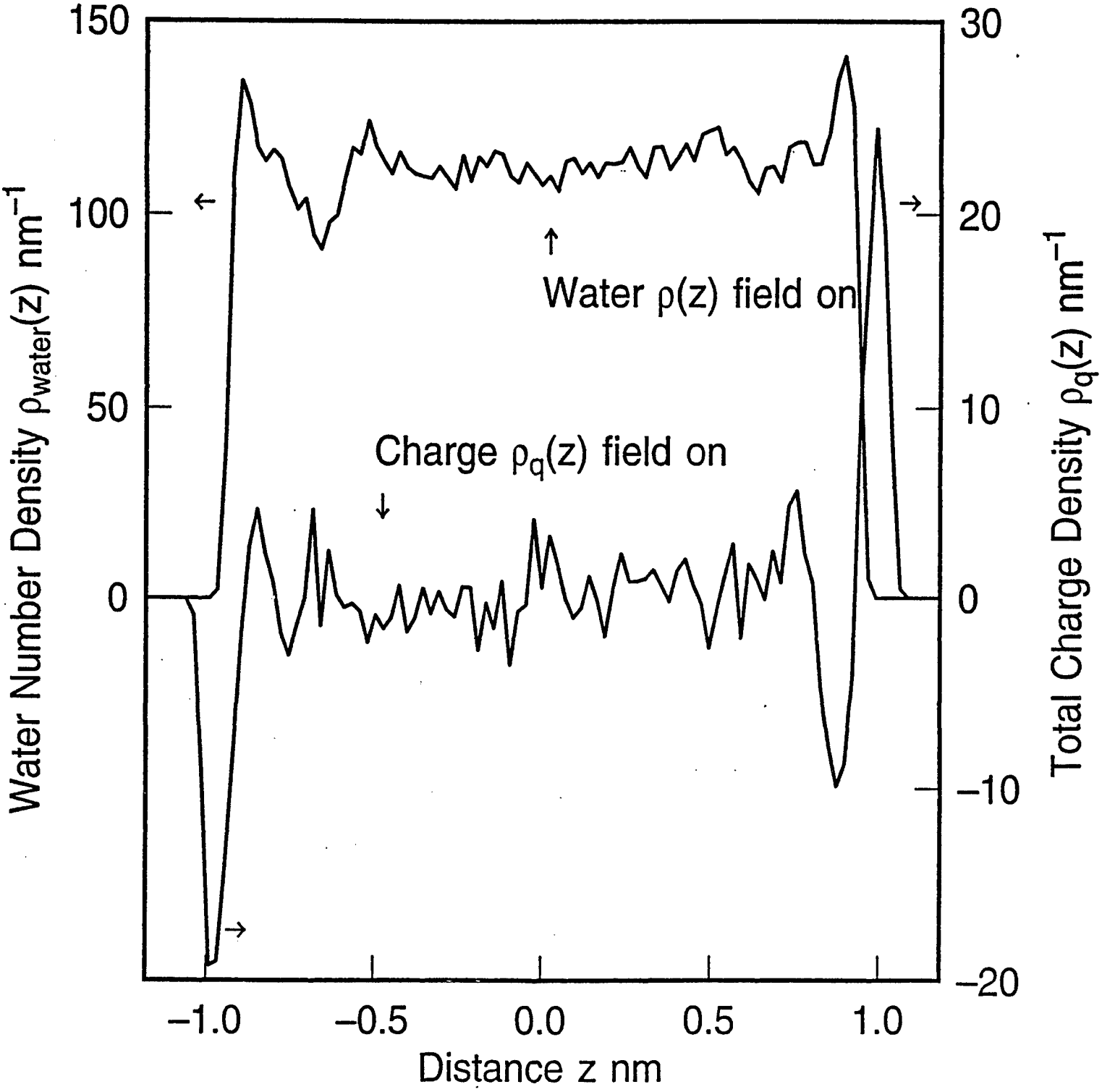
150
100
50
0
30
20
10
0
−10
−20
Water Number Density $\rho_{water}(z)$ nm^{-1}
Total Charge Density $\rho_q(z)$ nm^{-1}
Water ρ(z) field on
Charge $\rho_q(z)$ field on
−1.0
−0.5
0.0
0.5
1.0
Distance z nm

Figure 8

RJ 8846 (79228) June 22, 1992
Chemistry

Research Report

ADSORPTION OF HYDRATED HALIDE IONS ON CHARGED ELECTRODES. MOLECULAR DYNAMICS SIMULATION.

James N. Glosli
Michael Philpott

IBM Research Division
Almaden Research Center
650 Harry Road
San Jose, California 95120-6099

IBM Research Division
Yorktown Heights, New York • San Jose, California • Zurich, Switzerland

RJ 8846 (79228) June 22, 1992
Chemistry

Jun. 10, 1995

ADSORPTION OF HYDRATED HALIDE IONS ON CHARGED ELECTRODES. MOLECULAR DYNAMICS SIMULATION.

James N. Glosli
and
Michael R. Philpott

IBM Research Division
Almaden Research Center
650 Harry Road
San Jose, CA 95120-6099

ABSTRACT

Constant temperature molecular dynamics has been used to simulate the adsorption of hydrated lithium ion Li^+ and the halide ions X^- = F^-, Cl^-, Br^- and I^-, on a flat uniformly charged surface. All of the water molecules and ions interacted with the walls via a weak 9 - 3 potential. The simulations were done with either 214 water molecules and two ions (Li^+ and X^-) in a box 2.362 nm deep or with 430 water molecules and the two ions in a box 4.320 nm deep. The magnitude of the surface charge on the box ends was ± 0.11 e/(nm)^2, corresponding to an electric field of 2×10^7 V/cm. The lateral dimensions of the simulation cell were 1.862 nm × 1.862 nm (x × y) in each case. The ST2 water model and parameters optimized for alkali halides interacting with the model ST2 water molecule were used in the calculations. Common practices of truncating the interactions at a finite distance (0.82 nm) and switching off Coulomb interactions at small distances were followed. The temperature was set at T = 2.411 kJ/mole (290 K).

Some of the properties calculated were: ion - water pair correlation functions, distribution profiles for ions and water across the gap, and the number of water molecules in the first and second hydration shells of the ions as a function of time. The time spent by a water molecule in the hydration shell was calculated to be approximately ten times longer for lithium than any other ion. The correlation between distance from the electrode and hydration number was studied and generally found to be pronounced for the larger anions.

The smallest ion Li^+ remained fully solvated at all times. Comparison of the dynamics of the Li^+ for different anions revealed the subtle influence of a transcell interaction in the 2.362 nm film. The smallest anion fluoride was found to remain fully solvated and was at all times separated from the electrode by its primary solvation shell. Chloride behaved quite differently. Part of the time the chloride ion was far enough away from the electrode to be fully hydrated and part of the time it was in physical contact (ie., physisorbed) on the electrode with no water molecules interposed between it and the electrode. Bromide favoured contact

OCT. 21, 1992

Molecular Dynamics Modeling of Electric Double Layers

James N. Glosli and Michael R. Philpott
IBM Research Division, Almaden Research Center
650 Harry Road, San Jose, CA 95120-6099

Abstract

Constant temperature molecular dynamics calculations of a simple model of a charged metal electrode immersed in electrolyte show the following features known to exist experimentally : incipience of a compact layer, formation of a diffuse layer, presence of highly oriented water layer next to the metal, penetration of nominally diffuse layer species into inner Helmholtz region, ion pair formation between contact adsorbed ion and diffuse layer ion. All these effects emerge from calculations with the same basic model when either the electrolyte composition or the electrode charge are changed. The systems studied had the general composition $nI^- + mLi^+ + (158 - n - m)H_2O$ where (n,m) = (0,0), (1, 0), (0, 1), (1, 1), and (2, 1). The simulation cell had one metal electrode and one constraining dielectric surface. The surface charge on the metal was either zero, or $\pm e$ the latter corresponding to electric fields of $\pm 5.04 \times 10^7$ V/cm. The st2 water model and parameters for lithium iodide were used in all the calculations. The temperature was 290K. The fast multipole method for long range coulomb interactions was used to calculate all electrical forces. This is the first application of the use of the fast multipole method with molecular dynamics to study properties of electric double layers at a metal surface.

Molecular Dynamics Modeling of Electric Double Layers

James N. Glosli and Michael R. Philpott
IBM Research Division, Almaden Research Center
650 Harry Road, San Jose, CA 95120-6099

Abstract

Constant temperature molecular dynamics calculations of a simple model of a charged metal electrode immersed in electrolyte show the following features known to exist experimentally : incipience of a compact layer, formation of a diffuse layer, presence of highly oriented water layer next to the metal, penetration of nominally diffuse layer species into inner Helmholtz region, ion pair formation between contact adsorbed ion and diffuse layer ion. All these effects emerge from calculations with the same basic model when either the electrolyte composition or the electrode charge are changed. The systems studied had the general composition $nI^- + mLi^+ + (158 - n - m)H_2O$ where (n,m) = (0,0), (1, 0), (0, 1), (1, 1), and (2, 1). The simulation cell had one metal electrode and one constraining dielectric surface. The surface charge on the metal was $q_M = 0, \pm e$ the latter corresponding to electric fields of about $\pm 5 \times 10^7$ V/cm. Net charge in aqueous phase fixed at $q_{Aq} = -q_M$ The st2 water model and parameters for lithium iodide were used in the calculations. The temperature was 290K. The fast multipole method for long range coulomb interactions was used to calculate all electrical forces. This is the first application of molecular dynamics combined with the fast multipole method to study properties of electric double layers at a metal surface.

1 Introduction

This paper describes exploratory molecular dynamics simulations of electric double layers composed of water and monovalent ions adjacent to a metal surface modeled by a Lennard-Jones 9-3 potential and an image potential. The goal of this work was not to describe a particular electrochemical system in great detail, rather it was to determine whether a broad range of double layer phenomena [1, 2] were accessible to simulation using simple models based on the parameters that described bulk properties. For this reason we did not seek to model any particular metal surface, but rather chose only to imbue our model with minimum characteristics of a metal. In choosing ions we selected for known extremes of behaviour. Lithium ion was chosen because it is strongly hydrated and does not normally contact adsorb (same as physisorb) on noble metal electrodes [1]. Consequently lithium ion is expected to be confined to the diffuse part of any electric double layer that forms. Iodide was chosen because it does contact adsorb

and could participate in any compact layer that formed next to the electrode. These attributes of the st2 model Li and I ions were demonstrated by Glosli and Philpott [3, 4] for charged dielectric electrodes. In calculations with ions adjacent to metals electrostatic interactions can be large and long ranged due to the large dipole constituted by the ion and its image. Consequently when large scale interfacial structures organize in ionic systems it is imperative that the 'electrostatics' be calculated efficiently and with sufficient accuracy. For this reason we use the fast multipole method (fmm) of Greengard and Rokhlin [5], described briefly in a companion paper [6], to calculate the electrostatic interactions thereby avoiding the use of cut-offs, reaction fields and the like.

What is remarkable about the results of the calculations reported here is that sytems with a few independent ions display the richness of features found experimentally. Beyond the scope of this present report is an in depth study of concentration effects. We describe only some prelimary work on effects accompanying an increase in electrolyte concentration. This section is concluded with a brief summary of previous studies in this area. There have been simulations of films of pure water between uncharged dielectric walls [3, 7-9], and charged dielectric walls [3, 4, 10, 11]. Some of this work is noteworthy because of a predicted phase transition [10, 11]. There have been numerous reports for uncharged metal walls [12-16], [17-20], including one for jellium [18] and several for corrugated platinum surfaces [15-17, 19, 20] predicting water at on top sites oxygen down on Pt(111) and Pt(100). There have also been some for electrolyte solutions between uncharged and charged dielectric walls [3, 4, 21, 22] emphasising spacial distributions and hydration shell structure. There have been studies for electrolytes between uncharged metal walls [15, 23, 24]. The work of Rose and Benjamin [24] is particularly interesting because umbrella sampling was used to calculate the free energy of adsorption. Finally we mention the studies of water between charged metal walls [25], and electrolytes between charged metal walls [25]. In a lot but not all of this work the long range coulomb interactions were treated in an approximate way. The exceptions relied on the Ewald method or some modification. However the question of full image inclusion and the shape of the containing boundary has to be resolved even in some of these studies. Spherical boundaries are not appropriate for systems with a slab geometry. For the slab one has to perform the conditionally convergent Coulomb sums in a manifestly plane wise fashion [26]. This is a old problem that has occurred in other areas of physics in connection with long range electromagnetic fields inside samples of arbitary shape. It will not be discussed further here. In the calculations reported here a simulation of 100 ps used about 12 hours of cpu time on an IBM RS/6000 model 56F work station.

2 The Model

The immersed electrode was modelled as follows. Integral charge in the aqueous phase q_{Aq}, was exactly balanced by charge on the metal q_M. This is an essential constraint of our immersed electrode model. The advantage of the model is we have less than half the number of water molecules needed to simulate a system with two metal electrodes. The metal was represented by two linearly superimposed potentials. Pauli repulsion and dispersive attractive interactions were represented by a 9-3 potential, and the interaction with the conduction electrons by an image potential. In the calculations described here the image plane and origin plane of the 9-3 potential were coincident. This was tanta-

mount to choosing the image plane and the nuclear plane of the metal surface to be coincident. This was acceptable in our scheme because the Lennard-Jones core parameters σ are all large and the 'thickness' of the repulsive wall is also large (ca. 0.247 nm). On the other side of the simulation cell the electrolyte solution was constrained by the 9-3 potential of the second bounding surface (1.862 nm from the image plane of the metal). We refer to the second surface as a dielectric surface, it's main role was to limit the extent of the fluid phase and thereby make the calculations tractable. In summary of what's right with the model can be listed briefly. Long range coulomb interactions were included in essentially an exact way since all images generated by the metal surface were counted. The average 'mean field' molecular polarizabilities that get bulk properties right were included in the parameters defining the water model. Important effects omitted in this treatment: metal surface topology especially different sites, molecular polarizabilities, and molecular distortions.

In all the calculations reported here we use the parameters of the Stillinger [27, 28] st2 water model and the interaction parameters with Li and I ions developed by Heinzinger and coworkers [29]. The st2 water molecule model consists of a central oxygen atom (O_st2 or O for short) surrounded by two hydrogen atoms (H_st2 or H for short) and two massless point charges (PC_st2 or PC for short) in a rigid tetrahedral arrangement (bond angle = $\cos^{-1}(1/\sqrt{3})$). The O-H and O-PC bond lengths were 0.10 nm and 0.08 nm respectively. The only Lennard-Jones 'atom' in st2 model is the oxygen atom. The hydrogen H_st2 and point charges PC_st2 interact with their surroundings (i.e. other atoms and surfaces) only via Coulomb interactions. Their charges are $q_H = 0.23570|e|$ and $q_{PC} = -q_H$. The O atom has zero charge. The Li and and I ions were treated as non-polarizable Lennard-Jones atoms with point mass and charge. The atom-atom interaction parameters are taken from Heinzinger's review [29]. The (ε,σ) pairs are (0.3164, 0.3100), (0.1490, 0.2370) and (0.4080, 0.5400) for O_st2, Li ion and I ion respectively. The units are ε in kJ/mole and σ in nm . The usual combining rules were enforced for unlike species, namely: $\varepsilon_{AB} = (\varepsilon_{AA}\varepsilon_{BB})^{1/2}$ and $\sigma_{AB} = \frac{1}{2}(\sigma_{AA} + \sigma_{BB})$. The switching function interval ends R_L^{IJ} and R_U^{IJ} all vanish except for st2/st2 pairs, where $R_L^{ST2,ST2} = 0.20160$ nm and $R_U^{ST2,ST2} = 0.31287$ nm.

The atom-surface interaction parameters were those used by Lee at al [7], $A = 17.447\text{x}10^{-6}$ kJ(nm)^6/mole and $B = 76.144\text{x}10^{-3}$ kJ(nm)^3/mole for O, I ion and Li ion. The A and B parameters for H_st2 and PC_st2 were set to zero. The potential corresponding to these parameters describe a graphite-like surface. The Coulomb interaction between molecules was represented as sum of $1/r$ interactions between atomic point charges. These interactions were softened for small molecular separation in the established manner [7] by a switching function S . As already mentioned the short range part of the intermolecular interaction was modeled by Lennard-Jones potential between the atoms of each molecule. All molecule-molecule Lennard-Jones type interactions were cut-off in a smooth fashion at a molecular separation $R = 0.68$ nm by a truncation function T . The atoms of each molecule also interacted with the surfaces at $z = \pm z_o$ where z_o = 0.931 nm. Both surfaces were treated as flat featureless plates with a uniform electric charge density of σ on the metal plate at $+ z_o$. This gave rise to a uniform electric field, $E = 4\pi K\sigma$, in the z-direction where

K the electrostatic coupling constant had the value 138.936 kJ.nm/(mole.e^2) in the units used in this calculation. Recall total charge on the electrode was $q_M/e = 0, \pm 1$. The complete interaction energy U is,

$$U = \sum_{\substack{\beta \in A_j \\ i<j}} \left(\left\{ \frac{K q_\alpha q_\beta}{r_{\alpha\beta}} \left[S(R_{ij}, R_L^{ij}, R_U^{ij}) - 1 \right] + 4\varepsilon_{\alpha\beta} \left[\left(\frac{\sigma_{\alpha\beta}}{r_{\alpha\beta}} \right)^{12} - \left(\frac{\sigma_{\alpha\beta}}{r_{\alpha\beta}} \right)^{6} \right] \right\} T(R_{ij}) + \frac{K q_\alpha q_\beta}{r_{\alpha\beta}} \right) \tag{1}$$

$$+ \sum_\alpha \left\{ - q_\alpha E z_\alpha + \left(\frac{A_\alpha}{(z_\alpha + z_o)^9} - \frac{B_\alpha}{(z_\alpha + z_o)^3} \right) + \left(\frac{A_\alpha}{(z_\alpha - z_o)^9} - \frac{B_\alpha}{(z_\alpha - z_o)^3} \right) \right\}$$

where i and j were molecular indices, and, α and β were atomic indices. The symbol A_i represented the set of all atoms of molecular i . The symbol R_{ij} was the distance between the center of mass of molecules i and j. The symbol $r_{\alpha\beta}$ was the distance between atoms α and β. For small R we followed the practise of modifying the the Coulomb energy between st2 molecules and ions by the switching function $S(R, R_L, R_U)$ given by,

$$S(R, R_L, R_U) = \begin{cases} 0 & R < R_L \\ \dfrac{(R - R_L)^2 (3R_U - 2R - R_L)}{(R_U - R_L)^3} & R_L < R < R_U \\ 1 & R_U < R \end{cases} \tag{2}$$

The values of R_L and R_U were dependent on the types of the molecular species that were interacting.

As mentioned above the tails of the Lennard-Jones pair interactions were cut off by the truncation function T. The form of T was given by,

$$T(R) = \begin{cases} 1 & R < R_L^T \\ \left(1 - \left(\dfrac{R - R_L^T}{R_U^T - R_L^T} \right)^m \right)^n & R_L^T < R < R_U^T \\ 0 & R_U^T < R \end{cases} \tag{3}$$

The same truncation function has been applied to all non Coulombic molecular interactions, with $R_L^T = 0.63$ nm and $R_U^T = 0.68$ nm. The integers m and n controled the smoothness of the truncation function at R_L^T and R_U^T respectively. In this calculation $n = m = 2$ which insured that energy was smooth up to first spatial derivatives.

Bond lengths and angles were explicitly constrained by a quaternion formulation of the rigid body equations of motion [30]. The equations of motion were expressed as a set of first order differential equations and a fourth order multi-step numerical scheme with a 2 fs time step was used in the integration. At each time step a small scaling correction was made to the quaternions and velocities to correct for global drift. Also the global center of mass velocities in the x and y directions was set to zero at each time step by shifting the molecular translational velocities.

3 Electrodes Immersed in Electrolyte

This section describes briefly our studies of the immersed electrode using the model described in the last section. In the absence of ions 158 water molecules corresponded to about 4.5 layers of water. The layer was not complete in the sense that in the Lee model [7] the 216 water molecules organized roughly into six layers. Most of the simulations were run for 100 ps to anneal the film and then for a further 900 ps to gather configurations used in the construction of the density profiles shown in the figures. The density plots in Figures 1 and 2 used configurations stored every 1.0 ps. The density plots in Figures 3 to 6 used configurations stored every 0.5 ps.

3.1 158 st2 Waters. Immersed Metal Electrode

Uncharged Electrode. Figure 1 displays water component (molecule center of mass H_2O, proton H_st2, and point charge PC_st2) density profiles $\rho(z)$ for 158 st2 water molecules averaged in the xy plane with a bin size of 0.005 nm. The simulation time was 0.9 ns with configurations stored every 1 ps. There are four clearly visible peaks in H_st2, PC_st2 and H_2O, with some 'pile up' at the walls. Compared to the previous calculations of Glosli and Philpott [3, 4] the presence of the metal's image plane has almost no effect on the densities. The charge density shows weak positive deviations from zero at the boundaries due to the longer length of the O-H bond (0.1 nm) compared to the O-PC bond (0.08 nm). Qualitatively this appears little different from the two dielectric surface [3] result.

Anodically Charged Electrode. The results for field on resemble those published earlier for 216 st2 water molecules [3] in a weaker field of $2x10^7$ V/cm (equivalent to 0.11 e/(nm)^2). In the current simulation the field is about three times stronger and the film effectively 0.3 nm thinner. Figure 2 shows the density profiles for a field that repelled protons away from the metal. Notice that there is an overall loss in structure in the water density, which appeared distinctly flatter than the correponding profile in zero field (compare Figure 1). There was a distinct peak at the dielectric surface for H_st2 atoms that caused the left hand peak in the charge density. There was about 1.7e of charge in this peak and about -0.5e units in the adjacent negative going peak due to PC_atoms in the the first layer of water at the dielectric electrode. This negative charge comes from the main peak in the PC_density profile at -0.65 nm. At the metal electrode the oscillation in the charge density was less pronounced but qualitatively the same. The minimum at 0.75 nm was due to the distinct shoulder in the PC atom density and the peak at 0.6 nm was due to main peak in the H atom density at about 0.6 nm (see Figure 2).

In agreement with the earlier study, we see in the charge density a region that over compensated the charge next to the surface followed immediately by a layer of charge of opposite sign that in turn partially compensated the first. These layers were closer togther than the diameter of a water molecule and were due to closer packing of water molecules at the surface. This packing was the result of partial breaking of H-bonds by the applied electric field and 9-3 surface field.

3.2 I^- and 157 Waters. Compact Layer on an Anodically Charged Metal

Iodide represents one extreme case of adsorption. Experimentally iodide is known to contact adsorb, in contrast to hydrated lithium ion which does not. The simulation cell contained one iodide ion and 157 st2 water molecules. In this simulation the field across the system was an attractive field for anions equivalent to that generated by -1 unit of electronic charge smeared uniformly over the $z = +0.931$ nm plane. Figure 3 shows density profiles for all the components of the system as a function of distance across the gap. The bin size used in accumulating the densities was approximately 0.005 nm.

The high field behaviour of one iodide ion in 157 waters was found to be similar to that found previously for iodide in LiI and 214 waters between charged dielectric electrodes [3, 4]. Basically the iodide distribution here consisted of one sharp peak indicating that the ion spends almost all its time at the repulsive wall boundary of the metal, and this high field behaved like a strong contact adsorber. The narrowness of the distribution indicated that only short time excursions were made away from the surface. Figure 3 shows it to be rarely removed more than 0.1 nm from contact. The anion density profile was sharply peaked at $z = 0.700$ nm very close to the beginning of the repulsive wall at 0.684 nm. The point of closest approach was about 0.74 nm, and that farthest retreat was about 0.65 nm. In the charge density profile the iodide contributed a sharp negative peak on top of a rather broad negative density region centered around 0.72 nm due to the PC atoms of the first layer of water. We discuss this water layer next.

There was significant structure in water, H and PC densities near the metal boundary. The water density displayed four pronounced maxima and one minimum (see Figure 3): narrow peak at -0.67 nm due to water pile up at the dielectric boundary, a broad peak at 0.28 nm followed by an equally broad minimum at 0.43 nm likely due to water exclusion from the vicinity of iodide due to it's ssize, a peak at 0.56 nm due to 'non oriented surface water' and a sharp peak at 0.66 nm due to highly oriented surface water with one PC atom pointed directly at the metal.

This last feature must along with the sharp iodide peak be considered a key feature of the inner region of the double layer. The strongly oriented layer of surface water one molecule thick occurred when the applied field and anion and image field reinforced. The two peaks at $z = 0.74$ and 0.63 nm ($\delta z = 0.11$ nm) in the PC density arose from the negative charge on the same molecule, one pointing directly at the metal and the other away at the tetrahedral angle. The surface peak in the H density at 0.62 nm was approximately twice the area (over background) but at same position, clearly indicating that it belonged to the same highly oriented surface layer.

The PC density as mentioned already had two components near the surface. The peak at 0.74 nm contributed approximately -1.5|e| to the total negative charge (about -2.5|e|) in the large negative peak in the total charge density at 0.70 nm. Between -0.6 nm and 0.4 nm the H and PC densities are computed to be almost identical, so that this region was always neutral. Comparing the charge densities of pure water and this system we see that the presence of the ion and it's image created extensive polarization of the water. The metal boundary showed strong polar regions with alternating sign extending to out $z = 0.2$ nm as a result of water structure resulting from shielding of the fields of the charged electrode, adsorbed iodide ion, and the first layer of oriented water.

3.3 Li^+ and 157 waters. Diffuse Layer on a Cathodically Charged Metal

Figure 4 shows density profiles of the single lithium ion (normalized to unity), 157 waters, H and PC components, and the charge density across the system with a bin size of 0.005 nm. The density plots in this Figure used configurations from 100 ps to 1000 ps, stored every 0.5 ps.

In this simulation the field was reversed, the charge on the metal being -1.0|e|, so that the positive ion was attracted to the metal on the right side of the figure. First thing to notice is the over all similarity to Figure 3 in the water, H and PC profiles except that the profiles for H and PC are reversed in the case of Li compared to I due to change in field direction. This means that there was a highly oriented layer of surface water with protons H pointing directly at the metal. This reversal was of course quite consistent given the reversal in the field and the fact that the direction of ion field and that of it's image were also reversed. The peak heights were larger in the present case for three reasons. First the protons H_st2 could get closer to the image plane than in the case of PC_st2 because O_H bond was longer. Second the field af the Li ion and it's image was spread over a larger area of the electrode because it is located further from the electrode. Third the Li ions primary hydration shell penetrates to the wall and contributes localized water to the distributions.

The density profile for Li defines a bimodal diffuse region between -5.5 and 5.5 nm with a minimum at 0.15 nm. Thoughout this region the total charge was mostly zero. The distance of closest approach to the hard wall of the metal was approximately 0.13 nm or the radius of a water molecule. At this extremum the primary hydration shell of the lithium ion has to be mixed in with the highly oriented layer of water at the surface. The positive ion felt the influence of it's image and was 'splayed' against the hard wall thereby affording a further reduction in the distance of approach to less than $0.5(\sigma_{Li}+\sigma_O)$. Glosli and Philpott [3, 4] have discussed the adsorption of hydrated ions and their possible distances of approach. At the minimum of the bimodal Li ion distribution the distance from the hard wall was approximately 0.54 nm, which should be compared with 0.60 nm the distance correponding to separation from the wall by two water molecules. The interpretation of the Li distribution now seems clear. The peak between -0.55 and 0.15 nm is most likely a diffuse layer component with distance of closest approach being the outer Helmholtz plane, whilst the ssomewhat weaker diffuse-like component closer to the metal represents the smaller statistical probability of prenetrating past the outer plane into the inner layer. This latter process will dependent stongly on the exact nature of the forces acting at the surface (crystal plane sites, size of the ion, etc.) and in some experimental systems and might well be absent altogether. What is important here is the idea that nominally diffuse layer ions can penetrate the outer plane and comingle with inner layer species. As mentioned already the ability of an ion to do this will depend critically on double layer structure and topography of the electrode surface.

3.4 Li^+, I^- and 156 Waters. Weakly Oriented Water at the PZC

In this simulation the applied field was zero so there was no charge on the metal electrode. In some ways this case mimics the potential of zero charge (pzc). The main electrostatic fields are now amongst the charges making up the ions and water and their images in the metal surface at z = 0.931 nm. Figure 5 displays the density profiles for water, protons H_st2, point charges PC_st2, each ions and the total charge density as a function of position across the film.

Some of the features were similar to those discussed already. Emphasised here is on major points of difference. The surface electric fields due to ions and their images were weaker since there was no net applied field and the image fields of the ions tend to cancell on the average. We note first of all that all the water related densities were flatter across the whole film, the H and PC surface peaks appear only as shoulders, just as in the case already examined of water in zero field. This means that first layer of water was not well oriented as in the previous two examples. This is of course consistent with the experimental finding that at the pzc water is less well bound. Consistent with this conclusion was the observation that the charge density was positive at the extreme edge of the film. This is consistent with the known result for water without ions [3] snd the charge profile displayed in Figure 1.

Note that the iodide density has a tail not present in any of the simulations with non zero fields, that overlaps the tail of the Li ion distribution. This was a new feature that signals the possible formation of temporary ion pairs in the double layer. In this case the contact adsorbed ion attracted compensating ion of opposite sign from out of the diffuse layer. In the present case the separation between iodide peak and nearest Li peak was approximately 0.55 nm. This would seem to rule out an ion pair configured with nuclei along the surface normal with interposed water molecule from the primary solvation shell of the cation. This configuration would require a separation of 0.7 nm for all centers to be collinear.

That this interaction could locally alter the diffuse layer can be seen by comparing the diffuse regions of Li ion in Figure 4 with that shown in Figure 5. The idea of altering the position of the outer plane to change the field across the inner layer has been proposed many times. We cite only one example from our own experimental work [31]. References to the work of Bewick can be found there. Clearly this phenomenon could be studied further even with the primative model used here.

The minimum in the bimodal Li ion distribution was at approximately -0.1 nm. At this position the Li ion was separated from the hard wall by 0.784 nm, much more than two water molecules. At the pzc the Li ion was not bound by a charge originating on the metal. It was bound by the field of the contact adsorded species and its image. Since this was a dipole field the attraction between the iodide and lithium ions was weak. The Li ion in the density between -0.55 and -0.10 nm may be metastable and may well displace to larger separations if the water film were thicker.

3.5 Li^+, two I^- and 155 waters. Diffuse and Compact Layers

In this simulation there was a field of appproximately $5x10^7$ V/cm attracting negative ions to the metal. Figure 6 displays the density profiles for all components of the system and the charge density. The simulation time was 1000 ps with the first 100 ps discarded for equilibration, configurations were stored every 0.5 ps.

Note that both iodide ions were adsorbed in a sharply peaked distribution that resembled the single adsorbed iodide distribution in Figure 3 than the iodide distribution with the tail seen in Figure 5 of the last section. The single Li ion occupies a (possibly weakly bimodal) diffuse-like distribution between -0.6 nm and 0.3 nm. At large negative z this distribution has a gradually fall off that would be expected for an electrostatically bound species. In contrast the tail of Li ion in Figure 4 drops quickly suggesting it was modified by the presence of the confining dielectric wall. On the positive side the main component of the distribution ends at 0.05 nm. This latter position was 0.63 nm from the hard wall, and was roughly at the same place for the outer plane of Figure 4. The region between 0.05 and 0.3 nm defines, as in Figure 4, the region of greatly reduced probability of penetrating into inner layer and contacting the adsorbed iodide ions.

It was noticable that the water structure near the metal surface was less well defined than for either a single iodide or a single lithium ion. The reason for this was another new effect, water displacement from the interface as large ions contact adsorb. There was less water to orient next to the metal, and the density profiles mirror this fact.

4 Conclusions

In the introduction the question was could the behaviour of molecules and ions near a metal surface be qualitatively modeled with bulk parameters. Broadly speaking the answer appears to be yes. This means that the range of phenomena predicted is consistent with experimental observation. It does not mean that in any specific case we can model detailed behaviour. We have shown how a simple model suffices to reproduce many phenomena familiar from experiments on electric double layers at the electrolyte-metal interface. A key tool was the use of the fast multipole method to accurately and efficiently calculate coulomb interactions so that long range electric fields were computed correctly. This is very important for polar systems. The phenomena described included: contact adsorption of large ions on metals driven by image interactions, diffuse layers of strongly hydrated species, an oriented boundary layer of water next to the electrode when it is charged, relatively poorly oriented water next to uncharged electrode, and a zone of overlap between ions of opposite sign again when the electrode is not charged.

Finally we point out that these calculations suggest that modelling the electrochemical interface can be readily extended to such diverse systems as: nanosized structures, microelecrodes, and polymer coated electrodes. A more detailed analysis of phenomena such as these will be presented elsewhere.

Acknowledgements

This research was supported in part by the Office of Naval Research.

References

1 J. O. Bockris and A. K. Reddy, *Modern Electrochemistry, Vol.2* (Plenum Press, New York, 1973).

2 J. O. Bockris and A. Gonzalez-Martin, *Spectroscopic and Diffraction Techniques in* (Kluwer,Dordrecht,Holland, 1990), pp. 1-54.

3 J. N. Glosli and M. R. Philpott, J. Chem. Phys. **96**, 6962-6969 (1992).

4 J. N. Glosli and M. R. Philpott, J. Chem. Phys. **in press**, (1992).

5 L. Greengard and V. Rokhlin, J. Comp. Phys. **73**, 325-348 (1987).

6 J. N. Glosli and M. R. Philpott, ECS Symposium Proceedings, **Toronto**, (1992).

7 C. Y. Lee, J. A. McCammon, and P. J. Rossky, J. Chem. Phys. **80**, 4448-4455 (1984).

8 J. P. Valleau and A. A. Gardner, J. Chem. Phys. **86**, 4162-4170 (1987).

9 Y. J. Rhee, J. W. Halley, J. Hautman, and A. Rahman, Phys. Rev. B **40**, 36-42 (1989).

10 A. M. Brodsky, M. Watanabe, and W. P. Reinhardt, Electrochimica Acta **36**, 1695-1697 (1991).

11 M. Watanabe, A. M. Brodsky, and W. P. Reinhardt, J. Phys. Chem. **95**, 4593-4596 (1991).

12 N. G. Parsonage and D. Nicholson, J. Chem. Soc., Faraday Trans. 2, **82**, 1521-1535 (1986).

13 N. G. Parsonage and D. Nicholson, J. Chem. Soc. Faraday Trans. 2 **83**, 663-673 (1987).

14 A. A. Gardner and J. P. Valleau, J. Chem. Phys. **86**, 4171-4176 (1987).

15 E. Spohr and K. Heinzinger, Electrochimica Acta **33**, 1211-1222 (1988).

16 E. Spohr and K. Heinzinger, Ber. Bunsenges. Phys. Chem. **92**, 1358-1363 (1988).

17 K. Heinzinger and E. Spohr, Electrochimica Acta **34**, 1849-1856 (1989).

18 J. Hautman, J. W. Halley, and Y. Rhee, J. Chem. Phys. **91**, 467-472 (1989).

19 K. Foster, K. Raghavan, and M. Berkowitz, Chem. Phys. Lett. **162**, 32-388 (1989).

20 K. Raghavan, K. Foster, K. Motakabbir, and M. Berkowitz, J. Chem. Phys. **94**, 2110-2117 (1991).

21 R. Kjellander and S. Marcelja, Chemica Scripta **25**, 73-80 (1985).

22 E. Spohr and K. Heinzinger, J. Chem. Phys. **84**, 2304-2309 (1986).

23 J. Seitz-Beywl, M. Poxleitner, and K. Heinzinger, Z. Naturforsch. **46A**, 876 - 886 (1991).

24 D. A. Rose and I. Benjamin, J. Chem. Phys. **95**, 6856-6865 (1991).

25 K. Heinzinger, Pure Appl. Chem. **63**, 1733-1742 (1991).

26 G. E. Schacher and F. W. de Wette, Phys. Rev. **136A**, 78-91 (1965).

27 F. H. Stillinger and A. Rahman, J. Chem. Phys. **60**, 1545 (1974).

28 O. Steinhauser, Mol. Phys. **45**, 335-348 (1982).

29 K. Heinzinger, *Computer Modelling of Fluids Polymers and Solids,* (Kluwer,Dordrecht, 1990), pp. 357-404.

30 M. P. Allen and D. J. Tildesley, *Computer Simulation of Liquids* (Oxford University Press, Oxford, 1989), pp. 88-90.

31 K. Ashley, M. G. Samant, H. Seki, and M. R. Philpott, J. Electroanal. Chem. **270**, 349-364 (1989).

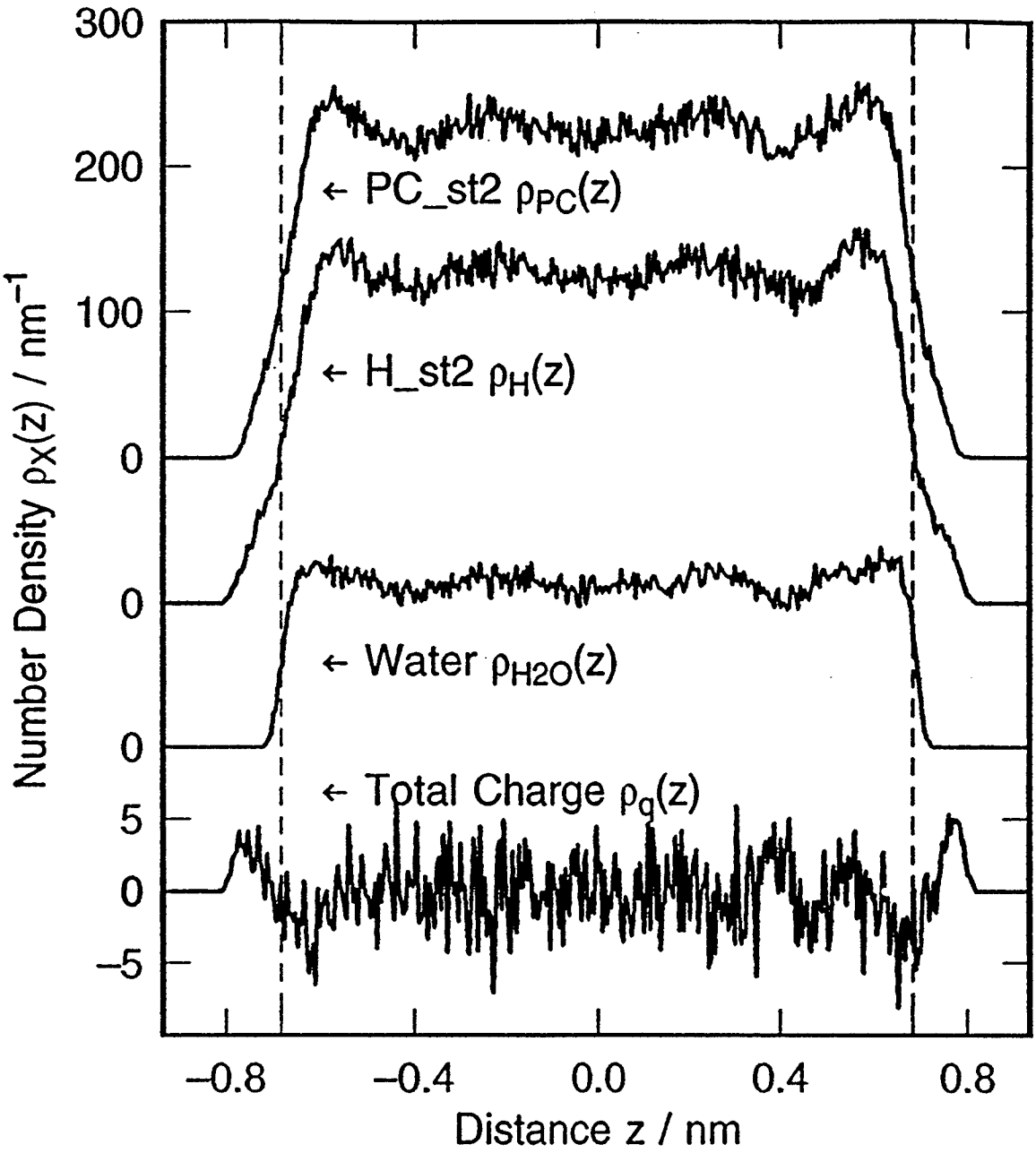

Figure 1. Water in zero field. Density profiles for 158 st2 water molecules adjacent to uncharged metal electrode on right side. Left side confining boundary is a dielectric surface with no image field. Gap between surfaces is $\Delta z = 1.862$ nm.

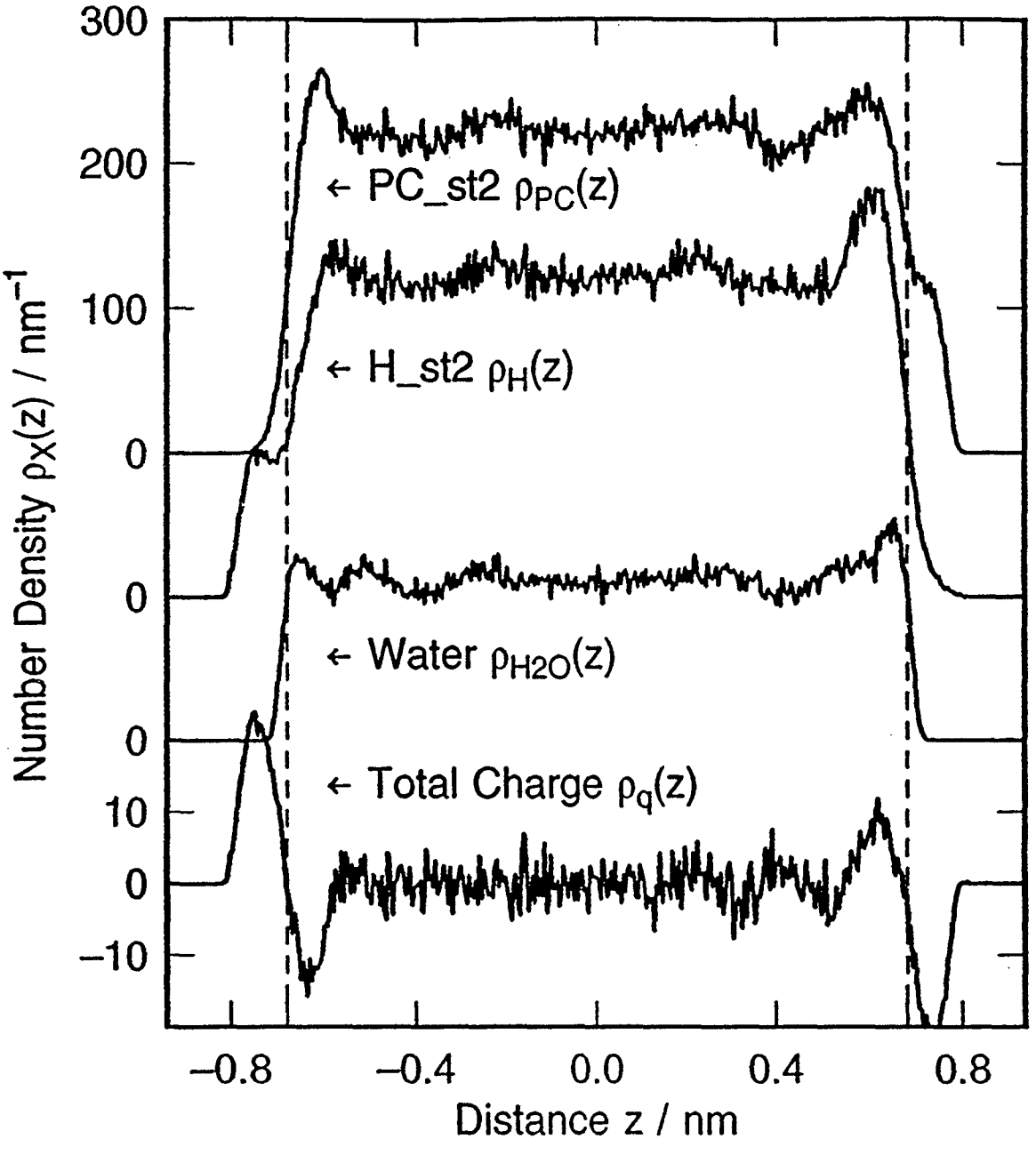

Figure 2. Water in field of 5×10^7 V/cm. Density profiles for 158 st2 water molecules adjacent to charged metal electrode on right side. Right confining boundary is a dielectric surface with no image field. Gap between surfaces is $\Delta z = 1.862$ nm.

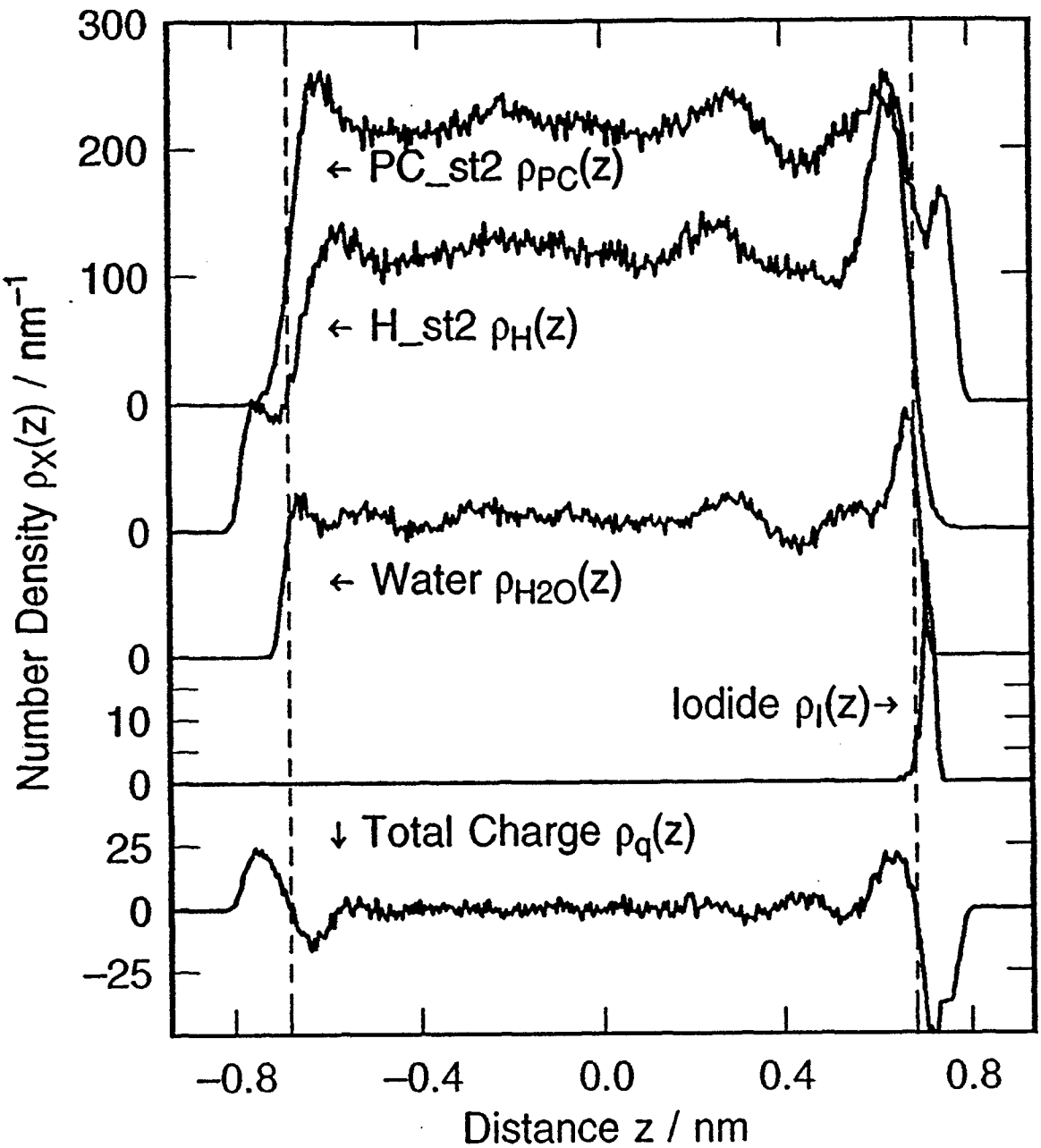

Figure 3. Density profiles for one iodide ion I^- and 157 st2 water molecules between a charged metal electrode and the dielectric boundary. The metal has anodic bias equivalent to a field of 5×10^7V/cm. Image plane at $z = 0.931$ nm . Repulsive portion of the wall potentials begin at $|z| = 0.682$ nm.

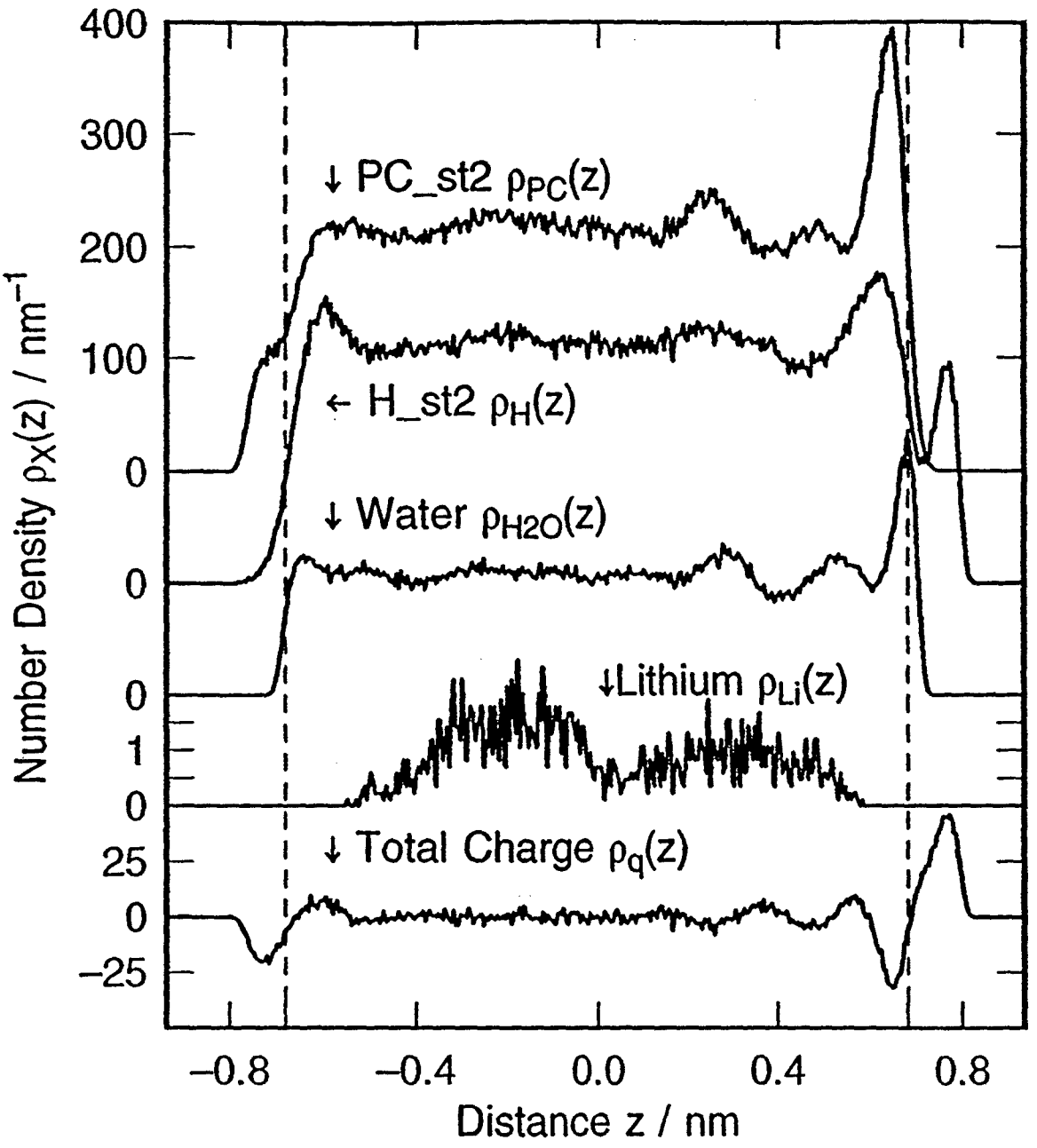

Figure 4. Density profiles for one Li^+ ion and 157 st2 waters near an immersed electrode with cathodic bias. Metal electrode on right hand side, dielectric on the left. Image plane at z = 0.931 nm and repulsive wall at $|z| = 0.682$ nm.

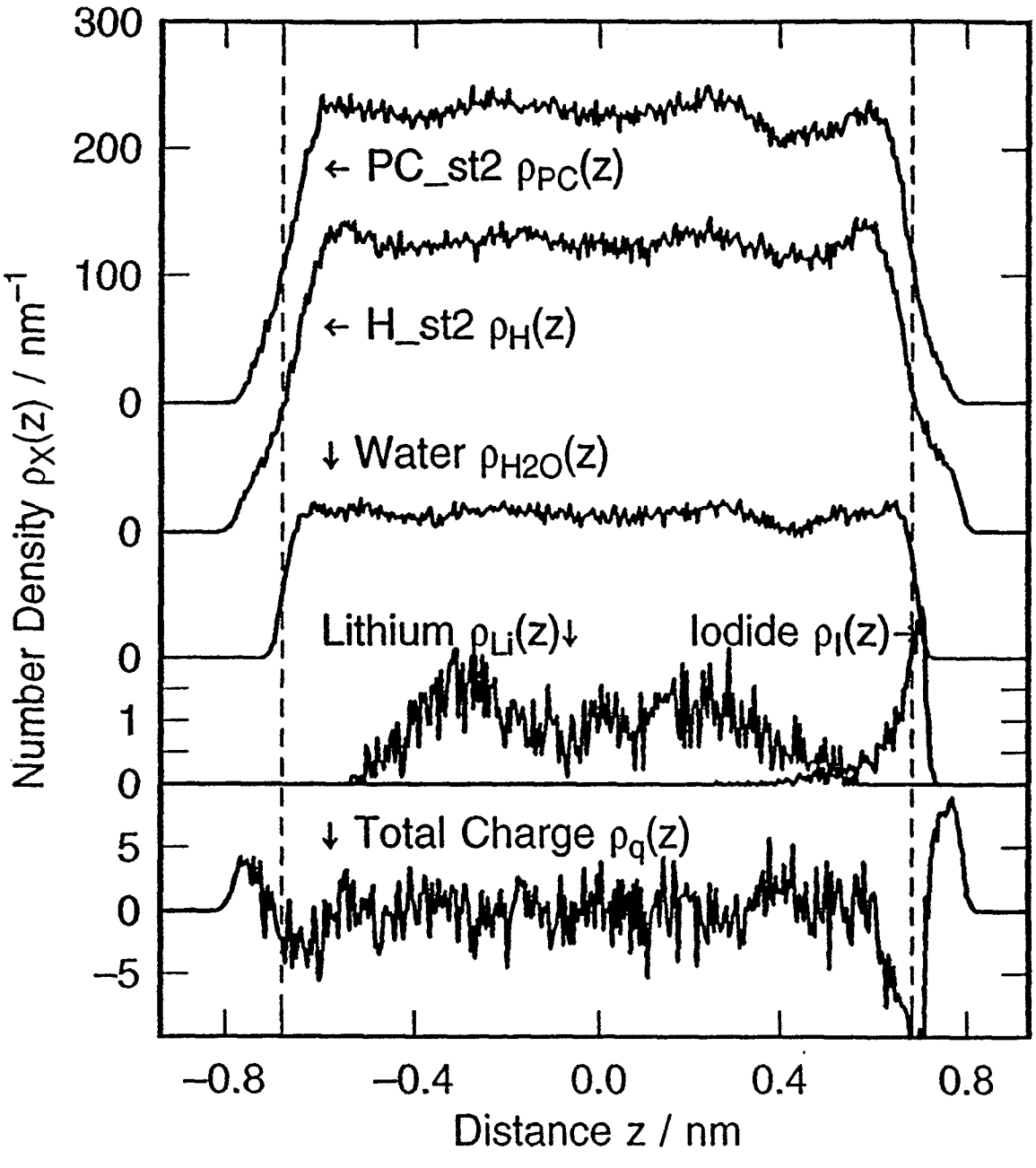

Figure 5. Density profiles for one Li^+ ion, one I^- ion and 156 st2 waters near an uncharged immersed electrode. Metal electrode on right hand side, dielectric on the left. Image plane at z = 0.931 nm and repulsive walls at $|z| = 0.682$ nm.

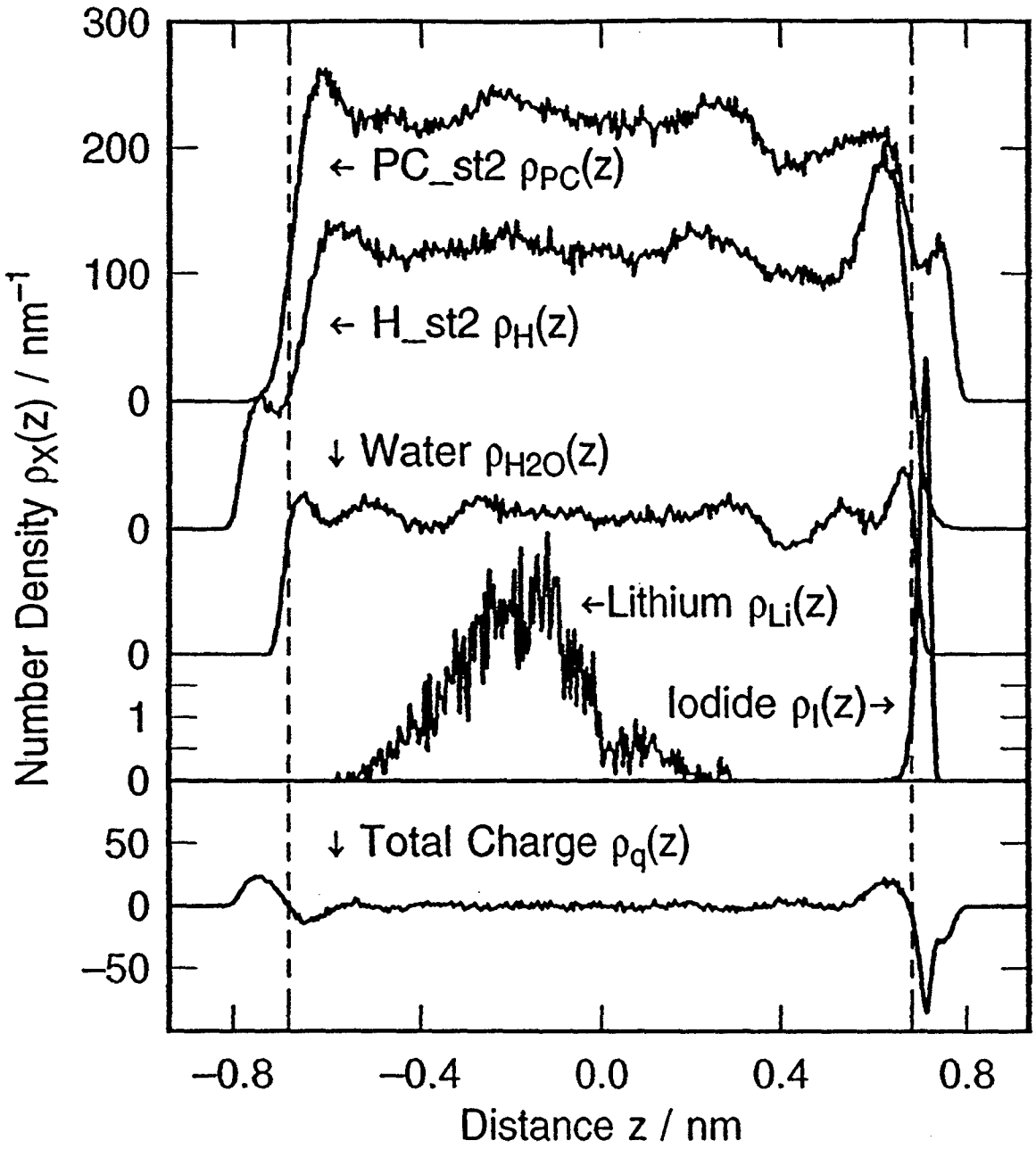

Figure 6. Density profiles for two I^-, one Li^+ and 155 st2 water molecules next to immersed electrode. Anodic bias corresponding to static electric field of $5x10^7$ V/cm.

ADSORPTION OF SULPHATE ON METAL ELECTRODES

Leslie A. Barnes
Michael R. Philpott
Bowen Liu

IBM Research Division
Almaden Research Center
650 Harry Road
San Jose, CA 95120-6099

1. Introduction

Non destructive in situ surface spectroscopies such as FTIR, surface enhanced Raman, second harmonic and sum frequency generation have provided useful information about adsorption, bonding and environment of sulphate. However more important are the fairly recent experiments using in situ surface exafs[1] on upd Cu monolayer on Au(111) and ex situ LEED on emersed Cu electrodes[2]. These experiments were analysed assuming the existence of a Cu-O bond perpendicular to the (111) plane, and an on-top adsorption site for sulphate was proposed, after IR spectroscopy showed the presence of surface sulphate. The original conjecture proposed that sulphate was adsorbed at an on-top site with a Cu-O-S bond perpendicular to the (111) plane.

The aim of the present work was to develope simple models to explore the interaction of sulphate and bisulphate with a metal surface. In previous work studies with Cu clusters and ligands such as O, CO, CN, and SCN had been useful in interpreting IR spectra. Studies with Ag clusters and the ligands F, Cl, Br, I, and N_2 had also provided in sight into the nature of the metal ligand bond and the effect of double layer field on vibrational frequency. However the polyatomic and multicharged ligands SO^{2-}_4 and HSO_4 were much more demanding due to the increased number of atoms and electrons (n^4 problem), and a large amount of cpu time was required to generate even qualitative results. An essential complication encountered with these ligands was their multidentate behaviour. They are able to bind to the surface in three ways (more substrate considered).

Theoretical Calculations

We have performed all electron ab initio SCF Hartree Fock calculations of sulphate and bisulphate oriented over neutral and charged clusters of one, four and ten copper atoms. Analytical derivative methods were used to determine optimal geometries, harmonic vibration frequencies and IR intensities. In some cases a strong electric field (5x10^7 V/cm) was used to mimic effects of the electric field in the double layer. The program CADPAC and the Cambridge Direct SCF program were used on an IBM 3090 mainframe and RS/6000 workstation.

In the first study we considered SO^{2-}_4, HSO_4, $Cu^0SO^{2-}_4$, $Cu^+SO^{2-}_4$, $Cu^0HSO^-_4$, and $Cu^+HSO^-_4$. Both zero and positively charged Cu^0 and Cu^+ were considered to investigate the effect of atomic charge on the bonding, structure and vibrational frequencies. The smallest basis set used on the sulphate and bisulphate molecules was approximately "double zeta": (12,7,1)/[6,4,1] on S, (9,5)/[4,2] on O and (4)/[2] on H. This was used to map out the potential energy surface and determine the important structures. These were then reoptimized using a larger basis set, which supplemented the DZ basis with an additional d function on S, and a diffuse p function and d function on O. For Cu we used the (14,11,6)/[8,6,4] contracted Gaussian basis. Altogether there were 156, 306, and 606 basis functions for $Cu^0SO^{2-}_4$, $Cu^0_4SO^{2-}_4$, and $Cu^0_{10}SO^{2-}_4$.

3. Results for Sulphate

Single atom cluster calculations predicted three different adsorption site geometries as having comparable stablity. Each had a different local symmetry. A fourth orientation with the three O atom down geometry was the less stable by 0.5 eV. Four atom tetrahedal shaped cluster calculations showed that the orientation with three oxygens down became a possible candidate for the top site adsorption, in either orientation of the cluster (see Figure). Four atom cluster calculations for the hollow site showed that the three down geometry (d) was the most stable. This necessitated a calculation on an even larger cluster in order to better represent essential properties of the (111) surface. Ten atom clusters calculations were performed to determine site with greatest binding energy. It was found that the most stable geometry corresponded to three O atoms down with one O over each of three triangularly disposed Cu atoms on the (111) surface. These and related results will be presented as time permits.

4. Conclusion and Significance

Theory predicts a different geometry to one the one originally proposed. In the new geometry there is one O atom above each Cu atom with the S atom positioned over the three fold hollow site. These results illuminate the complexities of large ligand adsorption and serve to demonstrate they can be investigated with help of theoretical calculations.

5. Acknowledgement

This research was supported in part by the Office of Naval Research.

6. References

1. L. Blum et al, J.Chem.Phys.85,6732-6738(1986).
2. C.B. Ehlers and J.L. Stickney, Surf. Sci.239,85-102(1990).

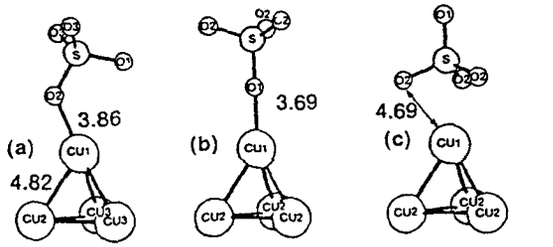

C_V ("1-1/2 down") 0 kcal/mole C_{3V} ("1 down") 4 kcal/mole C_{3V} ("3 down") 6 kcal/mole

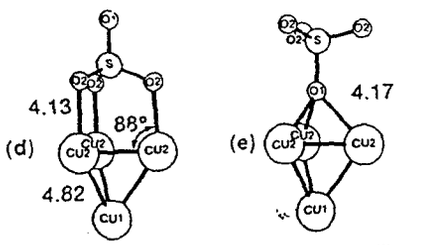

C_{3V} ("3 down") 0 kcal/mole C_{3V} ("1 down") 23 kcal/mole

RJ 9068 (80758) October 30, 1992
Chemistry

Oct. 19, 1992

FAST MULTIPOLE METHOD IN SIMULATIONS OF AQUEOUS SYSTEMS

James N. Glosli
Michael R. Philpott

IBM Research Division
Almaden Research Center
650 Harry Road
San Jose, California 95120-6099

ABSTRACT

The fast multipole method (fmm) for calculating electric fields developed by Greengard and Roklin (J. Comp. Phys. 73, 325(1987)), has been implemented specifically for molecular dynamics simulations of electrochemical problems including boundary conditions associated with metal electrodes. This order N (number of charged particles) algorithm, is known to be computationally much more efficient than direct or Ewald sum methods (order N^2) for systems with as few as one thousand charged particles (equivalent to 300 water molecules). Timings and accuracy estimates with system size N ($16 < N < 16000$) are given to illustrate the effectiveness and efficiency of the fmm.

As an application of fmm we describe it's use with constant temperature molecular dynamics to calculate the dielectric constant of the spce water model in bulk at temperatures 298K and 361K. Systems sizes of 27, 64, 125 and 216 water molecules were considered. Comparison with the Ewald and reaction field methods is made. At 298K the dielectric constant was calculated to be $\varepsilon = 77 \pm 6\%$ and at 361K $\varepsilon = 57 \pm 4\%$. Both values compare well with experiment and the theoretical reaction field simulations.

(80758) October 30, 1992
istry

Research Report

FAST MULTIPOLE METHOD IN SIMULATIONS OF AQUEOUS SYSTEMS

James N. Glosli
Michael R. Philpott

IBM Research Division
Almaden Research Center
650 Harry Road
San Jose, California 95120-6099

RJ 9299 (82229) April 14, 1993
Chemistry

April 08, 1993

Research Report

MOLECULAR DYNAMICS MODELING OF ELECTRONIC DOUBLE LAYERS

James N. Glosli
Michael R. Philpott

IBM Research Division
Almaden Research Center
650 Harry Road
San Jose, CA 95120-6099

IBM Research Division
Yorktown Heights, New York • San Jose, California • Zurich, Switzerland

RJ 9299 (82229) April 14, 1993
Chemistry

MOLECULAR DYNAMICS MODELING OF ELECTRIC DOUBLE LAYER

James N. Glosli
Michael R. Philpott

IBM Research Division
Almaden Research Center
650 Harry Road
San Jose, California 95120

Abstract: Constant temperature molecular dynamics calculations of a simple model of a charged metal electrode immersed in electrolyte show the following features known to exist experimentally : incipience of a compact layer, formation of a diffuse layer, presence of highly oriented water layer next to the metal, penetration of nominally diffuse layer species into inner Helmholtz region, ion pair formation between contact adsorbed ion and diffuse layer ion. All these effects emerge from calculations with the same basic model when either the electrolyte composition or the electrode charge are changed. The systems studied had the general composition $nI^- + mLi^+ + (158 - n - m)H_2O$ where (n,m) = (0,0), (1, 0), (0, 1), (1, 1), and (2, 1). The simulation cell had one metal electrode and one constraining dielectric surface. The surface charge on the metal was $q_M = 0, \pm e$ the latter corresponding to electric fields of about $\pm 5 \times 10^7$ V/cm. Net charge in aqueous phase fixed at $q_{Aq} = -q_M$ The st2 water model and parameters for lithium iodide were used in the calculations. The temperature was 290K. The fast multipole method for long range coulomb interactions was used to calculate all electrical forces. This is the first application of molecular dynamics combined with the fast multipole method to study properties of electric double layers at a metal surface.

MOLECULAR DYNAMICS STUDY OF INTERFACIAL ELECTRIC FIELDS

Michael R. Philpott, James N. Glosli† and Sheng-Bai Zhu
IBM Research Division, Almaden Research Center,
650 Harry Road, San Jose, CA 95120-6099
†Lawrence Livermore National Laboratory,
University of California, Livermore, CA 94550

Abstract

The calculation of interfacial electric fields is one of central importance in electrochemistry. In this paper we describe the structure and properties of electric double layers of selected aqueous electrolyte systems and show how to compute the electric field and potential across the system for a flat charged metal electrode-aqueous electrolyte interface using molecular dynamics. The source terms of the fields were derived from charge and polarization probabilities averaged in the plane parallel to the interface. Two methods were used, one based on source terms in vacuum and the other assuming that the ions and water are mutually exclusive sources of electric charge and electric polarization. Each method provides insight as does the resolution of differences in the computed fields. To illustrate these studies we chose examples from on going work in simulations of aqueous electrochemical interfaces that typify general classes of behaviour. The examples chosen are: non adsorbed hyrated lithium ion Li^+, contact adsorbed iodide ion I^-, a neutral solution of Li^+ and I^-, and coadsorbed Li^+ and two iodides $2I^-$. If time other examples will be drawn from: adsorbed neutral organics, spherical 'electrodes', AFM 'tips', and emersed layers. Interaction of the water and ions with the metal was modelled by a Lennard-Jones 9-3 potential for 'core electron' contribution and image potentials for all charged particles in the simulation cell. Screening of the charged surface and the transition to local neutral bulk electrolyte solutions were studied in simulations with 1600 water molecules and ions.

Williams-Wright Award Address

Do Publication Clearance

VIBRATIONAL SPECTROSCOPY OF MOLECULES ON SURFACES. THEORY AND EXPERIMENT

MICHAEL R. PHILPOTT, IBM Almaden Research Center, 650 Harry Road, San Jose, CA 95120-6099

Difficult problems often require a combination of techniques for their resolution. Examples from the areas of surface electrochemistry and computer disk drive tribology are described.

The discipline of surface electrochemistry is at the foundation of many technologies. This field has grown rapidly with application of ex situ techniques adapted from surface science and from the few in situ techniques that can access buried interfaces. In the last fifteen years vibrational spectroscopies have played an important role in increasing fundamental knowledge of metal electrodes immersed in aqueous electrolyte. We have used theory and experimental vibrational spectroscopy to probe the properties of ligands adsorbed on charged surfaces. The long range goal of this work is a detailed model of the structure and dynamics of electric double layers at charged metal surfaces. The early studies of Bewick and coworkers at the University of Southampton showed the power infra red spectroscopy in electrochemical studies. In our laboratories we took advantage of experimental developments in thin electrochemical cells, advances in Fourier Transform instrumentation, availability of fast polarization modulators, and electrochemical potential modulation, to make surface infra red spectroscopy a powerful technique able to lift minute adsorbate vibration signals out of the water continuum.

Here the story would have sputtered to an end without help from theory. Infra red spectroscopy alone did not provide a model of the adsorption site needed to forward our goal of understanding double layer properties. Fortunately in a number of cases, detailed quantum chemistry cluster calculations permitted

similar electric potential dependence in the stretching frequency ν_L near 2000 cm^{-1}. It was tempting to argue vaguely that because CO and CN^{-1} are isoelectronic their tuning rates $d\nu/dV$ should be similar. However quantum chemistry cluster calculations supplied a very different answer. The CO ligand was datively bonded to metal, with $d\pi$ donated from the metal orbitals into an empty $p\pi^*$, making its geometry quite rigid. The frequency shift comes from the coupling of the local electric field to the dynamic dipole to the CO bond. On the other hand the CN^- ligand was loosely bound, allowing its mass center to shift with change in electrode charge density or local electric field. It was subjected to a 'wall effect' arising from Pauli repulsion, which narrowed the potential wells and raised the stretching frequency as the ion was attracted to the metal surface. The tuning rate for the ν_{CN} stretch mode turned out to be accidentally similar to the rate for ν_{CO}.

An area where vibrational spectroscopy has yet to make a substantial impact is tribology, the science and technology of surfaces in close proximity and in relative motion. As time permits two applications will be described. First is the volatilization of perfluorinated lubricant molecules out of surface crevices on magnetic hard disks in computer disk drives. Second is the use of theory to understand the nature of vibrational spectra of amorphous a:C and a:CH films a few nanometers thick. Lubricants and carbon overcoats are essential to proper functioning of the computer disk in operating disk drives.

This work has been supported in part by the Office of Naval Research. Haj Seki, Bill Golden, Joe Gordon, Keiji Kunimatsu, Paul Bagus and Gianfrano Pacchioni are all due special thanks for their vital contributions over the years.

The spectroscopic exploration of 'buried' interfaces between condensed phases involve challenges that test scientific and technological ingenuity of mankind. Two 'buried'interfaces that impact the GNP of industrial nations are ones where corrosion occurs and where wear occurs. Ameliorating the conditions resulting from corrosion and wear has generally required the expenditure of vast sums of money.

May 28, 1994

Abstract Submitted
for the 1994 March Meeting of the
American Physical Society

21-25 March 1994

Suggested Session Title:
Complex Liquids: Interfacial phenomena

March Sorting Category
5(e) (November)

Molecular Dynamics Modeling of Electric Double Layers Near Flat and Spherical Surfaces as well as Metallic Tips.* M.R. PHILPOTT, S-B. Zhu IBM Almaden Research Center and J.N. GLOSLI, Lawrence Livermore National Laboratory. Molecular dynamics is used to model the structure and dynamics of electric double layers at charged surfaces in contact with water, ions and neutral organics. Surface geometries include small nanosized spheres and tips and flat metals. The electrostatic field is calculated using the fast multipole method of Greengard and Roklin. The focus is on the region between inter and diffuse layer which cannot be modeled by static compact layer or Gouy-Chapman diffuse layer models. Typically simulations last 1-2ns, with 200-1500 water molecules and 1-60 ions. The nature of the compact layer, diffuse-like layer, and the structure of the water next to a metal surface is explored as a function of ion concentration and field strength. The calculations provide microscopic basis for understanding of the dynamics of the outer and inner Helmholtz layers, macroscopic electric fields spanning the double layer and some aspects of surface sensitive spectroscopies.
*Work performed at LLNL under the auspices of the U.S. Department of Energy under contract No. W-7405-ENG-48 and at IBM in part under the auspices of the U.S. Office of Naval Research.

Prefer Standard Session

Submitted by:

James F. Belak

James Belak
Mail Stop L-299
Lawrence Livermore National Laboratory
P.O. Box 808
Livermore, CA 94551
APS Membership Number: MBE308842

May 28, 1994

pub req
5/26/94
dlw

MOLECULAR DYNAMICS MODELING OF ELECTRIC DOUBLE LAYERS NEAR FLAT, SPHERICAL AND 'TIPED' SURFACES. **M. R. Philpott, S-B. Zhu, and J. N. Glosli†, IBM Almaden Research Center, 650 Harry Road, San Jose, CA 95120-6099. †Lawrence Livermore National Laboratory, Livermore CA 94550.**

Molecular dynamics is used to model the structure and dynamics of electric double layers at charged surfaces in contact with water, ions and neutral organics. Surface geometries include small nanosized spheres and tips and flat metals. To avoid truncation artifacts the electrostatic field is calculated accurately using the fast multipole method of Greengard and Rokhlin with boundary conditions adapted for electrochemical interfaces. All molecule- and ion-image interactions were included. The focus is on the region between inner and diffuse layer which cannot be modeled by static compact layer or Gouy-Chapman diffuse layer models. Typical simulations last 1-2 ns, with 200-1500 water molecules and 1-60 ions, show structure corresponding to: compact layer, diffuse-like layer, highly oriented water next to a charged metal when ions are present, penetration of diffuse layer species into the inner layer, and poorly oriented surface water when the electrode is uncharged. Many of these features are known experimentally. The calculations provide microscopic basis for an understanding of the dynamics of the outer and inner Helmholtz layers, macroscopic electric fields spanning the double layer and some aspects of surface sensitive spectroscopies.

RJ 9665 (84105) January 11, 1994
Chemistry

Jan 7, 1994

Research Report

MOLECULAR DYNAMICS COMPUTER SIMULATIONS OF CHARGED METAL ELECTRODE-AQUEOUS ELECTROLYTE INTERFACES

Michael R. Philpott

IBM Research Division
Almaden Research Center
650 Harry Road
San Jose, CA 95120-6099

James N. Glosli

Lawrence Livermore National Laboratory
Livermore, CA 94550

IBM Research Division
Yorktown Heights, New York • San Jose, California • Zurich, Switzerland

RJ 9665 (84105) January 11, 1994
Chemistry

Molecular Dynamics Computer Simulations of Charged Metal Electrode-Aqueous Electrolyte Interfaces

Michael R. Philpott

IBM Research Division
Almaden Research Center
650 Harry Road
San Jose, CA 95120-6099

James N. Glosli

Lawrence Livermore National Laboratory
Livermore, CA 94550

Abstract:
When two different substances are joined, material flows across the interface (sometimes almost imperceptibly) until the chemical potentials of the component species are equalized. When the substances are solid or liquid and some of the chemical species are charged, then the interface develops a net electrical polarization due to the formation of an electric double layer. The main goal of this program of study is to give a molecular basis for understanding the structure and dynamics of electric double layers at charged metal-aqueous electrolyte interface. The aim is to unify current separate descriptions of surface adsorption and solution behavior and, ultimately, to include a detailed treatment of the surface crystalography and electronic properties of the metal.

Oct. 20, 1995

Paper for JEAC proceedings,
Snowdonia Electrified Interfaces Meeting,
Harlech, Wales, UK July 17-22, 1995.

ELECTRIC POTENTIAL NEAR A CHARGED METAL SURFACE IN CONTACT WITH AQUEOUS ELECTROLYTE

Michael R. Philpott
IBM Almaden Research Center,
650 Harry Road, San Jose, CA 95120-6099
and
James N. Glosli
Lawrence Livermore National Laboratory,
University of California, Livermore, CA 94550

Abstract

The time independent electric potential due to water and a lithium ion near a charged metal surface is calculated by space and ensemble averaging of trajectories generated by a molecular dynamics simulation. Since the cation does not contact adsorb variations in the electric potential near the metal surface are due to water oriented in the electric field of the charged surface. The potential is decomposed into separate contributions from monopoles (from the ions), and dipoles, quadrupoles and octopoles (from the water molecules). At distances greater than about 0.5 nm from the electrode (2 - 3 water molecules) the potential is 'flat' with the quadrupole contributing most due to a near cancellation of the ion and water dipole components. Approaching the surface weak features are encountered due to water packing and then a big oscillation due to water oriented in a layer next to the electrode. None of these effects are described in theories that approximate water as a continuum fluid.

Oct. 20, 1995

MOLECULAR DYNAMICS STUDY OF INTERFACIAL ELECTRIC FIELDS

James N. Glosli

Lawrence Livermore National Laboratory,

University of California, Livermore, CA 94550

and

Michael R. Philpott

IBM Research Division, Almaden Research Center,

650 Harry Road, San Jose, CA 95120-6099

Abstract

Electric fields and potentials of an equilibrated assembly of ions and water molecules adjacent to a charged metal surface are calculated as a function of perpendicular distance z from the surface from data derived from molecular dynamics trajectories. The spatial distributions of atoms or molecules along direction z are found by ensemble averaging of trajectories followed by averaging with a localized function with a well defined length scale. Two methods were used calculate z dependent charge density distributions. In the first, to be called the atom method, the trajectories of charged atoms are averaged. In the second, called the molecule method, a Taylor expansion of charged atom positions relative to molecular centers is performed and the charge density separated into monopole, dipole, quadrupole, octopole,... components. These distributions are used to calculate the electric potential and in one example to study progressive loss of structure due to water as the defined length parameter exceeds the dimension of a water

molecule. This latter result provides a link between simulations with detailed atomic modeling of intermolecular interactions and electric potentials derived from Gouy-Chapman theory. Illustrative examples are chosen from simulations of aqueous solutions of simple alkali halide electrolytes next to charged and uncharged flat metal surfaces. The smallest system has one ion and 157 water molecules, the largest 60 ions and 1576 water molecules.

ELSEVIER

Chemical Physics 00 (1995) CHP01964 T

Chemical Physics

Molecular dynamics simulation of the adsorption of benzene on charged metal electrodes in the presence of aqueous electrolyte

Michael R. Philpott [a], James N. Glosli [b]

[a] IBM Research Division, Almaden Research Center, 650 Harry Road, San Jose, CA 95120-6099, USA
[b] Lawrence Livermore National Laboratory, University of California, Livermore, CA 94550, USA

Received 14 January 1995; in final form 23 February 1995

Abstract

Classical molecular dynamics was used to model the adsorption of benzene on metal electrodes in a thin electrochemical cell containing aqueous NaCl solution. On uncharged electrodes benzene was adsorbed mostly flat and the ions formed a neutral diffuse region between the electrodes. As the charge on the electrode was increased the diffuse layer rearranged to shield the center of the film from the electric field. The remaining high electric field at the surface caused ordering of water molecules next to the metal, and this in turn promoted benzene desorption. Desorption occurred first from the cathode because of a higher surface electric field between the hydrated sodium ion in solution and the negative electrode. At the anode the field across the water layer was lower because the chloride ion was adsorbed in contact and so was closer to metal than the water layer. At the highest electrode charge density both ions were adsorbed in contact on their respective electrodes and benzene was desorbed from both surfaces into the central aqueous region.

1. Introduction

This paper describes the use of constant (N, V, T) classical molecular dynamics to model the adsorption–desorption of a neutral organic on a flat metal electrode as a function of charge on the surface in the presence of a simple electrolyte able to screen the electrodes. These calculations, though essentially qualitative in nature, reveal the important role in adsorption–desorption of surface electric fields arising from the screened electrode charge and the involvement of water layers localized and oriented near the surface. The ions are needed to localize the high electric field near the surface as in double layer experiments. Without the ions the electric field of the electrodes would span and polarizes the entire aqueous layer at field strengths much higher than are experimentally realizable. The molecular dynamics code [1–5] used was the same as that described before.

In the current set of calculations we model the surface as flat and featureless in order to focus on effects due to electrostatic interactions amongst the ions, water molecules, the benzene molecules and the two metal plates. This means that effects due to metal atomic corrugation [6–14] are not treated here. Probability density profiles averaged parallel with the surface for water, ions and benzene were calculated and used to monitor the change in the structure of the electric double layer (or at least what represents the double layer in the model) at each surface. We also leave for a separate study the calculation of

SSDI 0301-0104(95)00098-4

Harlech, Wales
March 17, 1995

MOLECULAR DYNAMICS SIMULATION OF IONS, NEUTRALS AND WATER IN ELECTRIC DOUBLE LAYERS BETWEEN CHARGED METAL ELECTRODES. **Michael R. Philpott and James N. Glosli†, IBM Almaden Research Center, 650 Harry Road, San Jose, CA 95120-6099, and †Lawrence Livermore National Laboratory, Livermore, CA 94550.**

Constant (N,V,T) molecular classical dynamics has been used to model the structure and dynamics of electric double layers sandwiched between charged metal surfaces and to ask questions about the process of adsorption of charged species and neutral organics in the presence of electrolyte[1]. These calculations represent a fairly comprehensive test of ideas derived from numerous electrochemical experiments over a period of fifty years. In the most primitive calculations we model the surface as flat and featureless. More advanced models introduce atomic topology and use a water-metal potential that describes top site adsorption of isolated molecules[2]. Interaction of the molecules with the metal was represented by a 9-3 potential for Pauli repulsion and attractive dispersive interactions, and an image potential for the interaction with the conduction electrons. Electrostatic fields were calculated exactly (no cut-offs) by the fast multipole method of Greengard and Rokhlin[3].

On uncharged electrodes benzene was adsorbed mostly flat and the ions formed a neutral diffuse region between the electrodes. As the charge on the electrode was increased the electrolyte layer rearranged to shield the center of the film from the electric field. This field remained high near the surface and promoted orientational ordering of water molecules near the metal. In small systems this assisted benzene desorption. The variation in the electric field and potential across the cell were calculated from average charge densities and showed how the contact adsorbed and diffuse layer ions contributed to the screening of electrode. Contact adsorption of ions occurred at the anode so the structure of the double layer was different on the two electrodes. Simulations were performed on systems with 200 to 2000 water molecules, salt concentrations from 0.3 to 3M. In the largest systems a bulk electrolyte zone in the middle of the cell was clearly identifiable.

Acknowledgement

This work was supported in part by the Office of Naval Research.

References

1 M. R. Philpott, J. N. Glosli, and S. Zhu, Surface Sci. **accepted**, (1995). "Molecular Dynamics Simulation of Adsorption in Electric Double Layers."

2 S. Zhu and M. R. Philpott, J. Chem. Phys. **100**, 6961-6968 (1994).

3 L. F. Greengard, *The Rapid Evaluation of Potential Fields in Particle Systems*. (The MIT Press, Cambridge, Massachusetts, 1987).

Honolulu. Invited

MOLECULAR DYNAMICS SIMULATION OF IONS, NEUTRALS AND WATER IN ELECTRIC DOUBLE LAYERS BETWEEN CHARGED METAL ELECTRODES. **Michael R. Philpott and James N. Glosli†, IBM Almaden Research Center, 650 Harry Road, San Jose, CA 95120-6099, and †Lawrence Livermore National Laboratory, Livermore, CA 94550.**

Classical molecular dynamics was used to model the adsorption of ions and neutrals, like benzene, on metal electrodes in a thin electrochemical cell containing aqueous NaCl solution. On uncharged electrodes benzene was adsorbed mostly flat and the ions formed a neutral diffuse region between the electrodes. As the charge on the electrode was increased the electrolyte layer rearranged to shield the center of the film from the electric field. This field remained high near the surface and promoted orientational ordering of water molecules near the metal. In small systems this assisted benzene desorption. The variation in the electric field and potential across the cell were calculated from average charge densities and showed how the contact adsorbed and diffuse layer ions contributed to the screening of electrode. Contact adsorption of ions occurred at the anode so the structure of the double layer was different on the two electrodes. Simulations were performed on systems with 200 to 2000 water molecules, salt concentrations from 0.3 to 3M, and in some cases for surfaces with (001) topography. In the largest systems a bulk electrolyte zone in the middle of the cell was clearly identifiable.

March 14, 1995
Xiamen, China
Invited

MOLECULAR DYNAMICS SIMULATIONS OF THE ELECTRODE-AQUEOUS ELECTROLYTE INTERFACE

MICHAEL R. PHILPOTT and JAMES N. GLOSLI†
IBM Almaden Research Center, 650 Harry Road San Jose, CA 95120-6099, USA
†Lawrence Livermore National Laboratory Livermore, CA 94550, USA

Constant (N,V,T) molecular classical dynamics has been used to model the structure and dynamics of electric double layers sandwiched between charged metal surfaces and to ask questions about the process of adsorption of charged species and neutral organics in the presence of electrolyte[1]. These calculations represent a fairly comprehensive test of ideas derived from numerous electrochemical experiments over a period of fifty years. In the most primitive calculations we model the surface as flat and featureless. More advanced models introduce atomic topology and use a water-metal potential that describes top site adsorption of isolated molecules[2]. Interaction of the molecules with the metal was represented by a 9-3 potential for Pauli repulsion and attractive dispersive interactions, and an image potential for the interaction with the conduction electrons. Electrostatic fields were calculated exactly (no cut-offs) by the fast multipole method of Greengard and Rokhlin[3].

On uncharged electrodes benzene was adsorbed mostly flat and the ions formed a neutral diffuse region between the electrodes. As the charge on the electrode was increased the electrolyte layer rearranged to shield the center of the film from the electric field. This field remained high near the surface and promoted orientational ordering of water molecules near the metal. In small systems this assisted benzene desorption. The variation in the electric field and potential across the cell were calculated from average charge densities and showed how the contact adsorbed and diffuse layer ions contributed to the screening of electrode. Contact adsorption of ions occurred at the anode so the structure of the double layer was different on the two electrodes. Simulations were performed on systems with 200 to 2000 water molecules, salt concentrations from 0.3 to 3M. In the largest systems a bulk electrolyte zone in the middle of the cell was clearly identifiable.

Acknowledgement

This work was supported in part by the Office of Naval Research.

References

1 M. R. Philpott and J. N. Glosli, Chem. Phys. **accepted**, (1995). "Molecular Dynamics Simulation of the Adsorption of Benzene on Charged Metal Electrodes in the Presence of Aqueous Electrolyte".

2 S. Zhu and M. R. Philpott, J. Chem. Phys. **100**, 6961-6968 (1994).

3 L. F. Greengard, *The Rapid Evaluation of Potential Fields in Particle Systems.* (The MIT Press, Cambridge, Massachusetts, 1987).

May 07, 1996

Molecular Dynamics Simulation of Interfacial Electrochemical Processes: Electric Double Layer Screening

Michael R. Philpott[1] and James N. Glosli[2]

[1]IBM Research Division, Almaden Research Center,
650 Harry Road, San Jose, CA 95120-6099
[2]Lawrence Livermore National Laboratory,
University of California, Livermore, CA 94551-9900

The status of computer simulations of electric double layers is briefly summarized and a road map with bottle necks for solving the important problems in the atomic scale simulation of interfacial electrochemical processes is proposed. As an example of recent activity, efforts to simulate screening in electric double layers are described. Molecular dynamics simulations on systems about 4 nm thick, containing up to 1600 water molecules and NaCl at 1M to 3M concentrations, are shown to exhibit the main components of electric double layers at charged metal surfaces. Ion and water density profiles across the system show: a bulk electrolyte zone, a diffuse layer that screens the charge on the electrode and a layer of oriented water on the surface.

7-3-96

MOLECULAR DYNAMICS SIMULATION OF ADSORPTION, DEPOSITION AND DISSOLUTION AT AQUEOUS ELECTROCHEMICAL INTERFACES

Michael R. Philpott*, James N. Glosli† and James Roberts

IBM Almaden Research Center, 650 Harry Road, San Jose, CA 95120-6099
†Lawrence Livermore National Laboratory, Livermore, CA 94550
* tel: (408) 927-2410(office/vm), -2100(fax); e-mail: philpott at almaden.ibm.com

Constant (N,V,T, electric potential or surface charge) molecular classical dynamics has been used to model the structure and dynamics of electric double layers of simple aqueous electrolytes between charged metal surfaces and make comparisons with Gouy-Chapman theory. In primitive calculations we model the surface as flat and featureless and in more advanced models we use surface potentials that describe the atomic topography and the tendency of water molecules to adsorb top site with oxygen down. All electric fields were calculated without cut-offs by the fast multipole method of Greengard and Rokhlin[1]. The simulations show: compact, diffuse, surface oriented water layers and an identifiable bulk zone. The electric field and potential across the cell deviate considerably from Gouy-Chapman predictions due to finite size of atoms, water layering and electrostatic quadrupole effects. A model describing aspects of metal deposition and dissolution will also be reported.

This work was supported in part by the Office of Naval Research. The contribution from JNG was performed under the auspices of US DOE contract W-7405-Eng-48.

1 < missing author >, < Missing journal >.

PACS 82.65.+z

ORAL presentation preferred Suggest symposium 8.

Michael R. Philpott
IBM Almaden Research Center